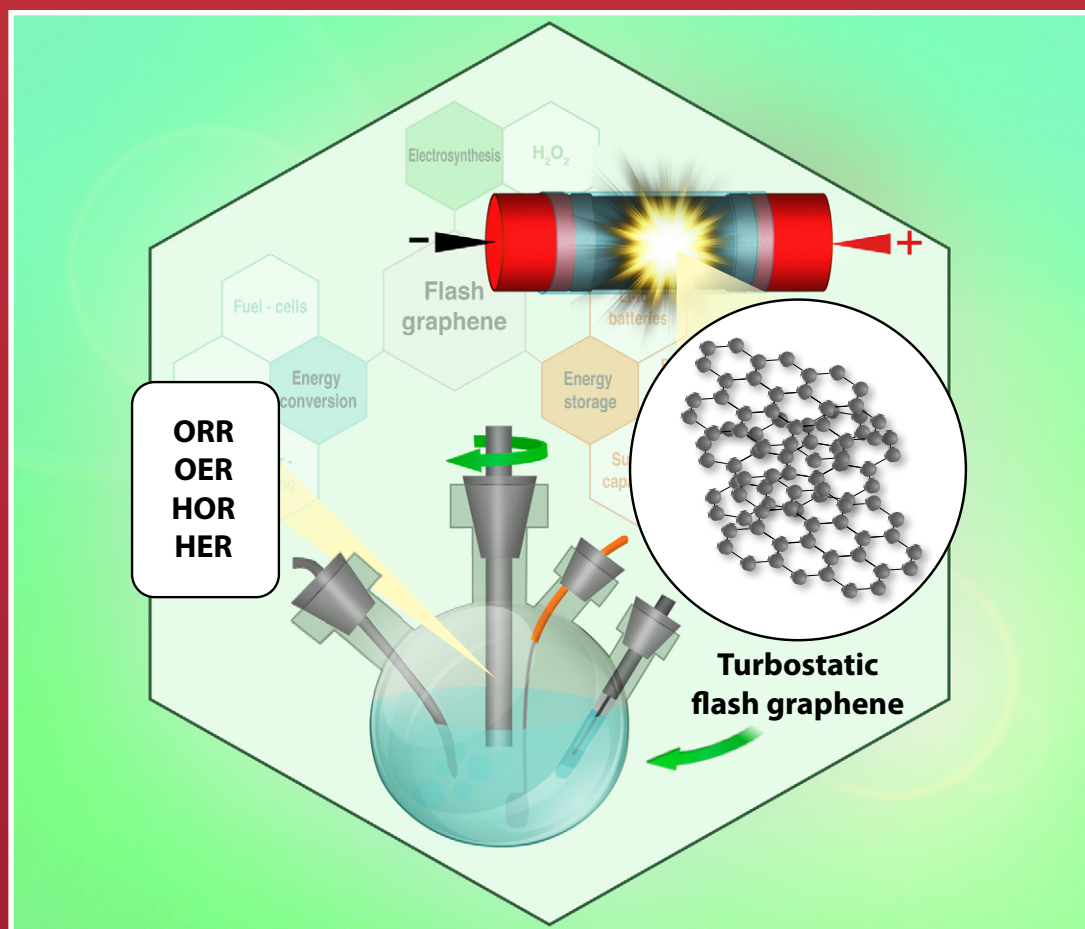




Acta Chimica Slo Acta Chimica Slo Slovenica Acta C

4

71/2024



EDITOR-IN-CHIEF

FRANC PERDIH

University of Ljubljana, Faculty of Chemistry and Chemical Technology, Večna pot 113, SI-1000 Ljubljana, Slovenija
E-mail: ACSi@fkk.uni-lj.si, Telephone: (+386)-1-479-8514

ASSOCIATE EDITORS

Alen Albreht, National Institute of Chemistry, Slovenia
Aleš Berlec, Jožef Stefan Institute, Slovenia
Janez Cerkovnik, University of Ljubljana, Slovenia
Mirela Dragomir, Jožef Stefan Institute, Slovenia
Krištof Kranjc, University of Ljubljana, Slovenia
Matjaž Kristl, University of Maribor, Slovenia
Maja Leitgeb, University of Maribor, Slovenia

Helena Prosen, University of Ljubljana, Slovenia
Jernej Stare, National Institute of Chemistry, Slovenia
Irena Vovk, National Institute of Chemistry, Slovenia

ADMINISTRATIVE ASSISTANT

Eva Mihalinec, Slovenian Chemical society, Slovenia

EDITORIAL BOARD

Wolfgang Buchberger, Johannes Kepler University, Austria
Alojz Demšar, University of Ljubljana, Slovenia
Stanislav Gobec, University of Ljubljana, Slovenia
Marko Goličnik, University of Ljubljana, Slovenia
Günter Grampp, Graz University of Technology, Austria
Wojciech Grochala, University of Warsaw, Poland
Danijel Kikelj, University of Ljubljana
Janez Košmrlj, University of Ljubljana, Slovenia
Mahesh K. Lakshman, The City College and
The City University of New York, USA
Blaž Likozar, National Institute of Chemistry, Slovenia

Janez Mavri, National Institute of Chemistry, Slovenia
Jiří Pinkas, Masaryk University Brno, Czech Republic
Friedrich Sreinc, University of Minnesota, USA
Walter Steiner, Graz University of Technology, Austria
Jurij Svete, University of Ljubljana, Slovenia
David Šarlah, University of Illinois at Urbana-Champaign, USA;
Università degli Studi di Pavia, Italy
Ivan Švancara, University of Pardubice, Czech Republic
Gašper Tavčar, Jožef Stefan Institute, Slovenia
Ennio Zangrando, University of Trieste, Italy
Polona Žnidaršič Plazl, University of Ljubljana, Slovenia

ADVISORY EDITORIAL BOARD

Chairman
Branko Stanovnik, Slovenia

Members
Udo A. Th. Brinkman, The Netherlands
Attilio Cesaro, Italy
Vida Hudnik, Slovenia
Venčeslav Kaučič, Slovenia

Željko Knez, Slovenia
Radovan Komel, Slovenia
Stane Pejovnik, Slovenia
Anton Perdih, Slovenia
Slavko Pečar, Slovenia
Andrej Petrič, Slovenia
Boris Pihlar, Slovenia
Milan Randić, Des Moines, USA

Jože Škerjanc, Slovenia
Đurđa Vasić-Rački, Croatia
Marjan Veber, Slovenia
Gorazd Vesnaver, Slovenia
Jure Zupan, Slovenia
Majda Žigon, Slovenia

Acta Chimica Slovenica is indexed in: *Academic Search Complete*, *Central & Eastern European Academic Source*, *Chemical Abstracts Plus*, *Chemical Engineering Collection (India)*, *Chemistry Citation Index Expanded*, *Current Contents (Physical, Chemical and Earth Sciences)*, *Digitalna knjižnica Slovenije (dLib.si)*, *DOAJ*, *ISI Alerting Services*, *PubMed*, *Science Citation Index Expanded*, *SciFinder (CAS)*, *Scopus*, *Web of Science and Portico*. Impact factor for 2022 is IF = 1.20.



Articles in this journal are published under the
Creative Commons Attribution 4.0 International License

Izdaja – Published by:

SLOVENSKO KEMIJSKO DRUŠTVO – SLOVENIAN CHEMICAL SOCIETY
Naslov redakcije in uprave – Address of the Editorial Board and Administration
Hajdrihova 19, SI-1000 Ljubljana, Slovenija
Tel.: (+386)-1-476-0252; Fax: (+386)-1-476-0300; E-mail: chem.soc@ki.si

Izdajanje sofinancirajo – Financially supported by:

National Institute of Chemistry, Ljubljana, Slovenia
Jožef Stefan Institute, Ljubljana, Slovenia
Faculty of Chemistry and Chemical Technology, University of Ljubljana, Slovenia
Faculty of Chemistry and Chemical Engineering, University of Maribor, Slovenia
University of Nova Gorica, Slovenia

Slovensko kemijsko društvo
Slovenian Chemical Society

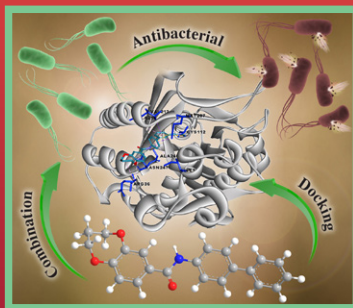


Acta Chimica Slovenica izhaja štirikrat letno v elektronski obliki na spletni strani <http://acta.chem-soc.si>. V primeru posvečenih številk izhaja revija tudi v tiskani obliki v omejenem številu izvodov.

Acta Chimica Slovenica appears quarterly in electronic form on the web site <http://acta.chem-soc.si>. In case of dedicated issues, a limited number of printed copies are issued as well.

Transakcijski račun: 02053-0013322846 Bank Account No.: SI56020530013322846-Nova Ljubljanska banka d. d., Trg republike 2, SI-1520 Ljubljana, Slovenia, SWIFT Code: LJBA SI 2X

Oblikovanje ovitka – Design cover: KULT, oblikovalski studio, Simon KAJTNA, s. p. Grafična priprava za tisk: OSITO, Laura Jankovič, s.p.

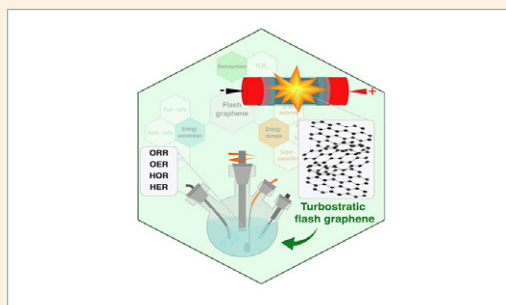


SCIENTIFIC PAPER

541–557 Feature Article

Flash Graphene: a Sustainable Prospect for Electrocatalysis

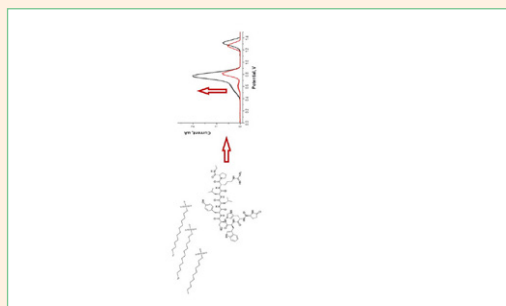
Ivo Bardarov, Desislava Yordanova Apostolova, Maris Minna Mathew, Miha Nosan, Pedro Farinazzo Bergamo Dias Martins and Bostjan Genorio



558–565 Analytical chemistry

A Reliable Voltammetric Method Utilizing the Effect of an Anionic Surfactant for the Determination of Leuprolide

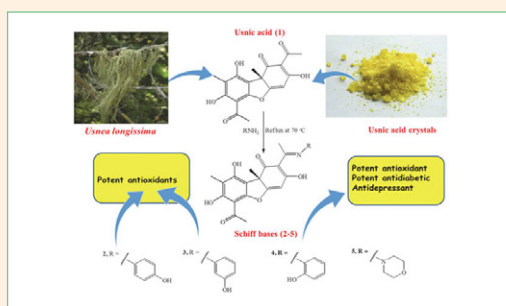
Begüm Evranos Aksöz and Burcu Dogan Topal



566–579 Organic chemistry

Synthesis of Schiff Bases of Usnic Acid and Investigation of Their Antidiabetic, Antidepressant, Anti-Parkinson's Disease, Neuroprotective and Antioxidant Potentials

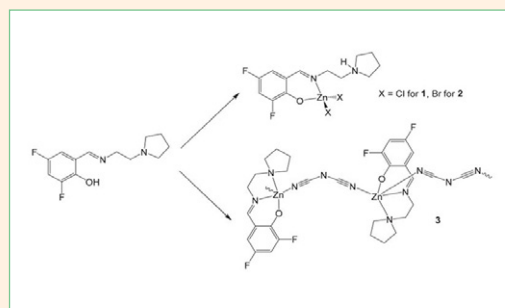
Lawali Yabo-Dambagi, Ahmet Cakir, Mehmet Akyuz, Aysegül Karakucuk-Iyidogan and Ali Aslan



580–586 Inorganic chemistry

Synthesis, Characterization and X-Ray Crystal Structures of Schiff Base Zinc(II) Complexes with Antibacterial Activity

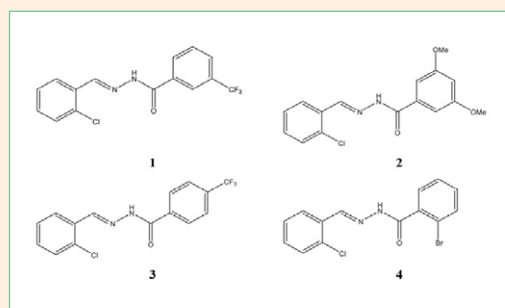
Yu-Hui Wu, Wan-Lin Wei, Wei Li and Zhonglu You



587–594 Organic chemistry

Synthesis, Characterization and X-Ray Crystal Structures of Aroylhydrazones Derived from 2-Chlorobenzaldehyde with Various Benzohydrazides

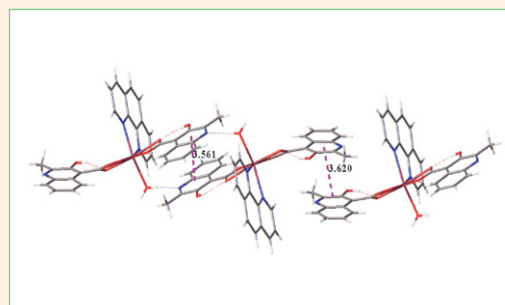
Jia-Xue Liu, Shi-Yu Zhang, Meng-Xiao Tai, Wei Li and Zhonglu You



595–602 General chemistry

Preparation, Characterization and Theoretical Calculation of a Cadmium Complex of 3-hydroxy-2-methylquinolin-4-carboxylate and 1,10-phenanthroline

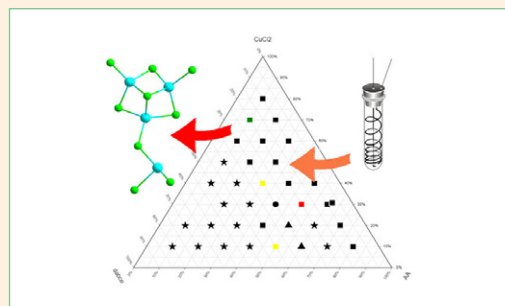
Ting-Qun Qiu, Zhi-Tao Lu, Zi-Jian He, Zheng-Ping Xie, Jin Guo and Xiu-Guang Yi



603–608 Inorganic chemistry

Investigation of the Composition Space Diagram CuCl-Allylamine-dabco. A New Mixed Ligand Compound of $(\text{H}_2\text{dabco})_2[\text{Cu}_4\text{Cl}_9(\text{allNH}_3)]$ Composition with Unique $\text{Cu}_4\text{Cl}_9^{5-}$ Cupro(I)-chloride Fragment

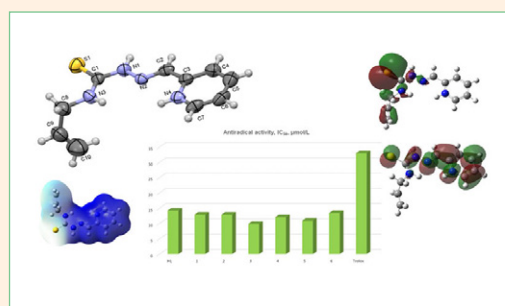
Evgeny Goreshnik, Olha Panteleieva



609–618 General chemistry

Insights into Antiradical Behavior: Crystal Structures and DFT Analysis of 2-Formylpyridine N4-Allylthiosemicarbazone Salts

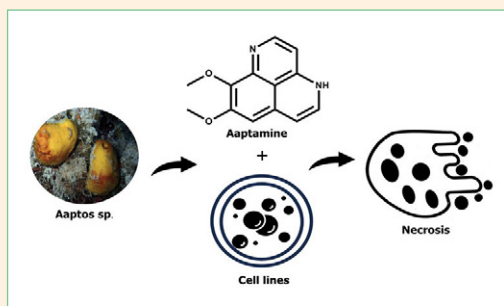
Yurii Chumakov, Vasiliu Graur, Ianina Graur, Victor Tsapkov, Olga Garbuz and Aurelian Gulea



619–626 Biomedical applications

Aaptamine, Isolated from the Bunaken National Park's Sponge, *Aaptos sp.*, Promotes Cell Cycle Arrest and Induces Necrotic Cell Death of Colorectal Cancers

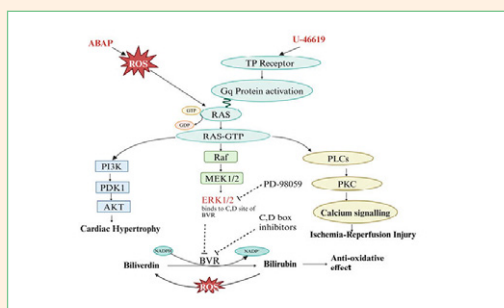
Annisa Elcentia Fajarwati, Mutia Hardhiyuna, Febby Nurdiya Ningsih, Adam Hermawan, Dyningtyas Dewi Pamungkas Putri, Nurul Fatimah, Asep Bayu, Andi Setiawan, Ucu Yanu Arbi, Tutik Murniasih, Aliyatur Rosyidah, Tri Aryono Hadi, Masteria Yunovilsa Putra, and Peni Ahmadi



627–645 Biomedical applications

Inhibition of Biliverdin Reductase Diminished the Protective Activity of Bilirubin and Biliverdin Against Oxidative Stress-Induced Injury in Human Vascular Endothelium

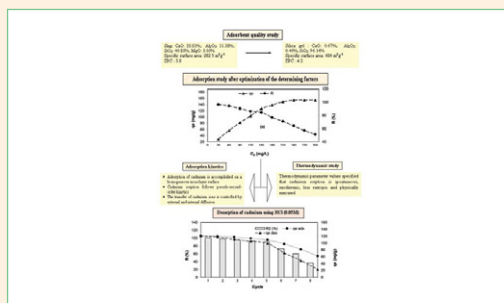
Kuldeepak Sharma, Irena Zajc, Alen Albreht and Lovro Žiberna



646–659 Chemical education

Elimination of Cadmium using Silica Gel Prepared from Blast Furnace Slag

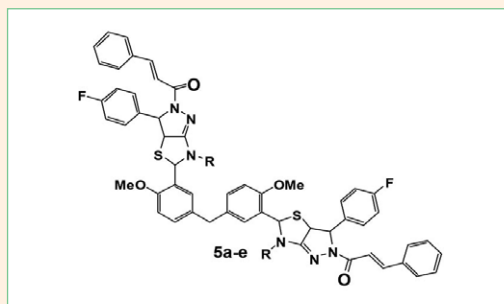
Toufik Chouchane, Mohamed Tayeb. Abedghars, Sabiha. Chouchane and Atmane Boukari



660–667 Organic chemistry

Microwave Assisted Synthesis of Methylene Bisthiazolo Arylvinyl Pyrazoles as Potential Biological Agents

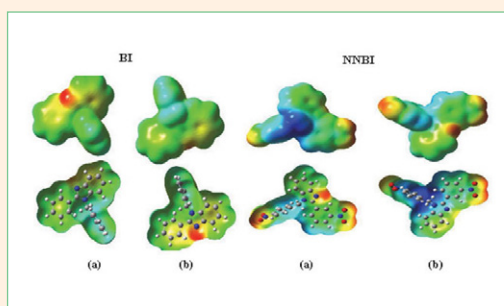
Avula Srinivas



668–684 Physical chemistry

Inhibition Effect of Benzimidazole Derivatives on the Corrosion of Mild Steel in Acidic Medium: Experimental and Theoretical Studies

Sonia Benabid and Linda Toukal

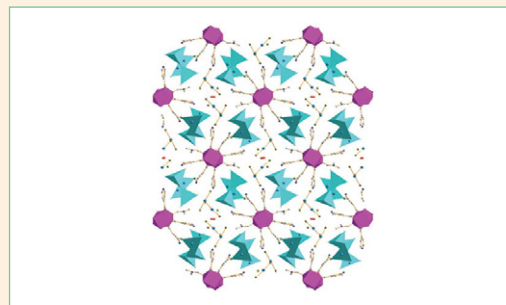


685–695

Organic chemistry

Syntheses, Crystal Structures and Characterization of Two New Lanthanide Mercury Halide Compounds

Xi-Yu Shao, Hao-Dong Liu, Long-Hua Zeng, Yu-Yue Xu, Wen-Tong Chen, Cheng Liu, Sheng-Ping Dai and Chang-Wang Pan

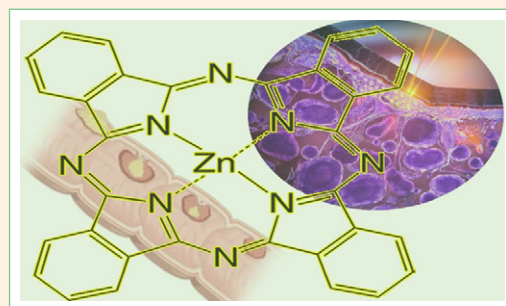


696–704

Biochemistry and molecular biology

Effect of Biphenyl Derivative of Coumarin Compounds Photodynamic Therapy on The Expression of Carcinoma-Associated Genes

Asiye Gok Yurttas, Tugba Elgun, Burcin Erkal Cam, Melike Kefeli and Kamil Cinar



Feature article

Flash Graphene: a Sustainable Prospect for Electrocatalysis

Ivo Bardarov^{1,2}, Desislava Yordanova Apostolova¹, Maris Minna Mathew¹, Miha Nosan¹, Pedro Farinazzo Bergamo Dias Martins^{1,2} and Bostjan Genorio^{1*}

¹ University of Ljubljana, Faculty of Chemistry and Chemical Technology, Večna pot 113, SI-1000 Ljubljana, Slovenia

² National Institute of Chemistry, Department of Materials Chemistry, D10, Hajdrihova 19, SI-1000 Ljubljana, Slovenia

* Corresponding author: E-mail: bostjan.genorio@fkkt.uni-lj.si

Received: 05-07-2024

Abstract

The increasing demand for sustainable and efficient energy conversion technologies requires ongoing exploration of new materials and methods. Flash Joule Heating (FJH) emerges as a promising technique for large-scale graphene production, boasting advantages over conventional methods. FJH rapidly heats carbon-based precursors to extreme temperatures using high electric currents, forming flash graphene upon rapid cooling. This approach offers rapid processing, high throughput, and can utilize diverse carbon sources, including biomass and waste, making it sustainable and cost-effective. Moreover, it generates minimal waste and yields flash graphene with enhanced conductivity, crucial for energy applications. FJH's scalability, versatility, and efficiency position it as a key method for commercializing graphene across industries, particularly in energy conversion. This review comprehensively discusses FJH synthesis principles, emphasizing efficiency, scalability, and sustainability. Additionally, it analyzes recent advancements in flash graphene-based electrocatalysts, exploring their impact on renewable energy and sustainable electrocatalysis. Challenges and opportunities are addressed, outlining future research directions. Continued advancements hold immense potential to revolutionize graphene production and integrate it into next-generation energy systems, driving the transition towards cleaner energy solutions.

Keywords: Synthesis of graphene; Flash Joule heating; Flash graphene; Electrocatalysis

1. Introduction

Graphene, the foundational two-dimensional (2D) structure of all carbon's graphitic forms, has captured significant attention since its groundbreaking isolation in 2004 by Geim and Novoselov.¹ The significance of this achievement cannot be overstated and was duly recognized by the scientific community in 2010 when it earned the Nobel Prize in Physics.^{2,3} Prior to its isolation, graphene's remarkable properties remained largely unexplored due to its inherent binding to substrates (e.g., platinum single crystal surface).⁴ These properties encompass a broad spectrum, including exceptional attributes like high electron mobility (measuring at $2.5 \times 10^5 \text{ cm}^2 \text{ V}^{-1} \text{ s}^{-1}$)⁵ and extraordinary intrinsic mechanical properties (reaching 130 GPa),⁶ making graphene a suitable candidate for applications in completely unrelated fields e.g., electronics⁷ and cement⁸ technologies. Unsurprisingly, researchers spanning various fields of expertise have enthusiastically embarked on graphene experimentation, considering it a

prime candidate for replacing conventional materials in established applications. Moreover, its extensive array of astonishing properties has sparked optimism about the potential birth of disruptive technologies.⁷ Consequently, this surge of interest has given rise to a metaphorical "gold rush" directed towards diverse applications of graphene.⁹ Among those, the use of graphene and graphene-based materials for energy storage and conversion have shown considerable improvement over the past years.^{10–13} The aim of this work is to discuss the pros and cons of different graphene production methods in terms of scalability and sustainability, considering specifically its application as electrocatalysts for sustainable technologies. Focus is given to a relatively new synthesis method based on a process called flash Joule heating (FJH), how its versatility may open new doors for the easy tuning of graphene properties toward applications in energy-related technologies, and the potential for breaking into the market due to its simplicity and low-cost.

2. A Brief Introduction of the Main Methods for Graphene Production and Their Application in Electrocatalysis

For almost 20 years graphene-related research continues to be enthusiastic, and the quest for a method to produce defect-free flat carbon monolayers in large-scale persists. This journey, in turn, also gave rise to a rather upsetting fact at first glance; that graphene and graphene-based materials properties (physical, electronic, and optical) vary strongly with the method employed for their synthesis.¹⁴ Therefore, the production method used to pre-

pare any graphene-like material will ultimately enable or impede its final application. In fact, during this period, a so called “graphene family”¹⁵ of 2D carbon forms varying in terms of morphology, lateral dimensions, number of layers, different types and number of structural defects emerged. Despite the abundance of scientific publications focused on large-scale graphene production and manufacturing technologies, the practical implementation of graphene remains limited. To achieve industrial-scale applications, a mass production technique must not only yield the necessary quantities but also ensure consistent quality. Unfortunately, current graphene manufacturing methods continue to be either cost prohibitive or underde-

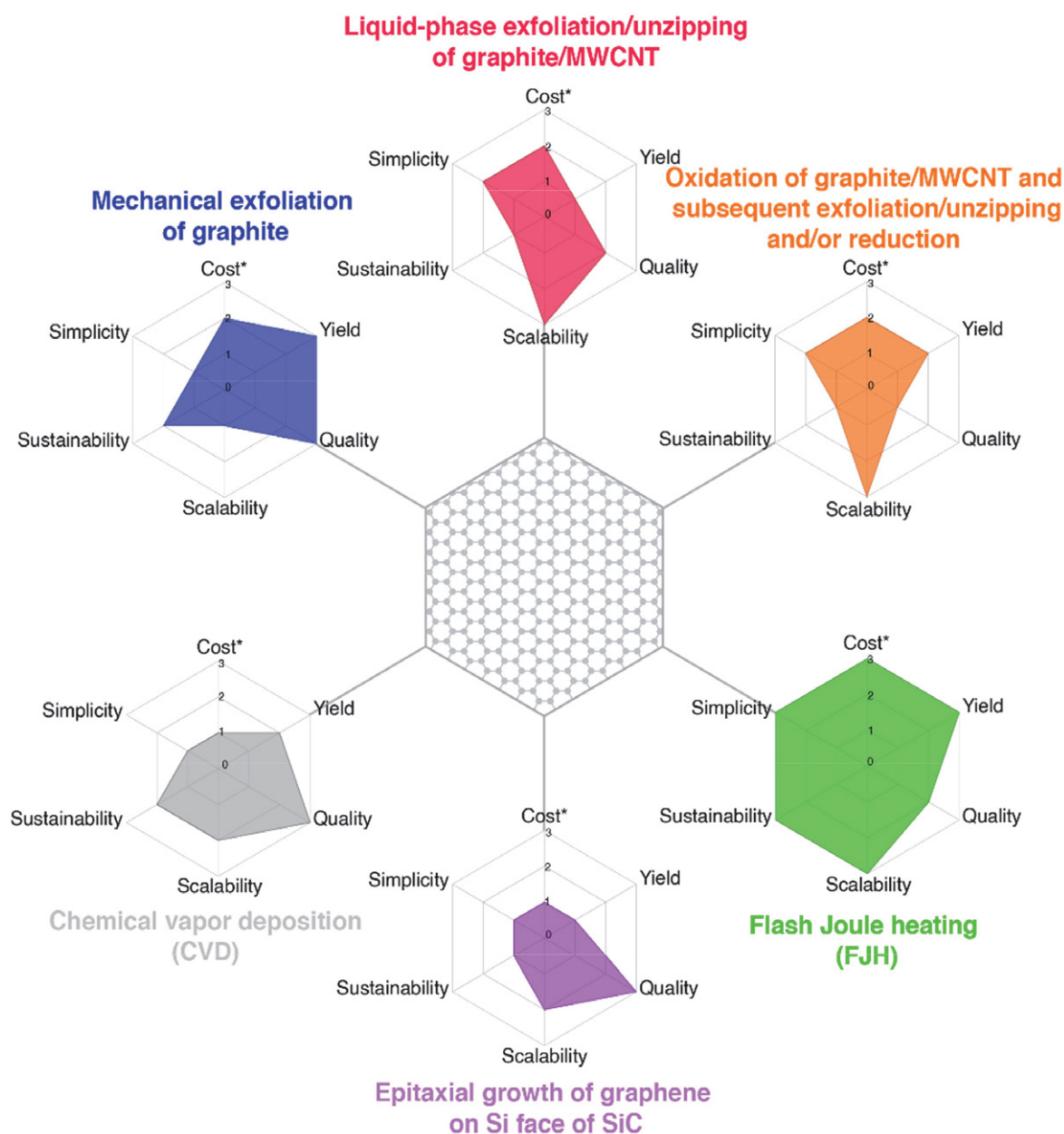


Figure 1. Schematic overview of common graphene production methods varying from top-down to bottom-up approaches. (*A low value represents a high-cost method).

veloped as new difficulties always emerge as the process is scaled from the research laboratory to the industry.^{16–28}

The main production methods of graphene and its derivative materials are shown in Figure 1. The produced graphene can be classified into two major characteristic groups, large area single layer graphene sheets and bulk graphene composed of graphene flakes having smaller lateral sizes. As it will be discussed later, bulk graphene is desirable for large-scale energy storage and conversion applications mainly due to its comparatively high surface area and relatively easy scalability.

2. 1. Mechanical Exfoliation

Mechanical exfoliation is a fundamental technique for producing graphene from graphite. This approach involves repeatedly cleaving a piece of highly ordered pyrolytic graphite (HOPG) with adhesive tape to obtain increasingly thin layers of graphene.¹ The pros of this method include its simplicity and the high quality of the graphene produced. It yields monolayer graphene with minimal defects and excellent electronic properties, making it suitable for various applications in electronics and nanotechnology. However, there are several cons associated with mechanical exfoliation. It is a time-consuming and labor-intensive process, limiting its scalability for large-scale production. Additionally, it is challenging to control the number of graphene layers produced, and it generates a substantial amount of waste material. As such, while mechanical exfoliation remains a crucial technique for research and fundamental studies of graphene, it may not be the most practical method for industrial scale production.²⁹

2. 2. Liquid-phase exfoliation (LPE)

Liquid-phase exfoliation (LPE) of graphite is widely employed by industries to produce graphene in large quantities. Its principle is based on weakening the interaction between graphite layers using non-aqueous solvents or aqueous solutions containing surfactants, followed by physical agitation or sonication to separate and disperse the graphene flakes. Due to incomplete delamination of the graphite precursor even after prolonged treatment, centrifugation is usually necessary to separate monolayer flakes from the bulk solution. Because of the presence of surfactants or organic solvents, a purification step is needed if the graphene flakes are to be used for energy storage and conversion applications. Moreover, LPE generates a lot of hazardous wastes, which renders it to be unsustainable for mass production of graphene.

2. 3. Oxidation with Successive Reduction

Another method heavily adopted by industry is the oxidation of graphite pellets, on which the graphite oxide

formed is ultrasonically exfoliated in aqueous solutions. The oxidation of graphite increases the inter-layer distance of individual sheets, hence facilitating its separation. The as-prepared graphene oxide (GO) flakes are isolated by centrifugation, followed by reduction to form reduced graphene oxide (rGO). The reduction process can be performed chemically or thermally; nevertheless, part of the product will always remain oxidized. One major drawback of this method is the introduction of structural defects in the rGO sheets, which may compromise the desired appealing properties of graphene. Like the LPE method, the production of rGO generates large quantities of harmful chemical waste, requiring extra-step(s) for its treatment before it can be discarded, which ultimately increases the overall cost of graphene production.

2. 4. Unzipping of Carbon Nanotubes

The top-down approach of graphene production through the unzipping of carbon nanotubes (CNTs) presents both advantages and drawbacks in the field of nanomaterial synthesis.³⁰ One key advantage is the inherent structural uniformity of carbon nanotubes, which facilitates the controlled production of graphene with well-defined characteristics.^{31,32} This approach allows for the tailoring of graphene sheets with specific dimensions and properties, offering versatility in applications ranging from electronics to energy storage.^{33–37} Moreover, the unzipping process enables the integration of functional groups onto the graphene surface, enhancing its compatibility with various matrices and facilitating the development of composite materials with tailored properties.^{38–40} Despite these advantages, drawbacks include the potential introduction of defects during the unzipping process, which can adversely impact the electrical and mechanical properties of the resulting graphene.^{31,38} Additionally, the scalability of this method may be limited, and the need for specialized equipment and precise control over reaction conditions poses challenges for large-scale production. For instance, the unzipping of carbon nanotubes (CNTs) through a solution-based oxidative treatment has been successfully demonstrated.⁴¹ This innovative method facilitates the longitudinal opening of multi-walled CNTs with an impressive yield approaching 100%, even on a large scale. However, it is noteworthy that this procedure is accompanied by certain limitations. Despite its efficiency, the resulting graphene ribbons exhibit a width surpassing 100 nm and are characterized by pronounced structural defects and oxidized sites, reminiscent of rGO. This outcome underscores the challenges associated with achieving precise control over the unzipping process, leading to the compromise of structural integrity and the introduction of undesirable chemical moieties. Consequently, while this approach presents a noteworthy step forward in the large-scale production of longitudinally opened CNTs, further refinement is essential to address the inherent issues relat-

ed to the dimensions and quality of the produced graphene materials. Advances in optimizing this methodology hold significant promise for unlocking the full potential of graphene-based structures across diverse scientific and technological applications.

2. 5. Chemical Vapor Deposition (CVD)

Chemical vapor deposition (CVD) is a prominent method for the large-scale production of graphene, offering several advantages and disadvantages in terms of cost, yield, reproducibility, and quality.^{42–48} It enables the synthesis of graphene on various substrates, mostly metals, such as copper or nickel surfaces, making it suitable for industrial applications.^{43,46,47,49–55} Moreover, CVD can yield high-quality graphene films with excellent electrical and mechanical properties, which are crucial for many advanced technologies.^{30,43,56–58} However, there are notable disadvantages associated with the CVD method. Cost can be a limiting factor, as it requires specialized equipment, precise control over reaction conditions, and the use of high temperatures and vacuum, making the initial setup and operation expensive. Additionally, the yield of high-quality graphene is greatly dependent on factors such as substrate quality and the need for post-processing steps to transfer graphene from the growth substrate. This can reduce the overall production efficiency and further increase costs. Reproducibility in CVD is another challenge, as slight variations in growth conditions can lead to differences in graphene quality and thickness. Achieving uniformity across large-scale production can be difficult, requiring tight process control.

Although the epitaxial growth of graphene on the Si crystal plane of silicon carbide (SiC) has emerged as a promising method to produce high-quality graphene, its distinct disadvantages, particularly in the context of large-scale production, inevitably restrict the use of graphene to fundamental research and restrict applications, such as electronic devices and high frequency transistors.⁵⁹ One significant advantage of this method is its ability to produce high-quality single-layer graphene directly on a technologically relevant substrate.^{42,60–63} The SiC lattice closely matches the graphene lattice, promoting epitaxial growth and reducing defects. This results in exceptional electronic quality, making it highly desirable for electronic and optoelectronic applications. Additionally, the method offers good reproducibility, as it relies on well-established semiconductor growth techniques.^{61–63} However, there are notable disadvantages to consider. First, the cost of SiC wafers and the epitaxial growth equipment can be relatively high, which poses a barrier to large-scale production. Second, while the quality of graphene produced through this method is exceptional, the process may not be as scalable as some other techniques. The growth rate may be limited, impacting overall yield and production speed. Furthermore, the requirement for spe-

cialized SiC substrates can limit versatility and increase costs.

2. 6. Polymerization from Organic Precursors

The organic synthesis of graphene is a bottom-up method based on the oxidative cyclodehydrogenation of oligophenylene and polyphenylene precursors to produce nanographene molecules and graphene nanoribbons (GNRs).^{30,64–70} The main advantage of this method is the possibility to create bandgap in the electronic structure of graphene and control its magnitude, which has enormous implications for application of graphene-based materials in electronic devices.^{71–81} For instance, by varying the width and edge termination of the GNRs, it is possible to tailor the magnitude of the bandgap with extreme precision, an essential step to design GNRs with accurate and reproducible electronic, optical, and magnetic properties for impending nanoelectronics, optoelectronics, and spintronics applications.^{29,82–86} However, the scalability of the organic synthesis of GNRs together with its transfer process remains challenging for practical application in devices.^{87,88}

2. 7. Graphene and Graphene-Based Materials as Passive Components for Electrocatalysis

Fuel cells are electrochemical devices that convert chemical energy directly into electrical energy. Graphene's high electrical conductivity, large surface area, and chemical stability make it an ideal candidate for various components in fuel cells. The use of graphene-based materials as catalyst supports, gas diffusion layers, and current collectors has shown remarkable improvements in the overall performance and durability of fuel cells.^{89–93} These advancements contribute to increased power density, faster reaction rates, and prolonged cell life. For instance, in a study conducted by Yoo et al., it was observed that sub-nano Pt clusters, when supported on graphene nanosheets (Pt/GNS), demonstrated superior CO tolerance during the hydrogen oxidation reaction (HOR) compared to Pt clusters dispersed on carbon black (Pt/CB).⁹⁴ Electrochemical characterization revealed that, under pure H₂ conditions, Pt/GNS, Pt/CB, and PtRu/CB exhibited comparable electrocatalytic activities for the HOR, notwithstanding the variation in the carbon material utilized. Notably, the Pt/GNS sustained a 52% activity level in the presence of H₂ and 500 parts per million (ppm) of CO, whereas the Pt/CB exhibited only 11% activity under the same conditions. Although the mechanism behind the improved CO tolerance for Pt/GNS remains unclear, these findings underscore the enhanced CO tolerance and high durability of Pt/GNS, positioning graphene-based electrocatalyst supports as promising candidates for improving the performance of fuel cells.

The oxygen reduction reaction (ORR) occurring at the cathodes of proton exchange membrane fuel cells (PEMFCs) is a crucial electrochemical process that significantly influences the overall efficiency of these energy conversion devices. Despite its importance, the slow kinetics associated with the ORR remains a major drawback, impeding the widespread deployment of practical fuel cells. The sluggish nature of the ORR can be primarily attributed to the complex four-electron transfer mechanism involved in reducing molecular oxygen to water. The intricate nature of this process, coupled with the inherently limited surface area of conventional cathode materials, results in substantial overpotential and hinders the rate of oxygen reduction. Kou et al. utilized functionalized graphene sheets (FGSs) as support for Pt nanoparticles as electrocatalyst for the ORR in acidic media.⁹⁵ Specifically, The FGSs were synthesized through the thermal expansion of graphite oxide, and Pt nanoparticles, featuring an average diameter of 2 nm, were homogeneously deposited onto FGSs utilizing impregnation methods. Comparative analysis revealed that Pt-FGS exhibited a superior electrochemical surface area and oxygen reduction activity, coupled with enhanced stability, in comparison to a commercially available catalyst (20% Pt supported on Vulcan XC-72 carbon). Complementary techniques such as transmission electron microscopy, X-ray photoelectron spectroscopy, and electrochemical characterization collectively indicate that the enhanced performance of Pt-FGS can be ascribed to the smaller particle size and reduced aggregation of Pt nanoparticles on the functionalized graphene sheets. This study highlights the significance of tailored catalyst-support systems in optimizing the electrocatalytic performance of oxygen reduction reactions for potential applications in energy conversion technologies.

A recent study about the influence of support's structure and chemistry on platinum-based electrocatalysts showed that graphene derivative (GD) support confers higher stability and activity during ORR compared to the commercial benchmark carbon black (CB) support.⁹⁶ Accelerated degradation testing, conducted utilizing a high-temperature liquid electrolyte disc electrode, revealed that reduced graphene oxide (rGO)-supported catalysts exhibited enhanced electrochemical stability in both electrochemically active surface area and mass activity retention compared to their CB-supported counterparts, including the commercially recognized benchmark from Umicore (Elyst Pt30 0690). X-ray photoelectron spectroscopy and Raman spectroscopy results suggested that the improved durability of the electrocatalyst is attributed to the increased content of sp^2 carbon and the reduction of structural defects in the rGO support. These alterations may induce a modified metal-support interaction, influencing the enhanced durability and performance of GD-supported catalysts. Furthermore, evaluation of high current density performance was conducted by measuring activity in a gas diffusion electrode half-cell. On average,

both electrocatalysts based on rGO exhibited superior kinetic performance and high current density, pertinent for industrial applications. Notably, the peak power density values of the rGO-supported materials in this study surpassed those reported in prior publications and exceeded the state-of-the-art commercial Pt-Co benchmark. This positions rGO-based materials as highly promising candidates for potential industrial applications as carbon-based catalyst supports, warranting further exploration in this direction.

Pavko et al. systematically assessed the durability of selected graphene derivatives (reduced graphene oxides, rGOs, and reduced graphene oxide nanoribbons, rGONRs) and carbon black (CB) employed as carbon supports for platinum-based ORR electrocatalysts.⁹⁷ Two distinct series of electrocatalysts, one based on PtCu and the other on Pt-Co nanoparticulate intermetallics, were uniformly dispersed on the specified carbon supports. Characterization through X-ray diffraction, transmission electron microscopy, and scanning electron microscopy indicated comparable metallic components in both series (PtCu and PtCo) of the composite samples, with the primary distinction lying in the nature of the carbon support - a critical consideration for investigating carbon support durability. In-depth X-ray photoelectron spectroscopy analysis affirmed substantial differences among the carbon supports in terms of total oxygen content, sp^2 carbon content, and the nature of oxygen functionalities. To assess carbon support durability, the authors conducted specialized electrochemical accelerated degradation tests (HT-ADTs), deliberately inducing carbon corrosion as the primary degradation mechanism. On average, electrocatalysts supported by rGO demonstrated superior electrochemical durability compared to their CB supported counterparts. Notably, the CB supported sample, despite exhibiting the lowest oxygen content, did not demonstrate the highest stability, suggesting that factors beyond total oxygen content significantly influence carbon support durability. Among these factors, the amount of sp^2 carbon and its corrosion stability emerged as crucial, specifically, higher sp^2 content correlated with increased durability of the carbon support. Finally, the paramount parameter influencing electrochemical durability was identified as the content of carboxyl functional groups; higher amounts of this functional group in the carbon support corresponded to lower electrochemical durability. These findings were corroborated by direct measurements of evolving CO_2 signals using an advanced *in-situ* electrochemical cell-mass spectrometry, which demonstrated carbon support degradation during potential cycling. The observed trend aligned with that of HT-ADTs, where the least stable catalyst exhibited the highest CO_2 signal, while the most stable catalyst exhibited the lowest, providing strong support for the results obtained from HT-ADTs. The knowledge gained can guide the development of more stable carbon supports, essential for the realization of practical and durable fuel cell systems.

Alkaline direct ethanol fuel cells (ADEFCs) have emerged as a significant fuel cell type, particularly for portable and transportation applications, owing to their high theoretical energy density (8 kWh kg⁻¹), environmental friendliness, and the ease of handling ethanol compared to other fuels like hydrogen.⁹⁸ Ethanol, with advantages such as production from agricultural products, relatively non-toxic fuel, and lower crossover from the anode to the cathode, presents distinct merits over methanol. Despite these benefits, ADEFCs face a critical challenge in the development of cost-effective, highly active, and stable electrocatalysts for the ethanol oxidation reaction (EOR) at the anode.⁹⁹ Addressing the impediment of sluggish kinetics in the EOR, Wolf et al. focused on the synthesis of a PdNiBi nanocatalyst supported on reduced graphene oxide (rGO) through a facile synthesis method.¹⁰⁰ Successful anchoring of PdNiBi nanoparticles onto the rGO support was achieved using the modified instant reduction method. Physicochemical analyses revealed a characteristic two-dimensional wrinkled sheet morphology associated with graphene-based materials. Additionally, the analyses demonstrated uniform and well-distributed metal particles, featuring an average diameter of 2.6 nm on the carbon support. This distribution was attributed to strong C–O–M (M = metal sites) bridges formed by the remaining oxygen functionalities of the rGO. Electrochemical tests highlighted the PdNiBi/rGO composite superior performance for EOR activity and stability compared to commercial Pd/C. The enhanced electrocatalytic activity was attributed to the generation of abundant active sites facilitated by the rGO support and the presence of oxophilic Ni and Bi elements.

2. 8. Graphene and Graphene-Based Materials as Active Components for Electrocatalysis

Among metal-free electrocatalysts the development of electrocatalysts, carbon-based nanomaterials exhibit many advantageous properties, such as variously tunable chemical structures, large surface area, thermal stability, conductivity, excellent mechanical properties, and high durability in various electrochemical environments.^{89–93,101–106} These properties ensure that the materials that serve as catalysts are inexpensive and have high tolerance to a wide pH range. In contrast, pristine carbon nanomaterials exhibit low electrocatalytic activity. Therefore, various approaches have been developed to modify carbon structures and generate electronic structures with highly active catalytic activities. These modifications are achieved by localized distribution of charge and spin density.¹⁰⁷

One strategy for fine-tuning the electronic properties of carbon nanostructures involves introducing intrinsic defects or increasing the edge structure. Among the various defects, the effect of point and line defects in

graphene clusters was investigated using the DFT method on the catalytic ORR activity. The point defects used in the study were Stone-Wales defect, single vacancies, double vacancies, and substituting pentagonal ring and for one dimensional line defects pentagon-heptagon and pentagon-pentagon-octagon chains were used. It was found that the defects can generate spin density and catalyze ORR, similar to the graphene edges.¹⁰⁸

Second possibility is to dope the carbon nanostructure with heteroatoms. The most popular heteroatoms are nitrogen (N), phosphorous (P) and boron (B)^{109–112} or bonds with oxygen (O), sulfur (S), chlorine (Cl), bromine (Br) and iodine (I)^{113,114} atoms at the edges. The different electronegativity of carbon and heteroatoms changes the local charge and spin density, which can have a positive effect on catalytic activity. The active sites in heteroatom-doped carbon nanostructures are the carbon atoms near the dopant, the carbon atoms at the edges, or the dopant itself. For ORR activity, the density functional theory (DFT) calculations showed that heteroatom doping with N, P, B, S, Cl, Br, and I significantly change the charge and spin density and further increases the activity. It was also shown that oxygen functional groups such as –C–OH–, –C=O and –COOH near the edge enhance the ORR activity.¹¹⁵

The third technique is physisorption of organic compounds to the graphene derivative nanostructures. It involves various organic molecules (TCNE, C₃N₄, etc.) adsorbed onto carbon nanotubes or graphene nanostructures. The catalytic potential results from electron transfer either between the organic compound and the graphene derivative. Electron transfer creates electrocatalytically active sites on carbon atoms with higher charge density.^{116,117}

In 2010, nitrogen-doped graphene (N-graphene) has been successfully synthesized through chemical vapor deposition (CVD) of methane in the presence of ammonia.¹¹⁸ This novel N-graphene exhibits remarkable electrocatalytic activity, long-term operational stability, and crossover tolerance superior to platinum when employed as a metal-free electrode for oxygen reduction through the four-electron pathway in alkaline fuel cells. This study marks the pioneering use of graphene and its derivatives as metal-free catalysts for oxygen reduction. The incorporation of nitrogen into the graphene structure plays a pivotal role in enhancing the oxygen reduction reaction (ORR). The N-graphene film outperforms Pt/C electrodes, showcasing a threefold increase in steady-state catalytic current over a broad potential range. Additionally, its long-term stability, crossover tolerance, and resistance to CO poisoning surpass those of Pt/C for oxygen reduction in alkaline electrolytes. This work not only underscores the versatility of N-doping in ORR, as demonstrated with nitrogen-doped carbon nanotubes and N-graphene, but also suggests broader implications for the development of diverse metal-free ORR catalysts for fuel cell applications.

Graphene derivatives doped with nitrogen have emerged as promising non-noble metal materials for the

ORR in both proton exchange membrane and alkaline fuel cells.^{118–120} Nosan et al. developed a rapid and scalable electrical induction heating method for the preparation of nitrogen-doped heat-treated graphene oxide derivatives.¹²¹ Materials synthesized using this method exhibited significantly elevated specific surface areas and demonstrated improved ORR activity compared to conventional synthesis approaches. Interestingly, the authors demonstrated that the temperature program of induction heating could finely modulate the concentration of nitrogen functionalities. Specifically, the amount of graphitic-N configuration increased directly proportional to the final temperature employed, coinciding with enhanced ORR activity in both alkaline and acidic electrolytes, suggesting that the concentration of graphitic-N could be responsible for the increased ORR activity. These findings contribute valuable insights for the development of non-metal nitrogen-doped heat-treated graphene oxide derivatives for applications in energy conversion systems.

The hydrogen evolution reaction (HER) and oxygen evolution reaction (OER) play a pivotal role in the field of electrocatalysis, particularly in the context of water electrolyzers, where they serve as the cathodic and anodic half-reactions, respectively.^{122–126} HER involves the reduction of protons to produce molecular hydrogen and OER involves the conversion of water into oxygen and protons, crucial processes for the sustainable generation of hydrogen gas as a clean and renewable energy carrier. Efficient electrocatalysis of the HER and OER are imperative for enhancing the overall performance and economic viability of water electrolyzers, as it determines the rate at which hydrogen and oxygen are produced and influences the system's energy efficiency.^{127–131} Electrodes with high catalytic activity for HER and OER facilitate lower overpotentials, reducing the energy input required for hydrogen and oxygen evolution.^{132–136} Consequently, advancements in the design and development of electrocatalysts for HER and OER have significant implications for the scalability and commercialization of water electrolysis technologies, offering a pathway towards the realization of a clean and sustainable hydrogen economy.

Zheng et al. study presents the synthesis of a metal-free electrocatalyst, comprising exclusively carbon and nitrogen components, achieved through the integration of graphitic carbon nitride (g-C₃N₄) and nitrogen-doped graphene (N-graphene; NG).¹³⁷ The resulting C₃N₄@NG hybrid exhibits distinctive molecular architecture and electronic characteristics, rendering it suitable for electrocatalytic hydrogen evolution reaction (HER) applications. Despite not reaching the activity levels of state-of-the-art Pt catalysts, this metal-free hybrid demonstrates HER performance comparable to well-established metallic counterparts, including nanostructured MoS₂ materials. Experimental observations, complemented by density functional theory (DFT) calculations unveil the unique electrocatalytic properties arising from a synergistic effect within this

hybrid nanostructure: g-C₃N₄ furnishes highly active hydrogen adsorption sites, while N-graphene facilitates the electron-transfer process during proton reduction. These results demonstrate the potential of well-designed metal-free catalysts, comparable to precious metals, for highly efficient electrocatalytic HER. Consequently, this work opens a promising avenue for the broader utilization of metal-free alternative materials, reducing reliance on noble metals across diverse applications.

Jiao et al. systematically explored the HER across a range of non-metal heteroatom-doped graphene materials, incorporating nitrogen, phosphorus, oxygen, sulfur, and boron.¹³⁸ Employing electrochemical reaction rate measurements and density functional theory (DFT) calculations to assess adsorption energetics, the study established a correlation between current density on each material and hydrogen adsorption strength on molecular models. The integrated experimental and theoretical analysis revealed that the suboptimal catalytic activity of carbon-based catalysts stems from weak hydrogen adsorption on graphene surfaces. A distinctive volcano-shaped relationship emerged, linking the activity (current density) to the free energy of hydrogen adsorption, with an optimal doped-graphene electrocatalyst predicted to reside at the volcano's apex. To validate this hypothesis, the researchers fabricated and evaluated three co-doped graphene samples (nitrogen-sulfur, nitrogen-phosphorus, and nitrogen-boron), calculating their hydrogen adsorption energy using DFT. Both experimental and theoretical results converged, demonstrating that nitrogen-sulfur co-doped graphene emerged as the most active catalyst, attributed to its lowest hydrogen adsorption energy. This enhancement in activity is postulated to arise from a synergistic coupling effect between the two heteroatoms, highlighting the potential for tailored multi-element doping or the introduction of structural defects to engineer idealized doped graphene electrocatalysts for improved HER performance.

Zhao et al. study presents an investigation into the electrocatalytic activity of nitrogen-doped graphite nano-materials derived from a nitrogen-rich polymer.¹³⁹ These materials exhibit superior performance in the oxygen evolution reaction (OER) in alkaline environments compared to conventional electrocatalysts. Remarkably, in the absence of transition metals, the optimized nitrogen/carbon materials demonstrate OER overpotentials as low as 0.38 V at a current density of 10 mA cm⁻² at pH 13, surpassing other non-metal OER electrocatalysts. Comprehensive electrochemical and physical analyses reveal that the improved OER activity of the nitrogen/carbon materials arises from active sites associated with pyridinic-N and/or quaternary-N functionalities. Specifically, carbon atoms adjacent to nitrogen atoms are postulated to be positively charged due to the electron-withdrawing nature of nitrogen atoms in a graphene π -system. This positive charge facilitates the absorption of OH⁻ ions by the positively charged carbon, a phenomenon crucial for OER. In the

context of the limiting step of OER, the authors consider one plausible explanation is that the neighboring positive-charged carbon atoms aid the facile recombination of two oxygen adsorbed species (O_{ads}). Finally, the authors suggest that another potential mechanism may involve nitrogen atoms, as their density of state in a graphitic sp^2 carbon network is proximate to the Fermi level.^{140,141} Noteworthy, further studies corroborated with these findings.^{142,143}

Hydrogen peroxide (H_2O_2) serves as an environmentally friendly oxidizing agent with diverse applications, prompting the exploration of alternative, efficient routes for its production. The two-electron oxygen reduction reaction ($2e^-$ ORR) emerges as a promising avenue, offering an attractive alternative to the energy-intensive anthraquinone oxidation process. However, conventional catalysts for $2e^-$ ORR fall short of meeting industrial demands. Addressing this, Lee et al. synthesized 3D graphene catalysts with controlled oxygen functional groups and defects, achieved through a one-step aerosol spray drying process.¹⁴⁴ A systematic investigation into the structure-electrochemical performance relationship of these graphene catalysts underscored the decisive role of oxygen functional groups and defects in facilitating H_2O_2 production. The optimized graphene catalyst demonstrated exceptional H_2O_2 selectivity (92–100%) across a wide potential range with remarkable stability and a high production rate at 0.4 V vs. RHE (ca. 450 mmol $g_{cat}^{-1} h^{-1}$). Complementary DFT calculations elucidated the contribution of diverse oxygen functional groups and defect sites to the $2e^-$ ORR pathway, establishing a scaling relation between OOH and O adsorption strengths. This thorough investigation establishes a critical structure-mechanism-performance relationship for nanostructured carbon systems in $2e^-$ ORR, offering crucial insights for the design of highly active and selective metal-free carbon electrocatalysts for H_2O_2 production, achievable through the precise tuning of oxygen functional groups and defect structures.

3. Flash Joule Heating (FJH) Method for Bulk Graphene Production

Flash Joule heating (FJH) is an electro-resistive method used for the synthesis of a broad spectrum of materials. As its name suggests, the method relies on the joule heat produced by the passage of rapid pulses of high-density electrical current through a conductive material. Unlike most other thermal methods where heat (or energy flux which gets converted to heat) from an external source is applied on the surface and then penetrates through the material in a process limited by the thermal conductivity of the sample, in FJH the heat is distributed uniformly throughout the whole volume. This feature allows very rapid heating rates in short periods of time, i.e. “in a flash”.

Joule heating has been in use for the sintering of materials for a long time and under different modifications lies in the basis of numerous processes. Under the umbrella term “resistance sintering”, Orrù et al. summarized 60 different process names by their first appearance in literature.¹⁴⁵ In another review article, Grasso et al. trace the history of the technology back to the patent submitted by Bloxam from 1906 as “the first patent on pure direct current (DC) resistance sintering”.¹⁴⁶ Despite the various processing parameters that differentiate the existing techniques, they are all based on the same physical phenomenon, the usage of the Joule heat for the synthesis of materials.

Since the early 20th century, the FJH technology has been applied to a wide variety of advanced materials, but only recently it was used for the synthesis of graphene by Luong and co-authors.⁸ The graphene and its derivatives synthesized using FJH deserve significant attention, because of the remarkable properties reported. These properties are attributed to the rotationally disordered or turbostratic structure of the flash graphene.¹⁴⁷ The turbostratic arrangement of the individual graphene layers (or rotational mismatching about the axis normal to the graphene sheets) is a direct result of the rapid cooling rate. Specifically, the extremely fast temperature change (on the order of $10^4 K s^{-1}$) during the cooling process impedes the produced flash graphene (FG) to not assume the thermodynamically favored arrangement and stacking of the graphene sheets (Bernal AB-stacked form).¹⁴⁸

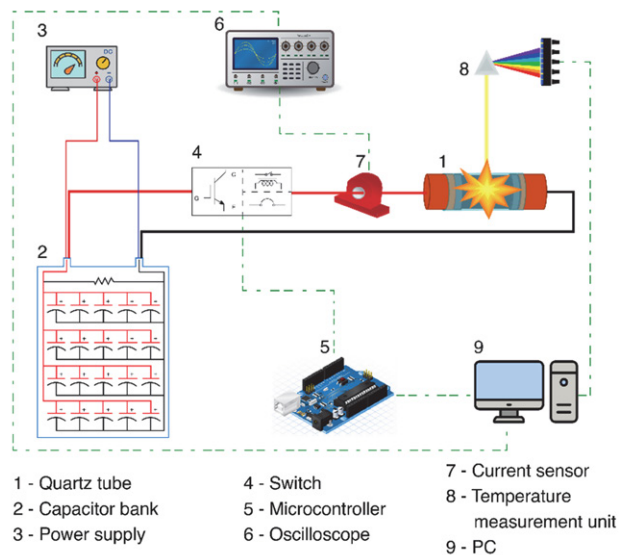


Figure 2. Typical flash Joule heating (FJH) setup diagram.

The Flash Joule Heating (FJH) process is typically conducted in a quartz tube (Figure 2 – element 1), chosen for its high thermal resistance. In this setup, a small quantity of carbonaceous material is placed between two graphite electrodes, which apply compression from both sides

until the desired electrical resistance is achieved. Since the FJH process requires rapid, high-current pulses that standard power grids cannot supply in such a brief time span, a large capacitor bank (Figure 2 – element 2) is generally used. This capacitor bank is charged to hundreds of volts, temporarily storing the necessary electrical energy, which is then swiftly discharged into the sample. A specialized electrical switch (Figure 2 – element 4), capable of handling the high current, is employed to control this discharge. As the flash process occurs within milliseconds, the switch is typically controlled by a microcontroller (Figure 2 – element 5) that manages the rapid release of the capacitor's energy into the sample and halts the process once the pre-set pulse duration is reached. During the process, an oscilloscope (Figure 2 – element 6) monitors the current and voltage in the system for detailed analysis. Temperature measurement is performed using an optical device (Figure 2 – element 8) that detects the light emitted by the heated carbon material, which is then compared to the spectrum of a grey body to estimate the temperature. When the pulse duration is completed, the electrical switch disconnects the circuit, ceasing the discharge and stopping further heat generation. From this point, the sample cools rapidly by natural means, typically 10^4 K s^{-1} . The temperatures reached in this process can exceed 3,000 K. At this temperature, all chemical bonds get broken and almost all the hetero atoms that are more volatile than carbon (O, H, N, S, P, etc.) leave the system through outgassing. This allows the use of a wide range of materials as precursors to produce turbostratic FG. Almost any carbon-based precursor can be transformed into bulk quantities of graphene.¹⁴⁹ Since no toxic and/or corrosive chemicals, solvents, and reactive gases are used, FJH offers a cheap and environmentally friendly method for the recycling of waste materials. Particularly, one of its key advantages over the traditional technologies for the synthesis of graphene is the possibility of upcycling low-value materials into high-value nanomaterials. Carbon-containing wastes and byproducts of different origins that often have little to no practical value require disposal or expensive utilization and even pose environmental hazards can be used as feedstock for flash graphene. For example, Luong and co-authors have shown the use of coal, coke, and even negative value materials such as waste plastics, rubber tires and discarded food can be processed into FG with purity greater than 99%.⁸

In terms of applicability, Tour and co-authors report that the FG produced shows higher quality compared to bulk graphene flakes produced using traditional methods (e.g., LPE and Oxidation with successive reduction). For instance, their carbon black-derived FG was used to prepare cement composites which showed compressive and tensile strength three times larger than those of other reported graphene-cement composites with the same loading.⁸ In another work, FG prepared from rubber waste was again used as a reinforcing additive to cement and led to a

~30% increase in concrete strength.¹⁵⁰ Hence, if the FG production can be implemented on industrial scale, it would have a significant impact on our world. Stronger cement would lead to a reduction in the amount of concrete needed, which in turn can result in significant carbon emission reduction as the cement industry is one of the main sources of greenhouse gases, accountable for 5–7% of the global anthropogenic carbon dioxide emissions,¹⁵¹ and at the same time represents ca. 7% of the industrial energy consumption.¹⁵²

When FG (in this case derived from metallurgical coke)¹⁵³ is applied as an additive in epoxy composites, the resulting composites have shown record high loading ratios that haven't been reported in the literature. Although graphene and other carbon nanomaterials have shown to improve the mechanical properties of epoxies, their high production costs limit their use on an industrial scale.¹⁵³ Since FG can be produced inexpensively and from low value material sources, it has been successfully used as a reinforcing and filler agent at weight ratios up to 50%. The resulting composites show a significant increase in Young's modulus, hardness, compressive strength and maximum elongation, as well as an impressive 496% increase in toughness compared to FG-free composites. Furthermore, the addition of such high amounts of FG to the epoxy composites resulted in a reduction of greenhouse gas emissions, and water and energy consumption during production by more than a third compared to the pure epoxy, making FG a promising candidate for a more sustainable chemical industry.¹⁵³ In terms of sustainability FJH offers additional advantages. Since the electrical energy used for the process is temporarily stored in a capacitor bank, FJH can act as a flexible load, meaning it can adjust its power consumption based on the availability of renewable electricity. Induction heating as well as other high temperature methods can benefit from the same source, but cannot compete with the ease, efficiency and speed offered by FJH.¹²¹ Moreover, it was demonstrated that the application of electric current through the sample can facilitate the crystallization of graphene, leading to the formation of a higher quality product.¹⁵⁴

4. Flash Graphene (FG) Applied to Electrocatalysis

The need to address rising energy consumption and environmental concerns requires the development of sustainable and environmentally friendly energy storage and conversion technologies. Promising innovations in the field of energy conversion include fuel cells and electrolyzers integrated into the electrochemical water cycle. This cycle revolves around oxygen reduction (ORR), oxygen evolution (OER), hydrogen evolution (HER), and hydrogen oxidation (HOR), central processes for the production of electricity, hydrogen, or chemical compounds. The effectiveness and accessibility of these energy solutions de-

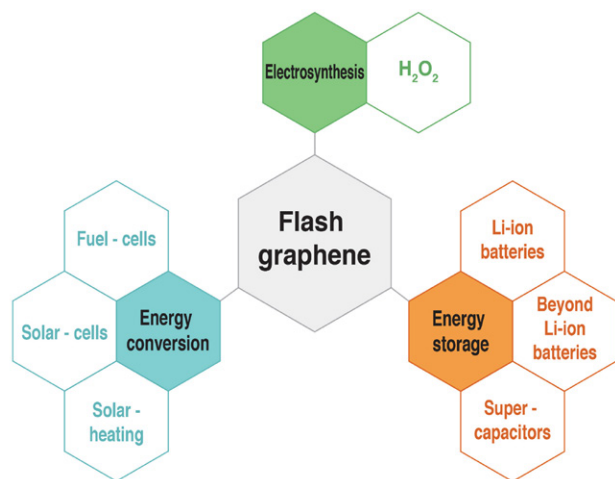


Figure 3. Diverse applications of flash graphene and other carbon allotropes.

pend largely on the catalysts used. The most effective catalysts are currently based on precious metals such as platinum, but their scarcity and exorbitant costs prevent their widespread use. Therefore, there is an urgent need for innovations in catalysts that not only offer better performance and longevity but are also economically viable and do not require precious metals.^{107,155}

Because the application of high-quality graphene and its derivatives for energy storage and conversion necessarily requires large quantities to be produced at industrial scale, FJH promises to have a tremendous influence in this field in the years to come (Figure 3). Although the use of FJH to produce FG and its derivatives is a relatively new technology, a few noteworthy examples for the application of FG in electrocatalysis already exist. Wyss and co-authors used the FJH process to produce holey and wrinkled flash graphene (HWFG) from mixed plastic waste. Among the applications demonstrated, HWFG was used as electrocatalyst for the hydrogen evolution reaction (HER) in acidic media in view of its high concentration of pores and edge defects.¹⁵⁶ When derived from high-density polyethylene (HDPE), HWFG electrocatalyst showed an overpotential of 613 mV (versus reversible hydrogen electrode, RHE) for hydrogen evolution in acidic media (Figure 4). Moreover, due to HWFG high surface area and porous structure, hydrogen gas (H_2) can easily escape as it evolves from HWFG active sites, allowing for constant H_2 production over time. Because FJH synthesis process does not involve the use of transition metals, the HWFG activity for HER is solely related to carbon-based surface-active sites. Consequently, HWFG showed very promising stability for 20 hours test, and even a slightly overpotential decrease (19 mV) over a -20 mA cm^{-2} current density, which was ascribed to the creation of more defects by cavitation caused by the H_2 constant evolution.

Graphene doping is a well-known strategy to create electrocatalytic active sites within graphene sheets.¹⁰² Because of the harsh reagents usually employed for top-down

synthesis of heteroatom-doped graphene (e.g., graphene oxide doping¹⁵⁷), the possibility of producing heteroatom-doped FG with high quality and impurity-free graphene flakes in bulk quantities at low-cost may open opportunities for its broad implementation in energy storage and conversion applications. In a recent work, Chen and co-authors used the FJH method to synthesize graphene doped by different heteroatoms in bulk quanti-

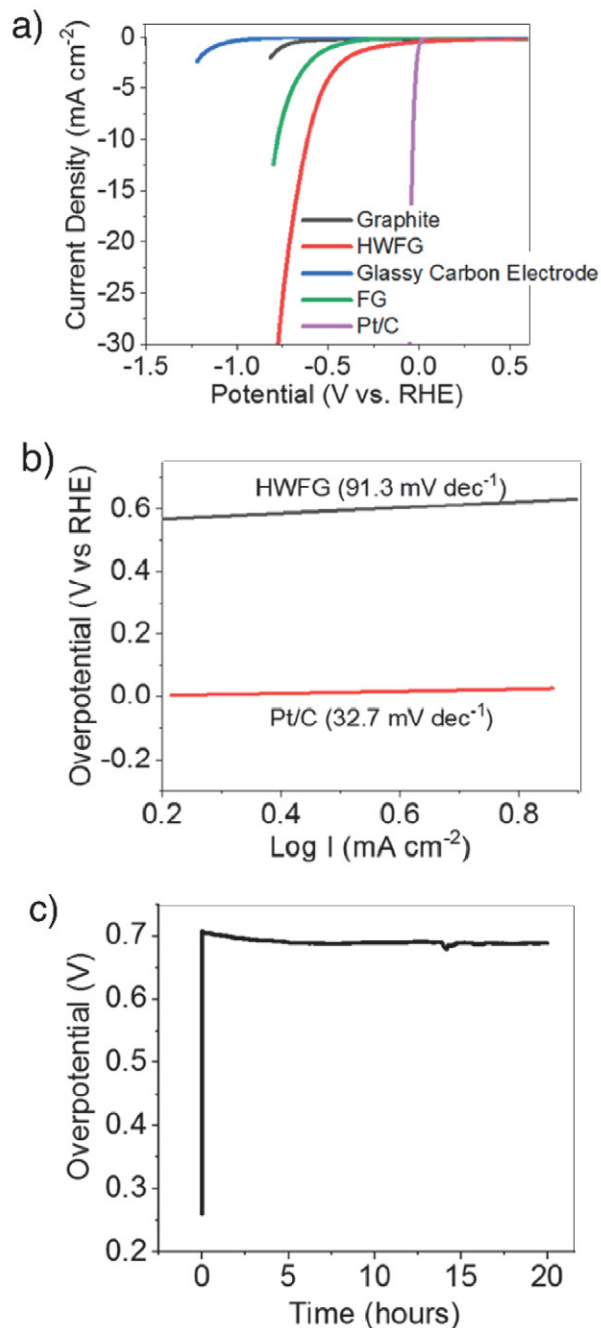


Figure 4. Assessment of HER electrochemical activity of mixed PW HWFG: a) Linear scan voltammograms; b) Tafel slope; c) Stability testing of HWFG at -20 mA/cm^2 . Graphs reproduced from reference.¹⁵⁶ HWFG = holey and wrinkled flash graphene. FG = flash graphene. Pt/C = platinum nanoparticles supported on carbon.

ties.¹¹¹ Both doped (boron, nitrogen, oxygen, phosphorous, and sulfur) and co-doped (when more than one element is used) FG showed high quality, similar to undoped FG, i.e. turbostratic structure, larger interlayer spacing between graphene sheets, and remarkable dispersibility. When applied as electrocatalysts for the oxygen reduction reaction (ORR) in alkaline media (Figure 5), sulfur-doped FG showed the highest activity, with a potential of 0.88 V (versus RHE) at a current density of -0.2 mA cm^{-2} , and a Tafel slope of 74 mV dec^{-1} . This result is in line with previous theoretical studies, where density functional theory (DFT) calculations revealed that sulfur-doped graphene

clusters can be a competitive electrocatalyst for ORR depending on their doping structures.¹¹⁴

A widely adopted strategy for enhancing and selectively tuning the electrocatalytic properties of graphene is the introduction of defects into its crystal structure. In a paper published by S. Dong and co-workers flash joule heating is used as a new approach for reducing graphene oxide using an exceptionally brief flash duration of a mere 1 ms. This approach enables the fabrication of defective graphene without intricate functional groups. The resulting material harbors a multitude of defects, and its unique three-dimensional structure allows it to withstand high

a) Flash Joule heating and doping

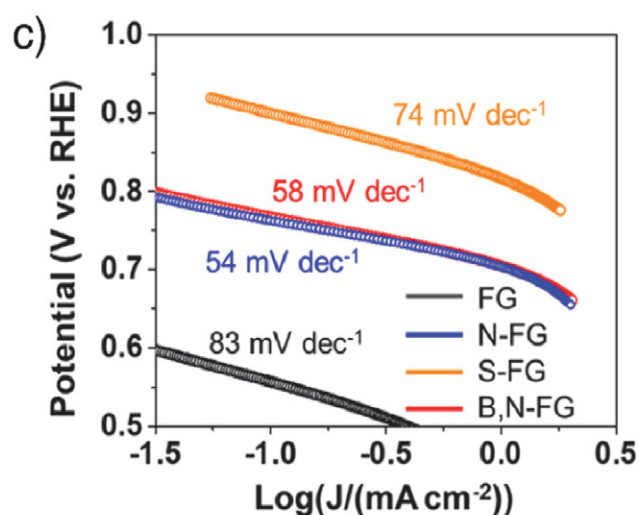
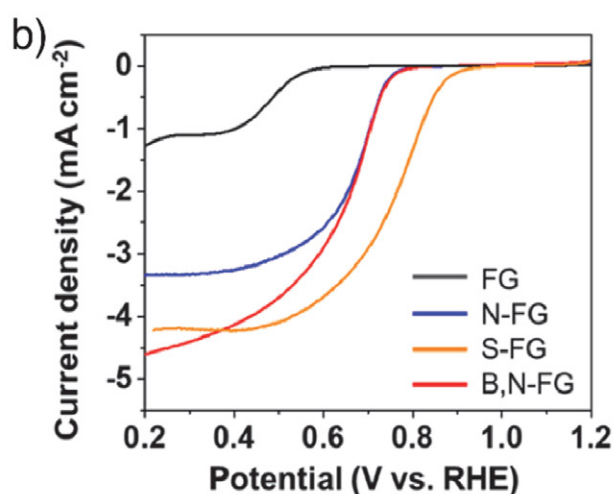
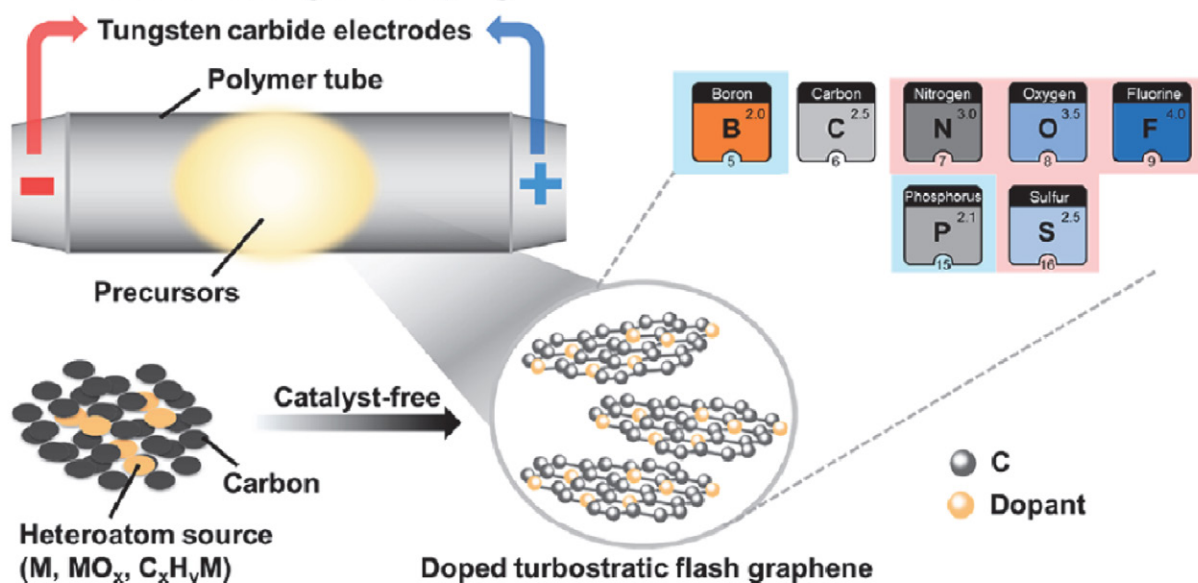


Figure 5. Electrochemical characterization of electrocatalysts synthesized by Flash Joule heating (FJH): a) Schematic representation of heteroatom-doped turbostratic graphene synthesis via FJH; b) Comparison of the oxygen reduction reaction performance among variously doped functionalized flash graphene in 0.1 M KOH solution at 1600 rpm; c) Corresponding Tafel plots. Image and graphs reproduced from reference.¹¹¹ FG = flash graphene. N-FG = nitrogen-doped flash graphene. S-FG = sulfur-doped flash graphene. B,N-FG = boron-nitrogen-doped flash graphene.

currents and prolonged cycles without drastic failures when used as an anode material in LIBs. It exhibits a remarkable reversible capacity of 1007 mAh/g after 5000 cycles at the current density of 5 A/g – surpassing the performance of graphene modified by other techniques.¹⁵⁸

Several studies have highlighted the feasibility of flash joule heating as an effective method for recycling and regenerating graphite from spent lithium-ion batteries. Natural graphite is classified as a critical raw material by the European Union, highlighting its strategic importance. To achieve true sustainability, it is essential to develop robust recycling programs for graphite, which are currently not widely established. In another study, S. Dong and co-workers utilized flash joule heating to recycle graphite from end-of-life lithium-ion batteries, demonstrating that the recycled graphite outperforms new commercial graphite in terms of electrical conductivity. Their comparison with other recent methods shows that the anodic graphite recovered through FJH exhibits higher initial Coulombic efficiency, near-complete capacity recovery, and is produced at significantly lower cost, all while requiring minimal processing time thus showing great potential for commercial applications.¹⁵⁹ In a more recent study, Tour et. al demonstrated an ultrafast flash recycling method to regenerate the graphite anode. During this process the intrinsic 3D layered graphite core structure is preserved and is coated with a solid-electrolyte-interphase derived carbon shell, contributing to high initial specific capacity, superior rate performance, and cycling stability, when compared to anode materials recycled using a high-temperature-calcination method. An additional advantage of the process is that it allows the extraction of metal ions from the flashed anode waste with average recovery efficiency reaching >99% using just 0.1M HCl.¹⁶⁰

Since this technology is in its initial state of development and application, the literature lacks comprehensive studies directly comparing the electrocatalytic properties of flash-graphene (FG) to those of the well-established carbon materials, the results available thus far affirm that flash joule heating is an exceptionally robust and sustainable method for synthesizing carbon-based electrocatalysts.

5. Perspective and Closing Remarks

In the fields of materials science and clean energy technologies, flash Joule heating (FJH) stands out as a groundbreaking method poised to revolutionize the large-scale production of graphene and simultaneously open new pathways for advanced recycling, upcycling and utilization of waste materials. This innovative technique harnesses the renewable power of high electric currents to rapidly elevate carbon-containing precursors to extreme temperatures, leading to the formation of turbostratic graphene (flash graphene (FG)). The remarkable attributes of FJH offer a new perspective on graphene manufacturing, effectively addressing longstanding challenges in the

industry. One of the most compelling aspects of FJH is its exceptional speed, with heating times measured in milliseconds. This rapid processing capability not only enables high production throughput but also promises to alleviate one of the critical bottlenecks in graphene manufacturing. Furthermore, FJH exhibits a unique ability to utilize a wide range of carbon sources, including biomass and waste materials, aligning with the pursuit of sustainability and economic viability in materials production. This versatility, combined with the method's minimal waste generation, results in flash graphene with exceptional crystallinity, endowing it with superior electrical and thermal conductivity. These attributes are of paramount importance for various energy-related applications. As we consider the implications of FJH on a broader scale, it becomes evident that its scalability, versatility, and efficiency position it as a game-changer in graphene production. This transformative approach offers a promising pathway toward unlocking the full commercial potential of graphene across various industries, particularly in energy storage and conversion. In the context of clean energy, the imperative for innovation extends beyond materials production to catalysis. Electrochemical processes such as oxygen reduction reaction (ORR), oxygen evolution reaction (OER), hydrogen evolution reaction (HER), and hydrogen oxidation reaction (HOR) are pivotal in energy conversion and storage devices like fuel cells, electrolyzers, and metal-air batteries. Catalysts play a crucial role in accelerating these reactions, but their efficiency and cost-effectiveness are of utmost importance. Traditional precious metal catalysts, notably platinum, face limitations due to their scarcity and high cost, driving the need for alternative, metal-free catalysts. Herein lies the significance of carbon-based nanomaterials as electrocatalysts, particularly in the context of graphene. These materials offer a plethora of advantages, high thermodynamic stability including tunable structures, high surface area, thermal stability, and conductivity. However, pristine carbon nanomaterials exhibit limited electrocatalytic activity. Innovative strategies such as introducing intrinsic defects or edge structures, doping with heteroatoms, and physisorption of organic compounds have emerged to enhance their catalytic performance. The manipulation of carbon nanostructures through these techniques has yielded promising results. Point and line defects, as well as heteroatom doping, can generate charge and spin density, catalyzing crucial electrochemical reactions. Moreover, the physisorption of organic compounds onto graphene derivatives fosters electron transfer and creates electrocatalytically active sites, contributing to improved performance. In the quest for large-scale production of high-quality graphene and its derivatives for energy applications, FJH holds great promise. Recent examples of its application in electrocatalysis, such as holey and wrinkled flash graphene (HWFG) for the hydrogen evolution reaction (HER), showcase its potential in energy conversion. Notably, FJH-derived materials exhibit impressive

stability and cost-effective performance, devoid of transition metals, reaffirming the pivotal role of carbon-based surface-active sites in electrocatalysis.

As this novel method was only developed relatively recently in 2020,⁸ there are still some challenges and obstacles to overcome for wider applicability. Many of the key challenges for scaling flash graphene production identified in the literature are related to the need for a deeper understanding and precise control of the processes occurring during FJH, which can vary depending on the specific feedstock used. In addition, life cycle assessments (LCA) of the production process and its overall environmental impact are essential. This requires the development of advanced computer models and process optimization as well as the implementation of comprehensive quality control protocols and standardization of the resulting graphene products.^{161,162} The reported ongoing industrial scaled up to 1 ton per day by early 2023 and targeted for 100 tons per day by 2024,¹⁶³ at an electricity cost of around \$100 per ton of graphene produced emphasize the promising future of the technology.

As we look ahead, the convergence of FJH and graphene-based electrocatalysis represents a paradigm shift in clean energy solutions. The integration of scalable and sustainable materials production with advanced catalytic systems holds the key to unlocking the full potential of renewable energy technologies. The journey of scientific exploration and development in these domains promises a brighter and more sustainable future, where the marriage of innovation and sustainability will lead us towards cleaner, more efficient energy solutions.

Acknowledgment

The authors would like to thank the Slovenian Research and Innovation Agency (ARIS) for funding through Research programme: P2-0423 and Research project J7-4636.

6. References

1. K. S. Novoselov, A. K. Geim, S. V. Morozov, D. Jiang, Y. Zhang, S. V. Dubonos, I. V. Grigorieva, A. A. Firsov, *Science* **2004**, *306*, 666–669. DOI:10.1126/science.1102896
2. K. S. Novoselov, *Rev. Mod. Phys.* **2011**, *83*, 837–849. DOI:10.1103/RevModPhys.83.837
3. A. K. Geim, *Rev. Mod. Phys.* **2011**, *83*, 851–862. DOI:10.1103/RevModPhys.83.851
4. T. A. Land, T. Michely, R. J. Behm, J. C. Hemminger, G. Comsa, *Surf. Sci.* **1992**, *264*, 261–270. DOI:10.1016/0039-6028(92)90183-7
5. M. Orlita, C. Faugeras, P. Plochocka, P. Neugebauer, G. Martinez, D. K. Maude, A.-L. Barra, M. Sprinkle, C. Berger, W. A. de Heer, M. Potemski, *Phys. Rev. Lett.* **2008**, *101*, 267601. DOI:10.1103/PhysRevLett.101.267601
6. C. Lee, X. Wei, J. W. Kysar, J. Hone, *Science* **2008**, *321*, 385–388. DOI:10.1126/science.1157996
7. A. C. Ferrari, F. Bonaccorso, V. Fal'ko, K. S. Novoselov, S. Roche, P. Bøggild, S. Borini, F. H. L. Koppens, V. Palermo, N. Pugno, J. A. Garrido, R. Sordan, A. Bianco, L. Ballerini, M. Prato, E. Lidorikis, J. Kivioja, C. Marinelli, T. Ryhänen, A. Morpurgo, J. N. Coleman, V. Nicolosi, L. Colombo, A. Fert, M. Garcia-Hernandez, A. Bachtold, G. F. Schneider, F. Guinea, C. Dekker, M. Barbone, Z. Sun, C. Galiotis, A. N. Grigorenko, G. Konstantatos, A. Kis, M. Katsnelson, L. Vandersypen, A. Loiseau, V. Morandi, D. Neumaier, E. Treossi, V. Pellegrini, M. Polini, A. Tredicucci, G. M. Williams, B. Hee Hong, J.-H. Ahn, J. Min Kim, H. Zirath, B. J. van Wees, H. van der Zant, L. Occhipinti, A. Di Matteo, I. A. Kinloch, T. Seyller, E. Quesnel, X. Feng, K. Teo, N. Rupesinghe, P. Hakonen, S. R. T. Neil, Q. Tannock, T. Löfwander, J. Kinaret, *Nanoscale* **2015**, *7*, 4598–4810. DOI:10.1039/C4NR01600A
8. D. X. Luong, K. V. Bets, W. A. Algozeeb, M. G. Stanford, C. Kittrell, W. Chen, R. V. Salvatierra, M. Ren, E. A. McHugh, P. A. Advincula, Z. Wang, M. Bhatt, H. Guo, V. Mancevski, R. Shahsavari, B. I. Yakobson, J. M. Tour, *Nature* **2020**, *577*, 647–651. DOI:10.1038/s41586-020-1938-0
9. A. K. Geim, K. S. Novoselov, *Nat. Mater.* **2007**, *6*, 183–191. DOI:10.1038/nmat1849
10. J. Hou, Y. Shao, M. W. Ellis, R. B. Moore, B. Yi, *Phys. Chem. Chem. Phys.* **2011**, *34*, 15384–15402. DOI:10.1039/c1cp21915d
11. R. Raccichini, A. Varzi, S. Passerini, B. Scrosati, *Nat. Mater.* **2015**, *14*, 271–279. DOI:10.1038/nmat4170
12. M. F. El-Kady, Y. Shao, R. B. Kaner, *Nat. Rev. Mater.*, **2016**, *7*, 1–14. DOI:10.1038/natrevmats.2016.33
13. X. Chen, R. Paul, L. Dai, *Natl. Sci. Rev.* **2017**, *4*, 453–489. DOI:10.1093/nsr/nwx009
14. K. S. Novoselov, V. I. Fal'ko, L. Colombo, P. R. Gellert, M. G. Schwab, K. Kim, *Nature* **2012**, *490*, 192–200. DOI:10.1038/nature11458
15. A. Bianco, H.-M. Cheng, T. Enoki, Y. Gogotsi, R. H. Hurt, N. Koratkar, T. Kyotani, M. Monthieux, C. R. Park, J. M. D. Tascon, J. Zhang, *Carbon N Y* **2013**, *65*, 1–6. DOI:10.1016/j.carbon.2013.08.038
16. L. Lin, H. Peng, Z. Liu, *Nat. Mater.* **2019**, *18*, 520–524. DOI:10.1038/s41563-019-0341-4
17. S. H. Choi, S. J. Yun, Y. S. Won, C. S. Oh, S. M. Kim, K. K. Kim, Y. H. Lee, *Nat. Commun.* **2022**, *13*, 1484. DOI:10.1038/s41467-022-29182-y
18. S. Park, *Nat. Rev. Mater.* **2016**, *1*, 1–2. DOI:10.1038/natrevmats.2016.80
19. W. Kong, H. Kum, S. H. Bae, J. Shim, H. Kim, L. Kong, Y. Meng, K. Wang, C. Kim, J. Kim, *Nat. Nanotechnol.* **2019**, *14*, 927–938. DOI:10.1038/s41565-019-0555-2
20. Editorial, *Nat. Mater.* **2019**, *18*, 519. DOI:10.1038/s41563-019-0394-4
21. P. Bøggild, *Nat. Commun.* **2023**, *14*, 1126. DOI:10.1038/s41467-023-36891-5
22. A. Zurutuza, C. Marinelli, *Nat. Nanotechnol.* **2014**, *9*, 730–734. DOI:10.1038/nnano.2014.225

23. W. Ren, H.-M. Cheng, *Nat. Nanotechnol.* **2014**, *9*, 726–730. DOI:10.1038/nnano.2014.229
24. C. A. Clifford, E. H. Martins Ferreira, T. Fujimoto, J. Herrmann, A. R. Hight Walker, D. Koltsov, C. Punckt, L. Ren, G. J. Smallwood, A. J. Pollard, *Nat. Rev. Phys.* **2021**, *3*, 233–235. DOI:10.1038/s42254-021-00278-6
25. S. Milana, *Nat. Phys.* **2021**, *17*, 1068–1068. DOI:10.1038/s41567-021-01339-4
26. A. P. Kauling, A. T. Seefeldt, D. P. Pisoni, R. C. Pradeep, R. Bentini, R. V. B. Oliveira, K. S. Novoselov, A. H. Castro Neto. *Adv. Mater.* **2018**, *30*, 1803784. DOI:10.1002/adma.201803784
27. P. Bøggild, *Nature* **2018**, *562*, 502–503. DOI:10.1038/d41586-018-06939-4
28. T. Barkan, *Nat. Nanotechnol.* **2019**, *14*, 904–906. DOI:10.1038/s41565-019-0556-1
29. X.-Y. Wang, A. Narita, K. Müllen, *Nat. Rev. Chem.* **2017**, *2*, 0100. DOI:10.1038/s41570-017-0100
30. M. Batzill, *Surf. Sci. Rep.* **2012**, *67*, 83–115. DOI:10.1016/j.surfrep.2011.12.001
31. A. L. Higginbotham, D. V Kosynkin, A. Sinitskii, Z. Sun, J. M. Tour, *ACS Nano* **2010**, *4*, 2059–2069. DOI:10.1021/nn100118m
32. L. Jiao, X. Wang, G. Diankov, H. Wang, H. Dai, *Nat. Nanotechnol.* **2010**, *5*, 321–325. DOI:10.1038/nnano.2010.54
33. C. Zhang, Z. Peng, J. Lin, Y. Zhu, G. Ruan, C.-C. Hwang, W. Lu, R. H. Hauge, J. M. Tour, *ACS Nano* **2013**, *7*, 5151–5159. DOI:10.1021/nn400750n
34. J. Lim, U. Narayan Maiti, N.-Y. Kim, R. Narayan, W. Jun Lee, D. Sung Choi, Y. Oh, J. Min Lee, G. Yong Lee, S. Hun Kang, H. Kim, Y.-H. Kim, S. Ouk Kim, *Nat. Commun.* **2016**, *7*, 10364. DOI:10.1038/ncomms10364
35. H. Wang, Y. Wang, Z. Hu, X. Wang, *ACS Appl. Mater. Interfaces* **2012**, *4*, 6827–6834. DOI:10.1021/am302000z
36. B. Xiao, X. Li, X. Li, B. Wang, C. Langford, R. Li, X. Sun, *J. Phys. Chem. C* **2014**, *118*, 881–890. DOI:10.1021/jp410812v
37. Y. Song, H. Hu, M. Feng, H. Zhan, *ACS Appl Mater Interfaces* **2015**, *7*, 25793–25803. DOI:10.1021/acsami.5b07700
38. A. Sinitskii, A. Dimiev, D. V Kosynkin, J. M. Tour, *ACS Nano* **2010**, *4*, 5405–5413. DOI:10.1021/nn101019h
39. Q. Shu, Z. Xia, W. Wei, X. Xu, R. Sun, R. Deng, Q. Yang, H. Zhao, S. Wang, G. Sun, *ACS Appl. Energy Mater.* **2019**, *2*, 5446–5455. DOI:10.1021/acsaem.9b00506
40. D. B. Shinde, J. Degupta, A. Kushwaha, M. Aslam, V. K. Pillai, *J. Am. Chem. Soc.* **2011**, *133*, 4168–4171. DOI:10.1021/ja1101739
41. D. V. Kosynkin, A. L. Higginbotham, A. Sinitskii, J. R. Lomeda, A. Dimiev, B. K. Price, J. M. Tour, *Nature* **2009**, *458*, 872–876. DOI:10.1038/nature07872
42. L. Sun, G. Yuan, L. Gao, J. Yang, M. Chhowalla, M. H. Ghahrahcheshmeh, K. K. Gleason, Y. S. Choi, B. H. Hong, Z. Liu, *Nat. Rev. Methods Primers* **2021**, *1*, 5. DOI:10.1038/s43586-020-00005-y
43. C. Mattevi, H. Kim, M. Chhowalla, *J. Mater. Chem.* **2011**, *21*, 3324–3334. DOI:10.1039/C0JM02126A
44. S. Marchini, S. Günther, J. Wintterlin, *Phys. Rev. B* **2007**, *76*, 075429. DOI:10.1103/PhysRevB.76.075429
45. P. Sutter, J. T. Sadowski, E. Sutter, *Phys. Rev. B* **2009**, *80*, 245411. DOI:10.1103/PhysRevB.80.245411
46. J. Lahiri, T. Miller, L. Adamska, I. I. Oleynik, M. Batzill, *Nano Lett* **2011**, *11*, 518–522. DOI:10.1021/nl103383b
47. L. Gao, J. R. Guest, N. P. Guisinger, *Nano Lett.* **2010**, *10*, 3512–3516. DOI:10.1021/nl1016706
48. C.-M. Seah, S.-P. Chai, A. R. Mohamed, *Carbon N Y* **2014**, *70*, 1–21. DOI:10.1016/j.carbon.2013.12.073
49. S. Bhaviripudi, X. Jia, M. S. Dresselhaus, J. Kong, *Nano Lett* **2010**, *10*, 4128–4133. DOI:10.1021/nl102355e
50. X. Li, C. W. Magnuson, A. Venugopal, R. M. Tromp, J. B. Hannon, E. M. Vogel, L. Colombo, R. S. Ruoff, *J. Am. Chem. Soc.* **2011**, *133*, 2816–2819. DOI:10.1021/ja109793s
51. M. Losurdo, M. M. Giangregorio, P. Capezzuto, G. Bruno, *Phys. Chem. Chem. Phys.* **2011**, *13*, 20836. DOI:10.1039/c1cp22347j
52. H. I. Rasool, E. B. Song, M. Mecklenburg, B. C. Regan, K. L. Wang, B. H. Weiller, J. K. Gimzewski, *J. Am. Chem. Soc.* **2011**, *133*, 12536–12543. DOI:10.1021/ja200245p
53. A. Dahal, M. Batzill, *Nanoscale* **2014**, *6*, 2548. DOI:10.1039/c3nr05279f
54. J. Wintterlin, M.-L. Bocquet, *Surf. Sci.* **2009**, *603*, 1841–1852. DOI:10.1016/j.susc.2008.08.037
55. Y. Zhang, L. Gomez, F. N. Ishikawa, A. Madaria, K. Ryu, C. Wang, A. Badmaev, C. Zhou, *J. Phys. Chem. Lett.* **2010**, *1*, 3101–3107. DOI:10.1021/jz1011466
56. Q. Yu, L. A. Jauregui, W. Wu, R. Colby, J. Tian, Z. Su, H. Cao, Z. Liu, D. Pandey, D. Wei, T. F. Chung, P. Peng, N. P. Guisinger, E. A. Stach, J. Bao, S.-S. Pei, Y. P. Chen, *Nat. Mater.* **2011**, *10*, 443–449. DOI:10.1038/nmat3010
57. Y. Zhang, L. Zhang, C. Zhou, *Acc. Chem. Res.* **2013**, *46*, 2329–2339. DOI:10.1021/ar300203n
58. L. P. Biró, P. Lambin, *New J. Phys.* **2013**, *15*, 035024. DOI:10.1088/1367-2630/15/3/035024
59. Y.-M. Lin, C. Dimitrakopoulos, K. A. Jenkins, D. B. Farmer, H.-Y. Chiu, A. Grill, Ph. Avouris, *Science* **2010**, *327*, 662–662. DOI:10.1126/science.1184289
60. I. Shteplyuk, V. Khranovskyy, R. Yakimova, *Semicond. Sci. Technol.* **2016**, *31*, 113004. DOI:10.1088/0268-1242/31/11/113004
61. P. N. First, W. A. de Heer, T. Seyller, C. Berger, J. A. Stroscio, J.-S. Moon, *MRS Bull.* **2010**, *35*, 296–305. DOI:10.1557/mrs2010.552
62. K. V. Emtsev, A. Bostwick, K. Horn, J. Jobst, G. L. Kellogg, L. Ley, J. L. McChesney, T. Ohta, S. A. Reshanov, J. Röhr, E. Rotenberg, A. K. Schmid, D. Waldmann, H. B. Weber, T. Seyller, *Nat. Mater.* **2009**, *8*, 203–207. DOI:10.1038/nmat2382
63. C. Berger, Z. Song, X. Li, X. Wu, N. Brown, C. Naud, D. Mayou, T. Li, J. Hass, A. N. Marchenkov, E. H. Conrad, P. N. First, W. A. de Heer, *Science* **2006**, *312*, 1191–1196. DOI:10.1126/science.1125925
64. L. Talirz, H. Söde, T. Dumschlaff, S. Wang, J. R. Sanchez-Valencia, J. Liu, P. Shinde, C. A. Pignedoli, L. Liang, V. Meunier, N. C. Plumb, M. Shi, X. Feng, A. Narita, K. Müllen, R. Fasel, P.

- Ruffieux, *ACS Nano* **2017**, *11*, 1380–1388.
DOI:10.1021/acsnano.6b06405
65. G. D. Nguyen, H.-Z. Tsai, A. A. Omrani, T. Marangoni, M. Wu, D. J. Rizzo, G. F. Rodgers, R. R. Cloke, R. A. Durr, Y. Sakai, F. Liou, A. S. Aikawa, J. R. Chelikowsky, S. G. Louie, F. R. Fischer, M. F. Crommie, *Nat. Nanotechnol.* **2017**, *12*, 1077–1082. DOI:10.1038/nnano.2017.155
66. J. Cai, C. A. Pignedoli, L. Talirz, P. Ruffieux, H. Söde, L. Liang, V. Meunier, R. Berger, R. Li, X. Feng, K. Müllen, R. Fasel, *Nat. Nanotechnol.* **2014**, *9*, 896–900.
DOI:10.1038/nnano.2014.184
67. A. Celis, M. N. Nair, A. Taleb-Ibrahimi, E. H. Conrad, C. Berger, W. A. de Heer, A. Tejeda, *J. Phys. D. Appl. Phys.* **2016**, *49*, 143001. DOI:10.1088/0022-3727/49/14/143001
68. A. J. Way, R. M. Jacobberger, N. P. Guisinger, V. Saraswat, X. Zheng, A. Suresh, J. H. Dwyer, P. Gopalan, M. S. Arnold, *Nat. Commun.* **2022**, *13*, 2992.
69. J. Cai, P. Ruffieux, R. Jaafar, M. Bieri, T. Braun, S. Blankenburg, M. Muoth, A. P. Seitsonen, M. Saleh, X. Feng, K. Müllen, R. Fasel, *Nature* **2010**, *466*, 470–473.
DOI:10.1038/nature09211
70. A. Narita, X.-Y. Wang, X. Feng, K. Müllen, *Chem. Soc. Rev.* **2015**, *44*, 6616–6643. DOI:10.1039/C5CS00183H
71. Y.-C. Chen, D. G. de Oteyza, Z. Pedramrazi, C. Chen, F. R. Fischer, M. F. Crommie, *ACS Nano* **2013**, *7*, 6123–6128.
DOI:10.1021/nn401948e
72. R. S. K. Houtsmma, J. de la Rie, M. Stöhr, *Chem. Soc. Rev.* **2021**, *50*, 6541–6568. DOI:10.1039/D0CS01541E
73. H. Wang, H. S. Wang, C. Ma, L. Chen, C. Jiang, C. Chen, X. Xie, A.-P. Li, X. Wang, *Nat. Rev. Phys.* **2021**, *3*, 791–802.
DOI:10.1038/s42254-021-00370-x
74. P. H. Jacobse, A. Kimouche, T. Gebraad, M. M. Ervasti, J. M. Thijssen, P. Liljeroth, I. Swart, *Nat. Commun.* **2017**, *8*, 119.
DOI:10.1038/s41467-017-00195-2
75. Y.-C. Chen, T. Cao, C. Chen, Z. Pedramrazi, D. Haberer, D. G. de Oteyza, F. R. Fischer, S. G. Louie, M. F. Crommie, *Nat. Nanotechnol.* **2015**, *10*, 156–160.
DOI:10.1038/nnano.2014.307
76. W. Niu, S. Sopp, A. Lodi, A. Gee, F. Kong, T. Pei, P. Gehring, J. Nägele, C. S. Lau, J. Ma, J. Liu, A. Narita, J. Mol, M. Burghard, K. Müllen, Y. Mai, X. Feng, L. Bogani, *Nat. Mater.* **2023**, *22*, 180–185. DOI:10.1038/s41563-022-01460-6
77. J. Wu, W. Pisula, K. Müllen, *Chem. Rev.* **2007**, *107*, 718–747.
DOI:10.1021/cr068010r
78. A. Narita, X. Feng, K. Müllen, *Chem. Rec.* **2015**, *15*, 295–309.
DOI:10.1002/tcr.201402082
79. M. Koch, F. Ample, C. Joachim, L. Grill, *Nat. Nanotechnol.* **2012**, *7*, 713–717. DOI:10.1038/nnano.2012.169
80. D. J. Rizzo, G. Veber, T. Cao, C. Bronner, T. Chen, F. Zhao, H. Rodriguez, S. G. Louie, M. F. Crommie, F. R. Fischer, *Nature* **2018**, *560*, 204–208. DOI:10.1038/s41586-018-0376-8
81. O. Gröning, S. Wang, X. Yao, C. A. Pignedoli, G. Borin Barin, C. Daniels, A. Cupo, V. Meunier, X. Feng, A. Narita, K. Müllen, P. Ruffieux, R. Fasel, *Nature* **2018**, *560*, 209–213.
DOI:10.1038/s41586-018-0375-9
82. L. Talirz, P. Ruffieux, R. Fasel, *Adv. Mater.* **2016**, *28*, 6222–6231. DOI:10.1002/adma.201505738
83. P. H. Jacobse, M. J. J. Mangnus, S. J. M. Zevenhuizen, I. Swart, *ACS Nano* **2018**, *12*, 7048–7056.
DOI:10.1021/acsnano.8b02770
84. S. Kawai, S. Nakatsuka, T. Hatakeyama, R. Pawlak, T. Meier, J. Tracey, E. Meyer, A. S. Foster, *Sci. Adv.* **2018**, *4*.
DOI:10.1126/sciadv.aar7181
85. X. Zhang, O. V. Yazyev, J. Feng, L. Xie, C. Tao, Y.-C. Chen, L. Jiao, Z. Pedramrazi, A. Zettl, S. G. Louie, H. Dai, M. F. Crommie, *ACS Nano* **2013**, *7*, 198–202. DOI:10.1021/nn303730v
86. J. Lawrence, A. Berdonces-Layunta, S. Edalatmanesh, J. Castro-Esteban, T. Wang, A. Jimenez-Martin, B. de la Torre, R. Castrillo-Bodero, P. Angulo-Portugal, M. S. G. Mohammed, A. Matěj, M. Vilas-Varela, F. Schiller, M. Corso, P. Jelinek, D. Peña, D. G. de Oteyza, *Nat. Chem.* **2022**, *14*, 1451–1458.
DOI:10.1038/s41557-022-01042-8
87. V. Saraswat, R. M. Jacobberger, M. S. Arnold, *ACS Nano* **2021**, *15*, 3674–3708. DOI:10.1021/acsnano.0c07835
88. V. Saraswat, R. M. Jacobberger, M. S. Arnold, *ACS Nano* **2021**, *15*, 9194–9194. DOI:10.1021/acsnano.1c03098
89. M. Liu, R. Zhang, W. Chen, *Chem. Rev.* **2014**, *114*, 5117–5160.
DOI:10.1016/j.cyto.2014.07.121
90. J. Hou, Y. Shao, M. W. Ellis, R. B. Moore, B. Yi, *Phys. Chem. Chem. Phys.* **2011**, *13*, 15384. DOI:10.1039/c1cp21915d
91. H. Su, Y. H. Hu, *Energy Sci. Eng.* **2021**, *9*, 958–983.
DOI:10.1002/ese3.833
92. A. Ambrosi, C. K. Chua, A. Bonanni, M. Pumera, *Chem. Rev.* **2014**, *114*, 7150–7188. DOI:10.1021/cr500023c
93. H. Jin, C. Guo, X. Liu, J. Liu, A. Vasileff, Y. Jiao, Y. Zheng, S.-Z. Qiao, *Chem. Rev.* **2018**, *118*, 6337–6408.
DOI:10.1021/acs.chemrev.7b00689
94. E. Yoo, T. Okada, T. Akita, M. Kohyama, I. Honma, J. Nakamura, *J. Power Sources* **2011**, *196*, 110–115.
DOI:10.1016/j.jpowsour.2010.07.024
95. R. Kou, Y. Shao, D. Wang, M. H. Engelhard, J. H. Kwak, J. Wang, V. V. Viswanathan, C. Wang, Y. Lin, Y. Wang, I. A. Aksay, J. Liu, *Electrochem. Commun.* **2009**, *11*, 954–957.
DOI:10.1016/j.elecom.2009.02.033
96. L. Pavko, M. Gatalo, M. Finšgar, F. Ruiz-Zepeda, K. Ehelebe, P. Kaiser, M. Geuß, T. Đukić, A. K. Surca, M. Šala, M. Bele, S. Cherevko, B. Genorio, N. Hodnik, M. Gaberšček, *ACS Catal.* **2022**, *12*, 9540–9548. DOI:10.1021/acscatal.2c01753
97. L. Pavko, M. Gatalo, T. Đukić, F. Ruiz-Zepeda, A. K. Surca, M. Šala, N. Maselj, P. Jovanović, M. Bele, M. Finšgar, B. Genorio, N. Hodnik, M. Gaberšček, *Carbon* **2023**, *215*, 118458.
DOI:10.1016/j.carbon.2023.118458
98. C. Lamy, E. M. Belgsir: *Handbook of Fuel Cells*, Wiley-VCH, Weinheim, Germany, **2010**.
99. A. L. Dicks, D. A. J. Rand: *Fuel Cell Systems Explained*, Wiley-VCH, Weinheim, Germany, **2018**.
DOI:10.1002/9781118706992
100. S. Wolf, M. Roschger, B. Genorio, N. Hodnik, M. Gatalo, F. Ruiz-Zepeda, V. Hacker, *J. Electrochem. Sci. Eng.* **2023**, *13*, 771–782. DOI:10.1126/sciadv.1500564
101. J. Zhang, Z. Xia, L. Dai, *Sci. Adv.* **2015**, *1*.
102. D. Deng, K. S. Novoselov, Q. Fu, N. Zheng, Z. Tian, X. Bao,

- Nat. Nanotechnol.* **2016**, *11*, 218–230.
DOI:10.1038/nnano.2015.340
103. X. Chia, M. Pumera, *Nat. Catal.* **2018**, *1*, 909–921.
DOI:10.1038/s41929-018-0181-7
104. F. Bonaccorso, L. Colombo, G. Yu, M. Stoller, V. Tozzini, A. C. Ferrari, R. S. Ruoff, V. Pellegrini, *Science* **2015**, *347*.
DOI:10.1126/science.1246501
105. Y. Li, W. Zhou, H. Wang, L. Xie, Y. Liang, F. Wei, J.-C. Idrobo, S. J. Pennycook, H. Dai, *Nat. Nanotechnol.* **2012**, *7*, 394–400.
DOI:10.1038/nnano.2012.72
106. J. Benson, Q. Xu, P. Wang, Y. Shen, L. Sun, T. Wang, M. Li, P. Papakonstantinou, *ACS Appl. Mater. Interfaces* **2014**, *6*, 19726–19736. DOI:10.1021/am5048202
107. Z. Zhao, L. Zhang, C.-Y. Lin, Z. Xia: *Carbon-Based Metal-Free Catalysts*, **2018**, Wiley-VCH, Weinheim, Germany, pp. 1–33. DOI:10.1002/9783527811458.vol1-ch1
108. L. Zhang, Q. Xu, J. Niu, Z. Xia, *Phys. Chem. Chem. Phys.* **2015**, *17*, 16733–16743. DOI:10.1039/C5CP02014J
109. Y. Sun, L. Silvioni, N. R. Sahraie, W. Ju, J. Li, A. Zitolo, S. Li, A. Bagger, L. Arnarson, X. Wang, T. Moeller, D. Bernsmeier, J. Rossmeis, F. Jaouen, P. Strasser, *J. Am. Chem. Soc.* **2019**, *141*, 12372–12381. DOI:10.1021/jacs.9b05576
110. J. Shui, M. Wang, F. Du, L. Dai, *Sci. Adv.* **2023**, *1*, e1400129.
111. W. Chen, C. Ge, J. T. Li, J. L. Beckham, Z. Yuan, K. M. Wyss, P. A. Advincula, L. Eddy, C. Kittrell, J. Chen, D. X. Luong, R. A. Carter, J. M. Tour, *ACS Nano* **2022**, *16*, 6646–6656.
DOI:10.1021/acsnano.2c01136
112. S. Wang, L. Zhang, Z. Xia, A. Roy, D. W. Chang, J.-B. Baek, L. Dai, *Angew. Chem. Int. Ed.* **2012**, *51*, 4209–4212.
DOI:10.1002/anie.201109257
113. I.-Y. Jeon, H.-J. Choi, M. Choi, J.-M. Seo, S.-M. Jung, M.-J. Kim, S. Zhang, L. Zhang, Z. Xia, L. Dai, N. Park, J.-B. Baek, *Sci. Rep.* **2013**, *3*, 1810.
114. L. Zhang, J. Niu, M. Li, Z. Xia, *J. Phys. Chem. C* **2014**, *118*, 3545–3553. DOI:10.1021/jp410501u
115. C. Su, M. Acik, K. Takai, J. Lu, S. Hao, Y. Zheng, P. Wu, Q. Bao, T. Enoki, Y. J. Chabal, K. Ping Loh, *Nat. Commun.* **2012**, *3*, 1298.
116. Y. Zheng, Y. Jiao, Y. Zhu, L. H. Li, Y. Han, Y. Chen, A. Du, M. Jaroniec, S. Z. Qiao, *Nat. Commun.* **2014**, *5*, 3783.
DOI:10.1038/ncomms4783
117. J. Wan, Z. Zhao, H. Shang, B. Peng, W. Chen, J. Pei, L. Zheng, J. Dong, R. Cao, R. Sarangi, Z. Jiang, D. Zhou, Z. Zhuang, J. Zhang, D. Wang, Y. Li, *J. Am. Chem. Soc.* **2020**, *142*, 8431–8439. DOI:10.1021/jacs.0c02229
118. L. Qu, Y. Liu, J.-B. Baek, L. Dai, *ACS Nano* **2010**, *4*, 1321–1326. DOI:10.1021/nn901850u
119. L. Dai (Ed.): *Carbon-Based Metal-Free Catalysts*, Wiley-VCH, Weinheim, Germany, **2018**.
DOI:10.1002/9783527811458
120. D. Guo, R. Shibuya, C. Akiba, S. Saji, T. Kondo, J. Nakamura, *Science* **2016**, *351*, 361–365. DOI:10.1126/science.aad0832
121. M. Nosan, L. Pavko, M. Finšgar, M. Kolar, B. Genorio, *ACS Appl. Energy Mater.* **2022**, *5*, 9571–9580.
DOI:10.1021/acsaem.2c01184
122. J. Durst, A. Siebel, C. Simon, F. Hasché, J. Herranz, H. A. Gasteiger, *Energy Environ. Sci.* **2014**, *7*, 2255–2260.
DOI:10.1039/C4EE00440J
123. J. K. Nørskov, T. Bligaard, A. Logadottir, J. R. Kitchin, J. G. Chen, S. Pandalov, U. Stimming, *J. Electrochem. Soc.* **2005**, *152*, J23. DOI:10.1149/1.1856988
124. A. Lasia: *Handbook of Fuel Cells*, Wiley-VCH, Weinheim, Germany, **2010**.
125. H. N. Nong, L. J. Falling, A. Bergmann, M. Klingenhof, H. P. Tran, C. Spöri, R. Mom, J. Timoshenko, G. Zichittella, A. Knop-Gericke, S. Piccinin, J. Pérez-Ramírez, B. R. Cuenya, R. Schlögl, P. Strasser, D. Teschner, T. E. Jones, *Nature* **2020**, *587*, 408–413. DOI:10.1038/s41586-020-2908-2
126. A. E. Thorarinsdottir, S. S. Veroneau, D. G. Nocera, *Nat. Commun.* **2022**, *13*, 1243.
DOI:10.1038/s41467-022-28723-9
127. D. Liu, X. Li, S. Chen, H. Yan, C. Wang, C. Wu, Y. A. Haleem, S. Duan, J. Lu, B. Ge, P. M. Ajayan, Y. Luo, J. Jiang, L. Song, *Nat. Energy* **2019**, *4*, 512–518.
DOI:10.1038/s41560-019-0402-6
128. Y. Zheng, Y. Jiao, A. Vasileff, S. Qiao, *Angew. Chem. Int. Ed.* **2018**, *57*, 7568–7579. DOI:10.1002/anie.201710556
129. N. Dubouis, A. Grimaud, *Chem. Sci.* **2019**, *10*, 9165–9181.
DOI:10.1039/C9SC03831K
130. A. Grimaud, O. Diaz-Morales, B. Han, W. T. Hong, Y.-L. Lee, L. Giordano, K. A. Stoerzinger, M. T. M. Koper, Y. Shao-Horn, *Nat. Chem.* **2017**, *9*, 457–465.
DOI:10.1038/nchem.2695
131. J. Herranz, J. Durst, E. Fabbri, A. Patru, X. Cheng, A. A. Permyakova, T. J. Schmidt, *Nano Energy* **2016**, *29*, 4–28.
DOI:10.1016/j.nanoen.2016.01.027
132. R. Subbaraman, D. Tripkovic, D. Strmcnik, K.-C. Chang, M. Uchimura, A. P. Paulikas, V. Stamenkovic, N. M. Markovic, *Science* **2011**, *334*, 1256–1260.
DOI:10.1126/science.1211934
133. D. Strmcnik, P. P. Lopes, B. Genorio, V. R. Stamenkovic, N. M. Markovic, *Nano Energy* **2016**, *29*, 29–36.
DOI:10.1016/j.nanoen.2016.04.017
134. P. P. Lopes, D. Y. Chung, X. Rui, H. Zheng, H. He, P. Farinazzo Bergamo Dias Martins, D. Strmcnik, V. R. Stamenkovic, P. Zapol, J. F. Mitchell, R. F. Klie, N. M. Markovic, *J. Am. Chem. Soc.* **2021**, *143*, 2741–2750.
DOI:10.1021/jacs.0c08959
135. D. Y. Chung, P. P. Lopes, P. Farinazzo Bergamo Dias Martins, H. He, T. Kawaguchi, P. Zapol, H. You, D. Tripkovic, D. Strmcnik, Y. Zhu, S. Seifert, S. Lee, V. R. Stamenkovic, N. M. Markovic, *Nat. Energy* **2020**, *5*, 222–230.
DOI:10.1038/s41560-020-0576-y
136. J. Suntivich, K. J. May, H. A. Gasteiger, J. B. Goodenough, Y. Shao-Horn, *Science* **2011**, *334*, 1383–1385.
DOI:10.1126/science.1212858
137. Y. Zheng, Y. Jiao, Y. Zhu, L. H. Li, Y. Han, Y. Chen, A. Du, M. Jaroniec, S. Z. Qiao, *Nat. Commun.* **2014**, *5*, 3783.
DOI:10.1038/ncomms4783
138. Y. Jiao, Y. Zheng, K. Davey, S.-Z. Qiao, *Nat. Energy* **2016**, *1*, 16130. DOI:10.1038/nenergy.2016.130
139. Y. Zhao, R. Nakamura, K. Kamiya, S. Nakanishi, K. Hashi-

- moto, *Nat. Commun.* **2013**, *4*, 2390.
DOI:10.1038/ncomms3390
140. R. Czerw, M. Terrones, J.-C. Charlier, X. Blase, B. Foley, R. Kamalakaran, N. Grobert, H. Terrones, D. Tekleab, P. M. Ajayan, W. Blau, M. Rühle, D. L. Carroll, *Nano Lett.* **2001**, *1*, 457–460. DOI:10.1021/nl015549q
141. Z. Hou, X. Wang, T. Ikeda, K. Terakura, M. Oshima, M. Kakimoto, *Phys. Rev. B* **2013**, *87*, 165401.
DOI:10.1103/PhysRevB.87.165401
142. S. Chen, J. Duan, M. Jaroniec, S. Qiao, *Adv. Mater.* **2014**, *26*, 2925–2930. DOI:10.1002/adma.201305608
143. T. Y. Ma, S. Dai, M. Jaroniec, S. Z. Qiao, *Angew. Chem. Int. Ed.* **2014**, *53*, 7281–7285. DOI:10.1002/anie.201403946
144. K. Lee, J. Lim, M. J. Lee, K. Ryu, H. Lee, J. Y. Kim, H. Ju, H.-S. Cho, B.-H. Kim, M. C. Hatzell, J. Kang, S. W. Lee, *Energy Environ. Sci.* **2022**, *15*, 2858–2866.
DOI:10.1039/D2EE00548D
145. R. Orrù, R. Licheri, A. M. Locci, A. Cincotti, G. Cao, *Mater. Sci. Eng. R Rep.* **2009**, *63*, 127–287.
DOI:10.1016/j.mser.2008.09.003
146. S. Grasso, Y. Sakka, G. Maizza, *Sci. Technol. Adv. Mater.* **2009**, *10*, 053001. DOI:10.1088/1468-6996/10/5/053001
147. K. M. Wyss, Z. Wang, L. B. Alemany, C. Kittrell, J. M. Tour, *ACS Nano* **2021**, *15*, 10542–10552.
DOI:10.1021/acsnano.1c03197
148. K. M. Wyss, J. L. Beckham, W. Chen, D. X. Luong, P. Hundi, S. Raghuraman, R. Shahsavari, J. M. Tour, *Carbon* **2021**, *174*, 430–438. DOI:10.1016/j.carbon.2020.12.063
149. B. I. Jakobson, J. M. Tour, M. G. Stanford, K. V. Bets, D. X. Luong, P. A. Advincula, W. Chen, J. T. Li, Z. Wang, E. A. McHugh, W. A. Algozeeb, *ACS Nano* **2020**, *14*, 13691–13699.
DOI:10.1021/acsnano.0c05900
150. P. A. Advincula, D. X. Luong, W. Chen, S. Raghuraman, R. Shahsavari, J. M. Tour, *Carbon* **2021**, *178*, 649–656.
DOI:10.1016/j.carbon.2021.03.020
151. E. Benhelal, G. Zahedi, E. Shamsaei, A. Bahadori, *J. Clean Prod.* **2013**, *51*, 142–161. DOI:10.1016/j.jclepro.2012.10.049
152. A. Cantini, L. Leoni, F. De Carlo, M. Salvio, C. Martini, F. Martini, *Sustainability* **2021**, *13*, 3810.
DOI:10.3390/su13073810
153. P. A. Advincula, W. Meng, L. J. Eddy, J. L. Beckham, I. R. Siqueira, D. X. Luong, W. Chen, M. Pasquali, S. Nagarajiah, J. M. Tour, *Macromol. Mater. Eng.* **2023**, *308*, 2200640.
DOI:10.1002/mame.202200640
154. J. Y. Huang, S. Chen, Z. F. Ren, G. Chen, M. S. Dresselhaus, *Nano Lett.* **2006**, *6*, 1699–1705.
DOI:10.1021/nl0609910
155. X. Liu, L. Dai, *Nat. Rev. Mater.* **2016**, *1*, 16064.
DOI:10.1038/natrevmats.2016.64
156. K. M. Wyss, W. Chen, J. L. Beckham, P. E. Savas, J. M. Tour, *ACS Nano* **2022**.
157. X. Wang, G. Sun, P. Routh, D.-H. Kim, W. Huang, P. Chen, *Chem. Soc. Rev.* **2014**, *43*, 7067–7098.
DOI:10.1039/C4CS00141A
158. S. Dong, Y. Song, M. Su, G. Wang, *J. Chem. Eng.* **2024**, *481*, 147988. DOI:10.1016/j.cej.2023.147988
159. S. Dong, Y. Song, K. Ye, J. Yan, G. Wang, *EcoMat* **2022**, *4*, 12212. DOI:10.1002/eom2.12212
160. W. Chen, R. Salvatierra, J. Li, C. Kittrell, J. Beckham, *Adv. Mater.* **2023**, *8*, 2207303.
161. K. Wyss, D. Luong, J. Tour, *Adv. Mater.* **2022**, *8*, 2106970.
162. X. Zhu, L. Lin, M. Pang, M. Nat. Commun. **2024**, *15*, 3218.
DOI:10.1038/s41467-024-48591-9
163. W. Chen, J. Chen, K. Bets, R. Salvatierra, K. Wyss, *Sci. Adv.* **2023**, *9*, 5131. DOI:10.1126/sciadv.adh5131

Povzetek

Naraščajoče povpraševanje po trajnostnih in učinkovitih tehnologijah za pretvorbo energije zahteva stalno raziskovanje novih materialov in metod. Metoda Flash Joule (FJH) se pojavlja kot obetavna tehnika za množično proizvodnjo grafena, saj ponuja prednosti pred tradicionalnimi metodami. FJH hitro segreje ogljikove prekurzorje do ekstremnih temperatur z uporabo visokih električnih tokov, pri čemer se po hitrem ohlajanju tvori bliskoviti grafen. Ta pristop omogoča hitro obdelavo, visoko zmogljivost in uporabo različnih ogljikovih virov, vključno z biomaso in odpadki, kar ga naredi trajnostnega in stroškovno učinkovitega. Poleg tega ustvarja minimalne odpadke in proizvaja bliskoviti grafen z izboljšano prevodnostjo, kar je ključnega pomena za energetske aplikacije. Zaradi možnosti razširitve, vsestranskosti in učinkovitosti se FJH postavlja kot ključna metoda za komercializacijo grafena v različnih industrijah, zlasti pri pretvorbi energije. Ta pregled celovito obravnava principe sinteze FJH, s poudarkom na učinkovitosti, razširljivosti in trajnosti. Poleg tega analizira nedavne napredke pri elektrokatalizatorjih, temelječih na bliskovitem grafenu, in raziskuje njihov vpliv na obnovljivo energijo ter trajnostno elektrokatalizo. Obravnavani so izzivi in priložnosti, pri čemer so načrtane smernice za prihodnje raziskave. Nadaljnji napredek ima velik potencial za revolucijo v proizvodnji grafena in njegovo vključitev v energetske sisteme nove generacije, kar bo prispevalo k prehodu na čistejšo energetske rešitve.



Except when otherwise noted, articles in this journal are published under the terms and conditions of the Creative Commons Attribution 4.0 International License

Scientific paper

A Reliable Voltammetric Method Utilizing the Effect of an Anionic Surfactant for the Determination of Leuprolide

Begüm Evranos Aksöz¹ and Burcu Dogan Topal^{2,*} ¹ Suleyman Demirel University, Faculty of Pharmacy, Department of Pharmaceutical Chemistry, Isparta, Turkey² Ankara University, Faculty of Pharmacy, Department of Analytical Chemistry, Tandogan, Ankara, Turkey

* Corresponding author: E-mail: doganb@ankara.edu.tr

Received: 10-08-2021

Abstract

Leuprolide acetate is a synthetic gonadotropin-releasing hormone agonist used in the treatment of central precocious puberty, uterine fibroids, endometriosis, and prostate cancer. In this study, the rapid, simple, environmentally friendly, and sensitive voltammetric method was developed for the quantification of leuprolide acetate in the presence of an anionic surfactant on a glassy carbon electrode. The effect of surfactant types, pH, and scan rate on the voltammetric response of leuprolide acetate were evaluated. Using square wave voltammetry, two anodic peaks were observed at 0.81 V and 1.26 V for the glassy carbon electrodes at pH 3.70 (acetate buffer solution). The oxidation peak currents of leuprolide acetate were enhanced in the presence of 8.0×10^{-2} mM sodium dodecyl sulfate. The sodium dodecyl sulfate monomer can be drawn to amino moieties in the drug structure through electrostatic interaction. The voltammetric behavior of leuprolide acetate exhibited irreversible and diffusion-adsorption mix-controlled processes by cyclic voltammetry. All stripping conditions and square wave voltammetric parameters were optimized at pH 3.21 (phosphate buffer). Under optimized conditions, the proposed method exhibits linearity in the concentration range of 3.64×10^{-6} – 2.00×10^{-4} mM with a nano-level detection limit of 4.70×10^{-7} mM by square wave adsorptive stripping voltammetry. The developed method was applied for the determination of leuprolide acetate in a pharmaceutical dosage form with a satisfactory recovery of 97.72%.

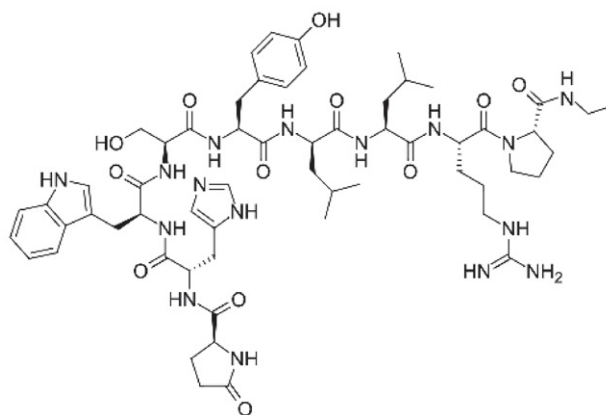
Keywords: Leuprolide acetate, voltammetry, determination, sodium dodecyl sulfate, validation

1. Introduction

Leuprolide acetate (LPA) in nonapeptide structure known by the chemical name 5-oxo-L-prolyl-L-histidyl-L-tryptophyl-L-seryl-L-tyrosyl-D-leucyl-L-leucyl-L-arginyl-N-ethyl-L-prolinamide acetate (Scheme 1) is a synthetic gonadotropin-releasing hormone agonist¹. It is more potent and durable to peptidases than the native hormone^{1,2}. LPA received its first FDA approval in 1985 for the symptomatic treatment of advanced prostate cancer. LPA acts to stimulate luteinizing hormone (LH) initially². But continuous utilization of LPA decreases gonadotropin-releasing hormone receptors' activity in the pituitary gland and causes complete suppression of LH, follicle-stimulating hormone and gonadal steroids. LPA is used in the treatment of central precocious puberty, uterine fibroids, endometriosis, in vitro fertilization and prostate cancer.

The elimination half-life of 1 mg LPA is 2.9 hours and 3.6 hours for intravenous injection and subcutaneous

injection, respectively. While the mean areas below the concentration-time curve are similar for short-acting leuprorelin subcutaneous or intravenous injection, a

**Scheme 1:** Structure of LPA

dose-dependent increase in the concentration-time curve was detected between 0 and 35 days after depot injection³. LPA binds to human plasma proteins at 43–49%. The maximum concentration of LPA is typically achieved 4–5 hours after injection regardless of the formulation and starting dose and varies widely in the range of 4.6–212.0 ng/mL. After administration of 3.75 mg of LPA depot suspension to 3 patients, less than 5% of LPA is excreted unchanged or as the pentapeptide metabolite in the urine.

The quantification of LPA has primarily been performed using methods based on liquid chromatography (LC) combined with mass spectrometry (MS)^{4–6}. A voltammetric method for the determination of LPA was developed by our group and the possible electrochemical mechanism of LPA was discussed⁷. The results revealed that the first oxidation process of LPA may occur on the hydroxyl group of the benzene ring of the molecule. It was concluded that a second oxidation step may occur on the nitrogen atom in the indole ring of the molecule leading finally to hydroxylation of the benzene ring.

The chromatographic studies need high volumes of organic solvents and time-consuming sample preparation procedures. Also, both LC and MS devices are expensive compared to electroanalytical instruments. The other advantages of electroanalytical methods include low sensitivity, low cost, environmentally friendly and short analysis time. The glassy carbon electrodes known for long-term stability can be used in drug analysis using electroanalytical methods. The surfactants that may provide significant enhancement of the response of drugs (even in trace quantities) were extensively utilized for various electroanalytical applications^{8–16}. The most valuable properties of surfactants in electrochemistry are the adsorption at interfaces and the aggregation into supra-molecular structures. For such properties, sodium dodecyl sulfate (SDS) is often employed, representing an anionic surfactant that contains a 12-carbon tail attached to a sulfate group.

The aim of this study was to develop the square wave adsorptive stripping (SWAdS) voltammetric method for the sensitive determination of LPA in the presence of SDS on a glassy carbon electrode (GCE). In addition, the proposed method was utilized for the quantification of LPA in pharmaceutical dosage forms.

2. Experimental

2.1. Apparatus and Electrochemical Procedure

PalmSens equipment (PSTrace 5.7) was used for electrochemical measurements. A GCE with a 3 mm diameter (working electrode, BAS MF-2012), a platinum wire (counter electrode, BAS MW-1032), and an Ag/AgCl (300 mM NaCl) (reference electrode, BAS MF-2052) were

used in the electrochemical cell. Experiments were implemented at room temperature. The GCE was polished with aluminium oxide slurry on a damp smooth polishing pad. A Model 538 (WTW, Austria) pH meter was used for all pH measurements.

Potential step was set at 5 mV, and the scan rate was set to 0.1 V/s for cyclic voltammetry. Differential pulse voltammetry (DPV) parameters were as follows: potential step: 5 mV; potential pulse: 20 mV; pulse time: 0.07s; scan rate 0.02V s⁻¹. Square wave voltammetry (SWV) parameters were potential step: 10 mV, amplitude: 0.1 V, frequency: 20 Hz.

The optimum conditions of square wave adsorptive stripping (SWAdS) voltammetry were found as a step potential of 18 mV; an amplitude of 100 mV; a frequency of 100 Hz; an accumulation potential of 200 mV, and an accumulation time of 180 s.

2.2. Chemicals

LPA was kindly supplied by Abbott Pharmaceutical Company (İstanbul, Turkey). Its pharmaceutical dosage form lucrin (5mg/mL), was purchased from a pharmacy. Cetyltrimethylammonium bromide (CTAB) (≥98%), SDS (≥99%), benzalkonium chloride (BAC) (≥95%), triton-X 100, tween 20, methanol, sulphuric acid, acetic acid, boric acid, phosphoric acid, sodium hydroxide and ultra-pure water were purchased from Merck (Darmstadt, Germany).

2.3. Preparation of Solutions

The stock solutions of 1.0×10^{-3} M SDS, BAC, triton-X 100, and tween 20 were freshly prepared in ultra-pure water and 1.0×10^{-3} M CTAB was prepared in methanol. Acetate buffer (pH 3.6–5.6), phosphate buffer (pH 2.0, 3.0, and pH 6.0–8.0), Britton-Robinson buffer solutions (BR, 0.4 M, pH 2.0–10.0), and 0.1 M sulphuric acid supporting electrolyte were prepared. All solutions were kept at 4 °C.

The stock solution of 1.0×10^{-3} M LPA was prepared in methanol. The working solutions of LPA (1.0×10^{-2} mM) were prepared by diluting the stock solution of LPA with buffer solution and 8.0×10^{-2} mM SDS containing 20% of methanol (v/v).

2.4. Analysis of LPA in Pharmaceutical Dosage Form

Adequate amount of lucrin injection solution (contain 5 mg LPA per mL of the solution) was dissolved in methanol to prepare the stock solution of 1.0×10^{-3} M injection solution.

The working solutions were prepared by diluting the stock solution of 1.0×10^{-3} M lucrin with pH 3.21 phosphate buffer solution and SDS containing 20% of methanol (v/v).

The nominal substance content in the pharmaceutical dosage form was determined using the regression data obtained from the calibration curve in concentration range from 3.64×10^{-6} to 2.00×10^{-4} mM. For recovery experiments, 2 mg of pure drug was added to the pharmaceutical dosage form, and % recovery was determined using the calibration regression data (More details are given in Section 3.5).

3. Results and Discussion

3.1. The Effect of Surfactant on Voltammetric Behaviour of LPA

Pulse techniques (DPV and SWV) were used to obtain the distinctive information on the voltammetric response of LPA. Due to the repeatable results, DPV was preferred to assess the effect of surfactant types on the electrochemical response of LPA on GCE. In acetate buffer (pH 3.70), LPA showed two anodic peak responses, namely, a first peak (E_{p1} , i_{p1}) and second peak (E_{p2} , i_{p2}) on bare GCE as seen in Table 1. The voltammetric behavior of 1.0×10^{-2} mM LPA was evaluated in the presence of 1.0×10^{-2} mM SDS, BAC, CTAB, Triton-X 100, and Tween 20 in acetate buffer (pH 3.70) (randomly selected) as seen in Table 1. The higher anodic peak currents of LPA were obtained in the presence of SDS. As a result of this study, SDS was chosen for all subsequent experiments. Table 1 shows that first peak current (i_{p1}) was significantly higher than the second peak current (i_{p2}) of LPA.

Table 1: The effect of surfactants on the voltammetric peak potentials and currents of LPA on GCE by DPV in acetate buffer (pH 3.70)

Surfactant types	E_{p1} (mV)	i_{p1} (μ A)	E_{p2} (mV)	i_{p2} (μ A)
–	0.821	0.083	1.249	0.035
SDS	0.806	0.192	1.310	0.048
Tween 20	0.816	0.115	–	–
Triton X-100	0.831	0.107	1.224	0.016
CTAB	0.831	0.114	1.284	0.006
BAC	0.841	0.074	–	–

3.2. The Effect of SDS Concentration on Voltammetric Response of LPA

The effect of SDS concentration on voltammetric responses of 1.0×10^{-2} mM LPA was performed in the range of 1.0×10^{-4} – 2.0×10^{-1} mM in acetate buffer (pH 3.70) using DPV and SWV. The critical micelle concentration of SDS is 8.2 mM. Once the concentration is lower than 8.2 mM, SDS is randomly dispersed as monomers in the aqueous solution¹⁹. Because of the higher peak current, SWV was selected to assess the effect of SDS concentration. As shown in Fig. 1, the i_{p1} of LPA en-

hanced with increasing concentration of SDS up to 8.0×10^{-2} mM and then i_{p1} was rather small. The high value of i_{p1} was obtained in the presence of 8.0×10^{-2} mM SDS, which was selected as the optimal concentration for subsequent experiments.

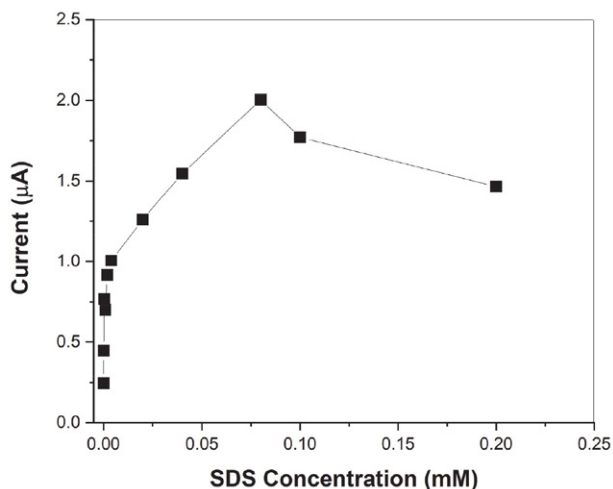


Figure 1: Effect of SDS concentration on i_{p1} of LPA (1.0×10^{-2} mM) in acetate buffer (pH 3.70) by SWV.

Fig. 2 depicts the effect of 8.0×10^{-2} mM SDS on the voltammograms of 1.0×10^{-2} mM LPA in acetate buffer (pH 3.70) by SWV. The i_{p1} of LPA was enhanced, and its peak potential (E_{p1}) slightly shifted to a less positive potential, while the i_{p2} of LPA also slightly increased and its peak potential shifted (E_{p2}) to a more positive potential (Fig. 2). It was concluded that the negatively charged SDS monomers can be attracted to the amino moiety on the LPA structure via electrostatic interaction¹⁷. Because of this interaction, more LPA molecules can rapidly reach the GCE surface, increasing the peak currents.

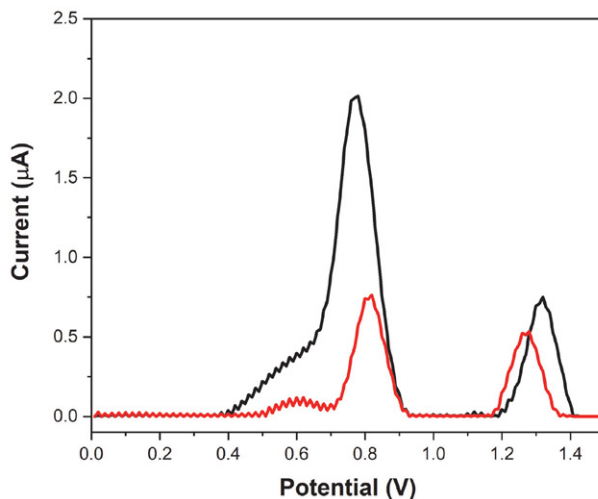


Figure 2: The SW voltammograms of LPA (1.0×10^{-2} mM) in the absence of SDS (red) and the presence (black) of SDS (8.0×10^{-2} mM) in acetate buffer (pH 3.70).

3. 3. The Influence of pH and Scan Rate on Voltammetric Response of LPA

The impact of pH on LPA response is significant for enlightening the voltammetric behaviour of LPA. The voltammetric responses of 1.0×10^{-2} mM LPA in the presence of 8.0×10^{-2} mM SDS in the pH range of 1.0–11.0 using acetate buffer, phosphate buffer, Britton-Robinson buffer solutions, and 0.1 M sulphuric acid supporting electrolyte were assessed by cyclic voltammetry, DPV, and SWV. Higher peak current was obtained using SWV, which was selected for further method development studies.

Fig. 3A exhibited the SW voltammograms of 1.0×10^{-2} mM LPA in the presence of 8.0×10^{-2} mM SDS in various pH values. The maximum i_p values were obtained in phosphate buffer with pH 3.21 (Fig. 3B), in which LPA showed two well-defined anodic peaks at 0.80 V (Ep_1) and

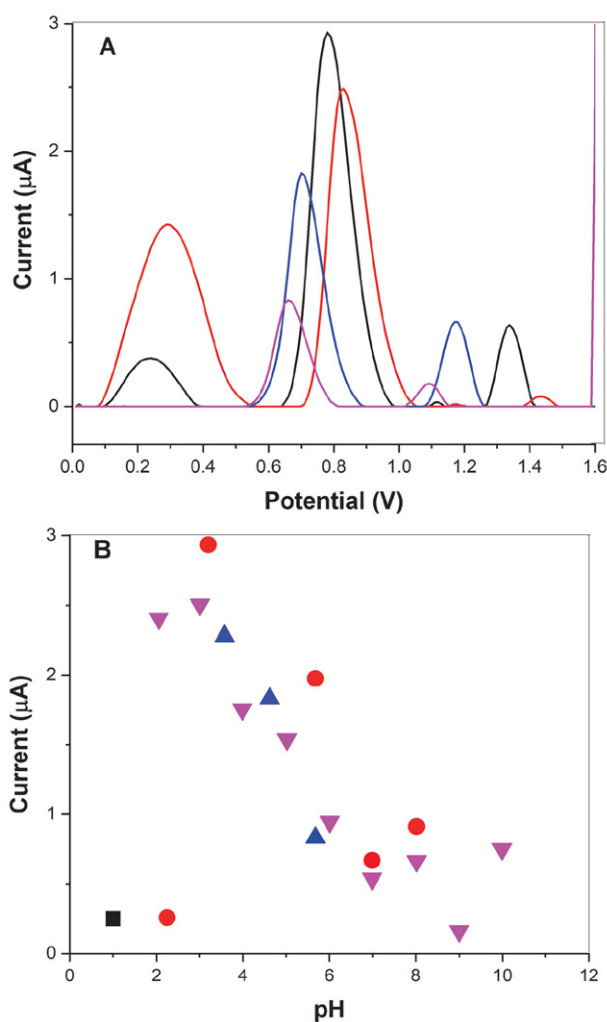


Figure 3: A: SW voltammograms of LPA (1.0×10^{-2} mM) in the presence of SDS (8.0×10^{-2} mM) on GCE at different pH values (pH 2.00 BR buffer (red), pH 3.21 phosphate buffer (black), pH 4.62 acetate buffer (blue), pH 5.68 acetate buffer (pink)). B: The effect of various supporting electrolyte and pH (▲: acetate buffer, ●: phosphate buffer, ▼: BR buffer, ■: 0.1M H_2SO_4) on i_{p1} (1.0×10^{-2} mM LPA).

1.35 V (Ep_2) (Fig. 3A). The i_{p1} of LPA was significantly higher than i_{p2} (Fig. 3A), which was selected for further method development studies.

By SWV, in the pH range of 1.0–9.0 (Figure 4), the Ep_1 and Ep_2 of LPA were shifted to lower positive values, which can be expressed by the following equations;

$$Ep_1 \text{ (V)} = -0.032 \text{ pH} + 0.872 \text{ (r: } -0.980) \quad (1)$$

$$Ep_2 \text{ (V)} = -0.073 \text{ pH} + 1.542 \text{ (r: } -0.989) \quad (2)$$

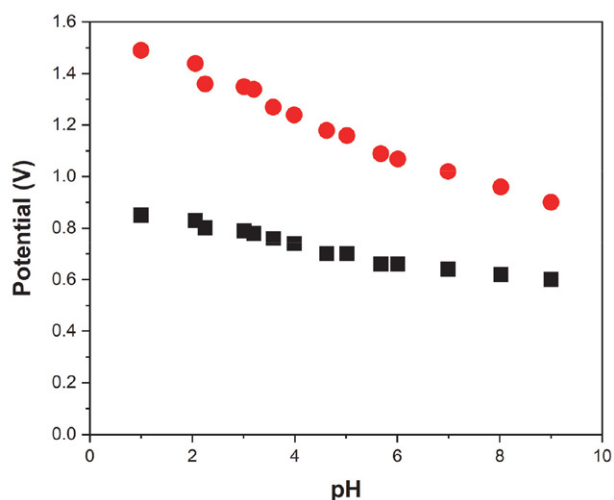


Figure 4: The effect of pH on Ep_1 (■, black color) and Ep_2 (●, red color) for LPA (1.0×10^{-2} mM) in the presence of SDS (8.0×10^{-2} mM).

This shifting indicated the changes in the acid-base protonation functions in LPA molecule.

The effect of scan rate on the first peak oxidation process of 4.0×10^{-2} mM LPA was investigated using cyclic voltammetry in the range of 0.005 – 0.5Vs^{-1} (Figure 5) in phosphate buffer (pH 3.21) in the presence of SDS (8.0×10^{-2} mM).

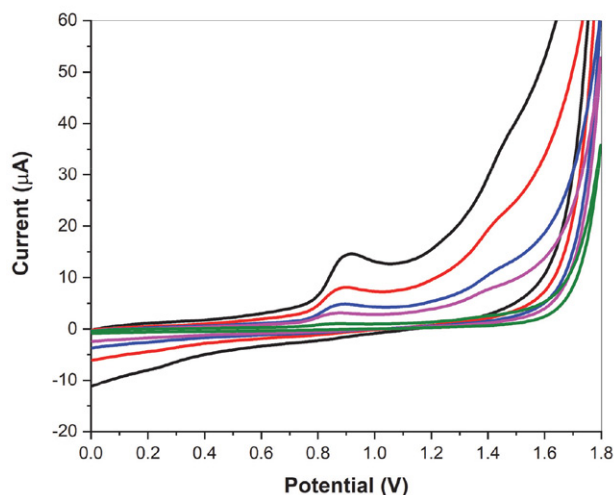


Figure 5: Cyclic voltammograms of LPA (4.0×10^{-2} mM) scanned at the following scan rates (mVs^{-1}); 500 (green), 200 (pink), 100 (blue), 50 (red) and 10 (black).

There was a linear relationship between ip_1 and the scan rate (ν) where n : number of data points as seen in the following equation;

$$ip_1 (\mu\text{A}) = 16.29 \nu (\text{Vs}^{-1}) + 0.703 \quad (r: 0.994; n: 9) \quad (3)$$

A plot of $\log ip_1$ - $\log \nu$ gave a straight line where n : number of data points as follows;

$$\log ip_1 (\mu\text{A}) = 0.69 \log \nu (\text{Vs}^{-1}) + 1.125 \quad (r: 0.999; n: 9) \quad (4)$$

The slope was found as 0.69. This suggests the electrochemical process was realized under diffusion-adsorption mixed controlled²¹.

3. 4. The Effect of Accumulation Potential/ Time and SWV Parameters on Peak Currents

Given that LPA may be adsorbed at the electrode surface, the influence of deposition potential (E_{acc}) and time (t_{acc}) were evaluated for LPA solution (1.0×10^{-3} mM) in the presence of SDS (8.0×10^{-2} mM) by SWV.

The t_{acc} was constant at 60 s, the effect of E_{acc} on peak currents was studied in the range from 0.0 to 1.5 V (Figure 6A). The 0.2 V was chosen due to the better repeatability and higher peak currents. Then the effect of t_{acc} on peak currents was varied in the range 0–360 s, and t_{acc} of 180 s was selected (Figure 6B). The optimal conditions of SWAdS voltammetric method were E_{acc} of 0.2 V and t_{acc} of 180 s.

The influence of parameters including step potential (E_{step}), frequency, and pulse amplitude on peak currents of 1.0×10^{-3} mM LPA in the presence of 8.0×10^{-2} mM SDS was evaluated. The step potential was selected in the range of 4 to 22 mV at a constant frequency of 20 Hz, amplitude of 100 mV, E_{acc} of 0.2 V, and t_{acc} of 180 s. The ip_1 and ip_2 increased up to 18 mV, which was chosen as the optimal value (Fig. 7A). The pulse amplitude varied from 10 to 150 mV, and the ip_1 and ip_2 were increasing up to 100 mV (Fig. 7B), which was chosen as the optimum. The effect of the frequency on peak currents was studied between 10–100 Hz and 100 Hz was chosen (Figure 7C).

3. 5. Analytical Method Development and Validation

Considering all the results thus far, due to the higher peak current, ip_1 of LPA was assessed for the development of the analytical method compared to ip_2 .

The LPA response improved in the presence of 8.0×10^{-2} mM SDS by performing deposition of 180 s at 0.2 V, step potential of 18 mV, pulse amplitude of 100 mV, and frequency of 100 Hz using the SWAdS voltammetric technique.

All analytical method validation parameters containing limit of detection (LOD), limit of quantification (LOQ), linearity, precision, and accuracy were calculated according to ICH guidelines¹⁷. The precision of the proposed method was evaluated in terms of repeatability and reproducibility by calculating the relative standard deviations (RSD %) with five replicates ($n = 5$). The accuracy of the proposed method was quantitatively given by the use of relative errors (Bias %) with three replicates ($n = 3$). LOD and LOQ values were calculated based on the following equations:

$\text{LOD} = 3s/m$; $\text{LOQ} = 10s/m$ where “ s ” is the standard deviation of the lowest concentration-response (three replicates) and m is the slope of the calibration line.

Using optimized conditions, the SWAdS voltammetric method was developed for the determination of LPA in the presence of SDS (8.0×10^{-2} mM) in phosphate buffer

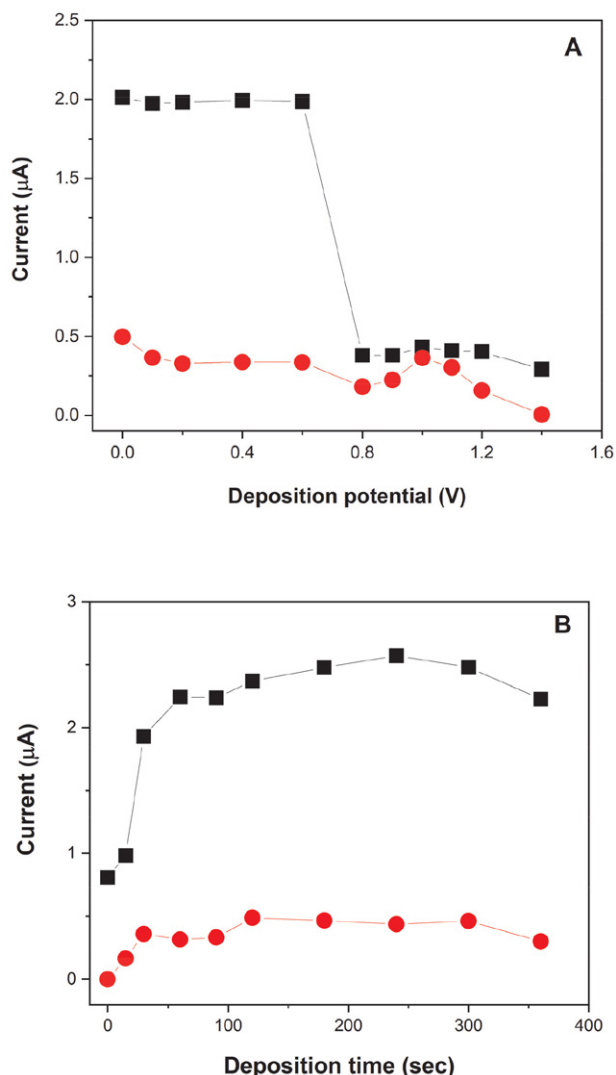


Figure 6: The effect of the E_{acc} (A) and t_{acc} (B) on ip_1 (■, black color) and ip_2 (●, red color) of LPA (1.0×10^{-3} mM) in phosphate buffer (pH 3.21) in the presence of SDS (8.0×10^{-2} mM) examined by SWAdV.

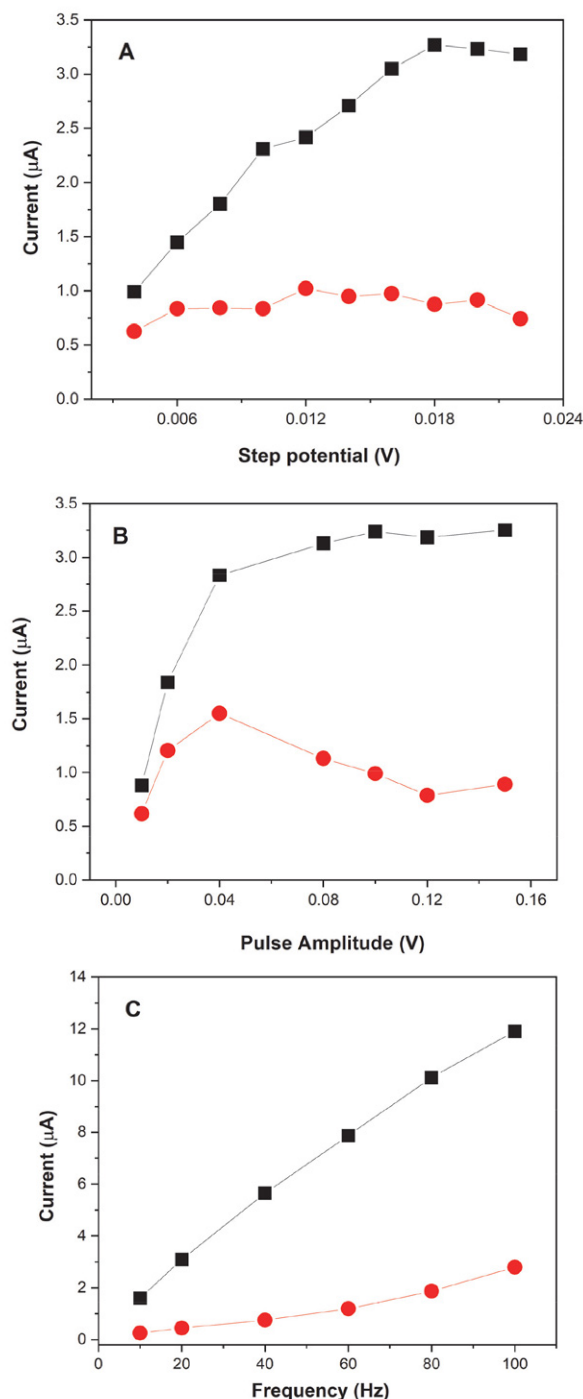


Figure 7: Influence of E_{step} (A), pulse amplitude (B), and frequency (C) on i_{p1} (■, black color) and i_{p2} (●, red color) of LPA (1.0×10^{-3} mM) in phosphate buffer (pH 3.21) in the presence of SDS (8.0×10^{-2} mM) examined by SWAdV.

(pH 3.21). The calibration curves were linear in the range from 3.64×10^{-6} – 2.00×10^{-4} mM. Equation for calibration curve was $i_p (\mu\text{A}) = 4.86 \times 10^7 C (\text{mM}) - 0.015$ with correlation coefficient of $r = 0.9986$. Some selected SWAdS voltammograms of calibration curve were given in Fig. 8. LOD was calculated to be 4.70×10^{-7} mM, while LOQ was calculated to be 1.42×10^{-6} mM. The RSD% \pm SE values of

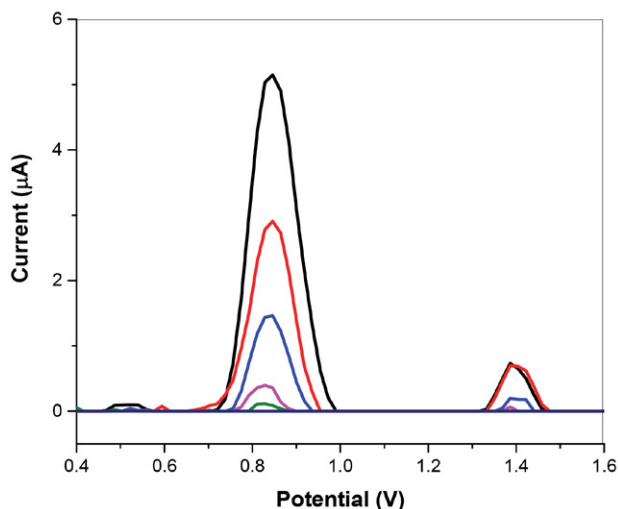


Figure 8: SWAd voltammograms of supporting electrolyte (purple), LPA levels of 1.0×10^{-5} mM (green), 2.0×10^{-5} mM (pink), 4.0×10^{-5} mM (blue), 8.0×10^{-5} mM (red), and 1.0×10^{-4} mM (black) at pH 3.21 (phosphate buffer) in the presence of 8.0×10^{-2} mM SDS.

repeatability and reproducibility of 5.46×10^{-5} mM LPA were 1.86 ± 0.05 and 2.11 ± 0.06 , respectively. The precision values suggest that the proposed method is convenient for quantification of LPA in pharmaceutical dosage forms.

For accuracy studies the developed method was applied to pharmaceutical dosage forms in the presence of SDS (8.0×10^{-2} mM) in phosphate buffer (pH 3.21). The sample preparation procedure was reported in the experimental part. The developed method was utilised to determine of LPA in pharmaceutical dosage forms (5mg/mL) without any matrix effects using the related linear regression equations of the bulk form. The recovery studies were performed by standard addition methods in which 2 mg of pure LPA solution were added to the pharmaceutical dosage form (Figure 9). The recovery parameters (Table 2) were calculated using the related calibration equations. The recovery value of 97.72% exhibited that the proposed method is free from interferences of the excipients in pharmaceutical dosage forms¹⁷.

Table 2: Analysis LPA in pharmaceutical dosage form and recovery studies.

Labeled claim (mg/mL)	5.00
Amount found ^a (mg/mL)	4.92 ± 0.05
RSD (%)	0.98
Bias (%)	-1.61
Added (mg)	2.00
Found ^a (mg)	1.95 ± 0.09
Average recovery (%)	97.72 ± 4.52
RSD (%) of recovery	4.63
Bias (%)	-2.28

^a Each value is the mean of three replicates given with standard error value

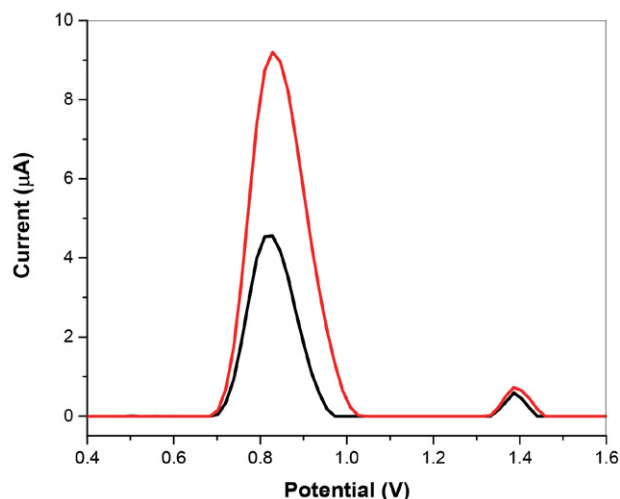


Figure 9: SWAdVs of labeled claim (black) and added amount (red) of LPA levels in pH 3.21 phosphate buffer in the presence of 8.0×10^{-2} mM SDS.

4. Conclusion

A reliable, sensitive, and low-cost SWAdS voltammetric method has been developed for the quantification of LPA in the presence of SDS on a glassy carbon electrode. The peak currents of LPA demonstrated higher sensitivity in the presence of 8.0×10^{-2} mM SDS. The monomer structure of anionic surfactant can be attracted to amino moieties in LPA structure via the electrostatic interaction. The developed method showed excellent analytical performance with nano-level detection limits and good reproducibility. The method enables measurement without time-consuming electrode modifications and sample pre-treatment. The developed method was administered for the determination of LPA in the pharmaceutical dosage form with satisfactory recovery. This simple and rapid electrochemical method may open the way for possible applications in the field of analytical chemistry for direct determination of LPA in pharmaceuticals.

5. References

- G. L. Plosker, R. N. Brogden, *Drugs* **1994**, *48*, 930–967. DOI:10.2165/00003495-199448060-00008
- P. Chrisp, E. M. Sorkin, *Drugs Aging* **1991**, *1*, 487–509. DOI:10.2165/00002512-199101060-00008
- P. Periti, T. Mazzei, E. Mini, *Clin. Pharmacokinet.* **2002**, *41*, 485–504. DOI:10.2165/00003088-200241070-00003
- Y. Zhan, X. Chen, X. Zhao, D. Zhong, *J. Chromatogr. B Anal. Technol. Biomed. Life Sci.* **2009**, *877*, 3194–3200. DOI:10.1016/j.jchromb.2009.08.023
- D. M. Xiong, S. L. Wen, H. Chen, X. Bao, L. M. Ye, *Asian J. Chem.* **2014**, *26*, 2321–2326. DOI:10.14233/ajchem.2014.15826
- M. Skiba, S. Fatmi, N. Elkasri, Y. Karrou, M. Lahiani-Skiba, *J. Chromatogr. B Anal. Technol. Biomed. Life Sci.* **2020**, *1160*, 122345. DOI:10.1016/j.jchromb.2020.122345
- B. Dogan-Topal, S. A. Ozkan, *Talanta* **2011**, *83*, 780–788. DOI:10.1016/j.talanta.2010.10.049
- P. Talay Pinar, Y. Yardım, Z. Şentürk, *Sensors Actuators, B Chem.* **2018**, *273*, 1463–1473. DOI:10.1016/j.snb.2018.07.068
- M. Zhu, R. Li, M. Lai, H. Ye, N. Long, J. Ye, J. Wang, *J. Electroanal. Chem.* **2020**, *857*. DOI:10.1016/j.jelechem.2019.113730
- A. M. Fekry, M. Shehata, S. M. Azab, A. Walcarius, *Sensors Actuators, B Chem.* **2020**, *302*, 127172. DOI:10.1016/j.snb.2019.127172
- S. Allahverdiyeva, P. Talay Pinar, E. Keskin, O. Yunusoğlu, Y. Yardım, Z. Şentürk, *Sensors Actuators, B Chem.* **2020**, *303*. DOI:10.1016/j.snb.2019.127174
- L. R. Rocha, J. de Cássica Mendonça, T. Boareto Capelari, R. Antigo Medeiros, C. R. Teixeira Tarley, *Sensors Actuators, B Chem.* **2020**, *310*, 127812. DOI:10.1016/j.snb.2020.127812
- X. Meng, Z. Xu, M. Wang, H. Yin, S. Ai, *Electrochim. Acta* **2013**, *95*, 200–204. DOI:10.1016/j.electacta.2013.02.050
- N. L. Teradal, S. S. Kalanur, S. N. Prashanth, J. Seetharamappa, *J. Appl. Electrochem.* **2012**, *42*, 917–923. DOI:10.1007/s10800-012-0473-6
- G. Ozcelikay, B. Dogan-Topal, S. A. Ozkan, *Electroanalysis* **2018**, *30*, 943–954. DOI:10.1002/elan.201700753
- C. E. Sener, B. Dogan Topal, S. A. Ozkan, *Anal. Bioanal. Chem.* **2020**, *412*, 8073–8081. DOI:10.1007/s00216-020-02934-9
- D. N. Lebard, B. G. Levine, R. DeVane, W. Shinoda, M. L. Klein, *Chem. Phys. Lett.* **2012**, *522*, 38–42. DOI:10.1016/j.cplett.2011.11.075
- D. K. Gosser, *Cyclic Voltammetry; Simulation and Analysis of Reaction Mechanisms*, VCH, **1994**, Vol. 24. DOI:10.1080/00945719408001398
- European Medicines Agency, *ICH Topic Q 2 (R1) Validation of Analytical Procedures: Text and Methodology, Step 5: Note for Guidance on Validation of Analytical Procedures: Text and Methodology (CPMP/ICH/381/95)*, **2006**, <http://www.emea.eu.int> (accessed January 8, 2021).

Povzetek

Leuprolid acetat (LA) je sintetični agonist gonadotropin sproščujočega hormona, ki se uporablja pri zdravljenju centralne prezgodnje pubertete, materničnih fibroidov, endometrioze in raka prostate. V tej študiji je bila razvita hitra, preprosta, okolju prijazna in občutljiva voltametrična metoda za kvantifikacijo LA v prisotnosti anionske površinsko aktivne snovi na elektrodi iz steklastega ogljika. Ovrednoten je bil vpliv površinsko aktivnih snovi, pH in hitrosti skeniranja na voltametrični odziv LA. Pri pH 3,70 (raztopina acetatnega pufra) sta bila z voltametrijjo s kvadratnim spreminjanjem potenciala ("square wave voltammetry") zaznana dva anodna vrha pri 0,81 V in 1,26 V. S "square wave" adsorptivno inverzno voltametrijjo ("square wave adsorptive stripping voltammetry") je bila pri optimiziranih pogojih umeritvena krivulja za LA linearna v koncentracijskem območju od $3,64 \times 10^{-6}$ do $2,00 \times 10^{-4}$ mM, meja zaznave pa je bila $4,70 \times 10^{-7}$ mM. Razvita metoda je bila uporabljena za določanje LA v farmacevtski obliki.



Except when otherwise noted, articles in this journal are published under the terms and conditions of the Creative Commons Attribution 4.0 International License

Scientific paper

Synthesis of Schiff Bases of Usnic Acid and Investigation of Their Antidiabetic, Antidepressant, Anti-Parkinson's Disease, Neuroprotective and Antioxidant Potentials

Lawali Yabo-Dambagi,^{1,*} Ahmet Cakir,^{2,3} Mehmet Akyuz,^{2,3}
Aysegul Karakucuk-Iyidogan¹ and Ali Aslan^{4,5}

¹ Department of Chemistry, Faculty of Science and Letters, Gaziantep University, Gaziantep, Türkiye

² Department of Chemistry, Faculty of Science, Kilis 7 Aralık University, 79000-Kilis, Türkiye

³ Advanced Technology Application and Research Center (ATARC), Kilis 7 Aralık University, 79000-Kilis, Türkiye

⁴ Department of Pharmacology, Faculty of Pharmacy, Yüzüncü Yıl University, 5080-Van, Türkiye

⁵ Department of Biology, Faculty of Arts and Science, Kyrgyz-Turkish Manas University, Bishkek, Kyrgyzstan

* Corresponding author: E-mail: dambagi91@gmail.com,
ld11012@mail2.gantep.edu.tr

Received: 02-16-2024

Abstract

Schiff bases have various pharmacological activities due to the azomethine ($-C=N-$) group. Usnic acid is the most famous lichen metabolite and it contains two carbonyl groups to synthesize the Schiff base derivatives with primary amines. Therefore, in the current study, the known Schiff base derivatives 2–5 of usnic acid (1) were synthesized to explore their antidiabetic, neuroprotective, antioxidant, antidepressant and anti-Parkinson's disease properties. Among the tested compounds, compound 4 exhibited the strongest antidiabetic and antidepressant activities, inhibiting α -glycosidase, α -amylase and MAO-A enzyme activities, respectively. Moreover, all of the tested compounds strongly scavenged the ABTS and DPPH radicals and the ABTS radical scavenging activities of 3 and 4 were found to be higher than the commercial antioxidants BHA and trolox. None of the tested compounds showed any significant anti-Parkinson's disease activity or neuroprotective action. In conclusion, compound 4 can be suggested as a drug candidate molecule for further studies due to its strong antioxidant, antidiabetic and antidepressant properties.

Keywords: Usnic acid; Schiff base; Biological activity; Antidiabetic; Antidepressant; Antioxidant

1. Introduction

Schiff bases or imine bases have been frequently used in various fields of industry, such as the paint industry, polymer technology, pharmaceutical industry, medicine, agriculture, preparation of rocket fuel, and explanation of biological events, as well as in many other areas due to the groups in their structures.¹ Schiff bases can be synthesized from an aliphatic or aromatic amine and a carbonyl compound by nucleophilic addition, forming a hemiaminal, followed by dehydration to generate an imine. They contain the imine or azomethine ($-C=N-$) group in their chemical structures. Schiff bases have been used in medicine for various pharmaceutical purposes, such as an-

ti-inflammatory, analgesic, antimicrobial, anticonvulsant, antituberculosis, anticancer, antioxidant and antihelminthic.^{1–8} Imine bases are also known as good nitrogen ligands due to their ability to form complexes with metal ions. These ligands provide one or more electron pairs to the metal ion during the coordination compound's formation. Schiff bases can form highly stable 4-, 5-, and 6-membered ring complexes if they donate more than one electron pair.^{2,9,10}

Medicinal plants or herbs have been used in the treatment of various diseases in traditional medicine practices since prehistoric times. The therapeutic properties of medicinal plants are frequently due to their secondary

metabolites.^{11,12} Although lichens and mosses are both called non-vascular plants, lichens are not plants. Lichens are a complex life form that is a symbiotic partnership of two separate organisms, a fungus and an alga. Lichens are widespread symbionts and play important roles in many terrestrial ecosystems due to their quick adaptation to all climatic and geographical conditions.¹³ Lichens, like plants, have been used in traditional medicine to treat various diseases since ancient times.^{14–16} Unlike plants, lichens synthesize unique and characteristic secondary metabolites such as dibenzofurans, diphenyl ethers, depsides, depsidones and the degradation products of depsides and depsidones etc.^{14,17–20} Usnic acid is a well-known metabolite synthesized by various lichen species and is notable for its diverse pharmacological properties, including analgesic, antibacterial, antiprotozoal, anti-inflammatory, antiulcer, anticholinergic, antiproliferative, and apoptotic effects against different cancer cell lines.^{21–32} Usnic acid has two carbonyl groups in its chemical structure and thus, its Schiff base derivatives can be synthesized via condensation reactions with primary amines.^{2–10,33–37} Therefore, in the current study, we aimed to evaluate the antidiabetic, antidepressant, anti-Parkinson's disease, anticholinesterases and antioxidant potentials of previously synthesized Schiff base derivatives of usnic acid with primary amines, 4-aminophenol, 3-aminophenol, 2-aminophenol and 4-aminomorpholine.

2. Experimental

2.1. Reagents and Instrumentation

Solvents and all of the required reagents used in the synthesis and isolation process were provided by Merck (Darmstadt, Germany), Riedel de Haen, Fluka and Sigma-Aldrich (St. Louis, MO, USA). The ¹H NMR spectra of the synthesized compounds were measured in DMSO-*d*₆ using a Bruker 400 MHz instrument. An Agilent (Cary 600 Series) (4000–400 cm⁻¹) instrument with an ATR attachment was used to obtain the FTIR spectra. Melting points were measured with a EZ-Melt apparatus. Bioassay experiments were recorded on a UV-Visible Spectrophotometer (T80 + UV PG Instrument Ltd.). Thin layer chromatography (TLC) was performed on the silica gel 60F-254 (Merck) plate. The spots on TLC were visualized with UV light (wavelengths of 365 and 254 nm), and spraying (1% vanillin-H₂SO₄) and then heating at 105 °C. Column chromatography (CC) was carried out using silica gel (Merck, 70–230 and 200–400 mesh).

2.2. Extraction of Lichen Sample and Isolation of Usnic Acid (1)

In this study, *Usnea longissima* used to isolate usnic acid was collected in the August–September period of 2021 from Northern Anatolian forests, then cleaned from other specimens and dried in a cool and shaded place by Dr. Ali

Aslan.²⁵ Dried thalluses were powdered using a laboratory blender. In order to isolate a sufficient amount of usnic acid to be used in the synthesis, the lichen sample (1.13 kg) was extracted with hexane (5 × 1.5 L) by maceration during 24 h at room temperature to remove chlorophyll and other lipophilic constituents (4.33 g, 0.38%). After extraction with the hexane, the lichen sample was macerated with CHCl₃ (5 × 5 L) at room temperature and the solvent was evaporated from the extract via a rotary evaporator at a low temperature (60 °C). Afterward, it yielded 35.35 g (3.04%) of the extract that consisted of a high amount of acicular yellow crystals of usnic acid.^{2,25} The crystals were quickly washed several times with hexane and then chloroform, and the purities of the chloroform phase and the crystals were controlled by TLC.

The chloroform phase containing usnic acid (1) with impurities was subjected to silica gel (70–230 mesh) column chromatography with CHCl₃ and CHCl₃-EtOAc (9:1) in order to isolate the remaining usnic acid (1) in the chloroform phase, and the fractions (25 mL) were checked by TLC. The fractions containing pure usnic acid (1) were combined, and the solvents were evaporated and weighed. At the end of the crystallization and chromatography processes, 25.35 g of usnic acid with a yield of 2.24% was purified as yellow acicular crystals.

2.3. Synthesis of the Schiff Bases 2–5

(*S,E*)-6-Acetyl-3,7,9-trihydroxy-2-(1-(4-hydroxyphenylimino)ethyl)-8,9b-dimethyldibenzo[*b,d*]furan-1(9*bH*)-one (2). In order to synthesize the Schiff base derivative of usnic acid and 4-aminophenol, usnic acid (2 g, 5.80 mmol) was dissolved in 25 mL of CHCl₃ in a two-neck glass balloon (70 °C) and added dropwise 4-aminophenol (0.634 g, 5.80 mmol) dissolved in methanol (25 mL) to the reaction medium every 10 minutes. The reaction was continued for 2 days at the same temperature (70 °C) by refluxing, and the medium was cooled to room temperature. At the end of the process, a yellowish product 2 precipitated, and then it was carefully separated from the liquid phase using a dropper. Yield: 2.28 g (86.56%) of yellowish solid; mp: 255 °C (decomp.). ¹H NMR (400 MHz, DMSO-*d*₆): δ 14.57 (s, 1H, OH₁), 13.36 (s, 1H, OH₂), 12.04 (s, 1H, OH₃, 8), 8.88 (s, 1H, OH₄, 4'), 7.17 (d, 2H, *J* = 8.68 Hz, 2' and 6'), 6.85 (d, 2H, *J* = 8.68 Hz, 3' and 5'), 5.89 (s, 1H, 4), 2.60 (s, 3H, 18), 2.49 (s, 3H, 15), 1.93 (s, 3H, 16), 1.65 (s, 3H, 13). ¹³C NMR (100 MHz, DMSO-*d*₆): 198.3 (1), 102.6 (2), 189.9 (3), 102.6 (4), 173.9 (5), 157.7 (6), 101.3 (7), 163.1 (8), 106.9 (9), 158.0 (10), 105.4 (11), 57.1 (12), 32.2 (13), 174.3 (14), 20.7 (15), 7.9 (16), 201.3 (17), 31.4 (18), 127.2 (1'), 127.3 (2'), 116.4 (3'), 156.1 (4'), 116.4 (5'), 127.3 (6'). FTIR (ATR, ν cm⁻¹): 3275 (strong Ar-OH bands), 3000–2860 (weak aliphatic C–H bands), 1689 and 1627 (C=O and –C=N– bands), 1600–1200 (aromatic C=C bands), 1200–1000 (C–O and C–N bands).² [α]_D²⁵ +141.2° (*c* = 0.08, CH₂Cl₂).

(S,E)-6-Acetyl-3,7,9-trihydroxy-2-(1-(3-hydroxyphenylimino)ethyl)-8,9b-dimethyldibenzo[b,d]furan-1(9bH)-one (3). Usnic acid (2 g, 5.80 mmol) was dissolved in 25 mL of CHCl_3 in two-neck glass balloon via refluxing (70 °C), and 3-aminophenol (0.634 g, 5.80 mmol) dissolved in 25 mL of methanol was added dropwise to the reaction medium every 10 minutes. The reaction mixture was refluxed at 70 °C for 2 days, and the reaction was visualized intervally by TLC with CH_2Cl_2 : ethyl acetate (9 : 1) mobile phase. At the end of the 2nd day, TLC showed that the spot belonging to usnic acid decreased and that of the product increased. In order to isolate the product, the reaction mixture (2.5 g) was fractionated over silica gel (30 g, 70–230 mesh) CC using CH_2Cl_2 : EtOAc (9 : 1), and the fractions (10 mL) were controlled on TLC using the same mobile phase. The fractions containing the product were collected, and the solvent was evaporated. Yield: 1.88 g (71.30%) of yellowish solid; mp: 220 °C (decomp.). ¹H NMR (400 MHz, DMSO-*d*₆): δ 14.72 (s, 1H, OH), 13.33 (s, 1H, OH), 11.92 (s, 1H, OH, 8), 9.97 (s, 1H, OH), 7.28 (t, 1H, *J* = 8.02 Hz, 5'), 6.81 (dd, 1H, *J*₁ = 8.19 Hz, *J*₂ = 1.88 and 1.92 Hz, 4'), 6.76 (d, 1H, *J*₁ = 7.92 Hz, 6'), 6.73 (d, 1H, *J*₁ = 1.84 Hz, 2'), 5.85 (s, 1H, 4), 2.56 (s, 3H, 18), 2.51 (s, 3H, 15), 1.91 (s, 3H, 16), 1.62 (s, 3H, 13). ¹³C NMR (100 MHz, DMSO-*d*₆): 198.5 (1), 102.7 (2), 190.1 (3), 102.5 (4), 173.9 (5), 157.9 (6), 101.2 (7), 163.1 (8), 107.0 (9), 158.8 (10), 105.3 (11), 57.1 (12), 32.1 (13), 174.2 (14), 20.8 (15), 7.9 (16), 201.1 (17), 31.4 (18), 137.1 (1'), 112.8 (2'), 156.0 (3'), 115.7 (4'), 130.9 (5'), 116.5 (6'). FTIR (ATR, ν cm⁻¹): 3400–3200 (Ar–OH bands), 3000–2850 (weak aliphatic C–H bands), 1694 and 1625 (C=O and –C=N– bands), 1600–1200 (aromatic C=C bands), 1100–1000 (C–O and C–N bands).² $[\alpha]_{\text{D}}^{23} +178.8^\circ$ (*c* = 0.08, CH_2Cl_2).

(S,E)-6-Acetyl-3,7,9-trihydroxy-2-(1-(2-hydroxyphenylimino)ethyl)-8,9b-dimethyldibenzo[b,d]furan-1(9bH)-one (4). In order to synthesize compound 4, 2 g of usnic acid (5.80 mmol) was dissolved in CHCl_3 (25 mL) in a two-neck glass balloon via refluxing at 70 °C, and 2-aminophenol (0.634 g, 5.80 mmol) dissolved in methanol (25 mL) was added dropwise to the reaction medium every 10 minutes. The reaction was refluxed at 70 °C for 3 days and was controlled intermittently with TLC using CH_2Cl_2 : hexane (8.5 : 1.5) and CH_2Cl_2 : EtOAc (9 : 1). At the end of the third day, the reaction mixture was cooled to room temperature, and the product 4 precipitated as a light brownish solid. The precipitate was carefully separated from the liquid part using a dropper, and then its purity was checked on TLC with CH_2Cl_2 : EtOAc (9 : 1). Yield: 2.18 g (82.76%); mp: 259 °C (decomp.). ¹H NMR (400 MHz, DMSO-*d*₆): δ 14.54 (s, 1H, OH), 13.37 (s, 1H, OH), 12.06 (s, 1H, OH, 8), 10.37 (s, 1H, OH), 7.28 (d, 1H, *J* = 7.88 Hz, 3'), 7.24 (td, 1H, *J*₁ = 7.82 and 7.76 Hz, *J*₂ = 1.15 and 1.40 Hz, 5'), 7.02 (d, 1H, *J* = 8.12 Hz, 6'), 6.90 (td, 1H, *J*₁ = 7.56 and 7.22 Hz, *J*₂ = 0.84 Hz, 4'), 5.93 (s, 1H, 4), 2.62 (s, 3H, 18), 2.50 (s, 3H, 15), 1.94 (s, 3H, 16), 1.67 (s, 3H,

13). ¹³C NMR (100 MHz, DMSO-*d*₆): 198.4 (1), 102.8 (2), 190.0 (3), 102.7 (4), 174.0 (5), 156.1 (6), 101.3 (7), 163.0 (8), 106.9 (9), 158.0 (10), 105.5 (11), 57.1 (12), 32.2 (13), 174.6 (14), 20.8 (15), 8.0 (16), 201.3 (17), 31.5 (18), 123.4 (1'), 152.0 (2'), 127.3 (3'), 119.8 (4'), 130.0 (5'), 116.9 (6'). FTIR (ATR, ν cm⁻¹): 3371 (Ar–OH bands), 3000–2850 (weak aliphatic C–H bands), 1687, 1624 and 1601 (strong C=O and –C=N– bands), 1600–1200 (strong aromatic C=C bands), 1100–1000 (strong C–O and C–N bands).² $[\alpha]_{\text{D}}^{23} +193.8^\circ$ (*c* = 0.08, CH_2Cl_2).

(S,E)-6-Acetyl-3,7,9-trihydroxy-8,9b-dimethyl-2-(1-(morpholinoimino)ethyl)dibenzo[b,d]furan-1(9bH)-one (5). For the synthesis of the Schiff base 5, usnic acid (3 g, 8.71 mmol) was dissolved in CHCl_3 (25 mL) at 70 °C using a two-neck glass balloon, and then 1.80 g (17.42 mmol) of 4-aminomorpholine dissolved in methanol (25 mL) was added dropwise to the reaction medium every 10 minutes. The reaction was refluxed (70 °C) for 3 days, and it was checked intermittently with TLC using CH_2Cl_2 : EtOAc (9 : 1). It was observed that the product 5 was synthesized at a high rate at the end of the 3rd day. The solvent was evaporated and the solid residue was subjected to silica gel (30 g, 70–230 mesh) CC with CH_2Cl_2 : EtOAc (9 : 1) and the collected fractions (15 mL) were controlled over TLC. Yield: 3.61 g (75.20%) of yellowish solid; mp 189–191 °C. ¹H NMR (400 MHz, DMSO-*d*₆): δ 14.62 (s, 1H, OH), 14.18 (s, 1H, OH), 11.43 (s, 1H, OH, 8), 5.71 (s, 1H, 4), 3.84 (m, 2H, 3' and 5'), 2.88 (m, 2H, 2' and 6'), 2.57 (s, 3H, 18), 2.15 (s, 3H, 18), 2.11 (s, 3H, 16), 1.67 (s, 3H, 13). ¹³C NMR (100 MHz, DMSO-*d*₆): 198.8 (1), 99.2 (2), 190.9 (3), 101.3 (4), 173.9 (5), 167.8 (6), 99.2 (7), 161.0 (8), 104.2 (9), 154.1 (10), 108.0 (11), 57.5 (12), 31.9 (13), 175.3 (14), 17.8 (15), 8.0 (16), 206.9 (17), 17.9 (18), 55.8 (2'), 65.9 (3'), 66.0 (5'), 55.4 (6'). FTIR (ATR, ν cm⁻¹): 3375 (Ar–OH bands), 3000–2800 (aliphatic C–H bands), 1639, 1624 and 1609 (strong C=O and –C=N– bands), 1600–1200 (strong aromatic C=C bands), 1100–1000 (strong C–O and C–N bands). $[\alpha]_{\text{D}}^{23} +233.8^\circ$ (*c* = 0.08, CH_2Cl_2).

2. 4. Enzyme Inhibition Assays

α -Glucosidase and α -amylase inhibition assays. α -Glucosidase and α -amylase enzyme measurements were made according to the previous methods,^{38,39} and the experimental details were published in our previous studies.^{6,40}

MAO sample preparation and MAO-A and MAO-B enzyme inhibition assays. A mitochondrial MAO sample was isolated by means of the previously described method from sheep liver.^{41,42} MAO-A and MAO-B enzymes inhibition tests were performed according to the previous method with minor modifications.⁴²

AChE and BChE enzyme inhibition assays. AChE and BChE enzyme measurements were made according to the previous method,⁴³ and the experimental details were published in our previous study.⁶

2. 5. Antioxidant Potentials

Radical scavenging activity. ABTS and DPPH radical scavenging activity assays of usnic acid and the synthesized Schiff bases were carried out according to the previous methods,^{38,39,43–45} and the experimental details were published in our previous studies.^{6,40,44}

Reducing powers. The experimental details for the total reducing powers of the Schiff bases and usnic acid were reported in our previous study.⁴⁴

3. Results and Discussion

3. 1. Synthesis of the Schiff Base Derivatives of Usnic Acid (1)

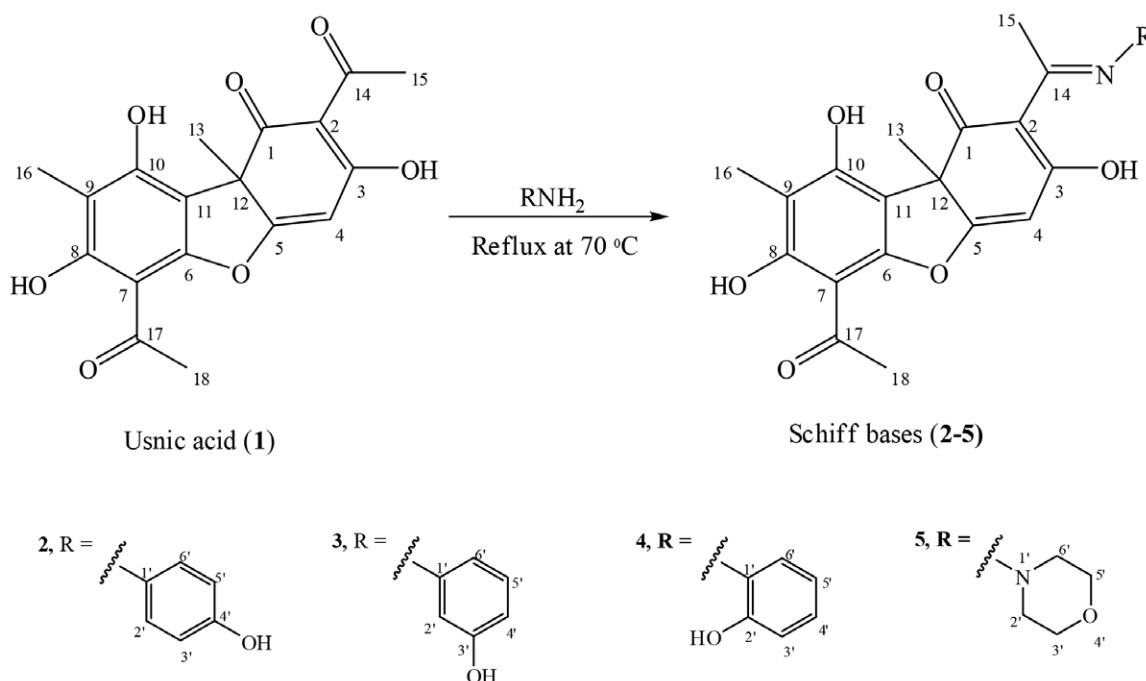
Schiff bases have different pharmacological activities such as anti-inflammatory, analgesic, antimicrobial, anti-convulsant, antituberculosis, anticancer, antioxidant, anti-helminthic, etc. due to the azomethine ($-C=N-$) group.^{1–8} Usnic acid is the most famous lichen metabolite, and it contains two carbonyl groups that enable the synthesis of the Schiff base derivatives with primary amines. Hence, in the literature, there are numerous reports on the Schiff bases derivatives of usnic acid synthesized with different primary amines and their various pharmacological activities.^{2,4,5,7,33–37} Therefore, in the current study, the known Schiff bases derivatives 2–5 of usnic acid (1) were synthesized via condensation reaction with 4-aminophenol, 3-aminophenol, 2-aminophenol and 4-aminomorpholine² (Scheme 1) to explore their new pharmacological activities. The chemical structures of the synthesized compounds

were characterized by means of FTIR, 1H and ^{13}C NMR, 1D- and 2D-NMR techniques (DEPT, APT 1H , 1H -COSY, HMQC and HMBC) and confirmed comparing with previously published spectroscopic data.^{2,4,5,7,35–37}

3. 2. Biological Activities of Usnic acid (1) and its Schiff Base Derivatives 2–5

3. 2. 1. Antidiabetic Activities

Diabetes is a chronic disease that occurs as a result of insulin production deficiency and/or insulin resistance and is characterized by hyperglycemia.^{46,47} Nowadays, uncontrolled hyperglycemia is considered one of the most important health problems, leading to blindness, amputation, kidney failure, heart attacks, retinopathy, neuropathy, nephropathy, stroke and lower limb amputation.^{46–50} There are two types of diabetes: type 1 (insulin-dependent) and type 2 (non-insulin-dependent).^{46,47} Type 2 diabetes corresponding to 80–90% of the patients—and is becoming more common gradually due to the increase in the world population, the aging of people in society, the increase in obesity and the sedentary lifestyle.^{49–52} Digestive enzymes, α -amylase and α -glucosidase, are primarily responsible enzymes for hyperglycemia in type 2 patients, and nowadays, the most preferred approach for the treatment of type 2 diabetes is to reduce hyperglycemia by inhibiting these enzymes after feeding.^{46,53–55} Herewith, in the current study, the inhibitory effects of the Schiff bases 2–5 and usnic acid (1) on α -glucosidase and α -amylase enzyme activities were investigated to explore potential new antidiabetic agent(s) (Table 1). The tested compounds exhibited



Scheme 1. The chemical structures of the Schiff bases derivatives 2–5 of usnic acid (1).

different inhibitory effects in a concentration-dependent manner on the digestive enzymes. Furthermore, IC_{50} and IC_{90} , whose low values point out a potent inhibitor, were computed to compare the inhibitory properties of the tested compounds and the antidiabetic agent acarbose on the digestive enzymes (Table 2). As shown in these tables, usnic acid (**1**) and the synthesized Schiff bases **2–5** exhibited a stronger inhibitory effect against the α -glycosidase enzyme compared to α -amylase. For instance, all of the tested compounds inhibited α -glycosidase at low concentrations with IC_{50} values of 0.21–1.32 mg/mL (0.48–3.08 mM). However, they showed significant inhibitory effects against α -amylase at much higher concentrations, with IC_{50} values ranging from 1.52 to 79.41 mg/mL (3.49–230.84 mM) (Table 2). Among the tested compounds, compound **2** (IC_{50} = 0.21 mg/mL, 0.48 mM) was found to be the strongest inhibitor for α -glycosidase, whereas compound **4** acted as the strongest inhibitor of both α -glycosidase (IC_{50} = 0.55 mg/mL, 1.26 mM) and α -amylase (IC_{50} = 1.52 mg/mL, 3.49 mM). These results suggest that compound **4** has an-

tidiabetic potential by inhibiting both digestive enzymes. Furthermore, our results indicate that usnic acid (**1**) and the Schiff bases **2–5** showed very strong inhibitory activity against α -glycosidase with lower IC_{50} values (0.21–1.32 mg/mL and 0.48–3.08 mM) compared to acarbose (IC_{50} = 22.41 mM and 14.47 mg/mL). On the other hand, acarbose was found to be more effective against α -amylase with an IC_{50} of 0.11 mg/mL compared to the inhibitory effects of usnic acid (**1**) and the Schiff bases **2–5**. Our findings are consistent with previous reports.^{6,40,44,56–58} Our results also reveal that the new functional groups introduced via azomethine bonds in usnic acid affect the antidiabetic activity of the synthesized compounds (Table 2). For instance, Schiff bases **2** (IC_{50} = 0.21 mg/mL), **3** (IC_{50} = 0.54 mg/mL), and **4** (IC_{50} = 0.55 mg/mL) were more effective against α -glycosidase than usnic acid (**1**) (IC_{50} = 0.67 mg/mL), whereas compound **5** (IC_{50} = 1.32 mg/mL) showed a weaker inhibitory effect compared to usnic acid (**1**). Similar results were also found against α -amylase; all synthesized Schiff bases **2–5**, with IC_{50} values ranging from 1.52

Table 1. Antidiabetic effects of usnic acid and the synthesized Schiff bases

Treatments	Conc. (mg/mL)	α -Glycosidase		Conc. (mg/mL)	α -Amylase	
		Abs \pm SS	Inh (%)		Abs \pm SS	Inh (%)
Enzyme + substrate	-	0.594\pm0.006f	-	-	0.433\pm0.008f	-
	0.156	0.522 \pm 0.004e	12.12*	10	0.397 \pm 0.08e	8.31
	0.312	0.422 \pm 0.006d	28.96*	20	0.370 \pm 0.005d	14.55*
Enzyme + substrate + 1	0.625	0.332 \pm 0.009c	44.10*	40	0.299 \pm 0.005c	30.95*
	1.25	0.052 \pm 0.009b	91.24*	80	0.227 \pm 0.007b	47.57*
	2.5	0.000 \pm 0.000a	100.00*	160	0.010 \pm 0.005a	97.69*
Enzyme + substrate	-	0.626\pm0.006e	-	-	0.446\pm0.011d	-
	0.062	0.488 \pm 0.006d	22.04*	10	0.240 \pm 0.011c	46.19*
	0.125	0.382 \pm 0.005c	38.97*	20	0.222 \pm 0.004c	50.22*
Enzyme + substrate + 2	0.25	0.228 \pm 0.005b	63.58*	40	0.146 \pm 0.003b	67.26*
	0.5	0.026 \pm 0.003a	95.84*	80	0.000 \pm 0.000a	100*
Enzyme + substrate	-	0.608\pm0.015e	-	-	0.356\pm0.003e	-
	0.125	0.559 \pm 0.010d	8.05	20	0.301 \pm 0.003d	15.45*
Enzyme + substrate + 3	0.25	0.504 \pm 0.006c	17.26*	40	0.205 \pm 0.002c	23.00*
	0.5	0.347 \pm 0.010b	42.93*	80	0.155 \pm 0.003b	56.00*
	1	0.006 \pm 0.000a	99.01*	160	0.000 \pm 0.000a	100*
Enzyme + substrate	-	0.363\pm0.011e	-	-	0.510\pm0.011e	-
	0.125	0.285 \pm 0.005d	21.49*	0.625	0.330 \pm 0.006d	35.30*
Enzyme + substrate + 4	0.25	0.247 \pm 0.003c	31.96*	1.25	0.258 \pm 0.017c	49.41*
	0.5	0.209 \pm 0.010b	42.42*	2.5	0.190 \pm 0.006b	62.74*
	1	0.061 \pm 0.004a	83.20*	5	0.000 \pm 0.000a	100*
Enzyme + substrate	-	0.369\pm0.037d	-	-	0.471\pm0.030e	-
	0.125	0.354 \pm 0.001d	4.06	20	0.337 \pm 0.003d	28.30*
	0.25	0.337 \pm 0.007d	8.67	40	0.256 \pm 0.003c	45.53*
Enzyme + substrate + 5	0.5	0.307 \pm 0.008c	16.80*	80	0.159 \pm 0.001b	66.17*
	1	0.231 \pm 0.006b	37.40*	160	0.000 \pm 0.001a	100*
	2	0.085 \pm 0.008a	76.80*			

Abs: Absorbance. Conc.: Concentration. Inh.: Inhibition. SD: Standard deviation.

*: Statistically different from enzyme + substrate applications ($p < 0.05$). The different letters in the lines are statistically different according to the Duncan test

to 77.33 mg/mL, acted as stronger inhibitors compared to usnic acid (**1**) ($IC_{50} = 79.41$ mg/mL) (Tables 1 and 2). In particular, compound **4** was noted to be a much stronger inhibitor of α -amylase, with IC_{50} values of 1.52 mg/mL and 2.58 mM. These results provide evidence that the new functional groups bonded to usnic acid (**1**) alter the interactions with the enzymes.

The previous reports indicated that the antidiabetic agents including acarbose, voglibose and miglitol strongly inhibit α -amylase but weakly inhibit α -glucosidase.^{40,56–58} These agents also have side effects including diarrhea and abdominal bloating and abdominal pain due to the strong inhibition of the α -amylase enzyme. Therefore, it is an important advantage in the treatment of type 2 diabetes that the α -glucosidase enzyme is strongly inhibited and the α -amylase enzyme is weakly inhibited.^{40,56–58} Tables 1 and 2 demonstrate that compounds **2**, **3**, and usnic acid (**1**) exhibited stronger inhibitory effects against α -glucosidase, while their inhibitory effects against α -amylase were comparatively weaker. Hereof, these compounds (**1**, **2**, and **3**) can also be recommended as potential antidiabetic agents besides compound **4**. Furthermore, it has been documented that potent α -glucosidase inhibitors can be used in the treatment of obesity as a result of slowing down glucose absorption from the blood.^{59,60} Hence, usnic acid (**1**) and the synthesized Schiff bases **2–5** are the potential molecules to be used in the treatment of obesity.

(N_2O_3).^{64,65} It is well known that ROS damage functional molecules such as DNA, proteins and lipids, which have important functions in tissues by leading to the oxidative stress.^{61–65} Cardiovascular diseases, cancer, diabetes, ischemia, asthma, arthritis, inflammation, rapid aging, Parkinson's, and Alzheimer's diseases are the diseases associated with the oxidative stress caused by ROS.^{61–66} Living organisms have an oxidant/antioxidant balance against the damage of ROS, whereas some external factors like depression, environmental pollution, radiation, an unbalanced diet, pesticides, drugs and smoking may disrupt this balance in favor of oxidants.^{64,65,67} Hence, it could be mandatory to use external antioxidants as a diet and/or medication to prevent or at least delay the development of the diseases mentioned above.^{31,32,64,65,67,69,70} It has been documented that the lichen metabolite, usnic acid (**1**) has some pharmacological properties closely related to oxidative stress.^{19,20,25,28,31,70–74}

The DPPH assay evaluates the capacity of antioxidants to scavenge free radicals by donating hydrogen, while the ABTS assay assesses antioxidant activity through a single-electron transfer mechanism. Previous research has demonstrated a lack of direct correlation between the outcomes of these two assays, suggesting that they evaluate antioxidant properties through different mechanisms. The DPPH and ABTS tests differ in their sensitivity to various types of antioxidants, and therefore, it is necessary to ap-

Table 2. IC_{50} and IC_{90} values for antidiabetic effects of the treatments

Treatments	α -Glycosidase				α -Amylase			
	IC_{50} (mg/mL) (mM)		IC_{90} (mg/mL) (mM)		IC_{50} (mg/mL) (mM)		IC_{90} (mg/mL) (mM)	
Acarbose*	14.47	22.41	29.66	45.94	0.11		0.23	
Usnic Acid (1)	0.67	1.95	1.24	3.61	79.41	230.84	147.77	429.56
synthesized Schiff bases								
2	0.21	0.48	0.45	1.03	17.33	39.84	68.02	156.37
3	0.54	1.24	0.93	2.14	77.33	177.56	141.80	325.98
4	0.55	1.26	1.12	2.58	1.52	3.49	4.31	9.91
5	1.32	3.08	2.34	5.46	54.76	127.94	135.73	317.13

*The data was acquired from our previous reports.⁶

3. 2. 2. Antioxidant Potentials

Reactive oxygen species (ROS) as unstable and highly reactive molecules are produced in normal or pathological cell metabolism as a result of cellular oxidation and play an important role in the pathogenesis of various diseases by causing tissue and organ damage.^{61–63} The most common types of ROS are the superoxide ($O_2^{\bullet-}$), peroxy (ROO^{\bullet}), hydroxyl (OH^{\bullet}), hydroperoxyl (HO_2^{\bullet}) and alkoxy (RO^{\bullet}), hydrogen peroxide (H_2O_2), ozone (O_3), singlet oxygen (1O_2), hypochlorous acid (HOCl), peroxytrite ($ONOO^-$), nitric acid (HNO_2) and nitrogen trioxide

ply both methods to comprehensively assess the antioxidant potential of samples.^{38,39,43–45} Thus, in the present research, the ABTS and DPPH radical scavenging potentials of the Schiff base derivatives **2–5** and usnic acid (**1**) were evaluated for the first time and the results are presented in Tables 3 and 4. As can be seen from these tables, usnic acid (**1**) and the synthesized Schiff bases **2–5** strongly scavenged the ABTS radicals with very low IC_{50} values ($IC_{50} = 0.002$ – 0.41 mM and 0.001 – 0.18 mg/mL). In particular, the ABTS radical scavenging activities of the Schiff bases **3** ($IC_{50} = 0.002$ mg/mL, 0.05 mM) and **4** ($IC_{50} = 0.001$ mg/mL, 0.002 mM) were found to be higher than the com-

Table 3. Radical scavenging effects of usnic acid and the synthesized Schiff base molecules

Treatments	Conc. (mg/mL)	DPPH Abs±SS	Scavenging (%)	Conc. (ppm)	ABTS Abs±SS	Scavenging (%)	
Control	-	0.502±0.007f	-	-	0.747±0.010f	-	
	1.25	0.344±0.002e	31.47*	31.25	0.447±0.006e	40.16*	
	2.5	0.332±0.004d	33.86*	62.5	0.354±0.002d	52.61*	
	5	0.317±0.008c	36.85*	125	0.284±0.006c	61.98*	
Usnic acid (1)	10	0.299±0.008b	40.44*	250	0.050±0.005b	93.19*	
	20	0.245±0.006a	51.20*	500	0.000±0.000a	100*	
	Control	-	0.450±0.006e	-	-	0.878±0.007e	-
	0.312	0.419±0.003d	6.89	62.5	0.613±0.005d	30.18*	
2	0.625	0.357±0.004c	20.67*	125	0.511±0.006c	41.80*	
	1.25	0.174±0.007b	61.33*	250	0.315±0.009b	64.12*	
	2.5	0.000±0.000a	100*	500	0.000±0.000a	100*	
	Control	-	0.443±0.004e	-	-	0.420±0.005e	-
3	1.25	0.286±0.006d	35.44*	6.25	0.203±0.011d	51.67*	
	2.5	0.266±0.005c	39.96*	12.5	0.155±0.006c	63.10*	
	5	0.236±0.006b	46.73*	25	0.103±0.008b	75.48*	
	10	0.199±0.005a	55.08*	50	0.000±0.000a	100*	
Control	-	0.437±0.002e	-	-	0.455±0.010f	-	
	0.125	0.346±0.004d	20.82*	1.25	0.231±0.010e	49.23*	
	0.25	0.261±0.002c	40.27*	2.5	0.207±0.006d	54.51*	
	0.5	0.189±0.003b	56.75*	5	0.188±0.003c	58.68*	
4	1	0.000±0.000	100*	10	0.118±0.006b	74.07*	
	20			20	0.005±0.001a	98.90*	
	Control	-	0.515±0.005e	-	-	0.601±0.006e	-
	10	0.367±0.006d	26.41*	12.5	0.513±0.002d	14.64	
5	20	0.367±0.008c	28.74*	25	0.472±0.006c	21.46*	
	40	0.348±0.007b	32.43*	50	0.358±0.006b	38.60*	
	80	0.305±0.011a	40.78*	100	0.190±0.006a	68.38	

* Abs: Absorbance. SD: Standard deviation. *: Statistically different from control application ($p < 0.05$). The different letters in the lines are statistically different according to the Duncan test

mercial antioxidants, BHA ($IC_{50} = 0.05$ mg/mL, 0.28 mM) and trolox ($IC_{50} = 0.07$ mg/mL, 0.28 mM). The current results also demonstrate that the groups newly bound to usnic acid (1) provide an enhancing effect on the ABTS radical scavenging activity when compared to the ABTS radical scavenging activities of the synthesized ligands 2–5 and usnic acid (1). However, Table 4 shows that the synthesized compounds 2–5 and usnic acid (1) exhibited reduced DPPH radical scavenging activities in contrast to their ABTS radical scavenging activities. As indicated by Table 4, both usnic acid (1) ($IC_{50} = 54.91$ mM and 18.89 mg/mL) and the Schiff bases 2–5 ($IC_{50} = 0.96$ – 293.22 mM and 0.42– 125.50 mg/mL) acted as weaker DPPH radical scavenging agents when compared to the commercial antioxidants, BHA ($IC_{50} = 0.83$ mM and 0.16 mg/mL) and trolox ($IC_{50} = 0.48$ mM and 0.12 mg/mL). On the other hand, the compounds 2–4 exhibited higher DPPH radical scavenging activities with lower IC_{50} values (0.42– 7.30 mg/mL, 0.96– 16.78 mM) compared to usnic acid (1) (Table 4). In accordance with the previous report,⁶ these present results demonstrate that the new hydroxyphenylimino

groups bound to usnic acid (1) have an enhancing effect on the DPPH radical scavenging activity. Nonetheless, the compound 5 displayed a weaker DPPH radical scavenging effect with $IC_{50} = 293.22$ mM, 125.50 mg/mL than usnic acid (1) ($IC_{50} = 18.89$, 54.91 mM). These findings conclude that the carbonyl group in the usnic acid (1) is more effective in DPPH radical scavenging than the $-CH=N-$ (azomethine) group. In conclusion, as can be seen from Table 4, the ligands 2–4 can be proposed as potent radical scavenging agents. However, further studies are needed to evaluate their safety and toxicities.

Another method to assess an agent's potential for antioxidant activity is the FRAP method, which is based on the reduction of iron(III) ions to iron(II) ions. According to this method, the high absorbance due to the high concentration of iron(II) measured in the medium indicates a high reduction potential.⁷⁵

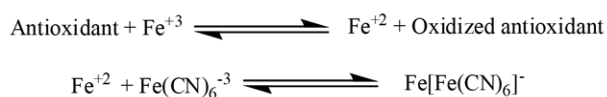


Table 4. IC₅₀ and IC₉₀ values for radical scavenging activities of the all treatments

Treatments	DPPH				ABTS			
	IC ₅₀ (mg/mL) (mM)		IC ₉₀ (mg/mL) (mM)		IC ₅₀ (mg/mL) (mM)		IC ₉₀ (mg/mL) (mM)	
BHA*	0.16	0.83	0.28	1.55	0.05	0.28	0.09	0.50
Trolox*	0.12	0.48	0.22	0.88	0.07	0.28	0.13	0.52
Usnic acid (1)	18.89	54.91	58.55	170.20	0.065	0.18	0.238	0.68
synthesized Schiff bases								
2	1.23	2.82	2.07	4.75	0.18	0.41	0.43	0.98
3	7.30	16.78	25.64	58.94	0.002	0.05	0.04	0.09
4	0.42	0.96	0.88	2.02	0.001	0.002	0.016	0.04
5	125.50	293.22	323.54	755.93	0.07	0.16	0.13	0.30

*The data was acquired from the previous reports published by our research group.⁶

Hereof, in the current investigation, the reducing powers of usnic acid (1) and the synthesized Schiff bases 2–4 were also evaluated via the FRAP method and the results are shown in Figure 1. As shown in this figure, the synthesized ligands 2–5 and usnic acid (1) showed lower reducing power than BHA and trolox. However, the compound 4 displayed the highest and noteworthy reducing power among the tested compounds.

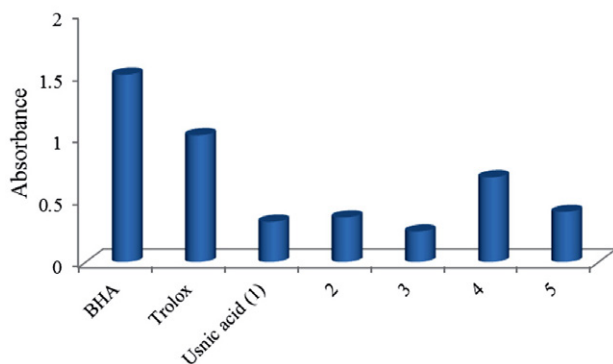


Figure 1. The reducing powers of the compounds 1–5

3. 2. 3. Antidepressant and anti-Parkinson's Disease Activities

Depression or major depressive disorder is a common and serious mental illness that negatively affects how you feel, the way you think, and how you act. Depression causes feelings of sadness and/or a loss of interest in activities you once enjoyed. Depression can lead to various emotional and physical problems such as feeling sad, weight loss or gain due to a lifestyle change, sleeping problems, increased fatigue, purposeless physical activities, feeling guilty and worthless, indecision, and thoughts of death or suicide.^{76–78} Moreover, it can be seen in all age and gender groups, and many patients are not aware of it.^{76–79} The syndromes observed in depressed patients are closely related to the decrease in the levels of some biogenic amine neu-

romediators such as serotonin, dopamine and noradrenaline in the central nervous system.^{77,78,80,81} It has also been shown that the levels of biogenic amines, serotonin, noradrenaline, norepinephrine, dopamine, catecholamines, homovalinic acid, and 5-OH indole acetic acid present in the blood, urine and brain fluids of patients suffering from depression are outside the normal range.^{77,78,80,81} Monoamine oxidases (MAO-A and MAO-B) in the cells are the enzymes responsible for catalyzing the oxidative deamination of the neurotransmitters and their levels increase with age in humans.^{78,82–85} It is well known that the decrease in the levels of neurotransmitters in the central nervous system causes the depressive syndroms as a result of increased activity of MAO's, in particular MAO-A.^{81–83} Hereof, in the present study, the inhibitory effects of different concentrations of the synthesized compounds 2–5 and usnic acid (1) were tested for the first time on MAO-A to reveal new potential antidepressant agent(s) (Table 5). The inhibitory potentials of the compounds were also compared with those of the positive control, clorgyline HCl (a selective MAO-A inhibitor). The IC₅₀ and IC₉₀ values for each treatment are also presented in Table 6. As can be seen from Table 6, clorgyline with an IC₅₀ value of 1.29 mg/mL (4.18 mM) was found to be a stronger inhibitor than usnic acid (1) (IC₅₀ = 5.70 mg/mL, 16.57 mM) and the synthesized compounds 2–5 (IC₅₀ = 3.18–14.83 mg/mL, 7.31–34.10 mM). However, among the tested compounds, compound 4 with an IC₅₀ value of 3.18 mg/mL (7.31 mM) exhibited the strongest antidepressant effect by displaying a remarkable inhibitory effect after clorgyline on MAO-A enzyme activity. Considering the IC₅₀ values presented in Table 6, the inhibition effects of the Schiff bases 2–5 were found to be lower than that of usnic acid (1) except for compound 4. These can be accounted for by the fact that the interaction with MAO-A is altered by the new groups bound to usnic acid (1).

We now know that MAO-B-catalyzed bioreactions raise the amount of H₂O₂ in cells.^{86,87} H₂O₂ is a neurotoxic substance that is involved in the pathogenicity of a number of illnesses, including depression, social anxiety,

Parkinson's, and Alzheimer's disease.^{86–88} Thus, selective MAO-A inhibitors are frequently used in the treatment of neurodegenerative diseases such as depression and social anxiety, while selective MAO-B inhibitors are usually preferred in the treatment of Parkinson's, and Alzheimer's diseases.^{79,83,86–91} In the current study, the inhibitory effects of the synthesized compounds 2–5 and usnic acid (1) at different concentrations were investigated for the first time on MAO-B and their inhibition effects were also compared

with a selective MAO-B inhibitor, pargyline HCl (Table 5). The IC₅₀ and IC₉₀ values for each treatment were also calculated (Table 6). As shown in this table, usnic acid (1) and its derivatives 2–5 acted as weak inhibitors with very high IC₅₀ values of 24.31–94.87 mg/mL or 55.86–264.80 mM as compared with pargyline (IC₅₀ = 5.06 mg/mL, 25.86 mM). Moreover, none of the tested compounds acted as selective inhibitors against MAO's and they were found to be stronger inhibitors against MAO-A in comparison to

Table 5. Antidepressant and anti-Parkinson's disease properties of usnic acid (1) and the synthesized Schiff bases 2–5

Treatments	MAO-A			MAO-B		
	Conc. (mg/mL)	Abs±SD (%)	Inh (mg/mL)	Conc. (%)	Abs±SD	Inh
Enzyme + substrate	-	0.474±0.004e	-	-	0.486±0.004e	-
Enzyme + substrate + 1	1.25	0.456±0.004d	3.80	20	0.438±0.009d	9.88
	2.5	0.408±0.010c	13.92*	40	0.389±0.005c	19.96*
	5	0.250±0.001b	47.26*	80	0.230±0.003b	52.67*
	10	0.033±0.003a	93.04*	160	0.081±0.001a	83.33*
Enzyme + substrate	-	0.562±0.007e	-	-	0.309±0.003e	-
Enzyme + substrate + 2	10	0.269±0.005d	52.14*	20	0.285±0.004d	7.77
	20	0.204±0.004c	63.70*	40	0.263±0.004c	14.89*
	40	0.033±0.005b	94.13*	80	0.123±0.00b	36.23*
	80	0.000±0.000a	100*	120	0.024±0.003a	92.23*
Enzyme + substrate	-	0.693±0.002e	-	-	0.374±0.006e	-
Enzyme + substrate + 3	5	0.479±0.001d	30.88*	5	0.361±0.008de	3.21
	10	0.440±0.001c	36.51*	10	0.332±0.010d	11.23*
	20	0.242±0.001b	65.08*	20	0.270±0.008c	27.81*
	40	0.007±0.006a	98.99*	40	0.154±0.012b	58.82*
	80	0.000±0.000a	100*			
Enzyme + substrate	-	0.496±0.010d	-	-	0.356±0.012f	-
Enzyme + substrate + 4	0.625	0.468±0.001cd	5.64	2.5	0.339±0.005e	4.76
	1.25	0.446±0.002c	10.08*	5	0.322±0.001d	9.55
	2.5	0.284±0.001b	42.74*	10	0.300±0.004c	15.73*
	5	0.094±0.003a	81.04*	20	0.171±0.003b	51.97*
	40	0.078±0.002a	78.09*			
Enzyme + substrate	-	0.498±0.007e	-	-	0.372±0.005e	-
Enzyme + substrate + 5	5	0.387±0.003d	22.29*	10	0.342±0.003d	8.06
	10	0.285±0.005c	42.77*	20	0.306±0.002c	17.74*
	20	0.072±0.002b	85.54*	40	0.207±0.001b	44.35*
	40	0.000±0.000a	100*	80	0.077±0.001a	79.30*
Enzyme + substrate	-	0.587±0.013f	-	-	0.431±0.004e	-
Enzyme + substrate + clorgyline	0.312	0.512±0.005e	12.78*			
	0.625	0.458±0.008d	21.98*			
	1.25	0.261±0.003c	55.54*			
	2.5	0.044±0.0004b	92.50*			
	5	0.000±0.000a	100.00*			
Enzyme + substrate				-	0.431±0.004e	-
Enzyme + substrate + pargyline				2.5	0.270±0.003d	37.35*
				5	0.215±0.002c	50.12*
				10	0.115±0.003b	73.32*
				20	0.000±0.000a	100.00*

Abs: Absorbance. SD: Standard deviation.

*:Statistically different from control application ($p < 0.05$). The different letters in the lines are statistically different according to the Duncan test.

MAO-B. These results point out that usnic acid (**1**) and the synthesized Schiff bases **2–5** do not have anti-Parkinson's disease activity due to their weak and non-selective inhibitory effects on MAO-B activity. Nevertheless, new 4-hydroxyphenylimino and 3-hydroxyphenylimino groups bound to usnic acid (**1**) ($IC_{50} = 91.09$ mg/mL, 264.80 mM) via an azomethine bond significantly increased the inhibition effect of the compounds **4** ($IC_{50} = 34.31$ mg/mL, 78.87 mM) and **3** ($IC_{50} = 24.31$ mg/mL, 55.86 mM) on the MAO-B activity.

It has been reported in the literature that pargyline and chlorgyline are potent inhibitors with extremely low IC_{50} values.^{6,28,92,93} However, in the current study, the IC_{50} values were calculated as higher values for chlorgyline ($IC_{50} = 1.29$ mg/mL, 4.18 mM) and pargyline ($IC_{50} = 5.06$ mg/mL, 25.86 mM). This could be accounted for by variations in the assaying techniques employed.^{6,28,92,93} Likewise, previously, 0.34 mg/mL and 1.25 mM IC_{50} values for chlorgyline were determined using a different assay method.⁶

nausea, vomiting, agitation, diarrhea, loose stools, night-time vivid dreams, dehydration, skin rash, bradycardia, peptic ulcer, seizures, weight loss, rhinorrhea, salivation, muscle cramps, and fasciculations.^{98,100,103,104} Therefore, further studies focused on new cholinesterase inhibitors that are safer and have fewer side effects are still important for human health.

Hence, in the present work, the inhibition effects of usnic acid (**1**) and the Schiff bases **2–5** at different concentrations were evaluated on AChE and BChE activities for the first time to discover new potentially neuroprotective compounds (Table 7). The IC_{50} and IC_{90} calculated for usnic acid (**1**), the Schiff bases **2–5** and commercial anticholinesterases, neostigmine and galantamine are also presented in Table 8. As shown in this table, the IC_{50} values for usnic acid (**1**) and the compounds **2–5** were determined to be very high with values 54.64–688.69 mM (23.77–294.76 mg/mL) and 24.81–56.12 mM (10.79–24.41 mg/mL) when compared with the inhibitory effects of neostigmine ($IC_{50} = 2.87$ mM, 0.64 mg/mL) and galantamine ($IC_{50} = 16.63$

Table 6. IC_{50} and IC_{90} values for the antidepressant, anti-Parkinson's disease effects of the treatments

Treatments	MAO-A				MAO-B			
	IC_{50} (mg/mL)	(mM)	IC_{90} (mg/mL)	(mM)	IC_{50} (mg/mL)	(mM)	IC_{90} (mg/mL)	(mM)
Chlorgyline HCl	1.29	4.18	2.37	7.68	-	-	-	-
Pargyline HCl	-	-	-	-	5.06	25.86	10.42	53.24
Usnic acid (1)	5.70	16.57	9.56	27.79	91.09	264.80	166.45	483.87
Synthesized Schiff bases								
2	9.23	21.22	37.45	86.09	94.87	218.09	159.91	367.60
3	14.83	34.10	34.78	79.75	34.31	78.87	59.48	136.73
4	3.18	7.31	5.42	12.46	24.31	55.86	43.90	100.92
5	11.62	27.15	21.09	49.28	49.82	116.40	88.82	207.52

3. 2. 4. Neuroprotective Effects

Alzheimer's disease is the most common dementia disease in older adults with a prevalence of 10% after the age of 65.^{94,95} Physical and mental behavioral disorders such as language, writing and reading difficulties, and memory loss are observed in Alzheimer's disease patients due to the gradual loss of cells in some parts of the brain.^{66,96–98} The loss of cholinergic neurotransmitters, acetylcholine (ACh) and butyrylcholine (BCh) in the brain is known to be one of the main causes of Alzheimer's disease.^{96–100} There is also evidence that the brain tissues of Alzheimer's disease patients have higher concentrations of the enzymes AChE and BChE, which use ACh and BCh, respectively, as substrates.^{98,99,101} Nowadays, the enhancement of cholinergic neurotransmission by the inhibition of cholinesterases is the main approach in the symptomatic treatment of Alzheimer's disease and dementia.^{96,98–102} The most widely used agents as cholinesterase inhibitors are donepezil, rivastigmine, and galantamine; however, they are associated with some side effects like appetite loss,

mM, 4.78 mg/mL).⁶ These results conclude that neither usnic acid (**1**) nor its derivatives **2–5** have any noteworthy neuroprotective potential as compared with commercial anticholinesterases. However, our results demonstrated that the new functional groups added to usnic acid (**1**) affect the neuroprotective activities of the synthesized compounds **2–5** (Tables 7 and 8). In particular, hydroxyphenylimino ligand derivatives **2–4** of usnic acid acted as stronger AChE enzyme inhibitors with 23.77–45.00 mg/mL or 103.44–54.64 mM of IC_{50} values than usnic acid (**1**) ($IC_{50} = 94.03$ mg/mL, 273.34 mM). On the other hand, the ligand **5** displayed a much weaker inhibitory effect with $IC_{50} = 294.76$ mg/mL or 688.69 mM against the AChE enzyme than usnic acid (**1**). Similar results for the treatments were also obtained against BChE activity (Table 8). As can be seen from Table 8, the inhibition effects of the synthesized compounds **2–5** with lower IC_{50} values ($IC_{50} = 10.79–24.41$ mg/mL, 24.81–56.12 mM) were found to be higher than that of usnic acid (**1**) ($IC_{50} = 38.61$ mg/mL, 112.24 mM).

Table 7. Neuroprotective effects of usnic acid (1) and the synthesized Schiff bases 2–4

Treatments	AChE			BChE		
	Conc. (mg/mL)	Abs±SS	Inh (%) (mg/mL)	Conc.	Abs±SS	Inh (%)
Enzyme + substrate	-	0.498±0.003e	-	-	0.374±0.003e	-
	20	0.462±0.007d	7.23	10	0.332±0.009d	11.23*
Enzyme + substrate + Usnic acid (1)	40	0.428±0.004c	14.06*	20	0.248±0.006c	33.69*
	80	0.302±0.003b	39.36*	40	0.169±0.005b	54.81*
	160	0.036±0.002a	92.77*	80	0.010±0.002a	97.33*
Enzyme + substrate	-	0.688±0.008f	-	-	0.390±0.006f	-
	10	0.517±0.015e	24.85*	5	0.345±0.014e	11.54
Enzyme + substrate + 2	20	0.395±0.009d	42.58*	10	0.287±0.010d	26.41*
	40	0.279±0.006c	59.44*	20	0.204±0.014c	47.69*
	80	0.086±0.003b	87.5*	40	0.090±0.006b	76.92*
	160	0.020±0.005a	97.07*	80	0.000±0.000a	100*
Enzyme + substrate	-	0.423±0.006e	-	-	0.378±0.012e	-
	20	0.218±0.007d	48.46*	10	0.318±0.005d	17.20*
Enzyme + substrate + 3	40	0.157±0.003c	62.88*	20	0.202±0.005c	46.50*
	80	0.017±0.006b	95.98*	40	0.052±0.005b	86.24*
	160	0.000±0.000a	100*	80	0.000±0.000a	100*
Enzyme + substrate	-	0.398±0.005e	-	-	0.336±0.007e	-
	20	0.317±0.009d	20.35*	5	0.239±0.009d	27.98*
Enzyme + substrate + 4	40	0.235±0.008c	40.95*	10	0.188±0.008c	44.04*
	80	0.020±0.002b	94.98*	20	0.037±0.006b	88.98*
	160	0.000±0.000a	100*	40	0.000±0.000a	100*
Enzyme + substrate	-	0.474±0.006d	-	-	0.370±0.004f	-
	40	0.452±0.013d	4.64	5	0.333±0.008e	10.00*
Enzyme + substrate + 5	80	0.412±0.010c	13.08*	10	0.285±0.011d	22.92*
	160	0.256±0.004b	24.89*	20	0.204±0.004c	44.60*
	320	0.214±0.006a	54.85*	40	0.075±0.005b	78.67*
				80	0.000±0.000a	100*

Abs: Absorbance. Conc.: Concentration. Inh.: Inhibition. SD: Standard deviation. *: Statistically different from enzyme + substrate applications ($p < 0.05$). The different letters in the lines are statistically different according to the Duncan test

Table 8. IC₅₀ and IC₉₀ values for the neuroprotective effects of the all treatments

Treatments	AChE				BChE			
	IC ₅₀		IC ₉₀		IC ₅₀		IC ₉₀	
	(mg/mL)	(mM)	(mg/mL)	(mM)	(mg/mL)	(mM)	(mg/mL)	(mM)
Neostigmine*	0.64	2.87	2.42	10.84	0.03	0.10	0.06	0.20
Galantamine*	4.78	16.63	15.31	53.34	0.31	1.08	0.94	3.28
Usnic acid (1)	94.03	273.34	157.83	458.81	38.61	112.24	71.91	209.04
Synthesized Schiff bases								
2	33.26	76.46	80.41	184.85	23.91	54.97	45.95	105.63
3	23.77	54.64	69.99	160.90	23.25	53.45	41.16	94.62
4	45.00	103.44	76.77	176.48	10.79	24.81	20.49	47.10
5	294.76	688.69	520.62	1216.40	24.41	56.12	45.11	103.70

*The data was acquired from the previous reports published by our research group.⁶

4. Conclusions

In the current study, the Schiff base derivatives 2–5 of a famous lichen metabolite, usnic acid (1) were synthe-

sized via the condensation reaction with 4-aminophenol, 3-aminophenol, 2-aminophenol and 4-aminomorpholine. The antidiabetic, antioxidant, antidepressant, anti-Parkinson's disease and neuroprotective activities of the com-

pounds were also evaluated for the first time. Our results conclude that the compound **4** was found to be a drug candidate molecule for further investigations due to its potent antidiabetic and antioxidant potentials, besides its noteworthy antidepressant effect.

Acknowledgements

The authors would like to more thanks Dr. Cavit Kazaz (Atatürk University) and Dr. Tuba Aydın (Ağrı İbrahim Çeçen University) for acquiring NMR spectra of the synthesized compounds.

Research Funding

The authors are grateful to the Scientific Research Project Governing Unit (BAPYB) of Gaziantep University (Project No. FEF.DT.22.11) for financial support of this research.

Conflicts of interest

The authors wish to confirm that there are no known conflicts of interest associated with this publication.

5. References

1. N. T. Subasi, in: T. Akitsu (Ed.): Schiff Base in Organic, Inorganic and Physical Chemistry, IntechOpen, **2022**. DOI:10.5772/intechopen.108178
2. S. Koçer, S. Uruş, A. Çakır, M. Güllüce, M. Dığrak, Y. Alan, A. Aslan, M. Tümer, M. Karadayı, C. Kazaz, H. Dal, *Dalton Trans.* **2014**, 43(16), 6148–6164. DOI:10.1039/C3DT53624F
3. X. J. Zhao, L. W. Xue, Q. R. Liu, *Acta Chim. Slov.* **2023**, 70, 524–532. DOI:10.17344/acsi.2023.8370
4. A. Pyrczak-Felczykowska, R. Narlawar, A. Pawlik, B. Guzow-Krzemińska, D. Artymiuk, A. Hac, K. Rys, L. M. Rendiņa, T. A. Reekie, A. Herman-Antosiewicz, M. Kassiou, *J. Nat. Prod.* **2019**, 82, 1768–1778. DOI:10.1021/acs.jnatprod.8b00980
5. E. Susithra, R. Meena, D. Chamundeeswari, Ch. Rajasekhar, J. Naveena Lavanya Latha, M. V. Basaveswara Rao, *Polycycl. Aromat. Compd.* **2022**, 42(8), 5020–5028.
6. N. Yuldasheva, N. Acikyildiz, M. Akyuz, L. Yabo-Dambagi, T. Aydın, A. Cakir, C. Kazaz, *J. Mol. Struct.* **2022**, 1270, 133883. DOI:10.1016/j.molstruc.2022.133883
7. G. A. Gunawan, G. Mariola, M. G. Gardiner, A. Herman-Antosiewicz, T. A. Reekie, *Bioorg. Med. Chem.* **2023**, 79, 117–157. DOI:10.1016/j.bmc.2023.117157
8. I. Tsacheva, Z. Todorova, D. Momekova, G. Momekov, N. Koseva, *Pharmaceuticals*, **2023**, 16(7), 938. DOI:10.3390/ph16070938
9. A. Kajal, S. Bala, S. Kamboj, N. Sharma, V. Saini, *J. Catal.* **2013**, 893512. DOI:10.1155/2013/893512
10. P. J. Sheetal, H. H. Kailas, S. D. Amruta, P. H. Apoorva, *World J. Pharm. Res.* **2017**, 6(12), 1361–1368.
11. T. Baytop, *Therapy with Medicinal Plants in Turkey*, Nobel Tıp Kitapevleri, İstanbul, Türkiye, **1999**.
12. P. M. Dewick, *Medicinal Natural Products: A Biosynthetic Approach*. John Wiley & Sons, Chichester, United Kingdom, **2009**. DOI:10.1002/9780470742761
13. U. Zeybek, V. John, *Pharmacia-JTPA* **1992**, 32, 37–38. DOI:10.1002/j.2161-007X.1992.tb00378.x
14. D. H. S. Richardson, in: M. Galun (Ed.): *Handbook of Lichenology*, CRC Press, Boca Raton, FL, USA, **1988**, pp. 1–16
15. A. Aslan, K. Yazici, Y. Karagoz, *Isr. J. Plant Sci.* **2002**, 50(1), 77–81. DOI:10.1092/RRXU-EX5Y-QRXX-H1HA
16. B. Dulger, F. Gucin, A. Kara, A. Aslan, *Turk. J. Biol.* **1997**, 21, 103–108. DOI:10.55730/1300-0152.2534
17. S. Huneck, I. Yoshimura, *Identification of Lichen Substances*, Springer Verlag, Berlin, Germany, **1996**. DOI:10.1007/978-3-642-85243-5
18. S. Huneck, *Naturwissenschaften* **1999**, 86, 559–576. DOI:10.1007/s001140050676
19. F. Atalay, M. Halici, A. Mavi, A. Cakir, F. Odabasoglu, C. Kazaz, A. Aslan, O. I. Kufrevioglu, *Turk. J. Chem.* **2011**, 35(4), 647–661.
20. Y. Bayir, F. Odabasoglu, A. Cakir, A. Aslan, H. Suleyman, M. Halici, C. Kazaz, *Phytomedicine* **2006**, 13, 584–590. DOI:10.1016/j.phymed.2005.07.002
21. E. Okuyama, K. Umeyama, M. Yamazaki, Y. Kinoshita, Y. Yamamoto, *Planta Med.* **1995**, 61(2), 113–115. DOI:10.1055/s-2006-958027
22. S. Kumar, K. Muller, *J. Nat. Prod.* **1999**, 62(6), 821–823. DOI:10.1021/np980378z
23. K. Ingolfsdottir, *Phytochemistry* **2002**, 61(7), 729–736. DOI:10.1016/S0031-9422(02)00383-7
24. C. Bezivin, S. Tomasi, I. Rouaud, J. G. Delcros, J. Boustie, *Planta Med.* **2004**, 70(9), 874–877. DOI:10.1055/s-2004-827240
25. F. Odabasoglu, A. Cakir, H. Suleyman, A. Aslan, Y. Bayir, M. Halici, C. Kazaz, *J. Ethnopharmacol.* **2006**, 103, 59–65. DOI:10.1016/j.jep.2005.06.043
26. E. Einarsdottir, J. Groeneweg, G. G. Bjornsdottir, G. Hardardottir, S. Omarsdottir, K. Ingolfsdottir, H. M. Ogmundsdottir, *Planta Med.* **2010**, 76(10), 969–974. DOI:10.1055/s-0030-1264341
27. N. K. Honda, F. R. Pavan, R. G. Coelho, S. R. de Andrade Leite, A. C. Micheletti, T. I. B. Lopes, M. Y. Misutsu, A. Beatriz, R. L. Brum, C. Q. F. Leite, *Phytomedicine* **2010**, 17(5), 328–332. DOI:10.1016/j.phymed.2009.07.018
28. K. C. Cakmak, I. Gulcin, *Toxicol. Rep.* **2019**, 6, 1273–1280. DOI:10.1016/j.toxrep.2019.11.003
29. A. Galanty, P. Pasko, I. Podolak, *Phytochem. Rev.* **2019**, 18, 527–548. DOI:10.1007/s11101-019-09605-3
30. K. Kumar, C. P. N. Misra, R. P. Singh, *Chem. Biol. Interact.* **2020**, 315, 108898. DOI:10.1016/j.cbi.2019.108898
31. S. Lee, Y. Lee, S. Ha, H. Y. Chung, H. Kim, J. S. Hur, J. Lee, *Brain. Res.* **2020**, 1730, 146642. DOI:10.1016/j.brainres.2019.146642
32. W. C. Qi, C. P. Lu, L. P. Huang, W. N. Zihang, S. F. Song, B.

- Liu, *Int. J. Mol. Sci.* **2020**, *21*(3), 876.
- 33..M. Takani, T. Yajima, H. Masuda, O. Yamauchi, *J. Inorg. Biochem.* **2002**, *9*, 139–150.
DOI:10.1016/S0162-0134(02)00439-7
- 34..M. Natic, Z. Tesic, K. Andelkovic, I. Brceski, S. Radulovic, S. Manic, D. Sladic, *Synth. React. Inorg. Met.* **2004**, *34*(1), 101–113.
- 35..M. B. Tomas, G. E. T. Chota, P.S. Cortavarria, P. F. Bonilla, M. A. I. Camones, *Rev. Colomb. Quim.* **2017**, *46*(3), 17–21.
DOI:10.15446/rev.colomb.quim.v46n3.61980
- 36..O. A. Luzina, N. F. Salakhutdinov, *Russ. J. Bioorganic. Chem.* **2016**, *42*(2), 115–132.
DOI:10.1134/S1068162016020084
- 37..D. Cirillo, E. Borroni, I. Festoso, D. Monti, S. Romeo, D. Mazier, L. Verotta, *Arch. Pharm.* **2018**, *351*(12), e1800177.
DOI:10.1002/ardp.201800177
- 38..B. Elya, K. Basali, A. Munim, W. Yulastuti, A. Bangun, E. K. Septiana, *J. Biomed. Biotechnol.* **2012**, *2012*, 281078.
DOI:10.1155/2012/281078
39. R. T. Dewi, S. Tachibana, S. Fajriah, M. Hanafi, *Med. Chem. Res.* **2015**, *24*, 737–743.
DOI:10.1007/s00044-014-1164-0
40. L. Yabo Dambagi, M. Akyuz, T. Aydin, A. Cakir, *Curr. Org. Chem.* **2020**, *24*, 785–797.
41. J. Castillo, J. Hung, M. Rodriguez, E. Bastidas, I. Laboren, A. Jaimés, *Anal. Biochem.* **2005**, *343*, 293–298.
DOI:10.1016/j.ab.2005.05.027
42. G. Huang, F. Zhu, Y. Chen, S. Chen, Z. Liu, X. Li, L. Gan, L. Zhang, Y. Yu, *Anal. Biochem.* **2016**, *512*, 18–25.
DOI:10.1016/j.ab.2016.06.020
43. G. L. Ellman, K. D. Courtney, V. Andres, R. Featherstone, *Biochem. Pharmacol.* **1961**, *7*, 88–95.
DOI:10.1016/0006-2952(61)90145-9
- 44..M. Akyuz, L. Yabo-Dambagi, T. Kilic, A. Cakir, S. Afr. J. Bot. **2022**, *147*, 443–456. DOI:10.1016/j.sajb.2022.01.040
45. R. Re, N. Pellegrini, A. Progettante, A. Pannala, M. Yang, C. Rice-Evans, *Free Radic. Biol Med.* **1999**, *26*, 1231–1237.
DOI:10.1016/S0891-5849(98)00315-3
46. G. Alper, in: T. Onat, K. Emerk, E. Y. Sözmen, (Ed.): *Diyabet, Palme Yayıncılık, Ankara, Türkiye*, **2002**. pp. 248–257.
47. S. Bastaki, *Int. J. Diabetes Metab.* **2005**, *13*, 111–134.
DOI:10.1159/000497580
48. T. Mazzone, A. Chait, J. Plutzky, *The Lancet*, **2008**, *371*(9626), 1800–1809. DOI:10.1016/S0140-6736(08)60768-0
49. S. Latha, R. Vijayakumar, *Galore Int. J. Health. Sci. Res.* **2019**, *4*, 64–75.
- 50..K. Ogurtsova, J. D. da Rocha Fernandes, Y. Huang, U. Linnenkamp, L. Guariguata, N. H. Cho, D. Cavan, J. E. Shaw, L. E. Makaroff, *Diabetes Res. Clin. Pr.* **2017**, *128*, 40–50.
DOI:10.1016/j.diabres.2017.03.024
51. A. Y. Y. Cheng, I. G. Fantus, *Can. Med. Assoc. J.* **2005**, *172*, 213–226. DOI:10.1503/cmaj.1031414
52. K. Sunguroglu, *Biochemistry, Akademisyen Tıp Kitapevi, Ankara, Türkiye*, **2014**.
53. H. Laube, *Clin. Drug. Investig.* **2002**, *22*, 141–156.
DOI:10.2165/00044011-200222030-00001
54. J. Singh, A. Dartois, L. Kaur, *Trends. Food. Sci. Technol.* **2010**, *21*, 168–180. DOI:10.1016/j.tifs.2009.12.001
55. G. Derosa, P. Maffioli, *Arch. Med. Sci.* **2012**, *8*, 899–906.
DOI:10.5114/aoms.2012.31621
56. I. Adyanthaya, Y. I. Kwon, E. Apostolidis, K. Shetty, *J. Food. Biochem.* **2010**, *34*, 31–49.
DOI:10.1111/j.1745-4514.2009.00257.x
57. Z. M. Dastjerdi, F. Namjoyan, M. E. Azemi, *Eur. J. Biol.* **2015**, *7*(1), 26–31.
58. S. Shobana, Y. N. Sreerama, N. G. Malleshi, *Food. Chem.* **2009**, *115*, 1268–1273. DOI:10.1016/j.foodchem.2009.01.042
59. K. Okada, T. Yanagawa, E. Warabi, K. Yamastu, J. Uwayama, K. Takeda, H. Utsunomiya, H. Yoshida, J. Shoda, T. Ishii. *Hepatol. Res.* **2009**, *39*, 490–500.
DOI:10.1111/j.1872-034X.2008.00478.x
60. Y. Hamada, H. Nagasaki, M. Fuchigami, S. Furuta, Y. Seino, J. Nakamura, Y. Oiso, *Metabolis.* **2013**, *62*, 734–742.
DOI:10.1016/j.metabol.2012.10.015
- 61..M. L. Rodriguez, S. Perez, S. Mena-Molla, M. C. Desco, A. L. Ortega. *Oxid. Med. Cell. Longev.* **2019**, e4940825.
- 62..D. Fraguas, C. M. Diaz-Caneja, M. Ayora, F. Hernandez-Alvarez, A. R. Quiroga, S. Recio, J. C. Leza, C. Arango. *Schizophr. Bull.* **2019**, *45*(4), 742–751. DOI:10.1093/schbul/sby125
- 63..M. A Sanchez-Rodriguez, V. M Mendoza-Nunez. *Oxid. Med. Cell. Longev.* **2019**, e4128152.
- 64..Y. Z. Fang, S. Yang, G. Wu, *Nutrition.* **2002**, *18*(10), 872–879.
DOI:10.1016/S0899-9007(02)00916-4
- 65..K. J. A. Davies, *IUBMB Life*, **2000**, *50*(4-5), 279–289.
DOI:10.1080/713803728
- 66..R. Sakakibara, T. Kawai, *Neurol. Clin. Neurosci.* **2020**, *8*, 232–240. DOI:10.1111/ncn3.12413
- 67..A. A. Hamid, O. O. Aiyelaagbe, L. A. Usman, O. M Ameen, A. Lawal. *Afr. J. Pure. Appl. Chem.* **2010**, *4*(8), 142–151.
- 68..J. M. Mates, C. Perez-Gomez, I. Nudes de Castro, *Clin. Biochem.* **1999**, *32*(8), 595–603.
DOI:10.1016/S0009-9120(99)00075-2
- 69..I. Gulcin, M. Oktay, E. Kirecci, O. I. Kufrevioglu. *Food. Chem.* **2003**, *83*, 371–382. DOI:10.1016/S0308-8146(03)00098-0
- 70..Y. Xiao, H. L. Zhang, Y. Sheng, F. Liu, J. J. Gao, G. S. Liu, S. H. Li, N. A. Jiang, C. Y. Yu, Y. Liu, *iScience.* **2022**, *25*(12), 105539.
DOI:10.1016/j.isci.2022.105539
71. A. A. S. Araujo, M. G. D. de Melo, T. K. Rabelo, P. S. Nunes, S. L. Santos, M. R. Serafini, M. R. V. Santos, L. J. Quintans, D. P. Gelain, *Nat. Prod. Res.* **2015**, *29*(23), 2167–2180.
DOI:10.1080/14786419.2015.1007455
72. C. Kohlhhardt-Floehr, F. Boehm, S. Troppens, J. Lademann, T. G. Truscott, *J. Photochem. Photobiol. B: Biol.* **2010**, *101*(1), 97–102. DOI:10.1016/j.jphotobiol.2010.06.017
73. V. Popovici, E. Matei, G. M. Cozaru, M. Aschie, L. Bucur, D. Rambu, T. Costache, I. E. Cuculea, G. Vochita, D. Gherghel, A. Caraine, V. Badea, *Antioxidants* **2021**, *10*(8), 1171.
DOI:10.3390/antiox10081171
74. C. A. Cazarin, A. P. Dalmagro, A. E. Gonçalves, T. Boeing, L. M. da Silva, R. Correa, L. C. Klein, B. Carlesso, T. S. Lorenzetti, T. U. D. Sobrinho, A. de Fátima, T. C. D. Lage, S. A. Fernandes, M. M. de Souza, *Behav. Brain Res.* **2021**, *397*, 112945.

- DOI:10.1016/j.bbr.2020.112945
75. I. G. Munteanu, C. Apetrei, *Int. J. Mol. Sci.* **2021**, *22*(7), 3380. DOI:10.3390/ijms22073380
76. R. Paul, *J. Psychiatry. Neurosci.* **2015**, *40*(4), 219–221. DOI:10.1503/jpn.150205
77. L. Agrawal, M. Korkutaba, S. K. Vimal, M. K. Yadav, S. Bhat-tacharyya, T. Shiga, *Neuropharmacology* **2020**, *166*, 107969. DOI:10.1016/j.neuropharm.2020.107969
78. Y. Jiang, D. Zou, Y. Li, S. Gu, J. Dong, X. Ma, S. Xu, F. Wang, J. S. Huang, *Pharmaceuticals (Basel)* **2022**, *15*(10), 1203. DOI:10.3390/ph15101203
79. A. Yesilada, N. *FABAD. J. Pharm. Sci.* **1995**, *20*, 157–172.
80. N. D. Volkow, G. J. Wang, S. H. Kollins, T. L. Wigal, J. H. Newcorn, F. Telang, J. S. Fowler, W. Zhu, J. Logan, Y. Ma, K. Pradhan, C. Wong, J. M. Swanson, *JAMA.* **2009**, *302*(10), 1084–1091. DOI:10.1001/jama.2009.1308
81. L. Perez-Caballero, S. Torres-Sanchez, C. Romero-López-Alberca, F. González-Saiz, J. A. Mico, E. Berrocoso. *Cell. Tissue. Res.* **2019**, *377*(1), 107–113. DOI:10.1007/s00441-018-2978-8
82. C. Binda, F. Hubalek, M. Li, D. E. Edmondson, A. Mattevi, *FEBS. Lett.* **2004**, *564*, 225–228. DOI:10.1016/S0014-5793(04)00209-1
83. A. W. K. Yeung, M. G. Georgieva, A. G. Atanasov, N. T. Tzvetkov. *Front. Mol. Neurosci.* **2019**, *12*, 143. DOI:10.3389/fnmol.2019.00143
84. P. Duarte, A. Cuadrado, R. Leon, in: H. H. H. W. Schmidt, P. Ghezzi, A. Cuadrado, (Ed.): *Reactive Oxygen Species. Handbook of Experimental Pharmacology*: Springer, Cham., Switzerland, **2020**, pp. 229–259. DOI:10.1007/164_2020_384
85. T. Karabin, G. Biala, M. Kruk-Slomka, *Curr. Issues. Pharm. Med. Sci.* **2023**, *36*, 108–113. DOI:10.2478/cipms-2023-0019
86. J. Saura, Z. Bleuel, J. Ulrich, A. Mendelowitsch, K. Chen, J. C. Shih, P. Malherbe, M. Da Prada, J. G. Richards. *Neuroscience.* **1996**, *70*, 755–774. DOI:10.1016/S0306-4522(96)83013-2
87. A. Parkinson, B. W. Ogilvie, in: C. D. Klaassen (Ed.): *Casarett & Doull's Toxicology: The Basic Science of Poisons*, McGraw-Hill Inc., New York, **2008**, pp. 161–304.
88. G. Cohen, *J. Neural. Transm.* **1990**, *32*, 229–238. DOI:10.1007/978-3-7091-9113-2_33
89. P. Dhiman, N. Malik, A. Khatkar, *BMC. Chem.* **2019**, *13*, 38. DOI:10.1186/s13065-019-0552-4
90. K. Zhi, Z. Yang, J. Sheng, Z. Shu, Y. Shi, *Iran. J. Pharm. Sci.* **2016**, *15*, 131–139.
91. Y. Y. Tan, P. Jenner, S. D. Chen, *J. Parkinsons Dis.* **2022**, *12*, 477–493. DOI:10.3233/JPD-212976
92. I. Khan, S. M. Bakht, A. Ibrar, S. Abbas, S. Hameed, J. M. White, U. A. Rana, S. Zaib, M. Shahide, J. Iqbal, *RSC. Adv.* **2015**, *5*, 21249–21267. DOI:10.1039/C5RA00906E
93. E. Palaska, F. Aydin, G. Uçar, D. Erol, *Arch. Pharm. Chem. Life Sci.* **2008**, *341*, 209–215. DOI:10.1002/ardp.200700159
94. W. Swardfager, K. Lanctôt, L. Rothenburg, A. Wong, J. Cappell, N. A. Herrmann, *Biol. Psychiatry.* **2010**, *68*, 930–941. DOI:10.1016/j.biopsych.2010.06.012
95. A. Gustavsson, N. Norton, T. Fast, L. Frölich, J. Georges, D. Holzapfel, T. Kirabali, P. Krolak-Salmon, P. M. Rossini, M. T. Ferretti, L. Lanman, A. S. Chadha, W. M. van der Flier, *Alzheimers Dement.* **2023**, *19*, 658–670. DOI:10.1002/alz.12694
96. R. T. Bartus, R. L. Dean, B. Beer, A. S. Lippa, *Science* **1982**, *217*, 408–417. DOI:10.1126/science.7046051
97. Q. Cao, C. C. Tan, W. Xu, H. Hu, X. P. Cao, Q. Dong, L. Tan, J. T. Yu, *J. Alzheimer's Dis.* **2020**, *73*, 1157–1166. DOI:10.3233/JAD-191092
98. G. Marucci, M. Buccioni, D. Dal Ben, C. Lambertucci, R. Volpini, F. Amenta, *Neuropharmacology* **2021**, *190*, 108352. DOI:10.1016/j.neuropharm.2020.108352
99. A. Nordberg, C. Ballard, R. Bullock, T. Darreh-Shori, M. Somogyi, *Prim. Care Companion CNS Disord.* **2013**, *15*, PCC.12r01412. DOI:10.4088/PCC.12r01412
100. K. Sharma, *Mol. Med. Rep.* **2019**, *20*, 1479–1487.
101. F. Amenta, L. Parnetti, V. Gallai, A. Wallin, *Mech. Ageing Dev.* **2001**, *122*, 2025–2040. DOI:10.1016/S0047-6374(01)00310-4
102. H. Cavdar, M. Senturk, M. Guney, S. Durdagi, G. Kayik, C. T. Supuran, D. Ekinci, *J. Enzyme Inhib. Med. Chem.* **2019**, *34*(1), 429–437. DOI:10.1080/14756366.2018.1543288
103. I. O. Korolev, *Med. Student Res. J.* **2014**, *4*, 24–33.
104. R. Khoury, J. Rajamanickam, G. T. Grossberg, *Ther. Adv. Drug Saf.* **2018**, *9*(3), 171–178. DOI:10.1177/2042098617750555

Povzetek

Schiffove baze imajo zaradi prisotnosti azometinske ($-C=N-$) skupine mnoge farmakološke aktivnosti. Usninska kislina je najbolj znan metabolit lišajev; vsebuje dve karbonilni skupini iz katerih je mogoče s primarnimi amini sintetizirati Schiffove baze. V okviru te študije smo iz usninske kisline (**1**) pripravili znane Schiffove baze **2–5** z namenom raziskati njihove antiadiabetične ter neurozaščitne lastnosti, antioksidativne aktivnosti in lastnosti delovanja proti depresiji ter Parkinsonovi bolezni. Med preizkušanimi spojinami, je spojina **4** izkazala najmočnejše delovanje proti diabetesu in depresiji, saj je inhibirala delovanje α -glikozidaze, α -amilaze in encima MAO-A. Poleg tega so se vse spojine izkazale kot dobri lovilci radikalov ABTS in DPPH; aktivnost spojin **3** in **4** za lovljenje radikalov ABTS je bila celo večja od aktivnosti komercialnih antioksidantov, kot sta BHA in troloks. Nobena od preizkušanih spojin pa ni pokazala občutnega delovanja proti Parkinsonovi bolezni in niti ni izkazala neurozaščitnega delovanja. Zaključimo lahko, da bi spojina **4** zaradi svojega antioksidativnega delovanja ter delovanja proti diabetesu in depresiji lahko bila kandidatka za nadaljnje študije.



Except when otherwise noted, articles in this journal are published under the terms and conditions of the Creative Commons Attribution 4.0 International License

Scientific paper

Synthesis, Characterization and X-Ray Crystal Structures of Schiff Base Zinc(II) Complexes with Antibacterial Activity

Yu-Hui Wu,¹ Wan-Lin Wei,² Wei Li^{1,*} and Zhonglu You²¹Department of Radiology, The Second Hospital of Dalian Medical University, Dalian 116023, P.R. China² Department of Chemistry and Chemical Engineering, Liaoning Normal University, Dalian 116029, P. R. China

* Corresponding author: E-mail: liwei_dlm@126.com

Received: 08-12-2024

Abstract

Two mononuclear zinc(II) complexes [ZnCl₂(HL)] (1) and [ZnBr₂(HL)] (2), and a polymeric zinc(II) complex [Zn(dca)L] (3), where HL is the zwitterionic form of the Schiff base 2,4-difluoro-6-(((2-pyrrolidin-1-yl)ethylimino)methyl)phenol (HL), L is the monoanionic form of HL, and dca is dicyanoamide, were prepared and characterized by elemental analysis and infrared spectroscopy, as well as X-ray single crystal determination. Complexes 1 and 2 are isostructural, in which the Zn atoms are in tetrahedral coordination. The Schiff base ligands in both complexes are coordinate to the Zn atoms through phenolate oxygen and imino nitrogen. The zinc atoms in complex 3 are in tetrahedral coordination and are bridged by dicyanoamide ligands. The Schiff base ligand in this complex is coordinates to the zinc atom through phenolate oxygen, imino nitrogen and pyrrolidine nitrogen. Molecules of the three complexes are stabilized by hydrogen bonds. The biological assay indicates that the complexes have good antimicrobial activities on the bacteria strains *Escherichia coli*, *Pseudomonas aeruginosa*, *Salmonella typhi* and *Staphylococcus aureus*.

Keywords: Schiff base; Zinc complex; X-Ray crystal structure; Antibacterial activity.

1. Introduction

In recent years, zinc complexes have received much attention for their interesting biological activities such as antibacterial, antifungi and antitumor.¹ Schiff base compounds derived from the condensation reaction of aldehydes with various amines are much attractive for their extensive biological applications and coordination capability to metal atoms.² In literature, a number of zinc complexes with Schiff base ligands have been reported to show effective antimicrobial activities.³ Halide and pseudohalide anions are versatile ligands in coordination chemistry. They play either terminal or bridging mode in the formation of metal complexes.⁴ Fluoro- and chloro-substituted compounds are reported to have effective antibacterial activities.⁵ Recently, our research group has reported some Schiff base complexes with biological activities.⁶ In continuation of the work, the present paper reports three new zinc(II) complexes, [ZnCl₂(HL)] (1), [ZnBr₂(HL)] (2) and [Zn(dca)L] (3), where HL is the zwitterionic form of the Schiff base 2,4-difluoro-6-[(2-pyrrolidin-1-ylethylimino)methyl]phenol (HL), L is the monoanionic form of HL, and dca is dicyanoamide.

2. Experimental

2. 1. Materials and Measurements

Commercially available 3,5-difluorosallylaldehyde and *N*-(2-aminoethyl)pyrrolidine were purchased from Sigma-Aldrich and used without further purification. Other solvents and reagents were made in China and used as received. The Schiff base HL was prepared according to the literature method.⁷ C, H and N elemental analyses were performed with a Perkin-Elmer elemental analyzer. Infrared spectra were recorded on a Nicolet AVATAR 360 spectrometer as KBr pellets in the 4000–400 cm⁻¹ region.

2. 2. Synthesis of [ZnCl₂(HL)] (1)

A methanolic solution (10 mL) of zinc chloride (0.10 mmol, 13.6 mg) was added to a methanolic solution (10 mL) of HL (0.10 mmol, 25.4 mg) with stirring. The mixture was stirred for 30 min at room temperature to give a colorless solution. The resulting solution was allowed to stand in air for a few days. Colorless block-shaped crystals suitable for X-ray single crystal diffraction were formed at the bottom of the vessel. The isolated products were

washed three times with cold ethanol and dried in air. Yield: 27 mg (69%). Analysis: Found: C 39.83%, H 4.20%, N 7.26%. Calculated for $C_{13}H_{16}Cl_2F_2N_2OZn$: C 39.98%, H 4.13%, N 7.17%. IR data (KBr, cm^{-1}): ν 3139 w (NH), 1623 s (C=N).

2. 3. Synthesis of [ZnBr₂(HL)] (2)

This complex crystallized as colorless block like single crystals was prepared by the same method as described for complex **1**, with zinc chloride replaced by zinc bromide (0.10 mmol, 22.5 mg). Yield: 35 mg (73%). Analysis: Found: C 32.37%, H 3.43%, N 5.92%. Calculated for $C_{13}H_{16}Br_2F_2N_2OZn$: C 32.56%, H 3.36%, N 5.84%. IR data (KBr, cm^{-1}): ν 3127 w (NH), 1623 s (C=N).

2. 4. Synthesis of [Zn(dca)L] (3)

A methanolic solution (10 mL) of zinc nitrate hexahydrate (0.10 mmol, 29.7 mg) was added to a methanolic solution (10 mL) of HL (0.10 mmol, 25.4 mg) with stirring. Then, sodium dicyanoamide (0.20 mmol, 17.8 mg) was added to the mixture. The final mixture was stirred for 30 min at room temperature to give a colorless solution. The resulting solution was allowed to stand in air for a few days. Colorless block-shaped crystals suitable for X-ray single crystal diffraction were formed at the bottom of the vessel. The isolated products were washed three times with cold ethanol and dried in air. Yield: 30 mg (79%). Analysis: Found: C 46.95%, H 3.86%, N 18.07%. Calculated for

$C_{15}H_{15}F_2N_5OZn$: C 46.83%, H 3.93%, N 18.20%. IR data (KBr, cm^{-1}): ν 2322 w, 2257 w, 2193 s (dca), 1617 sc (C=N).

2. 5. X-ray Crystallography

Diffraction intensities for the complexes were collected at 298(2) K using a Bruker D8 VENTURE PHOTON diffractometer with MoK α radiation ($\lambda = 0.71073$ Å). The collected data were reduced using the SAINT program,⁸ and multi-scan absorption corrections were performed using the SADABS program.⁹ The structures were solved by direct method and refined against F^2 by full-matrix least-squares method using the SHELXTL.¹⁰ All of the non-hydrogen atoms were refined anisotropically. The H atoms attached to the N atoms of pyrrolidine groups in complexes **1** and **2** were located from difference Fourier maps and refined isotropically, with N–H distances restrained to 0.90(1) Å. All other hydrogen atoms were placed in idealized positions and constrained to ride on their parent atoms. The crystallographic data for the complexes are summarized in Table 1. Selected bond lengths and angles are given in Table 2. Hydrogen bonding information is listed in Table 3.

3. Results and Discussion

The three complexes were facile prepared by reaction of the Schiff base HL and zinc salts in methanol in the presence of halide or pseudohalide anions (Scheme 1).

Table 1. Crystallographic data and refinement parameters for the complexes

	1	2	3
Chemical formula	$C_{13}H_{16}Cl_2F_2N_2OZn$	$C_{13}H_{16}Br_2F_2N_2OZn$	$C_{15}H_{15}F_2N_5OZn$
<i>Mr</i>	390.55	479.47	384.69
Crystal color, habit	Colorless, block	Colorless, block	Colorless, block
Crystal system	Monoclinic	Monoclinic	Monoclinic
Space group	$P2_1/c$	$P2_1/c$	$P2_1/n$
<i>a</i> (Å)	14.2038(16)	14.3819(11)	7.2966(4)
<i>b</i> (Å)	15.0934(12)	15.2563(11)	29.393(2)
<i>c</i> (Å)	14.6834(16)	14.8598(11)	7.5410(5)
α (°)	90	90	90
β (°)	101.804(1)	100.321(2)	94.478(1)
γ (°)	90	90	90
<i>V</i> (Å ³)	3081.3(5)	3207.7(4)	1612.36(18)
<i>Z</i>	8	8	4
<i>D</i> _{calc} (g cm ⁻³)	1.684	1.986	1.585
μ (mm ⁻¹)	1.960	6.533	1.557
<i>F</i> (000)	1584	1872	784
Number of unique data	5734	5959	2995
Number of observed data [$I > 2\sigma(I)$]	4566	3747	2383
Number of parameters	385	385	217
Number of restraints	2	2	0
<i>R</i> ₁ , <i>wR</i> ₂ [$I > 2\sigma(I)$]	0.0355, 0.0889	0.0461, 0.1277	0.0499, 0.1040
<i>R</i> ₁ , <i>wR</i> ₂ (all data)	0.0487, 0.0966	0.0839, 0.1466	0.0641, 0.1122
Goodness of fit on F^2	1.029	0.956	1.061

Table 2. Selected bond distances (Å) and angles (°) for the complexes

1			
Zn1–O1	1.931(2)	Zn1–N1	2.035(2)
Zn1–Cl1	2.2235(10)	Zn1–Cl2	2.2379(9)
O1–Zn1–N1	94.72(9)	O1–Zn1–Cl1	108.78(7)
N1–Zn1–Cl1	116.69(7)	O1–Zn1–Cl2	115.00(7)
N1–Zn1–Cl2	109.58(7)	Cl1–Zn1–Cl2	110.49(4)
2			
Zn1–O1	1.926(5)	Zn1–N1	2.046(5)
Zn1–Br1	2.3788(11)	Zn1–Br2	2.3567(11)
O1–Zn1–N1	95.1(2)	O1–Zn1–Br2	108.86(14)
N1–Zn1–Br2	116.92(15)	O1–Zn1–Br1	116.51(15)
N1–Zn1–Br1	108.59(15)	Br2–Zn1–Br1	110.36(4)
3			
Zn1–O1	1.986(3)	Zn1–N1	2.019(3)
Zn1–N3	2.008(3)	Zn1–N5A	2.039(3)
Zn1–N2	2.422(3)		
O1–Zn1–N3	96.27(12)	O1–Zn1–N1	91.42(11)
N3–Zn1–N1	128.72(11)	O1–Zn1–N5A	94.10(13)
N3–Zn1–N5A	106.06(12)	N1–Zn1–N5A	123.88(12)
O1–Zn1–N2	169.17(11)	N3–Zn1–N2	91.87(12)
N1–Zn1–N2	77.90(11)	N5A–Zn1–N2	90.48(12)

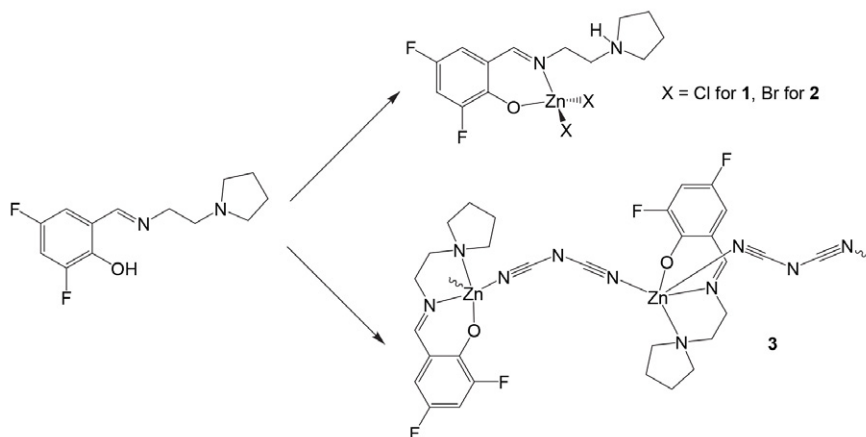
Symmetry code for A: $x, y, 1 + z$.**Table 3.** Hydrogen bond distances (Å) and bond angles (°) for the complexes

$D-H\cdots A$	$d(D-H)$, Å	$d(H\cdots A)$, Å	$d(D\cdots A)$, Å	Angle ($D-H\cdots A$), °
1				
N2–H2...F3 ^{#1}	0.90(1)	2.40(3)	3.032(3)	128(3)
N2–H2...O2 ^{#1}	0.90(1)	2.32(2)	3.129(3)	149(3)
N4–H4...Cl4	0.90(1)	2.55(2)	3.257(2)	136(3)
C10–H10A...F3 ^{#1}	0.97	2.47	2.992(3)	113
C10–H10B...O1 ^{#2}	0.97	2.36	3.315(4)	169
C13–H13A...Cl3 ^{#1}	0.97	2.80	3.760(3)	171
C25–H25B...F2	0.97	2.44	3.048(4)	122
2				
N2–H2...F4	0.90(1)	2.30(5)	3.020(6)	137(6)
N2–H2...O2	0.90(1)	2.40(4)	3.193(7)	147(6)
N4–H4...Br4	0.90(1)	2.63(5)	3.385(5)	142(6)
C10–H10B...O1 ^{#3}	0.97	2.37	3.333(9)	174
C24–H24A...F2 ^{#4}	0.97	2.45	3.144(9)	128
3				
C10–H10B...N5 ^{#5}	0.97	2.61	3.220(6)	122
C7–H7...F1 ^{#6}	0.93	2.34	3.208(4)	155

Symmetry codes: #1: $x, \frac{1}{2} - y, -\frac{1}{2} + z$; #2: $-x, \frac{1}{2} + y, \frac{1}{2} - z$; #3: $2 - x, \frac{1}{2} + y, 1\frac{1}{2} - z$; #4: $x, \frac{1}{2} - y, \frac{1}{2} + z$; #5: $1 - x, 1 - y, 1 - z$; #6: $x, y, 1 + z$.

Zinc chloride and zinc bromide were used in the synthesis of complexes **1** and **2**, respectively. The Cl and Br anions act as terminal ligands in both complexes. Complex **3** was synthesized from zinc nitrate and sodium dicyanoamide. As a result, the dicyanoamide anion participates in coordi-

nation and is a bridging ligand. The Schiff base ligands coordinate to the metal atoms in zwitterionic form for complexes **1** and **2**. While for complex **3**, it adopts deprotonated monoanionic form. All the complexes are soluble in DMF, DMSO, methanol, ethanol and aceton-



Scheme 1. The synthetic procedures for the complexes

trile, insoluble in water, chloroform and dichloromethane. Molar conductance of the complexes at concentration of 10^{-3} mol L $^{-1}$ is 23–45 Ω^{-1} cm 2 mol $^{-1}$, indicating they are non-electrolytes.¹¹

3. 1. Crystal Structure Description of Complexes 1 and 2

The molecular structures and atom numbering schemes of complexes **1** and **2** are shown in Figures 1 and 2, respectively. The asymmetric units of **1** and **2** possess two crystallographically independent molecules. Complexes **1** and **2** are isostructural mononuclear zinc(II) compounds. The Zn atom in each complex is in tetrahedral coordination and is coordinated by one phenolate oxygen and one imino nitrogen of a zwitterionic Schiff base ligand, and two halide anions (Cl for **1**, Br for **2**). The coordinate bond angles are in the ranges 94.72(9)–116.69(7) $^\circ$ for **1** and 95.1(2)–116.51(15) $^\circ$ for **2**, which are similar to those observed in similar Schiff base zinc complexes.¹² The Zn–O, Zn–N, Zn–Cl and Zn–Br bond lengths are comparable to those observed in the zinc complexes.¹²

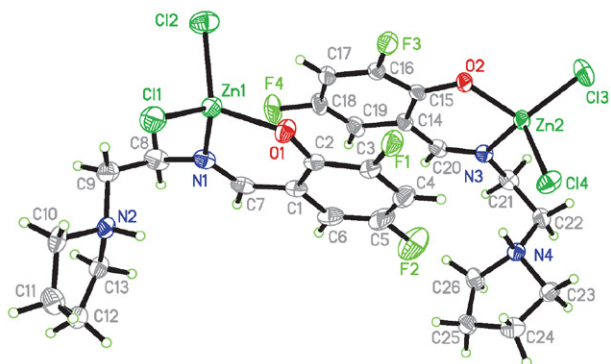


Figure 1. ORTEP plot of the crystal structure of complex **1**. Displacement ellipsoids of non-hydrogen atoms are drawn at the 30% probability level.

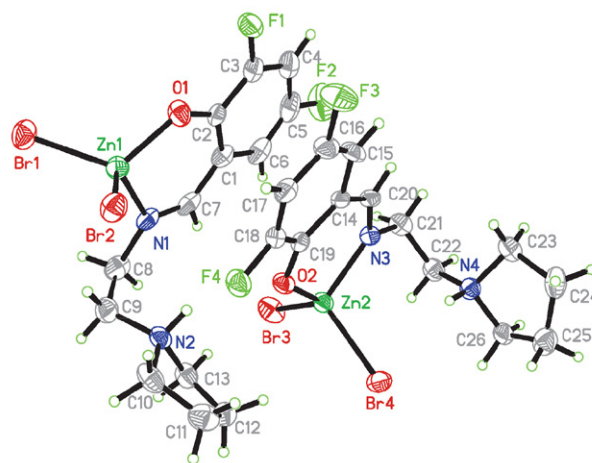


Figure 2. ORTEP plot of the crystal structure of complex **2**. Displacement ellipsoids of non-hydrogen atoms are drawn at the 30% probability level.

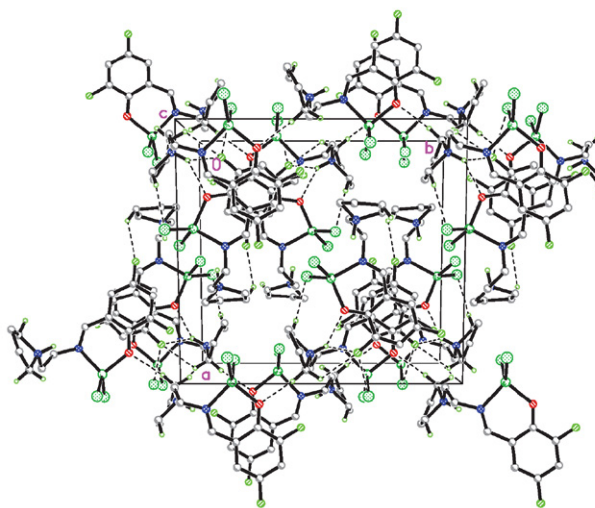


Figure 3. Molecular packing diagram of complex **1**. Viewed along the *c* axis. Hydrogen atoms not related to hydrogen bonding are omitted. Hydrogen bonds are shown as dashed lines.

In the crystal structures of the complexes, molecules are linked through intermolecular hydrogen bonds of types N–H...O, N–H...F, N–H...Cl/Br, C–H...O, C–H...F and C–H...Cl/Br (Table 3), to form three dimensional networks (Figures 3 and 4).

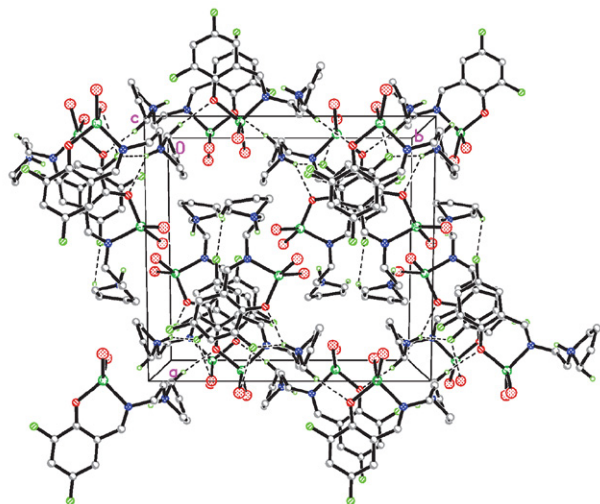


Figure 4. Molecular packing diagram of complex 2. Viewed along the *c* axis. Hydrogen atoms not related to hydrogen bonding are omitted. Hydrogen bonds are shown as dashed lines.

3. 2. Crystal Structure Description of Complex 3

The molecular structure and atom numbering scheme of complex 3 is shown in Figure 5. The asymmetric unit of the complex contains [Zn(dca)L] unit. The [ZnL] moieties are linked through dicyanoamide ligands, forming a polymeric structure. The Zn atom is in trigonal bipyramidal coordination, with the basal plane defined by the imino nitrogen (N1) of the Schiff base ligand L, and two N atoms from two dca ligands. The axial positions are occupied by one phenolate oxygen (O1) and one pyrrolidine nitrogen (N2). The Zn atom deviates from the least squares plane defined by the three basal donor atoms by 0.037(2) Å. The angular distortion in the trigonal bipyramidal environment comes from the five- and six-membered chelate rings taken by the Schiff base ligand, with angles of 77.90(11)° and 91.42(11)°. Distortion of the trigonal bipyramidal coordination can be observed from the coordinate bond angles, ranging from 106.06(12) to 128.72(11)° for the basal angles, and 169.17(11)° for the diagonal angle. The trigonal bipyramidal coordination can be calculated from the structural index value τ of 0.67.¹³ The Zn–O and Zn–N bonds are comparable to those observed in similar Schiff base zinc complexes.¹⁴

In the crystal structure of the complex, the [CuL] moieties are linked by dca ligands to form chain structure along the *c* axis. The chains are further linked by intermolecular hydrogen bonds of types C–H...N and C–H...F (Table 3), to form a three-dimensional network (Figure 6).

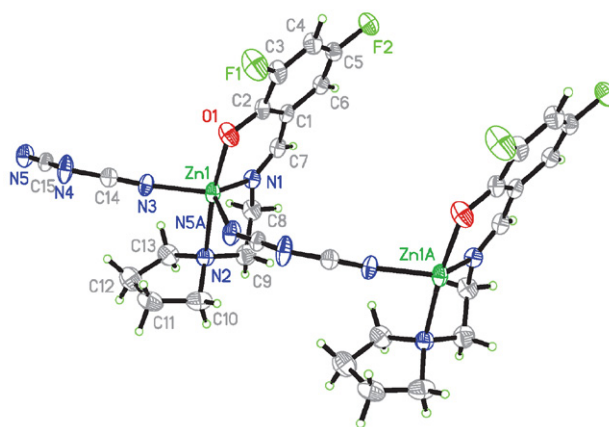


Figure 5. ORTEP plot of the crystal structure of complex 3. Displacement ellipsoids of non-hydrogen atoms are drawn at the 30% probability level. Atoms labelled with the suffix A are related to the symmetry position $x, y, 1 + z$.

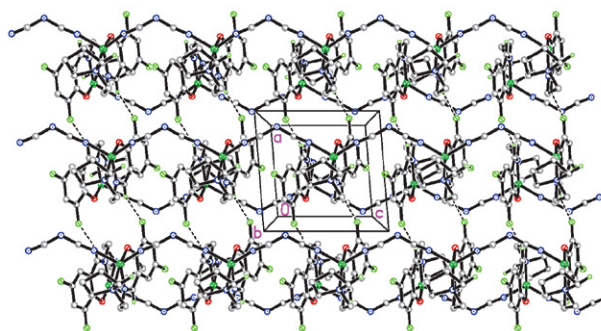


Figure 6. Molecular packing diagram of complex 3. Viewed along the *b* axis. Hydrogen atoms not related to hydrogen bonding are omitted. Hydrogen bonds are shown as dashed lines.

3. 3. Antibacterial Activity

The antibacterial assay was performed according to the literature method.¹⁵ Penicillin G was used as a standard drug. DMSO was used as solvent and the solutions were further diluted by distilled water. The DMSO at the tested concentration has no activity on the bacteria. The zone of inhibition for the 5000 $\mu\text{g mL}^{-1}$ test solutions on the four bacteria *Escherichia coli*, *Pseudomonas aeruginosa*, *Salmonella typhi* and *Staphylococcus aureus* is given in Table 4. The MIC values are given in Table 5. The results indicated that the metal complexes have from medium to strong activities against the bacteria, and stronger than the free Schiff base. The three zinc complexes have similar activities against all the bacterial strains, indicating the Cl, Br and dca ligands have similar effects on antibacterial activities. The complexes show strong activity on *E. coli* and *P. aeruginosa*, and medium activity on *B. subtilis* and *S. aureus*. The three metal complexes have better activities against *E. coli*, *P. aeruginosa* and *S. aureus* than the reference drug penicillin G.

Table 4 Antibacterial screening results

Compound	Zone of inhibition (mm)			
	<i>E. coli</i>	<i>P. aeruginosa</i>	<i>B. subtilis</i>	<i>S. aureus</i>
HL	8.2 ± 1.5	6.7 ± 1.6	6.1 ± 1.2	5.5 ± 1.3
1	23 ± 1.6	25 ± 1.3	16 ± 1.5	18 ± 1.7
2	22 ± 1.8	23 ± 2.0	15 ± 1.7	17 ± 1.4
3	20 ± 2.2	21 ± 2.0	15 ± 1.8	16 ± 1.5
Penicillin G	30 ± 2.8	26 ± 3.1	30 ± 3.2	24 ± 2.9

Table 5 Antibacterial activities as MIC values ($\mu\text{g mL}^{-1}$)

Compound	<i>E. coli</i>	<i>P. aeruginosa</i>	<i>B. subtilis</i>	<i>S. aureus</i>
HL	6.25	12.5	12.5	12.5
1	1.56	1.56	6.25	3.13
2	1.56	1.56	6.25	3.13
3	1.56	1.56	6.25	3.13
Penicillin G	3.13	6.25	1.56	6.25

4. Supplementary Material

CCDC 2376703–2376705 for the three complexes contains the supplementary crystallographic data for this paper. These data can be obtained free of charge at <http://www.ccdc.cam.ac.uk/const/retrieving.html> or from the Cambridge Crystallographic Data Centre (CCDC), 12 Union Road, Cambridge CB2 1EZ, UK; fax: +44(0)1223-336033 or e-mail: deposit@ccdc.cam.ac.uk.

5. References

- (a) H. Merazka, A. Bouchoucha, M. Nesaib, N. Bensouilah, K. S. Larbi, A. Bouzaheur, M. Brahimi, *J. Coord. Chem.* **2023**, 76, 798–829; DOI:10.1080/00958972.2023.2204512
(b) W.-G. Zhang, *Acta Chim. Slov.* **2023**, 70, 421–429; DOI:10.17344/acsi.2023.8144
(c) A. Zianna, E. Vradi, A. G. Hatzidimitriou, S. Kalogiannis, G. Psomas, *Dalton Trans.* **2022**, 51, 17629–17641; DOI:10.1039/D2DT02404G
(d) R. A. C. Souza, V. L. Cunha, J. H. De Souza, C. H. G. Martins, E. D. Franca, M. Pivatto, J. A. Ellena, L. A. Faustino, A. O. D. Patrocinio, V. M. Deflon, P. I. D. Maia, C. G. Oliveira, *J. Inorg. Biochem.* **2022**, 237, 111995; DOI:10.1016/j.jinorgbio.2022.111995
(e) P. S. Tessaro, M. D. Tomaz, G. Farias, C. P. Paula, M. C. Rocha, I. Malavazi, A. Cunha, B. F. Pimenta, H. F. Terenzi, S. R. Mendes, R. A. Gariani, F. R. Xavier, *J. Inorg. Biochem.* **2022**, 236, 111973; DOI:10.1016/j.jinorgbio.2022.111973
(f) J. Makhoulouf, Y. El Bakri, A. Valkonen, K. Saravanan, S. Ahmad, W. Smirani, *Polyhedron* **2022**, 222, 115937. DOI:10.1016/j.poly.2022.115937
- (a) Y. Z. Ng, K. W. Tan, L. Y. Chung, F. Salim, M. L. Low, I. H. Ooi, F. W. Yip, C. H. Ng, *J. Coord. Chem.* **2022**, 75, 1303–1324; DOI:10.1080/00958972.2022.2097869
(b) Q. Poladian, O. Sahin, T. Karakurt, B. Ilhan-Ceylan, Y. Kurt, *Polyhedron* **2021**, 201, 115164; DOI:10.1016/j.poly.2021.115164
(c) I. Demir, M. Bayrakci, K. Mutlu, A. I. Pekacar, *Acta Chim. Slov.* **2008**, 55, 120–124. DOI:10.1353/dss.2008.0061
- (a) F. Ramilo-Gomes, Y. Addis, I. Tekamo, I. Cavaco, D. L. Campos, F. R. Pavan, C. S. B. Gomes, V. Brito, A. O. Santos, F. Domingues, A. Luis, M. M. Marques, J. C. Pessoa, S. Ferreira, S. Silvestre, I. Correia, *J. Inorg. Biochem.* **2021**, 216, 111331; DOI:10.1016/j.jinorgbio.2020.111331
(b) H.-Y. Qian, *Acta Chim. Slov.* **2021**, 68, 638–644; DOI:10.17344/acsi.2021.6656
(c) L.-W. Xue, X. Fu, G.-Q. Zhao, Q.-B. Li, *Acta Chim. Slov.* **2021**, 68, 17–24; DOI:10.17344/acsi.2020.5817
(d) D.-L. Peng, N. Sun, *Acta Chim. Slov.* **2018**, 65, 895–901. DOI:10.17344/acsi.2018.4543
- (a) A. A. Sysoeva, A. S. Novikov, V. V. Suslonov, D. S. Bolotin, M. V. Ilin, *Inorg. Chim. Acta* **2024**, 561, 121867; DOI:10.1016/j.ica.2023.121867
(b) I. Yilmaz, *Polyhedron* **2024**, 250, 116816; DOI:10.1016/j.poly.2023.116816
(c) K. Jana, R. Maity, H. Puschmann, A. Mitra, R. Ghosh, S. C. Debnath, A. Shukla, A. K. Mahanta, T. Maity, B. C. Samanta, *Inorg. Chim. Acta* **2021**, 515, 120067; DOI:10.1016/j.ica.2020.120067
(d) R. J. Dubois, C. P. Landee, M. Rademeyer, M. M. Turnbull, *J. Coord. Chem.* **2019**, 72, 1785–1809; DOI:10.1080/00958972.2019.1629429
(e) H. Ogawa, K. Mori, K. Murashima, S. Karasawa, N. Koga, *Inorg. Chem.* **2016**, 55, 717–728. DOI:10.1021/acs.inorgchem.5b02159
- (a) L. C. Felton, J. H. Brewer, *Science* **1947**, 105, 409–410; DOI:10.1126/science.105.2729.409
(b) M. Gopalakrishnan, J. Thanusu, V. Kanagarajan, R. Govindaraju, *J. Enzym. Inhib. Med. Chem.* **2009**, 24, 52–58; DOI:10.1080/14756360801906632
(c) L. Shi, H.-M. Ge, S.-H. Tan, H.-Q. Li, Y.-C. Song, H.-L. Zhu, R.-X. Tan, *Eur. J. Med. Chem.* **2007**, 42, 558–564; DOI:10.1016/j.ejmech.2006.11.010
(d) M. Zhang, D.-M. Xian, H.-H. Li, J.-C. Zhang, Z.-L. You, *Aust. J. Chem.* **2012**, 65, 343–350. DOI:10.1071/CH11424
- (a) Y.-X. Zhou, W. Li, Z. You, *Acta Chim. Slov.* **2023**, 70, 240–246; DOI:10.17344/acsi.2023.8123
(b) X.-R. Tan, W. Li, M.-M. Duan, Z. You, *Acta Chim. Slov.* **2023**, 70, 509–515; DOI:10.17344/acsi.2023.8347
(c) W. H. Sun, K. H. Li, H. Liu, Y. T. Gu, Y. Zhang, Z. L. You, W. Li, *Russ. J. Coord. Chem.* **2017**, 43, 693–699. DOI:10.1134/S1070328417100104
- Y. Lei, Q. Yang, Z. Hu, S. Wang, *Polyhedron* **2024**, 259, 117071. DOI:10.1016/j.poly.2024.117071
- Bruker, SMART and SAINT, Bruker AXS Inc., Madison, Wisconsin, USA, **2012**.
- G. M. Sheldrick, SADABS Program for Empirical Absorption

- Correction of Area Detector, University of Göttingen, Germany, 1996.
10. G. M. Sheldrick, *Acta Crystallogr.* **2008**, *A64*, 112–122. DOI:10.1107/S0108767307043930
11. W. J. Geary, *Coord. Chem. Rev.* **1971**, *7*, 81–122. DOI:10.1016/S0010-8545(00)80009-0
12. (a) J. Ravichandran, P. Gurumoorthy, C. Kathick, A. K. Rahiman, *J. Mol. Struct.* **2014**, *1062*, 147–157; DOI:10.1016/j.molstruc.2014.01.026
(b) T. Chattopadhyay, M. Mukherjee, K. S. Banu, A. Banerjee, E. Suresh, E. Zangrando, D. Das, *J. Coord. Chem.* **2009**, *62*, 967–979; DOI:10.1080/00958970802385837
(c) D.-H. Shi, Z. L. Cao, W. W. Liu, R. B. Xu, L. L. Gao, Q. Zhang, Z. You, *Russ. J. Coord. Chem.* **2013**, *39*, 297–300. DOI:10.1134/S1070328413030111
13. A. W. Addison, T. N. Rao, J. Reedijk, J. van Rijn, G. C. Verschoor, *J. Chem. Soc., Dalton Trans.* **1984**, *7*, 1349–1356. DOI:10.1039/DT9840001349
14. (a) P. Chakraborty, J. Adhikary, S. Samanta, D. Escudero, A. C. Castro, M. Swart, S. Ghosh, A. Bauza, A. Frontera, E. Zangrando, D. Das, *Cryst. Growth Des.* **2014**, *14*, 4111–4123; DOI:10.1021/cg500717n
(b) M. Maiti, D. Sadhukhan, S. Thakurta, S. Roy, G. Pilet, R. J. Butcher, A. Nonat, L. J. Charbonniere, S. Mitra, *Inorg. Chem.* **2012**, *51*, 12176–12187. DOI:10.1021/ic3012958
15. (a) Y. M. Chumakov, B. Y. Antosyak, V. I. Tsapkov, N. M. Samus, *J. Struct. Chem.* **2001**, *42*, 335–339; DOI:10.1023/A:1010587923496
(b) Y.-J. Han, X.-Y. Guo, L.-W. Xue, *Acta Chim. Slov.* **2022**, *69*, 928–936; DOI:10.17344/acsi.2022.7817
(c) H.-Y. Zhu, *Acta Chim. Slov.* **2021**, *68*, 65–71. DOI: 10.17344/acsi.2020.6138

Povzetek

Sintetizirali smo dva enojedrna cinkova(II) kompleksa [ZnCl₂(HL)] (**1**) in [ZnBr₂(HL)] (**2**) ter polimerni cinkov(II) kompleks [Zn(dca)L] (**3**), kjer je HL zwitterionska oblika Schiffove baze 2,4-difluoro-6-(((2-pirolidin-1-il)etilimino)metil)fenol (HL), L je monoanionska oblika HL, dca pa je dicianoamid. Spojine smo okarakterizirali z elementno analizo in infrardečo spektroskopijo ter jim določili kristalne strukture z rentgensko monokristalno analizo. Kompleksa **1** in **2** sta izostrukturna, Zn centralni atomi imajo tetraedrično koordinacijo. Ligandi Schiffove baze so v obeh kompleksih koordinirani na Zn atome preko fenolatnega kisika in imino dušika. Cinkovi atomi v kompleksu **3** so tetraedrično koordinirani in jih povezujejo dicianoamidni mostnovni ligandi. Ligand Schiffove baze je v tem kompleksu koordiniran na cinkov atom preko fenolatnega kisika, imino dušika in pirolidinskega dušika. Molekule vseh treh kompleksov so stabilizirane z vodikovimi vezmi. Biološki testi kažejo, da imajo kompleksi dobro protimikrobno delovanje na bakterijske seve *Escherichia coli*, *Pseudomonas aeruginosa*, *Salmonella typhi* in *Staphylococcus aureus*.



Except when otherwise noted, articles in this journal are published under the terms and conditions of the Creative Commons Attribution 4.0 International License

Scientific paper

Synthesis, Characterization and X-Ray Crystal Structures of Aroylhydrazones Derived from 2-Chlorobenzaldehyde with Various Benzohydrazides

Jia-Xue Liu¹, Shi-Yu Zhang², Meng-Xiao Tai², Wei Li^{1,*} and Zhonglu You²¹ Department of Radiology, The Second Hospital of Dalian Medical University, Dalian 116023, P.R. China² Department of Chemistry and Chemical Engineering, Liaoning Normal University, Dalian 116029, P.R. China

* Corresponding author: E-mail: liwei_dlmu@126.com

Received: 08-31-2024

Abstract

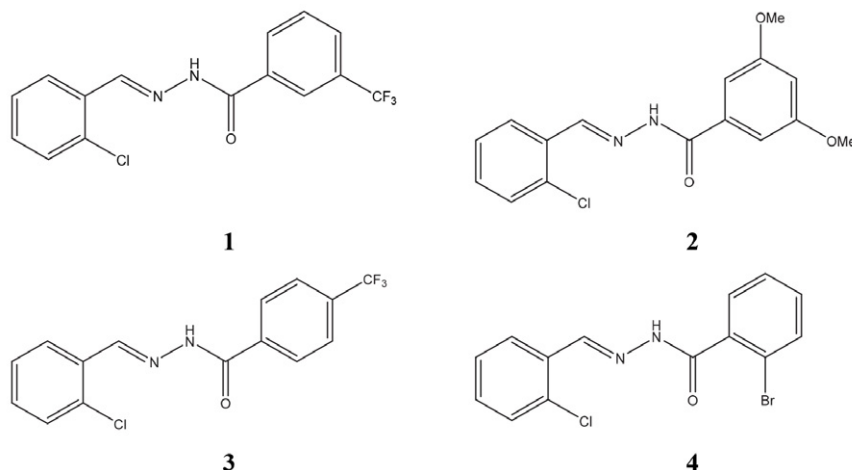
Reaction of 2-chlorobenzaldehyde with 3-trifluoromethylbenzohydrazide, 3,5-dimethoxybenzohydrazide, 4-trifluoromethylbenzohydrazide and 2-bromobenzohydrazide, respectively, in methanol afforded four new aroylhydrazones. The newly synthesized compounds were characterized by means of elemental analysis, IR and ¹H NMR spectroscopy, and their structures were further confirmed by X-ray single crystal determination. The compounds were assayed for their antibacterial activities against *E. coli*, *P. aeruginosa*, *B. subtilis*, and *S. aureus* and show interesting results.

Keywords: Aroylhydrazones; 2-chlorobenzaldehyde; crystal structure; antibacterial activity.

1. Introduction

Aroylhydrazones containing –C(O)–NH–N=CH– group can be prepared by a facile reaction of carbonyl containing compounds with hydrazides. The compounds have shown interesting biological application such as antibacterial activity,¹ antifungal activity,² antitumor activity,³ anti-inflammatory activity,⁴ and cytotoxic activity.⁵ The literature work indicates that compounds bearing halide substituents

have enhanced biological activities especially for the antibacterial and antifungal aspects.⁶ Rai et al. reported some fluoro, chloro, bromo and iodo-containing compounds that show improved antimicrobial activities.⁷ Recently, we have reported some hydrazones derived from 4-pyridinecarboxaldehyde.⁸ In continuation of such work, we report herein four new aroylhydrazones, *N*'-(2-chlorobenzylidene)methyl-3-trifluoromethylbenzohydrazide (**1**), *N*'-(2-chlorobenzylidene)methyl-3,5-dimethoxybenzohydrazide (**2**),



Scheme 1. The aroylhydrazones under study

N'-(2-chlorobenzylidenemethylene)-4-trifluoromethylbenzohydrazide (3), and 2-bromo-*N*'-(2-chlorobenzylidenemethylene)benzohydrazide (4), and evaluation of their antibacterial activities.

2. Experimental

2.1. Materials and Measurements

2-Chlorobenzaldehyde, 3-trifluoromethylbenzohydrazide, 3,5-dimethoxybenzohydrazide, 4-trifluoromethylbenzohydrazide, and 2-bromobenzohydrazide were purchased from Sigma-Aldrich, and used as received. The remaining chemicals were obtained from Aladin Chemical Co. Ltd. CHN elemental analyses were carried out with a Perkin-Elmer elemental analyzer. Infrared spectra of the compounds were recorded on a Nicolet AVATAR 360 spectrometer. ¹H NMR data were determined with a Bruker 500 MHz instrument. Single crystal X-ray diffraction was performed on a Bruker D8 VENTURE PHOTON diffractometer at room temperature equipped with Mo-K α radiation.

2.2. Preparation of the compounds

The four compounds were facile synthesized with the following method. 2-Chlorobenzaldehyde (1.0 mmol, 140 mg) was dissolved in MeOH (30 mL), which was slowly added to the methanolic solution (30 mL) containing 3-trifluoromethylbenzohydrazide (1.0 mmol, 204 mg), 3,5-dimethoxybenzohydrazide (1.0 mmol, 196 mg), 4-trifluoromethylbenzohydrazide (1.0 mmol, 204 mg), and 2-bromobenzohydrazide (1.0 mmol, 215 mg), respectively. The mixtures were magnetic stirred for 30 min at room temperature. Single crystals of the compounds with X-ray diffraction quality were grown from the solution after slow evaporation in air for several days.

N'-(2-Chlorobenzylidenemethylene)-3-trifluoromethylbenzohydrazide (1)

Colorless crystals. Yield: 273 mg (83%). Anal. calcd. for C₁₅H₁₀ClF₃N₂O: C, 55.15; H, 3.09; N, 8.57; found C, 54.93; H, 3.16; N, 8.65%. Characteristic IR data (cm⁻¹): 3184 (w), 1652 (s), 1598 (m), 1563 (s), 1434 (w), 1370 (w), 1330 (s), 1310 (m), 1276 (s), 1167 (s), 1117 (s), 1073 (m), 953 (w), 934 (w), 914 (w), 810 (w), 755 (m), 701 (s). ¹H NMR (500 MHz, *d*₆-DMSO): δ : 12.24 (s, 1H, NH), 8.88 (s, 1H, CN=N), 8.28 (s, 1H, ArH), 8.26 (d, 1H, ArH), 8.06 (t, 1H, ArH), 7.97 (d, 1H, ArH), 7.78 (t, 1H, ArH), 7.55 (d, 1H, ArH), 7.46 (m, 2H, ArH).

N'-(2-Chlorobenzylidenemethylene)-3,5-dimethoxybenzohydrazide (2)

Colorless crystals. Yield: 281 mg (88%). Anal. calcd. for C₁₆H₁₅ClN₂O₃: C, 60.29; H, 4.74; N, 8.79; found

C, 60.45; H, 4.81; N, 8.68%. Characteristic IR data (cm⁻¹): 3178 (w), 1652 (s), 1598 (s), 1565 (s), 1454 (m), 1360 (m), 1310 (m), 1206 (m), 1163 (s), 1063 (s), 945 (w), 854 (m), 760 (w), 700 (w), 538 (w). ¹H NMR (500 MHz, *d*₆-DMSO): δ : 11.98 (s, 1H, NH), 8.88 (s, 1H, CN=N), 8.03 (t, 1H, ArH), 7.53 (t, 1H, ArH), 7.45 (m, 2H, ArH), 7.10 (d, 2H, ArH), 6.73 (s, 1H, ArH), 3.83 (s, 6H, CH₃).

N'-(2-Chlorobenzylidenemethylene)-4-trifluoromethylbenzohydrazide (3)

Colorless crystals. Yield: 255 mg (78%). Anal. calcd. for C₁₅H₁₀ClF₃N₂O: C, 55.15; H, 3.09; N, 8.57; found C, 54.98; H, 3.16; N, 8.51%. Characteristic IR data (cm⁻¹): 3165 (w), 1655 (s), 1597 (m), 1561 (m), 1445 (w), 1372 (w), 1323 (m), 1313 (w), 1275 (m), 1163 (s), 1098 (m), 1065 (m), 971 (w), 946 (w), 902 (w), 823 (w), 757 (m), 689 (m). ¹H NMR (500 MHz, *d*₆-DMSO): δ : 12.17 (s, 1H, NH), 8.88 (s, 1H, CN=N), 8.19 (d, 2H, ArH), 7.79 (d, 2H, ArH), 7.67 (d, 1H, ArH), 7.53 (d, 1H, ArH), 7.45 (m, 2H, ArH).

2-Bromo-*N*'-(2-chlorobenzylidenemethylene)benzohydrazide (4)

Colorless crystals. Yield: 260 mg (77%). Anal. calcd. for C₁₄H₁₀BrClN₂O: C, 49.81; H, 2.99; N, 8.30; found C, 49.67; H, 3.12; N, 8.37%. Characteristic IR data (cm⁻¹): 3190 (w), 1653 (s), 1597 (s), 1563 (s), 1457 (m), 1371 (m), 1323 (w), 1211 (m), 1160 (m), 1073 (s), 953 (w), 846 (m), 757 (w), 723 (w), 612 (w). ¹H NMR (500 MHz, *d*₆-DMSO): δ : 12.10 (s, 1H, NH), 8.70 (s, 1H, CN=N), 8.03 (d, 1H, ArH), 7.73 (d, 1H, ArH), 7.57 (d, 1H, ArH), 7.51 (m, 3H, ArH), 7.38 (m, 2H, ArH).

2.3. Single Crystal X-ray Determination

Single crystal X-ray determination for the crystals of the compounds were carried out with Mo-K α radiation ($\lambda = 0.71073 \text{ \AA}$) at 298(2) K using Bruker D8 VENTURE PHOTON diffractometer. The data were reduced with SAINT.⁹ Multi-scan absorption corrections were performed with SADABS.¹⁰ All structures of the compounds were solved by direct method and refined against *F*² by full-matrix least-squares method using SHELXT and SHELXL programs.¹¹ All non-H atoms were refined anisotropically. The amino H atoms were located from electronic maps and refined isotropically. The N–H distances were restrained to 0.90(1) \AA . The remaining H atoms were placed in calculated positions. The crystallographic data are listed in Table 1. The trifluoromethyl groups in compounds **1** and **3** are disordered, with occupancies of 0.46(1) and 0.54(1), and 0.38(1) and 0.62(1), respectively.

Table 1. Crystal data for the compounds

	1	2	3	4
Formula	C ₁₅ H ₁₀ ClF ₃ N ₂ O	C ₁₆ H ₁₅ ClN ₂ O ₃	C ₁₅ H ₁₀ ClF ₃ N ₂ O	C ₁₄ H ₁₀ BrClN ₂ O
M _r	326.70	318.75	326.70	337.60
Crystal color, habit	Colorless, block	Colorless, block	Colorless, block	Colorless, block
Crystal system	Monoclinic	Monoclinic	Monoclinic	Monoclinic
Space group	P2 ₁ /c	P2 ₁ /c	P2 ₁ /c	P2 ₁ /n
Unit cell parameters				
a (Å)	13.2066(10)	21.6544(19)	12.6745(12)	7.4933(7)
b (Å)	12.9373(11)	8.9307(13)	13.1570(13)	25.3971(16)
c (Å)	8.5263(5)	16.3842(17)	8.8105(11)	7.7789(8)
β (°)	97.877(1)	99.034(1)	92.381(1)	114.043(1)
V (Å ³)	1443.0(2)	3129.2(6)	1468.0(3)	1351.9(2)
Z	4	8	4	4
D _{calc} (g cm ⁻³)	1.504	1.353	1.478	1.659
μ (mm ⁻¹)	0.300	0.258	0.295	3.230
F(000)	664	1328	664	672
Collected data	7045	18200	8618	7957
Number of unique data	2672	5821	2734	2511
Number of observed data [I > 2σ(I)]	1998	2765	1509	1876
Number of parameters	231	408	230	175
Number of restraints	49	2	49	1
R ₁ , wR ₂ [I > 2σ(I)]	0.0382, 0.0921	0.0559, 0.0949	0.0556, 0.1237	0.0353, 0.0661
R ₁ , wR ₂ (all data)	0.0556, 0.1053	0.1500, 0.1349	0.1161, 0.1550	0.0573, 0.0725
Goodness of fit on F ²	1.073	1.017	1.051	1.022

3. Results and Discussion

3. 1. Chemistry

The four compounds were prepared by facile condensation reaction of 2-chlorobenzaldehyde with aroylhydrazides in methanol. They have good solubility in MeOH, EtOH, acetonitrile, DMSO and DMF. The strong bands in the range 1652–1655 cm⁻¹ can be assigned to the vibration of ν(C=O). The bands in the range 1597–1598 cm⁻¹ can be assigned to the vibration of ν(C=N).^{8,12} The weak bands indicative of the ν(N–H) are observed at 3165–3190 cm⁻¹. The CHN elemental analyses agree well with the proposed chemical formulae by single crystal X-ray determination.

3. 2. Crystal Structure Description

The structures of the four compounds are shown in Figures 1–4. Characteristic bond lengths are given in Table 2. The asymmetric unit of **2** contains two independent molecules. There is only one aroylhydrazone molecule in the asymmetric unit in the remaining three compounds. The molecule of each compound has an *E* configuration about the C=N group. The methyldiene bonds have distances of 1.26–1.27 Å, which are similar to each other for the four compounds. The C–N bonds are shorter than usual, and the C=O bonds are longer than usual, suggesting the molecules present conjugation effects. The bond lengths in the compounds are within normal values.^{8,13} The two benzene rings form dihedral angles of 7.4(3)° for **1**, 35.3(5)° and 4.0(5)° for **2**, 4.3(5)° for **3**, and 15.7(3)° for

4. It is obvious that the dihedral angle between the two benzene rings in one molecule of compound **2** is larger than the other molecule, which might be caused by the hydrogen bonding. There are two acceptors (O1 and N1) for N4–H4 bond, *viz.* N4–H4...O1 and N4–H4...N1.

The aroylhydrazone molecules of **1** are linked through hydrogen bonds of N–H...O and C–H...O, to form one-dimensional chains along the *c*-axis direction (Table 3, Figure 5). The aroylhydrazone molecules of **2** are linked through hydrogen bonds of N–H...O, N–H...N and

Table 2. Selected bond distances (Å) for the four compounds

1			
N1–C7	1.268(2)	N1–N2	1.388(2)
N2–C8	1.341(2)	O1–C8	1.230(2)
2			
N1–C7	1.269(4)	N1–N2	1.378(4)
N2–C8	1.361(4)	O1–C8	1.229(4)
N3–C23	1.270(4)	N3–N4	1.381(4)
N4–C24	1.337(4)	O4–C24	1.228(4)
3			
N1–C7	1.261(4)	N1–N2	1.388(3)
N2–C8	1.349(4)	O1–C8	1.221(4)
4			
N1–C7	1.268(3)	N1–N2	1.387(3)
N2–C8	1.344(3)	O1–C8	1.220(3)

C–H...O, to form one-dimensional chains along the *c*-axis direction (Table 3, Figure 6). The aroylhydrazone molecules of **3** are linked through hydrogen bonds of N–H...O and C–H...O, to form one dimensional chains along the *c*-axis direction (Table 3, Figure 7). The aroylhydrazone molecules of **4** are linked through hydrogen bonds of N–H...O and C–H...O, to form one-dimensional chains along the *a* axis direction (Table 3, Figure 8).

3. 3. Antibacterial Activity

The antibacterial experiment was carried out with the method described in literature.¹⁴ Penicillin G was selected as a reference. DMSO was used as a solvent and the solutions were diluted by water. At the tested concentration, DMSO has no activity on the bacteria. The zones of inhibition for the bacteria *E. coli*, *P. aeruginosa*, *S. typhi* and *S. aureus* are summarized in Table 4. MIC values are

Table 3. Hydrogen bond distances (Å) and angles (°) for the four compounds

<i>D</i> –H... <i>A</i>	<i>d</i> (<i>D</i> –H), Å	<i>d</i> (H... <i>A</i>), Å	<i>d</i> (<i>D</i> ... <i>A</i>), Å	Angle (<i>D</i> –H... <i>A</i>), °
1				
N2–H2...O1 ⁱ	0.885(9)	2.036(11)	2.8978(18)	164(2)
C7–H7...O1 ⁱ	0.93	2.51	3.274(2)	139.5
2				
N2–H2...O4 ⁱⁱ	0.900(10)	2.04(3)	2.853(4)	149(5)
N4–H4...O1 ⁱⁱⁱ	0.901(10)	2.11(2)	2.948(4)	155(5)
C7–H7...O4 ⁱⁱ	0.93	2.27	3.089(5)	147.1
3				
N2–H2...O1 ^v	0.897(10)	1.996(16)	2.858(3)	161(3)
C7–H7...O1 ^v	0.93	2.34	3.137(4)	143.2
4				
C7–H7...O1 ^{vi}	0.93	2.52	3.292(3)	140.2
N2–H2...O1 ^{vi}	0.893(10)	1.975(13)	2.842(3)	163(3)

Symmetry codes: i) $x, 1\frac{1}{2} - y, \frac{1}{2} + z$; ii) $x, y, -1 + z$; iii) $x, \frac{1}{2} - y, \frac{1}{2} + z$; iv) $1 - x, -y, -z$; v) $x, 1\frac{1}{2} - y, \frac{1}{2} + z$; vi) $-\frac{1}{2} + x, \frac{1}{2} - y, -\frac{1}{2} + z$.

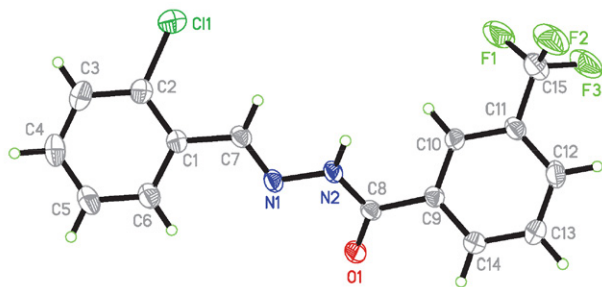


Figure 1. Molecular structure of compound **1** with 30% thermal ellipsoids.

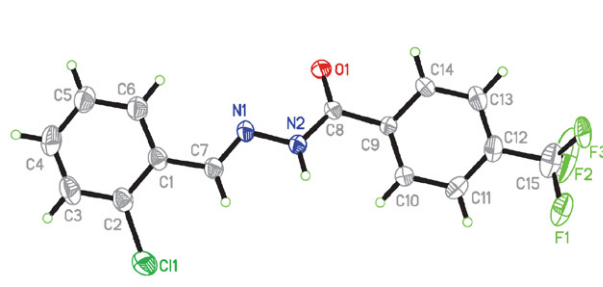


Figure 3. Molecular structure of compound **3** with 30% thermal ellipsoids.

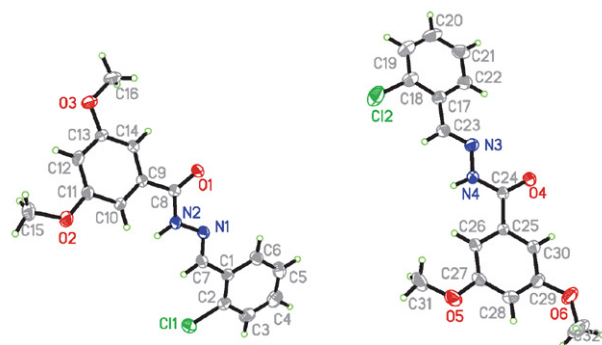


Figure 2. Molecular structure of compound **2** with 30% thermal ellipsoids.

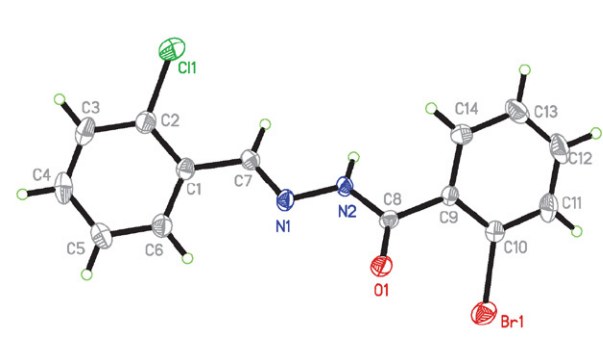


Figure 4. Molecular structure of compound **4** with 30% thermal ellipsoids.

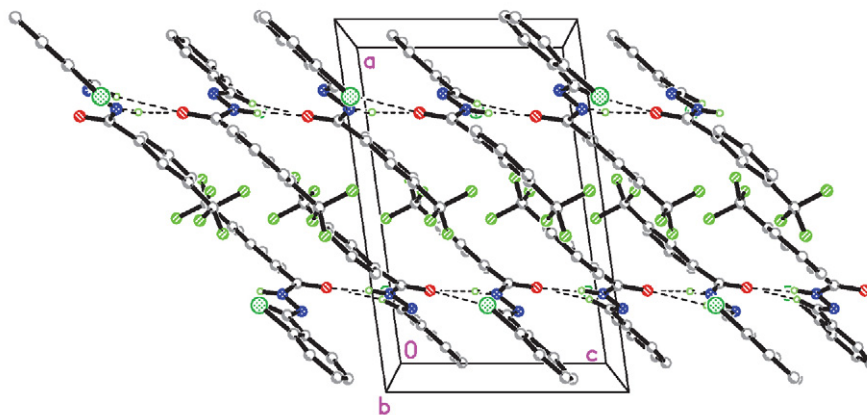


Figure 5. The hydrogen bonds (dashed lines) linked molecular structure of compound 1. Hydrogen atoms not involved in hydrogen bonding are deleted for clarity.

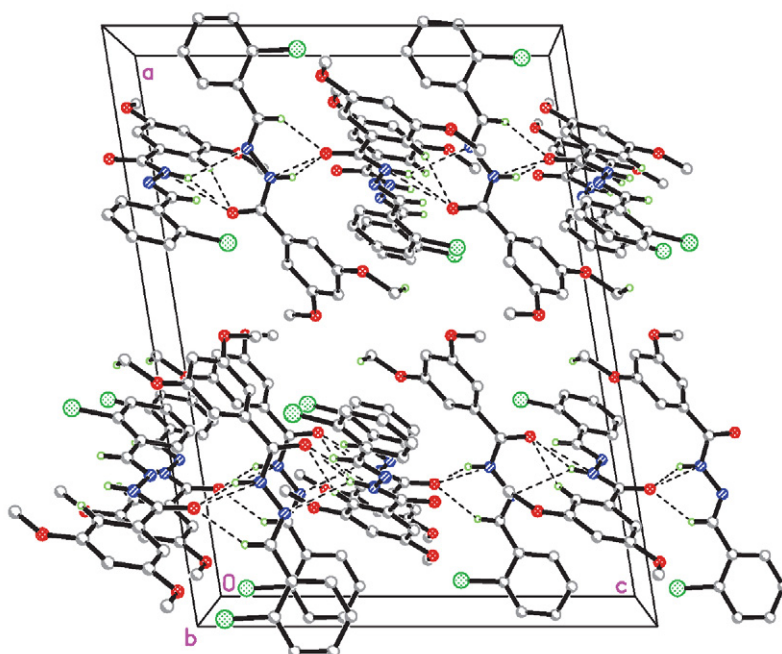


Figure 6. The hydrogen bonds (dashed lines) linked molecular structure of compound 2. Hydrogen atoms not involved in hydrogen bonding are deleted for clarity.

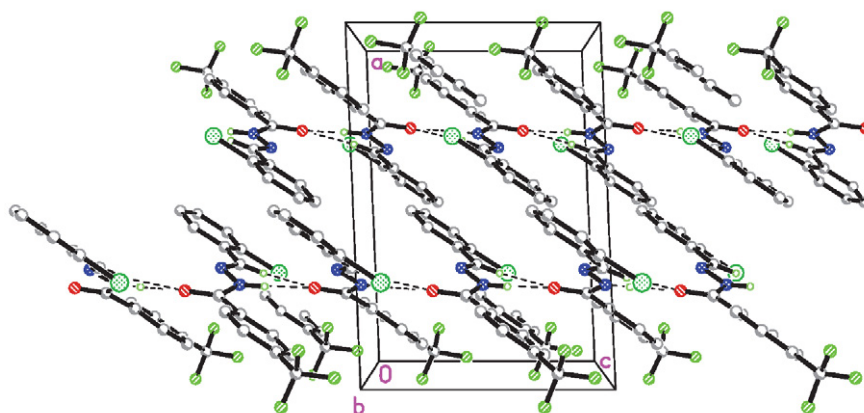


Figure 7. The hydrogen bonds (dashed lines) linked molecular structure of compound 3. Hydrogen atoms not involved in hydrogen bonding are deleted for clarity.

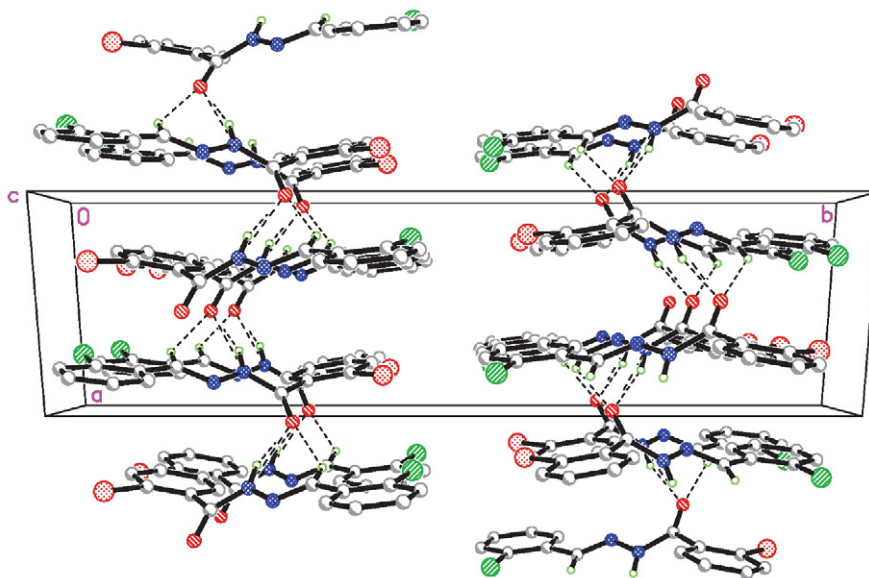


Figure 8. The hydrogen bonds (dashed lines) linked molecular structure of compound 4. Hydrogen atoms not involved in hydrogen bonding are deleted for clarity.

listed in Table 5. The compounds show from weak to strong activities on the bacteria strains. Compounds **1** and **3** have strong activity on *E. coli*, *P. aeruginosa* and *B. subtilis*, and medium activity on *S. aureus*. Compound **2** has medium activity on *E. coli*, *P. aeruginosa* and *B. subtilis*, and weak activity on *S. aureus*. Compound **4** has strong activity on *E. coli*, and medium activity on *P. aeruginosa*, *B. subtilis* and *S. aureus*. Among the compounds, compounds **1** and **3** have the most activity on *E. coli* and *P. aeruginosa* with MIC values of 1.56 and 6.25 $\mu\text{g mL}^{-1}$, respectively, which are stronger or similar to penicillin G. The compounds have higher activity on *E. coli*, *B. subtilis* and *S. aureus* than the pyrroles bearing thiazole moiety.¹⁵ The trifluoromethyl containing compounds **1** and **3** have better activity on the bacteria than the fluoro-substituted aroylhydrazones.¹⁶ The present compounds have higher activity than the benzohydrazones.⁸

After careful comparison we noticed that the electronic withdrawing substituent groups like Cl, CF_3 and Br might contribute to the activity on the bacteria strains. The trifluoromethyl group can enhance the activity.

Table 4 Antibacterial results

Compound	Zone of inhibition (mm)			
	<i>E. coli</i>	<i>P. aeruginosa</i>	<i>B. subtilis</i>	<i>S. aureus</i>
1	32 ± 2.2	23 ± 2.1	22 ± 1.7	15 ± 1.5
2	16 ± 1.7	15 ± 1.4	11 ± 1.5	9.3 ± 1.2
3	33 ± 1.8	21 ± 2.2	25 ± 2.0	16 ± 1.3
4	25 ± 2.0	17 ± 1.5	14 ± 1.7	12 ± 1.6
Penicillin G	30 ± 2.8	26 ± 3.1	30 ± 3.2	24 ± 2.9

Table 5 Antibacterial activities (MIC, $\mu\text{g mL}^{-1}$)

Compound	<i>E. coli</i>	<i>P. aeruginosa</i>	<i>B. subtilis</i>	<i>S. aureus</i>
1	1.56	6.25	3.13	12.5
2	12.5	6.25	25	25
3	1.56	6.25	3.13	12.5
4	6.25	12.5	12.5	12.5
Penicillin G	3.13	6.25	1.56	6.25

4. Conclusions

In conclusion, a series of four aroylhydrazones were synthesized and characterized. The antibacterial activities against *E. coli*, *P. aeruginosa*, *B. subtilis* and *S. aureus* were determined. *N*'-(2-Chlorobenzylidene)methylene)-3-trifluoromethylbenzohydrazide and *N*'-(2-chlorobenzylidene)methylene)-4-trifluoromethylbenzohydrazide have strong activity on *E. coli* and *P. aeruginosa*, with MIC values of 1.56 and 6.25 $\mu\text{g mL}^{-1}$, respectively. The trifluoromethyl substituent group is a preferred factor for the exploration of new antibacterial drugs.

5. Supplementary Material

CCDC–2380982 (**1**), 2380983 (**2**), 2380984 (**3**) and 2380985 (**4**) are the crystallographic data for this work. The data can be obtained at <http://www.ccdc.cam.ac.uk/const/retrieving.html> or from the Cambridge Crystallographic Data Centre (CCDC), 12 Union Road, Cambridge CB2 1EZ, UK; fax: +44(0)1223-336033 or e-mail: deposit@ccdc.cam.ac.uk.

6. References

1. (a) S. Verma, S. Lal, R. narang, K. Sudhakar, *Chem. Med. Chem.* **2023**. DOI:10.1002/cmcd.202200571
 (b) M. A. Shah, A. Uddin, M. R. Shah, I. Ali, R. Ullah, P. A. Hannan, H. Hussain, *Molecules* **2022**, *27*, 6770. DOI:10.3390/molecules27196770
 (c) M. Nabizadeh, M. R. Naimi-Jamal, M. Rohani, P. Azerang, A. Tahghighi, *Lett. Appl. Microbiol.* **2022**, *75*, 667–679. DOI:10.1111/lam.13692
 (d) G.-X. He, L.-W. Xue, *Acta Chim. Slov.* **2021**, *68*, 567–574. DOI:10.17344/acsi.2020.6333
 (e) K. Pyta, A. Janas, M. Szukowska, P. Pecyna, M. Jaworska, M. Gajecka, F. Bartl, P. Przybylski, *Eur. J. Med. Chem.* **2019**, *167*, 96–104. DOI:10.1016/j.ejmech.2019.02.009
 (f) I. Shabeeb, L. Al-Essa, M. Shtaiwi, E. Al-Shalabi, E. Younes, R. Okasha, M. Abu Sini, *Lett. Org. Chem.* **2019**, *16*, 430–436. DOI:10.2174/1570178616666181227122326
2. (a) M. Aydin, A. Ozturk, T. Duran, U. O. Ozmen, E. Sumlu, E. B. Ayan, E. N. Korucu, *J. Mycologie Medicale* **2023**, *33*, 101327. DOI:10.1016/j.mymed.2022.101327
 (b) I. R. Silva, T. Kronenberger, E. C. L. Gomes, I. C. Cesar, R. B. Oliveira, V. G. Maltarollo, *Eur. J. Pharm. Sci.* **2021**, *156*, 105575. DOI:10.1016/j.ejps.2020.105575
 (c) I. A. Khodja, H. Boulebd, C. Bensouici, A. Belfaitah, *J. Mol. Struct.* **2020**, *1218*, 128527. DOI:10.1016/j.molstruc.2020.128527
 (d) A. E. Dascalu, A. Ghinet, E. Lipka, C. Furman, B. Rigo, A. Fayeulle, M. Billamboz, *Bioorg. Med. Chem. Lett.* **2020**, *30*, 127220. DOI:10.1016/j.bmcl.2020.127220
 (e) N. R. Appna, R. K. Nagiri, R. B. Korupolu, S. Kanugala, G. K. Chityal, G. Thippaparapu, N. Banda, *Med. Chem. Res.* **2019**, *28*, 1509–1528. DOI:10.1007/s00044-019-02390-w
 (f) A. Erguc, M. D. Altintop, O. Atli, B. Sever, G. Iscan, G. Gormus, A. Ozdemir, *Lett. Drug Des. Discov.* **2018**, *15*, 193–202. DOI:10.2174/1570180814666171003145227
 (g) N. J. P. Subhashini, P. Janaki, B. Bhadraiah, *Russ. J. Gen. Chem.* **2017**, *87*, 2021–2026. DOI:10.1134/S1070363217090183
3. (a) M. S. A. Abdelrahman, F. M. Omar, A. A. Saleh, M. A. El-ghamry, *J. Mol. Struct.* **2022**, *1251*, 131947. DOI:10.1016/j.molstruc.2021.131947
 (b) B. Ay, O. Sahin, B. S. Demir, Y. Saygideger, J. M. Lopez-de-Luzuriaga, G. Mahmoudi, D. A. Safin, *New J. Chem.* **2020**, *44*, 9064–9072. DOI:10.1039/D0NJ00921K
 (c) E. M. Gungor, M. D. Altintop, B. Sever, G. A. Ciftci, *Lett. Drug Des. Discov.* **2020**, *17*, 1380–1392. DOI:10.2174/1570180817999200618163507
 (d) H. M. A. Abumelha, *J. Heterocycl. Chem.* **2018**, *55*, 1738–1745. DOI:10.1002/jhet.3211
 (e) H. F. He, X. Y. Wang, L. Q. Shi, W. Y. Yin, Z. W. Yang, H. W. He, Y. Liang, *Bioorg. Med. Chem. Lett.* **2016**, *26*, 3263–3270. DOI:10.1016/j.bmcl.2016.05.059
4. (a) M. A. M. B. Medeiros, M. G. E. Silva, J. D. Barbosa, E. M. de Lavor, T. F. Ribeiro, C. A. F. Macedo, L. A. M. D. Duarte-Filho, T. A. Feitosa, J. D. Silva, H. H. Fokoue, C. R. M. Araujo, A. D. Gonsalves, L. A. D. Ribeiro, J. R. G. D. Almeida, *Plos One* **2021**, *16*, e0258094. DOI:10.1371/journal.pone.0258094
 (b) M. X. Song, B. Liu, S. W. Yu, S. H. He, Y. Q. Liang, S. F. Li, Q. Y. Chen, X. Q. Deng, *Lett. Drug. Des. Discov.* **2020**, *17*, 502–511. DOI:10.2174/1570180816666190731113441
 (c) U. Debnath, S. Mukherjee, N. Joardar, S. P. S. Babu, K. Jana, A. K. Misra, *Eur. J. Pharm. Sci.* **2019**, *134*, 102–115. DOI:10.1016/j.ejps.2019.04.016
 (d) U. Kendur, G. H. Chimmalagi, S. M. Patil, K. B. Gudasi, C. S. Frampton, C. V. Mangannavar, I. S. Muchchandi, *J. Mol. Struct.* **2018**, *1153*, 299–310. DOI:10.1016/j.molstruc.2017.10.022
 (e) V. Gorantla, R. Gundla, S. S. Jadav, S. R. Anugu, J. Chimakurthy, S. K. Nidasanametla, R. Korupolu, *New J. Chem.* **2017**, *41*, 13516–13532. DOI:10.1039/C7NJ03332J
 (f) M. A. Abdelgawad, M. B. Labib, M. Abdel-Latif, *Bioorg. Chem.* **2017**, *74*, 212–220. DOI:10.1016/j.bioorg.2017.08.014
5. (a) E. Aydin, A. M. Senturk, H. B. Kucuk, M. Guzel, *Molecules* **2022**, *27*, 7309
 (b) M. A. Shah, A. Uddin, M. R. Shah, I. Ali, R. Ullah, P. A. Hannan, H. Hussain, *Molecules* **2022**, *27*, 6770. DOI:10.3390/molecules27196770
 (c) F. Beygi, A. Mostoufi, A. Mojaddami, *Chem. Biodivers.* **2022**, *19*, e202100754. DOI:10.1002/cbdv.202100754
 (d) Z. Ozdemir, N. Basak-Turkmen, I. Ayhan, O. Ciftci, M. Uysal, *Pharm. Chem. J.* **2019**, *52*, 923–929. DOI:10.1007/s11094-019-01927-y
 (e) J. C. Coa, W. Castrillon, W. Cardona, M. Carda, V. Ospina, J. A. Munoz, I. D. Velez, S. M. Robledo, *Eur. J. Med. Chem.* **2015**, *101*, 746–753. DOI:10.1016/j.ejmech.2015.07.018
6. (a) L. C. Felton, J. H. Brewer, *Science* **1947**, *105*, 409–410. DOI:10.1126/science.105.2729.409
 (b) M. Gopalakrishnan, J. Thanusu, V. Kanagarajan, R. Govindaraju, *J. Enzym. Inhib. Med. Chem.* **2009**, *24*, 52–58. DOI:10.1080/14756360801906632
 (c) L. Shi, H.-M. Ge, S.-H. Tan, H.-Q. Li, Y.-C. Song, H.-L. Zhu, R.-X. Tan, *Eur. J. Med. Chem.* **2007**, *42*, 558–564. DOI:10.1016/j.ejmech.2006.11.010
 (d) M. Zhang, D.-M. Xian, H.-H. Li, J.-C. Zhang, Z.-L. You, *Aust. J. Chem.* **2012**, *65*, 343–350. DOI:10.1071/CH11424
7. (a) N. P. Rai, V. K. Narayanaswamy, T. Govender, B. K. Manuprasad, S. Shashikanth, P. N. Arunachalam, *Eur. J. Med. Chem.* **2010**, *45*, 2677–2682. DOI:10.1016/j.ejmech.2010.02.021
 (b) N. P. Rai, V. K. Narayanaswamy, S. Shashikanth, P. N. Arunachalam, *Eur. J. Med. Chem.* **2009**, *44*, 4522–4527.
8. Y.-X. Zhou, W. Li, Z. You, *Acta Chim. Slov.* **2023**, *70*, 240–246. DOI:10.17344/acsi.2023.8123
9. Bruker, SMART and SAINT, Bruker AXS Inc., Madison, Wisconsin, USA, **2012**.
10. G. M. Sheldrick, SADABS Program for Empirical Absorption Correction of Area Detector, University of Göttingen, Germany, **1996**.
11. (a) G. M. Sheldrick, *Acta Crystallogr.* **2015**, *A71*, 3–8. DOI:10.1107/S2053273314026370

- (b) G. M. Sheldrick, *Acta Crystallogr.*, **2005**, C71, 3–8.
12. G. M. Sheldrick, *Acta Crystallogr.* **2008**, A64, 112–122.
DOI:10.1107/S0108767307043930
13. M. Zhang, D.-M. Xian, H.-H. Li, J.-C. Zhang, Z.-L. You, *Aust. J. Chem.* **2012**, 65, 343–350. DOI:10.1071/CH11424
14. (a) M. Kuriakose, M. R. P. Kurup, E. Suresh, *Spectrochim. Acta A* **2007**, 66, 353–358. DOI:10.1016/j.saa.2006.03.003
(b) L.-W. Xue, S.-T. Li, Y.-J. Han, X.-Q. Luo, *Acta Chim. Slov.* **2022**, 69, 385–392. DOI:10.17344/acsi.2021.7252
(c) G.-X. He, L.-W. Xue, *Acta Chim. Slov.* **2021**, 68, 567–574.
DOI:10.17344/acsi.2020.6333
15. (a) Y. M. Chumakov, B. Y. Antosyak, V. I. Tsapkov, N. M. Samus, *J. Struct. Chem.* **2001**, 42, 335–339.
DOI:10.1023/A:1010587923496
(b) Y.-J. Han, X.-Y. Guo, L.-W. Xue, *Acta Chim. Slov.* **2022**, 69, 928–936; (c) H.-Y. Zhu, *Acta Chim. Slov.* **2021**, 68, 65–71.
DOI:10.17344/acsi.2022.7817
16. M. A. Salem, S. Y. Abbas, M. A. M. Sh. El-Sharief, M. H. Helal, M. A. Gouda, M. A. Assiri, T. E. Ali, *Acta Chim. Slov.* **2021**, 68, 990–996. DOI:10.17344/acsi.2021.6980
17. F.-M. Wang, L.-J. Li, G.-W. Zang, T.-T. Deng, Z.-L. You, *Acta Chim. Slov.* **2021**, 68, 541–547.
DOI:10.17344/acsi.2020.6051

Povzetek

Reakcija 2-klorobenzaldehida s 3-trifluorometilbenzohidrazidom, 3,5-dimetoksibenzohidrazidom, 4-trifluorometilbenzohidrazidom in 2-bromobenzohidrazidom v metanolu je dala štiri nove aroilhidrazone. Na novo sintetizirane spojine smo okarakterizirali z elementno analizo, IR in ^1H NMR spektroskopijo, njihove strukture pa smo potrdili z rentgensko monokristalno analizo. Pri spojinah smo določili njihovo antibakterijsko delovanje proti *E. coli*, *P. aeruginosa*, *B. subtilis* in *S. aureus*.



Except when otherwise noted, articles in this journal are published under the terms and conditions of the Creative Commons Attribution 4.0 International License

Scientific paper

Preparation, Characterization and Theoretical Calculation of a Cadmium Complex of 3-hydroxy-2-methylquinolin-4-carboxylate and 1,10-phenanthroline

Ting-Qun Qiu¹, Zhi-Tao Lu¹, Zi-Jian He¹, Zheng-Ping Xie², Jin Guo^{1*}
and Xiu-Guang Yi^{1*}

¹ School of Chemistry and Chemical Engineering, Jinggangshan University, Ji'an 343009,
PR China

² School of Chemistry and Chemical Engineering, Jiangxi University of Science and Technology, Ganzhou 341000,
PR China

* Corresponding author: E-mail: E-mail: 39366276@qq.com
jayxgggchem@163.com

Received: 09-30-2024

Abstract

A novel organic-inorganic hybrid cadmium complex [Cd(MCA)₂(Phen)(H₂O)] (MCA = anion of 3-hydroxyquinoline-4-carboxylic acid; Phen = 1,10-phenanthroline) was synthesized by solvothermal method and characterized by single crystal X-ray diffraction. The complex exhibits a two-dimensional structure through hydrogen bonding and π - π packing interactions. Solid state photoluminescence specter shows that the complex displays an emission in the red region of the light spectrum that time-dependent density functional theory calculations reveal can be attributed to ligand-to-ligand charge transfer. Solid diffuse reflection specter shows that the energy band gap of the complex is 2.32 eV.

Keywords: Cadmium, crystal structure, solid state diffuse reflection, TDDFT.

1. Introduction

Due to their unique physical and chemical properties and wide application prospects, metal-organic complexes have shown extraordinary potential and value in many fields such as material science,^{1,2} catalytic chemistry,^{3,4} biomedicine,^{5,6} photoelectric technology and so on.^{7,8} These complexes are usually formed by metal ions or atoms binding to organic ligands through coordination bonds. Their structural diversity, adjustability, and functionality make them star molecules in scientific research and technological applications.

Quinolinecarboxylic acid,^{9–11} as a nitrogen-containing heterocyclic aromatic carboxylic acid compound, its unique structure gives it superior properties as a metal-organic complex ligand. The carboxyl group in quinolinecarboxylic acid can be coordinated with metal ions in many ways, such as monodentate, bidentate or bridged. The nitrogen atom on the quinoline ring also has certain coordination ability and can form additional coordination bonds

with metal ions, further enriching the structural types and properties of the complexes. The rigid planar structure of the quinoline ring and the high reactivity of carboxyl group enable quinoline carboxylic acid to form stable and structurally diverse complexes with various metal ions.

Transition metals can be combined with many ligands to form complex and functional complexes due to their unfilled *d* orbitals, variable oxidation states and high coordination number.^{12–14} These complexes play an important role in catalysis, medicine, materials science and other fields, and promote the rapid development of related fields.^{15,16}

Based on this, we are interested in crystal engineering of compounds containing group 12 elements with 3-hydroxy-2-methylquinolin-4-carboxylic acid (HMCA) as ligand.¹⁷ We report the solvothermal synthesis, X-ray crystal structure, photoluminescence and UV-visible diffuse reflectance spectral properties of a novel cadmium complex with a neutral isolated (0D) structure, and time-dependent density functional theory (TDDFT) calculations [Cd(MCA)₂(Phen)(H₂O)].

2. Experiment

2.1. Materials and Instruments

All reagents and chemicals are reagent grade, commercially available, and used directly for the reaction. The infrared spectrum of KBr disk was analyzed by PE-1 FT-IR spectrometer. Solid state UV/VIS diffuse reflection spectroscopy was performed on a computer-controlled TU1901 UV/VIS spectrometer. The fine ground powder was coated with barium sulfate to obtain 100% reflectance. The photoluminescence characteristics were studied on the F97XP photoluminescence spectrometer.

2.2. Synthesis of 3-hydroxy-2-methylquinoline-4-carboxylic acid (HMCA)

Synthesis of isatin: Indigo (0.262 g, 1.0 mmol), $K_2Cr_2O_7$ (0.147 g, 0.5 mmol) and distilled water (200 mL) were added to 500 mL three-neck flask and stirred. After cooling, dilute H_2SO_4 (10%, 250 mL) was added, stirred at 43°C for 1.5 h, diluted with twice the volume of distilled water, filtered out, dissolved in 10% NaOH solution, filtered again, and neutralized with 10% HCl until pH = 7.¹⁸ Yield: 0.23 g (90%); m.p. 210°C; HRMS m/z (ESI): calculated for $C_8H_5NO_2 [M+H]^+$ 147.0320, found 147.0826.

Synthesis HMCA: Isatin (0.147 g, 1.0 mmol) obtained in the previous step was added to the distilled water solution (200 mL) of NaOH (0.02 g, 0.5 mmol) to and filter. The filtrate and NaOH (0.02 g, 0.5 mmol) were added to chloroacetone (0.092 g, 1.0 mmol), and hydrochloric acid was added to adjust pH = 7, and filtration was done. Yield: 0.096 g (95%); m.p. 225°C; HRMS m/z (ESI): calculated for $C_{11}H_9NO_3 [M+H]^+$ 203.0582, found 203.0548. 1H NMR (400 MHz, DMSO) δ 9.15 (s, 1H), 7.93 (d, J = 8.0 Hz, 1H), 7.64 (t, J = 8.0 Hz, 1H), 7.60 7.52 (m, 2H), 2.70 (s, 3H).

2.3. Synthesis of Title Complexes

The ligand HMCA (0.1015 g, 0.5 mmol), cadmium acetate dihydrate (0.267 g, 1.0 mmol) and Phen (0.1 g, 0.5 mmol) were accurately weighed, and the above weighed samples were put into a 20 mL glass vial, followed by 10 mL water and 5 mL ethanol, and stirred with a glass rod. The substance in the glass bottle is placed in the oven at 80°C for four days. After cooling the mixture slowly down to room temperature, reddish block crystals suitable for X-ray analysis were collected and washed. Yield: 70% (based on cadmium). IR (KBr, cm^{-1}): 3420 (vs), 3044 (w), 2921 (w), 1592 (vs), 1516 (vs), 1423 (vs), 1355 (m), 1313 (m), 1216 (m), 1148 (m), 1094 (m), 1009 (m), 849 (vs), 777 (vs), 722 (vs), 642 (vs); Anal. Calcd. for $C_{34}H_{26}CdN_4O_7$ (%): C 57.11; H 3.67; N 7.84. Found (%): C 57.12; H 3.61; N 7.85.

2.4. X-ray Structure Determination

The single-crystal X-ray diffraction data set of the complex **1** was obtained by using a SuperNova CCD X-ray diffractometer. The micro-focus sealed X-ray tube is radiation source has Mo- $K\alpha$ radiation with being λ of 0.71073 Å. A mirror is acted as the diffraction radiation monochromator. The absorption corrections for complex **1** was made using the CrysAlis PRO programs.¹⁹ The structure of complex **1** was solved *via* direct method and subsequently refined using SHELXT and SHELXL programs, respectively^{20,21} with the OLEX2 graphical interface.²² All non-hydrogen atoms were located on the respective difference Fourier maps and anisotropically refined, while hydrogen atoms were theoretically found, allowed to attach on the parent atoms and isotropically refined. Selected crystal data and structural refinement details of the complex **1** are listed in Table 1. The selected bond lengths (Å) and bond angles (°) are listed in Table 2 and hydrogen bond interactions are shown in Table 3.

Table 1. Crystallographic data and structural analysis of the complex **1**

Empirical formula	$C_{34}H_{26}CdN_4O_7$
Formula weight	714.99
Temperature/K	293
Crystal system	triclinic
Space group	$P-1$
$a/\text{Å}$	9.6365(3)
$b/\text{Å}$	12.8942(4)
$c/\text{Å}$	13.6041(5)
$\alpha/^\circ$	108.980(3)
$\beta/^\circ$	98.922(3)
$\gamma/^\circ$	102.637(3)
Volume/ Å^3	1512.14(9)
Z	2
$\rho_{\text{calc}}/\text{g/cm}^3$	1.570
μ/mm^{-1}	0.779
$F(000)$	724.0
Reflections collected	13170
Independent reflections (R_{int})	6956 (0.0225)
Data/restraints/parameters	6956/0/420
Goodness-of-fit on F^2	1.044
$R_1, wR_2 [I > 2\sigma(I)]$	0.0391, 0.0772
R_1, wR_2 (all data)	0.0530, 0.0843
Largest diff. peak/hole / $e \text{ Å}^{-3}$	0.53/−0.34

3. Results and Discussion

3.1. Crystal Structure Analysis of Complex

X-ray single-crystal diffraction analysis reveals that the complex **1** that crystallizes in the triclinic system space group $P-1$ and is composed of a neutral isolated molecule as shown in Figure 1. The cadmium ion is surrounded by four oxygen atoms from two HMCA molecules, two nitrogen at-

oms from the auxiliary ligand, and one oxygen atom from water molecule, forming a seven-coordination structure mode. The observed Cd–O bonds lengths in the range 2.2774(19)–2.458(2) Å and Cd–N bond lengths in the range 2.342(2)–2.357(2) Å are comparable with those reported in the references.^{23,24} In the complex **1**, there are several O–H...O, O–H...N, C–H...O hydrogen-bonding interactions that allow the construction of a 3D supramolecular framework (the intramolecular hydrogen bond for O1–H1...O2, O4–H4...O5, C10–H10...O3, C21–H21...O6 and the intermolecular hydrogen bond for O7–H7A...N2ⁱ, O7–H7B...O2ⁱⁱ, C8–H8...O1ⁱⁱⁱ), as shown in Table 3 and Figure 2.

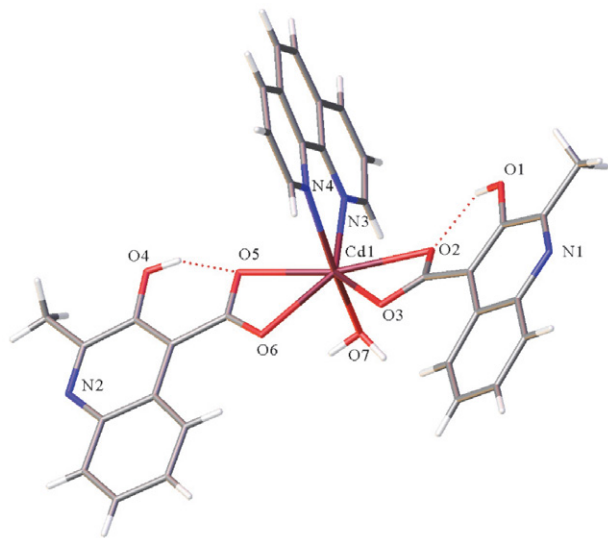


Figure 1. Intramolecular hydrogen bonds present in the complex **1**

Table 2. Selected bond lengths (Å) and bond angles (°) for the complex **1**

Distance	Length/Å	Distance	Length/Å
Cd1–O2	2.445(2)	Cd1–O7	2.2774(19)
Cd1–O3	2.3519(19)	Cd1–N3	2.357(2)
Cd1–O5	2.458(2)	Cd1–N4	2.342(2)
Cd1–O6	2.366(2)		
Angle	(°)	Angle	(°)
O2–Cd1–O5	166.62(7)	O2–Cd1–C1	27.59(7)
O3–Cd1–O2	54.15(7)	O3–Cd1–O5	137.41(7)
O3–Cd1–O6	86.12(7)	O3–Cd1–N3	137.51(7)
O3–Cd1–C1	26.69(8)	O5–Cd1–C1	162.43(8)
O6–Cd1–O2	139.51(7)	O6–Cd1–C1	112.74(8)
O7–Cd1–O2	94.08(7)	O7–Cd1–O3	104.99(8)
O7–Cd1–O5	88.76(7)	O7–Cd1–O6	88.63(8)
O7–Cd1–N3	88.63(8)	O7–Cd1–N4	159.53(9)
O7–Cd1–C1	102.70(8)	N3–Cd1–O2	85.40(7)
N3–Cd1–O5	81.60(7)	N3–Cd1–O6	135.09(7)
N3–Cd1–C1	111.57(8)	N4–Cd1–O2	88.83(8)
N4–Cd1–O3	93.14(8)	N4–Cd1–O5	84.06(7)
N4–Cd1–O6	102.23(8)	N4–Cd1–N3	71.39(8)
N4–Cd1–C1	89.18(8)		

Table 3. Hydrogen bond lengths (Å) and bond angles (°) in **1**

D–H...A	D–H (Å)	H...A (Å)	D...A (Å)	D–H...A (°)
O1–H1...O2	0.82	1.86	2.577(3)	145
O4–H4...O5	0.82	1.75	2.474(3)	146
O7–H7A...N2 ⁱ	0.86	1.92	2.756(3)	162
O7–H7B...O2 ⁱⁱ	0.86	2.31	2.782(3)	115
C8–H8...O1 ⁱⁱⁱ	0.95(3)	2.59(3)	3.387(4)	142(3)
C10–H10...O3	0.92(3)	2.33(3)	2.911(4)	121(2)
C21–H21...O6	0.92(3)	2.33(3)	2.880(3)	127(2)

Symmetry codes: (i) 1 – x, 2 – y, 2 – z; (ii) 1 + x, y, z; (iii) 1 – x, 2 – y, 1 – z.

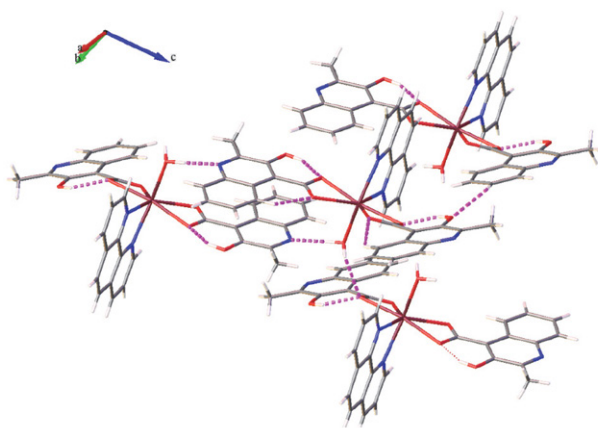


Figure 2. Hydrogen bonds in complex **1**

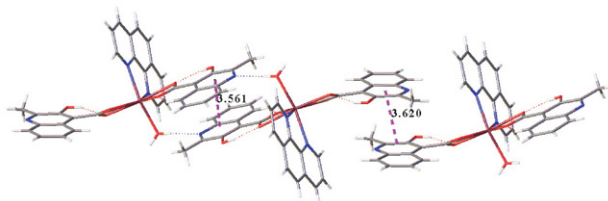


Figure 3. The π – π stacking interactions diagram of the complex **1**

In the structure, there are two strong offset face-to-face π – π stacking interaction between Cg1...Cg1ⁱ and Cg2...Cg2ⁱⁱ (Cg1 is the ring C2–C4/C6/C11/N1; Cg2 is the ring C13–C15/C17/C22/N2) as shown in Figure 3. The centroid-centroid distance of Cg1...Cg1ⁱ is 3.2620 Å, with a slippage distance of 0.941 Å, and with a dihedral angle of 0°. The centroid-centroid distance of Cg2...Cg2ⁱⁱ is 3.567 Å, with a slippage distance is 1.098 Å, and with a dihedral Angle of 0° as shown in Table 4.

Table 4. π - π stacking interactions of the complex 1

$Cg \cdots Cg$	Centroid-centroid distance (Å)	Slippage distance (Å)	Dihedral angle (Å)
$Cg1 \cdots Cg1^i$	3.620	0.941	0.000
$Cg2 \cdots Cg2^{ii}$	3.561	1.098	0.000

Symmetry codes: (i) $1 - x, 1 - y, 2 - z$; (ii) $1 - x, 2 - y, 1 - z$.

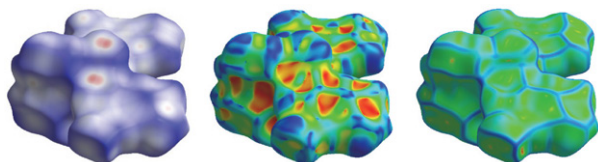


Figure 4. The Hirshfeld surface picture of the complex 1. From left to right are d_{norm} , shape index and curvature

3. 2. Hirshfeld Surface Analysis of the Complex 1

Hirshfeld surface analysis is gaining prominence as a technique in understanding the nature of intermolecular interactions within a crystal structure using a fingerprint plot. This allows easy identification of characteristic interactions throughout the structures or as a surface around the molecule. The size and shape of a Hirshfeld surface reflect the interplay between different atoms and intermolecular contacts in a crystal.^{25,26} Crystal Explorer 3.1 program was used to calculate the force distribution of Hirshfeld surface molecules of the title complex, and the morphology, shape index and curvature diagram were obtained, as shown in Figure 4. The d_{norm} , shape index and curve ranged from -0.6801 to 1.4037 , -1.0000 to 1.0000 , and -4.0000 to 0.4000 , respectively. The d_{norm} surface is used

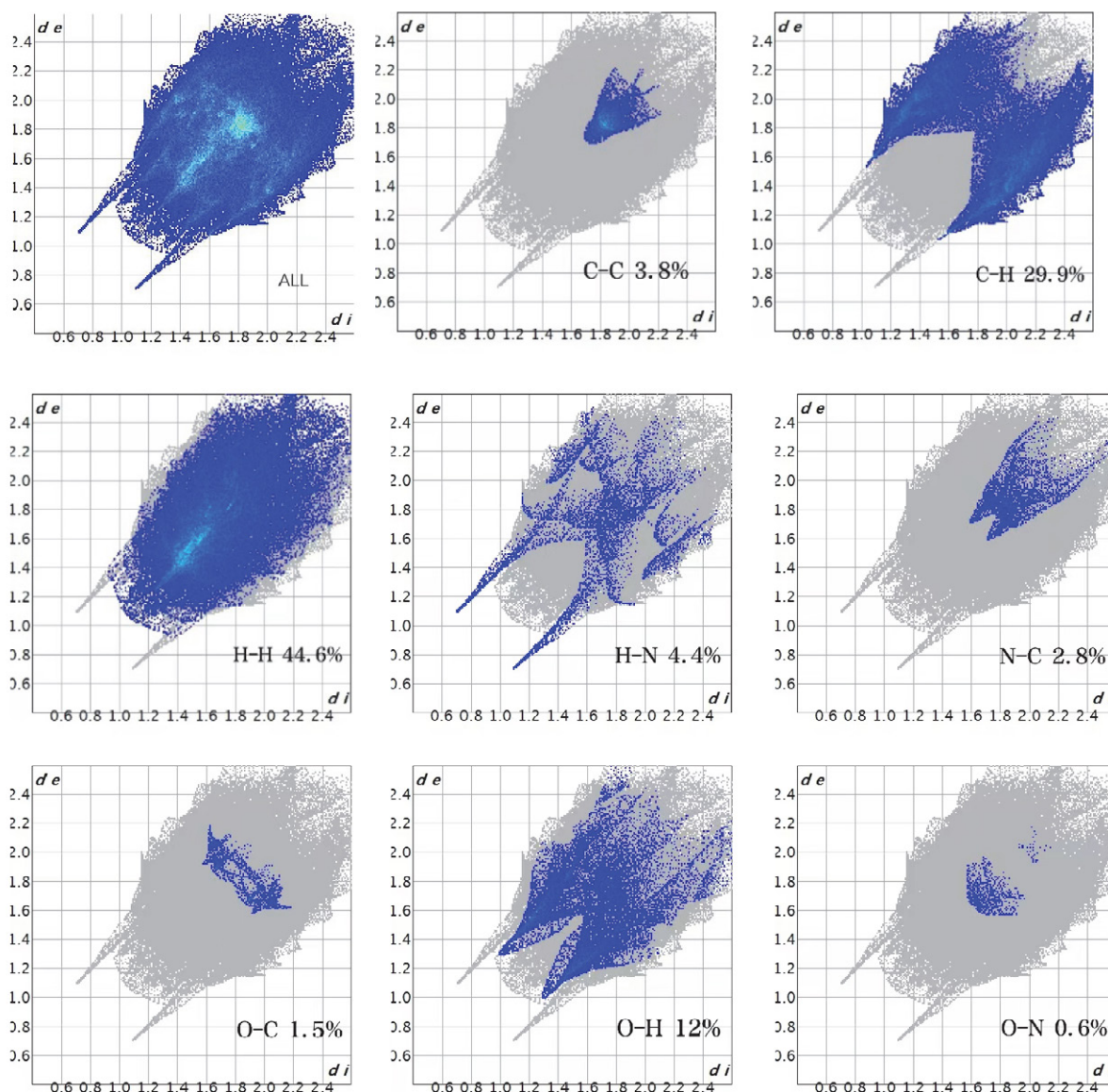


Figure 5. The 2D fingerprint of the complex 13.3 Photoluminescence measurements

for identification of very close intermolecular interactions. The red points on the d_{norm} surface of the title complex correspond to significant hydrogen bonding interaction. The shape index is most sensitive to very subtle changes in surface shape, the red triangle on the plane represents concave regions indicating atoms π -stacked molecule above them, and the blue represents convex regions indicating the ring atoms of the molecule inside the surface. The curvedness in the measurement of “how much shape”.

The 2D fingerprint plots complement the Hirshfeld surfaces, quantitatively summarizing the nature and type of intermolecular contacts experienced by molecules in the crystal. The five main modes of action are H...H, C...H, O...H, H...N, C...C and H...N, as shown in Figure 5. Among them, the action of H...H is distributed in the middle region of the fingerprint, and its contribution to the surface of Hirshfeld is the largest, reaching 44.6%, which is the most important mode of action. Followed by C...H, O...H, H...N, C...C and H...N, with a contribution ratio of 29.9%, 12%, 4.4% and 3.8%, respectively. C...H and O...H are conventional intramolecular hydrogen bonds, which are distributed in two-dimensional fingerprint region in a double wing shape. The distribution of the upper and lower spikes in the figure 5 corresponds to the donor of hydrogen bond and the acceptor of hydrogen bond (H...N and N...H).

The photoluminescence of complexes is increasingly gaining attention from scientists, making the study of photoluminescent materials from organic-inorganic complexes of great significance.²⁷ Based on this, we performed fluorescence spectroscopic analysis of the title complex at room temperature, and the experimental results are shown in Figure 6.

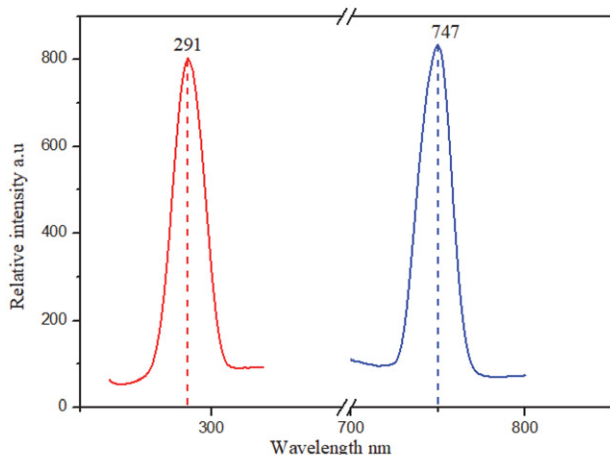


Figure 6. The solid-state excitation and emission spectra of the complex 1. The red is the emission spectrum, and the blue is the excitation spectrum

The complex **1** exhibits effective energy absorption in the wavelength range of 200–400 nm. When the excitation wavelength is 747 nm, there is obvious absorption at

291 nm. At 291 nm, the excitation spectrum has a corresponding absorption peak at 747 nm.

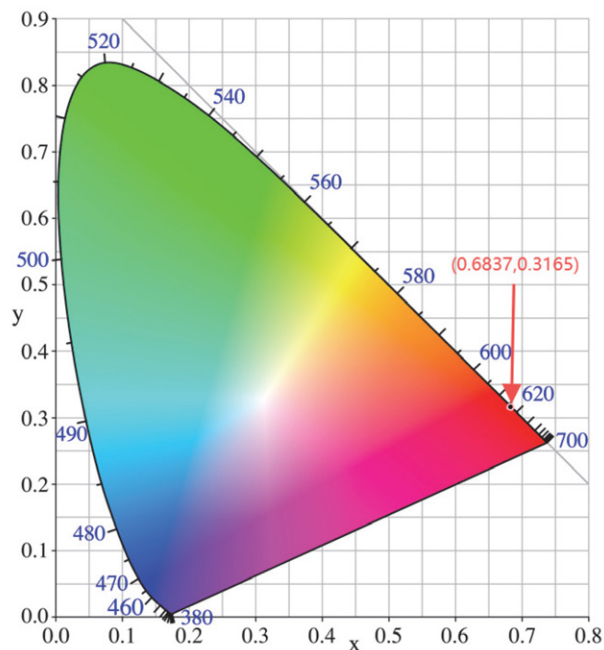


Figure 7. CIE chromaticity diagrams and chromaticity coordinates of the emission spectra of the complex 1

Solid state photoluminescence spectra show that they present a red emission band at 747 nm. The chromaticity coordinates of the title complex under radiation are calculated. The CIE estimate is $x = 0.6837$, $y = 0.3165$ (Figure 7). Therefore, we consider the complex **1** to be a promising red LED material.

3. 4. UV-vis Diffuse Reflection Spectra of Solid State

To study the optical properties of the crystal, the optical absorption properties of the crystal were measured by UV-vis diffuse reflection spectroscopy. At room temperature, using barium sulfate as 100% reflectance as a reference, the light absorption ability of the target complex was tested, and the band gap value of the material could be calculated by conversion. Energy band gap is an important concept to describe the distribution of electron energy states in solid materials, especially in crystalline materials.²⁸

In terms of data processing, the following formula is used for derivation^{29,30}

$$\alpha h\nu = B(h\nu - E_g)^m \quad (1)$$

where α is the molar absorption coefficient, h is Planck's constant, ν is the incident photon frequency, B is the proportionality constant, and E_g is the optical band gap of the semiconductor material.

According to Lambert-Beer law

$$A = \alpha bc \quad (2)$$

where A is the absorbance of the sample, b is the thickness of the sample, c is the concentration, where bc is a constant, if $B1 = (B/bc)^{1/m}$, formula (1) can be,

$$(Ah\nu)^{1/m} = B(h\nu - E_g) \quad (3)$$

$$E = h\nu = hc / \lambda \quad (4)$$

$$(Ahc / \lambda)^{1/m} = B(hc / \lambda - E_g) \quad (5)$$

there are different m values for different materials, and the relevant values can usually be obtained by referring to relevant literature (experience: n is $1/2$ for direct bandgap semiconductors, n is 2 for indirect bandgap semiconductors).

Then the final formula is

$$(Ahc / \lambda)^2 = B(hc / \lambda - E_g) \quad (6)$$

where c is the speed of light, h is the Planck constant, and the photon energy unit is eV.

First, the wavelength λ -absorbance A data of the complex were obtained through solid state UV-VIS diffuse

reflection spectroscopy experiment, as shown in the left side of Figure 8, then the corresponding $h\nu$ and $(Ah\nu)^2$ were calculated, and the corresponding $h\nu$ and $(Ah\nu)^2$ were plotted as shown in the right side of Figure 8. Finally, according to formula (6), when $(Ahc/\lambda)^2$ is equal to 0, the corresponding hc/λ is equal to E_g , that is, in the right side of Figure 8, the extreme point (x, y) is used as the tangent point as the tangent line, extrapolated to the horizontal axis ($y = 0$), and the intersection point is the band gap width value E_g .

The test results showed that the title complex showed light absorption in both ultraviolet and visible regions, and the prepared samples mainly showed absorption bands near 200 nm and 400 nm, corresponding to the absorption of transition metals in the MOF framework and ligand-based absorption. The energy band gap of the complex $E_g = 2.32$ eV is between metal and insulator, indicating that the complex **1** has semiconductor potential.

3. 5. Theoretical Calculation

In order to reveal the intrinsic fluorescence properties of Cd(II) complexes, we calculated them using the Gaussian09 program using TDDFT based on the B3LYP function (Cd as the basis set SDD and C, H, O and N as the basis set 6-31G^{*}). The single-crystal X-ray diffraction data set of the complex **1** was used to truncate the ground-state

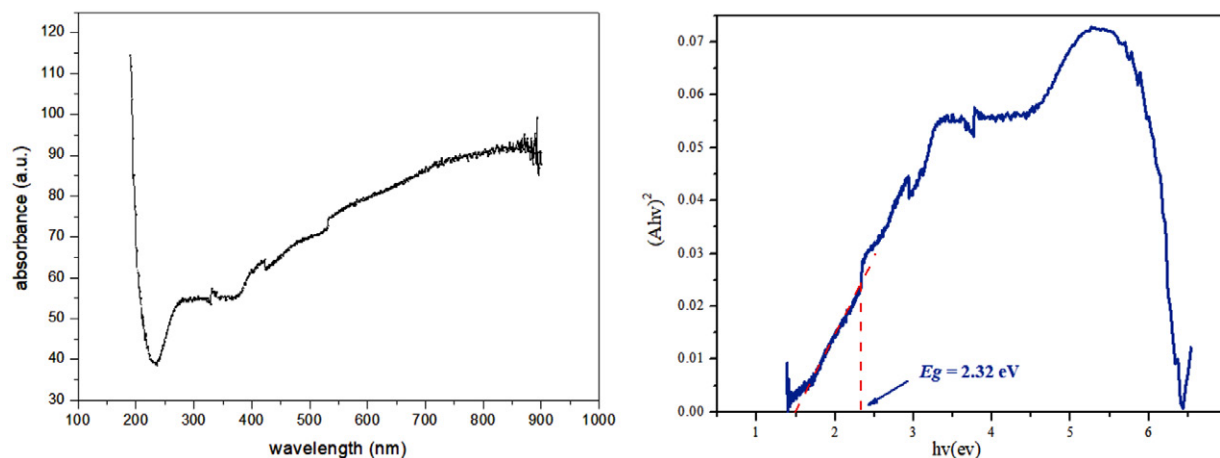


Figure 8. The UV-Vis spectra and the solid-state UV-Vis diffuse reflectance spectrum of the complex **1**

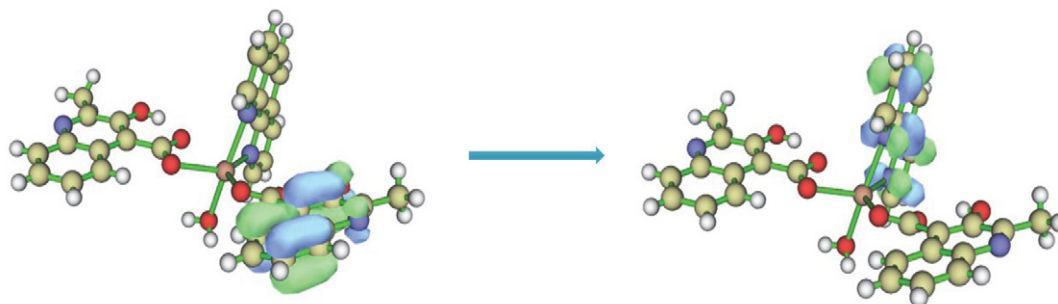


Figure 9. HOMO (left) and LUMO (right) of the complex **1**

geometry for the calculations, the X-ray diffraction data for the title complex was not optimized further.^{31–33} The characteristics of the highest occupied molecular orbital (HOMO) and the lowest unoccupied molecular orbital (LUMO) are shown in Figure 9.

The results show that the HOMO electron density distribution is located on the MCA⁻ ligand orbital, corresponding to the energy of -0.214699 a.u. (-5.842250 eV) in the π orbital, while the LUMO electron density distribution is completely located on the Phen ligand orbital. The corresponding energies are -0.098587 a.u. (-2.682690 eV). The HOMO–LUMO energy difference is 0.116112 a.u., that is 3.159559 eV and 304.851190 kJ/mol.

Based on this observation, the photoluminescent properties of the complex **1** can be attributed to the charge transfer between ligand and ligand (LLCT; from the HOMO of the π orbital of the MCA⁻ ligand to the LUMO of the π orbital of the Phen ligand. The calculated results agree well with the experimental results.

Supplementary Materials & Data Availability

Crystallographic data have been deposited with the Cambridge Crystallographic Data Center, CCDC 2384768. Copies of the data can be obtained free of charge from the Director, CCDC, 12 Union Road, Cambridge, CBZ, 1 EZ, UK; email: deposit@ccdc.cam.ac.uk or <http://www.ccdc.cam.ac.uk>.

Acknowledgements

The authors thank the National Natural Science Foundation of China (22168018), the National Natural Science Foundation of Jiangxi, China (20232BAB203048) and the National Natural Science Foundation of Jiangxi Ji'an, China for supporting this work.

Declaration of Competing Interest

The authors declare that they have no known competing financial interests or personal relationships that could have appeared to influence the work reported in this paper.

Data availability

Data will be made available on request.

4. References

- B. D. S. Deeraj, J. S. Jayan, A. Raman, A. Asok, R. Paul, A. Saritha, K. Joseph, *Surf. Interfaces*. **2023**, *43*, 103574. DOI:10.1016/j.surfin.2023.103574
- B. Jiang, C. W. Zhang, X. L. Shi, H. B. Yang, *Chinese J. Polym. Sci.* **2019**, *37*, 372–382. DOI:10.1007/s10118-019-2216-1
- A. Otero, J. Fernández-Baeza, A. Lara-Sánchez, L. F. Sánchez-Barba, *Coord. Chem. Rev.* **2013**, *257*, 1806–1868. DOI:10.1016/j.ccr.2013.01.027
- C. Li, D. Wu, D. S. Zhang, L. L. Wang, X. P. Zhang, J. Liu, S. M. Zhang, T. L. Li, Z. F. Shi, Q. Lin, *Chinese J. Inorg. Chem.* **2019**, *35*, 376–384. DOI:10.11862/CJIC.2019.035
- X. Cao, N. Feng, Q. Huang, Y. Liu, *ACS Appl. Bio Mater.* **2024**. DOI:10.1021/acsabm.3c01300
- S. Banerjee, C. T. Lollar, Z. Xiao, Y. Fang, H. C. Zhou, *Trends Chem.* **2020**, *2*, 467–479. DOI:10.1016/j.trechm.2020.01.007
- H. Chen, G. Lyu, Y. Yue, T. Wang, D. P. Li, H. Shi, J. Xing, J. Shao, R. Zhang, J. Liu, *J. Mater. Chem. C* **2019**, *7*, 7249–7258. DOI:10.1039/C9TC01520E
- G. Y. Lv, T. W. Wang, W. Y. Wang, R. Zhang, J. Liu, *Chinese J. Inorg. Chem.* **2020**, *36*, 1669–1674. DOI:10.11862/CJC.2020.189
- J. Zhang, W. Zhou, L. Yang, M. Dou, W. Qu, S. Lu, X. Chen, *Dyes Pigm.* **2024**, *229*, 112282. DOI:10.1016/j.dyepig.2024.112282
- M. Tabatabaee, S. Tabatabaee, M. Dusek, M. Krupickova Pobjarova, *Acta Crystallogr. A* **2011**, *67*, C617–C617. DOI:10.1107/S0108767311084418
- L. J. Xu, C. M. Wang, K. Yu, C. X. Wang, B. B. Zhou, *Coord. Chem. Rev.* **2023**, *481*, 215044. DOI:10.1016/j.ccr.2023.215044
- J. D. Rolfes, M. van Gastel, F. Neese, *Inorg. Chem.* **2020**, *59*, 1556–1565. DOI:10.1021/acs.inorgchem.9b03474
- J. C. Ott, D. Bürgy, H. Guan, L. H. Gade, *Acc. Chem. Res.* **2022**, *55*, 857–868. DOI:10.1021/acs.accounts.1c00737
- C. A. T. Zepeda, A. Coelho, O. Versiane, M. A. Mondragón, R. S. Pessoa, C. A. T. Soto, *J. Mol. Struct.* **2023**, *1287*, 135618. DOI:10.1016/j.molstruc.2023.135618
- P. Mantos, C. Ferrone, T. Ohta, P. Choudhury, S. Chowdhury, *Appl. Surf. Sci.* **2023**, *614*, 156204. DOI:10.1016/j.apsusc.2022.156204
- L. Ciolek, M. Chraniuk, P. Bollin, M. Biernat, M. Panasiuk, D. Nidzworski, B. Gromadzka, Z. Jaegermann, E. Pamuła, *Acta Bioeng. Biomech.* **2023**, *25*, 69–80. DOI:10.37190/ABB-02339-2023-02
- É. Quarez, A. Jouhara, S. Grolleau, F. Dolhem, N. Dupré, P. Poizot, *CrystEngComm.* **2020**, *22*, 1653–1663. DOI:10.1039/C9CE01674K
- X. G. Yi, X. N. Fang, J. Guo, J. Li, Z. P. Xie, *Acta Chim. Slov.* **2020**, *67*, 507–515. DOI:10.17344/acsi.2019.5532
- OD Rigaku (2022). *CrysAlis PRO*. Rigaku Oxford Diffraction, Yarnton, Oxfordshire, England.
- G. M. Sheldrick, *Acta Crystallogr. A* **2008**, *64*, 112–122. DOI:10.1107/S0108767307043930
- G. M. Sheldrick, *Acta Crystallogr. C* **2015**, *C71*, 3–8. DOI:10.1107/S2053229614024218
- O. V. Dolomanov, L. J. Bourhis, R. J. Gildea, J. A. K. Howard, H. Puschmann, *J. Appl. Crystallogr.* **2009**, *42*, 339–341. DOI:10.1107/S0021889808042726
- N. Palanisami, P. Rajakannu, R. Murugavel, *Inorg. Chim. Acta* **2013**, *405*, 522–531. DOI:10.1016/j.ica.2013.04.021
- X. J. Zhang, Y. P. Tian, S. L. Li, M. h. Jiang, A. Usman, S.

- Chantrapromma, H. K. Fun, *Polyhedron* **2003**, *22*, 397–402. DOI:10.1016/S0277-5387(02)01360-8
25. K. Z. Yang, R. Zou, X. G. Yi, J. B. Zhang, *Acta Chim. Slov.* **2023**, *70*, 310–317. DOI:10.17344/acsi.2023.8005
26. N. Abad, Y. Ramli, T. Hökelek, N. K. Sebbar, J. T. Mague, E. M. Essassi, *Acta Crystallogr. E* **2018**, *74*, 1648–1652. DOI:10.1107/S2056989018014561
27. M. H. You, M. H. Li, Y. M. Di, Y. W. Wang, M. J. Lin, *Dyes Pigm.* **2020**, *173*, 107943. DOI:10.1016/j.dyepig.2019.107943
28. F. D. E. Ghorabe, A. S. Novikov, P. V. Nesterov, A. R. Galina, A. E. Dudaev, E. I. Shishatskaya, E. V. Skorb, *Mater. Today Commun.* **2024**, *39*, 108886. DOI:10.1016/j.mtcomm.2024.108886
29. J. Tuac, R. Grigorovici, A. Vancu, *Phys. Stat. Sol.* **1966**, *15*, 627. DOI:10.1002/pssb.19660150224
30. E. A. Davis, N. F. Mott, *Philos. Mag.* **1970**, *22*, 903–822. DOI:10.1080/14786437008221061
31. H. U. Kim, S. Sohn, W. Choi, M. Kim, S. U. Ryu, T. Park, S. Jung, K. S. Bejoymohandas, *J. Mater. Chem. C* **2018**, *6*, 10640–10658. DOI:10.1039/C8TC04321C
32. W. Q. Zeng, W. Huang, C. H. He, R. Zou, W. K. Jin, X. G. Yi, K. Z. Yang, *J. Chem. Res.* **2023**, *47*, 1–9. DOI:10.1177/17475198231177955
33. N. H. Kwon, J. Park, X. Y. Jin, S. J. Kim, H. Kim, S. J. Hwang, *ACS Nano.* **2023**, *17*, 23732–23745. DOI:10.1021/acsnano.3c07566

Povzetek

S solvotermalno metodo smo sintetizirali nov organsko-anorganski hibridni kadmijev kompleks $[\text{Cd}(\text{MCA})_2(\text{Phen})(\text{H}_2\text{O})]$ (MCA = anion 3-hidroksikinolin-4-karbonsilne kisline; Phen = 1,10-fenantrolin) ter ga okarakterizirali z monokristalno rentgensko difrakcijo. Kompleks tvori dvodimenzionalno strukturo zaradi vodikovih vezi in $\pi\cdots\pi$ interakcij. Fotoluminiscenčni spekter v trdnem stanju kaže, da kompleks emitira v rdečem delu svetlobnega spektra, kar je mogoče pripisati prenosu naboja ligand-ligandi, kot kažejo časovno odvisni izračuni teorije gostotnostnega funkcionala. Spekter difuznega odboja kaže, da je energijska pasovna vrzel kompleksa 2,32 eV.



Except when otherwise noted, articles in this journal are published under the terms and conditions of the Creative Commons Attribution 4.0 International License

Scientific paper

Investigation of the Composition Space Diagram CuCl–Allylamine–dabco. A New Mixed Ligand Compound of $(\text{H}_2\text{dabco})_2[\text{Cu}_4\text{Cl}_9(\text{allNH}_3)]$ Composition with Unique $\text{Cu}_4\text{Cl}_9^{5-}$ Cupro(I)-chloride Fragment

Evgeny Goreshnik¹ , Olha Panteleieva^{1,2} ¹ Department of Inorganic Chemistry and Technology, Jožef Stefan Institute, Jamova 39, 1000 Ljubljana, Slovenia.² Department of Chemistry and Chemical Engineering, University of Technology, av. Dmytra Yavornitskogo 19, 49005 Dnipro, Ukraine.

* Corresponding author: E-mail: evgeny.goreshnik@ijs.si

Received: 09-30-2024

Abstract

The ternary system CuCl–allylamine–dabco (dabco = 1,4-diazabicyclo[2.2.2]octane) with an excess of HCl was explored. Starting from an ethanol solution of $\text{CuCl}_2 \cdot 2\text{H}_2\text{O}$, allylamine and dabco titrated with HCl, copper(I) salts were generated by means of electrochemical alternating current synthesis. In addition to the already known $(\text{H}_2\text{dabco})[\text{CuCl}_3]$, two modifications of the $(\text{allNH}_3)_2[\text{Cu}_2\text{Cl}_4]$ compound and some Cu(II) by-products, a new mixed ligand compound of the composition $(\text{H}_2\text{dabco})_2[\text{Cu}_4\text{Cl}_9(\text{allNH}_3)]$ was synthesized and structurally investigated. Its structure contains unique $\text{Cu}_4\text{Cl}_9^{5-}$ inorganic moiety bound via a η_2 -interaction allylammonium moiety and discrete $(\text{H}_2\text{dabco})^{2+}$ cations. The structure is stabilized by the system of N–H...Cl hydrogen bonds.

Keywords: copper, chloride, 1,4-diazabicyclo[2.2.2]octane, coordination polymers

1. Introduction

Copper(I) chloride coordination compounds amaze with a variety of inorganic fragments. Starting from the simplest neutral CuCl monomers,^{1,2} discrete Cu_2Cl_2 dimers,³ bicyclic Cu_3Cl_3 trimers,⁴ tetramers of cubane⁵ and stepped cubane types,⁶ prismane-like hexamers⁷ and many others were observed. An even broader spectrum of anionic moieties from CuCl_2^- dimers to infinite chains, layers and 3D frameworks were reported.^{8,9} A comprehensive review of the structural diversity of copper(I) halide aggregates was published nearly a decade ago.¹⁰

The carbon-carbon double bond successfully competes with the halide ions for the place in the coordination sphere of the Cu(I) ion. On the other hand, protonated organic amines form N–H...Hal hydrogen bonds with halide ions, thereby limiting the bridging ability of the halide ions to the metal centers. We hypothesized that the use of bulky organic amines and amino derivatives of unsaturated hydrocarbons in acidic media could promote the formation

of previously unknown copper-halide aggregates. In order to perform a complete study of such a system, we decided to investigate the entire CuCl–allylamine–dabco ternary system in acidic (HCl) medium using the Gibbs diagram.

The electrochemical technique has proven to be an effective tool for the synthesis of copper(I) derivatives.^{11,12} The absence of by-products and the possibility to grow high-quality single crystals in one step are the main advantages of such an approach.

It is worth noting that the CCDC contains only 26 entries for 20 compounds containing copper ions and diprotonated H_2dabco cations.¹³ Moreover, only six of the above compounds appear to be polymeric, and also six contain monovalent copper ions. On the other hand, only three cupro(I)chloride derivatives of allyl ammonium were found in the CCDC, four other entries contain mixed-anion derivatives.

The phase diagram of CuCl–allylamine–dabco in acidic media was investigated by means of electrochemical synthesis and by varying the ratios of the starting reagents.

A new $(\text{H}_2\text{dabco})_2[\text{Cu}_4\text{Cl}_9(\text{allNH}_3)]$ salt with a unique $\text{Cu}_4\text{Cl}_9^{5-}$ anion was found and characterized by single-crystal X-ray diffraction and Raman spectroscopy. The results are presented in this article.

2. Experimental Section

All chemicals were of commercial origin: $\text{CuCl}_2 \cdot 2\text{H}_2\text{O}$ from Zorka Šabac, p.a., hydrochloric acid from Sigma-Aldrich, ACS reagent, 37%, allylamine from Alfa Aesar, 98+%, 1,4-diazabicyclo[2.2.2]octane (Alfa Aesar, 98%); ethanol (Carlo Erba, p.a) were used without further purification.

2. 1. Syntheses

All experiments were carried out by electrochemical alternating current synthesis in ethanol. 5 mL of ethanol solution containing calculated amounts of $\text{CuCl}_2 \cdot 2\text{H}_2\text{O}$, dabco, allylamine and 1 mL of 37% aqueous HCl were placed in a small test tube. The technical details of the synthetic procedures were described earlier.^{10,11} An alternating current of 50 Hz and a voltage of 0.4 V was used. In case of discoloration of the solution and absence of crystals, the test tube was cooled in the refrigerator or the synthesis was repeated with larger amount of reagents.

Table 1. Crystallographic data, details of data collection and structure refinement parameters

	1
Compound	$(\text{H}_2\text{dabco})_2[\text{Cu}_4\text{Cl}_9(\text{allNH}_3)]$
Formula	$\text{C}_{15}\text{H}_{36}\text{Cl}_9\text{Cu}_4\text{N}_5$
M [g mol^{-1}]	859.70
T [K]	150
Crystal system	Triclinic
Space group	$P\bar{1}$
a [Å]	9.3468(4)
b [Å]	12.1301(6)
c [Å]	13.6361(5)
α [°]	112.695(4)
β [°]	91.951(3)
γ [°]	98.337(4)
V [Å ³]	1404.37(11)
Z	2
$F(000)$	860
ρ_{caled} [g cm^{-3}]	2.033
Radiation, λ [Å]	MoK α , 0.71073
μ [mm^{-1}]	3.862
Goodness-of-fit on F^2	1.072
Final R_1 [$I > 2\sigma(I)$]	0.0296
Final R_1 (all data)	0.0375
wR_2 [$I > 2\sigma(I)$]	0.0663
wR_2 (all data)	0.0720
Largest diff. peak and hole ($e \text{ \AA}^{-3}$)	0.603, -0.635

2. 2. X-ray Structure Determination

All crystals obtained were examined using the single-crystal X-ray technique. Single-crystal X-ray data for compound **1** were collected on a Gemini A diffractometer with an Atlas CCD detector, using graphite monochromated Mo-K α radiation. The data were processed using the CrysAlisPro program package.¹⁴ An analytical absorption correction was applied to the data set. The structure was solved using the dual-space algorithm of the program SHELXT¹⁵ and the structure refinement was performed using the software SHELXL-2014,¹⁶ both of which are implemented in the crystallographic software Olex.¹⁷ Hydrogen atoms bound to carbons were set to calculated positions (AFIX commands), their thermal parameters were set to $1.2U_{\text{eq}}$ of the corresponding C atoms. The positions of the hydrogen atoms bound to the nitrogen atoms were found on difference Fourier maps and refined freely. In some cases, the N–H bond lengths were constrained using the DFIX command. A summary of the crystallographic data and the structure refinement is given in Table 1. CCDC 2387343 (**1**) contains the supplementary crystallographic data for this paper. These data can be obtained free of charge from the Cambridge Crystallographic Data Centre via www.ccdc.cam.ac.uk/data_request/cif.

3. Results and Discussion

3. 1. Influence of Synthetic Conditions on a Formation of Definite Products

The preparation of the starting mixture $\text{CuCl}_2 \cdot 2\text{H}_2\text{O}$ –allylamine–dabco–HCl usually resulted in a multi-colored – from yellow to brown – solid.

Two series of experiments were carried out in the three-component system $\text{CuCl}_2 \cdot 2\text{H}_2\text{O}$ –allylamine–dabco (Fig. 1) in an acidic (HCl) environment. First, five points were selected on a ternary diagram and electrochemical syntheses were carried out. As expected, in dabco-reach region of ternary diagram the formation of H_2dabco salt, namely $(\text{H}_2\text{dabco})[\text{CuCl}_3]$ was observed.¹⁸ In contrast, an excess of allylamine led to the formation of the $(\text{allNH}_3)_2[\text{Cu}_2\text{Cl}_4]$ salt.¹⁹ The most remarkable result was achieved in a synthesis with 40 mol. % CuCl_2 , 15 mol. % allylamine and 45 mol. % dabco, in which the formation of earlier unknown yellow-orange crystals of the composition $(\text{H}_2\text{dabco})_2[\text{Cu}_4\text{Cl}_9(\text{allNH}_3)]$ was observed. Using the ratio of 40 mol. % CuCl_2 , 45 mol. % allylamine and 15 mol. % dabco resulted in a mixture of $(\text{H}_2\text{dabco})_2[\text{Cu}_4\text{Cl}_9(\text{allNH}_3)]$ and $(\text{allNH}_3)_2[\text{Cu}_2\text{Cl}_4]$ crystals. Further experiments were performed in steps of 10% for each component. In this way, 36 points of definite composition were determined on a Gibbs triangle, and the corresponding ratios of starting materials were used for subsequent syntheses (Table S1). No other mixed

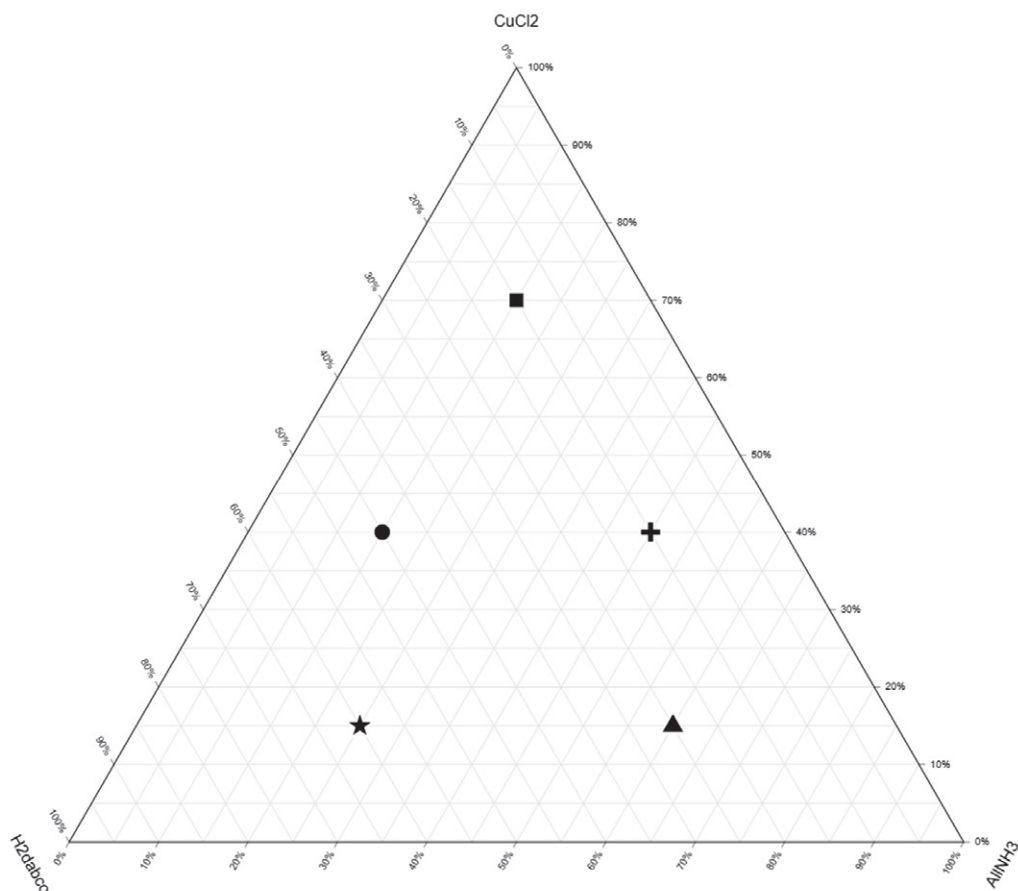


Figure 1. Ternary diagram of CuCl-allylammonium- H_2dabco . Square: region of formation $(\text{allNH}_3)_2[\text{Cu}_2\text{Cl}_4]$, circle – $(\text{H}_2\text{dabco})_2[\text{Cu}_4\text{Cl}_9(\text{allNH}_3)]$, cross – $(\text{H}_2\text{dabco})_2[\text{Cu}_4\text{Cl}_9(\text{allNH}_3)]$ and $(\text{allNH}_3)_2[\text{Cu}_2\text{Cl}_4]$, star and triangles – $(\text{H}_2\text{dabco})[\text{CuCl}_3]$.

cation salts were found during this detailed investigation. Crystals of another modification of the compound $(\text{allNH}_3)_2[\text{Cu}_2\text{Cl}_4]$ ²⁰ and undesired $(\text{H}_2\text{dabco})_2[\text{Cu}^{\text{II}}\text{Cl}_3(\text{H}_2\text{O})_2]\text{Cl}_3 \cdot \text{H}_2\text{O}$ ²¹ (copper(II) salt as a result of incomplete electrochemical reduction) were observed.

3. 2. Crystal Structure of 1

The compound $(\text{H}_2\text{dabco})_2[\text{Cu}_4\text{Cl}_9(\text{allNH}_3)]$ (**1**) crystallizes in the triclinic space group $P\bar{1}$. Three metal cations and three chloride anions form a six-membered ring with Cu...Cu distances of 2.9252(12)–2.9999(12) Å (Fig. 2). Each pair of copper ions is bound by a μ_2 chloride bridge with Cu– $\mu_2\text{Cl}$ distances of 2.302(2)–2.352(1) Å. The copper triangle is capped by a $\mu_3\text{Cl}_6$ center with significantly elongated Cu–Cl bonds with lengths of 2.632(2)–2.705(2) Å. The coordination of each copper center is completed to tetrahedral by another chloride ion: terminal chloride anions for Cu3 and Cu4 and a μ_2 bridge for Cu2. In the last case, the Cl2 bridge connects a Cu_3Cl_7 core with an $(\text{allNH}_3)\text{CuCl}_2$ fragment involving a π -coordinated Cu1 atom.

All three Cu ions in the Cu_3Cl_7 core are tetra-coordinated. τ_4 parameter values of 0.81, 0.89 and 0.86 for

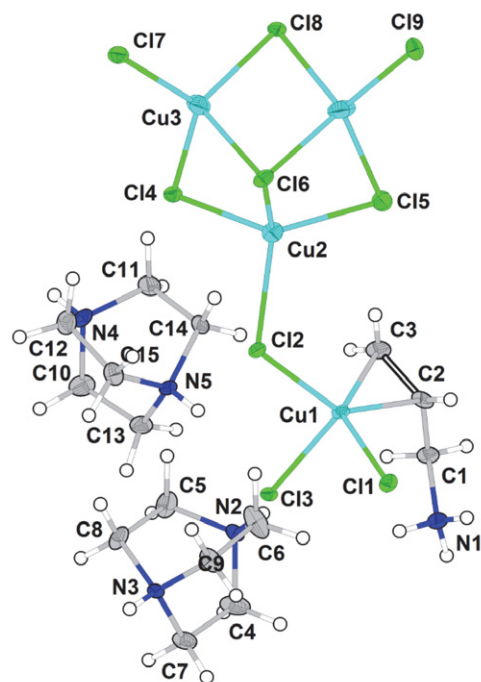


Figure 2. Asymmetric unit of structure **1**. Thermal ellipsoids are drawn with 50% probability. All

Cu2, Cu3 and Cu4 respectively indicate a slightly distorted tetrahedral surrounding in all cases (the value 1.00 corresponds to a perfect tetrahedral geometry, the value 0 to a perfect square planar geometry).²²

The Dewar-Chatt-Duncanson concept states that an effective Cu–(C=C) interaction leads to a transformation of the Cu coordination polyhedron from tetrahedral to trigonal pyramidal, with the olefin group

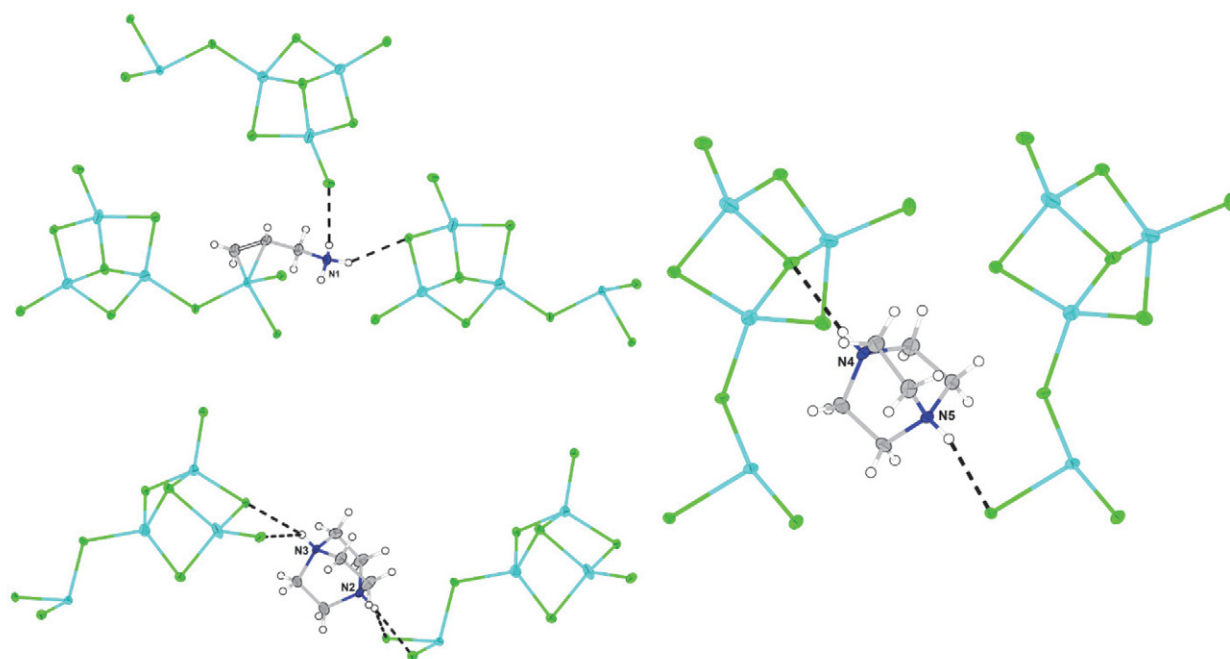


Figure 3. Hydrogen bonds around each organic cation in structure 1.

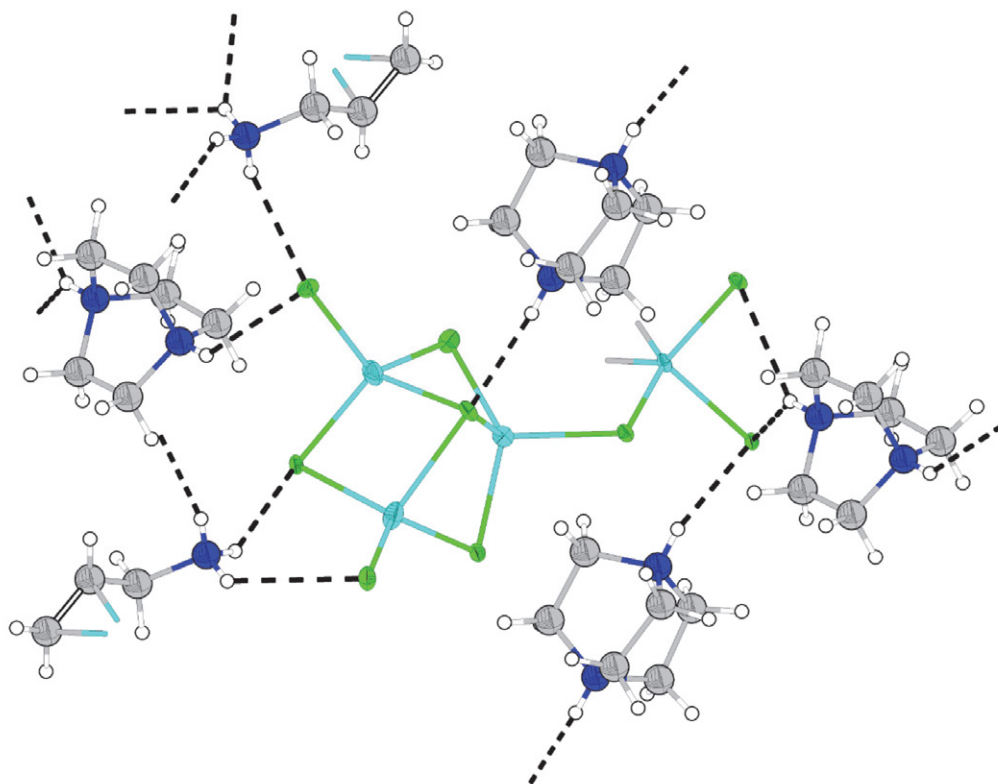


Figure 4. Hydrogen bonds around cupro(I) chloride fragment in structure 1.

located in the basal plane, and to an increase in the distance between the metal ion and the axial ligand.^{23,24} π -coordinated Cu1 center possess well-pronounced trigonal-pyramidal surrounding. The Cu1 ion in structure **1** lies practically in the basal plane (formed by Cl1, Cl2, C2 and C3 atoms) of the coordination polyhedron (distance metal–plane is 0.4 Å), the distance to the Cl3 atom in the apical position is much longer than the length of the Cu1–Cl1 and Cu1–Cl2 bonds (2.4906(6) Å versus 2.2905(7) and 2.3204(7) Å respectively). The C2=C3 bond coordinated to the metal center is tilted by about 2 degrees with respect to the basal plane of the coordination polyhedron. Despite this proper orientation and the relatively short distance Cu–m (m is the center of the C=C double bond) of 1.97 Å, the coordinated C=C-bond is very weakly elongated to 1.344(4) Å. For comparison, the mean length of the coordinated to copper(I) ion C=C bond of 1.360(17) Å was determined with the Mercury software²⁵ based on 44 records in CCDC¹³ containing a C=C + 3Cl environment of the Cu⁺ center (four records with a C=C bond length shorter than 1.3 Å or longer than 1.4 Å were excluded as equivocal from the analysis).

Protonated amino-groups of allylammonium and H₂dabco cations form a complex system of N–H...Cl hydrogen bonds (Figs. 3 and 4). Two H-atoms of the allylammonium group are bound to two different Cu₄Cl₉ fragments, and the third H-atom forms an intramolecular N1–H1c...Cl3 bond. Both N4H4 and N5H5 groups from one H₂dabco²⁺ cation form effective H-bonds and connect two chlorocuprate anions. Contrary, the N2H2 and N3H3 groups belong to another H₂dabco unit and form bifurcated hydrogen bonds. This organic cation acts also as a bridge between two Cu₄Cl₉ units.

3. 3. Raman Spectrum

A group of peaks observed in the Raman spectrum of **1** partially match those in the spectra of pure allylamine²⁶ and dabco²⁷ (Table 2).

Peaks arising from allylamine were found in **1** at 1207 cm⁻¹ (1209, –CH₂ twisting), 1253 cm⁻¹ (1283, =CH

bending), 1399 cm⁻¹ (1423) =CH₂ deformation (the values in parentheses correspond to the frequencies found in the spectrum of solid allylamine). ν_s and ν_{as} modes for =CH₂ were found in **1** in the range between 2909 and 3090 cm⁻¹

An important feature of the Raman spectra of **1** is that the ν_s mode of the C=C-bond is strongly shifted to 1565 cm⁻¹ compared to 1636 cm⁻¹ in solid allylamine due to the Cu–(C=C) interaction. A similar shift to lower wavenumbers was observed in a number of copper(I) p-complexes.²⁸

The broadened peak centered at 246 cm⁻¹ in spectrum **1** could be assigned to the ν_s mode of Cu–Cl bonds in (Cu₄Cl₉)⁵⁻ anion. The corresponding peak was observed at 255 cm⁻¹ in [H₂dabco][CuCl₃].

4. Conclusions

An idea for the synthesis of compound(s) with mixed organic cations and cupro(I) chloride anions was realized by the complete investigation of the CuCl–allylamine–dabco system in acidic media. A new compound of (H₂dabco)₂[Cu₄Cl₉(allNH₃)] composition was obtained and characterized by single crystal X-ray diffraction and Raman spectroscopy. This new compound contains earlier unknown Cu₄Cl₉⁵⁻ cupro(I)-chloride fragment. The formation of this compound was observed in a rather narrow region of the ternary diagram.

Supplementary Materials

Detailed list of all explored reagents compositions, expanded composition diagram and Raman spectrum of compound **1** are placed as Supplementary Materials.

Acknowledgements

Authors gratefully acknowledge the Slovenian Research Agency (ARRS) for the financial support of the present study within the research program P1-0045 Inorganic Chemistry and Technology. O.P. acknowledges the financial support from Erasmus+ program.

Table 2. Originated from the organic part peaks observed in Raman spectra of **1**, pure dabco and (H₂dabco)[CuCl₃] salt.

	in- δ (C–N–C)	out- ν_a (NC ₃)	in- ν_s (NC ₃)	in- ν_s (NC ₃), ν_s (C–C)	ν_a (C–C), in- γ_t (CH ₂)	ν_s (C–C), in- ν_s (NC ₃), in- δ_s (NC ₃)	in- ν_a (NC ₃), ν_a (C–C), in- γ_t (CH ₂)	in- γ_s (CH ₂)
dabco	430	579	598	807	894	972	1061	1459
(H ₂ dabco)[CuCl ₃]	406	560	601	803	893	977	1056	1461
1	404	557	606	804	887	979	1056	1456

5. References

1. A. Vakulka, E. Goreshnik, *J. Coord. Chem.* **2018**, *71*, 2426–2440. DOI:10.1080/00958972.2018.1481210
2. D. Rasale, K. Patil, B. Sauter, S. Geigle, S. Zhanybekova, D. Gillingham, *Chem. Comm.* **2018**, *54*, 9174–9177. DOI:10.1039/C8CC04476G
3. A. Szadkowska, R. Pawlowski, E. Zaorska, S. Staszko, D. Trzybiński, K. Woźniak, *Appl. Organomet. Chem.* **2019**, *33*, e4983. DOI:10.1002/aoc.4983
4. L. R. Collins, J. P. Lowe, M. F. Mahon, R. C. Poulten, M. K. Whittlesey, *Inorg. Chem.* **2014**, *53*, 2699–2707. DOI:10.1021/ic4031014
5. A. N. Paesch, A. K. Kreyenschmidt; R. Herbst-Irmer, D. Stalke, *Inorg. Chem.* **2019**, *58*, 7000–7009. DOI:10.1021/acs.inorgchem.9b00629
6. M. Munakata, T. Kuroda-Sowa, M. Maekawa, A. Honda, S. Kitagawa, *J. Chem. Soc. Dalton Trans.* **1994**, 2771–2775. DOI:10.1039/DT9940002771
7. E. A. Goreshnik, L. Z. Ciunik, Yu. K. Gorelenko, M. G. Mys'kiv, *Z. Anorg. Allg. Chem.* **2004**, *630*, 2743–2748. DOI:10.1002/zaac.200400218
8. Yu. Slyvka, E. Goreshnik, O. Pavlyuk, M. Mys'kiv, *Cent. Eur. J. Chem.* **2013**, *11*, 1875–1901. DOI:10.2478/s11532-013-0323-3
9. J. R. D. DeBord, Y. Lu, C. J. Warren, R. C. Haushalter, J. Zubietta, *Chem. Comm.* **1997**, 1365–1366. DOI:10.1039/a702053h
10. R. Peng, M. Li, D. Li. *Coord. Chem. Rev.* **2010**, *254*, 1–18. DOI:10.1016/j.ccr.2009.10.003
11. Yu. I. Slyvka, O. V. Pavlyuk, M. Yu. Luk'yanov, M. G. Mys'kiv Ukraine Patent UA 118819, **2017**, Bull. No. 16, August 28.
12. Z. N. Gafurov, A. O. Kanyukov, A. A. Kagilev, O. G. Sinyashin, D. G. Yakhvarov, *Coord. Chem. Rev.* **2021**, *442*, 213986. DOI:10.1016/j.ccr.2021.213986
13. C. R. Groom, I. J. Bruno, M. P. Lightfoot, S. C. Ward, *Acta Cryst.* **2016**, *B72*, 171–179. DOI:10.1107/S2052520616003954
14. CrysAlisPro, Agilent Technologies, Version 1.171.37.31 (release 14-01–2014 CrysAlis171 .NET).
15. G. M. Sheldrick, *Acta Cryst.* **2015**, *A71*, 3–8. DOI:10.1107/S2053273314026370
16. G. M. Sheldrick, *Acta Cryst.* **2015**, *C71*, 3–8. DOI:10.1107/S2053229614024218
17. O. V. Dolomanov, L. J. Bourhis, R. J. Gildea, J. A. K. Howard, H. Puschmann, *J. Appl. Cryst.* **2009**, *42*, 339–341. DOI:10.1107/S0021889808042726
18. E. Goreshnik, *J. Coord. Chem.* **2017**, *5*, 859–870. DOI:10.1080/00958972.2017.1285400
19. M. G. Mys'kiv, Kh. Fayad, V. E. Zavodnik. *Metalloorg. Khim. (Russ.) (Organomet. Chem. (USSR))* **1991**, *4*, 415–419.
20. V. V. Olijnik, M. G. Mys'kiv. *Koord. Khim. (Russ.) (Coord. Chem.)* **1996**, *22*, 876–879.
21. M. Wei, R. D. Willett, *Inorg. Chem.* **1996**, *35*, 6381–6385. DOI:10.1021/ic9602862
22. L. Yang, D. R. Powell; R. P. Houser, *Dalton Trans.* **2007**, 955–964. DOI:10.1039/B617136B
23. M. J. S. Dewar. *Bull. Soc. Chim. Fr.* **1951**, *18*, C71.
24. J. Chatt, L. A. Duncanson. *J. Chem. Soc.* **1953**, 2939–2947. DOI:10.1039/jr9530002939
25. C. F. Macrae, I. Sovago, S. J. Cottrell, P. T. A. Galek, P. McCabe, E. Pidcock, M. Platings, G. P. Shields, J. S. Stevens, M. Towler, P. A. Wood, *J. Appl. Cryst.* **2020**, *53*, 226–235. DOI:10.1107/S1600576719014092
26. J. R. Durig, J. F. Sullivan, C. M. Whang, *Spectrochim. Acta*, **1985**, *41*, 129–154. DOI:10.1016/0584-8539(85)80092-1
27. V. I. Kovalenko, A. A. Akhmediyarov, A. E. Vandyukov, A. R. Khamatgalimov, *J. Mol. Struct.* **2012**, *1028*, 134–140. DOI:10.1016/j.molstruc.2012.06.045
28. H. Masuda, M. Munakata, S. Kitagawa, *J. Organomet. Chem.* **1990**, *391*, 131–137. DOI:10.1016/0022-328X(90)80162-S

Povzetek







Raziskovali smo ternarni sistem CuCl–alilamin–dabco (dabco = 1,4-diazabiciklo[2.2.2]oktan) s presežkom HCl. Iz etanolne raztopine CuCl₂·2H₂O, alilamina in dabco titriranega s HCl, so bile s pomočjo elektrokemijske sinteze z uporabo izmeničnega toka generirane bakrove(I) soli. Poleg že znanih (H₂dabco)[CuCl₃], dveh modifikacij spojine (allN-H₃)₂[Cu₂Cl₄] in nekaterih Cu(II) stranskih produktov, smo sintetizirali novo spojino (H₂dabco)₂[Cu₄Cl₉(allNH₃)] in jo strukturno analizirali. Njena struktura vsebuje prej neznan anorganski del Cu₄Cl₉⁵⁻, ki je vezan preko η₂-interakcije z alilamonijem, in diskretnega kationa (H₂dabco)²⁺. Strukturno stabilizira sistem vodikovih vezi N–H...Cl.



Except when otherwise noted, articles in this journal are published under the terms and conditions of the Creative Commons Attribution 4.0 International License

Scientific paper

Insights into Antiradical Behavior: Crystal Structures and DFT Analysis of 2-Formylpyridine N^4 -Allylthiosemicarbazone Salts

Yurii Chumakov¹ , Vasiliu Graur^{2,*} , Ianina Graur² , Victor Tsapkov² ,
Olga Garbuz^{2,3}  and Aurelian Gulea² 

¹ Institute of Applied Physics, Moldova State University, Academiei 5, MD2028 Chisinau, R. Moldova

² Laboratory of Advanced Materials in Biopharmaceutics and Technics, Moldova State University, Mateevici 60, MD2028 Chisinau, R. Moldova

³ Laboratory of Systematics and Molecular Phylogenetics, Institute of Zoology, Moldova State University, Academiei 1, MD2028 Chisinau, R. Moldova

* Corresponding author: E-mail: vgraur@gmail.com

Received: 03-03-2024

Abstract

In this paper, six new salts of 2-formylpyridine N^4 -allylthiosemicarbazone ($[H_2L]X \cdot nH_2O$, where X is NO_3^- (1), $NH_2SO_3^-$ (2), Cl^- (3), Cl_3CCOO^- (4), Cl_2CHCOO^- (5), $ClCH_2COO^-$ (6); $n = 0$ (1, 3, 5, 6), 1 (2, 4)) were synthesized and physico-chemically characterized by elemental analysis, molar conductivity measurements, FT-IR studies, 1H and ^{13}C NMR. The crystal structures of compounds 1–5 were determined by single-crystal X-ray diffraction. Crystal data analysis shows that the structures of these compounds consist of protonated thiosemicarbazone H_2L^+ , anions of acid residue, and water molecules in 2 and 4. These compounds manifest antiradical activity toward $ABTS^{+ \cdot}$ cation radicals that exceeds the activity of non-protonated thiosemicarbazone HL and Trolox used in medical applications. The most active one is compound $[H_2L]Cl$ (3) with an IC_{50} value of 9.9 $\mu mol/L$. Density Functional Theory calculations showed that the electronic structure of cation H_2L^+ is more favorable for accepting electron if compared with HL.

Keywords: Crystal structure, thiosemicarbazone, theoretical calculation, antiradical activity

1. Introduction

Normal cellular metabolism consistently generates reactive oxygen species.¹ For example, during respiration, our cells convert oxygen to water. Sometimes, a portion of this oxygen escapes the complete transformation resulting in the formation of a highly reactive oxygen species known as the superoxide anion.^{2,3} Additional free radicals, such as hydrogen peroxide (HOO^\bullet) and nitric oxide (NO^\bullet), arise from diverse chemical reactions within our organism.⁴ Enzymatic or biochemical defense mechanisms typically remove these highly reactive molecules.⁵ There are also systems for repairing the detrimental effects caused by free radicals.⁶ However, when free radicals enter our body under the influence of factors such as smoking, pollution, and stress, the body's system is overloaded.^{7,8} Under such circumstances, the use of external antioxidant supple-

ments may be necessary to reinstate cellular redox homeostasis.⁹

In the design and synthesis of advanced antiradical drugs, thiosemicarbazones constitute a group of compounds with an exceptional pharmacological profile.^{10–12} Generally, thiosemicarbazones are produced through the condensation of the respective thiosemicarbazide with aldehydes or ketones.¹³ Various derivatives of thiosemicarbazones can be synthesized by incorporating substituents onto the ligand backbone, specifically by introducing substituents on the thioamide and hydrazine nitrogen atoms. Certain structural characteristics crucial for the biological functionality of thiosemicarbazones have been recognized.¹⁴ These include the substitution of sulfur in the thio-carbonyl group with selenium or oxygen, alteration of the attachment point of the thiosemicarbazones moiety in the original aldehyde or ketone, and substitution at the termi-

nal N4 position.^{15,16} Additional factors encompass electron density distributions, the characteristics of substituents, the geometry and symmetry of the initial ligand, metal binding capabilities, solubility, and the potential for interaction with the cell membrane.^{17–20}

2-Formylpyridine thiosemicarbazones and their coordination compounds of some 3d metals were studied as a potential antimicrobial,^{21–23} antifungal,^{24,25} antitumour,^{26–28} and antioxidant²⁹ agents. Moreover, various biological activities, such as antiproliferative, antibacterial, antifungal, and antiradical have been previously studied for 2-formylpyridine *N*⁴-allylthiosemicarbazone (**HL**) and its copper, nickel, cobalt, and zinc complexes.³⁰ In the case of antiradical activity, non-coordinated thiosemicarbazone showed higher activity than most of its metal complexes, and also higher than the activity of the Trolox standard. 2-Formylpyridine *N*⁴-allylthiosemicarbazone can act as a base and thus can form salts with different acids. Such type of salts is not described in the literature and nothing is known about their antiradical activity.

So, based on all of the above, in this study, new 2-formylpyridine *N*⁴-allylthiosemicarbazone salts were synthesized, characterized by FT-IR, elemental analysis, nuclear magnetic resonance (NMR), X-ray single crystal diffraction, and their antiradical activity was studied. At the same time, the synthesized compounds were also subjected to density functional theory (DFT) calculation.

2. Experimental Section

2.1. Materials and Measurements

In this work, all chemical reagents were commercial reagents and have not been further purified. 3-Isothiocyanatoprop-1-ene, hydrazine hydrate, 2-formylpyridine, nitric acid, sulfamic acid, hydrochloric acid, trichloroacetic acid, dichloroacetic acid, and chloroacetic acid were obtained from Sigma-Aldrich and were not additionally purified. The ¹H and ¹³C NMR spectra were recorded on a Bruker DRX-400. Chemical shifts are measured in ppm

relative to tetramethylsilane. CDCl₃ and DMSO-*d*₆ were used as solvents. FTIR spectra were obtained for powders on a Bruker ALPHA FTIR spectrophotometer at room temperature in the range of 4000–400 cm⁻¹. Elemental analysis was performed similar to the literature procedure.³¹ The resistance of solutions of the synthesized salts in DMF (20 °C, *c* 0.001 M) was measured using an R-38 rheochord bridge.

N-(Prop-2-en-1-yl)hydrazinecarbothioamide (*N*⁴-allyl-3-thiosemicarbazide) was synthesized by the reaction between 3-isothiocyanatoprop-1-ene (allyl isothiocyanate) and hydrazine hydrate.³²

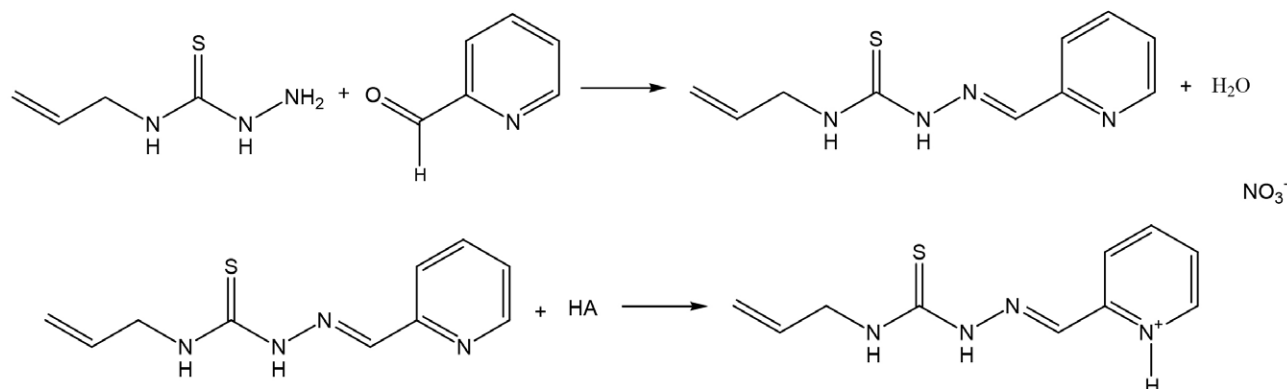
2.2. Synthesis of the Studied Substances

The compounds 1–6 were prepared by two steps as shown in Scheme 1. First, 2-formylpyridine *N*⁴-allylthiosemicarbazone was obtained by the method described in the literature.³³ *N*⁴-Allyl-3-thiosemicarbazide (20.0 mmol, 2.62 g) and 2-formylpyridine (20.0 mmol, 2.14 g) were mixed in 50 mL of 96% ethanol and stirred for about 1 h. The obtained pale-yellow precipitate was filtered, washed with a small amount of ethanol, and dried in air.

Second, the corresponding salts of 2-formylpyridine *N*⁴-allylthiosemicarbazone were obtained. 2-Formylpyridine *N*⁴-allylthiosemicarbazone (1.0 mmol, 0.22 g) and an equimolar amount of corresponding acid (1.0 M solution of HNO₃, NH₂SO₃H in water, 1.0 M solution of HCl, Cl₃CCOOH, Cl₂CHCOOH, ClCH₂COOH in water) were mixed in 25 mL of 96% ethanol and stirred for about 40 min on heating. Then, after cooling the corresponding salts of various shades of yellow crystallized from the solutions, were isolated by filtration, washed with ethanol and dried in air.

2-({2-[(Prop-2-en-1-yl)carbamothioyl]hydrazinylidene}methyl)pyridin-1-ium Nitrate [H₂L]⁺NO₃⁻ (1)

Yield: 0.20 g (71%). M. p. 159–160 °C. Anal. Calcd. for C₁₀H₁₃N₅O₃S: C, 42.39; H, 4.63; N, 24.72; S,



Scheme 1. Synthesis of the compounds 1–6.

11.32. Found: C, 42.26; H, 4.57; N, 24.68; S, 11.27. FT-IR (KBr, cm^{-1}) ν 3240, 3131, 3091 (N–H), 1641 ($\text{C}=\text{C}$)_{allyl}, 1619, 1578 (C=N), 1318 (C=S). ^1H NMR (Figure S1) (CDCl_3 , 400 MHz) δ 12.30 (br, 1H, NH), 9.17 (br, 1H, NH), 8.83 (d, 1H, CH arom.), 8.46 (m, 2H, CH arom.), 8.16 (s, 1H, CH=N), 7.86 (d, 1H, CH arom.), 5.93 (m, 1H, CH allyl), 5.17 (dd, 2H, $\text{CH}_2=\text{C}$), 4.28 (m, 2H, $\text{CH}_2\text{-N}$). ^{13}C NMR (Figure S2) (CDCl_3 , 100 MHz) δ 178.28 (C=S), 148.53, 134.54, 126.27, 124.90, 124.84 (C arom), 144.44 (C=N azometh.), 134.82 (CH allyl), 116.50 ($\text{CH}_2=$), 46.42 ($\text{CH}_2\text{-N}$). λ (DMF , $\Omega^{-1}\cdot\text{cm}^2\cdot\text{mol}^{-1}$) 83.

2-({2-[(Prop-2-en-1-yl)carbamothioyl]hydrazinylidene}methyl)pyridin-1-ium Sulfamate Hydrate [H_2L] $\text{SO}_3\text{NH}_2\cdot\text{H}_2\text{O}$ (2)

Yield: 0.25 g (75%). M. p. 173–174 °C. Anal. Calcd. for $\text{C}_{10}\text{H}_{17}\text{N}_5\text{O}_4\text{S}_2$: C, 35.81; H, 5.11; N, 20.88; S, 19.12. Found: C, 35.76; H, 5.06; N, 20.79; S, 19.05. FT-IR (KBr, cm^{-1}) ν 3428, 3365, 3285, 3188, 3085 (N–H), 1643 ($\text{C}=\text{C}$)_{allyl}, 1617, 1582 (C=N), 1320 (C=S). λ (DMF , $\Omega^{-1}\cdot\text{cm}^2\cdot\text{mol}^{-1}$) 88.

2-({2-[(Prop-2-en-1-yl)carbamothioyl]hydrazinylidene}methyl)pyridin-1-ium Chloride [H_2L] Cl (3)

Yield: 0.19 g (73%). M. p. 159–160 °C. Anal. Calcd. for $\text{C}_{10}\text{H}_{13}\text{ClN}_4\text{S}$: C, 46.78; H, 5.10; Cl, 13.81; N, 21.82; S, 12.49. Found: C, 46.68; H, 5.05; Cl, 13.75; N, 21.77; S, 12.40. FT-IR (KBr, cm^{-1}) ν 3190, 3116, 3098 (N–H), 1646 ($\text{C}=\text{C}$)_{allyl}, 1615, 1574 (C=N), 1312 (C=S). λ (DMF , $\Omega^{-1}\cdot\text{cm}^2\cdot\text{mol}^{-1}$) 66.

2-({2-[(Prop-2-en-1-yl)carbamothioyl]hydrazinylidene}methyl)pyridin-1-ium Trichloroacetate Hydrate [H_2L] $\text{Cl}_3\text{CCOO}\cdot\text{H}_2\text{O}$ (4)

Yield: 0.3 g (74%). M. p. 138–139 °C. Anal. Calcd. for $\text{C}_{12}\text{H}_{15}\text{Cl}_3\text{N}_4\text{O}_3\text{S}$: C, 35.88; H, 3.76; Cl, 26.48; N, 13.95; S, 7.98. Found: C, 35.78; H, 3.68; Cl, 26.40; N, 13.85; S, 7.89. FT-IR (KBr, cm^{-1}) ν 3336, 3146, 3084 (N–H), 1643 ($\text{C}=\text{C}$)_{allyl}, 1614, 1582 (C=N), 1314 (C=S). λ (DMF , $\Omega^{-1}\cdot\text{cm}^2\cdot\text{mol}^{-1}$) 72.

2-({2-[(Prop-2-en-1-yl)carbamothioyl]hydrazinylidene}methyl)pyridin-1-ium Dichloroacetate [H_2L] Cl_2CHCOO (5)

Yield: 0.26 g (76%). M. p. 126–127 °C. Anal. Calcd. for $\text{C}_{12}\text{H}_{14}\text{Cl}_2\text{N}_4\text{O}_2\text{S}$: C, 41.27; H, 4.04; Cl, 20.30; N, 16.04; S, 9.18. Found: C, 41.20; H, 3.94; Cl, 20.24; N, 15.96; S, 9.10. FT-IR (KBr, cm^{-1}) ν 3234, 3121, 3079 (N–H), 1645 ($\text{C}=\text{C}$)_{allyl}, 1602, 1572 (C=N), 1315 (C=S). λ (DMF , $\Omega^{-1}\cdot\text{cm}^2\cdot\text{mol}^{-1}$) 63.

2-({2-[(Prop-2-en-1-yl)carbamothioyl]hydrazinylidene}methyl)pyridin-1-ium Chloroacetate [H_2L] ClCH_2COO (6)

Yield: 0.23 g (73%). M. p. 128–129 °C. Anal. Calcd. for $\text{C}_{12}\text{H}_{15}\text{ClN}_4\text{O}_2\text{S}$: C, 45.79; H, 4.80; Cl, 11.26; N, 17.80; S, 10.19. Found: C, 45.58; H, 4.86; Cl, 11.17; N, 17.67; S, 10.10. FT-IR (KBr, cm^{-1}) ν 3252, 3133, 3084 (N–H), 1644 ($\text{C}=\text{C}$)_{allyl}, 1612, 1581 (C=N), 1317 (C=S). λ (DMF , $\Omega^{-1}\cdot\text{cm}^2\cdot\text{mol}^{-1}$) 61.

2. 3. X-Ray Crystallography

Single-crystal X-ray diffraction measurements of compounds 1–5 have been carried out on an Xcalibur E charge-coupled device (CCD) diffractometer equipped with a CCD area detector and a graphite monochromator utilizing MoK_α radiation at room temperature. Final unit cell dimensions were obtained and refined on an entire data set. All calculations necessary to solve the structures and to refine the proposed model were carried out with the SHELXS97 and SHELXL2015 program packages.^{34–36} The nonhydrogen atoms were treated anisotropically (full-matrix least-squares method on F^2). The H atoms were placed in calculated positions and were treated using riding model approximations with $U_{\text{iso}}(\text{H}) = 1.2U_{\text{eq}}(\text{C})$ and $U_{\text{iso}}(\text{H}) = 1.5U_{\text{eq}}(\text{O})$. The disordered allyl groups, solvent molecules, and Cl_3CCOO^- anion were found in compound 4. The X-ray data and the details of the refinement of studied compounds are summarized in Table 1, and the selected bond lengths, angles as well as hydrogen bond parameters are given in Tables S1, 2. The geometric parameters were calculated by PLATON program³⁷ and Mercury software³⁸ was used for visualization of structures. The hydrogen atoms that were not involved in the hydrogen bonding were omitted from the generation of the packing diagrams.

2. 4. Antiradical Evaluation

The ABTS^{•+} method³⁹ was utilized to assess the antiradical activity of the substances 1–6. Procedures for preparing standard solutions of ABTS^{•+} radical cation, as well as the studied substances, along with the spectrophotometric measurement conditions and inhibition calculations, were made as described.⁴⁰ To create 10 mM stock solutions of the compounds 1–6 and the reference compound (Trolox), 10 μmol of each compound were dissolved in 1 mL of DMSO. Subsequent solutions of 1, 10, 100, and 1000 μM concentrations were prepared by the dilution of stock solutions with DMSO. Following this, 20 μL of each solution of the tested compounds was transferred to a 96-well microtiter plate, and 180 μL of ABTS^{•+} working solution was added, resulting in final concentrations of tested compounds 0.1, 1, 10, and 100 μM , respectively.

2. 5. Computational Details

The electronic structure of H_2L^+ has been calculated by Density Functional Theory (DFT) of Gaussian16 suite

Table 1. Crystal data and structure refinement for 1–5.

Identification code	1	2	3
CCDC	2270396	2270395	2270397
Empirical formula	C ₁₀ H ₁₃ N ₅ O ₃ S	C ₁₀ H ₁₅ N ₅ O ₄ S ₂	C ₁₀ H ₁₃ ClN ₄ S
Formula weight	283.31	333.39	256.75
Temperature/K	293(2)	293(2)	293(2)
Crystal system	monoclinic	orthorhombic	orthorhombic
Space group	<i>P</i> 2 ₁ / <i>c</i>	<i>P</i> 2 ₁ 2 ₁ 2 ₁	<i>Pbca</i>
<i>a</i> /Å	5.1190(5)	5.1609(6)	14.4136(13)
<i>b</i> /Å	16.353(2)	16.9338(17)	9.9597(14)
<i>c</i> /Å	15.968(2)	17.463(2)	17.3614(19)
α /°	90	90	90
β /°	90.081(9)	90	90
γ /°	90	90	90
Volume/Å ³	1336.7(3)	1526.1(3)	2492.3(5)
<i>Z</i>	4	4	8
$\rho_{\text{calc}}/\text{g cm}^{-3}$	1.408	1.451	1.369
μ/mm^{-1}	0.255	0.371	0.453
<i>F</i> (000)	592.0	696.0	1072.0
Reflections collected	2965	3677	5649
Independent reflections (<i>R</i> _{int})	2054 (0.0359)	2579 (0.0343)	2240 (0.0585)
Data/restraints/parameters	2054/6/172	2579/0/193	2240/0/153
Goodness-of-fit on <i>F</i> ²	1.045	0.961	0.910
<i>R</i> ₁ , <i>wR</i> ₂ [<i>I</i> ≥ 2σ(<i>I</i>)]	0.0948, 0.1933	0.0596, 0.1083	0.0529, 0.0780
<i>R</i> ₁ , <i>wR</i> ₂ [all data]	0.1670, 0.2270	0.1025, 0.1260	0.1209, 0.0967
$\Delta\rho_{\text{max}}/\Delta\rho_{\text{min}} / \text{e Å}^{-3}$	0.26/−0.22	0.35/−0.28	0.22/−0.24
Identification code	4	5	
CCDC	2270394	2270398	
Empirical formula	C ₁₂ H ₁₂ Cl ₃ N ₄ O ₃ S	C ₁₂ H ₁₄ Cl ₂ N ₄ O ₂ S	
Formula weight	398.67	349.23	
Temperature/K	293(2)	293(2)	
Crystal system	monoclinic	triclinic	
Space group	<i>P</i> 2 ₁ / <i>c</i>	<i>P</i> -1	
<i>a</i> /Å	15.7525(6)	8.1644(6)	
<i>b</i> /Å	6.8339(2)	8.6556(6)	
<i>c</i> /Å	33.2529(10)	11.0961(9)	
α /°	90	91.468(6)	
β /°	95.272(3)	93.665(7)	
γ /°	90	100.901(6)	
Volume/Å ³	3564.6(2)	767.84(10)	
<i>Z</i>	8	2	
$\rho_{\text{calc}}/\text{g cm}^{-3}$	1.4857	1.511	
μ/mm^{-1}	0.648	0.567	
<i>F</i> (000)	1629.1	360.0	
Reflections collected	13159	4871	
Independent reflections (<i>R</i> _{int})	6254 (0.0192)	2848 (0.0188)	
Data/restraints/parameters	6254/0/4401	2848/0/199	
Goodness-of-fit on <i>F</i> ²	1.055	0.941	
<i>R</i> ₁ , <i>wR</i> ₂ [<i>I</i> ≥ 2σ(<i>I</i>)]	0.0664, 0.1754	0.0384, 0.1203	
<i>R</i> ₁ , <i>wR</i> ₂ [all data]	0.0869, 0.1897	0.0497, 0.1348	
$\Delta\rho_{\text{max}}/\Delta\rho_{\text{min}} / \text{e Å}^{-3}$	0.83/−0.54	0.31/−0.42	

of quantum chemical codes based on the B3LYP level of theory⁴¹ using Gaussian16 software.⁴² The molecular electrostatic potential was generated through a constant value of electron density. The molecular structure of the cation was optimized with 6-311G(d,p) basis set⁴³ in water using

the IEFPCM method.⁴⁴ The calculated frequencies were positive indicating that a definite absolute minimum was found on the potential energy surface. GaussView 05 software⁴⁵ was used for the visualization of molecular structures and analysis of obtained results.

Table 2. Hydrogen bonds (Å) and angles (deg.) in 1–5

D–H...A	d(H...A)	d(D...A)	∠(DHA)	Symmetry codes
1				
N1–H...O1	2.0	2.827(7)	162.0	x, y, z
N3–H...O3	2.05	2.910(7)	169.0	$x, 3/2 - y, -1/2 + z$
N4–H...O3	1.93	2.782(7)	174.0	$x, 3/2 - y, -1/2 + z$
C2–H...O1	2.48	3.323(8)	136	$x, 1/2 - y, -1/2 + z$
C7–H...O1	2.43	3.073(9)	127	$x, 3/2 - y, -1/2 + z$
2				
N1–H...O4	2.05	2.876(9)	150	x, y, z
N3–H...O1	2.12	2.950(8)	163	x, y, z
N4–H...O1	1.9	2.736(8)	165	x, y, z
O4–H...O4	2.08	2.916(8)	167	$1/2 + x, 1/2 - y, 1 - z$
O4–H...O2	2.08	2.904(7)	163	$1/2 - x, 1 - y, -1/2 + z$
N5–H...S1	2.71	3.479(6)	149	$x, 1/2 + y, 3/2 - z$
3				
N1–H...Cl1	2.4	3.222(3)	160	$-1/2 + x, 3/2 - y, 1 - z$
N4–H...Cl1	2.29	3.081(3)	153	x, y, z
N3–H...Cl1	2.52	3.278(3)	148	x, y, z
C2–H...Cl1	2.78	3.563(3)	143	$-1/2 + x, 3/2 - y, 1 - z$
C10–H...S1	2.85	3.806(5)	146	$1/2 - x, -1/2 + y, z$
4				
N1–H...Ow	1.95	2.7961(1)	166	x, y, z
N3–H...O4	2.41	3.1780(1)	150	x, y, z
Ow1–H...O6	2.03	2.8652(1)	168	$1 - x, 2 - y, -z$
N4–H...O4	1.98	2.7580(1)	165	x, y, z
Ow1–H...O1	1.89	2.7198(1)	165	$1 - x, 1 - y, -z$
N1a–H...Ow1	1.83	2.7826(1)	170	x, y, z
Ow–H...O3	1.89	2.7399(1)	172	x, y, z
Ow–H...O4	2.07	2.8977(1)	165	$x, -1 + y, z$
N3a–H...O6	2.47	3.2400(1)	149	$1 - x, 1 - y, -z$
N4a–H...O6	1.93	2.7363(1)	162	$1 - x, 1 - y, -z$
C2a–H...Ow1	2.58	3.3119(1)	136	x, y, z
5				
N1–H...O2	2.03	2.848(2)	158	$x, 1 + y, z$
N3–H...O1	2.13	2.946(2)	157	$1 - x, 1 - y, 1 - z$
N4–H...O1	1.86	2.687(2)	161	$1 - x, 1 - y, 1 - z$

3. Results and Discussion

Six new compounds **1–6** were synthesized in two steps. In the first step, 2-formylpyridine N^4 -allylthiosemicarbazone was obtained by the reaction between N^4 -allyl-3-thiosemicarbazide and 2-formylpyridine in ethanol. In the second step, 2-formylpyridine N^4 -allylthiosemicarbazone reacted with corresponding acids to form different salts. Single crystals of complexes **1–5** were obtained by recrystallization from ethanol. Elemental analysis was performed for all compounds, the results of which confirm the formula determined from the structure. The molar conductivity values of the synthesized compounds **1–6** are in the range 61–88 $\Omega^{-1}\text{cm}^2\text{mol}^{-1}$, indicating that they behave as 1:1 electrolytes in solution.

In order to determine the changes that appear upon protonation of the thiosemicarbazone **HL**, a comparative analysis of the NMR spectra of 2-formylpyridine N^4 -allylthiosemicarbazone, which is described in the literature,³⁰ and its nitric acid salt (**1**, Figures S2, S3) was performed. The protonation of the thiosemicarbazone **HL** led to an increase of chemical shift values of the protons from the pyridine moiety, which can indicate the protonation of the pyridine nitrogen atom.

3. 1. Structural Study of Compounds 1–5.

The X-ray structures of compounds **1–5** are presented in Figures 1–6. The structures of these compounds consist of a protonated ligand H_2L^+ , solvent molecules (in the

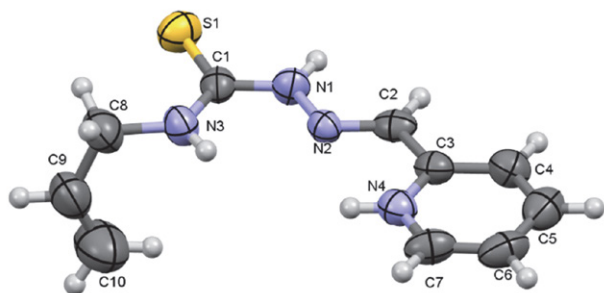


Figure 1. View of compounds with atom numbering. Thermal ellipsoids are drawn at a 50% probability level.

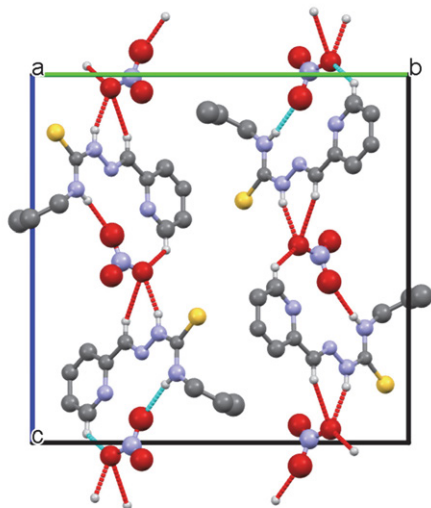


Figure 2. The crystal packing fragment of **1** with chains formation along the *c*-axis.

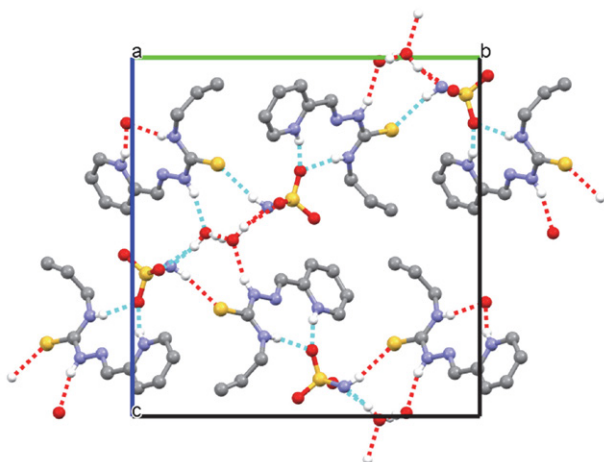


Figure 3. The fragment of 3D supramolecular network in **2**.

case of **2**, **4**) and counter ions NO_3^- , NH_2SO_3^- , Cl^- , Cl_3CCOO^- , $\text{Cl}_2\text{CHCOO}^-$ in **1–5** respectively. In H_2L^+ (Figure 1a, Table S1) the substituents at N1–C1 bond are in the *E* position. In compounds **1–5**, the A (S1–N1–N2–N3–C1–C2) core is practically planar within 0.05 Å and the dihedral angles between A and pyridine ring range

from 2.2 to 10.7°. Meanwhile, the cation is nonplanar in studied compounds because the C3H5 substituent in the thiosemicarbazone moiety, the dihedral angles between the best planes of A and allyl groups lie in interval 71.5–83.8°. The bond lengths and angles, as well as the aforementioned values, are in good agreement with those in neutral molecules of 2-formyl-, 3-formyl-, and 4-formylpyridine N^4 -allylthiosemicarbazones.³⁰

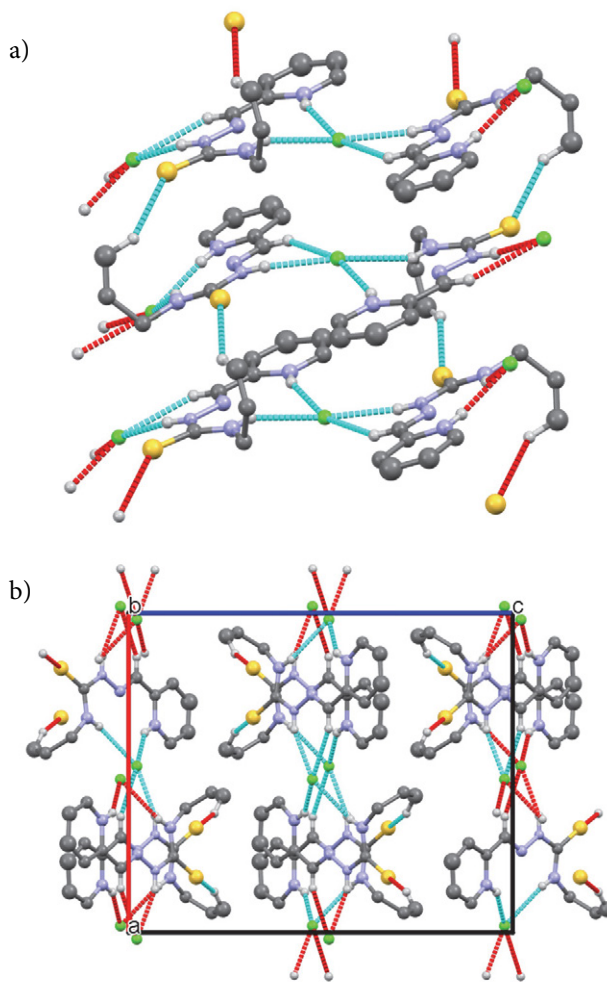


Figure 4. (a) Chains formation along *b*-direction via C10–H...S1 hydrogen bond; (b) fragment of layers in the crystal packing of **3**, where chains are joined by chlorine atoms.

The presence of anions (in substances **1–5**) and solvent molecules (in substances **2** and **4**) affects the architecture of hydrogen bonds in their crystal structures. In the crystal of **1**, the cations are joined by nitrate groups into the chains along the *c*-axis (Table 2, Figure 2). In the crystal of **2**, the 3D supramolecular network is formed by hydrogen-bonding interactions involving the ligands H_2L^+ and solvent molecules (Figure 3). In **3** the ligands are linked by C10–H...S1 hydrogen bonds in chains along the *b*-direction. In turn, these chains are joined by chlorine at-

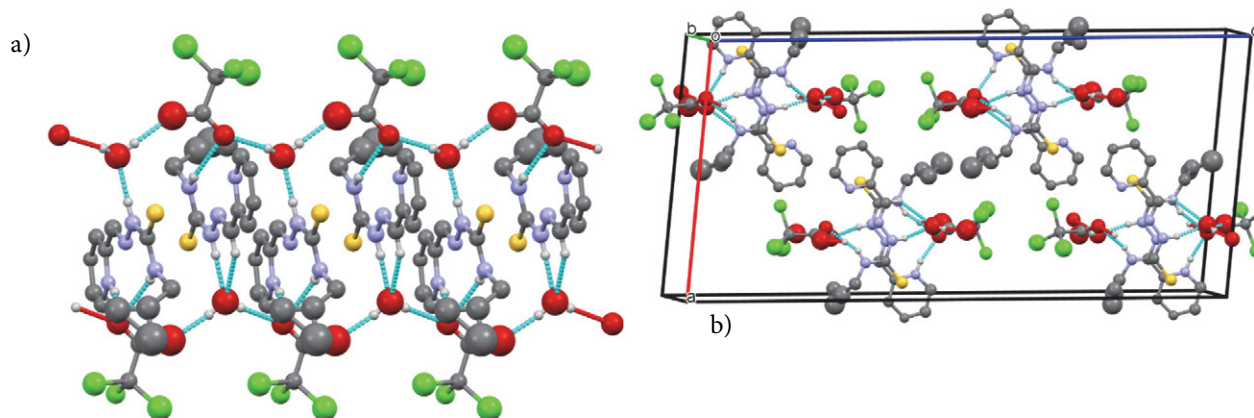


Figure 5. (a) Formation of chains along the *b*-axis through hydrogen bonds involving water molecules and anions; (b) fragment of crystal packing in **4**.

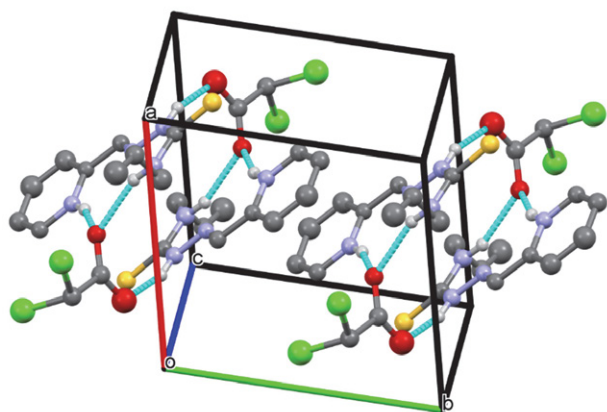


Figure 6. The centrosymmetric dimers in **5**, where monomers are held together by bridge solvent molecules.

oms into layers parallel to the (001) plane (Figure 4a, b). In **4** the cations form the chains along the *b*-axis *via* hydrogen bonds with two water molecules and anions (Figure 5a, b). In the crystal of **5**, the cations form the centrosymmetric dimers where the monomers are held together by bridge solvent molecules through hydrogen bonds (Figure 6). Between chains in **1** and **4**, layers in **3**, and dimers in **5** occur the van der Waals interactions.

3. 3. Antiradical Activity

The antiradical activity of the compounds **1–6** was determined by the ABTS^{•+} method (Table 3). In all cases, the obtained salts manifest a higher antiradical activity than the initial thiosemicarbazone **HL**.³⁰ The IC₅₀ values of the obtained salts **1–6** are 5–30% lower than that of non-protonated thiosemicarbazone. Based on the presented results we can conclude that the acidic residue in the composition of the thiosemicarbazone salts also has an influence on its antiradical activity. The antiradical activity of the studied compounds decreases according to the fol-

lowing series of dependences of acid residues: Cl⁻ > Cl₂CHCOO⁻ > Cl₃CCOO⁻ > NO₃⁻ ≈ SO₃NH₂⁻ > ClCH₂COO⁻. All the studied substances showed activity higher than Trolox, a standard antioxidant used for antioxidant capacity assays. Compound [H₂L]Cl (**3**) showed the greatest activity with an IC₅₀ value of 9.9 μmol/L, being three times more active than Trolox.

Compared with the literature data we have previously published,⁴⁰ the 2-acetylpyridine 4-allylthiosemicarbazone showed no antiradical activity, leading to conclusion that the presence of a 2-formylpyridine fragment in the structure of thiosemicarbazone enhances its antiradical activity.

Table 3. Antiradical activity of the studied substances in terms of IC₅₀ values toward ABTS^{•+}

Compound	IC ₅₀ , μmol/L
HL	14.2±1.8
1	12.9±0.4
2	12.9±1.0
3	9.9±1.0
4	12.1±0.7
5	10.9±0.9
6	13.4±0.8
Trolox	33.0±0.7

3. 3. DFT Calculations

It is known that the frontier molecular orbitals (FMOs) such as the highest occupied molecular orbitals (HOMO) and lowest unoccupied molecular orbitals (LUMO) may act as electron donors and acceptors, respectively. The energies of FMOs are used for the calculation of molecular descriptors which are important parameters for the characterization of the reactivity of molecules. The definition and detailed analysis of molecular descriptors and FMOs of neutral **HL** were done previously.^{30,46} The

contour plot of the ground state FMOs of cation is shown in Figure 2. The energy gaps between HOMO and LUMO in H_2L^+ and **HL** are different, being 2.04 and 3.771 eV, respectively. However, the composition of frontier molecular orbitals of these molecules is very similar. The HOMOs of H_2L^+ and **HL** are located mainly on the sulphur atoms with a small contribution of nitrogen atoms of the chains, while the LUMOs are distributed in thiosemicarbazone moieties and pyridine rings. Meanwhile, the molecular descriptors, namely electronegativity (χ), chemical hardness (η), and electrophilic index (ω) are significantly different in cations and neutral molecule. Compounds with high electronegativity are less likely to donate electrons. The lowest the chemical hardness value, the highest the activity of a molecule. The lowest electrophilic index is characterized by the highest electron donation ability. The values of χ , η , and ω for H_2L^+ and **HL** are 8.033, 1.02, 31.638 eV and 3.767, 1.886, 3.763 eV, respectively, and the main difference among these quantities is related to electronegativity and electrophilic index.

The molecular electrostatic potential (MEP) surface of H_2L^+ was mapped, using the optimized geometries (Figure 3). The MEPs of cations and neutral molecule are significantly different. The values of MEPs in H_2L^+ range from 0.0 to 62.75 kcal/mol, while in **HL** the MEP increase in the order $-31.7 \text{ kcal mol}^{-1} = \text{red} < \text{yellow} < \text{green} < \text{blue} = 31.7 \text{ kcal mol}^{-1}$. In the last compound, the negative (red and yellow) regions of MEP are related to electrophilic reactivity

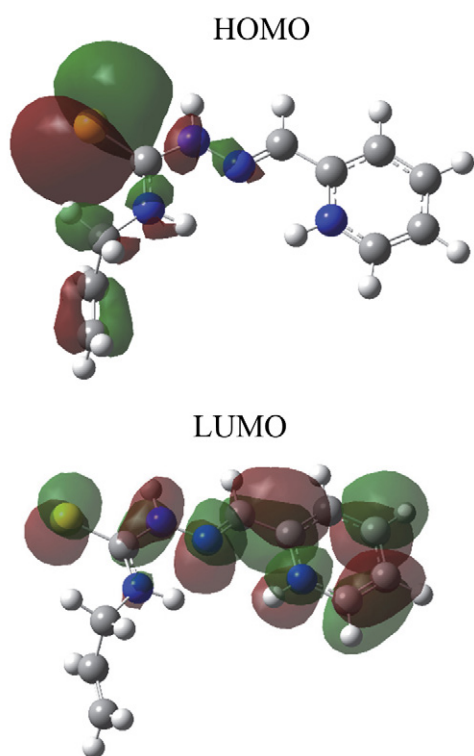


Figure 7. View of HOMO and LUMO of the studied molecule.

and the positive (blue) regions to nucleophilic reactivity whereas in H_2L^+ the molecular electrostatic potential is positive and corresponds to nucleophilic reactivity only.

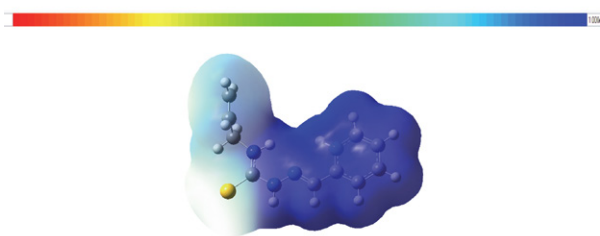


Figure 8. Electrostatic potentials mapped on the molecular surfaces of the studied molecule. The values of MEPs range from 0.0 to 62.75 kcal/mol.

Thus, the difference in molecular descriptors and molecular electrostatic potentials of H_2L^+ and **HL** may indicate different mechanisms of their antioxidant activity because the electronic structure of the cation is more favorable for accepting electrons if compared with **HL**.

4. Conclusions

We have described in this paper synthesis of six salts of 2-formylpyridine N^4 -allylthiosemicarbazone with nitric, hydrochloric, chloroacetic, dichloroacetic, trichloroacetic and sulfaminic acids, and crystal structure of five of them, as well as their antiradical activity toward $\text{ABTS}^{+\bullet}$ and compared them with the activity of neutral molecule of 2-formylpyridine N^4 -allylthiosemicarbazone and Trolox. Protonation of the thiosemicarbazone moiety led to an increase in antiradical activity. The corresponding IC_{50} values became lower by 5–30%.

Protonation of the pyridine fragment in this thiosemicarbazone induces changes in the molecular electrostatic potential surface and molecular descriptors, including electronegativity, chemical hardness, and electrophilic index. These alterations make the cation H_2L^+ more favorable for accepting electrons and thus contribute to the change in antiradical activity. Thus, all of the obtained salts manifest higher antiradical activity, which also depends on the nature of the acid moiety. The most active one is the salt with chloride anion, then the one with the dichloroacetate anion. So, the transformation of thiosemicarbazones into salts in this case leads to an increase in antiradical activity, and the continuation of this study on other N -substituted thiosemicarbazones represents an interest for enhancing antiradical activity of this important class of bioactive substances.

Acknowledgments

This work was fulfilled with the financial support of the subprograms 010602 and 010701.

Supplementary Materials

CCDC 2270394-2270398 contains the supplementary crystallographic data for the compounds 1-5. Copies of the data can be obtained free of charge on application to CCDC, 12 Union Road, Cambridge CB2 1EZ, UK (fax: 44-1223-336-033; e-mail: deposit@ccdc.cam.ac.uk or www: http://www.ccdc.cam.ac.uk)

5. References

- S. Vertuani, A. Angusti, S. Manfredini, *Curr. Pharm. Des.* **2004**, *10*, 1677–1694. DOI:10.2174/1381612043384655
- R. Mittler, *Trends Plant Sci.* **2002**, *7*, 405–410. DOI:10.1016/S1360-1385(02)02312-9
- B. Halliwell, R. Aeschbach, J. Löliger, O. I. Aruoma, *Food Chem. Toxicol.* **1995**, *33*, 601–617. DOI:10.1016/0278-6915(95)00024-V
- O. E. Ifeanyi, *Int. J. Curr. Res. Med. Sci* **2018**, *4*, 123–133.
- K. J. Davies, *IUBMB Life* **2000**, *50*, 279–289. DOI:10.1080/15216540051081010
- H. Sies, *Eur. J. Biochem.* **1993**, *215*, 213–219. DOI:10.1111/j.1432-1033.1993.tb18025.x
- F. Gagne: *Biochemical Ecotoxicology Principles and Methods*, Elsevier Academic Press Inc., **2014**, pp. 103–115. DOI:10.1016/B978-0-12-411604-7.00006-4
- A. Phaniendra, D. B. Jestadi, L. Periyasamy, *Indian J. Clin. Biochem.* **2015**, *30*, 11–26. DOI:10.1007/s12291-014-0446-0
- L. He, T. He, S. Farrar, L. Ji, T. Liu, X. Ma, *Cell Physiol. Biochem.* **2017**, *44*(2), 532–553. DOI:10.1159/000485089
- C. Bonaccorso, T. Marzo, D. La Mendola, *Pharmaceuticals* **2019**, *13*, 4. DOI:10.3390/ph13010004
- L. Yang, H. Liu, D. Xia, S. Wang, *Molecules* **2020**, *25*, 1192. DOI:10.3390/molecules25051192
- D. S. Kalinowski, P. Quach, D. R. Richardson, *Future Med. Chem.* **2009**, *1*, 1143–1151. DOI:10.4155/fmc.09.80
- M. A. Metwally, S. Bondock, H. El-Azap, E. E. M. Kandeel, *J. Sulphur Chem.* **2011**, *32*, 489–519. DOI:10.1080/17415993.2011.601869
- N. P. Prajapati, H. D. Patel, *Synth. Commun.* **2019**, *49*, 2767–2804.
- F. Kalso, A. Khalil, H. Noureddine, Y. El-Makhour, *Int. Immunopharmacol.* **2021**, *96*, 107778. DOI:10.1016/j.intimp.2021.107778
- P. F. Rapheal, E. Manoj, M. P. Kurup, *Polyhedron* **2007**, *26*, 818–828. DOI:10.1016/j.poly.2006.09.091
- M. N. M. Milunović, O. Palamarciuc, A. Sirbu, S. Shova, D. Dumitrescu, D. Dvoranová, P. Raptá, T. V. Petrasheuskaya, E. A. Enyedy, G. Spengler, M. Ilic, H. H. Sitte, G. Lubec, V. B. Arion, *Biomolecules* **2020**, *10*, 1213. DOI:10.3390/biom10091213
- S. Arora, S. Agarwal, S. Singhal, *Int. J. Pharm. Sci.* **2014**, *6*, 34–41.
- E. J. Siddiqui, I. Azad, A. R. Khan, T. Khan, *JDDT* **2019**, *9*, 689–703. DOI:10.22270/jddt.v9i3.2888
- S. Gupta, N. Singh, T. Khan, S. Joshi, *Results Chem.* **2022**, *4*, 100459. DOI:10.1016/j.rechem.2022.100459
- A. B. Ibrahim, M. K. Farh, S. A. El-Gyar, M. A. El-Gahami, D. M. Fouad, F. Silva, I. C. Santos, A. Paulo, *Inorg. Chem. Commun.* **2018**, *96*, 194–201. DOI:10.1016/j.inoche.2018.08.023
- S. Chandra, S. Parmar, Y. Kumar, *Bioinorg. Chem. Appl.* **2009**, 851316.
- A. P. Gulea, K. S. Lozan-Tyrshu, V. I. Tsapkov, I. D. Korzha, V. F. Rudik, *Russ. J. Gen. Chem.* **2012**, *82*, 1869–1872. DOI:10.1134/S1070363212110242
- D. X. West, D. L. Huffman, J. S. Saleda, A. E. Liberta, *Transition Met. Chem.* **1991**, *16*, 565–570. DOI:10.1007/BF01024187
- D. X. West, J. S. Saleda, A. E. Liberta, *Transit. Met. Chem.* **1991**, *17*, 568–572. DOI:10.1007/BF02910760
- G. Atassi, P. Dumont, J. C. E. Harteel, *Eur. J. Cancer* **1979**, *15*, 451–459. DOI:10.1016/0014-2964(79)90080-X
- E. W. Ainscough, A. M. Brodie, J. D. Ranford, J. M. Waters, *J. Chem. Soc.* **1991**, 2125–2131.
- K. C. Agrawal, B. A. Booth, S. M. DeNuzzo, A. C. Sartorelli, *J. Med. Chem.* **1976**, *19*, 1209–1214. DOI:10.1021/jm00232a008
- D. C. Ilies, S. Shova, V. Radulescu, E. Pahontu, T. Rosu, *Polyhedron* **2015**, *97*, 157–166. DOI:10.1016/j.poly.2015.05.009
- V. Graur, Y. Chumakov, O. Garbuz, C. Hureau, V. Tsapkov, A. Gulea, *Bioinorg. Chem. Appl.* **2022**, 2022. DOI:10.1155/2022/2705332
- J. Fries, H. Getrost: *Organic Reagents for Trace Analysis*, E. Merck Darmstadt, Germany, **1977**.
- W. Zhao, M. Zhao, *Chin. J. Org. Chem.* **2001**, *21*, 681.
- B. M. Zeglis, V. Divilov, J. S. Lewis, *J. Med. Chem.* **2011**, *54*, 2391–2398. DOI:10.1021/jm101532u
- O. V. Dolomanov, L. J. Bourhis, R. J. Gildea, J. A. K. Howard, H. Puschmann, *J. Appl. Cryst.* **2009**, *42*, 339–341. DOI:10.1107/S0021889808042726
- G. M. Sheldrick, *Acta Crystallogr., Sect. A: Found. Crystallogr.* **2008**, *64*, 112–122. DOI:10.1107/S0108767307043930
- G. M. Sheldrick, *Acta Crystallogr., Sect. C: Struct. Chem.* **2015**, *71*, 3. DOI:10.1107/S2053229614024218
- A. L. Spek, *Acta Crystallogr. D65* **2009**, 148–155. DOI:10.1107/S090744490804362X
- C. F. Macrae, P. R. Edgington, P. McCabe, E. Pidcock, G. P. Shields, R. Taylor, M. Towler, J. van De Streek, *J. Appl. Cryst.* **2006**, *39*, 453–457. DOI:10.1107/S002188980600731X
- R. Re, N. Pellegrini, A. Proteggente, A. Pannala, M. Yang, C. Rice-Evans, *Free Radicals Biol. Med.* **1999**, *26*, 1231–1237. DOI:10.1016/S0891-5849(98)00315-3
- V. Graur, I. Usataia, P. Bourosh, V. Kravtsov, O. Garbuz, C. Hureau, A. Gulea, *Appl. Organomet. Chem.* **2021**, *35*, e6172. DOI:10.1002/aoc.6172
- C. Lee, W. Yang, R. G. Parr, *Phys. Rev.* **1988**, *B. 37*, 785–789. DOI:10.1103/PhysRevB.37.785
- M. J. Frisch, G. W. Trucks, H. B. Schlegel, G. E. Scuseria, M. A. Robb, J. R. Cheeseman, G. Scalmani, V. Barone, G. A. Petersson, H. Nakatsuji, X. Li, Gaussian 16 Search PubMed. Gaussian Inc., Wallingford, CT, **2016**.
- E. V. R. Castro, F. E., J. Jorge, *Chem. Phys.* **1998**, *108*, 5225–5229. DOI:10.1063/1.475959

44. D. M. Chipman, *Theor. Chem. Acc.* **2002**, *107*, 80–89.
DOI:10.1007/s00214-001-0302-1
45. R. Dennington, T. Keith, J. Millam, Gauss View 2009, Version 5. Semichem Inc., Shawnee Mission.
46. Z. Lakbaibi, H. Abou El Makarim, M. Tabyaoui, A. El Hajbi, *J. Mater. Environ. Sci.* **2016**, *8*, 99–115.

Povzetek

Sintetizirali smo šest novih 2-formilpiridin N^4 -aliltiosemikarbazonskih soli ($[H_2L]X \cdot nH_2O$, kjer je $X NO_3^-$ (**1**), $NH_2SO_3^-$ (**2**), Cl^- (**3**), Cl_3CCOO^- (**4**), Cl_2CHCOO^- (**5**), $ClCH_2COO^-$ (**6**); $n = 0$ (**1**, **3**, **5**, **6**), 1 (**2**, **4**)) in določili njihove fizikalne ter kemijske lastnosti s pomočjo elementne analize, meritev prevodnosti, FT-IR ter 1H in ^{13}C NMR spektroskopije. Kristalne strukture spojin **1–5** smo določili s pomočjo rentgenske difrakcije na monokristalu. Podatki kristalne analize kažejo, da so strukture spojin sestavljene iz protonirane oblike tiosemikarbazonov H_2L^+ , ustreznega aniona (kislinskega ostanka) in molekule vode (v primerih **2** in **4**). Te spojine izkazujejo antiradikalno aktivnost proti $ABTS^{+\cdot}$ kation radikal, ki presega aktivnost neprotoniranega izhodnega tiosemikarbazona **HL** in tudi Troloksa, ki se standardno uporablja za medicinske namene. Najbolj aktivna spojina je $[H_2L]Cl$ (**3**) z IC_{50} vrednostjo $9.9 \mu mol/L$. Izračuni s teorijo gostotnega potenciala kažejo, da je elektronska struktura kationa H_2L^+ bolj dovzetna za sprejemanje elektronov kot pa **HL**.



Except when otherwise noted, articles in this journal are published under the terms and conditions of the Creative Commons Attribution 4.0 International License

Scientific paper

Aaptamine, Isolated from the Bunaken National Park's Sponge, *Aaptos* sp., Promotes Cell Cycle Arrest and Induces Necrotic Cell Death of Colorectal Cancers

Annisa Elcentia Fajarwati^{1,2}, Mutia Hardhiyuna¹, Febby Nurdiya Ningsih¹, Adam Hermawan^{3,4}, Dyaningtyas Dewi Pamungkas Putri^{3,4}, Nurul Fatimah^{3,4}, Asep Bayu¹, Andi Setiawan², Ucu Yanu Arbi⁵, Tutik Murniasih¹, A'liyatur Rosyidah¹, Tri Aryono Hadi⁵, Masteria Yunovilsa Putra¹, and Peni Ahmadi^{1,*}

¹ Research Center for Vaccine and Drugs, Health Research Organization, National Research and Innovation Agency (BRIN), Jl. Raya Bogor Km. 46, Cibinong, 16911, Indonesia

² Department of Chemistry, Faculty of Mathematics and Natural Sciences, Lampung University, Bandar Lampung 35145, Indonesia

³ Cancer Chemoprevention Research Center, Faculty of Pharmacy, Gadjah Mada University, Yogyakarta

⁴ Laboratory of Advanced Pharmaceutical Sciences, Faculty of Pharmacy, Gadjah Mada University, Yogyakarta, 55281, Indonesia

⁵ Research Center for Oceanography, National Research and Innovation (BRIN), Jl. Pasir Putih I, Ancol Timur, North Jakarta, 14430

* Corresponding author: E-mail: peni.ahmadi@brin.go.id

Received: 04-22-2024

Abstract

The sponge is one of the potential sources of bioactive compounds. Among them, the sponge *Aaptos* has been a promising source of leading drugs including aaptamine (1). This study investigated the aaptamine (1), spectroscopically determined, from *Aaptos* sp. collected from Bunaken National Park, Indonesia, as an anticancer agent, specifically targeting colorectal cancers (CRCs). Compound 1 showed potent cytotoxicity against DLD-1 and Caco-2 with IC₅₀ values of 30.3 and 236.8 µg/mL, respectively. In addition, the exposure of compound 1 on those colorectal cancer cells could promote cell cycle arrest and induce necrotic cell death.

Keywords: Sponge, *Aaptos*, aaptamine, DLD-1, Caco-2, Necrotic

1. Introduction

Colorectal cancer is the third most common cause of cancer-related deaths.¹ In 2020, colorectal cancer (CRC) resulted in approximately 1.9 million new cases and 0.9 million fatalities globally. The frequency of CRC has increased in developing countries because of the shifting in lifestyle and diet towards Westernization.² According to GLOBOCAN (2020), Indonesia contributed 34,189 (8.6%) cases of colorectal cancer in a total of 396,914 cases consisting of 21,764 cases for men and 12,425 cases for women.³ The elevated incidence of CRC in men may be attributed to a variety of factors. Unlike women, men appear to be more significantly impacted by environmental influ-

ences rather than genetic factors, including alcohol consumption, obesity, smoking, and bad dietary habits.⁴ The substantial occurrence and fatality rates associated with CRC, coupled with the limitations of current treatments and preventive measures, underscore the pressing necessity for the exploration and development of new drugs.

Natural products hold the promise to be a source of new drugs with minimum side effects and improved compatibility with the human body.⁵ Over the years, the potential of Marine Natural Products (MNPs) has attracted the attention of researchers. The immense expanses of the oceans and many levels of biodiversity in the marine environment make researchers eagerly explore novel active compounds from sponges.⁶

Sponges are marine invertebrates and have been recognized as a major source of bioactive compounds.⁷ For example, eribulin mesylate from the sponge *Halichondria okadai* has been reported to exhibit potential clinical activity against pre-treated metastatic breast cancer cells.⁸

Over various genera of sponges, *Aaptos* has been known as a genus of sponges that produce bioactive compounds. *Aaptos* is a cosmopolitan marine sponge with a wide geographical distribution including Indonesian waters.⁹ A unique bioactive compound identified from this genus is aaptamine, which exhibits various biological activities, including antibacterial,^{10,11} antioxidant,¹² antiproliferative,¹³ anti-mycobacterial,⁹ α -adrenoceptor blocking,¹⁴ sortase A inhibition,¹⁵ cholinesterase inhibition,¹⁶ antifungal,¹⁷ anti-HIV,¹⁷ and cytotoxic activities.¹⁸

Recently, Utkina and co-workers (2021) reported that iso-aaptamine isolated from *A. aaptos* could reduce the expression of enzymes in human colorectal adenocarcinoma DLD-1 cells from 100% to 64% at a concentration of 5 μ M.¹⁹ Another bioactive compound, 3-([9-methylhexadecyl] oxy) propane-1,2-diol 2,2,3-dihydro-2,3-dioxo-aaptamine, shows cytotoxic activity against lung cancer SK-LU-1, breast cancer MCF-7, liver cancer HepG2, and melanoma SK-Mel-2 with IC₅₀ of 41.27 \pm 2.63, 40.70 \pm 2.65, 34.31 \pm 3.43, and 36.63 \pm 1.40 μ M, respectively.²⁰

In this study, we will report bioactive compounds isolated from the marine sponge *Aaptos* sp. as anticancer agents against colorectal cancer cells, DLD-1 and Caco-2. Herein, we also describe the mechanism of action of the active compounds present in this sponge.

2. Method

2.1. Biological Material

The sponge was collected by scuba diving at a depth of 10–15 meters from Likuan 3, Bunaken Island, Bunaken National Park, North Sulawesi, Indonesia (N 01.60572 E 124.76818), in September 2022. The sample was immediately frozen and kept at the Genomics Laboratory, National Research and Innovation Agency (BRIN), Cibinong, West Java, Indonesia, until the extraction was performed. The specimen was identified by the analysis of morphology and the spicules which were identified as *Aaptos* sp.

2.2. Extraction

The extraction process was conducted according to Ahmadi et al. (2017).²¹ In brief, the sample (80.94 g, wet) was chopped and soaked in methanol (MeOH) overnight. Thereafter, the filtrate was collected by filtration and the spent biomass was reextracted using fresh methanol. The extraction was performed for at least three times. After maceration, all filtrate was combined and concentrated by

using a Rotary Vacuum Evaporator (Rotavapor Buchi R-300). Subsequently, the residue was partitioned exhaustively by using water and ethyl acetate (EtOAc) to give 388.97 mg of EtOAc fraction (SBM 066-1).

2.3. Thin Layer Chromatography (TLC)

As guidance to identify the components present in the extract, a thin layer chromatography (TLC) was performed using TLC sheets of silica gel 60 F₂₅₄ (Merck), with a mobile phase of n-hexane:EtOAc (7:3). Silica plates were exposed to UV light at 254 nm. Further, the plates were reacted using cerium sulfate Ce(SO₄)₂, ninhydrin, and Dragendorff's. The TLC plate was heated and examined to calculate the R_f value.

2.4. Open Column Chromatography (OCC) by Silica

The SBM 066-1 (~250 mg) was fractionated by using open-column chromatography (OCC) with normal-phased silica (7500 mg) as a stationary phase. Several mobile phases were used and started consecutively with n-hexane, followed by dichloromethane (DCM), EtOAc, and MeOH. Every solvent was collected and gave a corresponding yield of 80.53 mg (SBM 066-1-1), 26.13 mg (SBM 066-1-2), 112.76 mg (SBM 066-1-3), and 55.86 mg (SBM 066-1-4).

2.5. Spectroscopy Analysis

The sample was analyzed by using the Waters ACQUITY UPLC® H-Class System, which included an ACQUITY UPLC® HSS C₁₈ column (11.8 μ m, 2.1 Å, 100 mm) and coupled with the Xevo G2-S QTOF Mass Spectrometer, all from Waters, Beverly, MA, USA. The system utilized electrospray ionization (ESI) in a positive ion mode for the mass spectrometry. The elemental compositions were determined using the Waters MassLynx (v4.1) and Mestrenova software. Additionally, the compound type was compared to the PubChem database. Meanwhile, ¹H-NMR spectra were recorded by using BRUKER at 500 MHz for ¹H-NMR in CD₃OD.

2.6. Purification using Sep-pak C₁₈

Further purification was conducted by applying 53 mg of SBM 066-1-4 on Sep-pak C₁₈ and eluted with several eluent: 100% H₂O, 25% MeOH in H₂O, 50% MeOH in H₂O, 75% MeOH in H₂O, and 100% MeOH. Five fractions were yielded with amounts of 27.63 mg (SBM 066-1-4-1), 3.3 mg (SBM 066-1-4-2), 0.65 mg (SBM 066-1-4-3), 8.07 mg (SBM 066-1-4-4), and 13.35 mg (SBM 066-1-4-5) (Figure S1). Fraction SBM 066-1-4-1 was further identified to lead to an aaptamine compound with a purity of more than 90% (Figure S6).

2. 7. Cell Culture and Conditions

The study was conducted on two human colorectal cancer cells (DLD-1 and Caco-2) and normal cells (HEK293), all sourced from the American Type Culture Collection (ATCC, USA). These cell lines were grown in DMEM medium (Gibco, Germany) supplemented with 10% fetal bovine serum (FBS; Sigma-Aldrich), 1.5% Penicillin/Streptomycin (Sigma, Aldrich), and 0.5% fungizone (Sigma-Aldrich). The cells were maintained in a cell culture incubator set to 37°C with 5% CO₂ to create an optimal environment for their growth.

2. 8. MTT Assay

The colorectal cancer cells, DLD-1 and Caco-2, along with HEK293 as normal cells, were collected when they reached 70–80% confluence and then subjected to centrifugation at 1200 rpm at 21 °C for 5 minutes. The cells were enumerated using a microscope and a haemocytometer then were plated into a 96-well plate at a concentration of 1 × 10⁴ cells per well. These plates were placed in an incubator at 5% CO₂ and 37°C for 24 hours to facilitate cell attachment. After this incubation period, non-adherent cells were carefully removed. The cells were then exposed to a 100 mg/mL sample (for screening purposes) and a series of dilutions (100, 50, 25, 12.5, 6.25, 3.125 mg/mL for IC₅₀ purposes) of compound **1** and further incubated for 72 hours. All the samples were prepared by diluting them in DMSO and then in a culture medium. In this experiment, doxorubicin was used as a positive control with various concentrations corresponding to the sample's concentration. Following this incubation, MTT reagent (Sigma-Aldrich, Germany) (5 mg/mL) was introduced into each well and kept in the same incubation conditions (5% CO₂ and 37° C) for 4 hours. The mixture of MTT and media was subsequently discarded, and the purple formazan crystals were dissolved in sodium dodecyl sulfate (SDS) and further incubated in a dark environment. The absorbance at a wavelength of 570 nm was measured using Synergy HTX Multi-Mode Reader (Agilent Technologies, USA). All experiments were conducted in triplicate. The 50% inhibitory concentration (IC₅₀) of the samples was determined through statistical analysis. Cell viability was assessed using the following formula:

$$\text{Cell Viability} = (\text{Abs Treated cells} / \text{Abs Untreated cells}) \times 100\%$$

2. 9. Cell Cycle Assay

Cell cycle assay was conducted using a flow cytometer with a cell cycle staining kit from Abbkine (cat No. Cat #: KTA2020) according to the manufacturer's instructions. Briefly, colorectal cancer cells (DLD-1 and Caco-2) were harvested at 70–80% confluency before 5 × 10⁴ cells/mL of DLD-1 cells and 1 × 10⁴ cells/mL of Caco-2 cells were then seeded in a 6-well plate containing DMEM medium (10%

FBS, 1.5% penicillin- streptomycin, 0.5% fungizone) and incubation was set to 5% CO₂ at 37 °C for 24 h. Cells were then treated with half of the compound **1** IC₅₀ (µg/mL) in DLD-1 or Caco-2 cells (15.15 and 118.4 µg/mL, respectively) for 72 h. After that, cells were harvested to obtain pellets and then fixed with 70% ethanol at –20 °C overnight before being stained with PI staining solution. After 30 minutes of incubation at 37 °C in the dark, the cells were washed with PBS and analyzed with a BD Accuri™ C6 Plus Personal Flow Cytometer (BD Biosciences).

2. 10. Apoptosis Assay

Apoptosis assay was performed by Annexin V-FITC/PI staining using flow cytometry. After reaching confluency at 70–80%, a total of 5 × 10⁴ cells/mL of DLD-1 cells and 1 × 10⁴ cells/mL of Caco-2 cells were seeded in each well of a 6-well plate and then treated with half of the compound **1** IC₅₀ (µg/mL) in DLD-1 or Caco-2 cells (15.15 and 118.4 µg/mL, respectively) for 72 h. Cells were then harvested using trypsin-EDTA before being stained with an Annexin-V-FLUOS staining kit (Roche, Zhangjian Hi-Tech Park, Shanghai, China) and incubated for 15 minutes in the dark. The cells were then analyzed with a BD Accuri™ C6 Plus Personal Flow Cytometer (BD Biosciences) within 30 min of staining.

3. Results And Discussion

3. 1. Cytotoxic Activities

The preliminary cytotoxic evaluation of the ethyl acetate fraction of *Aaptos* sp. (SBM 066-1) was evaluated against DLD-1, Caco-2, and HEK293 cell lines. In this study, the IC₅₀ was observed at 20.91 and 21.64 µg/mL for DLD-1 and Caco-2, respectively. Meanwhile, the IC₅₀ value of SBM 066-1 against HEK293 shows less cytotoxic with an IC₅₀ value of 41.97 µg/mL (Figure S2, Table S1).

3. 2. Characterization of Major Compound (1) Contained in SBM 066-1 and its Purification

As a preliminary analysis, the characteristic compounds contained in fraction SBM 066-1 were conducted by using the TLC visualization method. The first visualization using UV light at 254 nm (short wavelength) showed the phosphorescent dark spot at Rf 0 (Figure S3a), cerium (IV) sulfate showed a brown spot in the polar region (Rf 0) and less polar region (Rf 0.7 and 0.8) (Figure S3b), Dragendorff's specific reagent showed an orange spot at Rf 0 (Figure S3c), and ninhydrin visualization analysis showed a purplish stain at Rf 0 (Figure S3d). Summarizing the TLC analysis, major compounds contained in fraction SBM 066-1 were characterized as alkaloid compounds bearing conjugated double-bonds and/ or aromatic rings, possess-

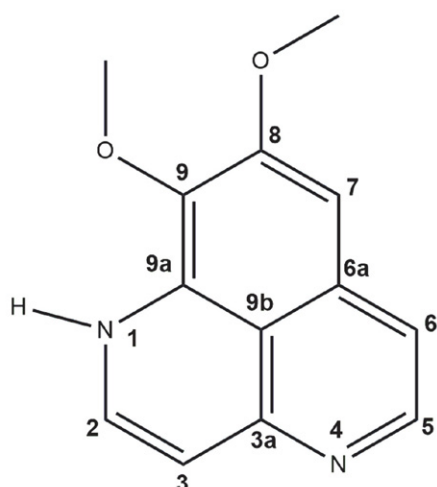


Figure 1 The planar structure of aptamine (1, SBM 066-1-4-1).

ing tertiary, primary, and/ or secondary amine moieties. These analyses elicited that the major compound contained in SBM 066-1 was similar to the characteristics of aptamine.

Further separation of SBM 066-1 on silica open column chromatography (OCC) gave four distinct fractions (SBM 066-1-1 – SBM 066-1-4). All the fractions were then tested against colorectal cancers (DLD-1) using an MTT assay at a final concentration of 100 mg/mL. Among the tested fractions, SBM 066-1-4 showed the highest activity with a % inhibition value of 83.3.

The LCMS/MS chromatogram (Figure S4) of SBM 066-1-4 showed a total of 13 peaks which is described in Table S2. The major peak, Rt 4.62 was selected for further analysis and presumed as the major compounds that are responsible for the anticancer activities in the fraction SBM 066-1-4. The peak at Rt 4.62 min, showed an m/z value at 229.0976 $[M+H]^+$ with chemical formula $C_{13}H_{13}N_2O_3$ (calcd for $C_{13}H_{13}N_2O_3$ 229.0977 ($\Delta - 0.1$ ppm)). This compound was identically 99.20% with aptamine and was supported by its mass-fragmentation patterns (Figure S5). Hence, SBM 066-1-4 was determined to contain aptamine as one of the major compounds.

The 1H -NMR-based metabolite profiling was then performed to identify the proton environments of compound 1 (Figure S6). There are distinct signals for two methoxy protons at δ_H 3.89 (s, 8-OCH₃) and δ_H 4.04 (s,

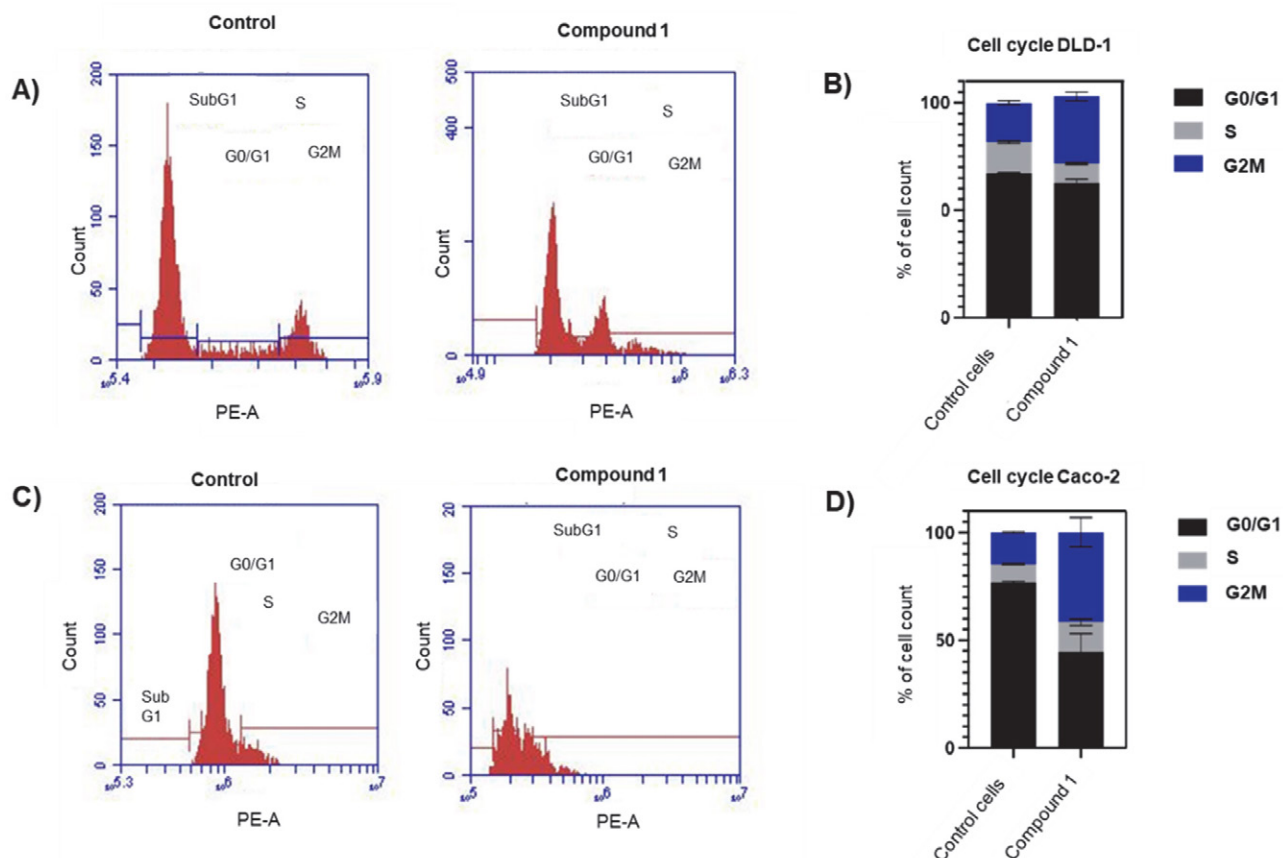


Figure 2. The effect of compound 1 on cell cycle distribution against DLD-1 and Caco-2 colorectal cancer cells (A) The DLD-1 cell cycle histogram (B) The cell distribution analysis of DLD-1 cells cycle (C) The Caco-2 cell cycle histogram (D) The cell distribution analysis of Caco-2 cell cycle. Both cell lines were treated with a 10 μ g/mL concentration of compound 1 for 72h and stained with PI to analyze cell distribution by flow cytometry. Vertical bars represent the standard deviation of means (SD) (n = 3).

9-OCH₃), two pairs of coupled protons at δ_{H} 7.78 (d, $J=7.5$ Hz, H-2), δ_{H} 6.35 (d, $J=7.5$ Hz, H-3), and δ_{H} 7.59 (d, $J=7.5$ Hz, H-5) and δ_{H} 6.88 (d, $J=7.5$ Hz, H-6). In addition, a single proton signal at δ_{H} 8.19 indicated a proton signal of H-7 (Table S3). These signals supported the chemical shifts for aaptamine.

3. 3. Further Isolation of aaptamine (1)

The major compounds in SBM 066-1-4 were further purified using Sep-pak C₁₈ to give a single compound aaptamine (1, SBM 066-1-4-1, 27.63 mg, Figure 1).

3. 4. Compound 1 Induces Cell Cycle Arrest on Colorectal Cancer Cells

The examination of several stages of the cell cycle is essential to get valuable knowledge about the mechanisms that govern cellular growth and division. To investigate cell cycle arrest, the treated colorectal cancer cells were analyzed by flow cytometry at the different cell cycle phases (G0/G1, S, and G2/M) on DLD-1 and Caco-2 cells. On the DLD-1 colorectal cancer cells, compound 1 treatment increased cell accumulation mainly in the G2/M phase

(Figure 2A and 2B), from 18.42% (control cells) to 31.28% (compound 1).

Meanwhile, on the Caco-2, the compound 1 administrations have increased in the S phase from 8.66% in the control cells to 13.81%. Moreover, compound 1 also increases the cell accumulation in the G2/M phase from 14.82% (control cells) to 41.80% (compound 1) (Figure 2C and 2D). Overall, the exposure of compound 1 on Caco-2 colorectal cancer cells induced cell cycle arrest because of the accumulation in the S phase and G2/M phase that influences the synthesis DNA process and inhibits the mitosis process in colorectal cells.

Overall, based on the cell cycle study, the G1 phase (%) was deficient, meanwhile, the G2/M phase (%) was increased in colorectal cancer cells (DLD-1 and Caco-2) (Figure 2B and 2D). Thus, the exposure of compound 1 on colorectal cancer cells DLD-1 and Caco-2 could relatively induce cell cycle arrest. These results also suggest that compound 1 inhibits the cell cycle of DLD-1 colorectal cancer cells through different mechanisms than Caco-2 colorectal cancer cells, specifically interfering with the preparatory phase of mitosis. Some anticancer drugs cause cell death by interfering with the cell cycle processes, including inhibiting the phase of mitosis.²² As a result, a mi-

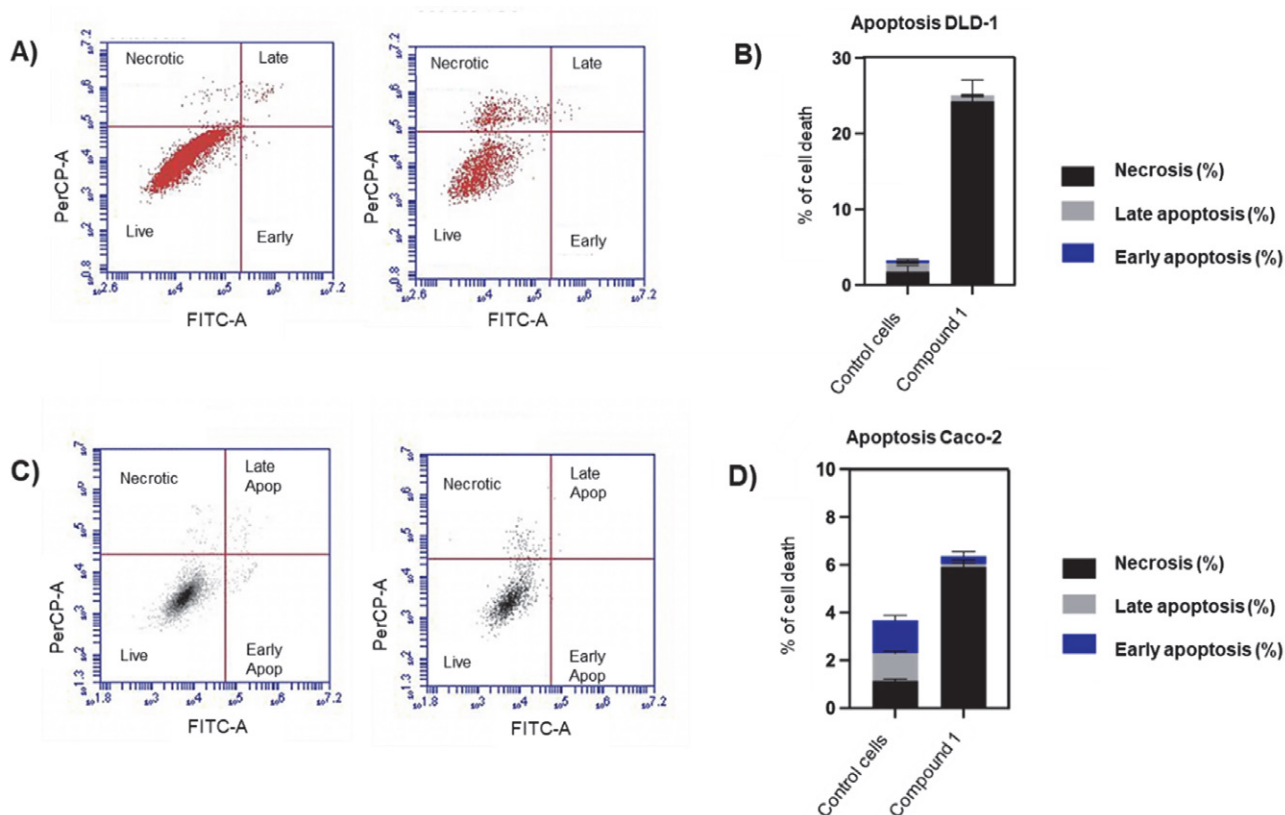


Figure 3. The effects of compound 1 treatment on apoptosis in DLD-1 and Caco-2 colorectal cancer cells (A) The DLD-1 cells death histogram (B) The cell distribution analysis of DLD-1 cell death (C) The Caco-2 cells death histogram (D) The cell distribution analysis of Caco-2 cell death. Both cell lines were treated with 10 $\mu\text{g}/\text{mL}$ of compound 1, stained with Annexin V, PI, and performed flow cytometry analysis. Vertical bars represent the standard deviation of means (SD) ($n = 3$).

otic catastrophe might happen, an oncosuppressive mechanism causing DNA damage and deformation of the microtubules associated with G2/M phase arrest. The characteristics or features of mitotic catastrophe are similar to necrosis where the cell size amplifies, and the DNA degrades in the first 24 h.²³

3. 5. Cells Apoptosis Induction

An investigation into apoptosis, the regulated process of cell death, is crucial for the development of anticancer drugs that can specifically induce apoptosis in cancer cells, ultimately resulting in enhanced patient outcomes. Annexin V-FITC/PI double staining was conducted to confirm whether the effects of compound 1 on the cytotoxicity of DLD-1 and Caco-2 colorectal cancer cells were related to apoptosis or necrotic cell death. In both cells, the treatments of compound 1 at 10 $\mu\text{g}/\text{mL}$ for 72 h show that the apoptotic cell population decreased, compared with

the untreated cell population (Figure 3). In contrast, the necrotic cells demonstrated an increasing population from 1.75% and 1.13% (untreated cells) to 24.25% and 5.91% (compound 1) in DLD-1 and Caco-2 cells, respectively. This result concludes that the compound could induce necrotic instead of apoptotic cell death in DLD-1 and Caco-2 colorectal cancer cells.

3. 6. The activity of Compound 1 against CRCs

To understand how compound 1 affects cell viability, this experiment assessed the cytotoxic activity by measuring cellular metabolic activity with MTT by converting a yellow dye into a purple formazan product. After treatment for 72 hours, a strong reduction was observed in doxorubicin-treated cells with 0% in DLD-1 and HEK293 and a 20% decline in Caco-2 cells (Figure 4A). A significant decrease in the number of viable cells was observed in

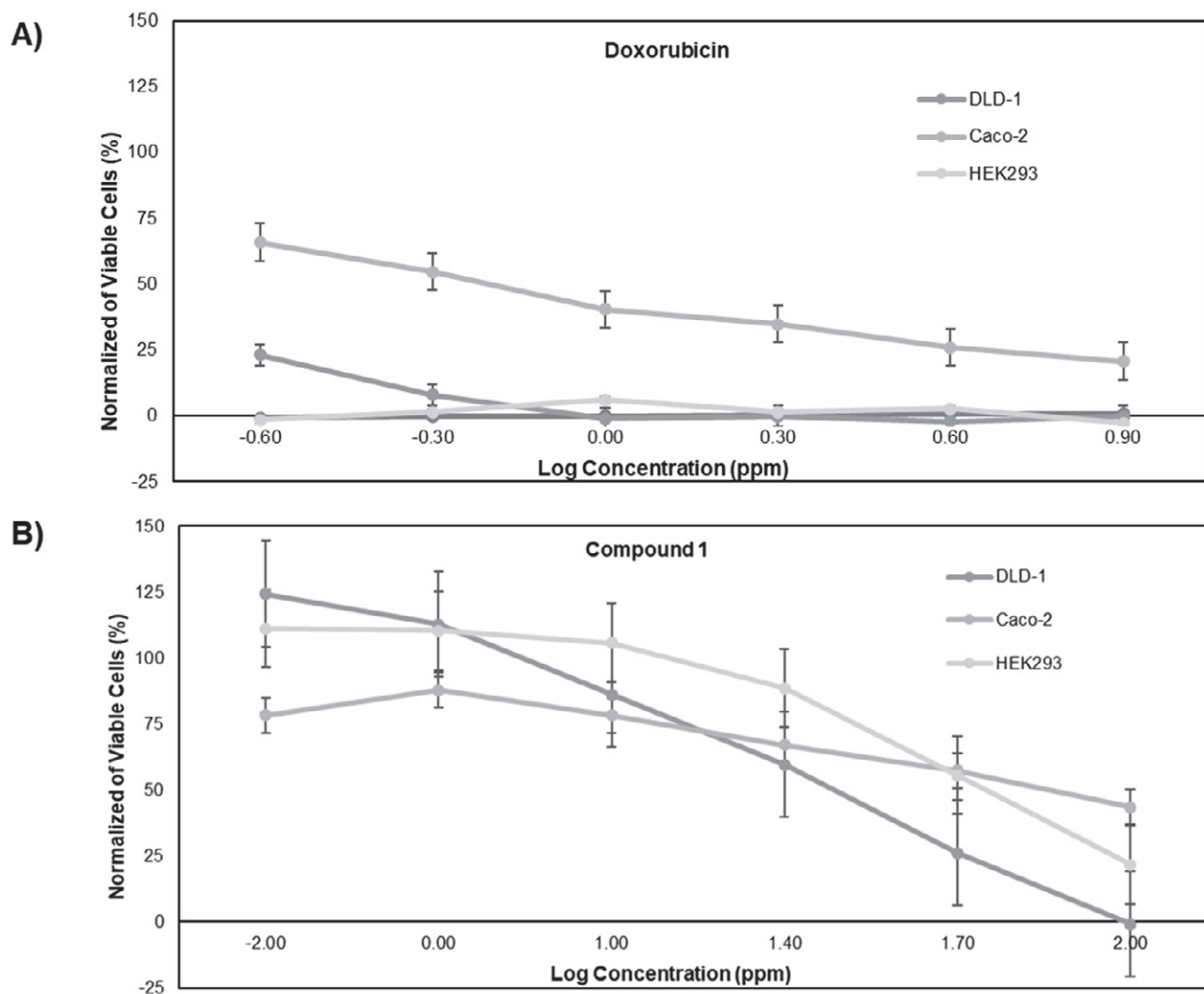


Figure 4. The viability of doxorubicin and compound 1 on DLD-1, Caco-2, and HEK293 cells. (A) The viability of doxorubicin-treated cells (B) The viability of compound 1-treated cells. Both were measured by using an MTT assay.

Table 1. The IC₅₀ values of compound **1** against several cell lines.

No	Cell lines	Compound	IC ₅₀ (µg/mL)	Selectivity Indeks (SI)
1.	DLD-1	Aptamine (1)	30.3	4.03630363
		Doxorubicin	0.1	0.055
2.	Caco-2	Aptamine (1)	236.8	0.51646959
		Doxorubicin	1.6641	0.00330509
3.	HEK293	Aptamine (1)	122.3	–
		Doxorubicin	0.0055	–

DLD-1, Caco-2, and HEK293 cell lines, reaching 0%, 43%, and 21%, respectively (Figure 4B). Thus, the effect of compound **1** on DLD-1, Caco-2, and HEK293 cell viability after 72 hours is dose-dependent, with higher concentrations leading to greater reductions in cell viability. These data also demonstrated that compound **1** is toxic to DLD-1 cells with an inhibitory concentration (IC₅₀) of 30.3 µg/mL, 236.8 µg/mL, and 122.3 µg/mL on DLD-1, Caco-2, and HEK293 cells, respectively (Table 1). However, in comparison to doxorubicin as a control, the IC₅₀ value of doxorubicin was higher than compound **1**. The IC₅₀ values of doxorubicin were 0.1 µg/mL, 1.6641 µg/mL, and 0.0055 µg/mL on DLD-1, Caco-2, and HEK293 cells, respectively (Table 1). Moreover, compound **1** exhibited dose-dependent cytotoxicity across both CRCs with particularly strong effects in DLD-1 cells with a selectivity index (SI) of 4.03, noticeably higher than Caco-2 cells with a selectivity index of 0.51. The SI results suggested that compound **1** preferentially targeted DLD-1 cells over Caco-2 cells, with an SI greater than doxorubicin (SI > 3). Taken together, these data indicated that the cytotoxic effect of compound **1** was both cell-type and dose-dependent.

4. Conclusions

Aptamine, a marine alkaloid derived from the sponge *Aaptos* sp. has shown promising anticancer properties in various studies. This study demonstrated that the extract of *Aaptos* sp. (SBM 066-1) is the potential source of anticancer against CRCs (DLD-1 and Caco-2), and considerably less cytotoxic against normal cells HEK293. Further isolation and purification of the bioactive compound from the EtOAc extract of this sponge (SBM 066-1) led to the discovery of aptamine (compound **1**). The LCMS/MS analysis and ¹H-NMR data showed a characteristic signal for a specific characteristic of **1** at *m/z* 229.0976 and aromatic rings at δ_H 7.78 (d, *J* = 7.5 Hz, H-2), δ_H 6.35 (d, *J* = 7.5 Hz, H-3), and at δ_H 7.59 (d, *J* = 7.5 Hz, H-5) as well as at δ_H 6.88 (d, *J* = 7.5 Hz, H-6) ppm. Then, the study reveals that compound **1** exhibits cytotoxicity against DLD-1 and Caco-2 cells with IC₅₀ values of 30.3 and 236.8 µg/mL. Compound **1** shows potential as a cytotoxic agent against CRCs. Meanwhile, previous research²⁴ was mainly concentrated on an aptamine-rich fraction, which exhibited a higher cytotoxic effect on DLD-

1 colorectal cancer cell viability (IC₅₀ value 9.597 µg/mL) compared with NIH-3T3 murine fibroblast cells (IC₅₀ value 12.23 µg/mL). Both papers revealed that aptamine could be promoted as a potent anticancer agent, and its ability to target DLD-1 cells selectively makes it a promising candidate for further research and potential development for colorectal cancer treatment. Notwithstanding, this current research discovered that aptamine could relatively induce necrotic cell death and promote cell cycle arrest in both DLD-1 and Caco-2 cells. This study revealed that compound **1** could relatively induce necrotic cell death and promote cell cycle arrest. Aptamine was found to interfere with the cell cycle of CRCs. Specifically, it causes arrest at the G2/M phase, preventing the cells from proceeding to mitosis, and thereby inhibiting their proliferation. Unlike apoptosis, which is a programmed and controlled form of cell death, aptamine induces necrosis in CRCs, which causes traumatic cell death, leading to the release of cellular contents and triggering inflammation in the tumor microenvironment. The study suggests that aptamine's cytotoxic and necrotic effects are mediated through oxidative stress, mitochondrial dysfunction, and the activation of specific signaling pathways related to cell cycle control and cell death. Overall, aptamine demonstrated selective toxicity toward DLD-1 cells, with an SI greater than 3. This selectivity is particularly notable due to its ability to induce necrotic cell death and arrest the cell cycle, making it a promising candidate for targeted therapies in CRCs. Further research is required to fully understand its molecular mechanisms and to evaluate its efficacy in vivo.

Acknowledgments

This research was partially supported by Research Assistance Program – Manajemen Talenta - BRIN, PEE (Pendanaan Ekspedisi dan Eksplorasi [Grant Code pee-2229172647]), Prioritas Riset Nasional (PRN) also known as RIIM (Riset dan Inovasi untuk Indonesia Maju) [Grant code prn-012917423], and RPVO (Pendanaan Rumah Program Vaksin dan Obat, Organisasi Riset Kesehatan BRIN) [Grant code RPVO-124.01.KB.6859.SDB.001].

Conflicts of interest

The authors report no conflicts of interest.

5. References

- J. Ferlay, I. Soerjomataram, R. Dikshit, S. Eser, C. Mathers, M. Rebelo, D.M. Parkin, D. Forman, F. Bray, *Int J Cancer*. **2015**, *136*, E359–E386. DOI:10.1002/ijc.29210
- Y. Xi, P. Xu, *Transl Oncol*. **2021**, *14*, 1–7. DOI:10.1016/j.tranon.2021.101174
- GLOBOCAN, Number of new cases in 2020. Global Cancer Observatory (GCO), <https://gco.iarc.fr/today/data/factsheets/populations/360-indonesia-fact-sheets.pdf> (assessed: January 24, 2024).
- N.N. Keum, E. Giovannucci, *Nat Rev Gastroenterol Hepatol*. **2019**, *16*, 713–732. DOI:10.1038/s41575-019-0189-8
- A. Bandiwadekar, J. Jose, M. Khayatkashani, S. Habtemariam, H.R. Khayat Kashani, S.M. Nabavi, *Journal of Molecular Neuroscience*. **2022**, *72*, 653–676. DOI:10.1007/s12031-021-01922-7
- A.R. Carroll, B.R. Copp, R.A. Davis, R.A. Keyzers, M.R. Prinssep, *Nat Prod Rep*. **2019**, *36*, 122–173. DOI:10.1039/C8NP00092A
- M.F. Mehub, J. Lei, C. Franco, W. Zhang, *Mar Drugs*. **2014**, *12*, 4539–4577. DOI:10.3390/md12084539
- J. Cortes, J. O'Shaughnessy, D. Loesch, J. L. Blum, L. T. Vahdat, K. Petrakova, P.Chollet, Twelves, C. *The Lancet*. **2011**, *377*, 914–923. DOI:10.1016/S0140-6736(11)60070-6
- M. Arai, C. Han, Y. Yamano, A. Setiawan, M. Kobayashi, *J Nat Med*. **2014**, *68*, 372–376. DOI:10.1007/s11418-013-0811-y
- L. Calcul, A. Longeon, A. Al Mourabit, M. Guyot, M.L. Bourguet-Kondracki, *Tetrahedron*. **2003**, *59*, 6539–6544. DOI:10.1016/S0040-4020(03)01069-X
- G. Rajivgandhi, S.N. kumar, G. Ramachandran, N. Manoharan, *Biocatal Agric Biotechnol*. **2019**, *17*, 628–637. DOI:10.1016/j.bcab.2019.01.007
- N.K. Utkina, N.N. Ome, *Chem Nat Compd*. **2009**, *45*, 712–715. DOI:10.1007/s10600-009-9424-9
- H. Luyao, H. Luesch, M. Uy, *Molecules*. **2021**, *26*, 1–13. DOI:10.3390/molecules26185618
- Y. Ohizumi, A. Kajiwara, H. Nakamura, J. Kobayashi, *Journal of Pharmacy and Pharmacology*. **1984**, *36*, 785–786. DOI:10.1111/j.2042-7158.1984.tb04876.x
- K.H. Jang, S.C. Chung, J. Shin, S.H. Lee, T.I. Kim, H.S. Lee, K.B. Oh, *Bioorg Med Chem Lett*. **2007**, *17*, 5366–5369. DOI:10.1016/j.bmcl.2007.08.007
- H.R. Putri, R. Kristiana, I.W. Mudianta, E. Setiawan, A. Widawaruyanti, N. Nuengchamnon, N. Suphrom, S. Suciati, *J Pharm Pharmacogn Res*. **2023**, *11*, 129–136. DOI:10.56499/jppres22.1511_11.1.129
- H.B. Yu, F. Yang, F. Sun, J. Li, W.H. Jiao, J.H. Gan, W.Z. Hu, H.W. Lin, *Mar Drugs*. **2014**, *12*, 6003–6013. DOI:10.3390/md12126003
- T. Hamada, Y. Matsumoto, C.S. Phan, T. Kamada, S. Onitsuka, H. Okamura, T. Iwagawa, N. Arima, F. Tani, C.S. Vairappan, *Nat Prod Commun*. **2019**, *14*, 1–3. DOI:10.1177/1934578X19863935
- N. Utkina, G. Likhatskaya, O. Malyarenko, S. Ermakova, L. Balabanova, L. Slepchenko, I. Bakunina, *Biomedicines*. **2021**, *9*, 1–17. DOI:10.3390/biomedicines9050510
- D.T. Trang, B.H. Tai, D.T. Hang, P.H. Yen, P. Thi, T. Huong, N.X. Nhiem, P. Van Kiem, *Nat Prod Res*. **2021**, *16*, 1–5. DOI:10.1080/14786419.2021.1917572
- P. Ahmadi, M. Higashi, N.J. De Voogd, J. Tanaka, *Mar Drugs*. **2017**, *15*, 1–8. DOI:10.3390/md15080249
- C.X. Deng, *Nucleic Acids Res*. **2006**, *34*, 1416–1426. DOI:10.1093/nar/gkl010
- M. Kimura, T. Yoshioka, M. Saio, Y. Banno, H. Nagaoka, Y. Okano, *Cell Death Dis*. **2013**, *4*, 1–10. DOI:10.1038/cddis.2013.108
- M. Hardhiyuna, U.Y. Arbi, Z. Zuraida, P. Ahmadi, *Asian Pacific Journal of Cancer Prevention*. **2024**, *25*(5), 1737–1743. DOI:10.31557/APJCP.2024.25.5.1737

Povzetek

Spužva je eden od potencialnih virov bioaktivnih spojin. Med njimi je spužva *Aaptos* obetaven vir spojin vodnic, vključno z aaptaminom (**1**). V tej študiji je bil spektroskopsko določen aaptamin (**1**) iz spužve *Aaptos* sp., nabrane v narodnem parku Bunaken v Indoneziji, in proučevan kot protirakavo sredstvo, usmerjeno predvsem proti raku debelega črevesa in danke. Spojina **1** je pokazala močno citotoksičnost proti DLD-1 in Caco-2 z vrednostmi IC₅₀ 30,3 oziroma 236,8 µg/ml. Poleg tega lahko dodatek spojine **1** celicam kolorektalnega raka povzroči zastoj celičnega cikla in nekrotično celično smrt.



Except when otherwise noted, articles in this journal are published under the terms and conditions of the Creative Commons Attribution 4.0 International License

Scientific paper

Inhibition of Biliverdin Reductase Diminished the Protective Activity of Bilirubin and Biliverdin Against Oxidative Stress-Induced Injury in Human Vascular Endothelium

Kuldeepak Sharma¹, Irena Zajc¹, Alen Albreht² and Lovro Žiberna^{1,3}¹ Institute of Pharmacology and Experimental Toxicology, Faculty of Medicine, University of Ljubljana, Ljubljana, Slovenia² Laboratory for Food Chemistry, Department of Analytical Chemistry, National Institute of Chemistry, Ljubljana, Slovenia³ Department of Biopharmacy and Pharmacokinetics, Faculty of Pharmacy, University of Ljubljana, Ljubljana, Slovenia

* Corresponding author: E-mail: lovro.ziberna@ffa.uni-lj.si

Received: 08-30-2024

Abstract

Endothelial dysfunction is an important risk factor for the development of cardiovascular diseases, and its condition is further aggravated by oxidative stress. Biliverdin (BV) and bilirubin (BR) are potent antioxidants that protect endothelial cells, with biliverdin reductase (BVR) converting BV to BR to maintain redox balance. This study explored BVR's role in mediating these protective effects under normoxic and hypoxia-reoxygenation conditions. Pharmacological inhibition of BVR reduced the protective effects of BV and BR, as evidenced by the decreased cell viability, cellular antioxidant activity, and intracellular bilirubin levels. Activation of ERK1/2 reduced BVR's protective function, while its inhibition enhanced it. Additionally, disruption of the BVR-ERK interaction further modulated these effects, highlighting BVR-ERK1/2 interaction sites as potential therapeutic targets for oxidative stress-induced endothelial dysfunction.

Keywords: Antioxidant, bilirubin, biliverdin, biliverdin reductase, human endothelium, oxidative stress

1. Introduction

Endothelial dysfunction, characterized by impaired vasodilation, increased oxidative stress, and inflammation, is a critical factor in the development of cardiovascular disorders. These conditions lead to pathologies such as atherosclerosis, hypertension, and myocardial infarction.¹ Importantly, hypoxia-reoxygenation (H/R) injury significantly contributes to endothelial dysfunction, particularly in ischemic heart disease and stroke.² During ischemia, reduced oxygen supply leads to the accumulation of metabolic byproducts and reactive oxygen species (ROS) after reperfusion, which are central to the pathophysiology of endothelial dysfunction.¹ These highly reactive molecules cause oxidative damage to lipids, proteins, and DNA, leading to endothelial damage and thereby exacerbating cardio-vascular disease. The key pathophysiological mechanism involves nitric oxide (NO) inactivation due to the superoxide anion reaction with NO to form peroxynitrite (ONOO⁻), which reduces NO availability, impairs vasodi-

lation, and increases vascular tone.³ Additionally, oxidative stress activates the NF- κ B pathway, promoting pro-inflammatory cytokines, adhesion molecules, and chemokines, leading to leukocyte adhesion and vascular inflammation. Excessive ROS can also induce endothelial cell apoptosis and senescence, thus reducing the regenerative capacity and compromising vascular integrity. In addition, ROS-mediated lipid peroxidation damages endothelial cell membranes and lipoproteins, thereby contributing to advanced atherogenesis¹. Consequently, mechanisms that mitigate ROS-induced damage are of significant interest for vascular health.⁴

In this regard, endogenous bile pigments such as biliverdin (BV) and bilirubin (BR) have gained attention because of their inherent antioxidant properties.^{5,6} Several studies have demonstrated an inverse correlation between bilirubin levels and the incidence of cardiovascular diseases, suggesting that higher bilirubin levels are associated with a reduced risk of conditions such as atherosclerosis

and coronary artery disease.⁷ The metabolic pathway involving the conversion of heme to biliverdin and subsequently to bilirubin is facilitated by the enzymes heme oxygenase-1 (HO-1) and biliverdin reductase (BVR), respectively.⁸ The addition of both BV and BR to endothelial cells can effectively neutralize ROS, thereby protecting the human endothelium from oxidative damage.⁹ Bilirubin, a potent antioxidant, reacts with ROS and is oxidized to biliverdin.¹⁰ BVR converts biliverdin back into bilirubin, thereby establishing an important cyclic antioxidant system.^{11,12}

Recent research has elucidated the multifaceted role of BVR, highlighting its function not only as an antioxidant enzyme, but also as a dual-specificity kinase (Ser/Thr/Tyr) that regulates the transcription of inflammatory mediators.^{13,14} Furthermore, there is a significant interplay between BVR and the extracellular signal-regulated kinase (ERK) pathway. BVR contains specific motifs known as C-box (cysteine-rich domain) and D-box (docking domain), through which it binds to ERK. In this way, BVR acts as a scaffold for ERK1/2 and modulates its cellular localization and activity within the cell.¹⁵ This influences various cellular processes, including cell survival, proliferation, and inflammation.^{16,17} The interaction of BVR with ERK1/2 involves phosphorylation of BVR, which subsequently facilitates the phosphorylation and activation of ERK1/2. Once activated, ERK1/2 translocates to the nucleus, where it modulates the activity of transcription factors such as NF- κ B and AP1, and thus influences the expression of genes involved in cell proliferation, differentiation, apoptosis, and cell survival.¹⁰ Additionally, BVR influences glucose metabolism and insulin signaling, contributing to metabolic homeostasis.¹⁸

Importantly, the knockout of BVR in human aortic endothelial cells leads to increased oxidative stress and endothelial-to-mesenchymal transition, which is characterized by the loss of endothelial markers.¹⁹ Similarly, another study indicated that silencing BVR in human endothelial cells results in increased levels of reactive oxygen and nitrogen species (RONS), and bilirubin, but not biliverdin, increases the expression of the protective protein GTP cyclohydrolase in cells.²⁰ This indicates that BVR and bilirubin have both direct and indirect antioxidant properties that are important for the protection of endothelial cells.²⁰ Interestingly, direct intrathecal application of BVR ameliorated the clinical and pathological signs of experimental autoimmune encephalomyelitis more efficiently than traditional antioxidant enzymes, further suggesting a crucial protective role for BVR against cellular oxidative stress.²¹

In this study, we aim to demonstrate that pharmacological inhibition of BVR can directly limit the conversion of biliverdin to bilirubin, leading to decreased bilirubin levels and consequently diminishing its antioxidant protective capacity. Reduced bilirubin levels make endothelial cells more vulnerable to oxidative damage. Our primary

goal is to delineate the impact of BVR on the protective activity of biliverdin (BV) and bilirubin (BR) on endothelial function under conditions of increased oxidative stress, both in normoxia and following hypoxia-reoxygenation injury. In addition, our study explored the complex role of BVR beyond its classical enzymatic functions. Recent evidence suggests that BVR may also act as a modulator of the ERK pathway, which is crucial for cellular response to oxidative stress. To specifically explore this modulation, we aim to inhibit the interaction between BVR and ERK by employing antagonists targeting the C-box and D-box binding sites. This approach aims to disrupt BVR's non-classical signaling functions, providing new insights into the dual contributions of its enzymatic activity and signaling pathways under oxidative stress conditions. Including normoxia with induced oxidative stress and hypoxia-reoxygenation (H-R) conditions allowed us to evaluate BVR's function under challenging stress conditions and its critical role during recovery. Under basal conditions, the BVR cycle of converting bilirubin back to biliverdin shows minimal changes upon inhibition, as the demand for antioxidant recovery is low. However, under conditions simulating cardiovascular pathologies where oxidative stress is elevated, efficient recovery of bilirubin through BVR is essential. This study aims to elucidate the role of BVR under these specific conditions.

2. Materials And Methods

2.1. Chemicals

Bilirubin, biliverdin, apomorphine, chlorpromazine, U-46619, PD-98059, CaCl₂, 2',7'-dichlorodihydrofluorescein diacetate (DCFH-DA), methanol (all Sigma Aldrich, Germany); fetal bovine serum (FBS), Dulbecco's Modified Eagle Medium (DMEM), Hanks' balanced salt solution (HBSS), HEPES Buffered Saline Solution (BSS), L-glutamine, penicillin-streptomycin solution, and dimethyl sulfoxide (DMSO) (all Merck, Germany); peptide FGF-PAFSG, peptide KKRILHCLGLA (both purchased from Biocat GmbH, Heidelberg, Germany).

2.2. Human Endothelial Cell Culture EA.hy926

All experiments were conducted using the human endothelial cell line EA.hy926. Cells were cultured in DMEM supplemented with 10% heatinactivated fetal bovine serum (FBS), 1 mM L-glutamine, and 1 mM penicillin-streptomycin solution. Cells were maintained at 37 °C in a humidified incubator with 95% air and 5% CO₂. The culture medium was changed every 2-3 days, and the cells were trypsinized using a 0.25% trypsin-EDTA solution for subculturing when confluence reached approximately 70–80%. The cells were then seeded in 96-well plates at a seeding concentration of 1×10^4 cells/well.

2. 3. Experimental Design

In Figure 1, we present a general overview of our experimental design, consisting of four experimental phases, namely i. normoxia (24 h) or hypoxia (15 h) – reoxygenation (9 h); ii. pharmacological protocols that influence BVR activity (incubation with inhibitors, antagonists, and activators); iii. condition of increased oxidative stress (1h incubation with peroxy-radical initiator); iv. functional cell assays (cell viability, cellular antioxidant assays, cell lysis for HPLC-MS measurements). In general, we aimed to perform three independent biological experiments for each experimental group and cell assay, each consisting of six technical replicates.

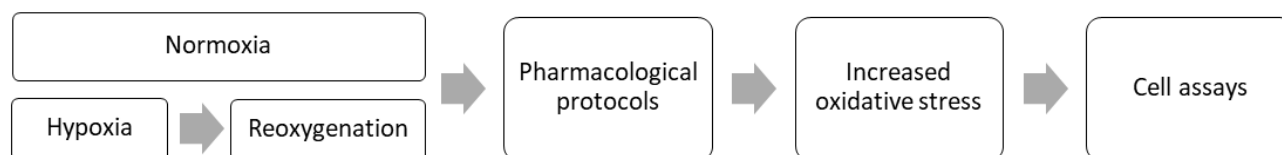


Figure 1. Schematic overview of experimental workflow. In the first phase, cells were introduced to either normoxia or the hypoxia-reoxygenation protocol for 24h, followed by various pharmacological treatments for 1-2h. All the cells were exposed to increased oxidative stress conditions with peroxy radical initiation. Finally, various cell assays (cell viability, cellular antioxidant assay, and cell lysis for HPLC-MS analysis) were performed.

2. 4. Phase 1. Normoxia and Hypoxia-Reoxygenation

To simulate hypoxia-reoxygenation (H/R) injury, endothelial cells were incubated in a hypoxic chamber with 1% O₂ and 5% CO₂ at 37 °C for 15 h. This was followed by reoxygenation under normoxic conditions (95% air and 5% CO₂) at 37 °C for 9 h, to mimic the pathological conditions of hypoxia-reoxygenation. In parallel, endothelial cells were incubated under normoxic conditions (95% air and 5% CO₂) for 24 h.

2. 5. Phase 2. Pharmacological Protocols Influencing BVR Activity

Inhibition of the Biliverdin Reductase (BVR)

To inhibit BVR, endothelial cells were incubated with 10 μM apomorphine (AP) for 1 h, followed by addition of bilirubin or biliverdin (10 nM and 100 nM) for 30 min. To exclude the role of dopamine receptor involvement in our observed phenomena with apomorphine (apomorphine is also a dopamine agonist), we performed another experimental series with pre-incubation with 10 μM chlorpromazine (CPZ), a non-selective dopamine receptor antagonist that blocks subtypes D₁, D₂, D₃, and D₄ receptors), for 60 min, followed by apomorphine addition at 10 μM for 60 min, followed by the addition of bilirubin and biliverdin (10 nM and 100 nM) for 30 min.

Activation and inhibition of extracellular signal-regulated kinases (ERKs)

To activate ERK1/2, endothelial cells were incubated for 30 min with U-46619 at 1 μM. The cells were then incubated with bilirubin (100 nM) for 30 min. To further

investigate the involvement of ERK1/2 in the protective activity of bilirubin, we inhibited ERK1/2 activity in endothelial cells with previously activated ERK1/2 enzymes (using U-46619) by incubating for 30 min with PD98059 at 20 μM, followed by incubation with bilirubin (100 nM) for 30 min.

Inhibition of BVR – ERK interaction using C-BOX and D-BOX inhibitors

The peptides FGFPAFSG (C-Box inhibitor) and KKRIHCLGLLENGTH (D-Box inhibitor) were introduced into endothelial cells using a calcium phosphate

transient transfection protocol. FGFPAFSG and KKRIHCLGLA peptides (15 μL at 250 mg/mL dissolved in PBS) were suspended in 50 μL of 2.5 M CaCl₂ buffer. Each peptide solution was prepared separately. Then, 500 μL of 2x HEPES Buffered Saline Solution (BSS) was placed in a 15 mL conical tube. The C-box inhibitor/CaCl₂ solution and D-box inhibitor/CaCl₂ were added dropwise to this tube while stirring. The precipitate was allowed to form at room temperature for 20 min and then spread evenly over the cells along with their medium. The cells were gently shaken to ensure even distribution and incubated at 37 °C with 95% air and 5% CO₂ atmosphere for 16 h. The medium was then removed, the cells were washed twice with PBS, and fresh complete medium was added. Subsequently, the cells were incubated with bilirubin and biliverdin at concentrations of 10 and 100 nM for 30 min.

Incubation with bilirubin and biliverdin

All pharmacological pretreatments ended with incubation with either bilirubin or biliverdin (10 nM and 100 nM) for 30 min. Bilirubin and biliverdin were prepared freshly just prior to the experiment in the dark conditions in the 5 mM DMSO stock solution, which was further diluted into the non-complete DMEM solution for the cell experiments.

2. 6. Phase 3. Increased Oxidative Stress

To simulate increased oxidative stress conditions, endothelial cells in all experimental groups were exposed to the peroxy-radical initiator 2,2'-azobis(2-methylpropionamide) dihydrochloride (ABAP) at 15 μM for 1 h before functional cell assays. ABAP was freshly prepared just

prior to experimental treatment. Endothelial cells in the control group were not exposed to oxidative stress, but continued incubation under normoxic conditions at 37 °C with 95% air and 5% CO₂ atmosphere for 1 h.

2. 7. Phase 4. Functional cell Assays

Cell viability assays

Cell viability was assessed using resazurin (Alamar Blue® reagent; Thermo Fisher, USA) at 37 °C for 3 h. The incubation time was optimized to maximize the signal-to-noise ratio without reaching saturation in preliminary experiments on Ea.hy926 cells. The fluorescence signal was recorded using a fluorescence reader (BioTek Synergy H1 multimode plate reader, Agilent, USA) in the filter detection mode with excitation at 530–570 nm and emission at 580–620 nm. Briefly, resazurin is a blue, non-fluorescent dye that serves as a redox indicator. In viable cells, metabolically active enzymes reduce resazurin to resorufin, a pink highly fluorescent compound. The conversion was directly proportional to the number of viable cells, allowing quantification of cell viability. Cell viability was calculated by comparing the fluorescence intensity of the treated samples with that of the untreated controls (100% viability). The following equation was used:

$$\text{Cell viability}(\%) = \left(\frac{\text{Fluorescence of treated samples}}{\text{Fluorescence of control samples}} \right) \times 100 \quad (1)$$

Equation 1. Cell viability assessment using resazurin reduction assay with fluorescence readings.

Cellular antioxidant assays

To assess the antioxidant capacity of endothelial cells EA.hy926, we performed a cellular antioxidant assay using the fluorescent probe 2',7'-dichlorofluorescein diacetate (DCFH-DA) and the peroxy radical-generating reagent 2,2'-azobis(2-methylpropionamide) dihydrochloride (ABAP), as previously described⁹. Endothelial cells were washed twice with PBS, and then incubated for 30 min with non-complete albumin-free DMEM, supplemented with 1 mM L-glutamine and 50 μM DCFH-DA. This step allows DCFH-DA to permeate cells and be hydrolyzed to non-fluorescent DCFH, which is then oxidized to fluorescent DCF in the presence of reactive oxygen species (ROS). After incubation, the DCFH-DA solution was removed, and cells were washed twice with PBS to eliminate excess probe. The cells were then treated with the peroxy radical-generating reagent ABAP at a concentration of 5 mM in 100 μL Hank's buffered saline solution (HBSS). The blank wells were filled with HBSS solution without ABAP, serving as a baseline control for the assay. Fluorescence emission was measured every 5 minutes for one hour at 538 nm with excitation at 485 nm using a fluorescence reader (BioTek Synergy H1 multimode plate reader, Agi-

lent, USA). The cellular antioxidant activity (CAA) was calculated as a percentage of the control value using the following equation:

$$\text{CAA units}(\%) = 100 - \left[\left(\frac{\int SA dt}{\int CA dt} \right) \times 100 \right] \quad (2)$$

Equation 2. Calculation of cellular antioxidant activity (CAA) of endothelial cells in the experimental group. Where $\int SA dt$ represents the integrated area under the fluorescence readings of the sample with the blank subtracted, measured over time, while $\int CA dt$ stands for the integrated area under the control fluorescence curve (with blank subtracted) over time.

This approach allows the quantification of antioxidant activity within cells by comparing the fluorescence intensity of treated samples against untreated controls. A higher percentage (expressed as CAA units in %) indicates a greater antioxidant capacity, reflecting the improved ability of cells to neutralize oxidative stress induced by ABAP.

Measurement of intracellular bilirubin and biliverdin levels in endothelial cells using HPLC-MS

For this set of experiments, human endothelial cells (EA.hy926) were cultured in 75 cm² cell culture flasks to provide sufficient material for bilirubin and biliverdin measurements. These larger culture flasks, as opposed to 96-well plates, were necessary to ensure adequate cell quantities for reliable HPLC-MS analysis. Following the completion of pharmacological treatments, as previously described, the cells were washed twice with PBS to remove residual media, dead cells, and other extracellular components. A 1:1 solution of DMSO and methanol was used to lyse cells. This solvent mixture is effective for the extraction of bilirubin and biliverdin, while preserving their stability. The flasks were gently scraped using Nunc™ Cell Scrapers (Thermo Fisher Scientific, USA) to mechanically harvest the adherent endothelial cells. Mechanical scraping was continued until all endothelial cells were completely detached and collected from the flask surface. All cell lysate samples were transferred into Eppendorf vials, which were then covered with aluminium foil to protect the samples from light exposure that could degrade bilirubin and biliverdin. The samples were stored at –80 °C until further analysis.

The intracellular levels of bilirubin and biliverdin were quantified using a validated high-performance liquid chromatography-mass spectrometry (HPLC-MS) method, as described previously^{22,23}. We utilized a reverse-phase ultra-high-performance liquid chromatography (UHPLC) system coupled with a mass spectrometer equipped with an electrospray ionization (ESI) source operating in the positive ion mode. The separation was achieved on a Kinetex C18 EVO column (100 × 2.1 mm i.d., 1.7 μm) with a

guard column, employing a gradient elution with 5 mM ammonium formate at pH 3 as solvent A and a mixture of acetonitrile, water, and ammonium formate as solvent B. The flow rate was set at 0.8 mL/min, and the column temperature was maintained at 35°C. Mass spectrometry detection was performed in selected reaction monitoring (SRM) mode, allowing precise quantification of bilirubin and biliverdin. The transitions monitored were m/z 583.2 \rightarrow 297.2 for biliverdin and m/z 585.2 \rightarrow 299.0 for bilirubin, ensuring high sensitivity and selectivity. This method has linearity over the concentration range of 0.5–100 nM, with limits of detection and quantitation at 0.1 nM and 0.5 nM, respectively²².

To ensure accurate and comparable results across samples, the total cellular protein content in each sample was determined using Bradford assay. Bilirubin and biliverdin concentrations were normalized to the total cellular protein content in each sample. This normalization accounts for any variability in cell number or size, allowing for the expression of bilirubin and biliverdin cellular levels in nanomoles per microgram of total protein (nmol/ μ g).

2. 8. Statistical Analysis

All results are expressed as mean \pm standard error of the mean (SEM). Statistical differences between groups were evaluated using one-way ANOVA followed by Bonferroni's post-hoc test. Differences were considered statistically significant at $p < 0.05$.

3. Results

3. 1. Inhibition of Biliverdin Reductase Diminished the Protective Activity of Bilirubin and Biliverdin After Increased Oxidative Stress

To investigate the role of biliverdin reductase (BVR) in protecting activity of bilirubin and biliverdin on the endothelium against oxidative stress, we conducted experiments using human endothelial cells (EA.hy926) exposed to varying conditions of oxidative stress and treatments with bilirubin, biliverdin, and the BVR inhibitor apomorphine.

3. 1. 1. Impact of BVR inhibition on cell viability of human endothelial cells

Oxidative stress induced by the peroxyl radical-generating reagent ABAP reduced endothelial cell viability, whereas bilirubin significantly increased cell viability. This increase in cell viability was concentration-dependent, with 100 nM bilirubin providing greater protection than 10 nM, as shown in Figure 2A. Apomorphine, used as a BVR inhibitor, did not decrease cell viability *per se* in con-

trol experiments without oxidative stress, indicating that it does not possess inherent cytotoxic effects under normoxic conditions. However, pre-incubation with apomorphine significantly decreased the protective effect of bilirubin, resulting in reduced cell viability compared to the bilirubin-treated groups without apomorphine ($p < 0.05$). This suggests that inhibition of BVR impairs the ability of bilirubin to protect endothelial cells from oxidative damage.

The effects of biliverdin treatment were examined in parallel experiments under normoxic conditions, as shown in Figure 2B. Similar to bilirubin, biliverdin treatment also enhanced cell viability after oxidative stress. The protective effect of biliverdin was concentration-dependent, with 100 nM showing more pronounced protection than 10 nM ($p < 0.05$). Pre-treatment with apomorphine significantly reduced the protective effect of biliverdin, as evidenced by decreased cell viability compared to the biliverdin-treated groups without apomorphine ($p < 0.05$), indicating that BVR inhibition also diminishes the protective capabilities of biliverdin.

To simulate more severe stress conditions, endothelial cells were subjected to hypoxia (15 h), followed by reoxygenation (9 h) before bilirubin treatment, as shown in Figure 2C. The injury induced by the pre-treatment protocol of hypoxia-reoxygenation was significantly greater than that under normoxic conditions, as evidenced by lower baseline cell viability in the oxidative stress-only group (group ABAP). Despite increased oxidative stress, bilirubin at both 10 nM and 100 nM concentrations maintained its protective role, enhancing cell viability compared to untreated controls ($p < 0.05$). Consistent with previous findings, apomorphine pre-treatment significantly reduced the protective effect of bilirubin, leading to decreased cell viability compared to that in the bilirubin-only treated groups ($p < 0.05$). Similar experiments were conducted with biliverdin treatment following hypoxia-reoxygenation injury (Figure 2D). Biliverdin demonstrated protective properties, increasing cell viability at 10 nM and 100 nM in a concentration-dependent manner under severe oxidative stress conditions. Pre-incubation with apomorphine diminished the protective effects of biliverdin, as shown by reduced cell viability in comparison to biliverdin-treated groups without apomorphine ($p < 0.05$).

3. 1. 2. Impact of BVR Inhibition on Cellular Antioxidant Activity (CAA) in Human Endothelial Cells

The effect of biliverdin reductase (BVR) inhibition on cellular antioxidant activity (CAA) in human endothelial cells was systematically examined under normoxic and hypoxia-reoxygenation conditions. These findings are depicted in Figure 3, with panels A and B corresponding to normoxic conditions and panels C and D to hypoxia-reoxygenation conditions. We observed that both bilirubin and

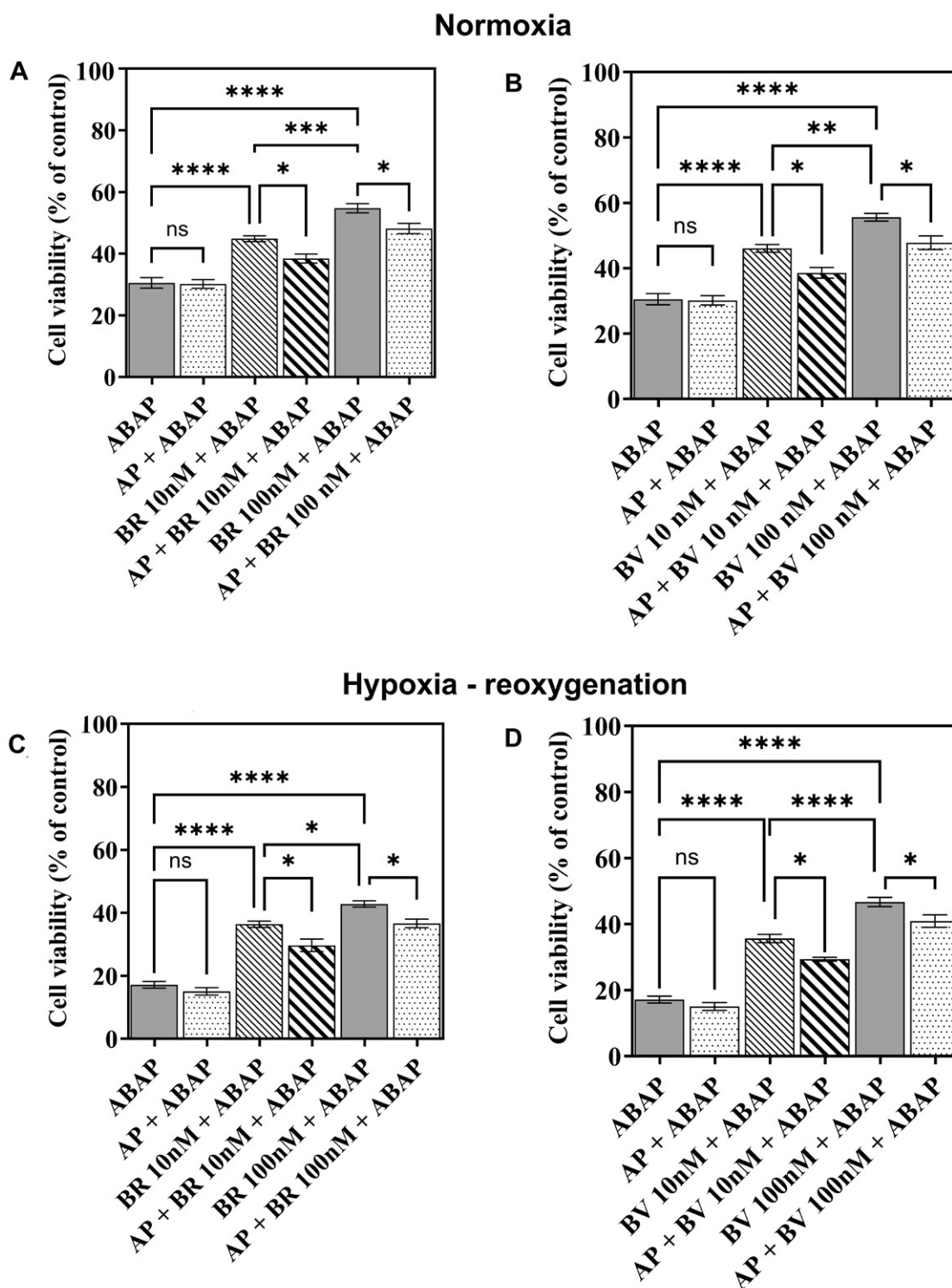


Figure 2. Assessment of cell viability of human endothelial cells EA.hy926 under various treatment conditions. This figure presents the impact of biliverdin reductase (BVR) inhibition on the protective effects of bilirubin and biliverdin against oxidative stress in EA.hy926 cells. Experimental groups included: (1) ABAP, where cells were subjected only to oxidative stress induced by 15 μ M ABAP; (2) AP + ABAP, inhibition of BVR with 10 μ M apomorphine (AP) prior to oxidative stress; (3) BR + ABAP, pre-treatment with bilirubin (10 nM or 100 nM) prior to oxidative stress; (4) AP + BR + ABAP, inhibition of BVR activity with 10 μ M AP, followed by bilirubin (10 nM or 100 nM) pre-treatment prior to oxidative stress; (5) BV + ABAP, pre-treatment with biliverdin (10 nM or 100 nM) prior to oxidative stress; and (6) AP + BR + ABAP, inhibition of BVR activity with 10 μ M AP, followed by biliverdin (10 nM or 100 nM) pre-treatment before oxidative stress. Cell viability was quantified and expressed as a percentage of control group viability, which was set as 100%. Data are presented as mean \pm SEM. Each data point represents the mean of three independent experiments, each consisting of six technical replicates. Statistical analysis was performed using one-way ANOVA with a post-hoc Bonferroni test to determine significance (* $p \leq 0.05$, ** $p \leq 0.01$, *** $p \leq 0.001$, **** $p \leq 0.0001$).

biliverdin exhibited slightly higher antioxidant activities under normoxic conditions than under hypoxic conditions.

Under normoxic conditions, the inhibition of BVR by apomorphine significantly reduced the CAA of both bilirubin and biliverdin. Specifically, Figure 3A shows that the antioxidant activity of bilirubin notably diminished

when BVR activity was inhibited. A similar reduction was observed for biliverdin (Figure 3B), indicating that the antioxidative capacity of both bile pigments is critically dependent on BVR activity.

When the experiment was extended to hypoxia-reoxygenation conditions, a comparable pattern was observed. As shown in Figure 3C, the CAA of bilirubin was

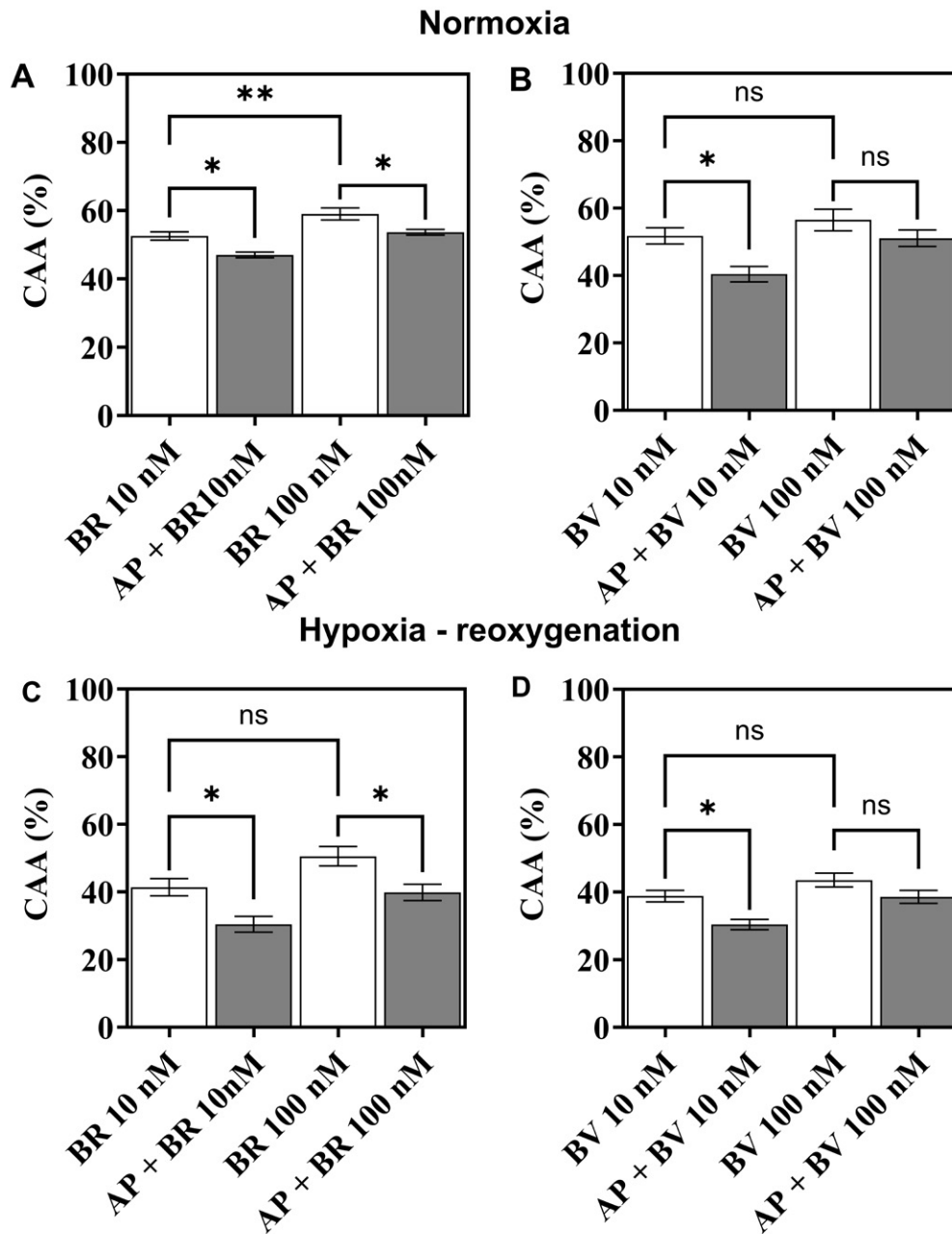


Figure 3. Assessment of cellular antioxidant activity in human endothelial cells EA.hy926 under various treatment conditions. This figure presents the effects of biliverdin reductase (BVR) inhibition on the cellular antioxidant activities of bilirubin and biliverdin in human endothelial cells EA.hy926. Experimental groups included: (1) BR, cells treated with bilirubin (10 nM or 100nM); (2) AP + BR, cells pre-incubated with 10 μ M apomorphine (BVR inhibitor) followed by treatment with 10 nM or 100 nM bilirubin; and (3) AP + BV, cells were pre-incubated with 10 μ M apomorphine, followed by treatment with 10 nM or 100 nM biliverdin. Following these treatments, the cellular antioxidant activity (CAA) was measured. The results are presented as the mean \pm SEM. Each data point represents the average of three independent experiments, each consisting of six technical replicates. Statistical analysis was performed using one-way ANOVA with a post-hoc Bonferroni test to determine significance. Labels indicate: ns, non-significant, * $p \leq 0.05$, ** $p \leq 0.01$.

reduced following BVR inhibition, mirroring findings under normoxic conditions. Similarly, Figure 3D shows a reduction in the antioxidant activity of biliverdin when BVR was inhibited during hypoxia-reoxygenation. An interesting exception was observed when 100 nM biliverdin was used in conjunction with apomorphine under hypoxia-reoxygenation conditions. In this case, the effect of BVR inhibition on CAA was not statistically significant, suggesting a potential differential response of biliverdin at this concentration.

3. 1. 3. Effects of BVR Inhibition on Cellular Bilirubin and Biliverdin Levels in Human Endothelial Cells

The impact of increased oxidative stress induced by ABAP, both under normoxic conditions and following hy-

poxia-reoxygenation, as well as the inhibition of biliverdin reductase (BVR), on cellular bilirubin and biliverdin levels in EA.hy926 cells is presented in Figure 4.

Under normoxic conditions, ABAP exposure significantly decreased cellular bilirubin levels (Figure 4A), with a similar reduction observed in biliverdin levels (Figure 4B). When bilirubin was added (100 nM), cellular bilirubin levels increased with minimal changes in biliverdin levels. In contrast, addition of biliverdin (100 nM) elevated both biliverdin and bilirubin levels. BVR inhibition by apomorphine slightly decreased cellular bilirubin levels when bilirubin was added, whereas biliverdin levels remained unchanged. In the presence of biliverdin and BVR inhibition, bilirubin levels decreased; however, biliverdin levels were unaffected.

Following hypoxia-reoxygenation, ABAP further decreased bilirubin levels, showing a threefold reduction

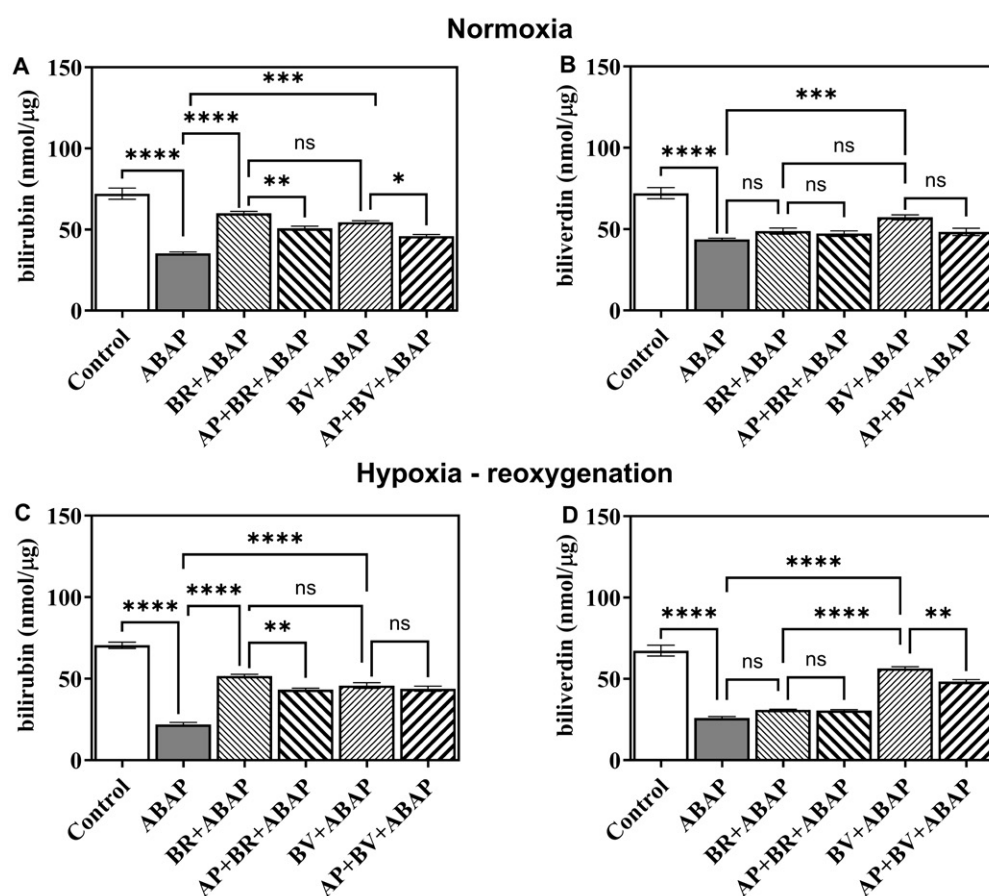


Figure 4. Measurement of bilirubin and biliverdin levels in human endothelial cells EA.hy926 using HPLC-MS. The experiments were performed using normoxic (panels A and B) and hypoxia-reoxygenation protocols (panels C and D). Results are presented as cellular bilirubin (panels A and C) or cellular biliverdin (panels B and D) levels normalized to the total quantity of cellular proteins (nmol/ μ g). Experimental groups included: (1) control group, in which cells were not exposed to any experimental protocol; (2) ABAP, oxidative stress induced by 15 μ M ABAP; (3) BR + ABAP, cells treated with 100 nM bilirubin (BR) prior to oxidative stress (15 μ M ABAP); (4) AP+BR+ABAP, cells pre-incubated with 10 μ M apomorphine (AP), then pre-treated with 100 nM bilirubin (BR) before oxidative stress (15 μ M ABAP); (5) BV + ABAP, cells treated with 100 nM biliverdin (BV) before oxidative stress (15 μ M ABAP); and (6) AP+BR+ABAP, cells pre-incubated with 10 μ M apomorphine (AP), then pre-treated with 100 nM biliverdin (BV) before oxidative stress (15 μ M ABAP). Results are expressed as mean \pm SEM. Each data point represents the mean of three independent experiments, each consisting of six technical replicates. Statistical analysis was performed using one-way ANOVA with a post-hoc Bonferroni test to determine significance. Labels indicate: ns, non-significant, * $p \leq 0.05$, ** $p \leq 0.01$, *** $p \leq 0.001$, **** $p \leq 0.0001$.

compared to controls (Figure 4C) and similarly reduced biliverdin levels (Figure 4D). Pre-incubation with 100 nM bilirubin significantly increased cellular bilirubin levels with a marginal increase in biliverdin levels. Conversely, biliverdin incubation raised bilirubin levels more than biliverdin itself. BVR inhibition caused a significant reduction in bilirubin levels after the addition of either bilirubin or biliverdin, with a minimal impact on biliverdin levels.

3. 2. Primary Mechanism of Apomorphine Involvement in Diminished Bilirubin and Biliverdin Protective Activity is Via Inhibition of BVR and Not Via Agonistic Activity on Dopamine Receptors in Endothelium

To assess whether the effects of apomorphine, a dopamine receptor agonist, on the protective activities of bilirubin and biliverdin were mediated by dopamine recep-

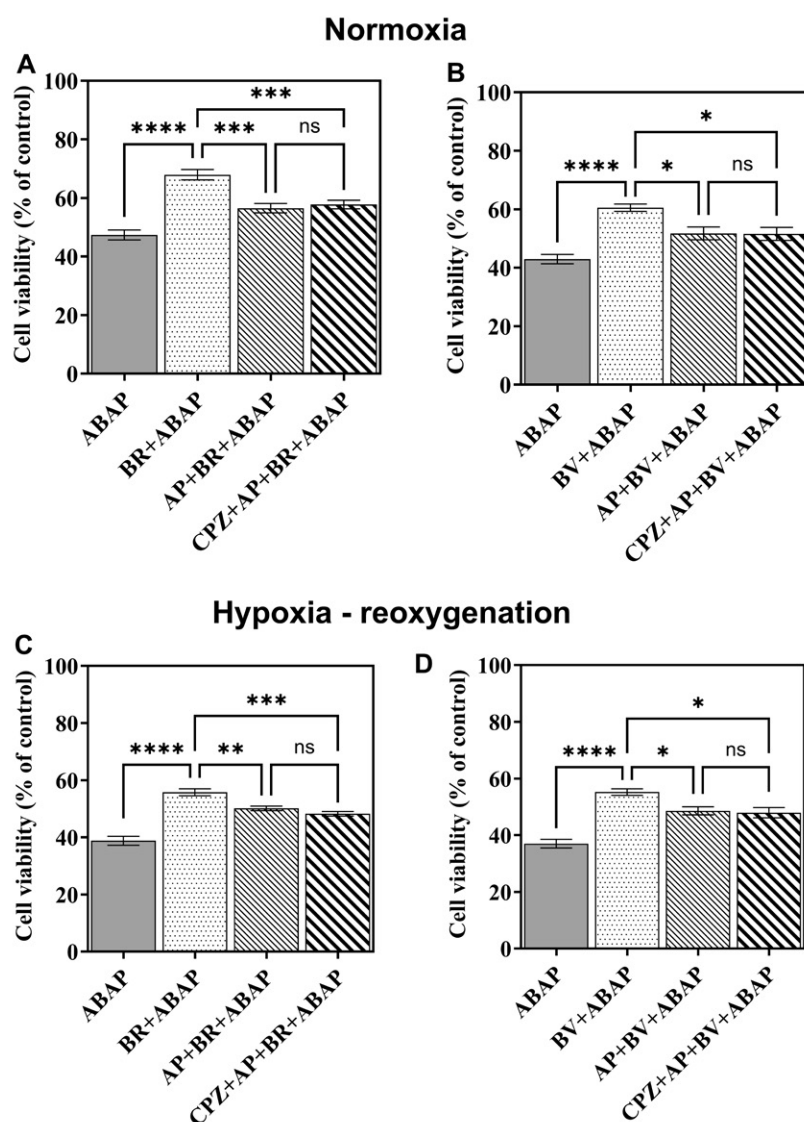


Figure 5. Evaluation of dopamine receptor involvement in the modulation of bilirubin and biliverdin protective activities by apomorphine in human endothelial cells EA.hy926. The results presented in this figure show that dopamine receptors, blocked by the dopamine receptor antagonist chlorpromazine, do not influence the effects of apomorphine on the protective activities of bilirubin and biliverdin under oxidative stress conditions. Experiments were performed under normoxic (panels A and B) and hypoxia-reoxygenation protocols (panels C and D). Experimental groups included: (1) ABAP – oxidative stress induced by 15 μ M ABAP; (2) BR + ABAP, cells treated with 100 nM bilirubin (BR) before oxidative stress (15 μ M ABAP); (3) AP+BR+ABAP, cells pre-incubated with 10 μ M apomorphine (AP), a BVR inhibitor, followed by treatment with 100 nM bilirubin (BR) before oxidative stress (15 μ M ABAP); (4) CPZ+AP+BR+ABAP, cells were pre-treated with 10 μ M chlorpromazine (CPZ), followed by 10 μ M apomorphine (AP), then cells were treated with 100 nM bilirubin (BR) before oxidative stress (15 μ M ABAP). Similar experiments were performed using 100 nM biliverdin (BV), as shown in panels B and D. Data are presented as mean \pm SEM. Each data point represents the mean of three independent experiments, each consisting of six technical replicates. Statistical analysis was performed using one-way ANOVA with a post-hoc Bonferroni test to determine statistical significance. Labels indicate: ns, non-significant, * $p \leq 0.05$, ** $p \leq 0.01$, *** $p \leq 0.001$, **** $p \leq 0.0001$.

tors, we conducted additional experiments using chlorpromazine, a non-selective dopamine receptor antagonist (Figure 5). Pre-incubation with chlorpromazine did not alter the observed effects of apomorphine on cell viability in either the bilirubin (Figure 5A) or biliverdin

(Figure 5B) treatment groups under normoxic and hypoxia-reoxygenation conditions. The reduction in protective activity observed with apomorphine was consistent, regardless of chlorpromazine pre-treatment, indicating that dopamine receptors were not involved in mediating the

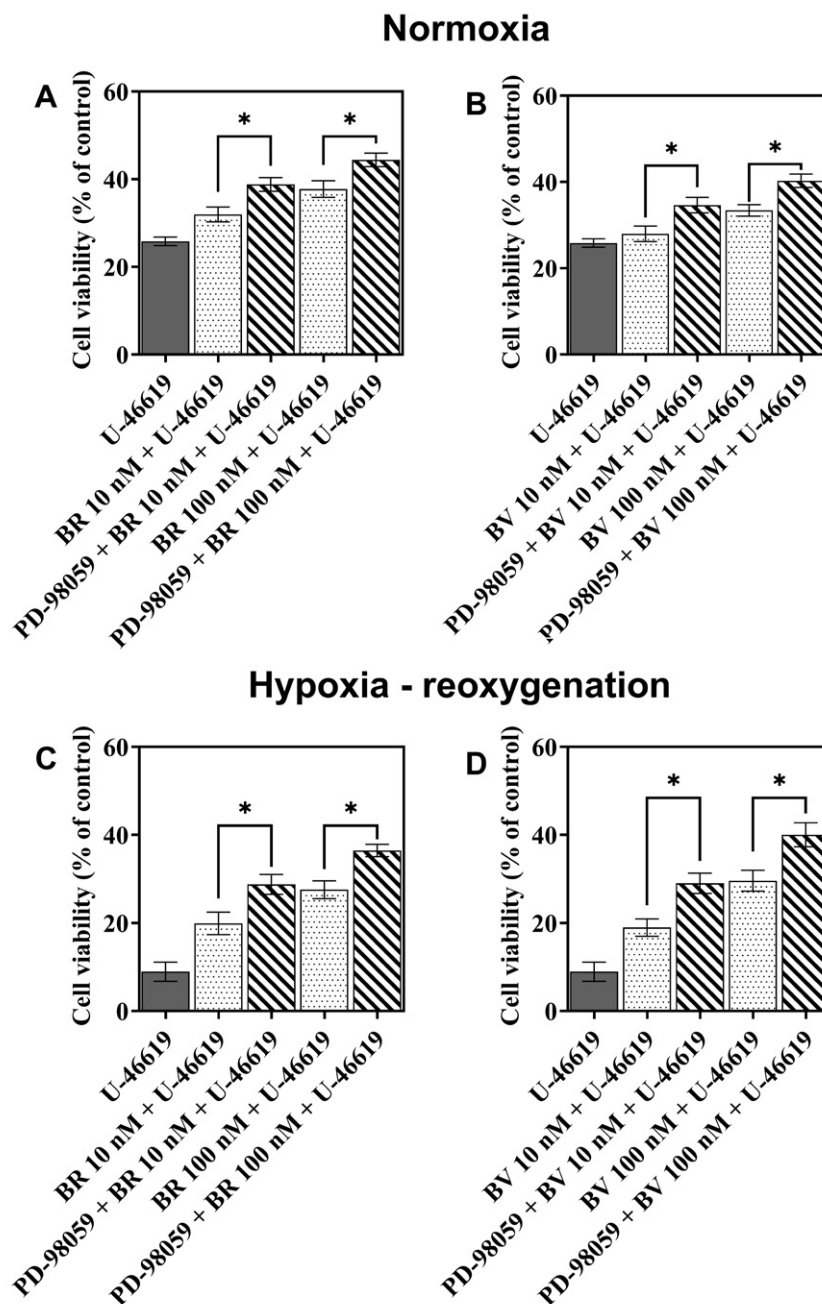


Figure 6. Assessment of ERK1/2 kinase modulation on the protective activity of bilirubin and biliverdin against oxidative stress in human endothelial cells EA.hy926. Experiments were conducted under normoxia (panels A and B) and hypoxia-reoxygenation conditions (panels C and D). The experimental setup involved the initial activation of ERK1/2 kinases using pretreatment with 1 μ M U46619, followed by different treatments, and subsequent cell viability assay. Experimental groups included: (1) U-46619 alone, for baseline activation of ERK1/2 kinases; (2) BR + U-46619, where cells were treated with bilirubin (BR) (10 nM or 100 nM) after initial ERK1/2 activation (1 μ M U-46619); (3) PD-98059 + BR + U46619, inhibition of ERK kinases by 20 μ M PD-98059 after U-46619 pre-treatment, then followed by bilirubin (10 nM or 100 nM). Similar experiments were performed with 10 and 100 nM biliverdin (BV) under normoxia (panel B) and hypoxia-reoxygenation (panel D). Data are presented as mean \pm SEM. Each data point represents the mean of three independent experiments, each consisting of six technical replicates. Statistical analysis was performed using one-way ANOVA with a post-hoc Bonferroni test to determine significance. Labels indicate: ns, non-significant, * $p \leq 0.05$.

effects of apomorphine. These findings confirm that the diminished protective effects of both bilirubin and biliverdin in the presence of apomorphine are due to the inhibition of BVR as a primary pharmacological mechanism rather than any agonistic activity of apomorphine on do-

pamine receptors located on the endothelial cell surface. In addition, the effect of apomorphine was evaluated following hypoxia-reoxygenation injury (Figure 5C for bilirubin and Figure 5D for biliverdin). In both scenarios, the presence of chlorpromazine did not influence the effect of

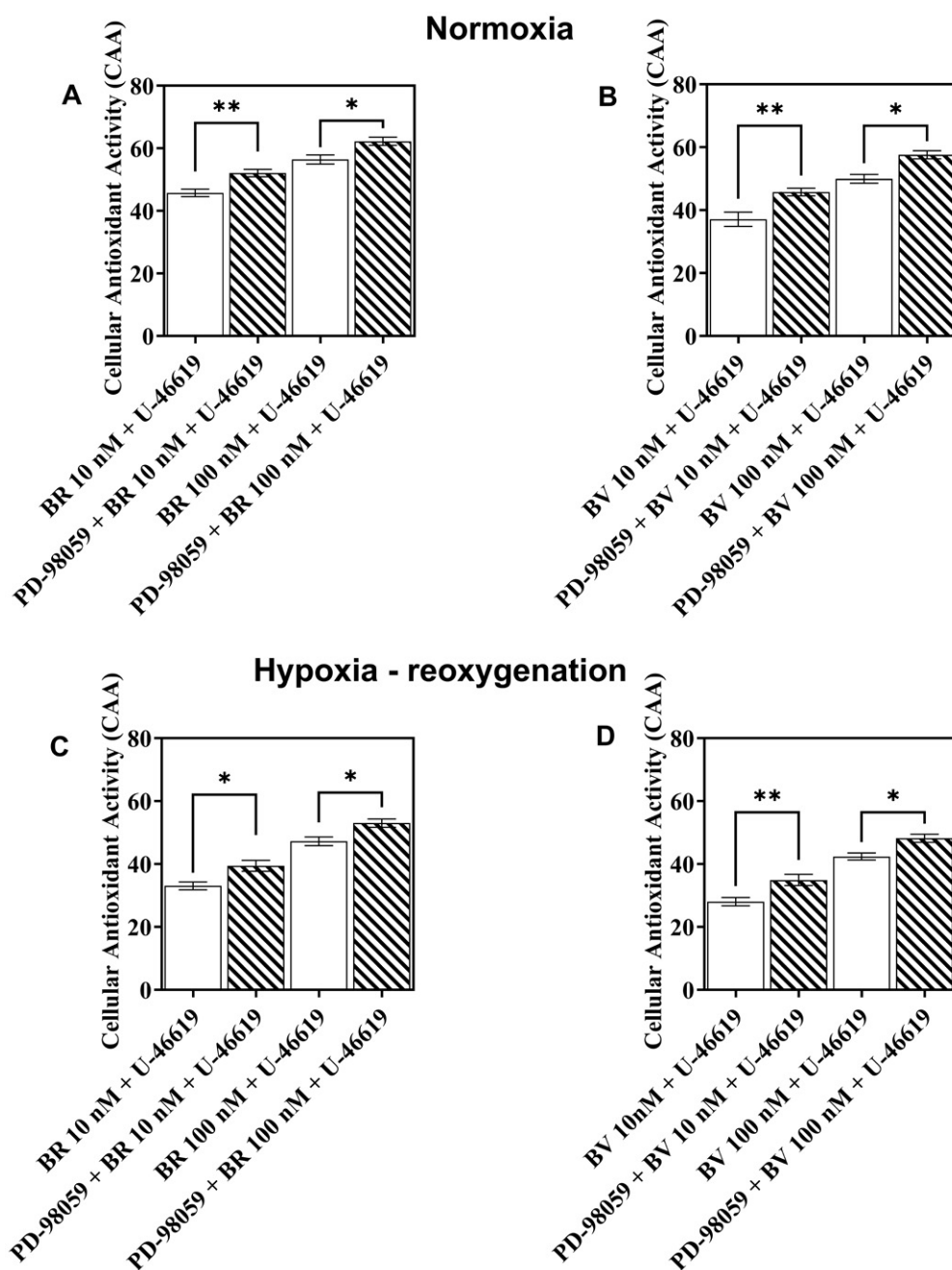


Figure 7. Evaluation of ERK1/2 kinase modulation on the cellular antioxidant activity (CAA) of bilirubin and biliverdin in human endothelial cells EA.hy926. Experiments were conducted under normoxia (panels A and B) and hypoxia-reoxygenation conditions (panels C and D). The experimental protocol involved the initial activation of ERK1/2 (by 1 μ M U-46619 pre-treatment), followed by different treatments, and a final CAA assay to measure the cellular antioxidant activity of bilirubin and biliverdin. Experimental groups included: (1) BR + U46619, where cells were treated with bilirubin (10 nM or 100 nM) after ERK1/2 activation by 1 μ M U-46619; (2) PD-98059 + BR + U46619, inhibition of ERK kinases by 20 μ M PD-98059 after 1 μ M U-46619 pre-treatment, then followed by bilirubin (10 nM or 100 nM). Similar experiments were performed with 10 and 100 nM biliverdin (BV) under normoxia (panel B) and hypoxia-reoxygenation (panel D). Data are presented as mean \pm SEM. Each data point represents the average of three independent experiments, each consisting of six technical replicates. Statistical analysis was performed using one-way ANOVA with a post-hoc Bonferroni test to determine significance. Labels indicate: * $p \leq 0.05$, ** $p \leq 0.01$.

apomorphine, further supporting the role of BVR inhibition as the primary mechanism of apomorphine.

3. 3. Activation or Inhibition of ERK1/2 Kinases Influences Bilirubin and Biliverdin Protective Activity

The effects of ERK1/2 kinase modulation on the protective activity of bilirubin and biliverdin on endothelial

cell viability are shown in Figure 6. Activation of ERK1/2 by U-46619 under normoxic conditions before oxidative stress injury significantly reduced cell viability. However, both bilirubin (Figure 6A) and biliverdin (Figure 6B) improved cell viability in a concentration-dependent manner, that is 100 nM provided greater protection than 10 nM did. Importantly, inhibition of pre-activated ERK1/2 with PD-98059 enhanced the protective effects of both bilirubin and biliverdin, as evi-

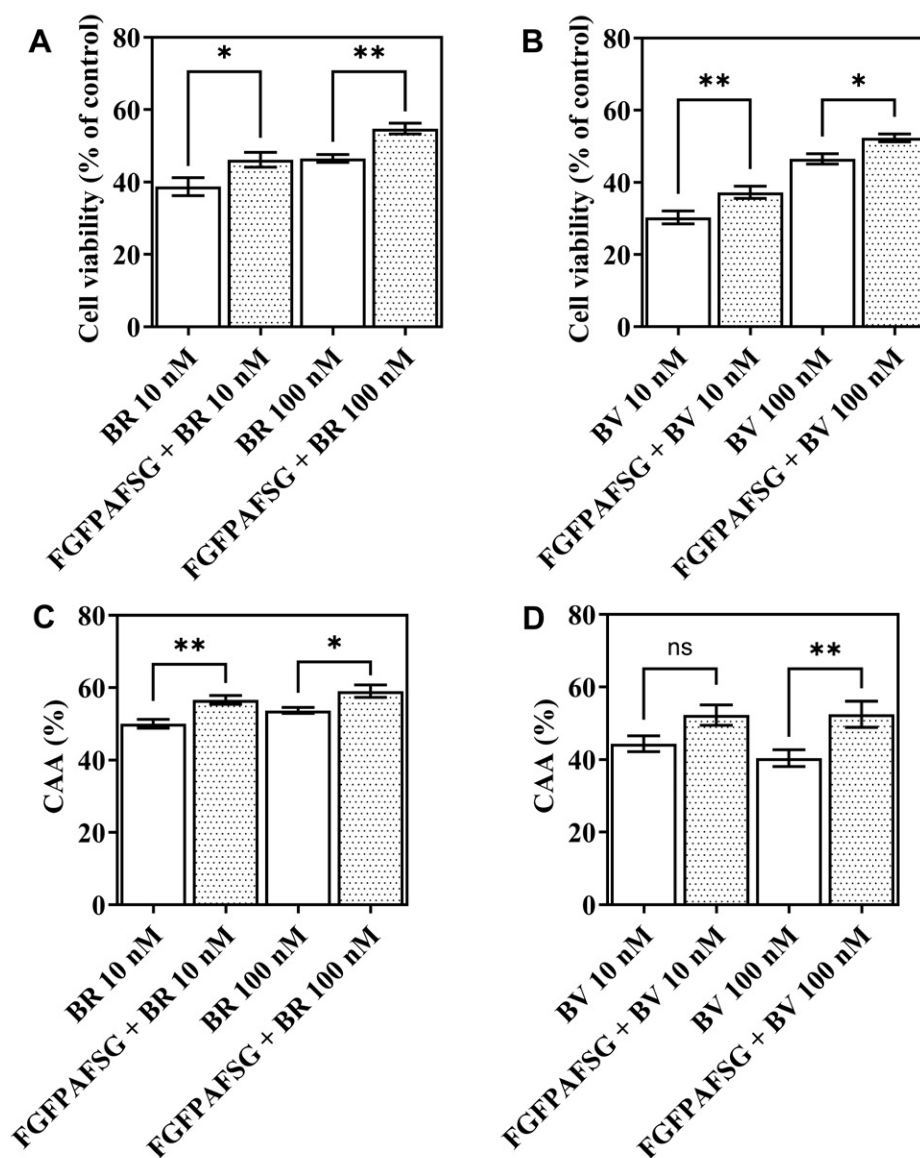


Figure 8. Assessment of the inhibition of BVR interaction with ERK1/2 kinases by C-Box inhibitor (peptide FGFPAFSG) on cell viability and cellular antioxidant activity in human endothelial cells EA.hy926. This figure depicts the effects of inhibiting BVR's interaction with ERK1/2 kinases using a CBox inhibitor, peptide FGFPAFSG, under normoxic conditions. Panels A and B show the effects on cell viability, and panels C and D show effects on cellular antioxidant activity with bilirubin and biliverdin, respectively. Experimental groups included: (1) BR, bilirubin (BR) treatment alone (10 nM and 100 nM) followed by ABAP-induced oxidative stress; (2) BV, biliverdin (BV) treatment alone (10 nM and 100 nM) followed by ABAP-induced oxidative stress; (3) FGFPAFSG + BR, pre-treatment with C-Box inhibitor, followed by bilirubin (BR) incubation (10 nM and 100 nM), and then followed by ABAP-induced oxidative stress; (4) FGFPAFSG + BV, pre-treatment with C-Box inhibitor, followed by biliverdin (BV) incubation (10 nM and 100 nM), and then followed by ABAP-induced oxidative stress. Data are presented as mean \pm SEM. Each data point represents the mean of three independent experiments, each consisting of six technical replicates. Statistical analysis was performed using one-way ANOVA with a post-hoc Bonferroni test to determine significance. Labels indicate: ns, non-significant, * $p \leq 0.05$, ** $p \leq 0.01$.

denced by the increased cell viability (Figure 6A and 6B).

Under hypoxia-reoxygenation conditions (Figures 6C and 6D), the negative impact of U-46619 on cell viability was even more pronounced, showing a 2.5-fold greater reduction in viability compared to normoxic conditions. In contrast, the inhibition of ERK1/2 by PD-98059 markedly increased the protective efficacy of bilirubin (Figure 6C) and biliverdin (Figure 6D), resulting in significantly higher cell viability.

Furthermore, inhibition of ERK1/2 with PD-98059 significantly increased the cellular antioxidant activity of both bilirubin (Figure 7A) and biliverdin (Figure 7B) under normoxic conditions. Under hypoxia-reoxygenation conditions, the inhibition of ERK1/2 with PD-98059 also resulted in a marked increase in the antioxidant activity of both bilirubin (Figure 7C) and biliverdin (Figure 7D).

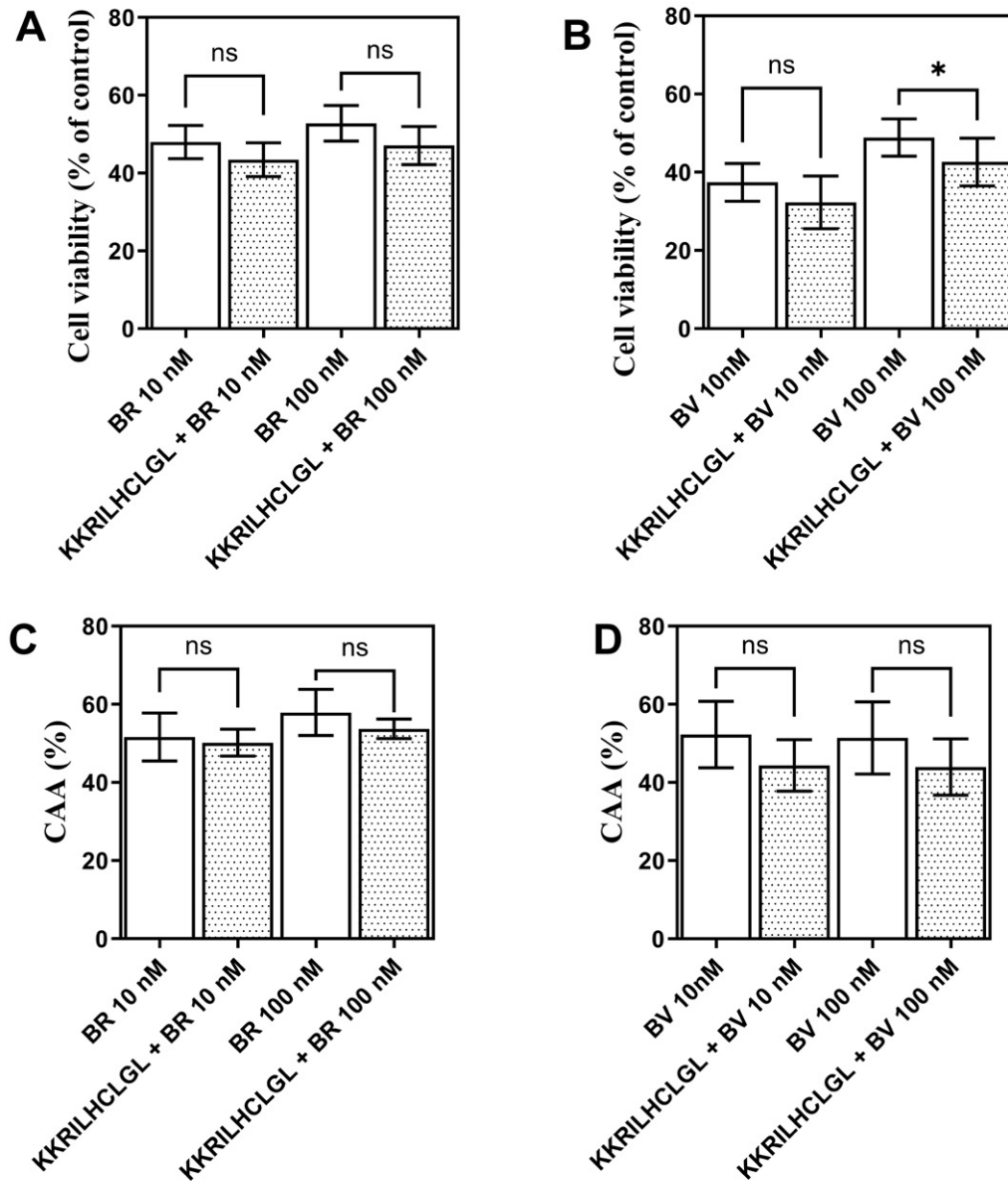


Figure 9. Assessment of the inhibition of BVR interaction with ERK1/2 kinases by D-Box inhibitor KKRILHCLGLA (D-Box inhibitor) on cell viability and cellular antioxidant activity in human endothelial cells EA.hy926. This figure depicts the effect of inhibiting the interaction between BVR and ERK1/2 kinases using the D-Box inhibitor KKRILHCLGLA under normoxic conditions. Panels A and B show the effects on cell viability, and panels C and D show effects on cellular antioxidant activity with bilirubin and biliverdin, respectively. Experimental groups included: (1) BR, bilirubin (BR) treatment alone (10 nM and 100 nM) followed by ABAP-induced oxidative stress; (2) BV, biliverdin (BV) treatment alone (10 nM and 100 nM) followed by ABAP-induced oxidative stress; (3) KKRILHCLGL + BR, pre-treatment with D-Box inhibitor, followed by bilirubin (BR) incubation (10 nM and 100 nM) and then followed by ABAP-induced oxidative stress; (4) KKRILHCLGL + BV, pre-treatment with D-Box inhibitor, followed by biliverdin (BV) incubation (10 nM and 100 nM), and then followed by ABAP-induced oxidative stress. Data are presented as mean \pm SEM. Each data point represents the average of three independent experiments, each consisting of six technical replicates. Statistical analysis was performed using one-way ANOVA with a post-hoc Bonferroni test. Labels indicate: ns, non-significant, * $p \leq 0.05$.

3. 4. Inhibition of BVR Interaction with ERK1/2 Kinases Enhances Bilirubin and Biliverdin Protective Activity

To study the influence of disruption of the interaction between biliverdin reductase (BVR) and ERK1/2 kinases on the protective activity of bilirubin and biliverdin, we used C-Box and D-Box inhibitors under normoxic conditions.

Inhibition of the BVR-ERK interaction via a C-Box inhibitor (FGFPAFSG peptide) resulted in a modest enhancement of the protective effects of bilirubin and biliverdin. Specifically, the C-Box inhibitor slightly increased cell viability in the presence of bilirubin (Figure 8A) and biliverdin (Figure 8B). Similarly, a minor elevation in cellular antioxidant activity was observed when the C-Box inhibitor was applied, as shown in Figure 8C for bilirubin and Figure 8D for biliverdin. Although these effects were statistically significant, they were relatively small, indicating a subtle contribution of the C-Box interaction in modulating the cytoprotective functions of these bile pigments.

Conversely, the D-Box inhibitor (KRILHCLGLA peptide) did not significantly affect the protective activity of bilirubin or biliverdin, as demonstrated by the lack of change in both cell viability (Figure 9A for bilirubin, Figure 9B for biliverdin) and cellular antioxidant activity (Figure 9C for bilirubin, Figure 9D for biliverdin). These findings suggest that the D-Box interaction between BVR and ERK1/2 kinases does not play a major role in the modulation of the protective mechanisms of bilirubin and biliverdin under the conditions tested.

4. Discussion

Our study provides compelling evidence for the critical role of biliverdin reductase (BVR) in mediating the protective effects of bilirubin and biliverdin against oxidative stress-induced injury in human vascular endothelial cells. Our findings demonstrate that the inhibition of BVR, particularly through the pharmacological agent apomorphine, significantly diminishes the cytoprotective and antioxidant activities of these bile pigments. Moreover, we elucidated the intricate interplay between BVR and the extracellular signal-regulated kinase (ERK1/2) pathway, highlighting how ERK1/2 activation modulates the efficacy of BVR-mediated protection.

Role of biliverdin reductase in endothelial protection conferred by bilirubin and biliverdin

Biliverdin reductase (BVR) is a critical enzyme in the heme catabolic pathway that catalyzes the reduction of biliverdin to bilirubin. This conversion is not merely a metabolic step; it represents a key aspect of the cellular antioxidant defence system.²⁴ Bilirubin, a product of

BVR activity, is a potent scavenger of reactive oxygen species (ROS), providing robust protection against oxidative damage in various cell types, including endothelial cells.⁹ Bilirubin is oxidized to biliverdin, and BVR converts biliverdin back to bilirubin.⁶ In case of high and intense oxidative stress, some bilirubin is lost and converted to bilirubin oxidizing products (BOXes).²⁵ Given that BOXes are vasoactive and capable of inducing significant vasoconstriction while further exacerbating oxidative stress,²⁶ it is crucial that biliverdin is efficiently recycled back into bilirubin under conditions of increased oxidative stress. Thus, BVR's contribution to the antioxidant defence is to ensure the availability of bilirubin, which can neutralize ROS and thus protect cellular components from oxidative damage. This cyclic mechanism is crucial for sustaining redox homeostasis within endothelial cells, particularly under conditions of increased oxidative stress, such as those encountered during ischemia-reperfusion injury.

Our results demonstrated that inhibition of BVR using apomorphine led to a significant reduction in both cell viability and cellular antioxidant activity. Recently, studies have begun to identify potential pharmacological tools for inhibiting BVR. For instance, screening of 1,280 FDA-approved compounds *in vitro* led to the identification of 26 compounds as BVR inhibitors.²⁷ Similarly, another study identified 20 inhibitors from a screening of 1,496 compounds.²⁸ To rule out the dopamine agonist activity of apomorphine, we pre-incubated samples with the non-selective dopamine receptor antagonist chlorpromazine. Our results showed that chlorpromazine, which effectively blocked dopamine receptors, did not reduce apomorphine activity. This suggests that the observed reduction in bilirubin and biliverdin's protective effects is attributable to apomorphine's role as a BVR inhibitor rather than its agonist activity on dopamine receptors. Our findings underscore the essential role of BVR in maintaining endothelial cell integrity under oxidative stress conditions. The observed reduction in cell viability following BVR inhibition was due to the decreased availability of bilirubin, impairing the cell's capacity to neutralize ROS-induced damage. Our experiments confirmed that intracellular bilirubin levels in endothelial cells were significantly reduced when BVR was inhibited with apomorphine compared to the control groups. Notably, we observed this reduction only under oxidative stress conditions, in both normoxic and hypoxia-reoxygenation pretreatments. However, under normal, non-stressed conditions (normoxia and without induced oxidative stress with ABAP), apomorphine incubation did not lead to significant changes in intracellular bilirubin or biliverdin levels. We also observed that the addition of biliverdin led to an increase in intracellular bilirubin levels, which could be explained by the rapid conversion of biliverdin to bilirubin by BVR. The data on intracellular bilirubin levels were consistent with the

findings from cell viability and cellular antioxidant activity (CAA) assays; higher intracellular bilirubin levels were associated with improved cell viability after oxidative stress and with improved intracellular antioxidant properties.

Our experimental findings align with previous research highlighting the protective role of BVR in various cellular contexts. For instance, BVR deficiency in human endothelial cells has been shown to increase oxidative stress and promote endothelial-to-mesenchymal transition, a process associated with vascular pathology.¹⁹ Similarly, in human endothelial cells (HUVECs) with silenced BVR expression, there was a notable rise in reactive oxygen and nitrogen species. Furthermore, a study on cyanobacteria demonstrated that inactivation of BVR resulted in higher ROS levels compared to cells with intact BVR activity.²⁹ From a pharmacological point of view, one study showed that atorvastatin significantly upregulated BVR expression and increased BVR protein levels in the parietal cortex.³⁰ This suggests that some protective drugs that increase the cellular bioavailability of bilirubin might act as inducers of BVR. However, the research field of increasing BVR levels in the endothelium has not yet been fully addressed. In conclusion, our study, along with several others, emphasizes the protective role of BVR in preventing oxidative damage and preserving endothelial function.

Impact of ERK1/2 Modulation on BVR Activity

The interaction between biliverdin reductase (BVR) and extracellular signal-regulated kinase 1/2 (ERK1/2) represents a significant intersection of cellular signaling pathways that govern both the oxidative stress response and cell survival mechanisms. In addition to its well-characterized role in the conversion of biliverdin to bilirubin, BVR also functions as a scaffold protein for ERK1/2 kinase and acts as a nuclear transporter of ERK,³¹ thereby influencing its activity and downstream signaling cascades. This dual role of BVR places it at a critical juncture, where metabolic and signaling pathways converge, impacting the overall cellular response to oxidative stress. Interestingly, several cellular stressor factors, including mitogens, cytokines, free radicals, and insulin, that activate MAPK also activate BVR.¹⁶

Our study elucidated the modulatory effects of ERK1/2 on BVR activity and its subsequent impact on the protective functions of bilirubin and biliverdin in endothelial cells. Specifically, activation of the ERK1/2 signaling pathway by the pharmacological agent U-46619 significantly impaired the cytoprotective effects of both bilirubin and biliverdin, as evidenced by reduced cell viability and antioxidant activity. We used U-46619, a thromboxane A₂ mimic, to activate the ERK1/2 pathway. It acts primarily through the thromboxane receptor, leading to the activation of G-proteins, which subsequently activate the MAPK/ERK pathway. These results were further em-

phasized under hypoxia-reoxygenation pre-treatment. We speculate that ERK1/2 activation compromises the ability of BVR to maintain adequate bilirubin levels, thereby diminishing its antioxidative capacity under stress conditions. The mechanistic basis for this impairment involves phosphorylation of BVR, which is facilitated by its interaction with ERK1/2. BVR contains specific docking sites, such as the C-box and D-box motifs, that enable its binding to ERK1/2.¹⁶ Once bound, ERK1/2 can phosphorylate BVR,¹⁶ potentially altering its enzymatic activity and its ability to convert biliverdin to bilirubin. We can hypothesize further that this phosphorylation event may also influence the subcellular localization of BVR, thereby impacting its accessibility to biliverdin and its role in the cellular antioxidant defence system. Furthermore, the role of phosphorylation in BVR's function extends beyond simple enzymatic modulation. As a scaffold protein, BVR facilitates the assembly of signaling complexes that include ERK1/2 and other kinases, thereby influencing the broader cellular response to stress.¹⁶ The phosphorylation of BVR by ERK1/2 may disrupt these scaffolding functions, leading to altered signaling outcomes that compromise cell survival pathways. This disruption can manifest as reduced activation of protective pathways, such as those mediated by nuclear factor kappa-light-chain-enhancer of activated B cells (NF- κ B) or activator protein 1 (AP-1), both of which are influenced by ERK1/2 signaling and are critical for cellular survival in the face of oxidative challenges.³² Similarly, BVR has been identified to form several other protein-protein interactions, such as with protein kinase C,³³ thereby suggesting that physical interaction between BVR and proteins of the signaling network is important for its mechanism of action.

Interestingly, our findings also demonstrated that inhibition of ERK1/2 activity enhances the protective effects of bilirubin and biliverdin. We achieved this inhibition using PD-98059, a specific inhibitor of MEK1 and MEK2, the upstream kinases in the MAPK/ERK pathway.³⁴ This protective enhancement is particularly evident in the context of oxidative stress, where the inhibition of ERK1/2 not only restores but also amplifies the antioxidant activity and cytoprotective functions of both bilirubin and biliverdin. The results of this experimental series further indicate that ERK1/2 activation serves as a negative regulator of BVR-mediated protection and that blocking this pathway can potentiate the antioxidative effects of bilirubin and biliverdin. In another study on arterial smooth muscle cells, the protective role of BVR under hypoxia was demonstrated, as well as the involvement of the ERK1/2 pathway.³⁵ In conclusion, modulation of BVR activity by ERK1/2 represents a critical control point in the cellular response to oxidative stress. Although ERK1/2 activation can impair the protective effects of bilirubin and biliverdin, its inhibition can enhance these effects, highlighting the potential of targeting

this pathway for therapeutic interventions aimed at preserving endothelial function in oxidative stress-related diseases.

Effects of C-Box and D-Box Inhibitors on BVR-ERK Interaction

The interaction between biliverdin reductase (BVR) and ERK1/2 kinases is mediated by specific motifs within the BVR, known as the C-box and D-box.¹⁶ These motifs facilitate the binding of BVR to ERK1/2, influencing downstream signaling events, and consequently, the cellular response to oxidative stress. In our study, we explored the effects of inhibiting these specific interactions using peptides that target the C-box and D-box motifs, thereby disrupting the BVR-ERK1/2 interaction. The differential effects of these inhibitors provide insights into the specific roles of these binding interactions in modulating the protective activities of bilirubin and biliverdin.

Modest Enhancement of Bilirubin Protective Activity with C-Box Inhibition

The inhibition of the C-box interaction using the FGFPAFSG peptide yielded a modest yet statistically significant enhancement of the protective activities of both bilirubin and biliverdin. We observed this enhancement in terms of increased cell viability and cellular antioxidant activity. The C-box motif within the BVR is also known as the high-affinity ERK binding site, and thus plays a crucial role in the docking and subsequent phosphorylation of BVR by ERK1/2.³⁶ Interestingly, the C-terminal part of BVR is critical for its catalytic activity, although it lies in a disordered region of the BVR molecule,³⁷ suggesting that various regions of BVR influence its catalytic function. By inhibiting this interaction, it is likely that the phosphorylation of BVR is reduced, thereby maintaining its enzymatic activity in converting biliverdin to bilirubin. This, in turn, may enhance the availability of bilirubin, allowing for more effective scavenging of reactive oxygen species (ROS) and greater protection of endothelial cells from oxidative damage.

The modest nature of the enhancement observed with C-box inhibition suggests that while this interaction is important, it may not be the sole determinant of BVR's protective function. The partial relief of the inhibitory effects of ERK1/2 on BVR through C-box inhibition indicates that other factors or interactions within the cell may also contribute to the overall regulation of BVR activity. Nonetheless, our data support the notion that disrupting the C-box-mediated interaction between BVR and ERK1/2 can positively influence the antioxidative capacity of bilirubin and biliverdin, albeit to a limited extent.

Lack of Significant Effects on Bilirubin Protective Activity with D-Box Inhibition

In contrast to the effects observed with C-box inhibition, disruption of the D-box interaction using the KRIL-

HCLGLA peptide did not yield significant changes in the protective activities of bilirubin and biliverdin. Both cell viability and cellular antioxidant activity remained unaffected by inhibition of the D-box motif. This lack of an effect suggests that the D-box-mediated interaction between BVR and ERK1/2 may not play a critical role in modulating the enzymatic activity of BVR or its ability to protect against oxidative stress.

Indeed, the D-box motif is considered a low-affinity binding site for several kinases, including ERK, and substrates in the MAPK signaling cascade, and is generally involved in stabilizing protein-protein interactions rather than directly influencing the catalytic activity of enzymes.³⁶ In the context of BVR, it is possible that the D-box interaction with ERK1/2 primarily facilitates the spatial organization of these proteins within the cell, without significantly altering the enzymatic function of BVR. Therefore, inhibition of this interaction may not affect the protective roles of bilirubin and biliverdin.

The differential effects observed with C-box and D-box inhibition highlight the distinct roles that these motifs play in BVR-ERK1/2 interaction. C-box is more directly involved in modulating BVR activity and, consequently, the protective effects of bilirubin and biliverdin. In contrast, the D-box may play a more structural or organizational role, which does not significantly affect the antioxidant functions of these bile pigments. These findings suggest that targeted modulation of the C-box interaction could be a potential strategy for enhancing the protective effects of BVR in endothelial cells under oxidative stress. However, the modest enhancement observed also indicates that this approach alone may not be sufficient to fully restore or amplify the antioxidative capacity of BVR. Future studies should explore combinatorial approaches that target multiple aspects of the BVR-ERK1/2 interaction or other related signaling pathways to achieve more robust protective effects.

Study limitations

Our study has several limitations that should be acknowledged. First, the experiments were conducted *in vitro* using human endothelial cells, which, while informative, do not fully replicate the complex *in vivo* environment of human vasculature. Second, the study primarily focused on the interaction between BVR and ERK1/2, potentially overlooking other signaling pathways that may also interact with BVR and influence its protective functions. Additionally, the use of pharmacological inhibitors, while effective in elucidating mechanisms, may have off-target effects that could confound our results. These limitations suggest the need for further research to validate our findings *in vivo* and to explore other pathways that might interact with BVR. More comprehensive studies are needed to fully understand the long-term effects of modulating BVR activity in the context of endothelial function.

5. Conclusions

In conclusion, this study highlights the critical role of biliverdin reductase (BVR) in protecting endothelial cells from oxidative stress. In Figure 10, we schematically present the interplay of BVR with ERK, the role of BVR in increased oxidative stress conditions, as well as all key approaches that we experimentally addressed in our study. Collectively, our results reinforce the importance of BVR as a key endothelial regulator of endogenous antioxidant activity of bilirubin. Building on the findings of this study, further research should investigate the interactions between BVR and other signaling pathways beyond ERK1/2, as this could reveal additional mechanisms through which BVR confers its protective effects. Finally, the development of specific BVR modulators that can selectively enhance or inhibit its activity could pave the way for novel therapeutic strategies aimed at preventing or treating endothelial dysfunction and related cardiovascular diseases. In addition, the development of novel small-molecule C-box inhibitors may lead to novel pharmacological strategies for treating endothelial dysfunction in both normoxia and after is-

chemia-reperfusion injury. However, the complexity of BVR interactions with several intracellular proteins and their versatile functions require cautious and well-targeted approaches for future clinical applications.

Conflicts of Interest

The authors declare no conflicts of interest. The funding sources were not involved in the study design, collection, analyses, interpretation of data, writing of the manuscript, or decision to publish the results.

Funding

This work was financially supported by the Slovenian Research and Innovation Agency (ARIS) for research project J38209 (Bilirubin as a protective factor against chronic degenerative disease: biomarker and potential for pharmacological modulation), and research programs P30067 and P1-0005. The authors gratefully acknowledge the support.

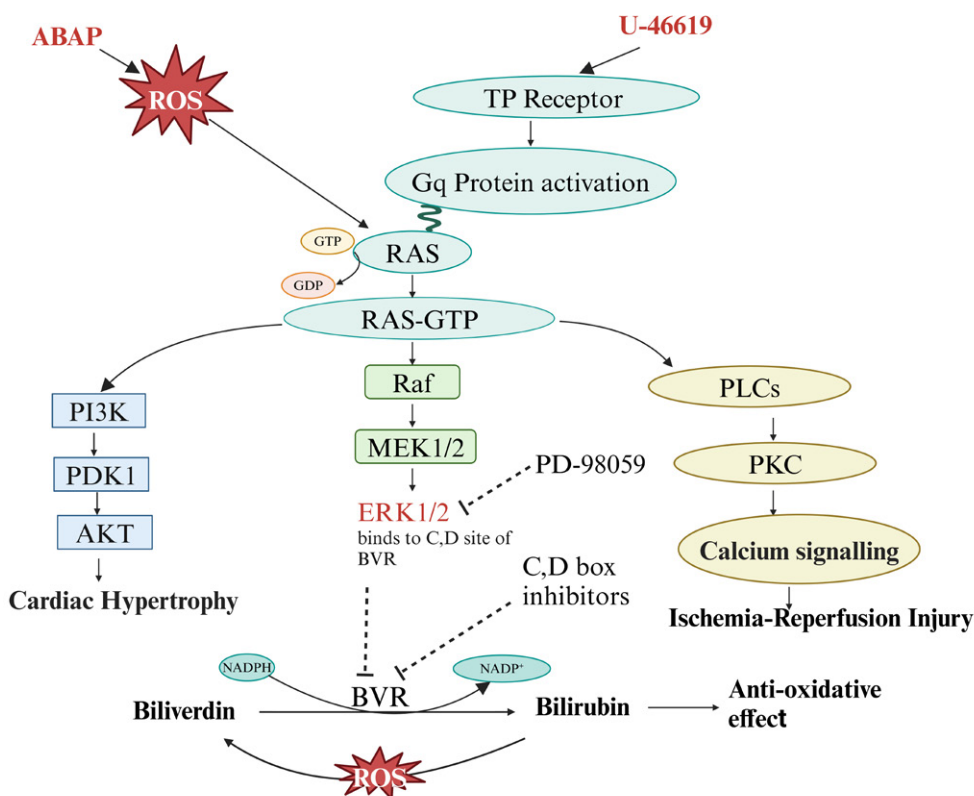


Figure 10. Schematic representation of the interplay between oxidative stress, ERK1/2 signaling, and biliverdin reductase (BVR) in endothelial cells. This figure illustrates the complex interactions between reactive oxygen species (ROS) generated by 2,2'-azobis (2-amidinopropane) dihydrochloride (ABAP) and the activation of thromboxane A2 (TXA2) receptors by U-46619, leading to activation of the Rat Sarcoma (RAS) protein. Activated RAS initiates several downstream pathways, including phosphoinositide 3-kinase/protein kinase B (PI3K/AKT) and rapidly accelerated fibrosarcoma/mitogen-activated protein kinase/extracellular signal-regulated kinase (Raf/MEK/ERK) signaling cascades. Additionally, phospholipase C/protein kinase C (PLC/PKC) - mediated calcium signaling is implicated in ischemia-reperfusion injury. Bilirubin, produced via the BVR pathway, provides important antioxidative protection, however its activity is modulated by the activity of ERK1/2. This hypothesis was experimentally tested in our study by the inhibition of BVR activity, by activation and inhibition of ERK1/2 kinase activity, and by using C-box and D-box inhibitors that interfere with ERK1/2 binding to BVR. The figure was created using graphical elements from BioRender.com.

6. References

- Park, K. H.; Park, W. J. *J Korean Med Sci* **2015**, *30* (9), 1213–1225. DOI:10.3346/jkms.2015.30.9.1213
- Singhal, A. K.; Symons, J. D.; Boudina, S.; Jaishy, B.; Shiu, Y. T. *Vasc Dis Prev* **2010**, *7*, 1–14. DOI:10.2174/1874120701007010001
- Ikonomidis, I.; Pavlidis, G.; Tsoumani, M.; Kousathana, F.; Katogiannis, K.; Tsilivarakis, D.; Thymis, J.; Kountouri, A.; Korakas, E.; Pliouta, L.; et al. *J Clin Med* **2022**, *11* (12). DOI:10.3390/jcm11123299
- Deanfield, J. E.; Halcox, J. P.; Rabelink, T. J. *Circulation* **2007**, *115* (10), 1285–1295. DOI:10.1161/CIRCULATIONAHA.106.652859
- Stocker, R.; Yamamoto, Y.; McDonagh, A. F.; Glazer, A. N.; Ames, B. N. *Science* **1987**, *235* (4792), 1043–1046. DOI:10.1126/science.3029864
- Sedlak, T. W.; Snyder, S. H. *Pediatrics* **2004**, *113* (6), 1776–1782. DOI:10.1542/peds.113.6.1776
- Suh, S.; Cho, Y. R.; Park, M. K.; Kim, D. K.; Cho, N. H.; Lee, M. K. *PLoS One* **2018**, *13* (2), e0193041. DOI:10.1371/journal.pone.0193041
- Tsai, M. T.; Tarng, D. C. *Int J Mol Sci* **2018**, *20* (1). DOI:10.3390/ijms20010117
- Ziberna, L.; Martelanc, M.; Franko, M.; Passamonti, S. *Sci Rep* **2016**, *6*, 29240. DOI:10.1038/srep29240
- Gibbs, P. E.; Maines, M. D. *Int J Cancer* **2007**, *121* (11), 2567–2574. DOI:10.1002/ijc.22978
- Jansen, T.; Daiber, A. *Front Pharmacol* **2012**, *3*, 30. DOI:10.3389/fphar.2012.00030
- Baranano, D. E.; Rao, M.; Ferris, C. D.; Snyder, S. H. *Proc Natl Acad Sci U S A* **2002**, *99* (25), 16093–16098. DOI:10.1073/pnas.252626999
- Cimini, F. A.; Perluigi, M.; Barchetta, I.; Cavallo, M. G.; Barone, E. *Int J Mol Sci* **2022**, *23* (10). DOI:10.3390/ijms23105574
- Gibbs, P. E.; Miralem, T.; Maines, M. D. *Faseb j* **2010**, *24* (9), 3239–3254. DOI:10.1096/fj.09-144592
- Lerner-Marmarosh, N.; Shen, J.; Torno, M. D.; Kravets, A.; Hu, Z.; Maines, M. D. *Proc Natl Acad Sci U S A* **2005**, *102* (20), 7109–7114. DOI:10.1073/pnas.0502173102
- Lerner-Marmarosh, N.; Miralem, T.; Gibbs, P. E.; Maines, M. D. *Proc Natl Acad Sci U S A* **2008**, *105* (19), 6870–6875. DOI:10.1073/pnas.0800750105
- Maines, M. D. *Physiology (Bethesda)* **2005**, *20*, 382–389. DOI:10.1152/physiol.00029.2005
- Hinds, T. D., Jr.; Stec, D. E. *Hypertension* **2018**, *72* (4), 788–795. DOI:10.1161/hypertensionaha.118.11130
- Kloska, D.; Kopacz, A.; Piechota-Polanczyk, A.; Neumayer, C.; Huk, I.; Dulak, J.; Jozkowicz, A.; Grochot-Przeczek, A. *Arch Biochem Biophys* **2019**, *678*, 108182. DOI:10.1016/j.abb.2019.108182
- Jansen, T.; Hortmann, M.; Oelze, M.; Opitz, B.; Steven, S.; Schell, R.; Knorr, M.; Karbach, S.; Schuhmacher, S.; Wenzel, P.; et al. *J Mol Cell Cardiol* **2010**, *49* (2), 186–195. DOI:10.1016/j.yjmcc.2010.04.011
- Liu, Y.; Liu, J.; Tetzlaff, W.; Paty, D. W.; Cynader, M. S. *Free Radic Biol Med* **2006**, *40* (6), 960–967. DOI:10.1016/j.freeradbiomed.2005.07.021
- Albrecht, A.; Martelanc, M.; Ziberna, L. *Anal Chim Acta* **2024**, *1287*, 342073. DOI:10.1016/j.aca.2023.342073
- Martelanc, M.; Ziberna, L.; Passamonti, S.; Franko, M. *Talanta* **2016**, *154*, 92–98. DOI:10.1016/j.talanta.2016.03.053
- Mancuso, C. *Free Radic Biol Med* **2023**, *207*, 133–143. DOI:10.1016/j.freeradbiomed.2023.07.015
- Wurster, W. L.; Pyne-Geithman, G. J.; Peat, I. R.; Clark, J. F. *Acta Neurochir Suppl* **2008**, *104*, 43–50. DOI:10.1007/978-3-211-75718-5_8
- Clark, J. F.; Sharp, F. R. *J Cereb Blood Flow Metab* **2006**, *26* (10), 1223–1233. DOI:10.1038/sj.jcbfm.9600280
- van Dijk, R.; Aronson, S. J.; de Waart, D. R.; van de Graaf, S. F.; Duijst, S.; Seppen, J.; Elferink, R. O.; Beuers, U.; Bosma, P. *J Sci Rep* **2017**, *7* (1), 1646. DOI:10.1038/s41598-017-01602-w
- Kim, M.; Ha, J. H.; Choi, J.; Kim, B. R.; Gapsys, V.; Lee, K. O.; Jee, J. G.; Chakrabarti, K. S.; de Groot, B. L.; Griesinger, C.; et al. *J Med Chem* **2022**, *65* (3), 2548–2557. DOI:10.1021/acs.jmedchem.1c01664
- Schluchter, W. M.; Babin, C. H.; Liu, X.; Bieller, A.; Shen, G.; Alvey, R. M.; Bryant, D. A. *Microorganisms* **2023**, *11* (10). DOI:10.3390/microorganisms11102593
- Barone, E.; Mancuso, C.; Di Domenico, F.; Sultana, R.; Murphy, M. P.; Head, E.; Butterfield, D. A. *J Neurochem* **2012**, *120* (1), 135–146. DOI:10.1111/j.1471-4159.2011.07538.x
- Mancuso, C. *Free Radic Biol Med* **2021**, *172*, 521–529. DOI:10.1016/j.freeradbiomed.2021.06.034
- Fujioka, S.; Niu, J.; Schmidt, C.; Sclabas, G. M.; Peng, B.; Uwagawa, T.; Li, Z.; Evans, D. B.; Abbruzzese, J. L.; Chiao, P. J. *Mol Cell Biol* **2004**, *24* (17), 7806–7819. DOI:10.1128/MCB.24.17.7806-7819.2004
- Maines, M. D.; Miralem, T.; Lerner-Marmarosh, N.; Shen, J.; Gibbs, P. E. *J Biol Chem* **2007**, *282* (11), 8110–8122. DOI:10.1074/jbc.M513427200
- Karpova, A. Y.; Abe, M. K.; Li, J.; Liu, P. T.; Rhee, J. M.; Kuo, W. L.; Hershenson, M. B. *Am J Physiol* **1997**, *272* (3 Pt 1), L558–565. DOI:10.1152/ajplung.1997.272.3.L558
- Song, S.; Wang, S.; Ma, J.; Yao, L.; Xing, H.; Zhang, L.; Liao, L.; Zhu, D. *Exp Cell Res* **2013**, *319* (13), 1973–1987. DOI:10.1016/j.yexcr.2013.05.015
- Gibbs, P. E.; Tudor, C.; Maines, M. D. *Front Pharmacol* **2012**, *3*, 31. DOI:10.3389/fphar.2012.00031
- Whitby, F. G.; Phillips, J. D.; Hill, C. P.; McCoubrey, W.; Maines, M. D. *J Mol Biol* **2002**, *319* (5), 1199–1210. DOI:10.1016/S0022-2836(02)00383-2

Povzetek

Endotelijska disfunkcija je pomemben dejavnik tveganja za razvoj srčno-žilnih bolezni, njeno stanje pa dodatno poslabša oksidativni stres. Biliverdin (BV) in bilirubin (BR) sta močna antioksidanta, ki ščitita endotelijske celice, pri čemer encim biliverdin reductaza (BVR) pretvarja BV v BR za vzdrževanje redoks ravnovesja. Naša raziskava je preučevala vlogo BVR pri posredovanju teh zaščitnih učinkov v normoksičnih pogojih in pogojih hipoksije-reoksigenacije. Farmakološka inhibicija BVR je zmanjšala zaščitne učinke BV in BR, kar se kaže v zmanjšani viabilnosti celic, znotrajcelični antioksidativni sposobnosti in nižjih ravneh znotrajceličnega bilirubina. Aktivacija ERK1/2 je zmanjšala zaščitno funkcijo BVR, medtem ko jo je njena inhibicija povečala. Poleg tega je zaviranje interakcije med BVR in ERK dodatno vplivalo na delovanje BV in BR, kar kaže, da bi lahko vezavna mesta interakcije BVR-ERK1/2 predstavljala potencialne terapevtske tarče za zdravljenje endotelijske disfunkcije, povzročene z oksidativnim stresom.



Except when otherwise noted, articles in this journal are published under the terms and conditions of the Creative Commons Attribution 4.0 International License

Scientific paper

Elimination of Cadmium using Silica Gel Prepared from Blast Furnace Slag

Toufik Chouchane^{1,*}, Mohamed Tayeb. Abedghars¹, Sabiha. Chouchane² and Atmane Boukari¹

¹ Research Center in Industrial Technologies CRTI, P.O. Box 64, Cheraga 16014 Algiers Algeria

² Faculty of Sciences, Badji Mokhtar University, Annaba Algeria

* Corresponding author: E-mail: chouchane_toufik@yahoo.fr
t.chouchane@crti.dz

Received: 02-13-2024

Abstract

In this work, the silica gel recovered from the blast furnace slag was exploited for the elimination of cadmium in batch mode under the action of different factors. Physico-chemical analyzes revealed that the modified slag is only composed of silica (96.14%). Its specific surface area is $484 \text{ m}^2\text{g}^{-1}$ and the pH corresponding to point of zero charge is 4.2. Adsorption isotherms demonstrated that the removal of cadmium on modified slag. The experiment revealed that at pH 6, the effect of the determining factors contributed to the progression of the sorption capacity, which was measured at 154.11 mg/g and was accomplished on a homogeneous monolayer surface ($R^2 = 0.99$). Kinetic analysis revealed that this process agreed with the pseudo-second-order kinetic model ($R^2 \geq 0.99$). In addition, it was indicated that the diffusion of the pollutant is ensured by external and intraparticle diffusion. The values of thermodynamic variables clarified that cadmium sorption is spontaneous, exothermic, less entropic and physically executed under the effect of electrostatic interaction. The desorption process revealed that the reuse of Silica gel was feasible over five consecutive cycles.

Keywords. Adsorption, Cadmium, Isotherm, Kinetics, slag, Silica gel

1. Introduction

Water contamination has become a major global problem, with its effects on humans and their environment. Indeed, used oils, organic materials (dioxins, polychlorinated biphenyls, polycyclic aromatic hydrocarbons, pesticides, etc.), and especially toxic metals (Cd, Hg, As, Pb, Cr, Ni, Zn, Mn, etc.) are continually released into the environment, causing serious pollution of fauna and flora, which will directly or indirectly affect the economy and the health of populations.¹ To guarantee a healthy environment and preserve this natural wealth (water), it is necessary to impose severe sanctions against all forms of pollution. In addition, it is essential to use innovative technological processes, namely ion exchange, solvent extraction, reverse osmosis, ultrafiltration, microextraction of magnetic nanomaterials, and adsorption.² In the latter process, the use of inexpensive adsorbents such as natural materials and industrial solid waste have been widely indicated in recent times.^{3,4} In this context, we opted for research to

eliminate cadmium in solution by adsorption on silica gel prepared from blast furnace slag from the El Hadjar steel complex in Algeria.

Cadmium is widely used in several industries, namely mining, surface coating, the manufacturing of zinc, batteries, alloys, and solar cells. It is considered very harmful. Its accumulation in the organs represents the most dangerous action. Indeed, its introduction could cause hypertension, kidney failure, loss of calcium, reduction of red blood cells, and other harmful consequences.^{1,4} These effects have prompted the World Health Organization and the International Agency for Research on Cancer to classify it as an enormously harmful contaminant.⁵ From the literature, it was noted that the elimination of cadmium in solution had been the subject of multiple research studies.^{6–15} It should be mentioned that the experimental results resulting from these applications displayed a good agreement and also an excellent affinity between the adsorbents examined and the cadmium ions in solution.

Blast furnace slag is a by-product regenerated during the production of cast iron from ores in steel blast furnaces. It is composed of lime, silica, alumina, magnesium oxide, and a small percentage of metal oxides.¹⁶ According to the bibliography, it has been cited that blast furnace slag was considered an adsorbent of choice for the removal of metal ions in solution.^{16–20} From the literature, it has also been cited that various adsorbents were formulated from blast furnace slag. For example, blast furnace slag was transformed into hydroxyapatite-zeolite material for the adsorption of Mn^{2+} , NH_4^+ and PO_4^{3-} ions,²¹ and it was also successfully converted to slag oxalate for the adsorption of Co(II) ions in solution.²² Furthermore, the synthesis of silica nanoparticles from blast furnace slag was carried out in order to use them as an adsorbent to remove azo dyes,²³ and the Tobermorite hydrothermal was formulated from blast furnace slag for the adsorption of Cs^+ and Sr^{2+} .²⁴

Silica gel (SG) is a silicon hydroxide $Si(OH)_4$ polymer of silicic acid prepared from sodium silicate. Silica can be obtained by different extraction techniques, including the alkaline fusion method,²⁵ and the reflux extraction method.²⁶ According to research studies, the alkaline fusion method is the most effective due to its ability to decompose silica and alumina at high temperatures.^{27,28} The fusion of silica with alkali hydroxide is a key factor in the extraction of metals from solids.²⁹

Due to its high porosity and large specific surface area, silica gel has been exploited as an adsorbent in waters containing metal ions.³⁰ Effectively, silica gel prepared from chemical waste bottles was used for the elimination of Zn(II) ions in solution.³¹ The chemically modified silica gel with a thiol group has been suggested for the removal of toxic metals from industrial liquid discharges,³² and modified with a chelating ligand has been proposed for the adsorption of mercury ions.³³ Additionally, silica gel has been recommended in the adsorption processes of ionic-imprinting polyamine,³⁴ and also for the adsorption of Pb(II) ions in an aqueous medium.³⁵

The aim of this study was to transform blast furnace slag into a silica gel and prove its effectiveness as an adsorbent in cadmium-containing wastewater. This work was implemented in several stages. To begin, we collected, treated, and modified the blast furnace slag in order to increase its specific surface area and thus improve its adsorption power. The treatment and modification of the slag were carried out according to appropriate experimental procedures. The solid's physicochemical characterization was carried out by X-ray fluorescence (XRF) and X-ray diffraction (XRD), and its specific surface area was defined by the BET model. Subsequently, we began the process of removing cadmium from silica gel by taking into consideration the determining factors, such as contact time (t_c), silica gel mass (m_s), solution stirring speed (V_{ag}), pH of solution, solution temperature (T), silica gel particle size (\varnothing_s), and initial concentration of the pollutant solution. Thirdly, we investigated the interactions reacting between

the silica gel and the cadmium ions (C_0), defined the nature of the adsorption, and identified the kinetics of pollutant elimination on modified slag. The Adsorbate-adsorbent interactions were detected following the involvement of appropriate adsorption isothermal models, such as Freundlich, Langmuir, and Temkin. The nature of the process was determined following the identification of the thermodynamic parameters, i.e., free enthalpy, enthalpy, entropy, and activation energy. The adsorption kinetics were explained following the use of appropriate models, namely the pseudo-order and diffusion models. In the last phase, we undertook the desorption process. The reuse process was accomplished by treating the saturated silica gel with distilled water and different eluents, namely hydrochloric acid, phosphoric acid and nitric acid. It is important to emphasize that the raw slag samples were collected, processed, and characterized using appropriate techniques. In addition, the influencing factors were maximized by following a rigorous and precise operating protocol (experimental plan) for optimal adsorption.

2. Experimental

2.1. Materials and Methods

The cadmium ions were assayed by atomic absorption spectrometry (Perkin Elmer 3110). The characterization of the solid samples was carried out by X-ray fluorescence (Siemens SRS 3000) and X-ray diffraction (Rigaku Ultim IV). The pH of the solution was measured by a pH meter (Ericsson). Heating of the adsorbent was carried out by a muffle furnace (Nabertherm HT16/17). Stirring was carried out using a mechanical stirrer operating at different speeds. The reagents used, namely hydrochloric acid (HCl), nitric acid (HNO_3), sulfuric acid (H_2SO_4), and sodium hydroxide (NaOH) were of analytical grade (Merck).

2.2. Treatment of Solid

The treatment of the blast furnace slag samples was carried out in accordance with a well-defined experimental protocol.² The modification of the slag into silica gel (SG) was carried out according to the following experimental approach:

- 50 g of treated slag were introduced into a beaker with a volume of 1 L containing NaOH (1 M).
- The mixture was stirred for 90 minutes at a partially low speed (100 rpm).
- The mixture was heated at 800 °C for 2 hours, then 20 ml of Na_2HPO_4 (10 mg/L) was added.
- The mixture obtained was further stirred (200 rpm) until homogenized;
- The treated solid was recovered by filtration, after standing for almost 8 h;
- The impurities ($Al(OH)_3$, $Ca(OH)_2$) were removed by filtration after the resting and cooling of the solution.

- The recovered filtrate was evaporated to dryness to provide sodium metasilicate Na_2SiO_3 as residue.
- The resulting sodium metasilicate (20 g) was dispersed in distilled water with gentle stirring (100 rpm) for 30 minutes.
- After this time, drops of H_2SO_4 (1M, 30 ml) were added to the stirred solution to obtain silica gel.
- Sodium sulfate (Na_2SO_4) was removed by the gradual addition of deionized water.
- The washed gel was steamed at 105°C for 8 hours and then heated in a muffle furnace at 600°C for 120 minutes.
- At the end, it was cooled, crushed, and stored in boxes.

2. 3. Specific Surface Area Determination

The specific surface area of the treated blast furnace slag and silica gel samples were determined from the amount of nitrogen adsorbed as a function of its pressure. This process was carried out at the boiling temperature of liquid nitrogen (-196°C) and under normal atmospheric pressure (760 mmHg).³⁶ The experimental data of N_2 gas desorption at 77 K were evaluated with the BET model.³⁷

2. 4. Adsorption Process

Batch mode tests were carried out to study the adsorption of cadmium on silica gel in solution. The experimental approach consisted of adding a certain mass of silica gel to a solution containing cadmium. The solutions examined were prepared from cadmium salt in beakers of 1 L volume. The experimental conditions applied are given below:

- Contact time (t_c) effects, and equilibrium estimation: $t_c = 0\text{--}180$ min; $C_0 = 30$ mg/L; $V_{ag} = 200$ rpm; $\text{pH} = 4.4$; $T = 20^\circ\text{C}$; $\text{Øs} = 500$ μm ; $m_s = 1$ g.
- Optimization of adsorbent mass (m_s): $t_c = 60$ min; $C_0 = 30$ mg/L; $V_{ag} = 200$ rpm; $\text{pH} = 5.4$; $T = 20^\circ\text{C}$; $\text{Øs} = 500$ μm ; $m_s = 0.4, 0.6, 0.8, 1, 1.2, 1.4$ g.
- Optimization of agitation speed (V_{ag}): $t_c = 60$ min; $C_0 = 30$ mg/L; $V_{ag} = 100, 200, 300, 400$ and 500 rpm; $\text{pH} = 5.4$; $T = 20^\circ\text{C}$; $\text{Øs} = 500$ μm ; $m_s = 1$ g.
- Optimization of pH: $t_c = 60$ min; $C_0 = 30$ mg/L; $V_{ag} = 300$ rpm; $\text{pH} = 2.5, 4.4, 4.7, 5.3, 6, 6.3$ and 6.6 ; $T = 25^\circ\text{C}$; $\text{Øs} = 400$ μm ; $m_s = 1$ g.
- Optimization of particle size (Øs): $t_c = 60$ min; $C_0 = 30$ mg/L; $V_{ag} = 300$ rpm; $\text{pH} = 5.8$; $T = 20^\circ\text{C}$; $\text{Øs} = 100, 200, 300, 400$ and 500 μm ; $m_s = 1$ g.
- Optimization of Temperature (T): $t_c = 60$ min; $C_0 = 30$ mg/L; $V_{ag} = 300$ rpm; $\text{pH} = 6$; $T = 20, 35, 45$ and 55°C ; $\text{Ø} = 200$ μm ; $m_s = 1$ g.
- Optimization of the initial concentration (C_0), and evaluation of the maximum adsorbed quantity (q_e): $t_c = 60$ min; $C_0 = 30\text{--}300$ mg/L; $V_{ag} = 300$ rpm; $\text{pH} = 5.8$; $\text{Øs} = 200$ μm , $T = 20^\circ\text{C}$; $m_s = 1$ g.
- Study of adsorption isotherms: $t_c = 60$ min; $C_0 = 30\text{--}300$ mg/L; $V_{ag} = 300$ rpm; $\text{pH} = 6$; $\text{Øs} = 200$ μm , $T = 20^\circ\text{C}$; $m_s = 1$ g.

- Study of adsorption kinetics: $t_c = 60$ min; $C_0 = 30, 60,$ and 90 mg/L; $V_{ag} = 300$ rpm; $\text{pH} = 6$; $\text{Øs} = 200$ μm , $T = 20, 35, 45, 55^\circ\text{C}$; $m_s = 1$ g.

The adsorbed quantity of cadmium, denoted by q_e and expressed in mg/g, and the adsorption yield, symbolized by R and expressed as a percentage, are obtained from equations 1 and 2.

$$q_e = \frac{C_0 - C_t}{m_s} \times V \quad (1)$$

$$R = \frac{C_0 - C_e}{C_0} \times 100 \quad (2)$$

Where: C_0 : initial solution concentration (mg/L), C_t : solution concentration after a time t (mg/L); C_e : Concentration at equilibrium (mg/L), V : volume of the solution (L) and m_s : adsorbent mass (g).

2. 5. Point of Zero Charge (pH_{pzc})

The zero point of charge (ZPC) is a very important parameter for the evaluation of the surface charge. Indeed, this quantity allows us to decide whether the surface charge is zero ($\text{pH} = \text{pH}_{\text{pzc}}$), positive ($\text{pH} < \text{pH}_{\text{pzc}}$) or negative ($\text{pH} > \text{pH}_{\text{pzc}}$).² The ZPC study involved the addition of 0.1 g of silica gel (SG) samples to a solution containing KNO_3 (0.1 M). This experiment was applied at different pH, namely 2, 4, 6, 8, 10, and 12. The pH adjustment was carried out by the addition of a few drops of H_2SO_4 . These solutions were shaken under operating conditions of 25°C and 200 rpm for 24 h. The ZPC was obtained at the intersection of the ΔpH ($\text{pH}_f - \text{pH}_i$) versus initial pH (pH_i) plot with the X axis.⁷

2. 6. Desorption Process

The process recommended by Chouchane et al.¹⁸ was applied to desorb cadmium ions from silica gel. The experimental approach below was used to carry out this work:

- Using filter paper, 10 g of saturated adsorbent were obtained.
- The recovered silica gel was dehydrated for 24 hours at 105°C .
- Utilizing H_2O and a number of eluents, including HCl , H_2SO_4 , and HNO_3 at 0.05 M concentration, the cadmium desorption study was investigated.
- The desorption process was completed after 150 minutes of agitation (150 rpm).

3. Results and Discussion

3. 1. Characterization of Adsorbent

In this work, the solid samples of blast furnace slag and silica gel were studied by XRF and XRD. The mass percentages of the materials examined are shown in Table 1,

while the XRD characterization is illustrated in Figures 1a and 1b. The new tests carried out by XRF of the blast furnace slag confirmed the results presented a recent research.¹⁷ Indeed, the slag examined was made up of lime (CaO: 35,2), silica (SiO₂: 40,85), alumina (Al₂O₃: 11,38), magnesium oxide (MgO: 5,03) and a fine quantity of metal

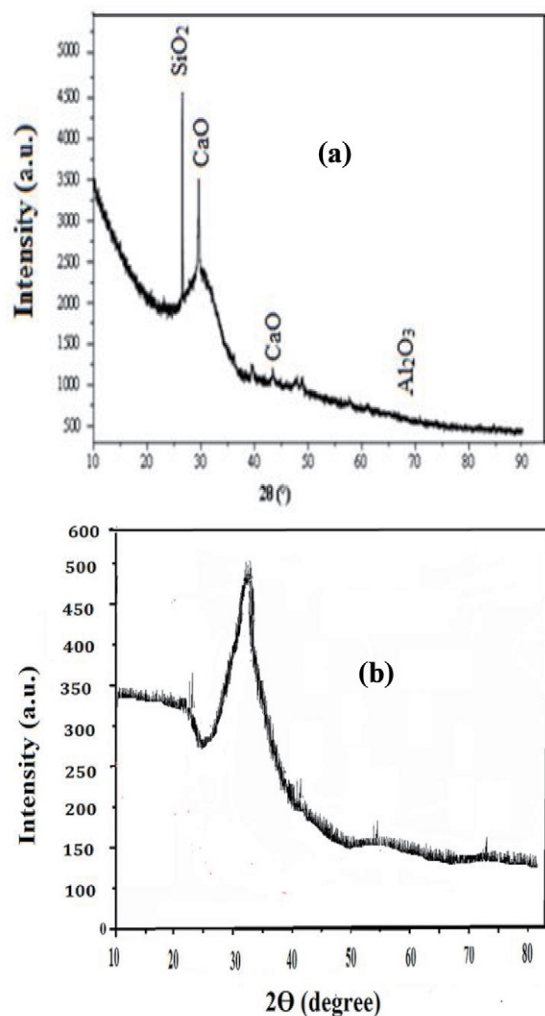


Figure 1. Diffractogram: (a) slag [19], (b) silica gel

Table 1. Chemical composition of treated blast furnace slag (BFS) [16], and silica gel (SG)

Element	Treated slag (BFS) Mass %	Silica gel (SG) Mass %
CaO	35.21	0.67
Al ₂ O ₃	11.38	0.46
SiO ₂	40.85	96.14
Fe ₂ O ₃	1.36	0
MgO	5.03	0
MnO	1.04	0
K ₂ O	0.2	0
Na ₂ O	0.99	0.61
P ₂ O ₅	0	0.35
LOI	3.94	1.77

oxide (Table 1). According to Table 1, silica gel consists of 96.14 % of silica (SiO₂).

In Figure 1a, it was determined that the results of the XRF analysis were consistent with those of the XRD analysis. High levels of lime, silica, and lower levels of alumina and magnesium oxide were detected. XRD analysis of silica gel obtained from converted blast furnace slag showed a significant increase in silica content and the absence of lime, alumina, sodium oxide and phosphorus pentoxide (Figure 2b), which have certainly dispersed in the structure.

3. 2. Contact Time Effect

The effect of contact time in adsorption processes is a crucial factor since it tells us about the equilibrium time and therefore allows us to reduce the number of tests. The impact of contact time is shown in Figure 2(a).

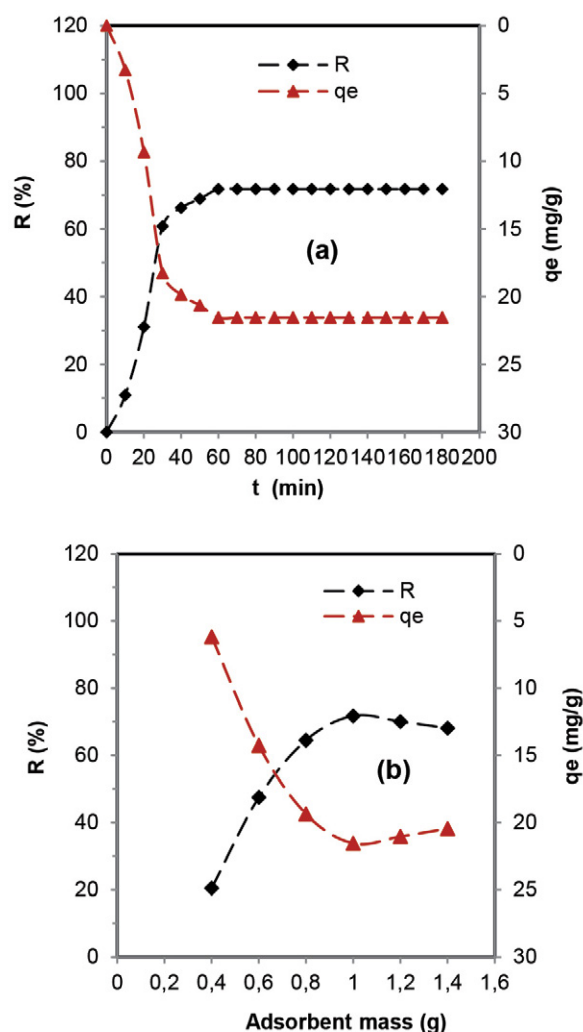


Figure 2. (a) Effect of contact time: $C_0 = 30$ mg/L; $V_{ag} = 200$ rpm; pH = 4.4; $T = 20$ °C; $\phi_s = 500$ μ m; $m_s = 1$ g, (b) Effect of adsorbent dosage: $t_c = 60$ min; $C_0 = 30$ mg/L; $V_{ag} = 200$ rpm; pH = 5.4; $T = 20$ °C; $\phi_s = 500$ μ m

According to the experimental tests, it was noticed that the saturation time of the adsorbent surface was achieved after 60 min. From Figure 2(a), we observed that this process went through three stages, namely fast, moderately slow, and stable. Between 0 and 30 min (rapid stage), the adsorption rate was 84.72%, and the adsorbed quantity increased from 0 to 18.25 mg/g. This outcome was certainly generated by the availability of multiple active adsorption sites.¹⁷ From 30 and 60 min (medium slow stage), the adsorption rate was 15.27%, and the adsorption capacity increased by 3.29 mg/g. This effect was probably due to the gradual decrease in free sites on the surface of the adsorbent.¹⁹ On the other hand, in the last stage, the adsorption rate and the sorption capacity remained constant despite the contact time increasing from 60 to 180 min. This result is undoubtedly caused by the absence of free adsorption sites, that is to say saturation of the adsorbent surface.²

According to the data in the bibliography, we observed that as cadmium adsorption of on silica gel prepared from blast furnace slag is moderately rapid. Indeed, the adsorption of cadmium on different adsorbents, such as natural Bolivian zeolite,³⁸ cellulose-embedded polyacrylonitrile/amidoxime,³⁹ biochar derived from a manure mix,⁴⁰ Mn oxide-modified pine biochar,⁴¹ and Fe₃O₄ nanoparticles loaded sawdust carbon,⁴² was accomplished after 60, 90, 120, 60, 30 and 90 min, respectively.

3. 3. Effect of Adsorbent Dosage

The effect of adsorbent mass on cadmium adsorption on silica gel prepared from blast furnace slag was examined using different masses, namely 0.4, 0.6, 0.8, 1, 1.2, and 1.4 g (Figure 2(b)).

According to the experimental tests, two stages were observed: one strongly increasing from 0.4 to 1g and the other slightly decreasing from 1 to 1.4g. At first, we observed that the adsorption rate and capacity increased by 52.26 % and 15.38 mg/g, respectively. While for the second stage, they had decreased by 3.66% and 1.1 mg/g, respectively. The increase in the adsorption rate and capacity were surely generated by the existence of many unoccupied adsorption sites.^{43,44} The reduction in adsorption efficiency is undoubtedly generated by the constant number of cadmium ions in solution in relation to the number of active sites in continuous growth.^{45,46} For this purpose we opted for 1g as the optimal mass of silica gel in this process.

3. 4. Effect of Agitation Speed

In these processes, medium agitation is a significant step since it contributes considerably to the pollutant transport from the liquid to the solid phase.¹⁷ For this purpose, we introduced this adsorption process. The stirring speeds (V_{ag}) exploited are 100, 200, 300, 400, and 500 rpm (Figure 3(a)).

According to the experimental test results, we discovered that the adsorption of cadmium was more efficient at 300 rpm. Indeed, it was observed that the adsorption yield and capacity systematically progressed between 100 and 300 rpm (Figure 3a). In this speed range, the values of adsorption efficiency and capacity increased from 59.46% to 78.26% and from 17.84 mg/g to 23.48 mg/g, respectively. The cadmium adsorption was certainly generated by an increase in the diffusion coefficient and, consequently, a better diffusion of cadmium ions from the solution to the adsorbent surface of the silica gel.^{47,48}

From the same source (Figure 3(a)), we observed that between 300 and 500 rpm, the adsorption rate and capacity remained constant (78.26 %, 23.48 mg/g). This result was certainly caused by the cessation of external diffusion and, consequently, the elimination of the liquid barrier to mass diffusion.¹⁹ Based on this information, we opted for a V_{ag} stirring speed of 300 rpm as the most suitable.

3. 5. Effect of Initial pH

It is widely recognized that solution pH has a significant influence on the adsorption process, particularly with respect to the adsorption of metal pollutants, due to its impact on adsorbent surface charge and speciation. metallic pollutants in aqueous environments.^{2,19} In order to better understand the experimental results from this stage, it is essential to identify the zero charge point (ZPC). The identification of the point of zero charge (ZPC or pH_{ZPC}) is demonstrated in Figure 3(b). The study of the influence of pH is shown in Figure 3(c).

From the analysis of Figure 3(c), we determined that the value of zero charge point (pH_{ZPC}) is 4.2. This outcome allowed us to predict that the adsorption of cadmium ions is more efficient at pH > 4.2. It is true that the cadmium removal efficiency greatly improved when the pH exceeded the pH_{ZPC}, resulting in an increase of 58.76% and 17.63%, respectively, in the yield and the amount removed between pH 4, 2 and 6 (Figure 3(c)). It is important to mention that the increase in the rate of cadmium elimination at pH > 6 was also generated by chemical precipitation. Indeed, it has been cited in the literature that the formation of Cd(OH)₂ starts progressively at pH > 6.^{49–52} From these details, we concluded that the adsorption of cadmium on silica gel took place efficiently at pH 6 under the effect of electrostatic interactions.^{53,54}

Regarding a pH varying from 2.5 to 4, we observed that the adsorption rates and the experimental adsorbed quantity were low. The adsorption inefficiency was mainly caused by the electrostatic repulsion effect instituted between the adsorbent and the adsorbate.²⁰ In addition, the excess H⁺ constituted a partial obstacle between cadmium ions and the adsorbent surface.¹⁷ The interaction between the adsorbent surface of silica and cadmium in solution is shown in Figure 4

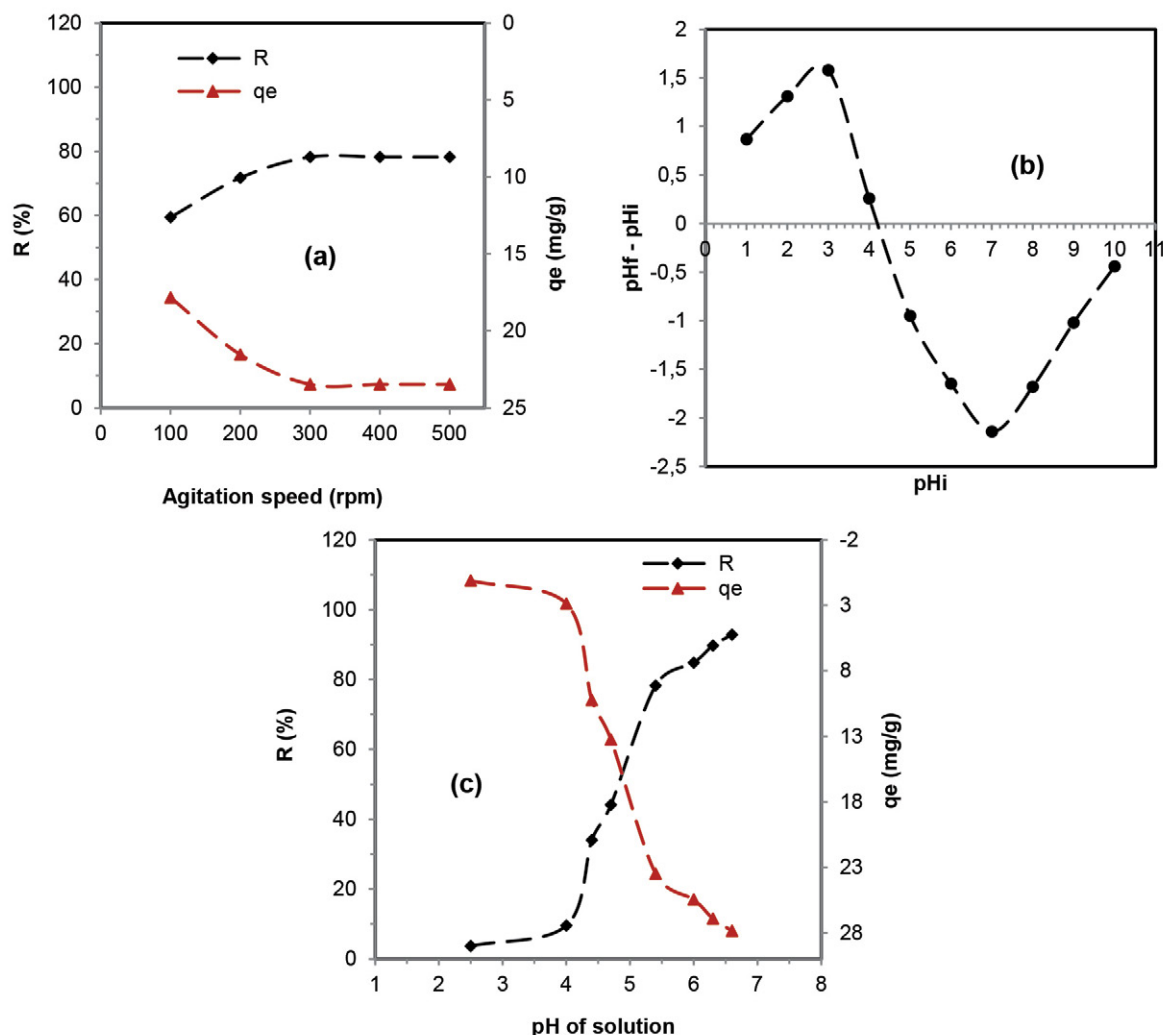


Figure 3. (a) Effect of agitation speed: $t_c = 60$ min; $C_0 = 30$ mg/L; $pH = 5.4$; $T = 20^\circ\text{C}$; $\varnothing_s = 500$ μm ; $m = 1$ g, (b) Zeta potential as a function of solution pH, (c) Effect of initial pH: $t_c = 60$ min; $C_0 = 30$ mg/L; $V_{ag.} = 300$ rpm; $pH = 2.5, 4.4, 4.7, 5.3, 6, 6.3$ and 6.6 ; $T = 25^\circ\text{C}$; $\varnothing_s = 400$ μm ; $m = 1$ g

According to the study by M'barek et al.,⁸ the ideal pH for the adsorption of cadmium on mesoporous silica, zeolite-supported zerovalent iron nanoparticles and cellulose was 6. In the same order of ideas, it has also been evoked that cadmium was efficiently adsorbed on natural Bolivian zeolite treated with NaCl,³⁸ on polyacrylonitrile/amidoxime covered with cellulose,³⁹ on wastewater treatment sludge,⁴⁰ and on kaolin,⁴³ with a pH ranging from 5 to 6.

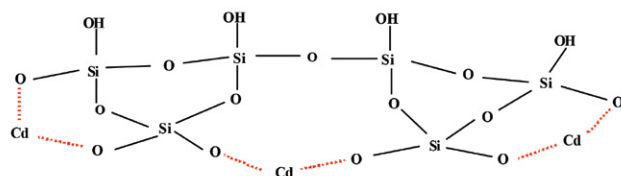


Figure 4. Diagram of the cadmium adsorption mechanism on the silica gel: Presentation of the electrostatic interaction between O^- and Cd^{++}

2. 6. Effect of Particle Size

The influence of solid particle size (\varnothing_s) on the sorption process of cadmium in solution by silica gel was discussed for different sizes, namely 100, 200, 300, 400, and 500 μm (Figure 5(a)).

The experimental results indicated that cadmium adsorbed efficiently at a particle size (\varnothing_s) of 200 μm . It was observed that by reducing the particle size from 500 to 200 μm , the experimental adsorption capacity and yield evolved by 17.73% and 5.32 mg/g, respectively (Figure 5(a)). It is highly plausible that the main reason for this efficiency lies in the reduction in the particle size of the solid, which resulted in an extension of the adsorption surface.^{16,55} Indeed, the larger the surface area, the more efficient the adsorption since this phenomenon is controlled by the ratio between the surface area of the adsorbent and the volume of the adsorbate.⁵⁶ It should be emphasized that for a particle size (\varnothing_s) of 100 μm , we observed a divergence from what was mentioned previously. Between 200 and 100 μm ,

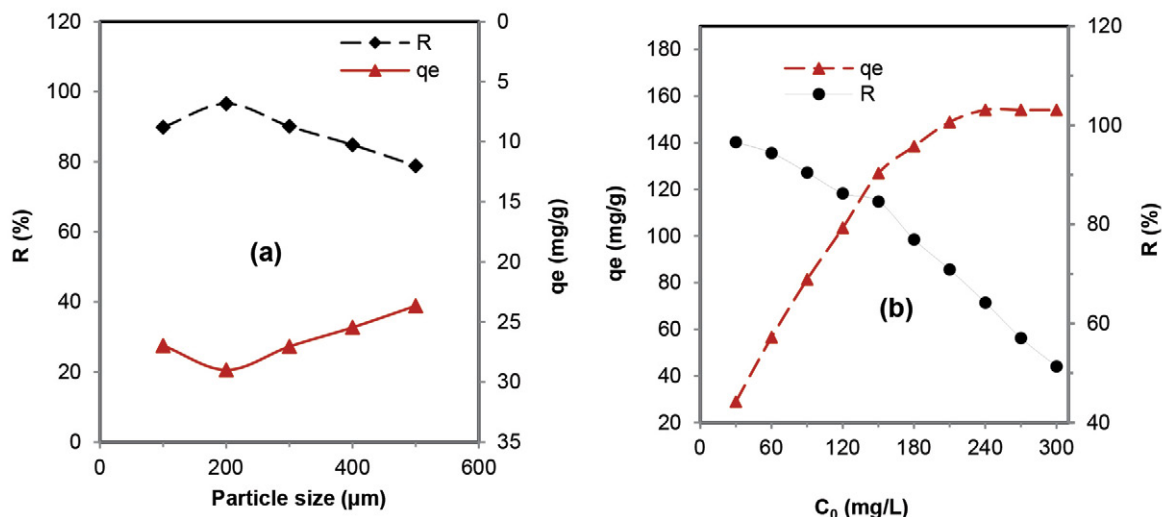


Figure 5. (a) Effect of particle size: $t_c = 60$ min; $C_0 = 30$ mg/L; $V_{ag} = 300$ rpm; pH = 5.8; $T = 20$ °C; $m_s = 1$ g, (b) Effects of Initial Concentration: $t_c = 60$ min; $V_{ag} = 300$ rpm; pH = 5.8; $\phi_s = 200$ μm, $T = 20$ °C; $m_s = 1$ g

the adsorption capacity and yield decreased by 6.73% and 2.02 mg/g, respectively. The regression in the efficiency of adsorption can certainly be due to the agglomeration of the silica gel particles, that is to say, to their evolution into larger particles (coalescence phenomenon).^{17,57}

3. 7. Effects of Initial Concentration

In this process, the study of the influence of the initial concentration is decisive since it allows us to trace the experimental adsorption isotherms and thus allows us to determine the maximum adsorption quantity. In order to achieve this objective, we examined the action of the initial concentration of 30 to 300 mg/L under specific operating conditions (Figure 5(b)).

From the experiments carried out, we observed that the value of the adsorption capacity progressed with the rise in the initial concentration, and then it became constant despite the supply of cadmium ions (Figure 5(b)). The adsorption capacity increased from 28.98 to 154.11 mg/g for an initial concentration of $30 \leq C_0 \leq 240$ mg/L. It is likely that this performance is attributable to the continued increase in the initial concentration, which generated a strong driving force. The latter made the transfer of cadmium ions from the solution to the adsorbent easier by reducing the resistance to mass transfer.^{17,58,59} On the other hand, from $C_0 \geq 240$ mg/L, the adsorption capacity remained constant (154.11 mg/g). The stability of the adsorption capacity was certainly due to the saturation of the adsorbent surface and also to the elimination of external diffusion resistances.^{16,19} The experiment results also showed that the cadmium adsorption rate decreased with increasing initial concentrations (Figure 5(b)), where its value gradually dropped from 96.6 to 51.37%. The progressive decrease in the adsorption rate was probably generated by the uninterrupted addition of cadmium ions by supply to an invariable active surface (constant number of active adsorption sites).^{2,18}

By examining the maximum amount of cadmium adsorbed by different adsorbents, including silica-coated metal organic framework (634 mg/g),⁵ mesoporous silica (3.62 mg/g),⁸ zerovalent iron supported by a zeolite (63.14 mg/g),⁸ orange peels (59.5 mg/g),⁸ cellulose chelating sulfur (54.7 mg/g),⁸ bone meal apatite (116.16 mg/g),¹⁴ egg-shell (217.4 mg/g),¹⁵ and NaCl-treated Bolivian natural zeolite (25.6 mg/g),³⁸ it has been established that silica gel prepared from blast furnace slag has a capacity fairly high adsorption rate (154.11 mg/g) and constitutes a promising adsorbent for the removal of cadmium in wastewater.

3. 8. Adsorption Isotherms

Adsorption isotherm models were approached to evaluate the maximum quantities adsorbed and also to specify the interactions reacting in this process. With this in mind, we selected for suitable models, namely the Freundlich, Langmuir and Temkin models.^{17,51} Their linear forms are represented by equations 3, 5, and 6, respectively. Equation 4 describes the separation factor R_L of the Langmuir model.

$$\log q_e = \log k_F + \frac{1}{n} \log C_e \quad (3)$$

$$\frac{C_e}{q_e} = \frac{1}{q_{max}} C_e + \frac{1}{q_{max} k_L} \quad (4)$$

$$R_L = \frac{1}{1 + C_0 b} \quad (5)$$

$$q_e = B_T \ln A_T + B_T \ln C_e \quad (6)$$

Where q_{max} : q_e : adsorbed capacity maximum and at equilibrium (mg/g), C_e , C_0 : concentration at equilibrium and initial (mg/L), k_L : Langmuir constant ($L \cdot mg^{-1}$), k_F : Freundlich constant ($mg \cdot g^{-1}$) ($ml \cdot mg^{-1}$)^{1/n}, $1/n$: adsorption Intensity, $B_T = \frac{RT}{b_T}$, A_T : equilibrium binding constant (L/g), R : universal gas constant (8.314 J/mol/K), T : absolute temperature in Kelvin, b_T : constant related to heat of sorption ($kJ \cdot kmol^{-1}$).

Table 2. Isotherm parameters for cadmium adsorption

Freundlich			Langmuir			Temkin			
k_F ($\text{mg}\cdot\text{g}^{-1}$)($\text{ml}\cdot\text{mg}^{-1}$) ^{1/n}	$1/n$	R^2	q_{max} (mg/g)	k_L ($\text{L}\cdot\text{mg}^{-1}$)	R^2	R_L	b_T (kJ/mol)	A_T (L/g)	R^2
27.81	0.34	0.94	153.84	0.154	0.99	0.021–0.17	0.92	2.26	0.95

The plots of the Freundlich, Langmuir Temkin models and their adsorption isotherms are reproduced in Figures 6(a), 6(b), 6(c), and 6(d). The parameter values of the models discussed are displayed in Table 4.

From the results obtained (Table 2), it was proven that the Langmuir model is the best fitted to the experimental points. Indeed, the correlation coefficient of the Langmuir model ($R^2 = 0.99$) was higher than those of Freundlich ($R^2 = 0.94$) and Temkin ($R^2 = 0.95$). In addition, the value of the theoretical adsorption capacity resulting from the Langmuir model (154.11 mg/g) was closer to the experimental adsorbed capacity (153.84 mg/g). From Figure 6(d), we observed that the shape of the plot of the Langmuir isotherm had the same shape as the shape of the

experimental isotherm (type 1). They increase gradually before stabilizing by establishing a saturation level. This outcome confirmed to us that the cadmium adsorption on the silica gel was accomplished on a monolayer and homogeneous surface.^{22,31,60} The value of $1/n$ corresponded to 0.34 (Table 2) and the value of R_L was between 0 and 1, thus affirming the favorability of the adsorption process.^{18,23} The value of the Temkin model parameter (b_T) indicated that the adsorption is physical ($b_T < 8 \text{ KJ/mol}$).⁶⁰

3. 9. Kinetics of Adsorption

Reputed models in the field of solid-liquid adsorption, namely, pseudo-first-order (PFO), pseudo-second-order (PSO), and

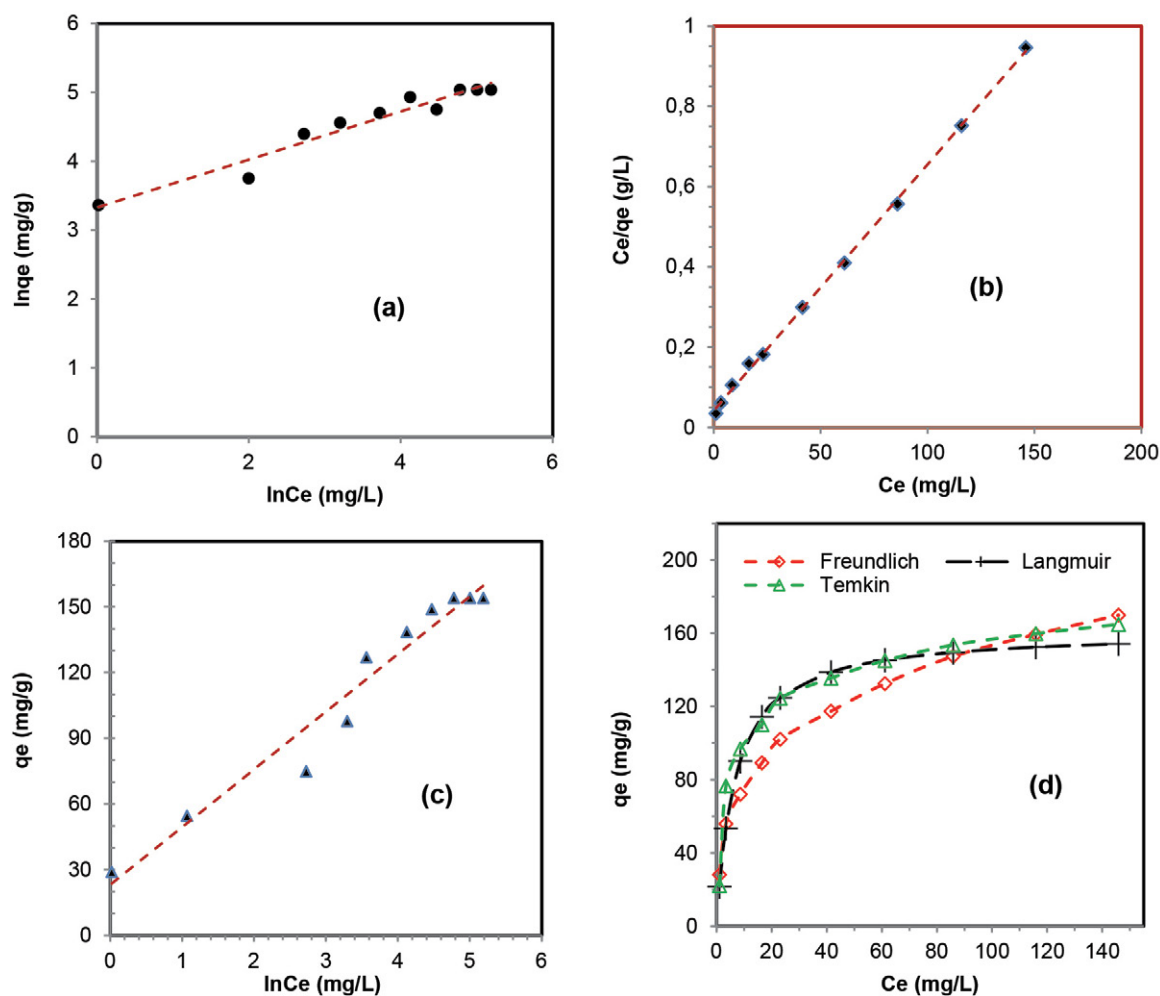


Figure 6. (a) Freundlich model presentation, (b) Langmuir model presentation, (c) Temkin model presentation, (d) Presentations of adsorption isotherms. $t_c = 60 \text{ min}$; $C_0 = 30\text{--}300 \text{ mg/L}$; $V_{ag} = 300 \text{ rpm}$; $\text{pH} = 6$; $\phi_s = 200 \mu\text{m}$, $T = 20 \text{ }^\circ\text{C}$; $m = 1 \text{ g}$

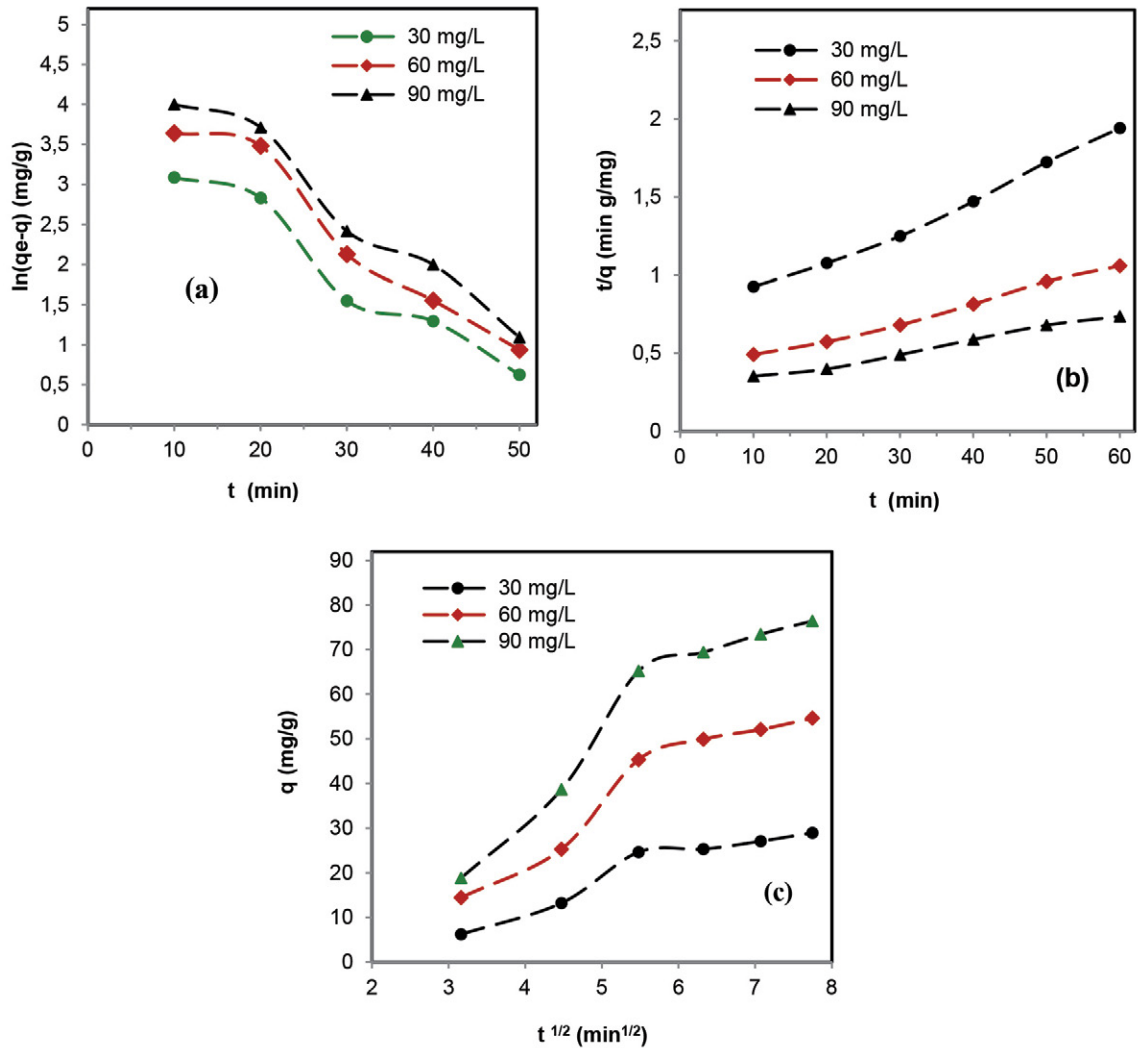


Figure 7. (a) pseudo-first-order model, (b) pseudo-second-order model, (c) internal diffusion: $t_c = 60$ min; $C_0 = 30\text{--}300$ mg/L; $V_{ag} = 300$ rpm; pH = 6; $\phi_s = 200$ μm , $T = 20$ $^\circ\text{C}$; $m = 1$ g

ond-order (PSO), and intraparticle diffusion (IPD) kinetic models, have been used to discuss the kinetics of adsorption of cadmium in solution on silica gel (SG) prepared from slag. The PFO, PSO and IPD models are described by equations 7, 8, and 9 respectively.^{18,35}

$$\ln(q_e - q) = -k_L t + \ln q_e \quad (7)$$

$$\frac{t}{q} = \frac{1}{k_B q_e^2} + \frac{t}{q_e} \quad (8)$$

$$q = k_W \sqrt{t} + C_{In} \quad (9)$$

where q and q_e : quantity adsorbed at time t and at equilibrium (mg/g), t : time of adsorption process, k_L : pseudo-first-order constant (min^{-1}), k_B : pseudo second order constant (g/mg min), k_W : internal diffusion constant ($\text{mg/m. min}^{1/2}$), and C_{In} : intercept.

Plots of $\ln(q_e - q)$ versus t , t/q versus t , and q versus \sqrt{t} are illustrated in Figures 7(a), 7(b), and 7(c), respectively. The adjustment results are produced in Table 3.

Table 3. Kinetic parameters

C_0 (mg/L)	$q_{e_{exp}}$ (mg/g)	Pseudo-first-order			Pseudo-second-order			Intraparticle diffusion		
		K_L (min^{-1})	$q_{e_{theo}}$ (mg/g)	R^2	K_B (g/mg min)	$q_{e_{theo}}$ (mg/g)	R^2	C_{int}	K_W (mg/g.min)	R^2
30	28.98	0.065	45.40	0.94	0.086	29.41	0.99	8.1	5.09	0.91
60	56.64	0.072	90.91	0.95	0.008	58.82	0.99	5.09	9.29	0.92
90	81.43	0.077	134.83	0.94	0.006	83.33	0.99	0.91	12.97	0.91

According to Table 3, it appears that the regression coefficients of PSO ($R^2 \geq 0.99$) are higher than those of PFO ($R^2 \leq 0.95$). Furthermore, the estimated adsorption capacities of PSO were practically equivalent to the actual capacities. From this information, we judged that the adsorption process of cadmium on SG follows pseudo-second order kinetics.^{16,35}

It is reported in the literature that cadmium adsorbed on various adsorbents, such as silica-coated metal organic framework, Canna indica-derived biochar, thermally activated sepiolite, layered double hydroxide nanoparticles stabilized on iron slag, modified biochar, virgin and acid-modified kaolinite clay, and calcium carbonate from eggshells, exhibits pseudo-second-order kinetics.^{5,6,9,12–15}

From Figure 7(c), it was observed that the plots were multilinear and did not converge towards the origin, which is not in agreement with the conditions formulated by Weber and Morris (linearity of straight lines and their passage through the origin).⁶¹ Furthermore, it was specified that the correlation coefficients were greater than 0.9 (Table 3). The mentioned data allowed us to conclude that intraparticle diffusion is not the only mechanism regulating the adsorption of cadmium on silica gel.^{17,62,63} Indeed, the adsorption of cadmium was first controlled by external diffusion due to agitation of the solution,⁴⁷ then by intraparticle diffusion.

3. 10. Effect of Temperature

In this passage, we discussed the effect of temperature on the adsorption of cadmium by silica gel, taking into consideration various temperature (Figure 8(a)). The experiments accomplished have unequivocally demonstrated that the adsorption efficiency of cadmium decreases when the temperature of the medium increases. In fact, a reduction of 28.73% in yield and 8.62 mg/L in adsorption capacity was recorded due to an increase in temperature. (Figure 8(a)). The lowering of cadmium adsorption efficiency with increasing solution temperature was certainly caused by the evolution of the random movement of cadmium ions, attenuating the interdependence between adsorbent and adsorbate.⁶⁴ Taking these results into account, we predicted that cadmium removal by adsorption on silica gel is exothermic.^{21,65,66}

It should be noted that, contrary to what has been observed, temperature can cause an increase in cadmium

adsorption, as reported in the literature. Significant improvements in the adsorption of cadmium in solution were found when the temperature was increased with different adsorbents, including pristine and acid-modified kaolinite clay, electrospun composite nanofibre, modified biochar, gel-like weak acid resin, acid-modified chili peppers, and NiO nanoparticles.^{10,13,14,67,68,69}

With the same purpose, a thermodynamic study was carried out to identify the nature and mechanisms of interaction favoring this process. The explanation of these effects (nature and mechanism of interaction) strongly depends on the values of the thermodynamic parameters, namely ΔG° , ΔH° , ΔS° and E_a . Equation 10 was used to calculate ΔG° , while equation 11 was used to determine ΔH° and ΔS° , and E_a was deduced from equation 13.^{2,16,17} Equation 12 describes the distribution coefficient K_d .¹⁹ The Arrhenius equation (Eq. 13) was used to calculate the activation energy.²

$$\Delta G^\circ = -RT \ln k_d \quad (10)$$

$$\ln k_d = \frac{\Delta H^\circ}{R} \times \frac{1}{T} + \frac{\Delta S^\circ}{R} \quad (11)$$

$$K_d = \frac{C_i - C_e}{C_e} \times \frac{V}{M} = \frac{q_e}{C_e} \quad (12)$$

$$\ln k_{app} = \ln A - \frac{E_a}{RT} \quad (13)$$

Where ΔG° is the Gibbs free energy (kJ/mol), ΔS° is entropy (kJ/K), ΔH° is enthalpy (kJ/mol), R is the universal gas constant (8.314 J/mol.K), K_d is distribution coefficient (L/g), E_a is activation energy (kJ/mol), k_{app} apparent constant (g/L.min), T is the absolute temperature (K) and A is frequency factor.

The apparent constant k_{app} was calculated from the function $\ln(Ct) = f(t)$ at different temperatures (20, 35, 45, and 55 °C). Van't Hoff and Arrhenius plots are represented by Figures 8(b) and 8(c). The values of free enthalpy, enthalpy, entropy, activation energy, apparent constant and distribution coefficient are displayed in Table 4.

From Figure 8(b), it was noticed that there was a good interdependence between the Van't Hoff model and the experimental data ($R^2 = 0.99$) (Table 4).² The decrease in the distribution coefficient (K_d) with increasing temperature made it possible to clarify that the adsorption of cadmium was favorable in the least heated solutions.^{19,70}

From Table 4, it was identified that the Gibbs energy values are negative and less than 20 kJ/mol, which ex-

Table 4. Thermodynamic parameters of cadmium adsorption

T (K)	ΔH° (kJ/mol)	ΔG° (kJ/mol)	ΔS° (kJ/K)	E_a (kJ/mol)	R^2	K_d (L/g)	k_{app} (g/L.min)
293		-18.11				1.79	5.22×10^{-2}
308		-18.87				1.69	6.32×10^{-2}
318	-6.98	-19.38	-25.67×10^{-3}	8.45	0.99	1.60	6.86×10^{-2}
328		-19.74				1.56	8.54×10^{-2}

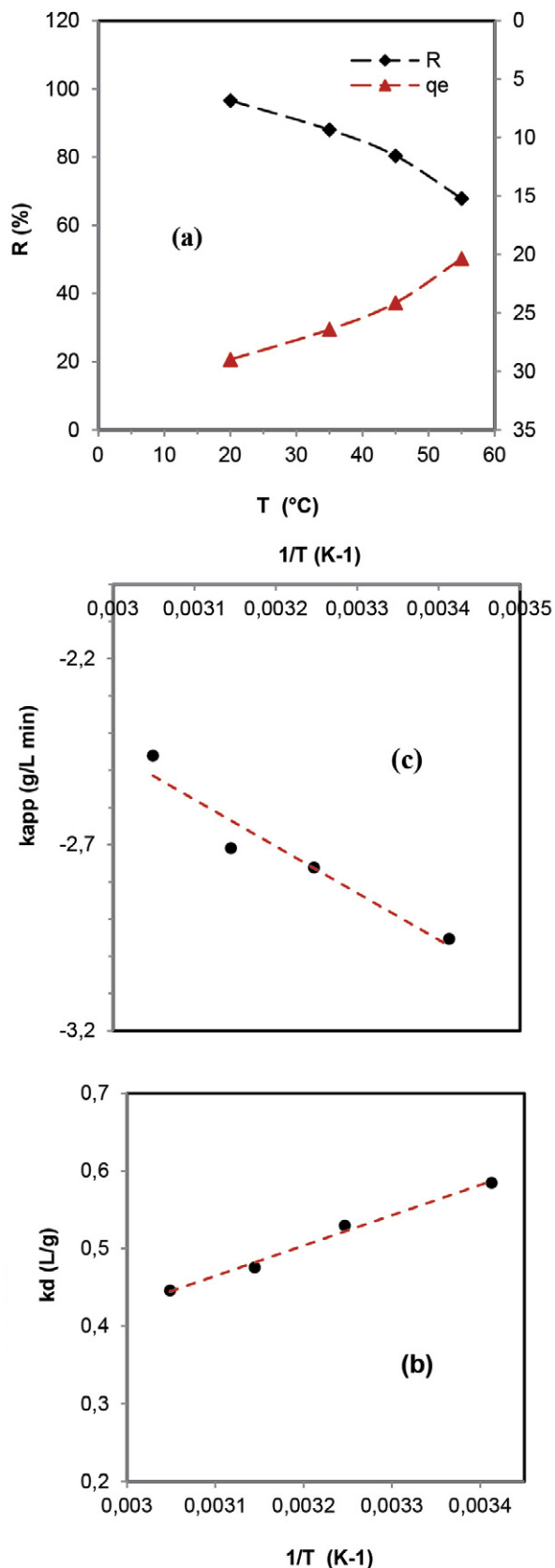


Figure 8. (a) Effect of temperature: $t_c = 60$ min; $C_0 = 30$ mg/L; $V_{ag} = 300$ rpm; pH = 6; $T = 20, 35, 45$ and 55 °C; $\varnothing = 200$ μ m; $m = 1$ g, (b) Van't Hoff equation plot, (c) Arrhenius equation plot

plained that the sorption of cadmium is spontaneous and occurred under the influence of physical interactions.^{17,39} The increase in the temperature of the solution resulted in a regression of ΔG° from -18.11 to -19.74 kJ/mol, thus demonstrating that mass transfer is inversely proportional to the temperature of the medium.^{65,71} The negative value of the enthalpy (-6.98 kJ/mol) revealed that this process is exothermic (Table 4).^{18,39} In addition, it also certified that this cadmium removal process is a physical adsorption, whose enthalpy value is less than 40 kJ/mol.^{20,72} The negative value of entropy highlighted the reduction of randomness at the adsorbent-adsorbate interface (Table 4).^{16,55} The reduction in random displacements at the solid-liquid interface was probably caused by the considerable electrostatic interaction between the cadmium ions and the adsorbent.^{73,74} Based on the activation energy value (Table 4), we reaffirmed that the removal of cadmium in solution by silica gel is physical adsorption.^{2,62,75}

From this information, we could conclude that the adsorption of cadmium on silica gel was spontaneous, exothermic, and less entropic. Furthermore, we deduced that the elimination was carried out by physical adsorption under the effect of electrostatic interactions. It should be emphasized that the adsorption of cadmium on various adsorbents is generally a spontaneous process, as clearly demonstrated in the literature.^{13,39,44,67,69,76}

3. 11. Reuse of Adsorbent

Figure 9(a) illustrates the kinetics of cadmium desorption from silica gel in the presence of different solutions. Figure 9 (b) illustrates the adsorption/desorption rate of cadmium under the effect of HCl at 0.05 M.

From the experimental data, it was noticed that the presence of HCl in solution significantly facilitated the desorption of cadmium ions from the saturated silica gel (Figure 9(a)). This outcome can be caused by the formation of a large number of H^+ protons, which will affect the nature of the adsorbent surface.⁷⁷ According to Figure 9(b), it was specified that the silica gel has the ability to be reused for five consecutive cycles using 0.05 M hydrochloric acid as the eluent. It should be clarified that the loss of mass and the exhaustion of active adsorption sites are surely responsible for the inefficiency of the desorption process after the fifth cycle.^{20,78}

It is important to mention that the desorption percentage of cadmium ions from the adsorbent surface of saturated silica gel was examined using Equation 14.

$$\text{Desorption rate} = \frac{q_{des}}{q_{ads}} \times 100 \quad (14)$$

Where q_{ads} is the adsorbed quantity at equilibrium (mg/g) for cycle I and q_{ads} is the desorbed quantity at equilibrium (mg/g) of each cycle.

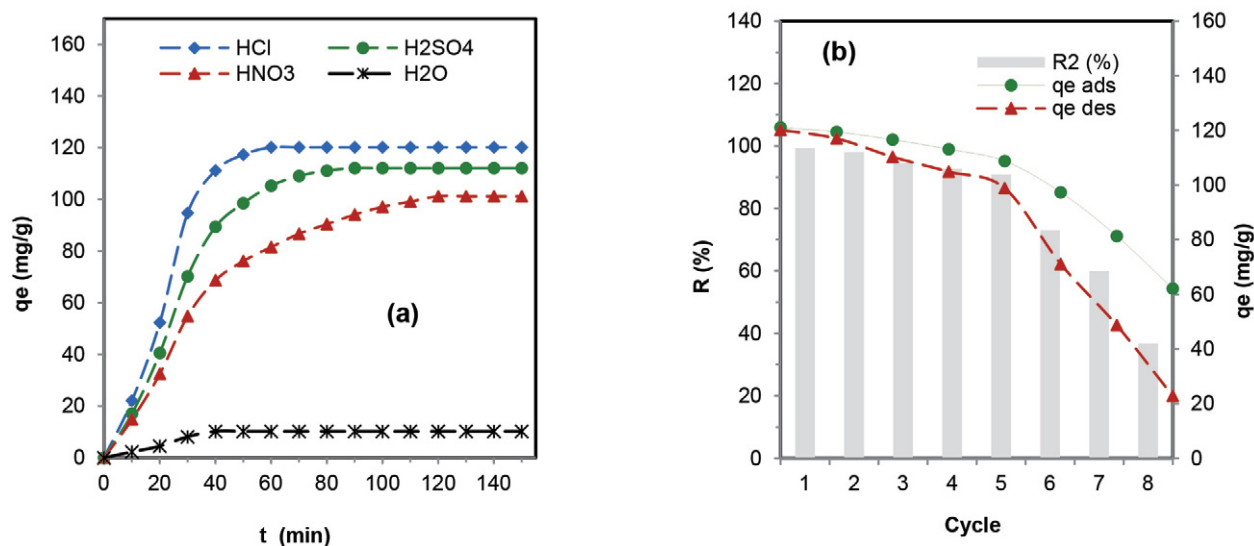


Figure 9. (a) desorption kinetics, (b) adsorption and desorption performance of cadmium

4. Conclusion

This study investigated the batch adsorption of cadmium ions onto silica gel (SG) prepared from blast furnace slag. The results demonstrated that silica gel contained 96.14% SiO₂. Its ZPC corresponds to pH 4.2, and its specific surface area is 484 m²/g. From the experimental results, it was found that the adsorption capacity of cadmium on the silica gel (q_e = 154.11 mg/g) was particularly influenced by the determining parameters, namely contact time (60 min), stirring speed (300 rpm), dosage of the adsorbent (1 g/L), pH (6), temperature (20 °C), particle size (200 μm), and initial concentration (240 mg/L). Modeling of experimental data indicated that the Langmuir model (R² = 0.99; q_{max} = 134.06 mg/g) is the most commonly adopted to represent the adsorption of cadmium on silica gel, thus affirming a monolayer adsorption on homogeneous active sites. The R_L and n values of the Langmuir and Freundlich models, respectively, revealed that the adsorption was favorable. The value of b_T from the Temkin model demonstrated that the adsorption was accomplished physically. The kinetic study showed that adsorption follows pseudo-second-order kinetics (R² ≥ 99). Furthermore, it clarified that the transport of cadmium was carried out through external and intraparticle diffusion. The values of Gibbs energy (ΔG° < 0 kJ/mol), enthalpy (ΔH° < 0 kJ/mol), and entropy (ΔS° < 0 J/K) demonstrated, respectively, that the adsorption of cadmium on silica gel is spontaneous, exothermic, and less entropic. The values of enthalpy (ΔH) and activation energy (E_a) revealed that this process was physically accomplished under the effect of electrostatic attraction. The desorption process demonstrated that the application of 0.05 M HCl as eluent significantly improved its reuse for five cycles. From this study, we reasoned that silica gel can be exploited as a reliable adsorbent to remove cadmium ions from wastewater.

Conflict of Interest

The authors declare that they have no known competing financial interests or personal relationships that could have appeared to influence the work reported in this paper. Competing interests.

5. References

- M. Mansoorianfar, H. Nabipour, F. Pahlevani, Y. Zhao, Z. Hussain, A. Hojjati-Najafabadi, H.Y. R. Hoang Pei, *Environ. Res.* **2022**, 214, 114113. DOI:10.1016/j.envres.2022.114113
- T. Chouchane, A. Boukari, *Anal. Bioanal. Chem. Res.* **2022**, 9, 381–399. DOI:10.22036/ABCR.2022.325691.1716
- V. K. Gupta, P. J. M. Carrott, M. M. L. Ribeiro Carrott, Suhas, *Crit. Rev. Environ. Sci. Technol.* **2009**, 39, 783–842. DOI:10.1080/10643380801977610
- K. Pyrzynska, *J. Environ. Chem. Eng.* **2019**, 7, 102795. DOI:10.1016/j.jece.2018.11.040
- S. Ul Mehdi, K. Aravamudan, *Mater. Today: Proc.* **2022**, 61, 487–497. DOI:10.1016/j.matpr.2021.12.304
- X. Cui, S. Fang, Y. Yao, T. Li, Q. Ni, X. Yang, Z. He, *Sci. Total Environ.* **2016**, 562, 517–525. DOI:10.1016/j.scitotenv.2016.03.248
- F. Zhou, G. Ye, Y. Gao, H. Wang, S. Zhou, Y. Liu, C. Yan, *J. Hazard. Mater.* **2021**, 423, 127104. DOI:10.1016/j.jhazmat.2021.127104
- I. M'barek, H. Slimi, A. K. D. AlSukaibi, F. Alimi, R. Hadj Lajimi, L. Mechi, R. ben Salem, Y. Moussaoui, *Arab. J. Chem.* **2022**, 15, 103679. DOI:10.1016/j.arabjc.2021.103679
- L. Semerjian, *J. Hazard. Mater.* **2010**, 173, 236–242. DOI:10.1016/j.jhazmat.2009.08.074
- S. Tasharofi, Z. Rouzitalab, D. M. Maklavany, A. Esmaeili, M. Rabieezadeh, M. Askarieh, A. Rashidi, H. Taghdisian, *Sci. Total Environ.* **2020**, 736, 139570.

- DOI:10.1016/j.scitotenv.2020.139570
11. M. Mousakhani, N. Sarlak, *Mater. Chem. Phys.* **2020**, *256*, 123578. DOI:10.1016/j.matchemphys.2020.123578
 12. T. S. Hussein, A. A. H., Faisal, *Arab. J. Chem.* **2023**, *16*, 105031. DOI:10.1016/j.arabjc.2023.105031
 13. T. Liu, Y. Lawluyv, Y. Shi, J. O. Ighalo, Y. He, Y. Zhang, P-S. Yap, *J. Environ. Chem. Eng.* **2022**, *10*, 106502. DOI:10.1016/j.jece.2021.106502
 14. L. S. Mustapha, A.S. Yusuff, P.E. Dim, *Heliyon* **2023**, *9*, e18634. DOI:10.1016/j.heliyon.2023.e18634
 15. K. Annane, W. Lemlikchi, S. Tingry, *Biomass Conv. Bioref.* **2021**, *13*, 6163–6174. DOI:10.1007/s13399-021-01619-2
 16. T. Chouchane, O. Khireddine, A. Boukari, *J. Eng. Appl. Sci.* **2021**, *68*, 00039–3. DOI:10.1186/s44147-021-00039-3
 17. T. Chouchane, S. Chibani, O. Khireddine, A. Boukari, *Iran. J. Mater. Sci. Eng.* **2023**, *20*, 1–13. DOI:10.22068/ijmse.3011
 18. T. Chouchane, A. Boukari, O. Khireddine, S. Chibani, S. Chouchane, *J. Eng. Appl. Sci.* **2023**, *70*, 58. DOI:10.1186/s44147-023-00218-4
 19. T. Chouchane, A. Boukari, O. Khireddine, S. Chibani, S. Chouchane, *Eurasian J. Chem.* **2023**, *38*, 115–130. DOI:10.31489/2959-0663/2-23-3
 20. T. Chouchane, O. Khireddine, S. Chibani, A. Boukari, *Anal. Bioanal. Chem. Res.* **2023**, *10*, 251–268. DOI:10.22036/ABCR.2022.365182.1843
 21. C. Li, X. Li, Y. Yu, Q. Zhang, L. Li, H. Zhong, S. Wang, *J. Ind. Eng. Chem.* **2022**, *105*, 63–73. DOI:10.1016/j.jiec.2021.08.017
 22. Q. T. N. Le, E. L. Vivas, K. Cho, *J. Ind. Eng. Chem.* **2021**, *95*, 57–65. DOI:10.1016/j.jiec.2020.12.003
 23. A.S. Dhmees, N.M. Klaleel, S.A. Mahoud, *Egypt. J. Pet.* **2018**, *27*, 1113–1121. DOI:10.1016/j.ejpe.2018.03.012
 24. T. Tsutsumi, S. Nishimoto, Y. Kameshima, M. Miyake, *J. Hazard. Mater.* **2014**, *266*, 174–181. DOI:10.1016/j.jhazmat.2013.12.024
 25. R.E. Kukwa, D. T. Kukwa, A. D. Oklo, T. T. Ligom, B. Ishwah, J.A. Omenka, *Am. J. Chem. Eng.* **2020**, *8*, 48–53. DOI:10.11648/j.ajche.20200802.12
 26. W. A. A. Sudjarwo, M. M. F. Bee, AIP Conf. Proc. 2017, 1855, 020019. DOI:10.1063/1.4985464
 27. F. Demir, E. M Derun, *J. Non-Cryst. Solids* **2019**, *524*, 119649. DOI:10.1016/j.jnoncrysol.2019.119649
 28. S.S. Owoeye, F. I. Jegede, S. G. Borisade, *Mater. Chem. Phys.* **2020**, *248*, 122915. DOI:10.1016/j.matchemphys.2020.122915
 29. Owoeye, S. S., Abegunde, S. M., Oji, B., *Nano-Struct. Nano-Objects* **2021**, *25*, 100625. DOI:10.1016/j.nanoso.2020.100625
 30. A. Bilgiç, A. Çimen, *RSC Adv.* **2019**, *9*, 37403–37414. DOI:10.1039/C9RA05810A
 31. Y.L. Nirmah, A.P.K Subandi., S. Suprpto, *Heliyon* **2022**, *8*, e11997. DOI:10.1016/j.heliyon.2022.e11997
 32. M. Najafi, R. Rostamian, A.A. Rafati, *Chem. Eng. J.* **2011**, *168*, 426–432. DOI:10.1016/j.cej.2010.12.064
 33. F. An, B. Gao, *Desalination* **2009**, *249*, 1390–1396. DOI:10.1016/j.desal.2009.04.004
 34. Y. Niu, R. Qu, C. Sun, C. Wang, H. Chen, C. Ji, Y. Zhang, X. Shao, F. Bu, *J. Hazard. Mater.* **2013**, *244–245*, 276–286. DOI:10.1016/j.jhazmat.2012.11.042
 35. L. Jinrong, W. Xiaonan, L. Yao, C. Wenquan, L. Yinghua, *Surf. Interfaces* **2018**, *12*, 108–115. DOI:10.1016/j.surfin.2018.04.005
 36. A. A. Basaleh, M. H. Al-Malack, T.A. Saleh, *J. Environ. Chem. Eng.* **2021**, *9*, 105126. DOI:10.1016/j.jece.2021.105126
 37. S. Brunauer, P. H. Emmett, E. J. Teller, *Am. Chem. Soc.* **1938**, *60*, 309–319. DOI:10.1021/ja01269a023
 38. L. Velarde, D. Nikjoo, E. Escalera, F.Akhtar, *Heliyon* **2024**, *10*, e24006. DOI:10.1016/j.heliyon.2024.e24006
 39. H.A. Abdelmonem, T. F. Hassanein, H. E. Sharafeldin, H. Gomaa, A. S. A. Ahmed, A. M. Abdel-lateef, E. M. Allam, M. F. Cheira, M. E. Eissa, A. H. Tilp, *Colloids Surf. A: Physicochem. Eng. Asp.* **2024**, *684*, 133081. DOI:10.1016/j.colsurfa.2023.133081
 40. Y. Jiang, Y. Xing, S. Liu, S. Tan, Q. Huang, X. Luo, W. Chen, *Biomass Bioenergy* **2023**, *173*, 106787. DOI:10.1016/j.biombioe.2023.106787
 41. E. Siswoyo, Y. Mihara, S. Tanaka, *Appl. Clay Sci.* **2014**, *97–98*, 146–152. DOI:10.1016/j.clay.2014.05.024
 42. N. Kataria, V.K. Garg, *Chemosphere* **2018**, *208*, 818–828. DOI:10.1016/j.chemosphere.2018.06.022
 43. S. Mustapha, M.M. Ndamitso, A.S. Abdulkareem, J.O. Tijani, A.K. Mohammed, D.T. Shuaib, *Heliyon* **2019**, *5*, e02923. DOI:10.1016/j.heliyon.2019.e02923
 44. Y. Zhao, S. Yang, D. Ding, J. Chen, Y. Yang, Z. Lei, C. Feng, Z. Zhang, *J. Colloid Interface Sci.* **2013**, *395*, 198–204. DOI:10.1016/j.jcis.2012.12.054
 45. R. Foroutan, R. Mohammadi, S. Farjadfard, H. Esmaeili, B. Ramavandi, G.A. Sorial, *Adv. Powder Technol.* **2019**, *30*, 2188–2199. DOI:10.1016/j.apt.2019.06.034
 46. P. Simha, P. Banwasi, M. Mathew, *Procedia Eng.* **2016**, *148*, 779–786. DOI:10.1016/j.proeng.2016.06.557
 47. A. Gupta, C. Balomajumder, *Appl. Water Sci.* **2017**, *7*, 4361–4374. DOI:10.1007/s13201-017-0582-9
 48. V. Yogeshwaran, A. K. Priya, *Mater. Today: Proc.*, **2021**, *37*, 486–495. DOI:10.1016/j.matpr.2020.05.467
 49. Z. H. Khan, M. Gao, W. Qiu, M. S. Islam, Z. Song, *Chemosphere* **2020**, *246*, 125701. DOI:10.1016/j.chemosphere.2019.125701
 50. S. Wang, T. Terdkiatburana, M.O. Tadé, *Sep. Purif. Technol.* **2008**, *62*, 64–70. DOI:10.1016/j.seppur.2008.01.004
 51. H. Çelebi, G. Gök, and O. Gök, *Sci. Rep.* **2020**, *10*, 1–12. DOI:10.1038/s41598-020-74553-4
 52. E. K. Toss, G. C. Feijoo, A. B. Botelho Junior, D. C. R. Espinosa, M. dos P. G. Baltazar, J. A. S. Tenório, *J. Sustain. Metall.* **2023**, *9*, 860–870. DOI:10.1007/s40831-023-00692-3
 53. R. Foroutan, M. Ahmadlouydarab, B. Ramavandi, R. Mohammadi, *J. Environ. Chem. Eng.* **2018**, *6*, 6049–6058. DOI:10.1016/j.jece.2018.09.030
 54. T. Shi, Z. Xie, Z. Zhu, W. Shi, Y. Liu, M. Liu, X. Mo, *Int. J. Biol. Macromol.* **2023**, *195*, 317–328. DOI:10.1016/j.ijbiomac.2021.12.039
 55. T. Chouchane, M. Yahi, A. Boukari, A. Balaska, S. Chouchane, *J. Mater. Environ. Sci.* **2016**, *7*, 2825–2842.

56. J. N. Wekoye, W.C. Wanyonyi, P. T. Wangila, M. K. Tonui, *Environ. Chem. Ecotoxicol.* **2020**, *2*, 24–1. DOI:10.1016/j.enceco.2020.01.004
57. T. Chouchane, S. Chouchane, A. Boukari, A. Mesalhi, *J. Mater. Environ. Sci.* **2015**, *6*, 924–941.
58. M. Naushad, A. Abdullah, A. A. Al-kahtani, T. Ahamad, R. Awual, T. Tatarchuk, *J. Mol. Liq.* **2019**, *296*, 112075. DOI:10.1016/j.molliq.2019.112075
59. H. Xu, Y. Li, F. Zhou, H. Su, E. Yao, J. Hu, Z. Chen, *Chem. Eng. J.* **2023**, *470*, 144070. DOI:10.1016/j.cej.2023.144070
60. S. Jellali, E. Diamantopoulos, K. Haddad, M. Anane, W. Durner, A. Mlayah, *J. Environ. Manage.* **2016**, *180*, 439–449. DOI:10.1016/j.jenvman.2016.05.055
61. W.J. Weber, J.C. Morriss, *ASCE* **1963**, *89*, 31–59. DOI:10.1061/JSEDAI.0000430
62. B. T. M. Nguyet, N. H. Nghi, N. A. Tien, D. Q. Khieu, H. D. Duc, N. V. Hung, *Acta Chim. Slov.* **2022**, *69*, 7567. DOI:10.17344/acsi.2022.7567
63. S. Jiang, L. Huang, T. A. H. Nguyen, O. K. Y. Sik, V. Rudolph, H. Yang, D. Zhang, *Chemosphere* **2016**, *142*, 64–71. DOI:10.1016/j.chemosphere.2015.06.079
64. X. Y. Wan, Y. Q. Zhan, Z. H. Long, G. Y. Zeng, Y. He, *Chem. Eng. J.* **2017**, *330*, 491–504. DOI:10.1016/j.cej.2017.07.178
65. J.-Y. Do, H. Moradi, D.-S. Kim, J.-K. Yang, Y.-Y. Chang, S. S. Choi, *Diam. Relat. Mater* **2023**, *136*, 110018. DOI:10.1016/j.diamond.2023.110018
66. Y. Zhang, C. Hui, R. Wei, Y. Jiang, L. Xu, Y. Zhao, L. Du, H. Jiang, *Appl. Surf. Sci.* **2022**, *573*, 151627. DOI:10.1016/j.apsusc.2021.151627
67. C. Xiong, C. Yao, L. Wang, J. Ke, *Hydrometallurgy* **2009**, *98*, 318–324. DOI:10.1016/j.hydromet.2009.05.008
68. N. Nkosi, N. D. Shooto, P. Nyamukamba, P. M. Thabede, *Energy Nexus* **2024**, *15*, 100313. DOI:10.1016/j.nexus.2024.100313
69. T. Sheela, Y. A. Nayaka, *Chem. Eng. J.* **2012**, *191*, 123–131. DOI:10.1016/j.cej.2012.02.080
70. Y. Zhang, C. Hui, R. Wei, Y. Jiang, L. Xu, Y. Zhao, L. Du, H. Jiang, *Appl. Surf. Sci.* **2022**, *573*, 151627. DOI:10.1016/j.apsusc.2021.151627
71. X. Y. Wan, Y. Q. Zhan, Z. H. Long, G. Y. Zeng, Y. He, *Chem. Eng. J.* **2017**, *330*, 491–504. DOI:10.1016/j.cej.2017.07.178
72. A. Sari, D. Citak M. Tuzen, *Chem. Eng. J.* **2010**, *162*, 521–527. DOI:10.1016/j.cej.2010.05.054
73. M. Sh. Gohr, A. I. Abd-Elhamid, A. A. El-Shanshory, H. M. A. Soliman, *J. Mol. Liq.* **2022**, *346*, 118227. DOI:10.1016/j.molliq.2021.118227
74. A. Nakhli, M. Bergaoui, C. Aguir, M. Khalfaoui, M. F. M'Henni, A.B. Lamine, *Desalination Water Treat.* **2016**, *57*, 12730–12742. DOI:10.1080/19443994.2015.1052564
75. M. Zhang, Q. Yao, C. Lu, Z. Li, W. Wang, *ACS Appl. Mater. Interfaces* **2014**, *6*, 20225–20233. DOI:10.1021/am505765e
76. I. Khoshkardar, H. Esmaeili, *Acta Chim. Slov.* **2019**, *66*, 208–216. DOI:10.17344/acsi.2018.4795
77. E. Daneshvar, A. Vazirzadeh, A. Niazi, M. Kousha, M. Naushad, A. Bhatnagar, *J. Clean. Prod.* **2017**, *152*:443–453. DOI:10.1016/j.jclepro.2017.03.119
78. E. Igberase, P. Osifo, A. Ofomaja, *J. Environ. Chem. Eng.* **2014**, *2*, 362–369. DOI:10.1016/j.jece.2014.01.008

Povzetek

V študiji je bil silikagel, pridobljen iz plavžne žindre, uporabljen za izločanje kadmija v šaržnem načinu pod delovanjem različnih dejavnikov. Fizikalno-kemijske analize so pokazale, da je modificirana žindra sestavljena samo iz kremena (96,14%). Njegova specifična površina je $484 \text{ m}^2\text{g}^{-1}$ in pH, ki ustreza točki ničelnega naboja, je 4,2. Eksperiment je pokazal, da je pri pH 6 vpliv determinantnih dejavnikov prispeval k povečanju sorpcijske kapacitete, ki je bila izmerjena pri 154,11 mg/g in je bila dosežena na homogeni enoslojni površini ($R_2 = 0,99$). Kinetična analiza je pokazala, da se ta proces ujema s kinetičnim modelom psevdodrugega reda ($R_2 \geq 0,99$). Poleg tega je bilo navedeno, da je difuzija onesnaževala zagotovljena z zunanjo difuzijo in difuzijo znotraj delcev. Vrednosti termodinamskih spremenljivk so pojasnile, da je sorpcija kadmija spontana, eksotermna, z nižjo entropijo in izvedena pod vplivom elektrostatične interakcije. Postopek desorpcije je pokazal, da je bila ponovna uporaba silikagela izvedljiva v petih zaporednih ciklih.



Except when otherwise noted, articles in this journal are published under the terms and conditions of the Creative Commons Attribution 4.0 International License

Scientific paper

Microwave Assisted Synthesis of Methylene Bisthiazolo Arylvinyl Pyrazoles as Potential Biological Agents

Avula Srinivas*

Department of Chemistry, Research and Development Division

Vaagdevi Degree & PG College, Ramnagar, Hanamkonda, Telangana-506001, India

* Corresponding author: E-mail: avula.sathwikreddy@gmail.com

Received: 07-01-2024

Abstract

(2*E*,2'*E*)-1,1'-(5,5'-(5,5'-methylenebis(2-methoxy-5,1-phenylene))bis(3-(4-fluorophenyl)-6-phenyl-3,3a,5,6-tetrahydro-2*H*-pyrazolo[3,4-*d*]thiazole-5,2-diyl))bis(3-phenylprop-2-en-1-ones) **5a–e** were synthesized from (5*Z*,5'*Z*)-2,2'-(5,5'-methylenebis(2-methoxy-5,1-phenylene))bis(5-(4-fluorobenzylidene)-3-phenylthiazolidin-4-ones) **4a–e** through cycloaddition reaction with cinnamic acid hydrazide and evaluated for their antibacterial, antifungal and antinematocidal activity. Among the tested compounds **5b** and **5d** containing chloro and nitro groups were shown to be the most effective against *Ditylenchus myceliophagus* and *Caenorhabditis elegans* with LD₅₀ between 160 and 190 ppm, 190 and 210 ppm respectively. Compounds **5b** and **5e** showed good zone of inhibition against *Bacillus subtilis*, compounds **5c** and **5d** were active against *Staphylococcus aureus*, compounds **5a**, **5c** and **5e** were active against *Chromobacterium violaceum* and compounds **5b**, **5a** and **5d** were the most active against *Klebsiella aerogenes*, *Pseudomonas aeruginosa* and *Bacillus sphaericus*. Compounds **5b** and **5d** showed good inhibition towards *Candida albicans* at the concentration of 3.12 µg/mL which is less than the value for amphotericin B, used as the standard.

Keywords: Methylene bis Heterocycles, Thiazolo 2-arylvinylpyrazoles, Microwave irradiation, Biologically active molecules

1. Introduction

Hybrid heterocycles play very important role in drug discovery. Aza heterocyclic derivatives are widely used for the development of therapeutic molecules,^{1–3} as they are active against different microorganisms. Following the COVID-19 pandemic, this approach received a lot of attention. Natural and synthetic five membered aza heterocycles exhibit different pharmacological activities, cytotoxic and COX inhibitory activity.^{4–10} In recent years, pyrazole derivatives have been used to generate some FDA-approved and commercialized medications, including patented products.

Sulphur-bearing heterocycles create wide interest due to their diverse biological actions. Their derivatives have a variety of biological effects;^{11–21} aza heterocyclic ring (pyrazole ring), when combined with other heterocycles, is an advantageous pharmacophore for the synthesis of novel lead compounds.^{22–25} The pyrazole-tethered thiazole has attracted a lot of interest in recent years because

of its amazing biological properties, which include antimicrobial,^{26–30} antibiofilm,²² as an apoptosis inducer,³¹ anti-inflammatory,^{29,32} anti tubercular,³³ and anti mycobacterial activity.³⁴ Pyrazoles bearing 2-arylvinyl (staryl) group at pyrazole nucleus exhibit powerful biological activity^{35,36} as well as noteworthy physicochemical features.^{37,38}

Microwave processing is an efficient green technology for the conversion of reactants into products.³⁹ Due to the simplicity, atom economy and better yields of multi component reactions⁴⁰ a lot of interest was devoted to this approach.

With this introduction of thiazoles, pyrazoles, 2-arylvinylpyrazoles, microwave processing, inspired by the biological profile of thiazoles, pyrazoles, 2-arylvinylpyrazoles, and part of routine work on development of new hybrid molecules,^{41–46} we have synthesized a series of novel methylene bis(2-arylvinyl)thiazolo pyrazoles, and evaluated their antibacterial, antifungal and antinematocidal activities.

2. Experimental

All the reagents and solvents (of analytical grade) were purchased from Sigma Aldrich. Reactions were monitored and purity of the compounds was checked by thin-layer chromatography (TLC) on pre-coated Merck silica gel plates, and spots were observed by exposing them to UV light or immersing the plates in a 1% aqueous potassium permanganate solution. Separations were performed using silica gel chromatographic columns (60–120 mesh). Microwave reactions were carried out in a compact lab microwave catalytic reactor (ZZKD, WBFY-201), and reaction mixture temperatures were recorded using an immersed fiber optic sensor. All melting points are uncorrected and measured using Fisher John's apparatus. IR spectra were recorded using KBr disks on a Perkin–Elmer FT IR spectrometer. The ^1H NMR and ^{13}C NMR spectra were obtained using a Varian Gemini spectrometer (300 MHz for ^1H and 75 MHz for ^{13}C). Chemical shifts are presented in δ (ppm) with TMS as the internal reference, while coupling constants (J) are reported in Hz units. Mass spectra were collected using a VG micro mass 7070H spectrometer. The Perkin–Elmer 240 CHN elemental analyzer was used to obtain elemental analyses (C, H, N) that were within $\pm 0.4\%$ of theoretical values.

General method for production of compounds 4a–e: A mixture of compound **3** (5 mmol), *para*-bromobenzaldehyde (10 mmol), and sodium acetate (5 mmol) in anhydrous glacial acetic acid (10 mL) was refluxed for 3 hours. The reaction mixture was concentrated and then poured into ice cold water. The solid thus separated was filtered, washed with water and the crude product obtained was purified by column chromatography on silica gel with hexane-ethyl acetate as eluent to yield pure product.

(5*Z*,5'*Z*)-2,2'-(5,5'-Methylenebis(2-methoxy-5,1-phenylene))bis(5-(4-bromobenzylidene)-3-phenylthiazolidin-4-one) (4a). M.p. 165–167 °C. ^1H NMR (300 MHz, CDCl_3) δ 7.60 (d, $J = 6.2$ Hz, 4H, Ar-H), 7.46–7.43 (m, Ar-H, 8H), 7.35 (s, 2H, =CH), 7.30 (d, $J = 5.4$ Hz, 2H, Ar-H), 7.37 (m, 4H, Ar-H), 7.26 (s, 2H, Ar-H), 6.93 (d, $J = 5.2$ Hz, 2H, Ar-H), 3.80 (s, 6H, $2\times\text{CH}_3$), 3.73 (s, 2H, CH_2). ^{13}C NMR (60 MHz, CHCl_3) δ 172.9, 154.6, 135.7, 135.5, 133.9, 132.9, 131.9, 130.4, 129.3, 128.8, 126.2, 125.4, 125.0, 123.5, 114.1, 62.1, 56.7, 42.3. MS m/z 915 $[\text{M}+\text{H}]^+$. Anal. calcd. for $\text{C}_{47}\text{H}_{36}\text{Br}_2\text{N}_2\text{O}_4\text{S}_2$: C, 61.55; H, 3.93; N, 3.04. Found: C, 61.58; H, 3.96; N, 3.06.

(5*Z*,5'*Z*)-2,2'-(5,5'-Methylenebis(2-methoxy-5,1-phenylene))bis(5-(4-bromobenzylidene)-3-(4-chlorophenyl)thiazolidin-4-one) (4b). M.p. 212–214 °C. ^1H NMR (300 MHz, CDCl_3) δ 7.60 (d, $J = 6.9$ Hz, 4H, Ar-H), 7.38–7.42 (m, 12H, Ar-H and CH), 7.32 (s, 4H, =CH), 7.22 (s, 2H, Ar-H), 7.08 (d, $J = 5.9$ Hz, Ar-H), 6.91 (d, $J = 6.8$ Hz,

2H, Ar-H), 3.84 (s, 6H, $2\times\text{CH}_3$), 3.52 (s, 2H, CH_2). ^{13}C NMR (60 MHz, CHCl_3) δ 172.9, 154.66, 135.5, 133.9, 132.0, 131.9, 129.4, 125.4, 124.9, 123.5, 114.1, 62.1, 56.7, 42.3. MS m/z 983 $[\text{M}+\text{H}]^+$. Anal. calcd. for $\text{C}_{47}\text{H}_{34}\text{Br}_2\text{Cl}_2\text{N}_2\text{O}_4\text{S}_2$: C, 57.27; H, 3.48; N, 2.84. Found: C, 57.24; H, 3.45; N, 2.81.

(5*Z*,5'*Z*)-2,2'-(5,5'-Methylenebis(2-methoxy-5,1-phenylene))bis(5-(4-bromobenzylidene)-3-(4-bromophenyl)thiazolidin-4-one) (4c). M.p. 195–197 °C. ^1H NMR (300 MHz, CDCl_3) δ 7.60 (d, $J = 6.2$ Hz, 4H, Ar-H), 7.54 (d, $J = 6.9$ Hz, 4H, Ar-H), 7.38–7.42 (m, 10H, Ar-H and C-H), 7.32 (s, 2H, =CH), 7.22 (s, 2H, Ar-H), 7.07 (d, $J = 6.9$ Hz, 2H, Ar-H), 6.91 (d, $J = 6.3$ Hz, 2H, Ar-H), 3.85 (s, 6H, $2\times\text{CH}_3$), 3.52 (s, 2H, CH_2). ^{13}C NMR (60 MHz, CHCl_3) δ 172.9, 154.6, 135.5, 134.8, 133.9, 132.5, 132.1, 132.0, 131.9, 130.4, 128.8, 125.9, 125.4, 124.9, 123.5, 117.1, 114.1, 62.1, 56.7, 42.38. MS m/z 1071 $[\text{M}+\text{H}]^+$. Anal. calcd. for $\text{C}_{47}\text{H}_{34}\text{Br}_2\text{N}_2\text{O}_4\text{S}_2$: C, 52.53; H, 3.19; N, 2.61. Found: C, 52.51; H, 3.16; N, 2.59.

(5*Z*,5'*Z*)-2,2'-(5,5'-Methylenebis(2-methoxy-5,1-phenylene))bis(5-(4-bromobenzylidene)-3-(4-nitrophenyl)thiazolidin-4-one) (4d). M.p. 209–210 °C. ^1H NMR (300 MHz, CDCl_3) δ 8.29 (d, $J = 5.9$ Hz, 4H, Ar-H), 7.71 (d, $J = 6.2$ Hz, 4H, Ar-H), 7.60 (d, $J = 5.9$ Hz, 4H, Ar-H), 7.44–7.43 (m, 6H, Ar-H and CH), 7.39 (s, 2H, =CH), 7.18 (s, 2H, Ar-H), 7.10 (d, $J = 7.2$ Hz, 2H, Ar-H), 6.93 (d, $J = 6.0$ Hz, 2H, Ar-H), 3.87 (s, 6H, $2\times\text{CH}_3$), 3.60 (s, 2H, CH_2). ^{13}C NMR (60 MHz, CHCl_3) δ 172.9, 154.6, 144.3, 143.0, 135.5, 133.9, 132.1, 132.0, 131.9, 130.4, 128.8, 126.7, 125.4, 124.9, 123.5, 121.6, 114.1, 62.1, 56.7, 42.3. MS m/z 1005 $[\text{M}+\text{H}]^+$. Anal. calcd. for $\text{C}_{47}\text{H}_{34}\text{Br}_2\text{N}_4\text{O}_8\text{S}_2$: C, 56.07; H, 3.40; N, 5.57. Found: C, 56.05; H, 3.36; N, 5.49.

(5*Z*,5'*Z*)-2,2'-(5,5'-Methylenebis(2-methoxy-5,1-phenylene))bis(5-(4-bromobenzylidene)-3-*para*-tolylthiazolidin-4-one) (4e). M.p. 194–196 °C. ^1H NMR (300 MHz, CDCl_3) δ 7.58 (d, $J = 5.9$ Hz, 4H, Ar-H), 7.42–7.39 (m, 10H, Ar-H), 7.33 (s, 2H, =CH), 7.23 (d, $J = 6.4$ Hz, 4H, Ar-H), 7.17 (d, $J = 6.1$ Hz, 2H, Ar-H), 6.98 (d, $J = 6.4$ Hz, 2H, Ar-H), 6.71 (s, 2H, CH), 3.85 (s, 2H, CH_2), 3.75 (s, 6H, $2\times\text{CH}_3$), 2.34 (s, 6H, $2\times\text{CH}_3$). ^{13}C NMR (60 MHz, CHCl_3) δ 172.9, 154.6, 135.5, 134.7, 134.5, 132.1, 132.0, 131.9, 130.6, 130.4, 128.8, 125.4, 124.9, 123.5, 122.5, 114.1, 62.1, 56.7, 42.3, 21.1. MS m/z 943 $[\text{M}+\text{H}]^+$. Anal. calcd. for $\text{C}_{49}\text{H}_{40}\text{Br}_2\text{N}_4\text{O}_4\text{S}_2$: C, 62.29; H, 4.27; N, 2.97. Found: C, 62.27; H, 4.25; N, 2.96.

General procedure for synthesis of compounds 5a–e: A mixture of compound **4** (5 mmol), cinnamic acid hydrazide (10 mmol), and anhydrous sodium acetate (5 mmol) with a catalytic quantity of glacial acetic acid in water was heated in a microwave oven (280 W) up to 8 minutes at 100 °C. The reaction mixture was concentrated and cooled to room temperature, the separated solid was fil-

tered and thoroughly washed with water, and the crude product was purified using column chromatography on silica gel with hexane-ethyl acetate as eluent to get pure compounds.

(2*E*,2'*E*)-1,1'-(5,5'-(5,5'-Methylenebis(2-methoxy-5,1-phenylene))bis(3-(4-fluorophenyl)-6-phenyl-3,3a,5,6-tetrahydro-2*H*-pyrazolo[3,4-*d*]thiazole-5,2-diyl))bis(3-phenylprop-2-en-1-one) (5a). M.p. 246–248 °C. ¹H NMR (300 MHz, CDCl₃) δ 7.51–7.49 (m, 6H, Ar-H and =CH), 7.41–7.39 (m, 6H, Ar-H), 7.32 (d, *J* = 7.0 Hz, 4H, Ar-H), 7.20–7.16 (m, 8H, Ar-H), 7.09 (m, 4H, Ar-H), 6.97 (d, *J* = 6.2 Hz, 2H, Ar-H), 6.78 (t, *J* = 7.4 Hz, 2H, Ar-H), 6.61 (d, *J* = 6.8 Hz, 4H, Ar-H), 6.53–6.52 (m, 4H, Ar-H), 5.61 (s, 2H, N-CH-S), 5.11 (d, *J* = 5.9 Hz, 2H, CH), 3.85 (s, 6H, 2×CH₃), 3.72 (s, 2H, CH₂). ¹³C NMR (60 MHz, CHCl₃) δ 163.0, 161.8, 155.0, 146.6, 137.3, 135.8, 133.9, 131.8, 132.3, 132.0, 131.8, 129.5, 129.0, 128.0, 126.7, 126.6, 124.6, 120.2, 115.7, 114.3, 72.2, 66.6, 58.4, 56.7, 42.38. MS *m/z* 1083 [M+H]⁺. Anal. calcd. for C₆₅H₅₂F₂N₆O₄S₂: C, 72.07; H, 4.84; N, 7.76. Found: C, 72.04; H, 4.80; N, 7.73.

(2*E*,2'*E*)-1,1'-(5,5'-(5,5'-Methylenebis(2-methoxy-5,1-phenylene))bis(6-(4-chlorophenyl)-3-(4-fluorophenyl)-3,3a,5,6-tetrahydro-2*H*-pyrazolo[3,4-*d*]thiazole-5,2-diyl))bis(3-phenylprop-2-en-1-one) (5b). M.p. 271–273 °C. ¹H NMR (300 MHz, CDCl₃) δ 7.58–7.53 (m, 6H, Ar-H and =CH), 7.41–7.38 (m, 8H, Ar-H), 7.24–7.17 (m, 10H, Ar-H), 7.04 (m, 4H, Ar-H), 6.94 (d, *J* = 5.8 Hz, 2H, Ar-H), 6.67 (d, *J* = 6.8 Hz, 2H, =CH), 6.59 (d, *J* = 6.2 Hz, 4H, Ar-H), 6.49 (d, *J* = 7.2 Hz, 2H, CH), 5.61 (s, 2H, CH), 4.95 (d, *J* = 6.2 Hz, 2H, CH), 3.80 (s, 2H, CH₂), 3.76 (s, 6H, 2×CH₃). ¹³C NMR (60 MHz, CHCl₃) δ 163.0, 161.8, 155.0, 146.6, 135.8, 135.6, 133.9, 132.3, 131.8, 131.6, 130.3, 129.6, 129.0, 128.0, 127.6, 124.6, 120.2, 115.7, 114.3, 72.2, 66.6, 58.4, 56.7, 42.3. MS *m/z* 1151 [M+H]⁺. Anal. calcd. for C₆₅H₅₀Cl₂F₂N₆O₄S₂: C, 67.76; H, 4.37; N, 7.29. Found: C, 67.74; H, 4.35; N, 7.26.

(2*E*,2'*E*)-1,1'-(5,5'-(5,5'-Methylenebis(2-methoxy-5,1-phenylene))bis(6-(4-bromophenyl)-3-(4-fluorophenyl)-3,3a,5,6-tetrahydro-2*H*-pyrazolo[3,4-*d*]thiazole-5,2-diyl))bis(3-phenylprop-2-en-1-one) (5c). M.p. 257–259 °C. ¹H NMR (300 MHz, CDCl₃) δ 7.46 (s, 4H, Ar-H), 7.39–7.34 (m, 12H, Ar-H and CH), 7.29 (d, *J* = 6.2 Hz, 4H, Ar-H), 7.23 (s, 2H, Ar-H), 7.12–7.06 (m, 8H, Ar-H), 6.53 (d, *J* = 6.2 Hz, 2H, =CH), 6.45 (d, *J* = 6.2 Hz, 4H, Ar-H), 6.29 (d, *J* = 7.4 Hz, 2H, CH), 5.61 (s, 2H, CH), 4.86 (d, *J* = 7.2 Hz, 2H, CH), 3.84 (s, 2H, CH₂), 3.74 (s, 6H, 2×CH₃). ¹³C NMR (60 MHz, CHCl₃) δ 163.0, 161.1, 155.0, 146.6, 137.6, 135.8, 133.9, 133.2, 132.0, 132.3, 131.0, 129.4, 129.0, 128.8, 128.0, 126.6, 124.6, 120.2, 118.8, 115.7, 114.3, 72.2, 6.6, 58.4, 56.79, 42.38. MS *m/z* 1239 [M+H]⁺. Anal. calcd. for C₆₅H₅₀Br₂F₂N₆O₄S₂: C, 62.91; H, 4.06; N, 6.77. Found: C, 62.89; H, 4.04; N, 6.72.

(2*E*,2'*E*)-1,1'-(5,5'-(5,5'-Methylenebis(2-methoxy-5,1-phenylene))bis(3-(4-fluorophenyl)-6-(4-nitrophenyl)-3,3a,5,6-tetrahydro-2*H*-pyrazolo[3,4-*d*]thiazole-5,2-diyl))bis(3-phenylprop-2-en-1-one) (5d). M.p. 246–248 °C. ¹H NMR (300 MHz, CDCl₃) δ 7.96 (d, *J* = 6.9 Hz, 4H, Ar-H), 7.64–7.61 (m, 6H, Ar-H and =CH), 7.46 (d, *J* = 6.4 Hz, 4H, Ar-H), 7.40 (m, 2H, Ar-H), 7.25–7.21 (m, 6H, Ar-H), 7.11 (d, *J* = 5.6 Hz, 2H, Ar-H), 7.05 (m, 4H, Ar-H), 6.92–6.88 (m, 6H, Ar-H), 6.68 (d, *J* = 6.1 Hz, 2H, CH), 6.41 (d, *J* = 5.2 Hz, 2H, CH), 5.61 (s, 2H, CH), 4.80 (d, *J* = 6.1 Hz, 2H, CH), 3.83 (s, 6H, 2×CH₃), 3.57 (s, 2H, CH₂). ¹³C NMR (60 MHz, CHCl₃) δ 163.0, 161.8, 155.0, 146.5, 143.9, 135.8, 133.9, 132.2, 132.0, 131.8, 129.0, 128.8, 128.0, 126.8, 126.2, 124.6, 120.2, 114.3, 115.7, 72.2, 66.6, 58.4, 56.7, 42.3. MS *m/z* 1173 [M+H]⁺. Anal. calcd. for C₆₅H₅₀F₂N₈O₈S₂: C, 66.54; H, 4.30; N, 9.55. Found: C, 66.50; H, 4.28; N, 9.51.

(2*E*,2'*E*)-1,1'-(5,5'-(5,5'-Methylenebis(2-methoxy-5,1-phenylene))bis(3-(4-fluorophenyl)-6-*para*-tolyl-3,3a,5,6-tetrahydro-2*H*-pyrazolo[3,4-*d*]thiazole-5,2-diyl))bis(3-phenylprop-2-en-1-one) (5e). M.p. 276–278 °C. ¹H NMR (300 MHz, CDCl₃) δ 7.49 (s, 4H, Ar-H), 7.40–7.37 (m, 8H, Ar-H and =CH), 7.31 (d, *J* = 6.4 Hz, 4H, Ar-H), 7.09–7.08 (m, 8H, Ar-H), 7.03–7.02 (m, 6H, Ar-H), 6.57 (m, 6H, Ar-H and =CH), 6.03 (d, *J* = 6.4 Hz, 2H, CH), 5.61 (s, 2H, CH), 4.78 (d, *J* = 6.4 Hz, 2H), 3.81 (s, 2H, CH₂), 3.76 (s, 6H, 2×OCH₃), 2.32 (s, 6H, 2×CH₃). ¹³C NMR (60 MHz, CHCl₃) δ 163.3, 161.8, 155.0, 146.6, 137.0, 136.5, 135.8, 133.9, 132.3, 132.0, 131.8, 130.7, 129.0, 128.6, 128.0, 127.1, 124.6, 120.2, 114.3, 115.7, 72.2, 66.6, 58.4, 56.7, 42.3, 21.1. MS *m/z* 1111 [M+H]⁺. Anal. calcd. for C₆₇H₅₆F₂N₆O₄S₂: C, 72.41; H, 5.08; N, 7.56. Found: C, 72.39; H, 5.06; N, 7.53.

2. 1. Antibacterial Assay

Standard inoculums (1–2·10⁻⁷ colony forming unit (c.f.u.)/mL 0.5 McFarland standards) were applied to the surface of sterile agar plates for the antibacterial assay, and a sterile glass spreader was employed to ensure equal distribution of the inoculums. The discs, measuring 6.26 mm in diameter, were made from Whatman no. 1 filter paper and sterilized with dry heat at 140 °C for 1 hour. The sterile discs had previously been soaked in a known concentration of the test substances and were put in nutritional agar medium. The plates were inverted and incubated for 24 hours at 37 °C. The inhibitory zones were measured and compared to standards. For determining MIC bacteria were cultured overnight in Luria–Bertani (LB) broth at 37 °C, centrifuged, and washed twice with sterile distilled water. Stock solutions for the series of chemicals were produced in DMSO. Each stock solution was diluted with standard method broth (Difco) to generate successive two-fold dilutions ranging from 50 to 0.8 mg/mL. Ten microtiters of broth containing about 105 CFU/mL of test bacteria were added to each well

of a 96-well microtiter plate. Culture plates were incubated at 37 °C for 24 hours, and growth was measured both visually and spectroscopically. The minimum inhibitory concentration (MIC, mg/mL) was discovered to be the lowest concentration required to stop bacterial growth compared to the criteria. To determine the minimum bacterial concentration (MBC), 0.1 mL of each tube was extracted and placed on agar plates. The number of CFUs was counted after 18–24 hours of incubation at 35 °C.

2. 2. Antifungal Assay

For antifungal assay Sabouraud's agar media was made by dissolving peptone (1 g), D-glucose (4 g), and agar (2 g) in distilled water (100 mL) and setting the pH to 5.7. To generate a suspension of fungal spores for lawns, normal saline was employed. A loopful of a certain fungal strain was added to 3 mL saline to create a suspension of the corresponding species. 20 mL of agar media were placed into each petri dish, the excess suspension was decanted, and the plates were dried in an incubator at 37 °C for 1 hour. Wells were produced with an agar punch and labeled individually. A control was likewise produced in triplicate and kept at 37 °C for 3–4 days. The MIC of compounds **5a–e** was measured using the broth dilution method.³⁸ *C. albicans* was cultured for 48 hours at 28 °C in YPD broth (1% yeast extract, 2% peptone, and 2% dextrose), collected by centrifugation, and washed twice with sterile distilled water. *Aspergillus fumigatus*, *Trichophyton rubrum*, and *Trichophyton mentagrophytes* were plated on potato dextrose agar (PDA) (Difco) and cultured for two weeks at 28 °C. Spores were washed three times with sterile distilled water and resuspended in distilled water to yield an initial inoculum of 10⁵ spores/mL. Each tested compound was dissolved in DMSO and diluted with potato dextrose broth (Difco) to produce serial two-fold dilutions ranging from 100 to 0.8 mg/mL. Each well received ten microtiters of the broth with approximately 10³ (for yeast) and 10⁴ (for filamentous fungus) cells/mL of test fungi. Culture plates were incubated at 28 °C for about 48–72 hours. To determine the minimum fungicidal concentration (MFC), 0.1 mL was extracted from each tube and put on agar plates. The number of c.f.u. was recorded after 48 hours of incubation at 35 °C.

3. Result and Discussion

The reaction of methylene bis(phenyl thiazolidenones) **3a–e**,⁴⁷ with 4-bromobenzaldehyde in acetic acid and sodium acetate for 3 hours produced arylidine thiazolidenones **4a–e**. The latter were converted to 2-arylvinylnpyrazoles **5a–e** in dimethyl sulphoxide via microwave irradiation at 50 °C, yielding unusually high yields of thiazolo 2-arylvinylnpyrazoles **5a–e**. Their structures were confirmed using FT-IR, mass spectrometry, ¹H and ¹³C

NMR spectroscopy techniques. The IR spectra of compounds **5a–e** showed the disappearance of the amide carbonyl absorption band at about 1700 cm⁻¹, which was present in compounds **4a–e**, confirming the involvement of the α,β -unsaturated carbonyl system. The bands around 1300–1337 cm⁻¹, characteristic for N–C–S bending vibration, provided confirmatory evidence for ring closure. In addition, the absorption bands corresponding to the C=N of the pyrazole moiety were detected at 1600 cm⁻¹. Further support was provided from the ¹H NMR spectra, which revealed that the N–CH–S protons of the thiazole ring appeared at δ 5.61 ppm as a singlet and the protons of the pyrazole ring at δ 6.59 ppm as a doublet. These signals indicated that the cyclisation step had occurred. In the ¹³C NMR spectra, strong signals corresponding to the carbons of the thiazolo 2-arylvinylnpyrazolo ring in all compounds are seen near δ 161.8, 146.6, 120.2, 72.2 and 66.6 ppm, providing further evidence of their structures. In conclusion, all of the synthesized compounds produced satisfactory spectral data compatible with their structures.

3. 1. Antinematicidal Activity

For antinematicidal activity⁴⁸ against *D. myceliophagus* and *C. elegans* by aqueous *in vitro* screening technique at various concentrations the compounds **5a–e** were screened. Median lethal dose at which 50% nematodes became immobile and the results was expressed in terms of LD₅₀. The screened data of the compound **5b** and **5d** reveal that they are the most effective against *D. myceliophagus* and *C. elegans* with LD₅₀ values 160–190 ppm, and 190–210 ppm, respectively.

3. 2. Antibacterial Activity

The analysis of antibacterial screening^{49–51} data reveals that practically all of compounds **5a–e** (Tables 2 and 3) are active and exhibit moderate to good antibacterial activity. Compounds **5b** and **5e** demonstrated good zone of inhibition against *B. subtilis*. Compounds **5c** and **5d** were effective against *S. aureus*. Compounds **5a**, **5c**, and **5e** were active against *C. violaceum*, while compounds **5b**, **5a**, and **5d** were most effective against *K. aerogenes*, *P. aeruginosa*, and *B. sphaericus* (Table 2). Compounds **5d** and **5e** effectively inhibited Gram-positive bacteria at a concentration of 6.12 μ g/mL, as shown by their MIC and MBC values (Table 3). The majority of the compounds displayed good antibacterial activity almost similar compared to the standard. Few compounds have the same MBC as the MIC, but many have values that are two to four times greater than the corresponding MIC values.

Antifungal Activity

The compounds **5a–e** were further tested for antifungal activity against four fungal organisms: *C. albicans*

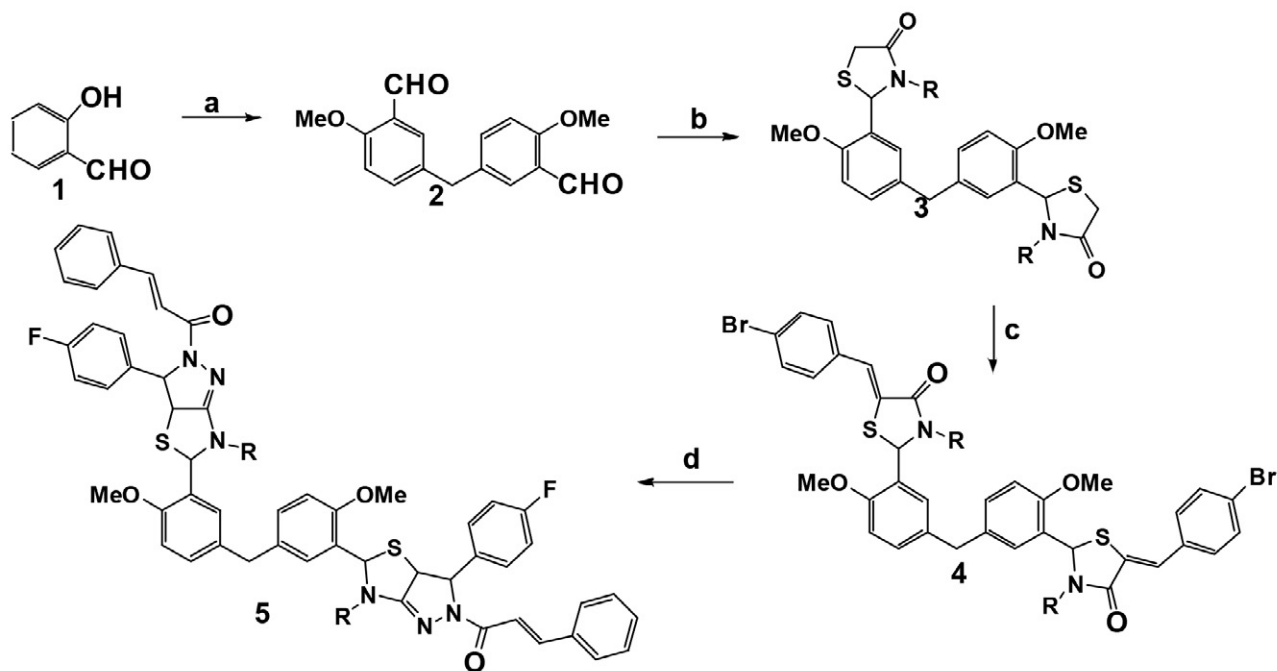
(10231), *A. fumigatus* (HIC 094), *T. rubrum* (IFO 9185), and *T. mentagrophytes* (IFO 40996) in dimethyl sulphoxide (DMSO) using the agar diffusion method.⁵² Amphotericin B was employed as the reference medication, and the zones of fungal inhibition values are shown in Table 4. Table 5 also includes the MIC and MFC (minimum fungicidal concentration) values computed using the broth dilution method.⁵¹ The antifungal screening data presented in Tables 4 and 5 show that the majority of the novel compounds are active and exhibit moderate to good antifungal activity. Among the screened compounds the compound **5e** in which thiazolo 2-arylvinylpyrazole moiety bearing *para*-methylphenyl group showed highest activity against all of the microorganisms employed. The activity of this compound is almost equal to the standard. Compounds **5b** and **5d** showed good inhibition towards *C. albicans* at the concentration

of 3.12 µg/mL which is less than amphotericin B standard.

Reagents and conditions: (a) Trioxane, H₂SO₄, AcOH, reflux, 81%; (b) MeI, K₂CO₃, DMF, rt, 83%; (c) R-NH₂, HSCH₂COOH, ZnCl₂, MWI, 81–90%; (d) *para*-Br-C₆H₄CHO, AcOH, NaOAc, reflux, 80%; (e) 2-arylvinylhydrazide, AcOH, NaOAc, MWI, 80–85%.

Table 1. Nematicidal activity of compounds **5a–e**.

S. No	Compound	<i>D. myceliophagus</i>	<i>C. elegans</i>
1	5a	840	650
2	5b	160	190
3	5c	240	360
4	5d	190	210
5	5e	380	420
6	Levamisole	160	180



Scheme 1. R = H, Cl, Br, NO₂, CH₃

Table 2. Inhibitory zone (diameters, mm) of compounds **5a–e** against tested bacterial strain by disc diffusion method.

Compound	<i>B. subtilis</i>	<i>B. sphaericus</i>	<i>S. aureus</i>	<i>P. aeruginosa</i>	<i>K. aerogenes</i>	<i>C. violaceum</i>
5a	14	22	18	20	22	20
5b	24	24	17	21	24	23
5c	16	15	23	16	15	16
5d	18	20	21	19	21	21
5e	26	16	16	18	16	15
Streptomycin	30	20	41	15	25	20
Neomycin	25	28	40	25	30	25

Table 3. Minimum inhibitory concentration (MIC) and minimum bacterial concentration (MBC) in µg/mL of compound 5a–e

Compound	<i>B. subtilis</i>		<i>B. sphaericus</i>		<i>S. aureus</i>		<i>P. aeruginosa</i>		<i>K. aerogenes</i>		<i>C. violaceum</i>	
	MIC	MBC	MIC	MBC	MIC	MBC	MIC	MBC	MIC	MBC	MIC	MBC
5a	12.5	25.0	25.0	50.0	12.5	12.5	12.5	50.0	12.5	50.0	25.0	25.0
5b	12.5	25.0	25.0	50.0	50.0	12.5	25.0	25.0	25.0	50.0	12.5	25.0
5c	12.5	50.0	12.5	25.0	25.0	12.5	12.5	25.0	12.5	25.0	12.5	50.0
5d	6.25	12.5	6.5	12.5	6.25	6.25	12.5	25.0	12.5	50.0	12.5	12.5
5e	6.25	12.5	6.5	50.0	6.25	25.0	12.5	50.0	6.25	12.5	6.25	6.25
Streptomycin	6.25	12.5	6.25	25.0	6.25	12.5	1.56	6.25	1.56	6.25	3.12	6.25
Penicillin	1.26	6.25	3.12	25.0	1.56	6.25	6.25	12.5	6.25	12.5	12.5	12.5

Table 4. Inhibitory zone diameters (mm) of compounds 5a–e against tested fungal strains by disc diffusion method

Compound	Mean zone inhibition (MZI) in mm			
	<i>C. albicans</i>	<i>A. fumigatus</i>	<i>T. rubrum</i>	<i>T. mentagrophytes</i>
5a	11	10	—	9
5b	22	16	15	16
5c	18	15	13	17
5d	21	17	14	16
5e	20	20	20	18
Amphotericin B	25	20	20	18

hibited *Candida albicans* at a concentration of 3.12 µg/mL, lower than the conventional amphotericin B.

Acknowledgements

The authors are grateful to Principal of Institution for moral support.

Conflict of Interest

Authors declared no conflict of interest.

Table 5. Minimum inhibitory concentration (MIC) and minimum fungicidal concentration (MFC) in µg/mL of compounds 5a–e

Compound	<i>C. albicans</i>		<i>A. fumigatus</i>		<i>T. rubrum</i>		<i>T. mentagrophytes</i>	
	MIC	MBC	MIC	MBC	MIC	MBC	MIC	MBC
5a	—	—	25.0	25.0	25.0	50.0	25.0	25.0
5b	3.12	6.25	25.0	25.0	12.5	25.0	25.0	25.0
5c	12.5	25.0	6.25	12.5	6.25	12.5	6.25	12.5
5d	3.12	6.25	6.25	12.5	6.25	12.5	12.5	25.0
5e	3.12	3.12	3.12	6.25	3.12	6.25	6.25	12.5
Amphotericin B	6.25	12.5	3.12	6.25	3.12	12.5	3.12	12.5

4. Conclusion

A series of new methylene bis 2-arylvinyl thiazolo pyrazoles were synthesized and tested for their antinematocidal, antibacterial, and antifungal properties. Among the studied compounds, 5b and 5d containing chloro and nitro substituents are the most efficient against *Ditylenchus myceliophagus* and *Caenorhabditis elegans*, with LD 50 between 160 and 190 ppm, 190 and 210 ppm, respectively. Compounds 5b and 5e inhibited *Bacillus subtilis* effectively, compounds 5c and 5d inhibited *Staphylococcus aureus*, compounds 5a, 5c, and 5e inhibited *Chromobacterium violaceum*, and compounds 5b, 5a, and 5d inhibited *Klebsiella aerogenes*, *Pseudomonas aeruginosa* and *Bacillus sphaericus* the most. Compounds 5b and 5d effectively in-

5. References

- O. Ebenezer, M. Shapi, J. A. Tuszyński, *Biomedicines* **2022**, *10*, 1124–1181. DOI:10.3390/biomedicines10051124
- D. Havrylyuk, O. Roman, K. R. Lesy, *Eur. J. Med. Chem.* **2016**, *113*, 145–166. DOI:10.1016/j.ejmech.2016.02.030
- R. F. Costa, L. C. Turones, K. V. N. Cavalcante, I. A. Rosa Junior, C. H. Xavier, L. P. Rosseto, H. B. Napolitano, P. Castro, M. L. F. Neto, G. M. Galvão, R. Menegatti, G. R. Pedrino, E. A. Costa, J. L. R. Martins, J. O. Fajemiroye, *Front. Pharmacol.* **2021**, *12*, 666725–666734. DOI:10.3389/fphar.2021.666725
- S. J. Takate, A. D. Shinde, B. K. Karale, H. Akolkar, L. Nawale, D. Sarkar, P. C. Mhaske, *Bioorg. Med. Chem. Lett.* **2019**, *29*, 1199–1202. DOI:10.1016/j.bmcl.2019.03.020
- V. Rachakonda, S. S. Kotapalli, R. Ummanni, M. Alla, *Chem-*

- istrySelect* **2017**, *2*, 6529–6534. DOI:10.1002/slct.201701241
6. R. S. Keri, K. Chand, T. Ramakrishnapa, B. M. Nagaraja, *Arch. Pharm.* **2015**, *348*, 299–314. DOI:10.1002/ardp.201400452
7. A. M. Vijesh, A. M. Isloor, P. Shetty, S. Sundershan, H. K. Fun, *Eur. J. Med. Chem.* **2013**, *62*, 410–415. DOI:10.1016/j.ejmech.2012.12.057
8. A. A. Bekhit, H. M. A. Ashour, Y. S. Abdel Ghany, A. E.-D. A. Bekhit, A. Baraka, *Eur. J. Med. Chem.* **2008**, *43*, 456–463. DOI:10.1016/j.ejmech.2007.03.030
9. H. Kumar, D. Saini, S. Jain, N. Jain, *Eur. J. Med. Chem.* **2013**, *70*, 248–258. DOI:10.1016/j.ejmech.2013.10.004
10. A. A. Bekhit, A. M. M. Hassan, H. A. Abd El Razik, M. M. M. El-Miligy, E. J. El-Agroudy, A. E.-D. A. Bekhit, *Eur. J. Med. Chem.* **2015**, *94*, 353–366. DOI:10.1016/j.ejmech.2015.02.038
11. D. van Duin, D. L. Paterson, *Infect. Dis. Clin. North. Am.* **2016**, *30*, 377–390. DOI:10.1016/j.idc.2016.02.004
12. O. B. Bekker, D. N. Sokolov, O. A. Luzina, N. I. Komarova, Y. V. Gatilov, S. N. Andreevskaya, T. G. Smirnova, D. A. Maslov, L. N. Chernousova, N. F. Salakhutdinov, V. N. Danilenko, *Med. Chem. Res.* **2015**, *24*, 2926–2931. DOI:10.1007/s00044-015-1348-2
13. S. F. P. Braga, N. C. Fonseca, J. P. Ramos, E. M. Souza-Fagundes, R. B. Oliveira, *Braz. J. Pharm. Sci.* **2016**, *52*, 299–307. DOI:10.1590/S1984-82502016000200008
14. A. V. Galochkina, R. K. Bollikanda, V. V. Zarubaev, D. D. Tentler, I. N. Lavrenteva, A. V. Slita, N. Chirra, S. Kantevari, *Arch. Pharm.* **2019**, *2*, 352–361.
15. P. Ottanà, R. Paoli, A. Naß, G. Lori, V. Cardile, I. Adornato, A. Rotondo, A. C. E. Graziano, G. Wolber, R. Maccari, *Eur. J. Med. Chem.* **2017**, *127*, 840–858. DOI:10.1016/j.ejmech.2016.10.063
16. I. Sharma, M. Sullivan, T. F. McCutchan, *Antimicrob. Agents Chemother.* **2015**, *59*, 3174–3182. DOI:10.1128/AAC.04294-14
17. E. Schadich, A. Kryshchshyn-Dylevych, S. Holota, P. Polishchuk, P. Džubak, S. Gurska, M. Hajdych, R. Lesyk, *Bioorg. Med. Chem. Lett.* **2020**, *30*, 127616–127620. DOI:10.1016/j.bmcl.2020.127616
18. R. D. Kamble, R. J. Meshram, S. V. Hese, R. A. More, S. S. Kamble, R. N. Gacche, B. S. Dawane, *Comput. Biol. Chem.* **2016**, *61*, 86–96. DOI:10.1016/j.compbiolchem.2016.01.007
19. A. H. Abdelazeem, M. T. El-Saadi, A. G. Safi El-Din, H. A. Omar, S. M. El-Moghazy, *Bioorg. Med. Chem.* **2017**, *25*, 665–676. DOI:10.1016/j.bmc.2016.11.037
20. S. Thota, K. Nadipelly, A. Shenkesi, R. Yerra, *Med. Chem. Res.* **2015**, *24*, 1162–1169. DOI:10.1007/s00044-014-1184-9
21. K. Z. Łączkowski, N. Konklewska, A. Biernasiuk, A. Malm, K. Sałat, A. Furgała, K. Dzitko, A. Bekier, A. Baranowska-Łączkowska, A. Paneth, *Med. Chem. Res.* **2018**, *27*, 2125–2140. DOI:10.1007/s00044-018-2221-x
22. B. Yu, S. Zhou, L. Cao, Z. Hao, D. Yang, X. Guo, N. Zhang, V. A. Bakulev, Z. J. Fan, *Agric. Food. Chem.* **2020**, *68*, 7093–7102. DOI:10.1021/acs.jafc.0c00062
23. G. S. Masaret, *ChemistrySelect* **2021**, *6*, 974–982. DOI:10.1002/slct.202004304
24. B. Patel, M. Zunk, G. Grant, S. Rudrawar, *Bioorg. Med. Chem. Lett.* **2021**, *39*, 127853–127859. DOI:10.1016/j.bmcl.2021.127853
25. B. Sharifzadeh, N. O. Mahmoodi, M. Mamaghani, K. Tabatabaeian, A. S. Chirani, I. Nikokar, *Bioorg. Med. Chem. Lett.* **2013**, *23*, 548–551. DOI:10.1016/j.bmcl.2012.11.024
26. R. Gondru, K. Sirisha, S. Raj, S. K. Gunda, C. G. Kumar, M. Pasupuleti, R. Bavantula, *ChemistrySelect* **2018**, *3*, 8270–8276. DOI:10.1002/slct.201801391
27. N. D. Gaikwad, S. V. Patil, V. D. Bobade, *J. Heterocycl. Chem.* **2013**, *50*, 519–527. DOI:10.1002/jhet.1513
28. S. M. Ronkin, M. Badia, S. Bellon, A. Grillot, C. H. Gross, *Bioorg. Med. Chem. Lett.* **2010**, *20*, 2828–2831. DOI:10.1016/j.bmcl.2010.03.052
29. P. Khloya, S. Kumar, P. Kaushik, P. Surain, D. Kaushik, P. K. Sharma, *Bioorg. Med. Chem. Lett.* **2015**, *25*, 1177–1181. DOI:10.1016/j.bmcl.2015.02.004
30. J. Nalawade, A. Shinde, A. Chavan, S. Patil, M. Suryavanshi, M. Modak, P. Choudhari, V. D. Bobade, P. C. Mhaske, *Eur. J. Med. Chem.* **2019**, *179*, 649–659. DOI:10.1016/j.ejmech.2019.06.074
31. K. K. Bansal, J. K. Bhardwaj, P. Saraf, V. K. Thakur, P. C. Sharma, *Mater. Today Chem.* **2020**, *17*, 433–438. DOI:10.1016/j.mtchem.2020.100335
32. L. D. Khillare, M. R. Bhosle, A. R. Deshmukh, R. A. Mane, *Med. Chem. Res.* **2015**, *24*, 1380–1386. DOI:10.1007/s00044-014-1222-7
33. K. Chaudhari, S. Surana, P. Jain, H. M. Patel, *Eur. J. Med. Chem.* **2016**, *124*, 160–185. DOI:10.1016/j.ejmech.2016.08.034
34. S. M. Jagadale, Y. K. Abhale, H. R. Pawar, A. Shinde, V. D. Bobade, A. P. Chavan, D. Sarkar, P. C. Mhaske, *Polycycl. Arom. Compd.* **2022**, *42*, 3216–3237. DOI:10.1080/10406638.2020.1857272
35. P. A. Datar, S. R. Jadhav, *Lett. Drug. Discov.* **2014**, *11*, 686–703. DOI:10.2174/1570180810666131113212354
36. V. L. M. Silva, A. M. S. Silva, D. C. G. A. Pinto, P. Rodríguez, M. Gomez, N. Jagerovic, L. F. Callado, J. A. S. Cavaleiro, J. Elguero, J. Fernandez-Ruiz, *Arkivoc* **2010**, (x), 226–247. DOI:10.3998/ark.5550190.0011.a19
37. V. P. Perevalov, L. I. Baryshnenkova, G. V. Sheban, A. K. K. Karim, S. S. Kramarenko, T. Y. Koldaeva, B. I. Stepanov, *Chem. Heterocycl. Compd.* **1990**, *26*, 887–894. DOI:10.1007/BF00480863
38. V. Garg, P. Kumar, A. K. Verma, *J. Org. Chem.* **2017**, *82*, 10247–10262. DOI:10.1021/acs.joc.7b01746
39. C. O. Kappe, *Angew. Chem. Int. Ed.* **2004**, *43*, 6250–6284. DOI:10.1002/anie.200400655
40. J. Fairsoo, S. Saranya, S. Radhika, G. Anilkumar, *Chem. Select* **2020**, *5*, 5180–5197. DOI:10.1002/slct.202000683
41. A. Srinivas, *Russ. J. Org. Chem.* **2024**, *12*, 84–93.
42. A. Srinivas, *Res. J. Chem. Environ.*, **2024**, *28*, 61–73. DOI:10.25303/283rjce061069
43. A. Srinivas, *Russ. J. Org. Chem.* **2023**, *11*, 1940–1951. DOI:10.1134/S107042802311012X
44. A. Srinivas, S. Rajitha, P. Suresh, *Russ. J. Gen. Chem.* **2023**, *5*, 1201–1209. DOI:10.1134/S1070363223050213

45. A. Srinivas, S. Shamili, S. Kavitha, I. Farheen, *J. Heterocycl. Chem.*, **2023**, *60*, 116–122. DOI:10.1002/jhet.4568
46. A. Srinivas, *Indian J. Chem.* **2022**, *60B*, 1199–1204.
47. Ch. Sanjeeva Reddy, A. Srinivas, A. Nagaraj, *J. Heterocycl. Chem.* **2008**, *45*, 999–1003. DOI:10.1002/jhet.5570450409
48. C. W. McBeth, G. B. Bergeson, *Phytopathology*, **1953**, *43*, 264–268.
49. R. Cruickshank, J. P. Duguid, B. P. Marmion, R. H. A. Swain: *Medicinal Microbiology*, 12th Ed., Vol. II, Churchill Livingstone, London, 1975, 196–202.
50. A. H. Collins: *Microbiological Methods*, 2nd Ed., Butterworth, London, 1976.
51. National Committee for Clinical Laboratory Standards (NC-CLS). Standard methods for dilution antimicrobial susceptibility tests for bacteria, which grows aerobically. Nat. Comm. Lab. Stands, Villanova, 1982, p. 242.
52. Z. K. Khan: Proc. Int. Workshop UNIDO-CDRI, 1997, p. 210.

Povzetek

S pomočjo cikloadicijske reakcije hidrazida cimetine kisline in (5*Z*,5'*Z*)-2,2'-(5,5'-metilenbis(2-metoksi-5,1-fenilen))bis(5-(4-fluorobenziliden)-3-feniltiazolidin-4-onov) **4a–e** smo pripravili (2*E*,2'*E*)-1,1'-(5,5'-(5,5'-metilenbis(2-metoksi-5,1-fenilen))bis(3-(4-fluorofenil)-6-fenil-3,3a,5,6-tetrahidro-2*H*-pirazolo[3,4-*d*]tiazol-5,2-diil))bis(3-fenilprop-2-en-1-one) **5a–e**. Za pripravljene spojine smo raziskali delovanje proti bakterijam, glivam in nematodam. Izmed testiranih spojin sta se spojini **5b** and **5d**, ki vsebujeta kloro oz. nitro skupino, pokazali kot najbolj učinkoviti proti *Ditylenchus myceliophagus* in *Caenorhabditis elegans* z LD₅₀ vrednostmi med 160 in 190 ppm, oz. 190 in 210 ppm. Spojini **5b** in **5e** sta izkazali dobro inhibicijo proti *Bacillus subtilis*, spojini **5c** in **5d** sta bili aktivni proti *Staphylococcus aureus*, spojine **5a**, **5c** in **5e** proti *Chromobacterium violaceum*, spojine **5b**, **5a** in **5d** pa so bile najbolj aktivne proti *Klebsiella aerogenes*, *Pseudomonas aeruginosa* in *Bacillus sphaericus*. Spojini **5b** in **5d** v koncentraciji 3.12 µg/mL dobro inhibirata *Candida albicans*; ta vrednost je manjša od vrednosti za amfotericin B, ki smo ga uporabili kot standard.



Except when otherwise noted, articles in this journal are published under the terms and conditions of the Creative Commons Attribution 4.0 International License

Scientific paper

Inhibition Effect of Benzimidazole Derivatives on the Corrosion of Mild Steel in Acidic Medium: Experimental and Theoretical Studies

Sonia Benabid^{1,*} and Linda Toukal²

¹ Laboratory of Electrochemistry of Molecular and Complex Materials (LEMMC), Department of Process Engineering, Faculty of Technology, Ferhat Abbas University Setif-1, Setif 19000, Algeria

² Laboratory of Electrochemistry and Materials (LEM), Department of Engineering Process, Faculty of Technology, Ferhat Abbas University Setif-1, Setif 19000, Algeria

* Corresponding author: E-mail: sonia_benabid@yahoo.fr
Tel: +213552755767

Received: 08-08-2024

Abstract

The effect of heterocyclic compounds, derived from benzimidazole (BnZ), namely 1-Benzyl-2-phenyl 1H-benzimidazole (BI) and 1-(4-Nitrobenzyl)-2-(4-nitrophenyl)-1H-benzimidazole (NNBI), on the carbon corrosion steel in 1M HCl medium was assessed by electrochemical impedance spectroscopy (EIS) and potentiodynamic polarization (PDP). The effects of the concentration and the temperature were studied. The determined electrochemical parameters showed that the two inhibitors are of mixed type. The inhibition efficiency of NNBI was lesser than that of BI. The most electron-withdrawing substituent offers the lowest efficiency. The mechanism of action of these inhibitors has been defined by the thermodynamic study. Calculated ΔG_{ads}° , E_{av} , ΔH_{av}° and ΔS_a° values confirmed that BI and NNBI adsorb through a chemical and physical process. The adsorption process was found to be spontaneous and followed the Langmuir adsorption isotherm. The quantum chemical parameters calculated by density functional theory (DFT) and molecular dynamics simulation (MDS) corroborate both the experimental data and those of the literature.

Keywords: Corrosion; steel; organic inhibitors; benzimidazole; DFT; MDS.

1. Introduction

Acid solutions widely used in various industrial processes (e.g., acid pickling, acid cleaning, oil well acidification, and acid descaling) cause severe corrosion of mild steel.

A number of physical, chemical, and mechanical properties favor the use of mild steel (MS) for construction and manufacturing purposes. Since MS is mainly used as structural and instrumental material, which often needs to use acids such as hydrochloric acid for pickling, descaling and various petrochemical processes, the prevention of its corrosion is necessary.¹ The use of organic corrosion inhibitors has proven to be the most practical and effective methods for protecting metals against corrosion in acidic media.²

During the last few decades, benzimidazole (BnZ) and its non-toxic derivatives have attracted considerable

attention due to their inhibitive action which proceeds via their adsorption on the metal surface by displacing pre-adsorbed water molecules at the interface forming subsequently an isolating barrier film.³ The adsorption of these heterocyclic compounds on the metal surface occurs due to the interaction of their unshared electron pairs on nitrogen atoms and the π -electrons in the phenyl rings with d-orbitals of the metal surface.⁴ These electronic features contribute to their effectiveness as corrosion inhibitors.

This paper deals with the study of the inhibition efficiency of two benzimidazole derivatives namely 1-Benzyl-2-phenyl-1H-benzimidazole (BI) and 1-(4-Nitrobenzyl)-2-(4-nitrophenyl)-1H-benzimidazole (NNBI) against the corrosion of mild steel in 1 M HCl medium.

The molecular structures of the inhibitors BI and NNBI are shown in Fig. 1.

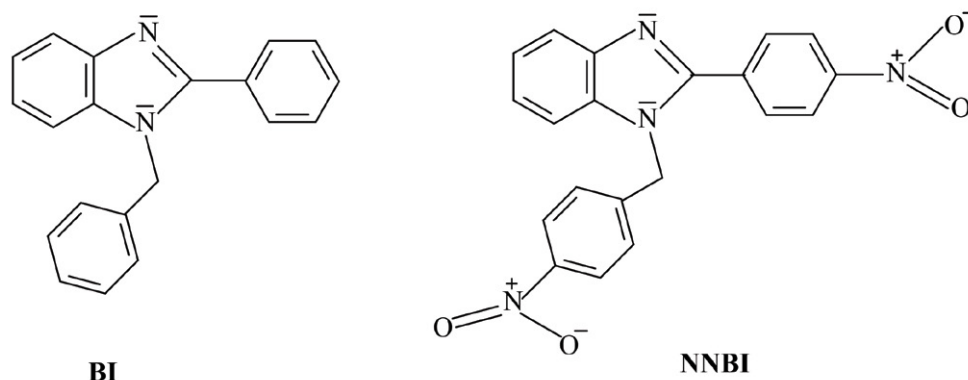


Figure 1. Molecular structures of 1-Benzyl-2-phenyl-1H-benzimidazole (BI) and 1-(4-Nitrobenzyl)-2-(4-nitrophenyl)-1H-benzimidazole (NNBI) inhibitors

To ensure a deep understanding of the process of corrosion prevention, various experimental techniques such as potentiodynamic polarization (PDP) and electrochemical impedance spectroscopy (EIS) were performed. The thermodynamic and kinetic parameters were determined and discussed. The electronic properties of tested compounds and their interactions with the iron surface were obtained from theoretical studies using DFT and MD simulations. The theoretical and experimental results corroborate.

2. Experimental

2.1. Materials and Solutions

The mild steel XC52 used in this study was determined from its technical sheet supplied by Sonatrach which is a big oil company located in Hassi Messaoud (southern Algeria).

The chemical composition (wt. %) of the mild steel was: C = 0.1038, Si = 0.1261, Mn = 0.971, P = 0.002, S = 0.0021, Cr = 0.01, Mo = 0.005, Ni = 0.005, Al = 0.0032, Co = 0.50, Cu = 0.01, No = 0.0419, Ti = 0.0025, V = 0.005, W = 0.05, Sn = 0.005, Fe = 98.67.

A conventional three-electrode cell was used for the electrochemical experiments. A platinum plate with a surface area of 1 cm² served as the counter electrode and Ag/AgCl as reference electrode. The working electrode is a square shaped mild steel coated with Teflon so that only the cross section (0.25 cm²) is exposed to the acid solution.

For reliable and reproducible data, the surface of the working electrode was mechanically polished prior to each test (before immersion in the acid solution), using abrasive Silicon Carbide (SiC) paper of increasingly fine particle size (i.e., 180, 320, 600, 800, 1000, 1200 and 2500), followed by rinsing with double distilled water (ddH₂O), degreasing with acetone and finally drying at room temperature.

The test solution 1 M HCl, was prepared from analytical grade reagent HCl (37%) purchased from Sigma

Aldrich and distilled water. Four different concentrations (5×10^{-6} , 1×10^{-5} , 5×10^{-5} and 1×10^{-4} M) of the studied inhibitors were prepared for analysis. This range was determined after studying the solubility of the inhibitors in the corrosive environment.

2.2. Electrochemical Measurements

The electrochemical measurements were performed using a set-up comprising a Voltalab40, controlled by “Voltmaster 4” analysis software, and were recorded in a three-electrode Pyrex cell. The potential applied to the sample varied continuously, with a scanning speed of 2mV/s. The working electrode potential reached stability after 30 minutes waiting period. All potentials were measured relative to the KCl-saturated Ag/AgCl reference electrode.

The electrochemical impedance diagrams were recorded in the frequency range 100 kHz–10 Hz with disturbance amplitude of 10 mV.

2.3. Quantum Chemical Study

All theoretical calculations were done with the GAUSSIAN 09 software, and the geometry of the BnZ derivatives was entirely optimized using the DFT method at the B3LYP level with base 6-31G (d, p).^{5,6}

2.4. Molecular Dynamic Simulation Study (MDS)

MDS was realized using BIOVIA Materials Studio 8.0 software, developed by Accelrys Inc. USA.^{7, 8} In this study, we used three modules: (i) the molecular structure of the inhibitor in gas, (ii) the aqueous phase, geometrically optimized using the Forcite module, (iii) the adsorption localization module was used to identify possible adsorption configurations. A simulation box with dimensions 17.38 Å × 17.38 Å × 27.16 Å, was used to determine the interaction between the studied inhibitors molecules and the

Fe (110) surface. Periodic boundary conditions were used in all three directions, and the equations of motion were integrated into the canonical (constant-volume) NVT ensemble. The Fe plate, the water plate containing the studied inhibitors, and a vacuum layer were included in the simulation box. We worked at a temperature of 298 K (about 25 °C) using the Condensed-phase Optimized Molecular Potentials for Atomistic Simulation Studies (COMPASS) force field.

3. Results and Discussion

3.1. Electrochemical Measurements

3.1.1. Concentration effect of BI and NNBI by PDP

Potentiodynamic polarization experiment was performed to assess the kinetics of cathodic and anodic reactions. The polarization curves in the absence and presence of different concentrations of BI and NNBI in 1 M HCl solution at 20 °C are shown in Fig. 2.

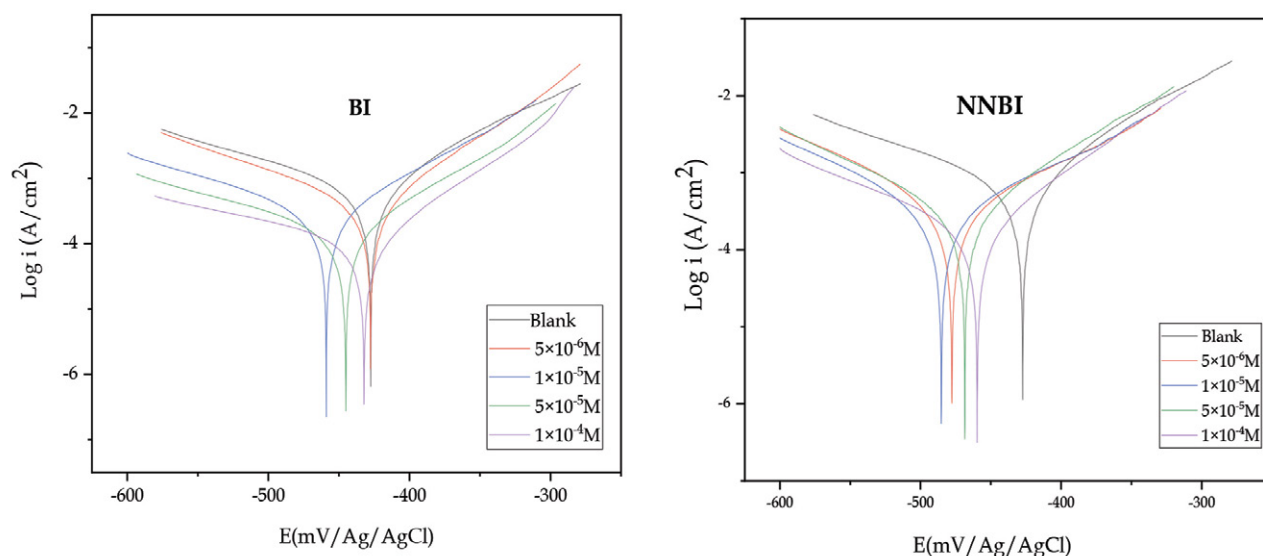


Figure 2. Polarization curves of mild steel in 1 M HCl in the absence and presence of different concentrations of BI and NNBI at 20 °C.

The electrochemical parameters such as the corrosion potential (E_{corr}), the current densities (I_{corr}), the cathodic and anodic tafel slopes (β_c and β_a), the surface coverage rate (θ) and the inhibitory efficiency (IE %) are listed in Table 1.

The inhibition efficacy (IE %) and the surface coverage rate (θ) of BI and NNBI were determined from the two equations below:

$$IE \% = \left(\frac{i_{corr}^0 - i_{corr}}{i_{corr}^0} \right) \times 100 \quad (1)$$

$$\theta = \left(\frac{i_{corr}^0 - i_{corr}}{i_{corr}^0} \right) \quad (2)$$

Table 1. Electrochemical parameters and corrosion inhibition efficiency of mild steel in 1M HCl in the absence and presence of different concentrations of BI and NNBI at 20 °C

Inhibitor	C (M)	E_{corr} (mV/Ag/AgCl)	i_{corr} (mA/cm ²)	β_a (mV/dec)	β_c (mV/dec)	IE %	θ
BI	Blank	-427	0.63	82	-159	-	-
	5×10^{-6}	-428	0.33	67	-125	48	0.48
	1×10^{-5}	-459	0.30	91	-160	52	0.52
	5×10^{-5}	-445	0.16	85	-177	75	0.75
	1×10^{-4}	-432	0.10	72	-202	84	0.84
NNBI	5×10^{-6}	-477	0.4	131	-128	37	0.37
	1×10^{-5}	-485	0.33	134	-125	48	0.48
	5×10^{-5}	-468	0.28	87	-116	56	0.56
	1×10^{-4}	-460	0.18	82	-149	71	0.71

i_{corr}^0 and i_{corr} represent the current densities in the absence and presence of BI and NNBI inhibitors, respectively.

Analysis of the potentiodynamic polarization curves (Fig. 2) reveals that increasing the concentration of both

inhibitors causes a decrease in cathodic and anodic current densities. This result suggests that the addition of BI and NNBI reduces anodic dissolution and also retards the hydrogen evolution. This phenomenon is due to the creation of an inhibitor barrier between the corrosive medium and the metal surface.⁹

Inspection of Table 1 shows that the corrosion potential (E_{corr}) of BI and NNBI shifts towards negative values in comparison with the corrosion potential of the blank solution. This shift is less than 85 mV, suggesting that BI and NNBI act as mixed type inhibitor with predominance on the cathodic reaction.¹⁰

On the other hand, the values of both anodic and cathodic Tafel slopes (β_a , β_c) slightly change when the concentration of the inhibitors increases, which means that the

addition of inhibitors reduces the anodic dissolution of mild steel as well as retards the cathodic hydrogen evolution reaction without affecting the reactions mechanism.^{10,11}

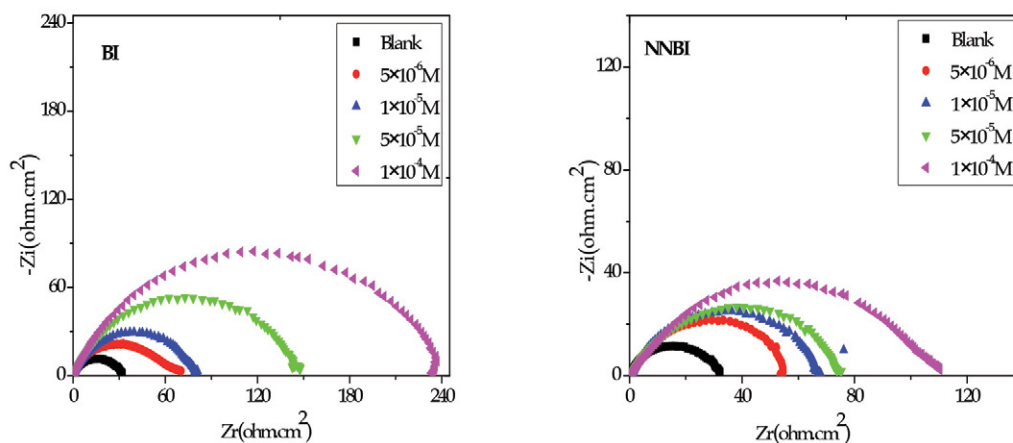


Figure 3. Nyquist diagrams of mild steel in 1M HCl in the absence and presence of different concentrations of the inhibitors BI and NNBI at 20 °C.

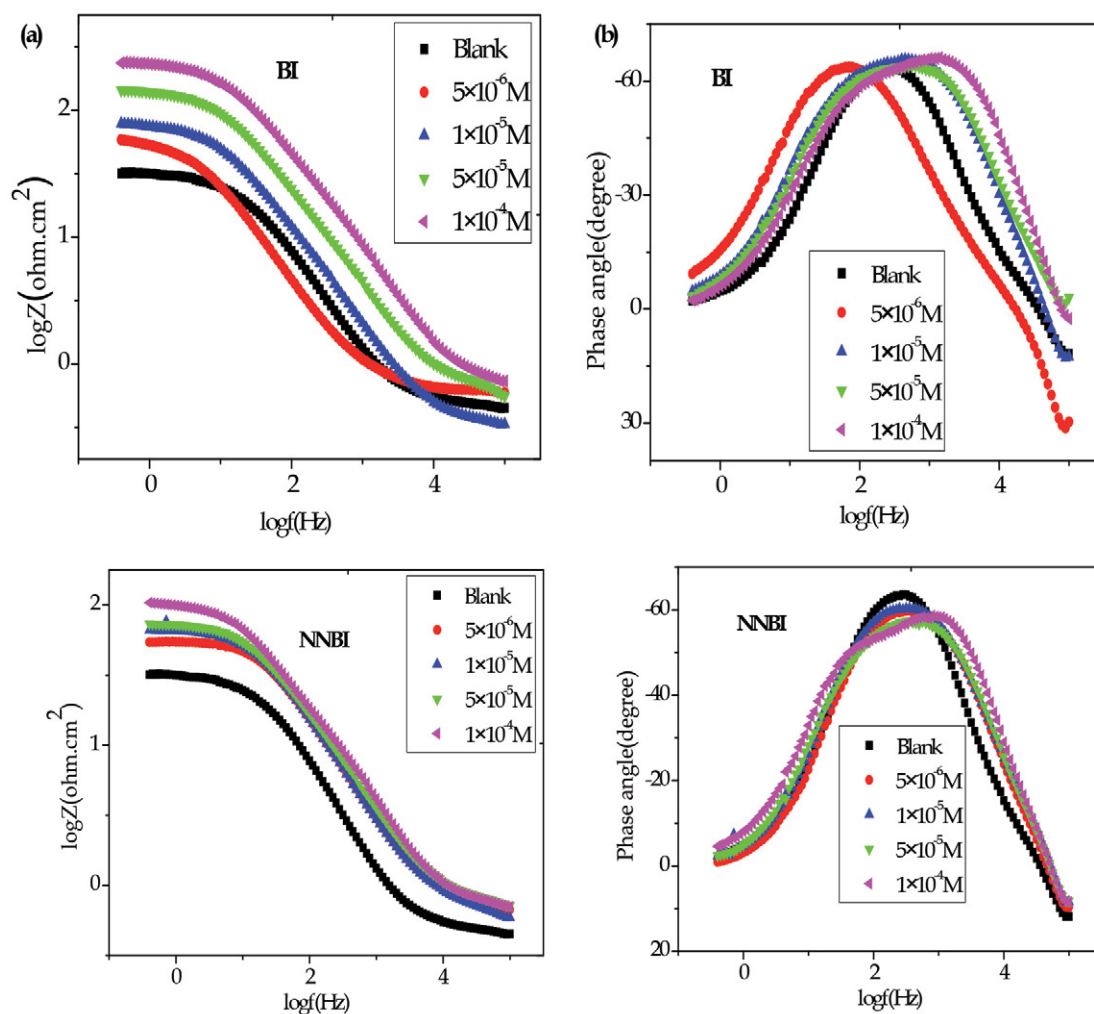


Figure 4. Bode (a) and phase angle (b) plots for mild steel in 1M HCl in the absence and presence of different concentrations of BI and NNBI at 20 °C.

3. 1. 2. Concentration Effect of BI and NNBI by EIS

In order to evaluate the electrochemical phenomenon which occurs at the metal/solution interface, Nyquist plots of mild steel in 1 M HCl in the absence and presence of various concentrations of BI and NNBI at 20 °C are represented in Fig. 3.

We can notice that for all concentrations, the presence of a single capacitive loop corresponding to the charge transfer resistance (R_{ct}) generally indicates that the dissolution reaction of XC52 in 1 M HCl is controlled by a single process charge transfer which is not affected by the presence of inhibitors.¹² Nyquist curves are not perfect semicircles due to the heterogeneity of the electrode surface. This heterogeneity can result from the surface roughness, impurities, dislocations, grain boundaries, adsorption and desorption phenomena of the inhibitor.^{13,14}

The Bode diagrams (Fig. 4) reveals the existence of an equivalent circuit containing a single constant phase element in the metal/solution interface. The increase in absolute impedance at low frequencies in the Bode plots confirms that the protection is better at high inhibitor concentrations. The observation of a single-phase peak in the central frequency range indicates the existence of a unique constant, linked to the electrical double layer.¹⁵

To define a model for the steel/solution interface in the absence and presence of the inhibitors BI and NNBI, the data obtained by EIS were adjusted to the electrical equivalent circuit, as illustrated in Fig. 5.

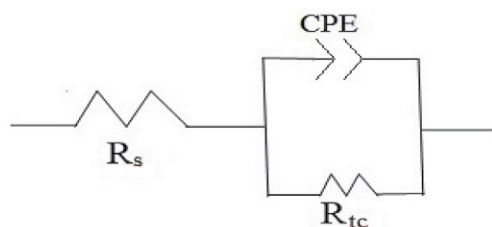


Figure 5. Equivalent electrochemical circuit representing the steel/solution interface used for the simulation of BI and NNBI impedance diagrams.

Where R_c is the solution resistance, R_{ct} denotes the charge transfer resistance, and CPE is the constant phase element which replaces the double layer capacitance (C_{dl}) allowing a more precise fit to the experimental results.

The double layer capacitance (C_{dl}) is obtained through the following equation (3):

$$C_{dl} = \frac{1}{2\pi f_{max}} \times \frac{1}{R_{ct}} \quad (3)$$

Where f_{max} is the frequency with maximal impedance of the imaginary component.

The inhibition efficiency is calculated from the following formula (4):

$$IE (\%) = \frac{R_{ct} - R_{ct}^0}{R_{ct}} \times 100 \quad (4)$$

Where R_{ct}^0 and R_{ct} represent the charge transfer resistances in the absence and presence of the inhibitors BI and NNBI, respectively.

From the diagrams of Nyquist, the values of (R_s), (R_{ct}), (C_{dl}), and consequently the inhibition efficiency (IE) of BI and NNBI were obtained. These different impedance parameters are summarized in Table 2.

Table 2. Electrochemical impedance parameters for mild steel in 1 M HCl in the absence and presence of different concentrations of BI and NNBI at 20 °C.

Inhibitor	C (M)	R_s ($\Omega \text{ cm}^2$)	R_{ct} ($\Omega \text{ cm}^2$)	C_{dl} ($\mu\text{F}/\text{cm}^2$)	IE (%)
BI	Blank	0.368	32	249	–
	5×10^{-6}	0.24	67	597	52
	1×10^{-5}	0.29	80	199	60
	5×10^{-5}	0.7	146	98	78
	1×10^{-4}	1	237	48	87
NNBI	5×10^{-6}	1	54	147	41
	1×10^{-5}	0.83	67	136	52
	5×10^{-5}	1	74	132	57
	1×10^{-4}	1.7	108	117	70

Examination of Table 2 shows that the addition of 1×10^{-4} M of BI and NNBI inhibitors augmented the values of R_{ct} . This increase can be attributed to the adsorption of the inhibitors on the metal surface by forming a protective layer against immediate exposure to the aggressive acidic microenvironment.¹⁶ On the other hand, (C_{dl}), in the presence of the inhibitors decreased compared to that of the solution without inhibitors; this decrease may be due to the displacement of the water molecules present at the metallic interface in favor of the adsorbed BI and NNBI molecules. Indeed, there is a positive correlation between the adsorption of the inhibitors and the thickness of the organic deposit, whereas the capacity of the double layer decreases proportionally.¹⁴

3. 1. 3. Temperature Effect

Temperature is one of the crucial steel behavior-modifying factors in a corrosive environment; Thereby, it can alter the nature of the metal/inhibitor interaction. Increasing temperature can impact significantly the formation of the inhibitor film. Indeed, a rise in temperature would promote the inhibitor desorption as well as a quick dissolution of the formed organic compounds or complexes, subsequently causing a weakening of the steel corrosion resistance.¹⁷

In order to analyze the effect of temperature on the inhibition efficiency of BI and NNBI, polarization curves of mild steel in 1 M HCl solution, without and with ad-

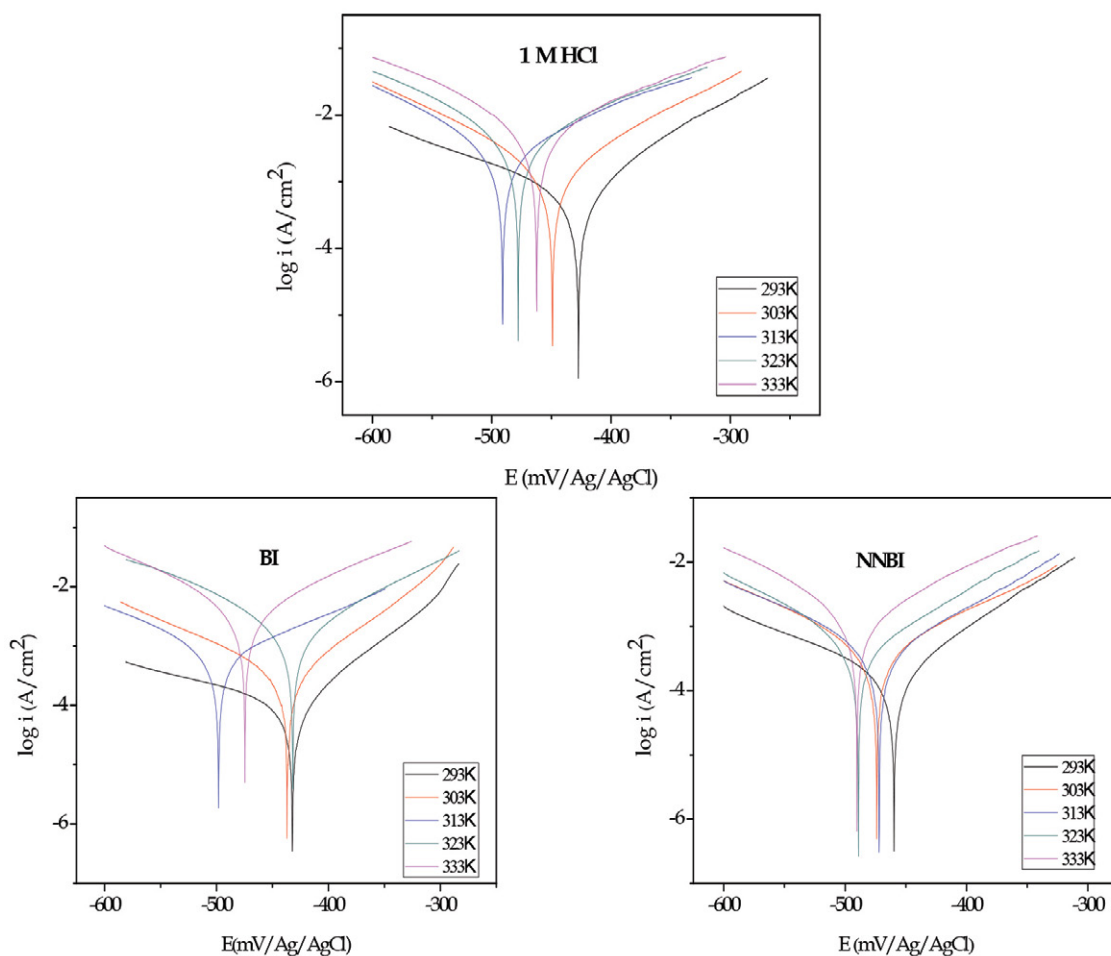


Figure 6. Tafel curves for corrosion of mild steel in 1 M HCl in the absence and presence of 1×10^{-4} M of BI and NNBI at different temperatures.

Table 3. Influence of temperature on the electrochemical parameters of mild steel in 1 M HCl medium in the absence and presence of 1×10^{-4} M of BI and NNBI

	Temperature (K)	E_{corr} (mV/Ag/AgCl)	i_{corr} (mA/cm ²)	β_a (mV/dec)	β_c (mV/dec)	IE (%)
1 M HCl	293	-427	0.63	82	-159	-
	303	-449	1.76	114	-121	-
	313	-491	3.21	145	-118	-
	323	-478	6.13	173	-140	-
	333	-462	8.65	168	-147	-
1 M HCl + BI 1×10^{-4} M	293	-432	0.1	72	-202	84
	303	-437	0.30	7	-119	83
	313	-498	0.64	134	-111	80
	323	-432	1.6	120	-137	74
	333	-475	2.81	135	-126	68
1 M HCl + NNBI 1×10^{-4} M	293	-460	0.18	82	-149	71
	303	-474	0.52	124	-124	70
	313	-472	1.1	108	-129	66
	323	-490	2.21	108	-109	64
	333	-490	3.5	88	-76	60

dition of 1×10^{-4} M of BI and NNBI, were conducted at temperature ranging from 293 to 333 K as shown in Fig. 6.

The electrochemical parameters obtained from the polarization curves of mild steel in 1M HCl before and after addition of the optimal concentration (1×10^{-4} M) of BI and NNBI at different temperatures are shown in Table 3.

According to Table 3, we can notice that E_{corr} is altered by increasing temperatures and moves towards more negative values i_{corr} values increase with increasing temperatures but they remain much lower compared to those observed for HCl alone, thereby confirming that BI and NNBI inhibit corrosion in the temperature range (293–333 K) albeit they appeared less efficient at the highest temperatures. The decrease in IE (%) with increasing temperatures is explained by the desorption of the previously adsorbed inhibitors, which leads a larger metallic surface to be exposed to the corrosive solution.¹⁸ This phenomenon may be the result of Van Der Waals interactions (weak forces) between the metal surface and the inhibitor.¹⁹ These interactions are very sensitive to thermal agitation and are very easy to break according to increased temperatures. The increase in temperature shifts the adsorption-desorption balance toward the desorption process, thus reducing the inhibition efficiency of the compounds studied.^{19,20}

3. 1. 4. The Activation Parameters

Temperature is a critical factor that has a considerable effect on the behavior of steel in acidic medium. As the temperature increases, it can modify the metal/inhibitor interaction interface. To assess the impact of this parameter on the kinetics of protective film formation, the activation parameters of the corrosion process such as the activation energy (E_a), the activation enthalpy (ΔH_a°) and activation entropy (ΔS_a°) were calculated at different temperatures (293–333 K), in the absence and presence of 1×10^{-4} M of BI and NNBI inhibitors.

Activation energy (E_a) was determined using the i_{corr} values obtained from the polarization curves following the

equation (5):²¹

$$i_{corr} = A \exp\left(\frac{-E_a}{RT}\right) \quad (5)$$

Where i_{corr} is the corrosion current density, A is a pre-exponential factor, E_a denotes the activation energy, R represents the universal gas constant, and T is the temperature.

Fig. 7 represents the variation of the corrosion current density as a function $1/T$ ($\ln i_{corr} = f(1/T)$). This variation is a straight line both in the absence and presence of 1×10^{-4} M of BI and NNBI at different temperatures.

An alternative Arrhenius equation can determine the activation enthalpy (ΔH_a°) and the activation entropy (ΔS_a°) using the following equation (6):

$$i_{corr} = \frac{RT}{Nh} \exp\left(\frac{\Delta S_a^\circ}{R}\right) \exp\left(-\frac{\Delta H_a^\circ}{RT}\right) \quad (6)$$

Where h is the Planck's constant, N denotes the Avogadro number, R represents the universal gas constant.

The variation of $\ln(i_{corr}/T)$ as a function $1/T$ is a straight line (Fig. 8), with a slope of $(-\Delta H_a^\circ/R)$ and an intercept equal to $(\ln R/Nh) + \Delta S_a^\circ/R$. Therefore, it was possible to calculate ΔH_a° and ΔS_a° .

The activation parameters such as the activation energy (E_a) the activation enthalpy (ΔH_a°) and activation entropy (ΔS_a°) in the absence and presence of 1×10^{-4} M of BI and NNBI given in Table 4 are calculated from the Arrhenius relation.

Table 4. Activation parameters of the corrosion process of mild steel in 1M HCl solution in the absence and presence of 1×10^{-4} M of BI and NNBI

Inhibitor	E_a (kJ/mol)	ΔH_a° (kJ/mol)	ΔS_a° (J/mol K)
1M HCl	53.6	51.19	-72.23
1M HCl + 1×10^{-4} M BI	69.27	66.72	-36
1M HCl + 1×10^{-4} M NNBI	71.6	69	-27

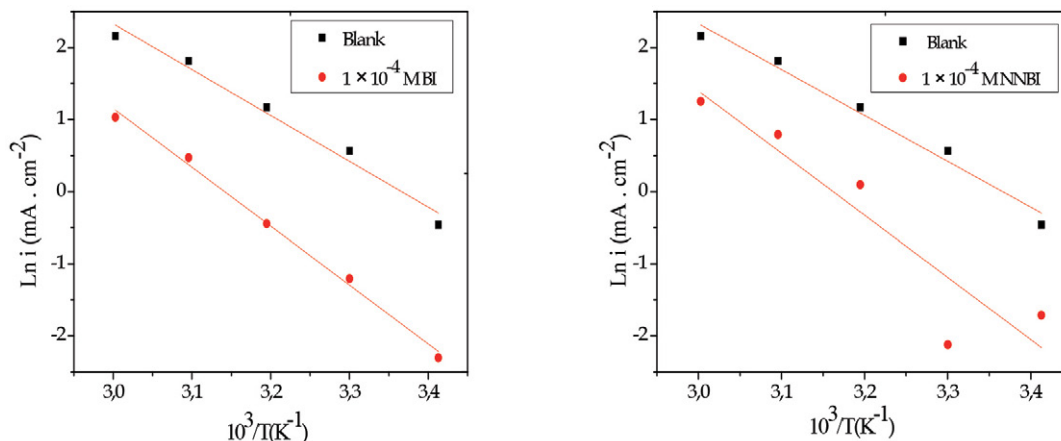


Figure 7. Arrhenius plots of the corrosion of mild steel in 1M HCl in the absence and presence of 1×10^{-4} M of BI and NNBI at different temperatures

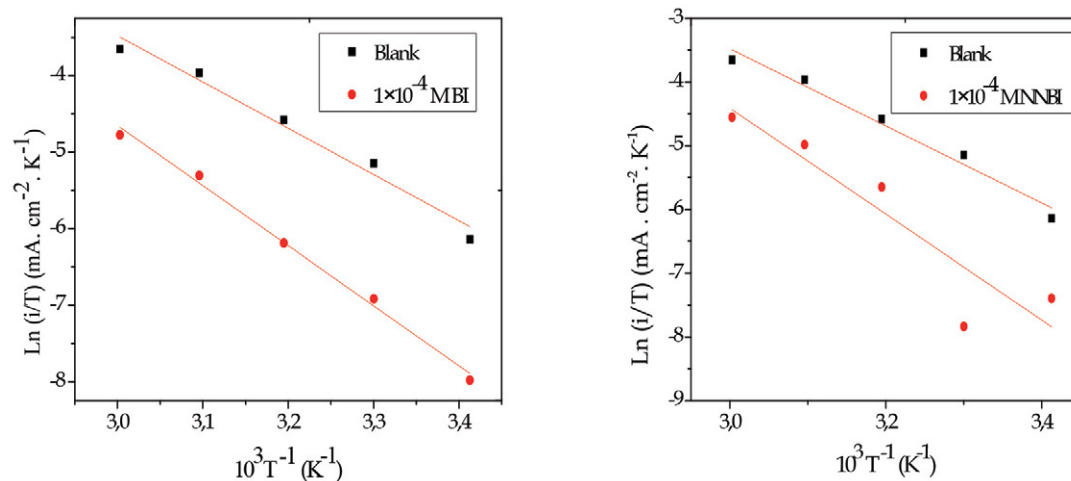


Figure 8. Alternative Arrhenius plots for mild steel in 1 M HCl in the absence and presence of 1×10^{-4} M of BI and NNBI.

From Table 4, we can observe that is higher in the presence of inhibitor compared to the blank. The increase in values in the presence of the benzimidazole derivatives is typical of the physisorption of these molecules on the steel surface.²² The high values of E_a can also be attributed to the increase in the thickness of the double layer.^{23,24} Furthermore, the augmentation of E_a after addition of BI or NNBI indicates that physisorption, through electrostatic interactions, occurred in the first step of the inhibition mechanism.²⁵ Besides, the positive signs of the enthalpies reflect the endothermic nature of the steel dissolution process.^{26,27} ΔH°_a values closer to 100 kJ/mol imply chemisorption while those below 40 kJ/mol correspond to physisorption. In this study, the values in the presence of inhibitors are positive, similarly closer to 100 kJ/mol, and higher than those found in the solution exempt of inhibitor. This reflects a mixed type adsorption process²⁸ and shows that the dissolution of the steel is endothermic. Concordantly, higher negative values of the entropy ΔS°_a in the presence of inhibitors signifies that there was a reduction in disorder during the transformation of the reactants into the activated iron-molecule complex in the medium.^{29, 30}

3. 1. 5. Adsorption Parameters

The effectiveness of organic corrosion inhibitors principally depends on their adsorption capacity at the metal/solution interface. Therefore, it is essential to know the adsorption isotherm, a thermodynamic parameter, which can inform us about the interaction between the inhibitor and the metal surface. To identify the type of adsorption corresponding to this inhibitor, various isotherms were tested: Langmuir, Temkin and Frumkin (Fig. 9).

Based on these isotherms, the recovery rate θ is linked to the inhibitor concentration C_{inh} ^{31,32} following these respective equations:

$$\frac{C_{inh}}{\theta} = \frac{1}{K_{ads}} + C_{inh} \quad \text{Langmuir adsorption isotherm (7)}$$

$$\exp(-2a\theta) = K_{ads} C_{inh} \quad \text{Temkin adsorption isotherm (8)}$$

$$\left(\frac{\theta}{1-\theta}\right) \exp(2a\theta) = K_{ads} C_{inh} \quad \text{Frumkin adsorption isotherm (9)}$$

Where a represents the interaction constant between adsorbed particles, K_{ads} denotes the adsorption equilibrium constant, and C_{inh} stands for the inhibitor concentration.

We can notice from the Fig. 9, that the Langmuir adsorption isotherm is the most appropriate for adjusting the obtained experimental results (R^2 close to unity), which means that the adsorption of 1×10^{-4} M of BI and NNBI on the mild steel surface, in 1 M HCl solution at 293 K, obeys the Langmuir adsorption isotherm. In the same experimental conditions, K_{ads} and the free energy of adsorption (ΔG°_{ads}) of BI and NNBI (Table 5) were calculated from the following relations:

$$K_{ads} = \frac{1}{C_{inh}} \times \frac{\theta}{1-\theta} \quad (10)$$

$$\Delta G^\circ_{ads} = -RT \ln (55,5 \cdot K_{ads}) \quad (11)$$

Where θ denotes the surface coverage rate, C_{inh} is the inhibitor concentration, R represents the gas constant, T is the absolute temperature, and 55.5 is the concentration of water in solution (mol/L).

Table 5. Thermodynamic parameters of adsorption of 1×10^{-4} M of BI and NNBI on mild steel in 1 M HCl solution at 293 K

Inhibitor	K_{ads} (M ⁻¹)	ΔG°_{ads} (kJ/mol)
BI	5.25×10^4	-36.24
NNBI	2.44×10^4	-34.37

The high values of K_{ads} (5.25×10^4 M⁻¹ for BI and 2.44×10^4 M⁻¹ for NNBI) mean that a strong adsorption of the inhibitors occurred on the steel surface.^{33,34}

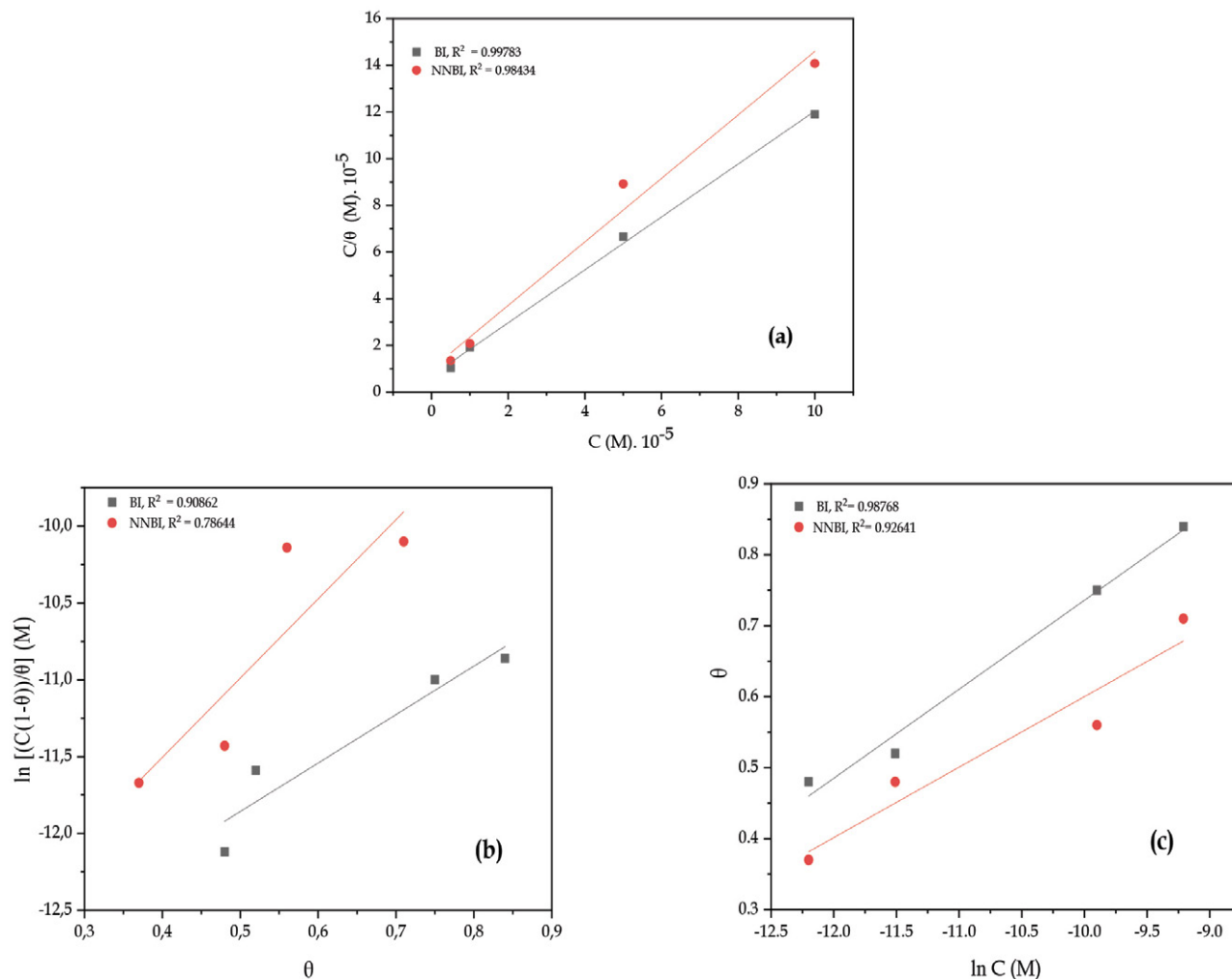


Figure 9. (a) Langmuir, (b) Freundlich and (c) Temkin adsorption isotherms for mild steel in 1 M HCl of BI and NNBI at 20 °C

The negative values of ΔG_{ads}° reflect the spontaneity of the interaction between the inhibitor, the metal surface, and the stability of the formed layer.³⁵

Furthermore, adsorption free energies ΔG_{ads}° ranged from -20 and -40 kJ/mol, which strongly suggests that the adsorption of BI or NNBI on the steel surface is a mixed type (both chemical and physical).^{36,37}

3. 2. Theoretical Study by DFT

The theoretical calculation by DFT is implemented to study the correlation between the inhibition efficiency (IE) and the molecular reactivity of the inhibitor.

The energy of the highest occupied molecular orbital (E_{HOMO}), the energy of the lowest unoccupied molecular orbital (E_{LUMO}), the energy gap ($\Delta E_{gap} = E_{LUMO} - E_{HOMO}$), the dipole moment (μ), the absolute electronegativity (χ), the absolute hardness (η), the global softness (σ), the number of electrons transferred (ΔN), and the electrophilicity index (ω) were determined,³⁸ following equations 12–18:

$$I = -E_{HOMO} \quad (12)$$

$$A = -E_{LUMO} \quad (13)$$

Where I: Ionization potential (eV), A: Electron Affinity (eV).

The values of χ and η were calculated, according to Pearson:

$$\chi = (I + A)/2 \quad (14)$$

$$\eta = (I - A)/2 \quad (15)$$

σ , which describes the capacity of an atom to receive electrons,¹³ was estimated by:

$$\sigma = 1/\eta \quad (16)$$

ΔN is calculated as follows:

$$\Delta N = (\chi_{Fe} - \chi_{inh})/2 (\eta_{Fe} + \eta_{inh}) \quad (17)$$

Where χ_{Fe} , χ_{inh} , η_{Fe} and η_{inh} designate the absolute electronegativity and the absolute hardness of iron and inhibitor, respectively.

The theoretical values χ and η of iron are equal to 7 and 0 eV. mol⁻¹ respectively.⁴⁰

Eventually, ω was obtained as follows:

$$\omega = \chi^2/2\eta \quad (18)$$

Adsorption on the metal surface is due to donor-acceptor interactions between the π electrons of the inhibitor and the vacant d orbitals on the surface atoms of the metal.⁴¹

The electron donor (molecule having a high E_{HOMO}) interacts with a suitable acceptor (molecule having a low E_{LUMO}). Thus, high values of E_{HOMO} facilitate the adsorption of the inhibitor to the metal surface by influencing the electronic transfer process through the adsorbed layer. On the other hand, E_{LUMO} highlights on the electron acceptor character of the molecule (e.g., inhibitor).

The decrease in the E_{LUMO} value is an indicator of the ability of the molecule to accept electrons from the metal surface.⁴² As established in the literature, a good corrosion inhibitor is often the one which not only gives up its electrons, but is also capable of accepting electrons from the metallic surface; the lower the E_{LUMO} is, the higher the IE.

The gap between the E_{HOMO} and E_{LUMO} is another important parameter; the low values of ΔE_{gap} are a sign of good inhibitory activity.⁴³ A high ΔE_{gap} value characterizes a hard molecule and a low ΔE_{gap} value characterizes a soft one.

Hard molecules are facing difficulties to donate electrons to an acceptor, and consequently their reactivity is lower than that of soft molecules. Adsorption occurs in the molecular region where σ has the highest value.²⁵ IE increases with increasing values of σ but with decreasing values of ω .

According to Lukovits, if $\Delta N < 3.6$, the inhibitor is an electron donor and therefore it is a valuable inhibitor, since its IE increases with its capacity to donate electrons.⁴⁴

The dipole moment is mostly used to describe the molecular polarity.⁴⁵ Organic compounds with high dipole moments are good inhibitors.⁴⁶

The optimized molecular structures and the frontier molecular orbital density distributions of the organic compounds BI and NNBI are represented in Fig. 10.

Fig. 10 shows that the HOMO density distribution on the BI molecule is identical to that of LUMO, centered essentially on the planar benzimidazole group and its phenyl substituent bonded to C13.⁴⁷ For the NNBI molecule,

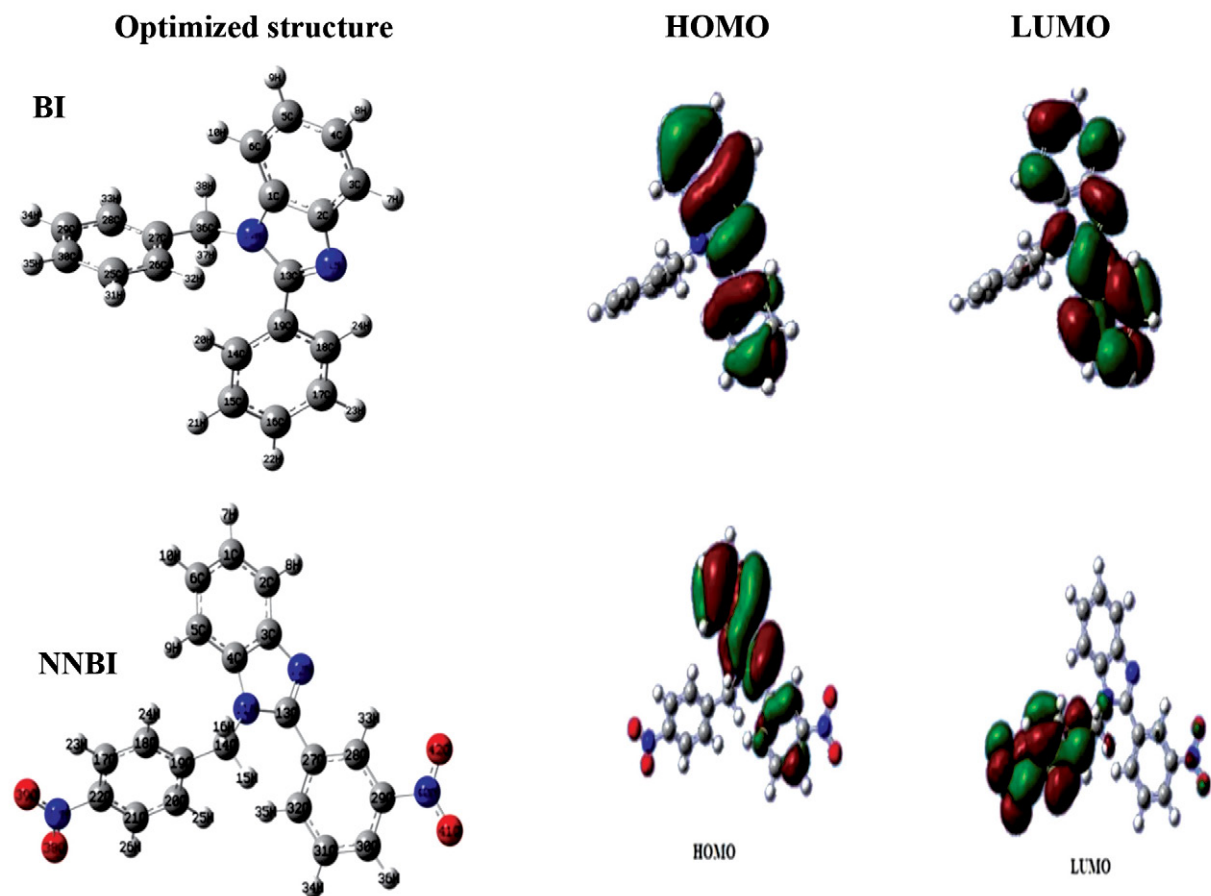


Figure 10. Optimized molecular structures and the frontier molecular orbital density distributions of the organic compounds BI and NNBI given byB3LYP/6-31G (d, p).

the HOMO density is located mostly on the planar benzimidazole ring and on some atoms of the phenyl group bonded to C13, while the LUMO density is centered on the N11 nitrogen of benzimidazole, the nitro group of phenyl linked to C13 and nitro group, and the phenyl linked to C14.⁴⁸

The quantum parameters of BI and NNBI in the gas and aqueous phases have been summarized in Table 6.

Table 6. Quantum parameters of BI and NNBI in gas and aqueous phase calculated by DFT (B3LYP) using the 6-31G basis (d, p).

Parameters	BI		NNBI	
	gas phase	aqueous phase	gas phase	aqueous phase
E_{tot} (eV)	-23981.67	-23981.95	-35111.14	-35111.14
E_{HOMO} (eV)	-5.72	-6	-6.34	-6.21
E_{LUMO} (eV)	-1	-1.07	-2.74	-2.70
ΔE_{gap} (eV)	4.72	4.94	3.60	3.50
μ (Debye)	3.45	4.97	4.21	5.69
η (eV)	2.36	2.47	1.80	1.75
σ (eV ⁻¹)	0.42	0.40	0.55	0.57
χ (eV)	3.36	3.55	4.54	4.46
ω (eV)	2.4	2.54	5.73	5.67
ΔN	0.77	0.70	0.68	0.72

The data in the Table 6 show that BI and NNBI have high HOMO (-05.72 and -06.34 eV for BI and NNBI, respectively) and low LUMO energies, as well as low energy gap (ΔE) implying easy adsorption to the steel surface and consequently high inhibition efficacy (IE). This property is confirmed by the high dipole moment (μ) values (3.45

and 4.21 Debye for BI and NNBI, respectively); these inhibitors can therefore easily transfer electrons to the vacant d orbitals of iron. Molecular reactivity depends on the hardness (η) which was found low (2.36 and 1.80 eV for BI and NNBI, respectively) and softness (σ), which was found high (0.42 and 0.55 eV for BI and NNBI, respectively).⁴⁹ The electronegativity (χ) values (3.36 and 4.54 eV for BI and NNBI, respectively) were lower than that of iron, which implied a transfer of electrons from the HOMO orbital of the inhibitor to the empty 3d orbital of iron.⁵⁰ BI and NNBI displayed ΔN values lower than 3.6 (0.77 and 0.68 for BI and NNBI, respectively), which indicate that they are electron donors and the metal surface is an acceptor. The IE increases with the ability of the molecule to donate electrons to the steel surface, this ability follows the sequence BI > NNBI, which is in accordance with previous data.⁵¹

The global electrophilicity index (ω) reflects the ability of a chemical species to accept electrons. A high value of electrophilicity index describes a good electrophile while a small one describes a good nucleophile. The electrophilicity indices (ω) of NNBI being higher than BI (2.4 and 5.73 eV for BI and NNBI, respectively) confirms the electrophilic nature of NNBI especially since it includes an electron-withdrawing NO₂ group in its structure.⁵²

Molecular electrostatic potential (MEP) was used to identify electrophilic and nucleophilic sites (Fig. 11). In the case of BI, the electron-rich regions are located around the heteroatoms and the conjugated double bonds. The nucleophilic active sites that promote nucleophilic reactions in the corrosion inhibition process of mild steel are the nitrogen atom N11 and the electrons of the conjugated double bonds.⁵³ In the case of NNBI, the nucleophilic ac-

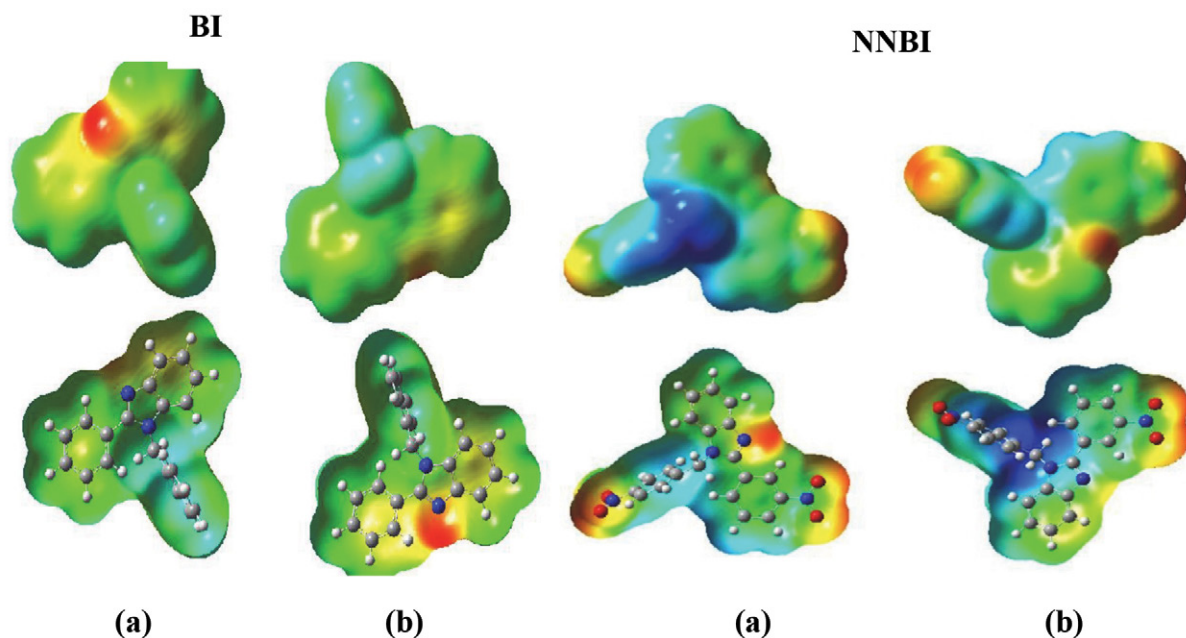


Figure 11. MEP map and counter plot of BI and NNBI inhibitors. (a) Front view and (b) Rear view.

tive sites are located on one of the nitrogen atoms and on the oxygen atoms of the two nitro groups of the substituted phenyl.⁵⁴

The distribution of Mulliken charges for BI and NNBI is shown in Table 7.

The Mulliken analysis, that estimates the adsorption centers of inhibitors, was mainly used for the calculation of the charge distribution across the entire backbone of the molecule. In the case of the BI, N11 and N12 atoms displayed negative charges with a high electron density, which means that they behave like nucleophilic centers when they interact with the mild steel surface.⁵⁵

The nitrogen and carbon atoms of the benzimidazole ring of BI exhibited negative charges, making them ideal sites for adsorption on mild steel.⁵³ In the case of the NNBI, we can observe that all the nitrogen and oxygen atoms have significant negative charges (−0.541, −0.389, −0.385, −0.390, −0.384 for N11, O38, O39, O41 and O42, respectively) and negative charges on some carbon atoms of the imidazole ring like C29 (−0.137) and C17 (−0.135). This indicates that these atoms are the likely active sites for the adsorption of NNBI on the mild steel surface. As a result, the NNBI molecules form a barrier, thereby preventing the arrival of aggressive ions at the metal surface, and thus reducing the rate of corrosion.

Table 7. Mulliken atomic charges calculated for BI and NNBI.

BI			NNBI		
Atom	Gas phase	Aqueous phase	Atom	Gas phase	Aqueous phase
C1	−0.087	−0.101	C1	0.226	0.221
C2	−0.131	−0.151	C2	0.284	0.283
C3	0.249	0.246	C3	−0.121	−0.133
C4	0.197	0.196	C4	−0.095	−0.110
C5	−0.117	−0.129	C5	−0.099	−0.112
C6	−0.108	−0.119	C6	−0.118	−0.136
H7	0.088	0.106	H7	0.096	0.113
H8	0.097	0.105	H8	0.095	0.110
H9	0.156	0.172	H9	0.107	0.113
H10	0.086	0.109	H10	−0.546	−0.575
N11	−0.554	−0.564	N11	−0.541	−0.551
N12	−0.527	−0.557	N12	0.400	0.408
C13	0.387	0.391	C13	0.151	0.157
C14	−0.107	−0.108	C14	−0.127	−0.130
H15	0.119	0.136	H15	−0.087	−0.084
H16	0.131	0.137	H16	0.257	0.264
C17	−0.100	−0.112	C17	−0.135	−0.126
C18	−0.167	−0.182	C18	−0.066	−0.059
C19	0.120	0.108	C19	0.140	0.139
C20	−0.136	−0.147	C20	0.145	0.150
C21	−0.078	−0.094	C21	0.146	0.156
C22	−0.085	−0.102	C22	0.011	0.013
H23	0.073	0.096	H23	−0.119	−0.118
H24	0.152	0.157	H24	0.095	0.109
H25	0.076	0.096	H25	0.153	0.176
H26	0.085	0.102	H26	0.092	0.118
C27	0.093	0.091	C27	0.023	0.017
C28	−0.107	−0.120	C28	0.034	0.036
C29	−0.090	−0.101	C29	−0.137	−0.132
C30	−0.077	−0.088	C30	0.269	0.275
C31	−0.093	−0.105	C31	−0.094	−0.095
C32	−0.124	−0.131	C32	−0.109	−0.113
H33	0.119	0.114	H33	0.119	0.131
H34	0.093	0.112	H34	0.139	0.142
H35	0.091	0.112	H35	0.139	0.142
H36	0.106	0.117	H36	0.107	0.132
H37	0.081	0.111	N37	0.354	0.365
H38	0.090	0.098	O38	−0.389	−0.418
			O39	−0.385	−0.416
			N40	0.357	0.368
			O41	−0.390	−0.417
			O42	−0.384	−0.413

3. 3. Molecular Dynamic Simulation Study (MDS)

For a better understanding of the interactions between BI, NNBI and the Fe (110) surface, MDS was carried out in the presence or absence of solvent molecules (H₂O). The equilibrium adsorption configurations of BI and NNBI on the Fe (110) surface, using of the Monte Carlo simulation, are illustrated in Fig. 12.

According to Fig. 12, it clearly appears that BI and NNBI adsorb in a parallel manner to the Fe (110) surface. The nitrogen atoms in BI and NNBI molecules can donate electrons to unoccupied iron d orbitals to form coordination bonds while the electron orbitals of aromatic rings can accept electrons from the iron orbitals to form coordination bonds.⁵⁶

The descriptors obtained by the MDS for BI and NNBI on the Fe (110) surface, are listed in Table 8.

The interaction (adsorption) energy (E_{inter}), between the inhibitor and the Fe (110) surface was calculated by the following equation:⁵⁷

Table 8. Molecular dynamics simulation (MDS) results for the lowest adsorption configurations of BI and NNBI compounds on the Fe (110) interface.

Systems		BI/Fe (110)	NNBI/Fe (110)
Total energy (E_s)	(kJ/mol)	-105	-153
Adsorption energy (E_{ads})	(kJ/mol)	-216	-405
Rigid adsorption energy	(kJ/mol)	-122	-151
Deformation energy (D_E)	(kJ/mol)	-93	-254
dE_{ads}/dN_i	(kJ/mol)	-216	-405

$$E_{inter} = E_{tot} - (E_{surf+sol} + E_{inh}) \quad (19)$$

Where, E_{tot} is the total energy of the iron crystal with the adsorbed inhibitor molecule, (E_{inter}) is the interaction energy, $E_{surf+sol}$ represents the energy of the iron surface with H₂O molecules, and E_{inh} denotes the energy of the free inhibitor molecule.

The binding energy is the negative value of E_{inter} . The total energy is defined as the sum of the rigid adsorption

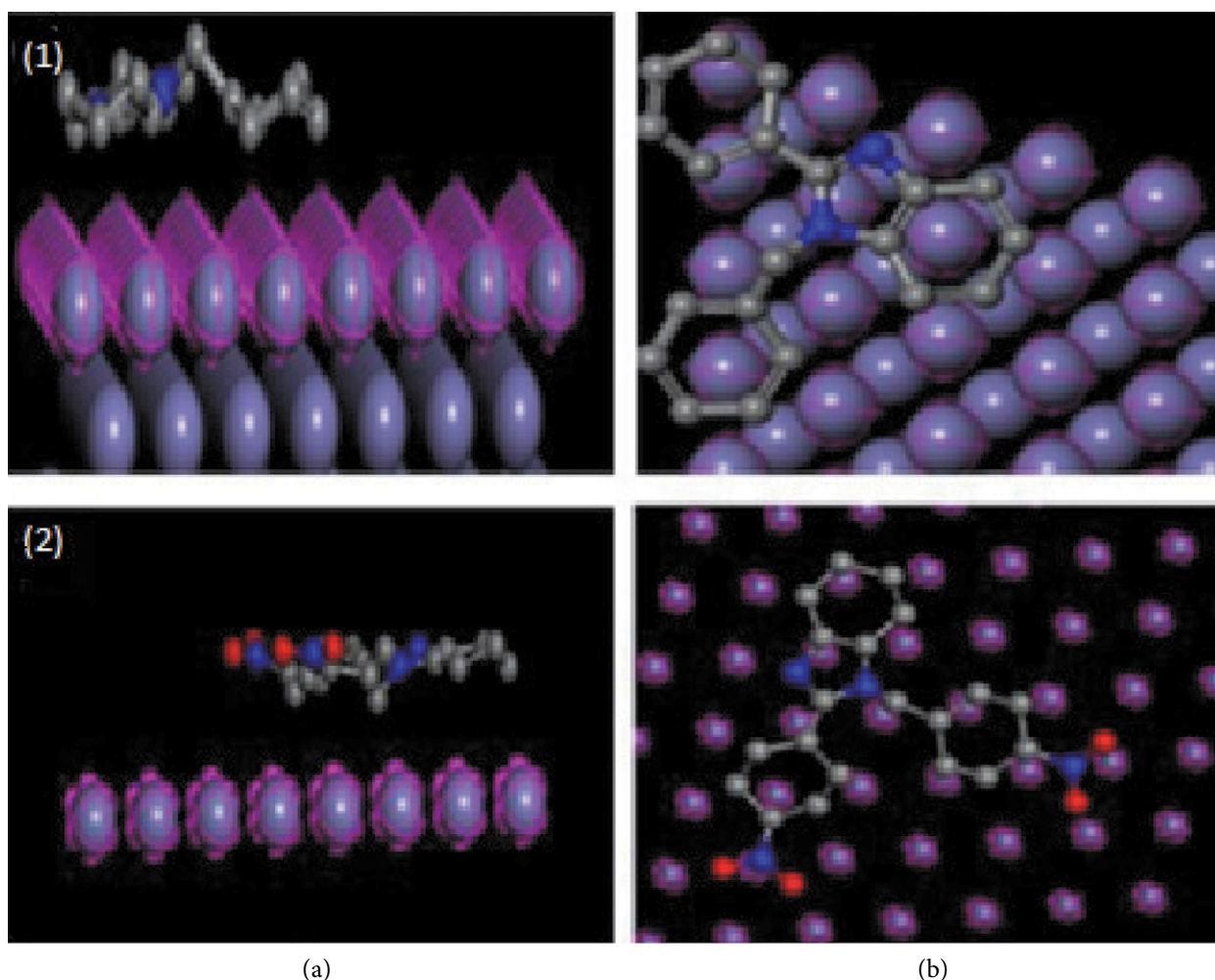


Figure 12. Equilibrium adsorption configurations of BI (1) and NNBI (2) molecules on the Fe (110) surface, (a) side view (b) top view.

energy (R.A.E) and the deformation energy (E_{def}). R.A.E reports the energy released when unrelaxed adsorbed components (i.e., before the geometry optimization step) are adsorbed onto the substrate. E_{def} is the energy released when adsorbed components are released to the substrate surface.¹² Adsorption energy (E_{ads}) is the energy released when relaxed inhibitor molecules are adsorbed on the metal surface. The energy of the substrate (surface of the iron) is taken equal to zero.

The differential adsorption energy (dE_{ads}/dNi) is the energy of removal of an adsorbate from a particular component.²¹

The data summarized in Table 8 shows that BI and NNBI exhibit high negative adsorption energy during the simulation process, which indicates spontaneous and stronger adsorption of the inhibitors on the steel surface.⁵⁸

MDS was performed to further study the adsorption behavior of BI and NNBI on the Fe (110) surface in aqueous phase. The most stable low-energy adsorption configurations of BI and NNBI inhibitors on a Fe (110)/50 H₂O molecules system using Monte Carlo simulations are shown in Fig. 13.

From Fig. 13, it is evident that, when adsorbed on the Fe (110) surface in the presence of water, BI and NNBI adopt a flat orientation as they approach the iron surface with close contact, thereby confirming a strong adsorption of the inhibitors on the iron surface.⁵³

The values for the outputs and descriptors of the Monte Carlo simulations are listed in Table 9. It includes the total energy, the adsorption energy, the rigid adsorption energy and the strain energy of the inhibitors adsorbed on Fe (110) in the presence of 50 water molecules, as well as the differential adsorption energies of inhibitors and water.

In all cases, the adsorption energies of BI and NNBI are much higher than those of H₂O molecules. This suggests a gradual substitution of H₂O molecules on the iron surface, leading to the formation of a stable layer capable of protecting the iron from aqueous corrosion.⁴⁹

It can also be noted that BI and NNBI exhibit high negative adsorption energy during the simulation process, which indicates a stable and stronger adsorption of these inhibitors on a steel surface.⁵⁸

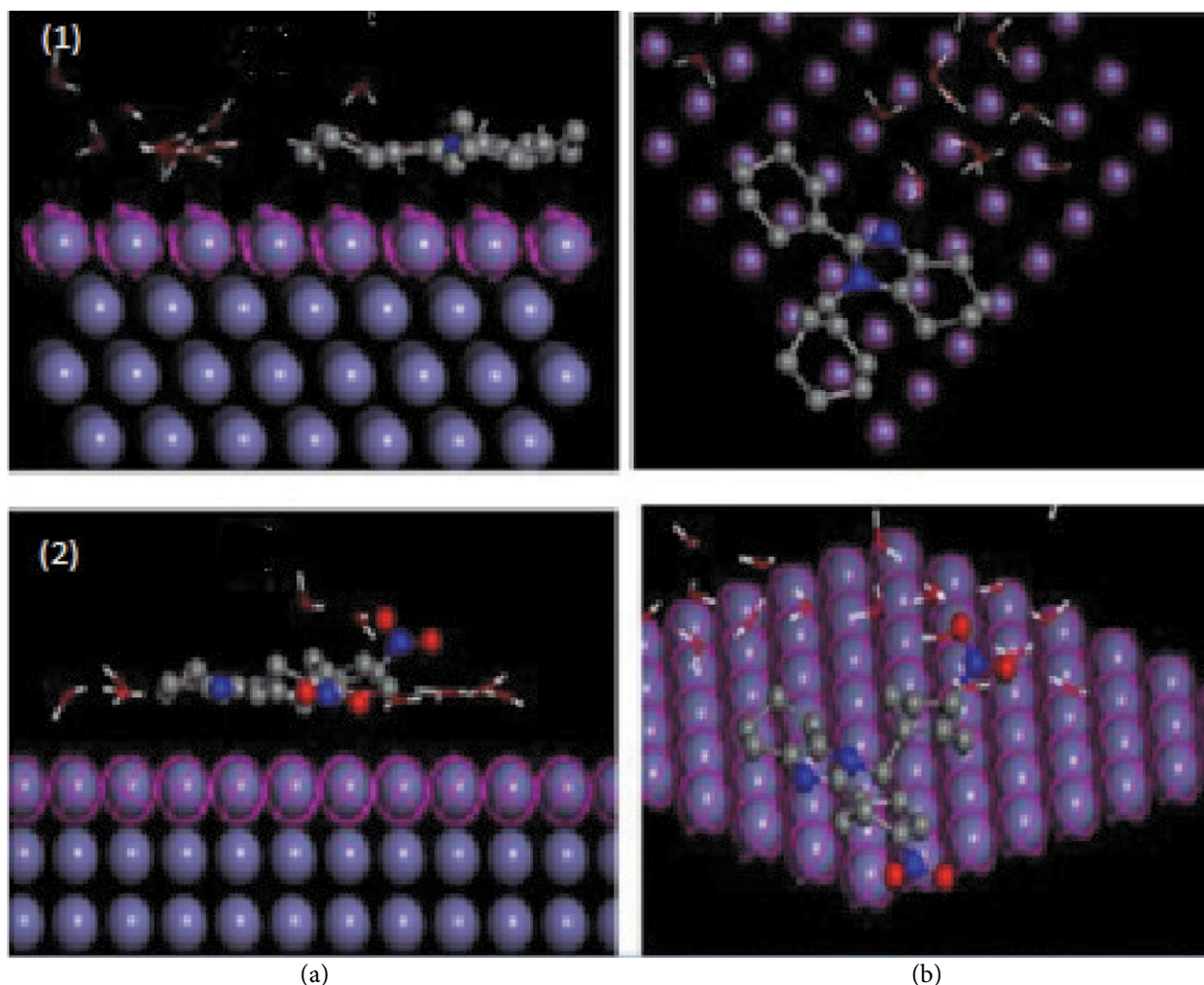


Figure 13. Equilibrium adsorption configurations of BI (1) and NNBI (2) molecules on the Fe (110) surface in presence of water, (a) side view (b) top view.

Table 9. Molecular dynamics simulation (MDS) results for the lowest adsorption configurations of BI and NNBI compounds on the Fe (110)/50 H₂O interface.

Systems		BI/Fe (110)/H ₂ O	NNBI/Fe (110)/H ₂ O
Total energy (E_t)	(kJ/mol)	-845	-891
Adsorption energy (E_{ads})	(kJ/mol)	-1929	-2116
Rigid adsorption energy	(kJ/mol)	-899	-924
Deformation energy (D_E)	(kJ/mol)	-1029	-1191
dE_{ads}/dN_i compounds	(kJ/mol)	218	409
dE_{ads}/dN_i H ₂ O	(kJ/mol)	-35	-33

4. Conclusion

Two new benzimidazole derivatives namely 1-Benzyl-2-phenyl 1H-benzimidazole (BI) and 1-(4-Nitrobenzyl)-2-(4-nitrophenyl)-1H-benzimidazole (NNBI) were investigated as corrosion inhibitors for mild steel in 1 M HCl medium using a combined experimental and theoretical approaches.

The electrochemical analysis revealed that the inhibition efficiency of both inhibitors increases as their concentration increase according to the sequence BI > NNBI, the substitution with the nitro electron-withdrawing group (NO₂) reduces the protective power of NNBI. EIS plots indicated that the addition of inhibitors increases the charge-transfer resistance of the corrosion process, and hence the inhibition performance. The outcomes obtained from potentiodynamic polarization data indicate that the investigated compounds are mixed type inhibitors. The inhibitors adsorption on the metal surface follow the Langmuir isotherm model which is attributed to the monolayer formation of the inhibitors molecules on the steel surface. The obtained values of kinetic and thermodynamic parameters (E_w , ΔG_{ads}°) suggest that the adsorption process of BI and NNBI on mild steel surface in 1 M HCl occurred by physical and chemical ways.

The data achieved by electrochemical techniques corroborate. The inhibition rates determined are close and evolve in the same way. The inhibitory effectiveness of the two benzimidazole derivatives is confirmed even at high temperatures, indicating their strong thermostability.

Quantum chemical calculations extend the understanding of the experimental findings and show that heteroatoms and aromatic backbones play a crucial role in adsorption process thus a correlation between the inhibition efficiency and the molecular structure of the two inhibitors was established.

Molecular dynamics simulation (MDS) indicates that both investigated molecules adsorb in a parallel manner to the steel surface suggesting a better surface coverage of the metal and the high negative adsorption energies of

BI and NNBI indicates their spontaneous and stronger adsorption on the steel surface. The computational studies confirmed experimental results.

This work provides a step forward the best understanding of the role of two benzimidazole derivatives as new efficient corrosion inhibitors for steel corrosion in 1 M HCl medium and their behavior could be assessed with similar compounds in order to step up the search for more efficient organic corrosion inhibitors.

Authors' contributions:

S. B. and L. T. conceived and designed the experiments; S. B. and L. T. performed the experiments and analyzed the data; S. B. and L. T. revised the paper.

CRediT authorship contribution statement:

This statement is to certify that all Authors of the article "Inhibition effect of benzimidazole derivatives on the corrosion of mild steel in acidic medium: Experimental and theoretical studies" have approved the manuscript being submitted. We warrant that the article is original and has not received prior publication and is not under consideration for publication elsewhere.

Declaration of Competing Interest

The authors declare no conflict of interest.

Data Availability: upon reasonable request by contacting the corresponding author(s).

Funding

This research received no external funding.

5. References

1. M. Yadav, S. Kumar, T. Purkait, L. O. Olasunkanmi, I. Bahadur, E. E. Ebenso, *J. Mol. Liq.* **2016**, *213*, 122–138. DOI:10.1016/j.molliq.2015.11.018
2. E. E. Ebenso, I. B. Obot, L. C. Murulana, *Int. J. Electrochem. Sci.* **2010**, *5*, 1574–1586. DOI:10.1016/S1452-3981(23)15412-5
3. Y. Tang, F. Zhang, S. Hu, Z. Cao, Z. Wu, W. Jing, *Corros. Sci.* **2013**, *74*, 271–282. DOI:10.1016/j.corsci.2013.04.053
4. L. Toukal, M. Foudia, D. Haffar, N. Aliouane, M. Al-Noaimi, Y. Bellal, H. Elmsellem, I. Abdel-Rahman, *J. Indian Chem. Soc.* **2022**, *99*, 100634. DOI:10.1016/j.jics.2022.100634
5. C. Lee, W. Yang, R. G. Parr, *Phys. rev. B.* **1988**, *37*, 785–789. DOI:10.1103/PhysRevB.37.785
6. M. Frisch, G. Trucks, H. Schlegel, G. Scuseria, M. Robb, J. Cheeseman, G. Scalmani, V. Barone, B. Mennucci, G. Petersson, Gaussian 09, Revision A. 1, Gaussian Inc., Wallingford, CT., **2009**.

7. N. Metropolis, A. W. Rosenbluth, M. N. Rosenbluth, A. H. Teller, E. Teller, *J. Chem. Phys.* **1953**, *21*, 1087.
DOI:10.1063/1.1699114
8. F. El Hajjaji, I. Merimi, M. Messali, R. J. Obaid, R. Salim, M. Taleb, B. Hammouti, *Mater. Today Proc.* **2019**, *13*, 822–831. DOI:10.1016/j.matpr.2019.04.045
9. C. Boulechar, H. Ferkous, S. Djellali, M. A. Amin, S. Boufas, A. Djedouani, A. Delimi, Y. Ben Amor, K. Kumar Yadav, B. H. Jeon, Y. Benguerba, *J. Mol. Liq.* **2021**, *344*, 117874.
DOI:10.1016/j.molliq.2021.117874
10. S. Prifiharni, G. Mashanafie, G. Priyotomo, A. Royani, A. Ridhova, B. Elya, J. W. Soedarsono, *J. Indian Chem. Soc.* **2022**, *99*, 100520. DOI:10.1016/j.jics.2022.100520
11. R. Khanna, V. Kalia, R. Kumar, R. kumar, P. Kumar, H. Dahiya, P. Pahuja, G. Jhaa, H. Kumar, *J. Mol. Struct.* **2024**, *1297*, 136845. DOI:10.1016/j.molstruc.2023.136845
12. S. Abdoune, N. Aliouane, A. Hellal, M. Al-Noaimi, N. Sait, N. Chafai, L. Toukal, N. Ait Ahmed, *J. Mol. Struct.* **2024**, *1295*, 136673. DOI:10.1016/j.molstruc.2023.136673
13. W. Ettahiri, M. Adardour, E. Ech-chihbi, M. Azam, R. Salim, S. Dalbouha, K. Min, Zakia Rais, A. Baouid, M. Taleb, *Colloids Surf. A Physicochem. Eng. Asp.* **2024**, *681*, 132727.
DOI:10.1016/j.colsurfa.2023.132727
14. T. Yan, S. Zhang, L. Feng, Y. Qiang, L. Lu, D. Fu, Y. Wen, J. Chen, W. Li, B. Tan, *J. Taiwan Inst. Chem. Eng.* **2020**, *106*, 118–129. DOI:10.1016/j.jtice.2019.10.014
15. D. Daoud, H. Hamani, T. Douadi, *J. Adhes. Sci. Technol.* **2021**, *35*, 2319–2345. DOI:10.1080/01694243.2021.1885923
16. Q. Wang, X. Wu, H. Zheng, X. Xiao, L. Liu, Q. Zhang, P. Gao, Z. Yan, Y. Sun, Z. Li, X. Li, *Colloids Surf. A Physicochem. Eng. Asp.* **2022**, *640*, 128458. DOI:10.1016/j.colsurfa.2022.128458
17. D. S. Zinad, M. Hanoon, R. D. Salim, S. I. Ibrahim, A. A. Al-Amiery, M. S. Takriff, A. A. H. Kadhum, *Int. J. Corros. Scale Inhib.* **2020**, *9*, 228–243.
DOI: 10.17675/2305-6894-2020-9-1- 14.
18. A. Alamiery, L. M. Shaker, T. Allami, A. H. Kadhum, M. S. Takriff, *Mater. Today Proc.* **2021**, *44*, 2337–2341.
DOI:10.1016/j.matpr.2020.12.431
19. M. Husaini, U. Bishir, I. M. Adamu, I. M. Bashir, *Res. J. Chem. Environ.* **2020**, *24*, 99–106.
20. M. Mahdavian, M. M. Attar, *PCCC.* **2015**, *8*, 177–196.
DOI:10.1590/s1517-707620210002.1278
21. A. Ziouani, S. Atia, H. Hamani, T. Douadi, M. Al-Noaimi, N. Gherraf, *J. Indian Chem. Soc.* **2023**, *100*, 100832.
DOI:10.1016/j.jics.2022.100832
22. M. Oubaaqa, M. Ouakki, M. Rbaa, F. Benhiba, M. Galai, R. Idouhli, M. Maatallah, A. Jarid, I. Warad, B. Lakhrissi, A. Zarrouk, M. EbnTouhami, *J. Phys. Chem. Solids* **2022**, *169*, 110866. DOI:10.1016/j.jpss.2022.110866
23. N. Sait, N. Aliouane, N. Ait Ahmed, L. Toukal, M. Al-Noaimi, *J. Adhes. Sci. Technol.* **2022**, *36*, 109–133.
DOI:10.1080/01694243.2021.1916250
24. S. Boukazoula, D. Haffar, R. Bourzami, L. Toukal, V. Dorcet, *J. Mol. Struct.* **2022**, *1261*, 132852.
DOI:10.1016/j.molstruc.2022.132852
25. L. Raisemche, I. Kaabi, T. Douadi, M. Al-Noaimi, A. Alrashed, M. S. Mubarak, N. Elboughdiri, A. Zouaoui, Y. Benguerba, *J. Environ. Chem. Eng.* **2024**, *12*, 112354.
DOI:10.1016/j.jece.2024.112354
26. A. Boutouil, I. Elazhary, M. R. Laamari, H. Ben El Ayouchia, H. Anane, M. El Had- dad, S. E. Stiriba, *J. Adhes. Sci. Technol.* **2020**, *34*, 549–578. DOI:10.1080/01694243.2019.1681741
27. R. Haldhar, D. Prasad, N. Mandal, F. Benhiba, I. Bahadur, O. Dagdag, *Colloids Surf. A Physicochem. Eng. Asp.* **2021**, *614*, 126211. DOI:10.1016/j.colsurfa.2021.126211
28. P. R. Ammal, A. R. Prasad, *Joseph, Egypt. J. Pet.* **2018**, *27*, 1067–1076. DOI:10.1016/j.ejpe.2018.03.006
29. N. Bounedjar, M. Fouad Ferhat, L. Toukal, R. Messai, *Mater. Chem. Phys.* **2024**, *311*, 128555.
DOI:10.1016/j.matchemphys.2023.128555
30. M. Alahiane, R. Oukhrib, Y. AitAlbrimi, H. AbouOualid, H. Bourzi, R. AitAkbour, A. Assabbane, A. Nahle, M. Hamdani, *RSC Adv.* **2020**, *10*, 41137–41153.
DOI:10.1039/D0RA06742C
31. M. Galai, M. Rbaa, M. Ouakki, K. Dahmani, S. Kaya, N. Arrousse, N. Dkhireche, S. Briche, B. Lakhrissi, M. EbnTouhami, *Chem. Phys. Lett.* **2021**, *776*, 138700.
DOI:10.1016/j.cplett.2021.138700
32. N. B. Iroha, V. C. Anadebe, N. J. Maduelosi, L. A. Nnanna, L. C. Isaiah, O. Dagdag, A. Berisha, E. E. Ebenso, *Colloids Surf. A Physicochem. Eng. Asp.* **2023**, *660*, 130885.
DOI:10.1016/j.colsurfa.2022.130885
33. S. Benabid, T. Douadi, S. Issaadi, C. Penverne, S. Chafaa, *Measurement* **2017**, *99*, 53–63.
DOI:10.1016/j.measurement.2016.12.022
34. V. Shenoy K, P. P. Venugopal, P. D. ReenaKumari, D. Chakraborty, *Mater. Chem. Phys.* **2022**, *281*, 125855.
DOI:10.1016/j.matchemphys.2022.125855
35. N. N. Hau, D. Q. Huong, *J. Mol. Struct.* **2023**, *1277*, 134884.
DOI:10.1016/j.molstruc.2022.134884
36. F. H. Zaidon, K. Kassim, H. M. Zaki, Z. Embong, N. Z. N. Hashim, *J. Mol. Liq.* **2021**, *329*, 115553.
DOI:10.1016/j.molliq.2021.115553
37. S. A. Al Kiey, A. A. El-Sayed, A. M. Khalil, *Colloids Surf. A Physicochem. Eng. Asp.* **2024**, *683*, 133089.
DOI:10.1016/j.colsurfa.2023.133089
38. E. Ech-chihbi, R. Salim, M. Ouakki, M. Koudad, L. Guo, M. Azam, N. Benchat, Z. Rais, M. Taleb, *Mater. Today Sustain.* **2023**, *24*, 100524. DOI:10.1016/j.mtsust.2023.100524
39. A. Saady, Z. Rais, F. Benhiba, R. Salim, K. Alaoui, N. Arrousse, F. Elhajjaji, M. Taleb, K. Jarmoni, Y. Rodi, I. Warad, A. Zarrouk, *Corros. Sci.* **2021**, *189*, 109621.
DOI:10.1016/j.corsci.2021.109621
40. M. Ouakki, M. Galai, Z. Benzekri, Z. Aribou, E. Ech-Chihbi, L. Guo, K. Dahmani, K. Nouneh, S. Briche, S. Boukhris, M. Cherkaoui, *J. Mol. Liq.* **2021**, *344*, 117777.
DOI:10.1016/j.molliq.2021.117777
41. O. Moumeni, M. Mehri, R. Kerkour, A. Boubli, F. Mihoub, K. Rebai, A. Ali Khan, A. Erto, A. S. Darwish, T. Lemaoui, N. Chafai, Y. Benguerba, *J. Taiwan Inst. Chem. Eng.* **2023**, *147*, 104918. DOI:10.1016/j.jtice.2023.104918
42. H. Hamani, D. Daoud, S. Benabid, T. Douadi, *J. Indian Chem.*

- Soc. **2022**, 99, 100492. DOI:10.1016/j.jjics.2022.100492
43. K. V. Shenoy, P. P. Venugopal, P. D. R. Kumari, D. Chakraborty, *Mater. Chem. Phys.* **2022**, 281, 125855. DOI:10.1016/j.matchemphys.2022.125855
44. L. Toukal, D. E. Belfennache, M. Foudia, R. Yekhlef, F. Benghanem, B. Hafez, H. Elmsellem, I. Abdel-Rahman, *Int. J. Corros. Scale Inhib.* **2022**, 11, 438–464. DOI:10.17675/2305-6894-2022-11-1-26
45. P. P. Kumari, G. Anusha, J. N. Cheerlin Mishma, R. K. Sinha, A. S. Suvarna, S. L. Gaonkar, *Heliyon* **2023**, 9, e21014. DOI:10.1016/j.heliyon.2023.e21014
46. M. Al-Noaimi, S. Benabid, H. Hamani, Q. F. A. Salman, M. Binsabt, F. F. Awwadi, K. Douadi, T. Douadi, *Chem. Data Collect.* **2022**, 40, 100877. DOI:10.1016/j.cdc.2022.100877
47. P. R. Ammal, M. Prajila, A. Joseph, *J. Environ. Chem. Eng.* **2018**, 6, 1072–1085. DOI:10.1016/j.jece.2018.01.031
48. A. Dutta, S. Kr. Saha, U. Adhikari, P. Banerjee, D. Sukul, *Corros. Sci.* **2017**, 123, 256–266. DOI:10.1016/j.corsci.2017.04.017
49. W. M. I. W. M. Kamaruzzaman, M. S. Shaifudin, N. A. M. Nasir, M. A. Badruddin, N. Yusof, A. Adnan, N. Abdul Aziz, W. M. N. W. Nik, J. Haque, M. Murmu, P. Banerjee, M. S. M. Ghazali, *Mater. Chem. Phys.* **2024**, 312, 128642. DOI:10.1016/j.matchemphys.2023.128642
50. Ö. Uguz, M. Gümüş, Y. Sert, I. Koca, A. Koca, *J. Mol. Struct.* **2022**, 1262, 133025. DOI:10.1016/j.molstruc.2022.133025
51. A. A. Abdulridha, M. A. A. H. Allah, S. Q. Makki, Y. Sert, H. Edan Salman, A. A. Balakit, *J. Mol. Liq.* **2020**, 315, 113690. DOI:10.1016/j.molliq.2020.113690
52. M. A. Abbas, M. A. Bedair, O. E. El-Azabawy, E. S. Gad, *ACS Omega* **2021**, 6, 15089–15102. DOI:10.1021/acsomega.1c01274
53. Y. El Aoufir, Y. El Bakri, H. Lgaz, A. Zarrouk, R. Salghi, I. Warad, Y. Ramli, A. Guenbour, E. M. Essassi, H. Oudda, *J. Mater. Environ. Sci.* **2017**, 8, 3290–3302
54. Z. Salarvand, M. Amirnasr, M. Talebian, K. Raeissi, S. Meghdadi, *Corros. Sci.* **2017**, 114, 133–145. DOI:10.1016/j.corsci.2016.11.002
55. M. Yadav, D. Behera, S. Kumar, R. R. Sinha, *Ind. Eng. Chem. Res.* **2013**, 52, 6318–6328. DOI:10.1021/ie400099q
56. Z. Rouifi, M. Rbaa, A. S. Abousalem, F. Benhiba, T. Laabaissi, H. Oudda, B. Lakhrissi, A. Guenbour, I. Warad, A. Zarrouk, *Surf. Interfaces* **2020**, 18, 100442. DOI:10.1016/j.surf.2020.100442
57. H. EL Hassouni, A. Elyousfi, F. Benhiba, N. Setti, A. Romane, T. Benhadda, A. Zarrouk, A. Dafali, *Inorg. Chem. Commun.* **2022**, 143, 109801. DOI:10.1016/j.inoche.2022.109801
58. E. H. Akroujai, S. Chetioui, N. Benzbiria, A. Barrahi, A. Chraka, A. Djedouani, S. Chtita, B. Dikici, I. Warad, A. Bellaouchou, M. Assouag, A. Zarrouk, *Int. J. Corros. Scale Inhib.* **2023**, 12, 1441–1475. DOI:10.17675/2305-6894-2023-12-4-5

Povzetek

Z uporabo elektrokemijske impedančne spektroskopije (EIS) in potenciodinamične polarizacije (PDP) smo ocenili učinek dveh heterocikličnih spojin, derivatov benzimidazola (BnZ), in sicer 1-benzil-2-fenil-1H-benzimidazola (BI) ter 1-(4-nitrobenzil)-2-(4-nitrofenil)-1H-benzimidazola (NNBI), na korozijo ogljikovega jekla v mediju 1M HCl. Proučevali smo vpliv koncentracije in temperature. Določeni elektrokemijski parametri so pokazali, da sta oba inhibitorja mešanega tipa. Inhibicijska učinkovitost NNBI je bila manjša od učinkovitosti BI. Najbolj elektronsko privlačna substituenta zagotavlja najnižjo učinkovitost. Mehanizem delovanja teh inhibitorjev smo ovrednotili s termodinamično študijo. Izračunane vrednosti, inso potrdile, da se BI in NNBI adsorbirata s kemijskim in fizikalnim procesom. Proces adsorpcije je spontan in sledi Langmuirovi adsorpcijski izotermi. Kvantno kemijski parametri, izračunani z uporabo teorije gostotnega funkcionala in simulacije molekularne dinamike, so potrdili tako eksperimentalne podatke kot tudi podatke iz literature.



Except when otherwise noted, articles in this journal are published under the terms and conditions of the Creative Commons Attribution 4.0 International License

Scientific paper

Syntheses, Crystal Structures and Characterization of Two New Lanthanide Mercury Halide Compounds

Xi-Yu Shao, Hao-Dong Liu, Long-Hua Zeng, Yu-Yue Xu, Wen-Tong Chen*, Cheng Liu*, Sheng-Ping Dai and Chang-Wang Pan

School of Chemistry and Chemical Engineering, Jian Key Laboratory of Photoelectric Crystal Materials and Device, Key Laboratory of Jiangxi Province for Special Optoelectronic Artificial Crystal Materials, Humic Acid Utilization Engineering Research Center of Jiangxi Province, Institute of Applied Chemistry, Jingtangshan University, 343009, Jian, Jiangxi, China

* Corresponding author: E-mail: wtchen_2000@aliyun.com (W.-T. Chen); 234871279@qq.com (C. Liu)
Tel.: +86(796)8100490; fax +86(796)8100490

Received: 08-17-2024

Abstract

Two new lanthanide mercury halide compounds with isonicotinic acid as a ligand, namely, $[\text{Gd}(\mu_2\text{-HIA})_2(\mu_3\text{-IA})(\text{H}_2\text{O})_2(\text{HgCl}_2)]_n(n\text{HgCl}_4)\cdot 3n\text{H}_2\text{O}$ (**1**) (HIA = isonicotinic acid) and $\{[\text{Nd}(\mu_2\text{-HIA})_3(\text{DMF})(\text{H}_2\text{O})]_n\}[(\text{Hg}_4\text{Br}_{11})_n](2\text{HgBr}_2)(n\text{Br})\cdot n\text{H}_3\text{O}$ (**2**), were synthesized with solvothermal reactions and characterized by single-crystal X-ray diffraction. Compound **1** is characterized by a two-dimensional (2-D) layer-like structure, while compound **2** features a one-dimensional (1-D) chain-like structure. The lanthanide ions in both compounds are eight coordinated and show a square antiprism geometry. The mercury ions exhibit various coordination motifs. Compound **1** exhibits ultraviolet upconversion photoluminescence emission, whereas compound **2** displays red photoluminescence. The photoluminescence emissions arise from the characteristic 4f electron intrashell transitions of the ${}^6P_{7/2} \rightarrow {}^8S_{7/2}$ of the Gd^{3+} ions in compound **1** and the ${}^4F_{9/2} \rightarrow {}^4I_{9/2}$, ${}^4F_{7/2} + {}^4S_{3/2} \rightarrow {}^4I_{9/2}$, ${}^4F_{5/2} + {}^2H_{9/2} \rightarrow {}^4I_{9/2}$, ${}^4F_{3/2} \rightarrow {}^4I_{9/2}$ of the Nd^{3+} ions in compound **2**. Compound **2** has CIE (Commission Internationale de l'Éclairage) chromaticity coordinates of (0.7142, 0.2857) and its CCT (correlated color temperature) is 138,224 K. Solid-state UV/Vis diffuse reflectance spectra revealed that the semiconductor band gaps of the compounds are 3.12 eV and 3.23 eV, respectively. Elemental analyses and FT-IR spectroscopy were carried out to confirm the purity of the compounds.

Keywords: gadolinium; band gap; neodymium; photoluminescence; solvothermal reaction

1. Introduction

Over the course of several decades, lanthanide coordination compounds have increasingly garnered interest from researchers in chemistry and materials science. This heightened attention arises from the fact that these compounds often exhibit valuable physicochemical properties, including photoluminescence, catalytic activity, magnetic capabilities, and biochemical sensing abilities, thus making them highly sought-after for applications in displays, catalysis, medicine, and numerous other fields.^{1–6} The intriguing physicochemical attributes of lanthanide coordination compounds primarily arise from the abundant 4f electrons present in the lanthanide ions. Among these properties, which are captivating, photoluminescence stands out as particularly fascinating. Lanthanide coordination compounds typically exhibit robust photoluminescence emission when 4f electron transitions occur effi-

ciently. To explore their potential applications in domains such as electrochemical displays, luminescent sensors, medicine, magnetic materials, light-emitting diodes, and more, extensive research has been conducted on lanthanide coordination compounds.^{7–12}

Zinc, cadmium, and mercury, classified as Group 12 elements, have garnered considerable attention for a multitude of reasons, including zinc's pivotal role in biological systems, the diverse coordination motifs they exhibit, as well as their enticing photoelectric and photoluminescence behaviors, among others.^{13–16} Furthermore, the Group 12 elements also hold potential for use in the synthesis of semiconductor materials, and numerous semiconductor materials incorporating these elements have been documented to date.^{17–20}

Organic molecules featuring diverse functional groups are invaluable in the synthesis of metal coordina-

tion compounds. Specifically, N-containing heterocyclic molecules, such as isonicotinic acid, nicotinic acid, 4,4'-bipyridine, 2,2'-bipyridine, and others, have been extensively utilized in the preparation of these compounds due to their abundant coordination sites and versatility in coordination modes.^{21–23} To our understanding, isonicotinic acid serves as a valuable building block due to its unique structural features, namely, two carboxylic oxygen atoms on one side and a nitrogen atom on the other. This arrangement enables isonicotinic acid molecules to bind with various metal ions, facilitating the formation of novel compounds. Consequently, isonicotinic acid is regarded as an excellent chelating and bridging ligand for constructing metal coordination compounds with extended, high-dimensional structures. Additionally, the pyridyl ring in isonicotinic acid possesses delocalized π -electrons, which renders it a promising candidate for the development of luminescent materials in diverse fields, including organic light-emitting diodes (OLEDs), chemical sensors, solar energy conversion, and more.^{24–26}

For many years, our team has been aiming at research on photoluminescence and semiconductor compounds.^{27–29} We have recently become interested in the design and preparation of lanthanide mercury halide compounds with new structural geometries and fascinating properties. In this paper, we report the syntheses, single crystal structures, FT-IR, and semiconductor bandgaps, as well as the photoluminescence, CIE, and CCT of two new lanthanide mercury halide compounds with isonicotinic acid as a ligand, namely, $[\text{Gd}(\mu_2\text{-HIA})_2(\mu_3\text{-IA})(\text{H}_2\text{O})_2(\text{HgCl}_2)]_n(n\text{HgCl}_4)\cdot 3n\text{H}_2\text{O}$ (**1**) and $\{[\text{Nd}(\mu_2\text{-HIA})_3(\text{DMF})(\text{H}_2\text{O})]_n\}[(\text{Hg}_4\text{Br}_{11})_n](2\text{HgBr}_2)(n\text{Br})\cdot n\text{H}_3\text{O}$ (**2**). Both compounds were synthesized via solvothermal reactions. It is noteworthy that compound **1** exhibits ultraviolet up-conversion photoluminescence.

2. Experimental

2.1. Instruments and Chemicals

All reagents and chemicals applied for the syntheses of the title compounds were commercially available and directly used. The elemental analyses of carbon, hydrogen and nitrogen were conducted on an Elementar Vario EL elemental analyzer. The FT - IR spectroscopy was carried out on a PE Spectrum - One FT - IR spectrophotometer with KBr pellets in the wavenumber of $4000\text{ cm}^{-1} \sim 400\text{ cm}^{-1}$. The photoluminescence spectra were measured on a F97XP photoluminescence spectrometer with 200 nm \sim 900 nm wavelength. The solid - state UV/Vis diffuse reflectance spectra (DRS) were carried out on a TU1901 UV/Vis spectrometer with 190 nm \sim 900 nm wavelength. The band gap energy (E_g) of the title compounds was calculated from DRS data using the Kubelka–Munk equation ($\alpha h\nu = A(h\nu - E_g)^{1/2}$); where α is absorption coefficient; h is Planck constant, ν is light frequency, A is Tauc's constant, and E_g is absorption coefficient.³⁰

2.2. Preparation of $[\text{Gd}(\mu_2\text{-HIA})_2(\mu_3\text{-IA})(\text{H}_2\text{O})_2(\text{HgCl}_2)]_n(n\text{HgCl}_4)\cdot 3n\text{H}_2\text{O}$ (**1**)

The $\text{GdCl}_3\cdot 6\text{H}_2\text{O}$ (1 mmol, 372 mg), HgCl_2 (2 mmol, 542 mg), isonicotinic acid (3 mmol, 369 mg) and distilled water (15 mL) were loaded into a 25 mL Teflon-lined stainless steel autoclave. This autoclave was kept at 473 K for seven days. After naturally cooling to room temperature, colorless block-like crystals suitable for the single-crystal X-ray diffraction measurements were obtained, washed with distilled water and dried in air. The yield was 35% (based on $\text{GdCl}_3\cdot 6\text{H}_2\text{O}$). $\text{C}_{18}\text{H}_{24}\text{Cl}_6\text{GdHg}_2\text{N}_3\text{O}_{11}$: calc. C, 17.58; H, 1.97; N, 3.42; Found C, 17.68; H, 1.99; N, 3.48. FT-IR peaks (cm^{-1}) of **1**: 3514(vs), 3440(vs), 3206(w), 3134(m), 3073(s), 2892(w), 2803(w), 1699(m), 1590(vs), 1501(w), 1408(vs), 1230(m), 1077(w), 1048(m), 1004(w), 846(s), 761(vs), 676(s), 547(m) and 413(s). FT-IR peaks (cm^{-1}) of isonicotinic acid: 3453(vs), 3105(w), 3052(m), 2923(w), 2850(w), 2806(w), 1961(m), 1714(vs), 1613(s), 1565(m), 1476(w), 1411(s), 1335(s), 1302(w), 1229(s), 1140(m), 1023(s), 857(m), 764(s), 692(m), 671(w) and 485(m).

2.3. Preparation of $\{[\text{Nd}(\mu_2\text{-HIA})_3(\text{DMF})(\text{H}_2\text{O})]_n\}[(\text{Hg}_4\text{Br}_{11})_n](2\text{HgBr}_2)(n\text{Br})\cdot n\text{H}_3\text{O}$ (**2**)

The $\text{Nd}(\text{NO}_3)_3\cdot 6\text{H}_2\text{O}$ (0.5 mmol, 218 mg), HgBr_2 (2 mmol, 720 mg), isonicotinic acid (1.5 mmol, 185 mg), 1 mL DMF and 10 mL distilled water were loaded into a 25 mL Teflon-lined stainless steel autoclave. The autoclave was heated at 433 K for ten days and powered off. After naturally cooling to room temperature, yellow block-like crystals suitable for the single-crystal X-ray diffraction measurement were collected, washed with distilled water and dried in air. The yield was 23% (based on $\text{Nd}(\text{NO}_3)_3\cdot 6\text{H}_2\text{O}$). $\text{C}_{21}\text{H}_{27}\text{Br}_{16}\text{Hg}_6\text{N}_4\text{NdO}_9$: calc. C, 8.12; H, 0.88; N, 1.80; Found C, 8.20; H, 0.85; N, 1.87. FT-IR peaks (cm^{-1}): 3465(vs), 3081(w), 1618(s), 1590(s), 1408(s), 1380(vs), 1242(w), 1101(w), 1048(w), 842(w), 761(m), 681(m), 543(w) and 470(w).

2.4. X-ray Single Crystal Structure Characterization

The X-ray single crystal data of complexes **1** and **2** were obtained from a Rigaku Mercury CCD X-ray diffractometer equipped with a graphite monochromated Mo-K α radiation source, and the radiation wavelength is 0.71073 Å. The measurement was carried out using the ω scan mode. The single crystal data reduction and empirical absorption correction were conducted using the CrystalClear software. The single crystal structures of complexes **1** and **2** were solved using the direct method with the Siemens SHELXTL™ Version 5 software packages. All non-hydrogen atoms were generated based on the subsequent dif-

Table 1: Crystallographic data and structural analyses for complexes **1** and **2**

Compound	1	2
Formula	C ₁₈ H ₂₄ Cl ₆ GdHg ₂ N ₃ O ₁₁	C ₂₁ H ₂₇ Br ₁₆ Hg ₆ N ₄ NdO ₉
<i>M_r</i>	1229.53	3105.81
Color and Habit	colorless block	yellow block
Crystal size/mm	0.23 × 0.07 × 0.05	0.14 × 0.06 × 0.04
Crystal system	Monoclinic	Monoclinic
Space group	<i>P</i> 2 ₁ / <i>c</i>	<i>P</i> 2 ₁ / <i>c</i>
<i>a</i> (Å)	9.7208(3)	9.7418(3)
<i>b</i> (Å)	19.8355(7)	27.1490(9)
<i>c</i> (Å)	17.1090(5)	21.4775(12)
β (°)	101.521(3)	100.772(4)
<i>V</i> (Å ³)	3232.44(18)	5580.3(4)
<i>Z</i>	4	4
2θ _{max} /°	50	50
Reflections collected	18390	30735
Independent, observed reflections (<i>R</i> _{int})	5712, 4737 (0.0276)	9756, 6788 (0.0444)
<i>d</i> _{calcd.} (g/cm ³)	2.526	3.697
μ/mm ⁻¹	12.054	28.854
<i>T</i> /K	293(2)	293(2)
<i>F</i> (000)	2268	5412
<i>R</i> 1, <i>wR</i> 2	0.0317, 0.0629	0.1108, 0.3030
<i>S</i>	1.037	1.051
Largest and mean Δ/ <i>σ</i>	0.001, 0.000	0.000, 0.000
Δρ(max, min) (e/Å ³)	1.116, -1.081	6.358, -5.117

ference electron density maps and refined anisotropically, while all hydrogen atoms were placed theoretically. The final single crystal structures of complexes **1** and **2** were refined using the full-matrix least-squares refinement on *F*². Crystallographic data and structural analyses of complexes **1** and **2** are given in Table 1. Selected bond lengths and bond angles are shown in Table 2. Hydrogen bonding geometry (Å, °) are listed in Table 3.

3. Result and Discussions

Compound **1** was prepared by using GdCl₃·6H₂O, HgCl₂, isonicotinic acid and distilled water in a Teflon-lined stainless steel autoclave at 473 K under hydrothermal conditions. Compound **2** was synthesized by using Nd(NO₃)₃·6H₂O, HgBr₂, isonicotinic acid, DMF and distilled water in a Teflon-lined stainless steel autoclave at 433 K under hydrothermal conditions. It is known that the hydrothermal reaction with organic molecules is a powerful way for the preparation of novel compounds. Under hydrothermal conditions, the properties of water behave very different from normal conditions, namely, water is superheated with obviously lowered viscosity. Solids are easily extracted into this water and the diffusion rate of reagents increases under hydrothermal conditions. So, many reactions can occur. Lee and co-authors reported a mercury bromide complex [Hg₄Br₆L₂][Hg₂Br₆] which was prepared by using a slow evaporation method of solution.³¹ Hu et al documented a mercury bromide complex

(TMP)(Hg₂Br₅)·0.5H₂O which was also obtained by using a slow evaporation method of solution.³² Song and co-authors reported a mercury bromide complex [Cu₂(bipy)₄HgBr₄][Hg₂Br₆] which was also synthesized by using a slow evaporation method.³³

The FT-IR spectroscopy of compounds **1** and **2** were carried out under room temperature. The FT-IR bands of both compounds are dominantly located in the frequency span of 600 ~ 1700 cm⁻¹. The very strong intensity bands residing at 3440 cm⁻¹, 3514 cm⁻¹ and 3465 cm⁻¹ should be ascribed to the O–H asymmetric vibration of the water molecules. The bands locating at 1618 cm⁻¹ and 1590 cm⁻¹ could be assigned to the stretching and bent vibrations of the C–N bonds of the pyridyl rings of the isonicotinic acid ligands. The bands at 1501 cm⁻¹, 1408 cm⁻¹, 1380 cm⁻¹, 1242 cm⁻¹ and 1230 cm⁻¹ could be assigned to the C–O stretching vibrations of the pyridyl rings of the isonicotinic acid ligands. The bands residing in the span of 842 ~ 1101 cm⁻¹ should be ascribed to the bending vibration of the pyridyl rings of the isonicotinic acid ligands. The bands locating at 413 cm⁻¹ ~ 761 cm⁻¹ could be assigned to the stretching vibrations of the Hg–Cl/Br bonds.³⁴ The very strong band 1714 cm⁻¹ of the free ligand isonicotinic acid disappeared in the FT-IR spectroscopy of compounds **1** and **2**. This verifies that the carboxylic groups of the isonicotinic acid molecules are coordinated with metal. It is in good line with the single-crystal X-ray diffraction results.

The single-crystal X-ray diffraction experiments showed that both title compounds crystallize in the space group *P*2₁/*c* of the monoclinic system with four formula

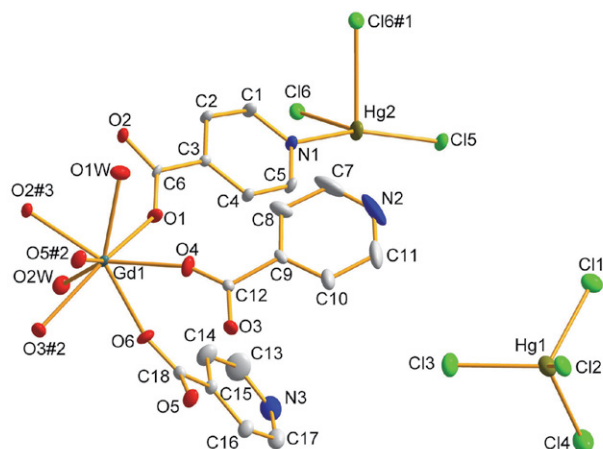


Fig. 1: An ORTEP figure of the asymmetric unit of complex **1** with 20% thermal ellipsoids. Lattice water molecules and hydrogen atoms were omitted for clarity.

molecules in each cell unit (Table 1). The crystallographically asymmetric unit of compound **1** consists of two Hg^{2+} cations, one Gd^{3+} cation, six Cl^- anions, two isonicotinic acid molecules, one isonicotinate anion, two coordination

water molecules and three lattice water molecules, as displayed in Fig. 1. All crystallographic independent atoms are located at general positions. The Gd^{3+} ions are bound by eight oxygen atoms: two from coordination water molecules, two from isonicotinic acid anions, and four from isonicotinic acid molecules, forming a GdO_8 square antiprismatic geometry. As listed in Table 2, the $\text{Gd}-\text{O}_{\text{isonicotinic acid}}$ bond lengths of compound **1** locate in the span of $2.319(4) \text{ \AA} \sim 2.391(4) \text{ \AA}$ with an average value of $2.358(4) \text{ \AA}$, while the $\text{Gd}-\text{O}_{\text{water}}$ bond lengths are $2.438(4) \text{ \AA}$ and $2.499(4) \text{ \AA}$. The $\text{Gd}-\text{O}_{\text{isonicotinic acid}}$ bond lengths are obviously shorter than the $\text{Gd}-\text{O}_{\text{water}}$ bond lengths. This suggests that the Gd^{3+} ions have much stronger affinity to the isonicotinic acid ligands than to the water molecules. These $\text{Gd}-\text{O}$ bond lengths are in the normal span and comparable with the values documented in the references.^{35,36} The $\text{O}-\text{Gd}-\text{O}$ bond angles fall within the range of $69.60(15)^\circ \sim 145.98(15)^\circ$.

The Hg1 ion is coordinated by four chloride ions to form an isolated HgCl_4 tetrahedron. The Hg2 ion is bound by one terminal chloride ion, two μ_2 -bridging chloride ions and one pyridine nitrogen atom to yield a distorted tetrahedron. The $\text{Hg}-\text{Cl}$ bond lengths fall within the range

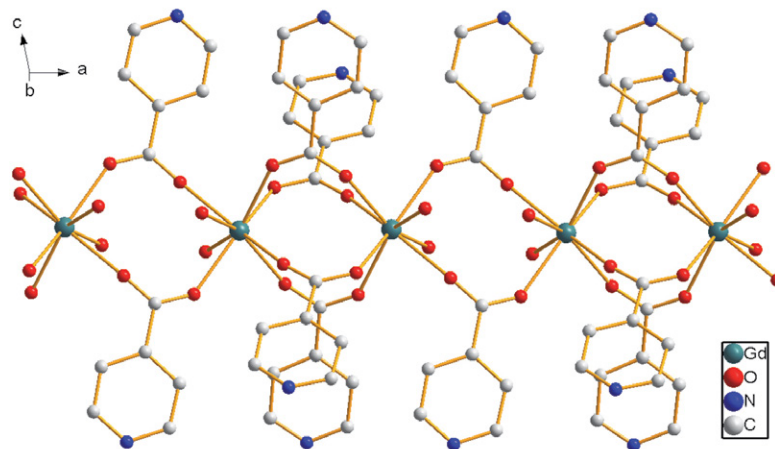


Fig. 2: A 1-D $-\text{Gd}-(\text{IA})_2-\text{Gd}-(\text{HIA})_4-\text{Gd}-$ chain in complex **1**

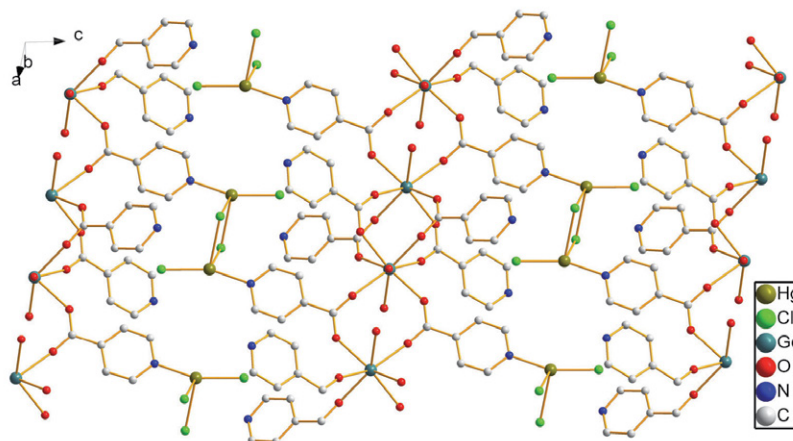


Fig. 3: A 2-D layer in complex **1**

Table 2: Selected bond lengths (Å) and angles (°) of complexes 1 and 2

Complex 1			
Bond Lengths (Å)		Bond Angles (°)	
Hg(1)-Cl(1)	2.5081(18)	Cl(3)-Hg(1)-Cl(4)	112.03(8)
Hg(1)-Cl(2)	2.5306(18)	Cl(3)-Hg(1)-Cl(1)	115.60(7)
Hg(1)-Cl(3)	2.438(2)	Cl(4)-Hg(1)-Cl(1)	106.63(7)
Hg(1)-Cl(4)	2.451(2)	Cl(3)-Hg(1)-Cl(2)	98.82(7)
Hg(2)-N(1)	2.161(5)	Cl(4)-Hg(1)-Cl(2)	118.07(8)
Hg(2)-Cl(5)	2.3205(16)	Cl(1)-Hg(1)-Cl(2)	105.82(6)
Hg(2)-Cl(6)	2.7730(16)	N(1)-Hg(2)-Cl(5)	156.31(14)
Hg(2)-Cl(6)#1	2.6795(17)	N(1)-Hg(2)-Cl(6)#1	97.53(13)
Gd(1)-O(2)	2.319(4)	Cl(5)-Hg(2)-Cl(6)#1	102.80(6)
Gd(1)-O(6)#2	2.336(4)	N(1)-Hg(2)-Cl(6)	92.48(13)
Gd(1)-O(1)#3	2.358(4)	Cl(5)-Hg(2)-Cl(6)	100.46(5)
Gd(1)-O(4)#2	2.361(4)	Cl(6)#1-Hg(2)-Cl(6)	87.26(5)
Gd(1)-O(5)	2.388(4)	Hg(2)#1-Cl(6)-Hg(2)	92.74(5)
Gd(1)-O(3)	2.391(4)	O(2)-Gd(1)-O(4)#2	145.98(15)
Gd(1)-O(1W)	2.438(4)	O(5)-Gd(1)-O(1W)	69.60(15)
Gd(1)-O(2W)	2.499(4)		
Symmetry transformations used to generate equivalent atoms: #1 -x, -y+1, -z-1; #2 -x, -y+1, -z; #3 -x+1, -y+1, -z			
Complex 2			
Bond Lengths (Å)		Bond Angles (°)	
Hg(1)-Br(1)	2.70(5)	Hg(5)-Br(1) #1	3.298(5)
Hg(1)-Br(2)	2.38(5)	Hg(6)-Br(14)	2.41(2)
Hg(1)-Br(3)	2.60(6)	Hg(6)-Br(15)	2.416(15)
Hg(1)-Br(5)	3.228(6)	Nd(1)-O(3)	2.36(5)
Hg(2)-Br(3)	3.10(2)	Nd(1)-O(5)	2.39(4)
Hg(2)-Br(4)	2.39(2)	Nd(1)-O(2)	2.39(5)
Hg(2)-Br(5)	2.406(18)	Nd(1)-O(6)	2.42(5)
Hg(2)-Br(6)	3.214(18)	Nd(1)-O(4)#2	2.45(5)
Hg(3)-Br(7)	2.343(19)	Nd(1)-O(1)#2	2.46(5)
Hg(3)-Br(8)	2.373(18)	Nd(1)-O(1W)	2.51(5)
Hg(4)-Br(6)	2.646(18)	Nd(1)-O(7)	2.52(4)
Hg(4)-Br(9)	2.860(18)		
Hg(4)-Br(10)	2.455(16)	Br(9)-Hg(3)-Br(1)#3	89.1(5)
Hg(4)-Br(11)	2.623(19)	Br(14)-Hg(6)-Br(15)	176.9(9)
Hg(5)-Br(12)	2.33(5)	Hg(1)-Br(3)-Hg(2)	89.4(15)
Hg(5)-Br(12)#1	3.144(5)	Hg(4)-Br(9)-Hg(3)	166.64(5)
Hg(5)-Br(13)	2.41(2)	O(6)#1-Nd(1)-O(1)#2	145.3(18)
		O(6)#1-Nd(1)-O(1W)	72.0(16)
Symmetry transformations used to generate equivalent atoms: #1 -x-1, -y+3, -z+4; #2 -x, -y+3, -z+4; #3 x+1, y, z.			

of 2.3205(16) Å ~ 2.7730(16) Å with an average value of 2.5287(18) Å, while the Hg–N bond length is 2.161(5) Å. The Hg–Cl and Hg–N bond lengths are within normal ranges and comparable with the values documented in the references.^{37,38} The Cl–Hg–Cl and N–Hg–Cl bond angles locate in the range of 87.26(5)° ~ 118.07(8)° and 92.48(13)° ~ 156.31(14)°, respectively. Two neighboring Hg(2) ions are linked by two μ_2 -bridging chloride ions to form a Hg₂Cl₄ moiety. The Hg(2)#1-Cl(6)-Hg(2) bond angle is 92.74(5)° that is close to a right angle. The neighboring Gd³⁺ ions are interbridged together alternately by two isonicotinic acid anions and four isonicotinic acid molecules, to yield

a one-dimensional (1-D) chain running along the *a* axis, as shown in Fig. 2. The distances are 4.533 Å and 5.220 Å between adjacent Gd³⁺...Gd³⁺ ions. The 1-D chains are connected by Hg₂Cl₄ moieties to form a two-dimensional (2-D) layer extending along the *ac* plane, as presented in Fig. 3. The deviation of the six atoms of the pyridyl rings of the three isonicotinic acid are in the range of -0.011 Å ~ 0.010 Å, -0.009 Å ~ 0.006 Å and -0.009 Å ~ 0.014 Å, respectively. Such small deviation suggests that each of the pyridyl rings of the three isonicotinic acid are almost coplanar. The torsion angles from the carboxylic groups to the pyridyl rings are 170.5(5)°, 168.2(5)°, -173.3(5)°,

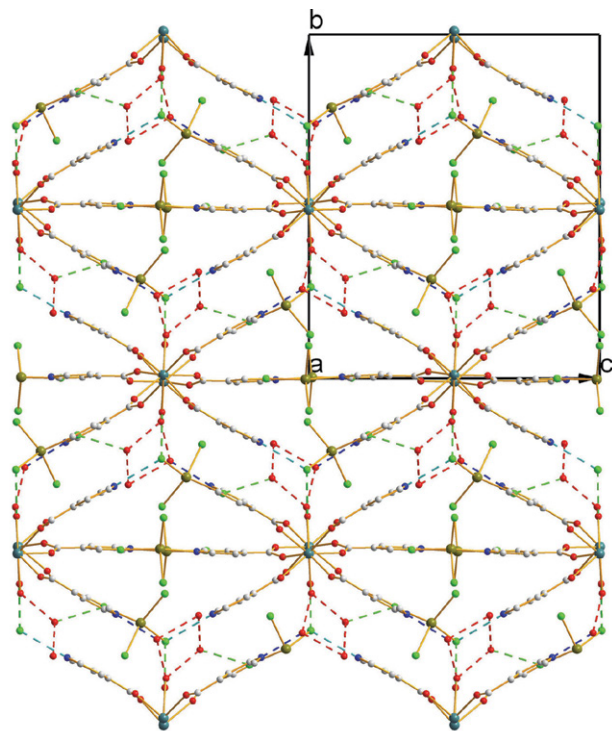


Fig. 4: The packing structure of complex 1 with the dashed lines representing hydrogen bonding interactions

$-178.0(5)^\circ$, $-173.7(5)^\circ$ and $-169.8(5)^\circ$, respectively. The neutral isonicotinic acid molecule acts as a μ_2 -bridging ligand with two oxygen atoms binding to two Gd^{3+} cations, while the isonicotinic acid anion acts as a μ_3 -bridging ligand with two oxygen atoms binding to two Gd^{3+} cations and one nitrogen atom linking to one Hg^{2+} cation (see Fig. 3). There are eight hydrogen bonding interactions which can be grouped into five types, namely, O-H...O, N-H...Cl, O-H...Cl, N-H...O and C-H...Cl, as shown in Table 3. These hydrogen bonding interactions solidify the crystal packing

structure and construct a three-dimensional (3-D) supramolecular framework of complex 1, as presented in Fig. 4.

The single-crystal X-ray diffraction analysis results revealed that the crystallographically asymmetric unit of complex 2 is comprised of six Hg^{2+} cations, one Nd^{3+} cation, sixteen Br^- anions, three neutral isonicotinic acid molecules, one DMF molecule, one coordination water molecule and one lattice water molecule, as displayed in Fig. 5. All crystallographic independent atoms are located at general positions. The six crystallographically independent Hg^{2+} cations have two kinds of coordination geometries. The Hg1, Hg2, Hg4 and Hg5 ions are bound by four bromide ions to yield distorted tetrahedra. The Hg3 and Hg6 ions are coordinated by two terminal bromide ions to give a linear motif with the bond angles of Br(7)-Hg(3)-Br(8) and Br(14)-Hg(6)-Br(15) being of $169.2(9)^\circ$ and $176.8(6)^\circ$, respectively. The Hg-Br bond lengths fall within the range of $2.33(5) \text{ \AA} \sim 3.298(5) \text{ \AA}$. The Hg-Br bond lengths are in the normal span and comparable with the values reported in the references.^{39,40} The Br-Hg-Br bond angles fall within the range of $89.1(5)^\circ \sim 176.9(9)^\circ$, while Hg-Br-Hg bond angles reside in the span of $89.4(15)^\circ \sim 166.64(5)^\circ$. The Hg1, Hg2, Hg4 and Hg5 ions are connected by the μ_2 -bridging bromide ions to form a 1-D -Hg-Br-Hg-Br- chain running along the *a* axis, as shown in Fig. 6. Lee and co-authors reported a mercury bromide complex with two rhomboidal clusters $[Hg_2Br_6]^{2-}$.³¹ Hu et al reported a complex (TMP)(Hg_2Br_5) $\cdot 0.5H_2O$ containing a $(Hg_2Br_5)^-$ anion.³² Song and co-authors reported a mercury bromide complex $[Cu_2(bipy)_4HgBr_4][Hg_2Br_6]$ that contains a $[Hg_2Br_6]^{2-}$ anion.³³

The Nd^{3+} ion is surrounded by eight oxygen atoms, of which one is offered by one coordination water molecule, one comes from one DMF molecule, six are offered by six isonicotinic acid molecules, to yield a NdO_8 square antiprismatic geometry. As shown in Table 2, the $Nd-O_{isonicotinic\ acid}$ bond lengths of compound 1 fall within

Table 3: Hydrogen bonding geometry (\AA , deg) of complexes 1 and 2

Complex 1				
D-H...A	D-H	H...A	D...A	D-H...A
O2W-H2WA...O3W(-x, -1/2+y, -1/2-z)	0.82	2.16	2.971(7)	169
N2-H2B...Cl1(-1+x, 1/2-y, -1/2+z)	0.86	2.53	3.269(10)	145
O1W-H1WB...Cl1(1-x, 1-y, -z)	0.90(5)	2.30(5)	3.158(4)	159(7)
N3-H3A...O3W	0.86	1.98	2.795(9)	159
O5W-H5WA...Cl3(x, 1/2-y, 1/2+z)	0.94(9)	2.62(10)	3.118(9)	114(10)
O3W-H3WA...O4W(-x, 1/2+y, -1/2-z)	0.90(4)	2.23(3)	3.000(16)	144(2)
C17-H17A...Cl3(1-x, 1/2+y, -1/2-z)	0.93	2.80	3.434(9)	126
C13-H13A...Cl2(-x, 1/2+y, -1/2-z)	0.93	2.79	3.468(10)	131
Compound 2				
D-H...A	D-H	H...A	D...A	D-H...A
C7-H7A...Br2(-1-x, 1/2+y, 7/2-z)	0.94	2.92	3.80(8)	158

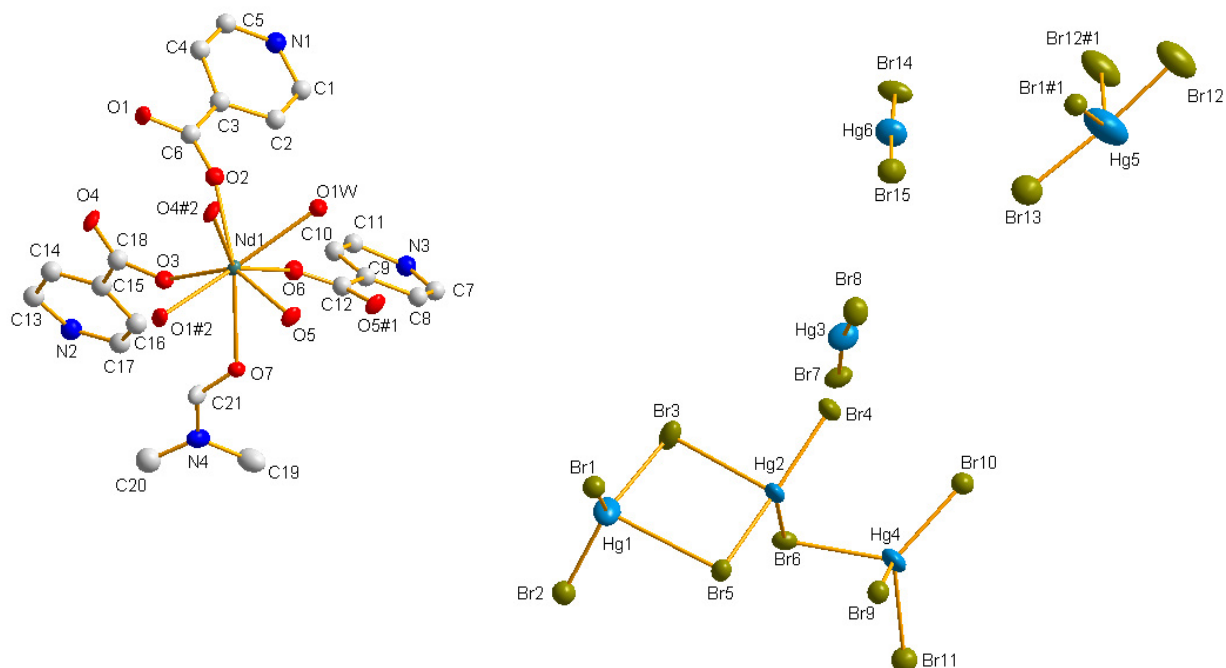


Fig. 5: An ORTEP drawing of complex 2 with 20% thermal ellipsoids. Lattice water molecules, isolated bromide ions, disordered atoms and hydrogen atoms were omitted for clarity.

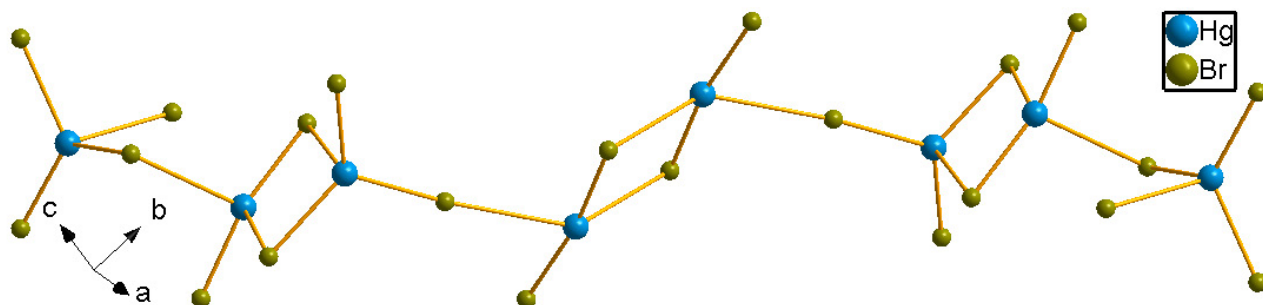


Fig. 6: A 1-D -Hg-Br-Hg-Br-Hg- chain in complex 2

the range of 2.36(5) Å ~ 2.46(5) Å with an average value of 2.41(5) Å, while the Nd–O_{water} and Nd–O_{DMF} bond lengths are 2.51(5) Å and 2.52(4) Å, respectively. The Nd–O_{isonicotinic acid} bond length is the shortest and the Nd–O_{DMF} bond length is the longest. This suggests that the Nd³⁺ ion has much more stronger affinity to the isonicotinic acid ligands than to the DMF molecules. These Nd–O bond lengths lie in the normal range and comparable with the values documented in the references.^{41,42} The O–Nd–O bond angles fall within the range of 72.0(16)° ~ 145.3(18)°. The neighboring Nd³⁺ ions are interbridged together alternately by two and four isonicotinic acid molecules, to form a one-dimensional (1-D) –Nd–(HIA)₄–Nd–(HIA)₂–Nd–(HIA)₄–Nd– chain running along the *a* axis, as shown in Fig. 7. The distances are 4.639 Å and 5.141 Å between adjacent Nd³⁺...Nd³⁺ ions. All of the isonicotinic acid molecule acts as a μ_2 -bridging ligand with two oxygen atoms binding to two Nd³⁺ cations (see Fig. 7). The deviation of the six

atoms of the pyridyl rings of the three isonicotinic acid are in the range of –0.042 Å ~ 0.061 Å, –0.060 Å ~ 0.047 Å and –0.029 Å ~ 0.026 Å, respectively. Such small deviation suggests that each of the pyridyl rings of the three isonicotinic acid are almost coplanar. The torsion angles from the carboxylic groups to the pyridyl rings are 174.6(7)°, 167.7(7)°, –172.2(7)°, –174.9(7)°, –172.8(5)° and –177.9(4)°, respectively. There is only one hydrogen bonding interaction in compound 2, namely, C7–H7A...Br2(–1–*x*, 1/2+*y*, 7/2–*z*). This hydrogen bonding interaction connects the above mentioned 1-D –Hg–Br–Hg–Br–Hg– chains and –Nd–(HIA)₄–Nd–(HIA)₂–Nd–(HIA)₄–Nd– chains together to yield a 2-D supramolecular layer extending along the *ac* plane, as shown in Fig. 8. Hydrogen bonding interactions and electrostatic forces enhance the stability of the crystal packing structure of complex 2, as presented in Fig. 9.

It is well-known that a large number of lanthanide and mercury complexes can display photoluminescence

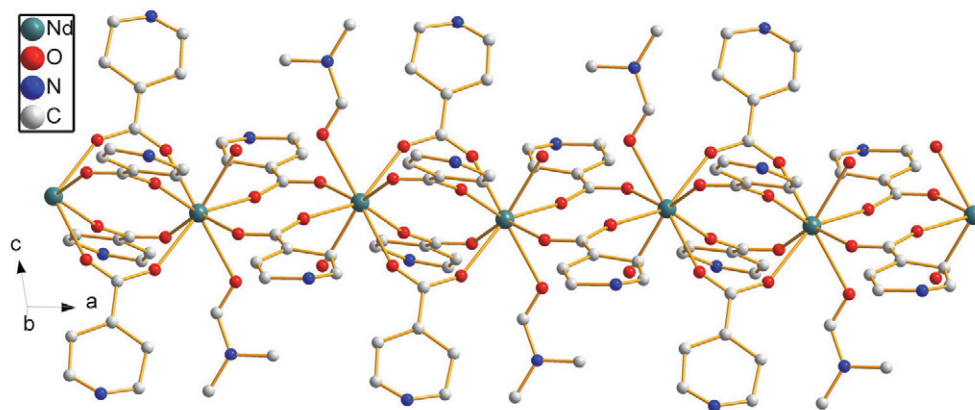


Fig. 7: A 1-D $\text{-Nd-(HIA)}_4\text{-Nd-(HIA)}_2\text{-Nd-(HIA)}_4\text{-Nd-}$ chain in complex 2

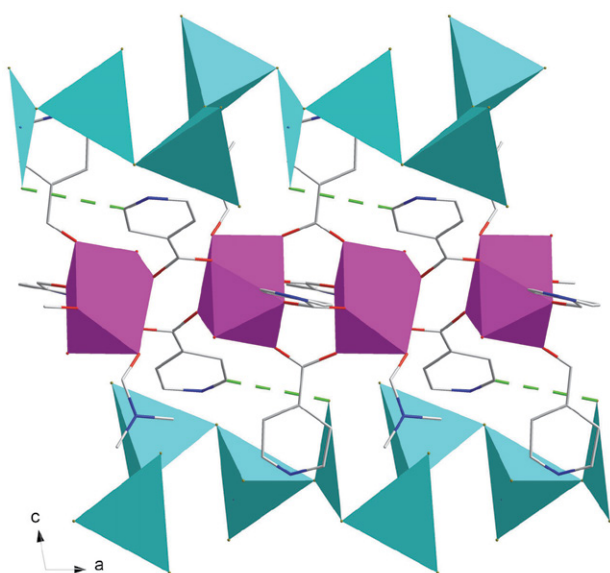


Fig. 8: A 2-D supramolecular layer in complex 2 with the green dashed lines representing hydrogen bonding interactions. The turquoise and pink are Hg- and Nd-centered polyhedra, respectively.

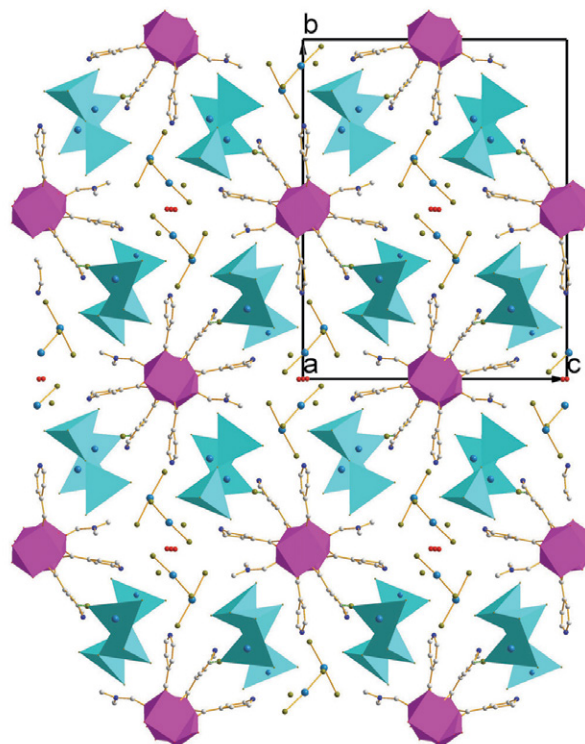


Fig. 9: The packing structure of complex 2. The turquoise and pink are Hg- and Nd-centered polyhedra, respectively.

emissions. As a result, it is supposed that both title complexes should exhibit photoluminescence emissions because they possess lanthanide and mercury ions simultaneously. Based on this consideration, the powder samples of both title complexes were applied to conduct the photoluminescence experiments at room temperature. The results of the photoluminescence experiments of both title complexes are presented in Fig. 10 and Fig. 11. As for complex 1, when it was excited by the UVA light of 386 nm, it exhibited the UVB photoluminescence with an emission band locating at 312 nm, as displayed in Fig. 10. The photoluminescence emission originates from the characteristic emissions of the $4f$ electron intrashell transitions of the Gd^{3+} ions in complex 1.⁴³ UVB includes the wavelength 280–320 nm of the spectrum therefore, complex 1 is a potential UVB photoluminescence emission material. With regard to complex 2, the photoluminescence absorption

is located in the span of 480 nm \sim 550 nm with an adsorption peak at 496 nm. When it was excited by the 496 nm light, complex 2 exhibits red photoluminescence emissions in the span of 620 nm \sim 900 nm with four emission bands locating at 682, 745, 823 and 885 nm, of which 745 nm is the strongest one, as shown in Fig. 11. These photoluminescence emission bands come from the characteristic emissions of the $4f$ electron intrashell transitions of the Nd^{3+} ions in compound 2.⁴⁴ As presented in Fig. 12, compound 2 has CIE chromaticity coordinates (0.7142, 0.2857) in the red region and its CCT is 138224 K. As a result, complex 2 is supposed to be a potential red light photoluminescent material.

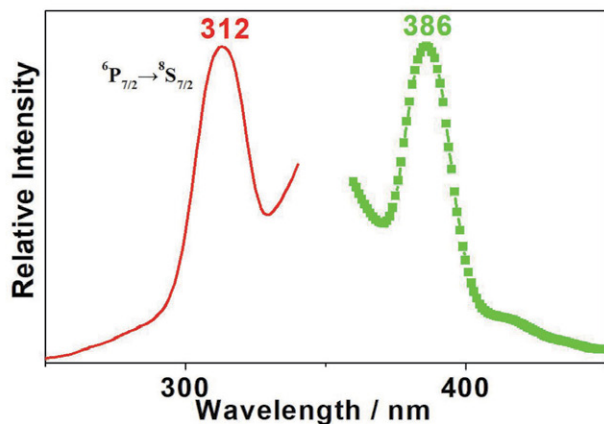


Fig. 10: Solid state photoluminescence spectra of complex 1 with the green and red lines representing excitation and emission spectra, respectively.

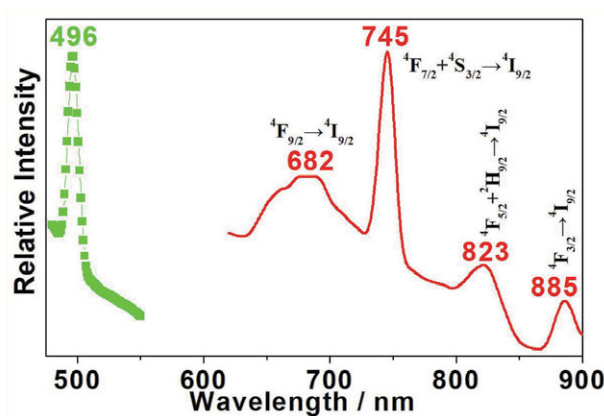


Fig. 11: Solid state photoluminescence spectra of complex 2 with the green and red lines representing excitation and emission spectra, respectively.

As for lanthanide materials, their photoluminescence, magnetic and catalytic properties have been widely explored so far, but their semiconductive properties have been relatively rarely investigated. Considering this reason and in order to more deeply explore the photophysical performances of compounds **1** and **2**, their solid state UV/Vis diffuse reflection measurements were carried out with a finely ground powder sample at room temperature. The solid state UV/Vis diffuse reflectance spectra data for complexes **1** and **2** were processed with the famous Kubelka-Munk formula $\alpha/S = (1-R)^2/2R$, where α refers to the absorption coefficient, S is the scattering coefficient, R is the reflection coefficient. The converted solid state UV/Vis diffuse reflectance spectra are given in Figs. 13 and 14 for complexes **1** and **2**, respectively. The semiconductive bandgaps for complexes **1** and **2** can be found by virtue of the straight line extrapolation technique from the maximum absorption edges of the α/S versus energy diagrams. Based on such a technique, the semiconductive bandgaps for complexes **1** and **2** can be found to be 3.12 eV and 3.23 eV,

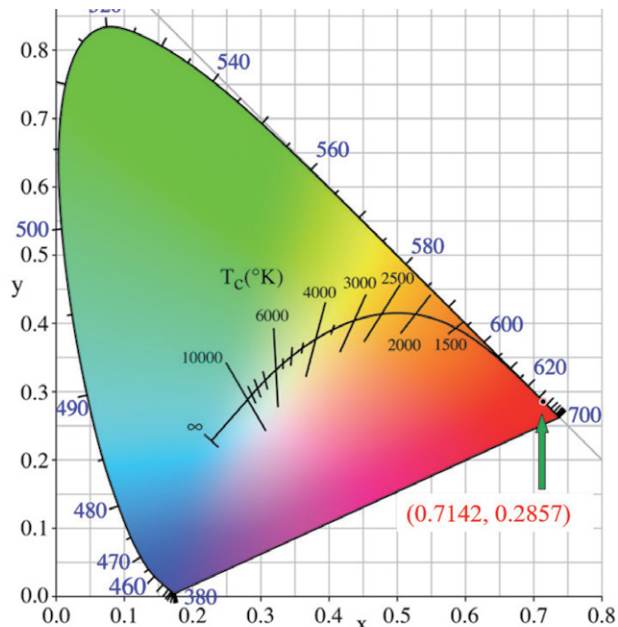


Fig. 12: The CIE diagram of complex 2.

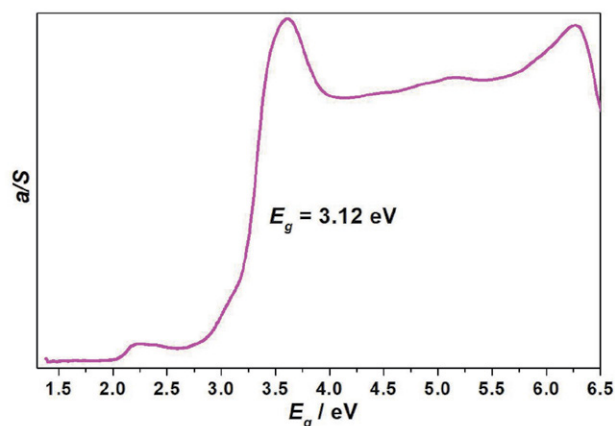


Fig. 13: The UV-vis diffuse reflectance diagram measured with a solid state sample of complex 1.

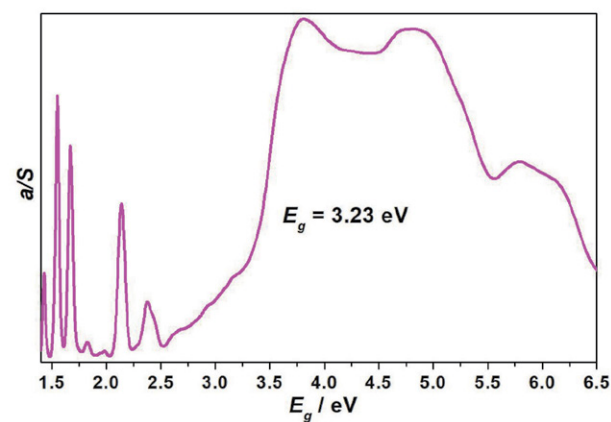


Fig. 14: The UV-vis diffuse reflectance diagram measured with a solid state sample of complex 2.

respectively. Furthermore, the solid state UV/Vis diffuse reflectance curves of complexes **1** and **2** reveal that the maximum absorption edges are not very steep, which indicates that both of them should go through an indirect transition process.⁴⁵ As a result, complexes **1** and **2** are potentially a candidate for wide bandgap semiconductive materials.

4. Conclusions

In brief, we have synthesized two new lanthanide mercury halide compounds each possessing distinct crystal structures: one exhibits a 2-D layer-like structure, while the other features a 1-D chain-like structure. One compound has a ultraviolet upconversion photoluminescence emission, while the other shows red photoluminescence. These emissions originate from the characteristic emissions of the 4f electron intrashell transitions of the $^6P_{7/2} \rightarrow ^8S_{7/2}$ of the Gd³⁺ ions and the $^4F_{9/2} \rightarrow ^4I_{9/2}$, $^4F_{7/2} + ^4S_{3/2} \rightarrow ^4I_{9/2}$, $^4F_{5/2} + ^2H_{9/2} \rightarrow ^4I_{9/2}$, $^4F_{3/2} \rightarrow ^4I_{9/2}$ of the Nd³⁺ ions. The neodymium compound possesses CIE chromaticity coordinates of (0.7142, 0.2857) and a CCT of 138224 K. Solid-state UV/Vis diffuse reflectance spectra revealed that they are potential wide bandgap semiconductive materials. Further investigations on the relationship between the crystal structures and the physicochemical properties in this field are in progress in our lab.

Acknowledgements

We greatly thank for the financial support of the National Natural Science of Foundation of China (22265014, 22262015), the Natural Science of Foundation of Jiangxi Province (20242BAB26034, 20224BAB204008, 20212BAB213020, 20232BCJ23026), Key Laboratory of Jiangxi Province for Special Optoelectronic Artificial Crystal Materials (20242BCC32037), as well as the Science and Technology Project of Jiangxi Provincial Department of Education (GJJ2201602).

Supplementary Material

Crystallographic data for the structure reported in this paper have been deposited with the Cambridge Crystallographic Data Centre as supplementary publication No. CCDC 2377406 and 2377012 for complexes **1** and **2**, respectively. Copies of the data can be obtained free of charge on application to CCDC, 12 Union Road, Cambridge CB2 1EZ, UK (fax: (44) 1223 336-033; e-mail: deposit@ccdc.cam.ac.uk).

5. References

- M. Rakhmanova, T. Sukhikh, E. Kovalenko, *CrystEngComm* **2024**, *26*, 3954–3963. DOI:10.1039/D4CE00375F
- A. Mortis, R. Anwander, *Eur. J. Inorg. Chem.* **2024**, *27*, e202400127. DOI:10.1002/ejic.202400127
- E. A. Sanzhenakova, K. S. Smirnova, I. P. Pozdnyakov, E. V. Lider, *J. Struct. Chem.* **2024**, *65*, 786–797. DOI:10.1134/S0022476624040140
- R. Huo, T. Zhang, G. Zeng, C. Wang, Y. H. Xing, F. Y. Bai, *Chinese J. Chem.* **2024**, *42*, 283–293. DOI:10.1002/cjoc.202300448
- M. O. Savchuk, O. O. Litsis, N. S. Kariaka, V. O. Trush, V. V. Dyakonenko, S. S. Smola, J. A. Rusanova, T. Y. Sliva, S. V. Shishkina, V. M. Amirkhanov, *Inorg. Chim. Acta* **2024**, *559*, 121783. DOI:10.1016/j.ica.2023.121783
- C. Chen, C. Lu, B. Zhao, *J. Org. Chem.* **2023**, *88*, 16391–16399. DOI:10.1021/acs.joc.3c01905
- B. Alnami, J. G. C. Kragoskow, J. K. Staab, J. M. Skelton, N. F. Chilton, *J. Am. Chem. Soc.* **2023**, *145*, 13632–13639. DOI:10.1021/jacs.3c01342
- D. I. Galimov, S. M. Yakupova, R. G. Bulgakov, *J. Photochem. Photobio. A* **2023**, *438*, 114559. DOI:10.1016/j.jphotochem.2023.114559
- Y. F. Wang, X. Gao, C. S. Cao, S. M. Li, Z. L. Wu, *Inorg. Chim. Acta* **2023**, *546*, 121327. DOI:10.1016/j.ica.2022.121327
- Y. W. Wang, M. H. Yang, Z. C. Cui, H. H. Zeng, X. Zhang, J. Q. Shi, T. F. Cao, X. L. Fan, *J. Mater. Sci.* **2023**, *58*, 268–280. DOI:10.1007/s10853-022-08024-8
- H. Reuter, M. Boeltken, M. Horstmann, M. Haase, *Crystals* **2023**, *13*, 1043. DOI:10.3390/cryst13071043
- K. Wydra, V. Kinzhyballo, J. Lisowski, *Dalton Trans.* **2023**, *52*, 11992–12001. DOI:10.1039/D3DT01948A
- L. X. Meng, J. L. Wang, Y. Zhang, B. X. Zhou, J. J. Shi, K. Xiao, *Sensor. Actuat. B- Chem.* **2024**, *414*, 135897. DOI:10.1016/j.snb.2024.135897
- C. Yu, Y. Shan, J. Zhu, D. Sun, X. Zheng, N. Zhang, J. Hou, Y. Fang, N. Dai, Y. Liu, *Materials* **2024**, *17*, 1864. DOI:10.3390/ma17081864
- Y. Tian, H. Luo, M. Chen, C. Li, S. V. Kershaw, R. Zhang, A. L. Rogach, *Nanoscale* **2023**, *15*, 6476–6504. DOI:10.1039/D2NR07309A
- Y. Selmani, H. Labrim, R. E. L. Bouaydi, L. Bahmad, *Phys. B* **2022**, *644*, 414204. DOI:10.1016/j.physb.2022.414204
- H. Song, S. Y. Eom, G. Kim, Y. S. Jung, D. Choi, G. S. Kumar, J. H. Lee, H. S. Kang, J. Ban, G. W. Seo, *Commun. Mater.* **2024**, *5*, 60. DOI:10.1038/s43246-024-00499-z
- S. Padwal, R. Wagh, J. Thakare, R. Patil, *Appl. Phys. A* **2024**, *130*, 34. DOI:10.1007/s00339-023-07202-y
- Y. Xie, F. Guo, W. Tong, H. Chang, *Inorg. Chem.* **2024**, *63*, 4160–4167. DOI:10.1021/acs.inorgchem.3c03969
- S. Kukreti, S. Ramawat, A. Dixit, *Phys. Stat. Sol. B* **2023**, *260*, 2200524.
- Y. L. Liu, Y. X. Zhao, J. H. Zhang, Y. Ye, Q. Q. Sun, *J. Solid State Chem.* **2022**, *313*, 123332. DOI:10.1016/j.jssc.2022.123332
- S. Wang, Y. Li, B. Wang, *J. Chem. Res.* **2021**, *45*, 934–941. DOI:10.1177/17475198211032835
- L. B. Zhu, F. Li, M. L. Sun, Y. Y. Qin, Y. G. Yao, *Chinese J. Struct. Chem.* **2021**, *40*, 1031–1038.
- J. F. Zhang, J. J. Wu, G. D. Tang, J. Y. Feng, F. M. Luo, B. Xu, C.

- Zhang, *Sensor Actuat. B-Chem.* **2018**, *272*, 166–174.
DOI:10.1016/j.snb.2018.05.121
25. N. N. Pang, D. X. Lin, Z. Y. Zhan, X. D. Ding, T. T. Shi, Q. X. Meng, P. Y. Liu, W. G. Xie, *Mat. Sci. Semicon. Proc.* **2022**, *145*, 106639. DOI:10.1016/j.mssp.2022.106639
26. F. E. Özbek, M. Sertçelik, M. Yüksek, G. Ugurlu, A. M. Tonbul, H. Necefoglu, T. Hökelek, *J. Fluoresc.* **2019**, *29*, 1265–1275.
DOI:10.1007/s10895-019-02440-x
27. X. Zhang, W.-T. Chen, *J. Mol. Struct.* **2024**, *1301*, 137257.
DOI:10.1016/j.molstruc.2023.137257
28. H.-D. Liu, Y.-Y. Xu, X.-Y. Shao, L.-H. Zeng, W.-T. Chen, C. Liu, S.-P. Dai, C.-W. Pan, *J. Mol. Struct.* **2024**, *1305*, 137762.
DOI:10.1016/j.molstruc.2024.137762
29. H.-D. Liu, X.-Y. Shao, L.-H. Zeng, Y.-Y. Xu, C. Liu, S.-P. Dai, C.-W. Pan, W.-T. Chen, *J. Porphy. Phthalocya.* **2024**, *28*, 157–165. DOI:10.1142/S108842462450010X
30. P. Makuła, M. Pacia, W. Macyk, *J. Phys. Chem. Lett.* **2018**, *9*, 6814–6817. DOI:10.1021/acs.jpcclett.8b02892
31. H.-H. Lee, I.-H. Park, S. S. Lee, *Inorg. Chem.* **2014**, *53*, 4763–4769. DOI:10.1021/ic500594f
32. N.-H. Hu, K. Aoki, A. O. Adeyemo, G. N. Williams, *Inorg. Chim. Acta* **2022**, *333*, 63–71.
33. J.-L. Song, J.-G. Mao, H.-Y. Zeng, Z.-C. Dong, *Eur. J. Inorg. Chem.* **2004**, 38–543. DOI:10.1002/ejic.200300554
34. Y. J. Nie, Y. H. Deng, H. X. Guo, S. M. Ying, *Chinese J. Struct. Chem.* **2020**, *39*, 1029–1034. DOI:10.1002/cjoc.202190052
35. M. T. Kaczmarek, R. Jastrzab, M. Kubicki, M. Gierszewski, M. Sikorski, *Inorg. Chim. Acta* **2015**, *430*, 108–113.
DOI:10.1016/j.ica.2015.02.026
36. H.-D. Liu, X.-Y. Shao, Y.-Y. Xu, W.-T. Chen, Ch. Liu, S.-P. Dai, C.-W. Pan, *Acta Chim. Slov.* **2024**, *71*, 380–387.
DOI:10.17344/acsi.2024.8661
37. P. Nockemann, G. Meyer, *Z. Anorg. Allg. Chem.* **2003**, *629*, 123–128. DOI:10.1002/zaac.200390003
38. X. Zhang, W. Chen, *J. Mol. Struct.* **2024**, *1301*, 137257.
DOI:10.1016/j.molstruc.2023.137257
39. S.-C. Chen, H.-H. Hsueh, C.-H. Chen, C. S. Lee, F.-C. Liu, I. J. B. Lin, G.-H. Lee, S.-M. Peng, *Inorg. Chim. Acta* **2009**, *362*, 3343–3350. DOI:10.1016/j.ica.2009.03.014
40. W.-J. Zhang, Y.-Y. Xu, L.-J. Wei, J.-Y. Lin, W.-T. Chen, W.-S. Lin, *Inorg. Chim. Acta* **2023**, *547*, 121328.
DOI:10.1016/j.ica.2022.121328
41. I. V. Kalinovskaya, A. Y. Mamaev, V. E. Karasev, *Russ. J. Gen. Chem.* **2011**, *81*, 1407–1410.
DOI:10.1134/S1070363211070012
42. D.-Y. He, L.-J. Wei, Y.-Y. Xu, Z.-G. Luo, W.-T. Chen, W.-S. Lin, *J. Iran. Chem. Soc.* **2023**, *20*, 1323–1331.
DOI:10.1007/s13738-023-02757-2
43. V. Singh, G. Sivaramaiah, N. Singh, J. L. Rao, P. K. Singh, M. S. Pathak, D. A. Hakeem, *Optik* **2018**, *158*, 1227–1233.
DOI:10.1016/j.ijleo.2017.12.185
44. S. Insiripong, S. Kaewjeang, U. Maghanemi, H. J. Kim, N. Chanthima, J. Kaewkhao, *Appl. Mechan. Mater.* **2014**, *548–549*, 124–128.
DOI:10.4028/www.scientific.net/AMM.548-549.124
45. S. F. M. Schmidt, C. Koo, V. Mereacre, J. Park, D. W. Heermann, V. Kataev, C. E. Anson, D. Prodius, G. Novitchi, R. Klingeler, A. K. Powell, *Inorg. Chem.* **2017**, *56*, 4796–4806.
DOI:10.1021/acs.inorgchem.6b02682

Povzetek

S solvotermalno sintezo smo sintetizirali dve novi spojini z lantanoidi in živim srebrom ter izonikotinsko kislino kot ligandom in sicer $[\text{Gd}(\mu_2\text{-HIA})_2(\mu_3\text{-IA})(\text{H}_2\text{O})_2(\text{HgCl}_2)]_n(\text{nHgCl}_4) \cdot 3n\text{H}_2\text{O}$ (**1**) (HIA = izonikotinska kislina) in $\{[\text{Nd}(\mu_2\text{-HIA})_3(\text{DMF})(\text{H}_2\text{O})]_n\}[(\text{Hg}_4\text{Br}_{11})_n](2\text{HgBr}_2)(\text{nBr}) \cdot n\text{H}_3\text{O}$ (**2**). Obe spojini smo karakterizirali z monokristalno rentgensko difrakcijo. Spojina **1** ima dvodimenzionalno (2-D) plastovito strukturo, medtem ko ima spojina **2** enodimenzionalno (1-D) verižno zgradbo. Lantanoidni ioni v obeh spojinah so osemštevno koordinirani v obliki kvadratne antiprizme, medtem ko ima živosrebrov ion različne koordinacijske motive. Spojina **1** kaže ultravijolično fotoluminiscenco, medtem ko ima spojina **2** rdečo fotoluminiscenco. Razlog za fotoluminiscenčno emisijo so karakteristični prehodi $4f$ elektronov ${}^6P_{7/2} \rightarrow {}^8S_{7/2}$ Gd^{3+} ionov v spojnini **1** in ${}^4F_{9/2} \rightarrow {}^4I_{9/2}$, ${}^4F_{7/2} + {}^4S_{3/2} \rightarrow {}^4I_{9/2}$, ${}^4F_{5/2} + {}^2H_{9/2} \rightarrow {}^4I_{9/2}$, ${}^4F_{3/2} \rightarrow {}^4I_{9/2}$ prehodi Nd^{3+} ionov v spojnini **2**. Spojina **2** ima barvne koordinate (0.7142, 0.2857) CIE (Commission Internationale de l'Éclairage) in vrednost CCT (korelirana barvna temperatura) 138,224 K. Iz UV/Vis spektrov v trdnem stanju smo izračunali polprevodniške širine prepovedanega pasu, ki znašajo 3.12 eV in 3.23 eV. Elementna analiza in FT-IR spektri potrjujejo čistost obeh spojin.



Except when otherwise noted, articles in this journal are published under the terms and conditions of the Creative Commons Attribution 4.0 International License

Scientific paper

Effect of Biphenyl Derivative of Coumarin Compounds Photodynamic Therapy on The Expression of Carcinoma-Associated Genes

Asiye Gok Yurttas^{1,*} , Tugba Elgun^{2,6}, Burcin Erkal Cam³, Melike Kefeli⁴ and Kamil Cinar⁵

¹ Department of Biochemistry, Faculty of Pharmacy, Istanbul Health and Technology University, Istanbul, Türkiye

² Medical Biology, Faculty of Medicine, Istanbul Biruni University, Istanbul, Türkiye

³ Department of Molecular Biology and Genetics, Yildiz Technical University, Istanbul, Türkiye

⁴ Molecular Biology and Genetics, Istanbul University, Istanbul, Türkiye

⁵ Department of Physics, Faculty of Science, Gebze Technical University, Kocaeli, Türkiye

⁶ Biruni University Research Center (B@MER), Biruni University, 34015, Istanbul, Türkiye

* Corresponding author: E-mail: asiye.yurttas@istun.edu.tr

Phone/Fax: +90 533 280 87 07

Received: 08-22-2024

Abstract

Photodynamic Therapy (PDT) is a cancer treatment. Singlet oxygen is produced as a result of the photochemical reaction between light, photosensitizer (PS), and molecular oxygen, which kills cells. Colon cancer, affecting 1.23 million people worldwide, often requires surgery but has high recurrence and metastasis rates. Photodynamic therapy (PDT) represents an alternative treatment for colon cancer. This study used MTT assays to evaluate cell viability and applied Zinc (II) Phthalocyanine (ZnPc) photosensitizers to the colorectal adenocarcinoma (HT-29) cell line to investigate cancer pathways via flow cytometry and q-PCR. The results showed that PDT with ZnPc significantly reduced cell viability in HT-29 cells and induced apoptosis at a rate of 53%. According to q-PCR results, CT values of ten out of thirty genes were significant, and their association with cancer was evaluated.

Keywords: Photodynamic therapy, HT-29 cancer cell, Coumarin, Phthalocyanine, Gene expression

1. Introduction

The second most significant cause of death in the world is cancer.¹ Popular cancer therapies include surgery, chemotherapy, radiation, and immunotherapy. However, numerous regulatory cell signaling pathways, such as cell cycle arrest, apoptosis, or migration, have been discovered to impair therapeutic effectiveness process. Cancer cells' cellular heterogeneity may restrict the treatment options available to treat the illness.² The vast heterogeneity in tumor cell populations at the patient and cell level is a significant barrier to effective cancer treatment.³ Different cancer cells have different responses to therapy in terms of acquiring drug tolerance, surviving, and having the potential to spread. Subsets of hematological and solid tumors,

including breast, ovarian, lung, and lower gastrointestinal tract malignancies, have been found to evolve the multidrug-resistant genotype.³

The continuous accumulation of genetic and epigenetic changes is the hallmark of the complex colorectal cancer (CRC) illness.⁴ The fourth most common cause of cancer-related deaths worldwide and the third most dangerous malignancy overall are CRCs.⁵ Surgery, chemotherapy or radiotherapy are the standard curative therapies for CRC patients. However, these procedures have a lot of side effects and need a lot of recovery time. With the creation of fresh medications and therapeutic regimens, significant advancements in the therapy of CRC have been made.^{6,7} However, because tumor cells are resistant to existing treatment approaches.

Due to its excellent specificity and selectivity, photodynamic therapy (PDT) is an appealing anticancer treatment.⁸ PDT is a recognized medical procedure worldwide, including in Canada, Japan, Brazil, Chile, Argentina, the US, and the EU.⁹ PDT is a minimally invasive treatment technique that has been clinically established and can selectively kill cancer cells.¹⁰ PDT has the following benefits over other cancer therapy modalities: 1- Low side effect profile in the dark; 2- Because tissues differ physiologically, photosensitizers accumulate more in tumor tissues than in healthy tissues; 3- It can be used in conjunction with other treatments; 4- It can be used without surgery; 5- The effects are seen in 24 to 48 hours; and 6- The risk of cancer recurrence is low after PDT.¹¹ PDT is presently employed in numerous fields, such as ophthalmology, photo-immunotherapy, vascular targeting, and the treatment of cancer and acne.¹²

A wide range of biological actions, anti-tumor potential¹³, including antifungal, anticoagulant, vasodilator, estrogenic, dermal, photosensitizing, sedative, hypnotic, analgesic, antimicrobial, anti-inflammatory, anti-HIV, and anti-ulcer effects, are displayed by compounds with a coumarin moiety.¹⁴ Phthalocyanines are used commercially as dyes and pigments in printing inks, coloring plastic and metal surfaces, laser technology, optical and electrical materials, photodynamic cancer therapy, and chemical sensors. Functional phthalocyanines are needed for the development of different reactions on phthalocyanine complexes. These two functional compounds, coumarins, and phthalocyanines, can be combined in a single compound by synthetic methods to obtain soluble-fluorescent phthalocyanines. According to the experimental results; the addition of coumarin derivatives to the peripheral positions of the phthalocyanine ring increased the fluorescence properties and solubility of phthalocyanines.¹⁴ The original metal phthalocyanine, a new biphenyl derivative of coumarin compounds Zinc (II) Phthalocyanine (ZnPc), was synthesized.¹⁴

This article investigated the cytotoxicity of ZnPc against colorectal adenocarcinoma cell line (HT-29 cells). It has been demonstrated that PDT and particular photosensitizers (PSs) kills cancer cells.¹⁵ The underlying mechanism of cell death induction must be identified to evaluate the effectiveness of PDT utilizing particular PSs. Therefore, in this study, we compare the effects of ZnPc on HT-29 cells and the cancer pathways to better understand the etiopathogenesis of human colorectal adenocarcinoma. This knowledge will facilitate innovative therapeutic approaches in the future.

2. Material and Methods

2. 1. Procedure for the Synthesis of ZnPc

In our previous study, biphenyl derivative of coumarin [7-(2,3-dicyanophenoxy)-3-biphenylcoumarin 2

(0.10 g, 0.227 mmol)] with metal salt [Zn(OAc)₂·2H₂O (0.01 g, 0.046 mmol)], and two drops of DBU in 3 mL dry hexanol in a sealed glass tube was heated at 180 °C and stirred for 30 h under an argon atmosphere. After cooling to room temperature, the mixture was treated with 10 mL ethanol. The obtained products were filtered off and washed first with hot water then ethanol, ethylacetate and dried.¹⁴

2. 2. Photodynamic Therapy Treatment of Cell and Cell Viability Assay

The HT-29 colorectal adenocarcinoma cell line from (ATCC, USA) was routinely cultured in Dulbecco's Modified Eagle's Medium (DMEM) with the addition of 10% heat-inactivated fetal bovine serum (FBS), 1% penicillin-streptomycin (Sigma, USA), and 37 °C in a humid environment with 5% CO₂. Adherent monolayer cells were passaged at 70-80% confluence using trypsin EDTA (Sigma, USA). Each cell line was seeded onto 96-well plates with 100 μL of media per well (1 × 10⁴ cells), and the wells were attached after 24 hours of incubation at 37 °C. Cells were gathered to perform viability tests. The HT-29 cells of 1 × 10⁴ cell density were cultured for 24 h before being exposed to eight concentrations of ZnPc, as 0.5, 1, 3, 5, 10, 15, 20, and 40 μM prepared from the leading stocks of ZnPc, which were prepared according to literature.¹⁶ ¹⁷ The cells were first grown with PSs for 24 hours before being photosensitized with a diode laser at 660 nm with a fluence of 5.4 J/cm² for phototoxicity tests. The cells were then collected, and their vitality was assessed.¹⁶ Each well's culture media was taken out, and the cells were then treated with ZnPc and rinsed with PBS. Using the MTT test kit, the cell viability (%) was calculated (Thiazolyl Blue Tetrazolium Bromide, Sigma Aldrich, Missouri, ABD, Cas: 298-93-1). HT-29 cell line was then cultured for 3 hours at 37 °C before being slowly rinsed in PBS with a pH of 7.4. A spectrophotometer (540nm) was used to determine the cell viability, which was then computed using the formula below: Viability = (Sample-Blank)/(Control-Blank). Three times during three different weeks, the experiments were repeated.¹⁸

2. 3. Flow Cytometry

At 24 hours after treatment with increasing doses of ZnPc, apoptosis, and necrosis were identified using a flow cytometric assay.¹⁷ This was done using the Annexin V/7-Aminoactinomycin D (7-AAD) kit from Invitrogen/Biolegend in San Diego, California, USA. According to the manufacturer's recommendations, the HT-29 cell line (8 × 10⁵ cells/well) was seeded in 6-well plates with 2 mL of medium and cultivated at 37 °C for 24 hours. The cells underwent two cold PBS washes after being collected into individual eppendorf tubes. After all cells were centrifuged at 1500 rpm for 5 minutes, the supernatant was gathered. After adding the annexin V binding buffer, cells

were counted at a density of 10^6 cells per milliliter. Cells were treated for 15 minutes at room temperature in the dark with 5 μ L of Annexin V and 5 μ L of 7-AAD. After 400 μ L of binding buffer was injected on ice, the percentages of apoptosis and necrosis were calculated by flow cytometry (BD Accuri™ C6 Plus) (Figure 1–2).

2. 4. RNA Isolation and Global Dna Methylation Assessment

Total RNA was isolated using a TRIzol reagent (Life Technologies, Carlsbad, CA, USA). Total RNA concentrations were determined using a Nanodrop 2000c (Thermo Fisher Scientific). cDNA was synthesized with Wonder RT- cDNA Synthesis kit (Euroclone, Milan, Italy). Following cDNA synthesis, the level of global DNA methylation was estimated using the Methyl flash™ Global DNA methylation (5-mC) ELISA Easy Kits (Epigentek Group Inc, USA) according to the manufacturer's protocol.

2. 5. qPCR

According to the manufacturer's recommendations, total RNA was extracted from cell and tumor tissue samples using the TRIzol reagent (Life Technologies, Carlsbad, CA, USA). Following reverse transcription, complementary DNA (cDNA) was produced and put through real-time PCR using the proper primers and SYBR Green Mix (Thermo Fisher Scientific). Glyceraldehyde 3-phosphate dehydrogenase (GAPDH) was used as an internal control. Each experiment was performed in triplicate. Each data item was calculated using the $2^{-\Delta\Delta CT}$ method (Table 1).¹⁹

2. 6. Gene Enrichment Analysis of Significant Genes

Protein-protein interactions (PPI) of the prominent genes between groups were performed using the STRING

tool. PPI analyses were visualized using the Cytoscape program. Pathway and Gene ontology analyses of these genes were also performed using both STRING and cancer hallmarks tool. The expression status of these genes in COAD data (Cancer vs. normal) was also evaluated using the UALCAN tool, which performs analyses using TCGA datasets. In addition, survival analysis of the prominent genes was performed using the TIMER 2.0 tool. P value < 0.05 was accepted as statistically significant.

2. 7. Statistical Analyses

Mean SD were the descriptive statistics used to report all values. Welch correction and a t-test without pairings were employed to compare two unpaired variables. ANOVA was used to analyze more than two parametric variables, and the Tukey-Kramer Multiple Comparisons Test was used for a post hoc analysis. The cutoff for significance in all statistical studies is fixed at P < 0.05. GraphPad InStat (GraphPad Software, San Diego, CA, USA) was used to conduct the analyses.

3. Results

3. 1. Cytotoxicity Studies and Phototherapeutic Effect of Znpc Photosensitizer *In Vitro*

According to the morphological examination, 20 μ M ZnPc significantly suppressed the cell growth of the HT-29 cell line when compared to the control groups. According to the MTT experiment, the effective dose of ZnPc, specifically for the HT-29 cell line, was 20 μ M ($P^{****} < 0.001$). The increasing doses of ZnPc dramatically lowered the cell viability of HT-29 cells. These findings indicate a dose-dependent inhibition of cell viability by the ZnPc treatment in HT-29 cells. The concentrations between 0.5 and 10 μ M

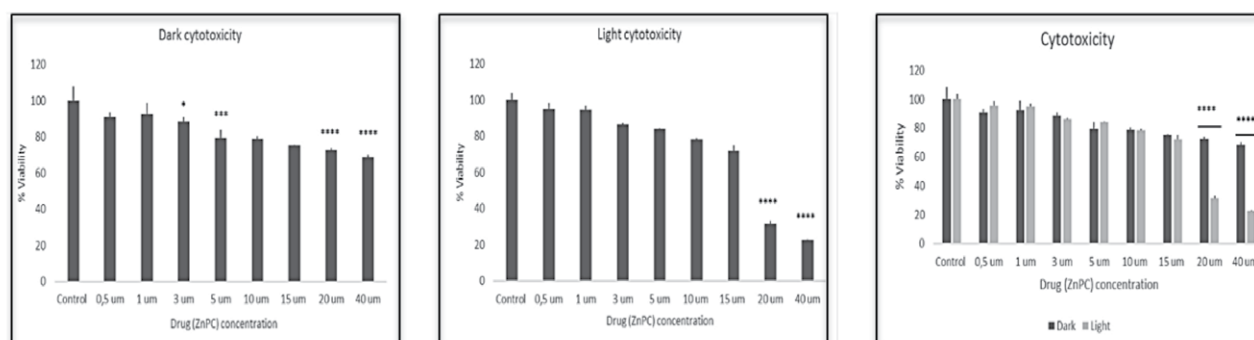


Figure 1. The cell viabilities (%) of HT29 cells calculated according to the results of MTT assay

Survival ratios of HT-29 cells incubated in ZnPc were analyzed using dark and light toxicity assays. $****P < 0.001$ vs normal cells. All data shown are the mean \pm standard deviation of three experiments performed independently. * $P < 0.05$, ** $P < 0.01$ and *** $P < 0.001$ are the statistically significance levels. ns: not significant. 3 μ m vs. Control * $P < 0,05$; 5 μ m vs. Control *** $P < 0,001$; 20 μ m vs. Control **** $P < 0,001$; 40 μ m vs. Control **** $P < 0,001$ analyzed by dark toxicity assays. 20 μ m vs. Control **** $P < 0,001$; 40 μ m vs. Control **** $P < 0,001$ analyzed by light toxicity assays. 20 μ m (dark) vs 20 μ m (light); 40 μ m (dark) vs 40 (light) **** $P < 0,001$ analyzed by dark and light toxicity assays.

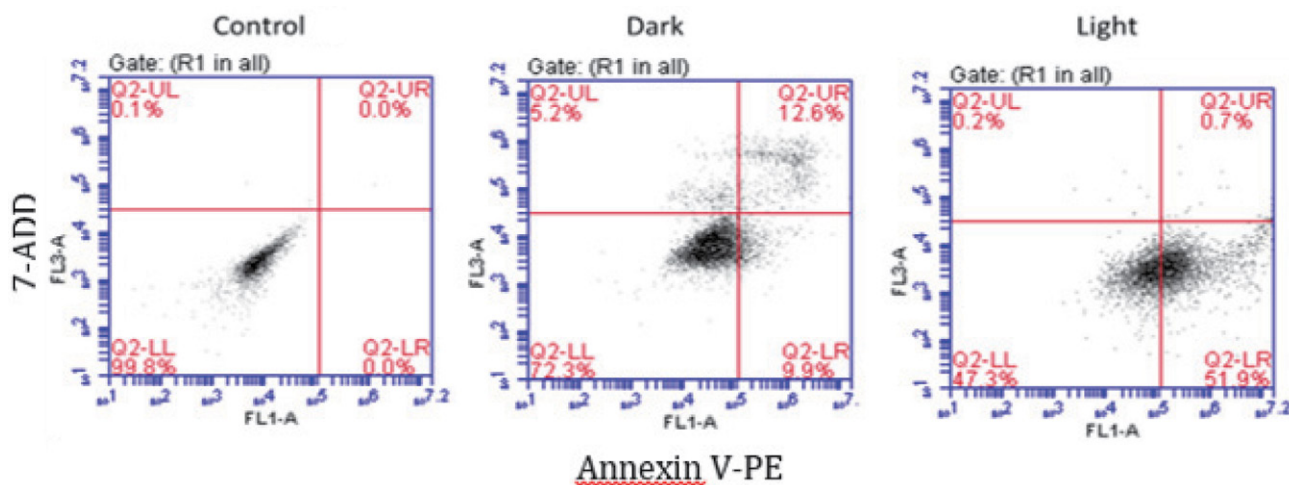


Figure 2. Analysis of Annexin-V/7AAD in HT-29 cells.

were also examined but did not give significant results in this range. One of the desirable characteristics of an efficient ZnPc is to have a high toxicity in the light and a low toxicity in the dark [17]. This was accomplished for ZnPc at a concentration of 20 μM , per the MTT results from the current investigation. Statistical analysis used One-Way Analysis of Variance (ANOVA) and the Tukey-Kramer Multiple Comparison Test with Post-hoc Test. This concentration of ZnPc, showed minimal toxicity in the dark (75%, $P^{***} < 0.001$), and their survival ratio decreased significantly (lower than 35%, $P^{***} < 0.001$) under light irradiation. While ZnPc (at 20 μM concentration) toxicity showed was showing minimal toxic effects in the dark, a high rate of toxicity was observed at 5.4 J/cm^2 light dose at the same concentration in the light (Figure1).

3. 2. Irradiation on HT-29 Cell

In our meticulously designed experimental configuration, we utilized a red laser diode emitting light at a central wavelength of 660 nm to irradiate a precisely defined area of 0.2 cm^2 on HT-29 cell samples. The laser's Gaussian beam profile played a crucial role in our calculations, as it excluded the tails, whose contribution to exposure fluence was deemed negligible. This meticulous approach ensured a high level of precision in assessing the intricate interactions between light and matter.

In a related experiment, we exposed HT-29 cells to a specific fluence using a continuous wave diode laser, following which we evaluated the subsequent biological responses after a 24-hour incubation period in fresh, photosensitizer-free media. This post-exposure evaluation allowed us to gain valuable insights into the longer-term effects of laser irradiation on cellular responses.

Our investigation focused on the dynamic interplay between ZnPc and HT-29 cells, maintaining a cell density 10^4 . The diode laser, with a power output of 5 mW and a central wavelength of 660 nm, delivered an irradiation

that deposited an energy density of 5.4 J/cm^2 . Notably, the study honed in on the energy absorption characteristics of ZnPc solutions, specifically at a concentration of 20 μM . The results unveiled a remarkable finding; the solution of ZnPc at 20 μM in a particular solvent exhibited the highest photo-toxicity among the examined conditions.

3. 3. Apoptotic Effect of ZnPc on HT-29 Cell

When HT-29 cells were exposed to a specific concentration (of 20 μM) of ZnPc and a diode laser with a fluence of 5.4 J/cm^2 was used for light toxicity experiments, the data were analyzed using flow cytometry. HT-29 cells treated with ZnPc showed a higher of cell death opposed to untreated cells ($**P < 0.01$; Figure 2). ZnPc compound led to 53% apoptosis in light, but 22% apoptosis in dark environment. The desired result is minimum death in the dark and maximum death in the light environment. These findings strongly imply the ZnPc's ability to induce apoptosis in HT-29 cells (Figure 2).

3. 4. Analyses of Deregulated Genes and Their Related Molecular Mechanism

In cells whose cell viability experiments were finished and whose IC_{50} value was 20 μM , the expression levels of about thirty genes were assessed. The $2^{-\Delta\Delta\text{CT}}$ method was used to calculate the analyses of ten cancer-related genes from the expression levels of thirty genes. The results of the examination of the genes involved in particular cancer pathways showed changes expression levels. The $2^{-\Delta\Delta\text{CT}}$ explain analyzed ten genes in this pathway and explain their molecular mechanism. To calculate the true fold change at this point, we balance the scales of the genes that are up- and down-regulated using the log base 2 of this value. If not, the scale for upregulation is 2-infinity, while the scale for downregulation is less than 0.5. According to gene expression analyses ten genes including APC, APC2, EIF4E,

Table 1. Gene expression in HT-29 cells. Up-regulated genes had a fold change ($2^{(-\Delta\Delta Ct)}$) above 2, while down-regulated genes had a $2^{(-\Delta\Delta Ct)}$ below 0.5. Only statistically significant genes are shown. <https://www.genecards.org/>.

Gene Symbol	Gene Name	Dark FoldChange 2- $\Delta\Delta Ct$	P value 2- $\Delta\Delta Ct$	Light FoldChange	P value
APC	Adenomatous polyposis coli	9,48	**<0.001	1,33	*<0.05
APC2	Adenomatous polyposis coli	6,08	**<0.001	1,25	*<0.05
EIF4E	Eukaryotic translation initiation factor 4E	5,35	**<0.001	1,46	*<0.05
GLI2	GLI family zinc finger 2	1,76	*<0.05	9,48	**<0.001
GLI3	GLI family zinc finger 3	1,43	*<0.05	3,14	**<0.001
BMP2	Bone morphogenetic protein 2	2,9	*<0.05	0,88	>0.05
BMP4	Bone morphogenetic protein 4	2,87	*<0.05	1,44	*<0.05
IFNA1	human interferon-Alpha1	2,11	>0.05	1,21	*<0.05
LEF1	Lymphoid enhancer binding factor 1	2,32	>0.05	1,39	*<0.05
LRP2	Lipoprotein-receptor-related protein 2	2,18	>0.05	0,84	*<0.05

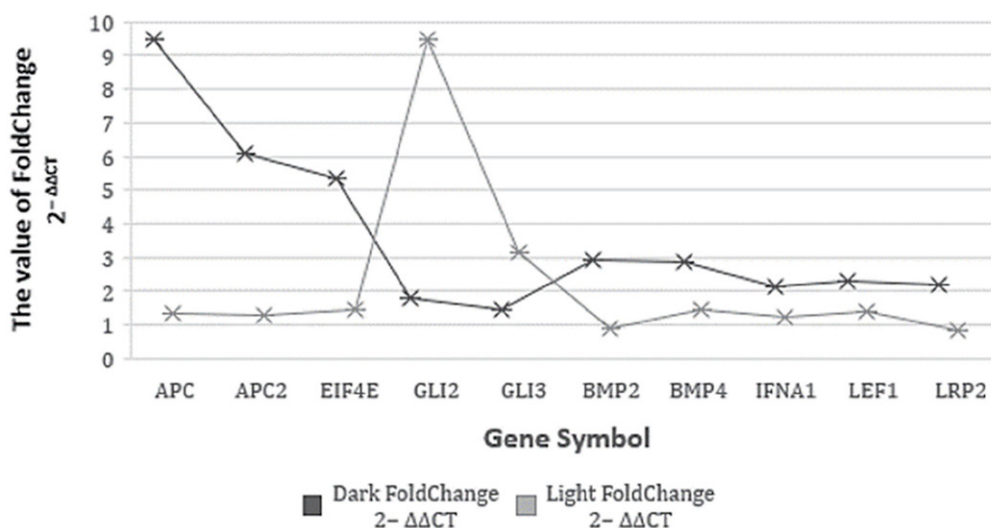


Figure 3. Gene expression in HT-29 cells.

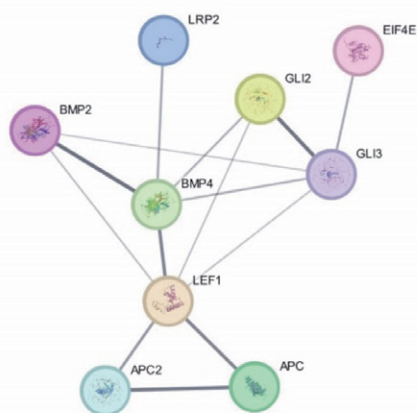
GLI2, GLI3, BMP2, BMP4, IFNA1, LEF1, and LRP2 were found statistically significant (Table 1).

Only two genes (GLI2, GLI3) out of ten were significantly ($p < 0.001$) increased compared to the treatment

(light) of the group, while the expression of the rest of the genes was decreased (Figure 3).

PPI network is shown for APC, APC2, EIF4E, GLI2, GLI3, BMP2, BMP4, IFNA1, LEF1, and LRP2 genes in

4.a



4.b

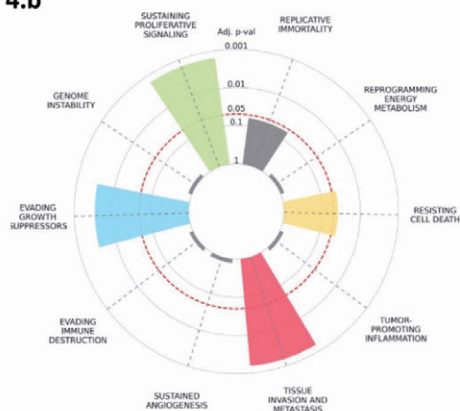


Figure 4. PPI network (4. a) and hallmark cancer analyses (4. b).

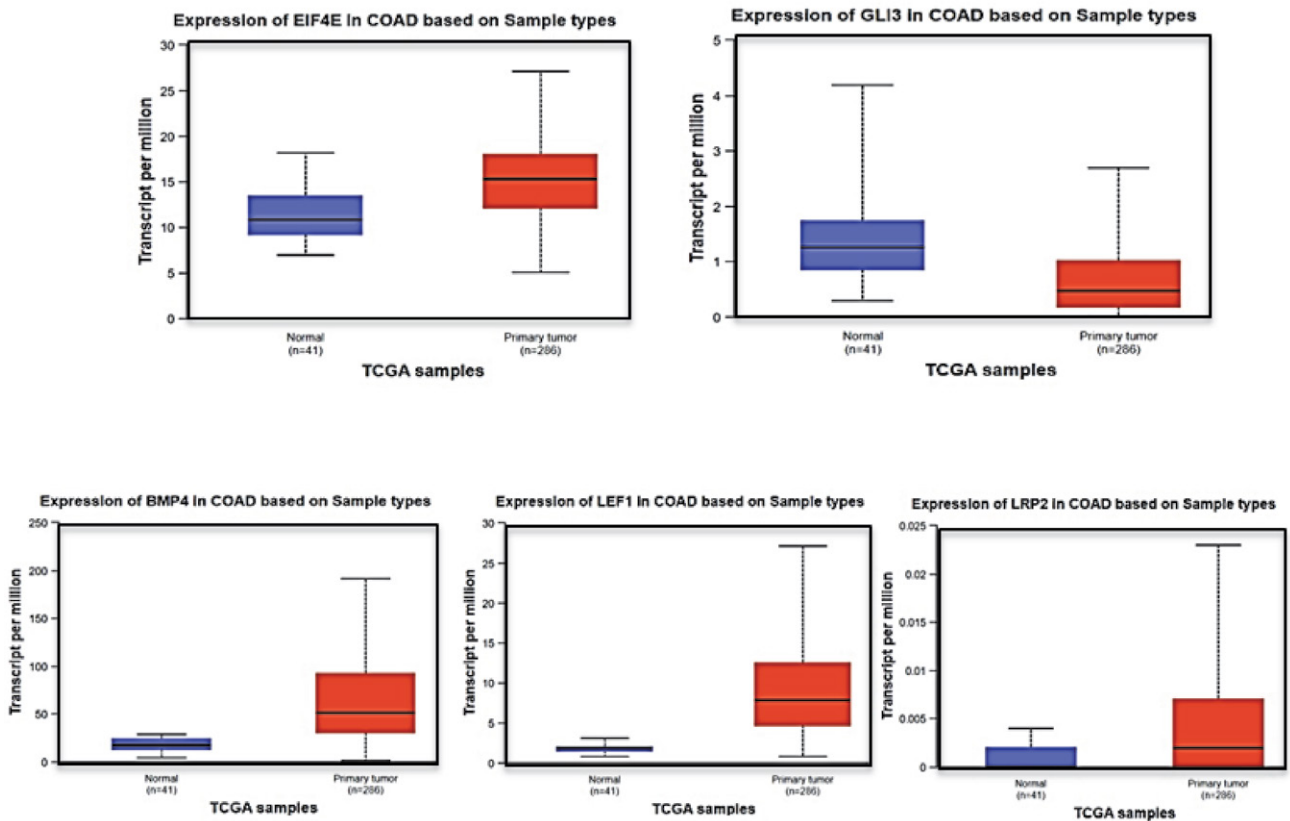


Figure 5. Expression of EIF4E, GLI3, BMP4, LEF1, and LRP2 genes in COAD data using UALCAN tool

Figure 4.a. Enrichment of hallmark cancer analyses shows that our prominent genes have a potential role in sustaining proliferative signaling (LEF1; GLI2; BMP2; BMP4), evading growth suppressors (APC; BMP2; BMP4), tissue invasion and metastasis (APC; LEF1; APC2; BMP2), and resisting cell death (APC; BMP4) molecular mechanisms (Figure 4. b).

In the GO-Biological process analyses using STRING tool, it was determined that all of these 10 genes, which showed expression changes especially with the effect of treatment, were involved in cell differentiation and system development processes. Regarding GO-Molecular process analysis, the beta-catenin binding mechanism (APC; APC2; LEF1; GLI3) emerged in the foreground.

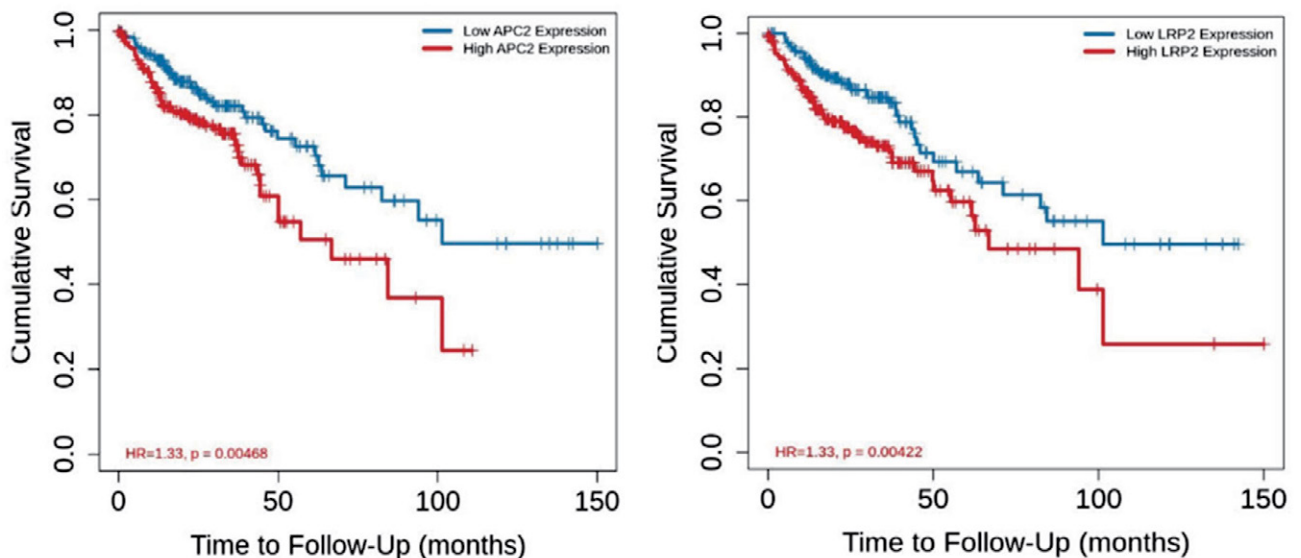


Figure 6. Survival analysis of APC2 and LRP2 genes.

According to the UALCAN tool the genes including EIF4E, BMP4, LEF1, and LRP2 were found increased expression levels and GLI3 was found, the genes including EIF4E, BMP4, LEF1, and LRP2 were found to have increased expression levels, and GLI3 was found to have decreased expression levels in cancer samples compared to normal (Figure 5). In our study expression of EIF4E, BMP4, LEF1, and LRP2 genes decreased and GLI3 increased compared to non-treated (dark) group.

APC and APC2 genes are tumor suppressor genes. In our study, their expression levels were decreased in the treated group compared to the non-treated group. Regarding survival analysis, the APC2 gene has a higher survival rate when its expression level decreases. Moreover, LRP2 gene was also higher survival rate when its expression level decreases (Figure 6).

4. Discussion

4.1. In Terms of Cellular Analysis

In certain tumor types, the use of photosensitizers (PS) is favored, and photodynamic therapy (PDT) has long been used as an anti-tumor treatment strategy. Light has long been used effectively to treat disease. It is known that cancer cells use various cell systems to avoid death. They frequently exhibit anti-apoptotic protein overexpression, mutations in proapoptotic proteins, and lysosomal hydrolases that block the initiation of cell death signals.²⁰ In the flow cytometry experiments, after ZnPc was applied to the HT-29 cells at a concentration of 20 μM , the light power was applied as 5.4 J/cm^2 . Consider analysis results, 52.6% apoptosis was observed in the light environment, while 22.5% apoptosis was observed in the dark. Another study observed 5–20% apoptosis because of PDT applied to HT-29 cells.²¹ Thus, we have observed the success of the ZnPc compound, which we use as a photosensitizer, leading to apoptosis.

Jamier et al. investigated the structure-activity relationship of various coumarin derivatives for cytotoxicity against human and mouse carcinoma cell lines (HT29, HepG2, A549, MCF7, OVCAR and CT26). Among the coumarin derivatives, (E)-7-methoxy-4-(3-oxo-3-phenylprop-1-enyl)-2H-chromon-2-one and (E)-7-hydroxy-4-(3-(4-hydroxyphenyl)-3-oxoprop-1-enyl)-2H-chromon-2-one showed the strongest cytotoxic effect on colon cancer cells CT26 ($\text{IC}_{50} = 4.9 \mu\text{M}$) due to their pro-oxidant properties.²² In our study, according to morphological examination, 20 μM ZnPc significantly suppressed cell growth of HT-29 cell line compared to control groups. According to MTT assay, the effective dose of ZnPc especially for HT-29 cell line was 20 μM ($P^{****} < 0.001$).

4.2. In Terms of Molecular Mechanism

APC and APC2 genes act as tumor suppressors. In our study, the expression of these genes showed a decrease

in the response to treatment between the groups compared to the cancer group. In studies, it has been reported that a decrease in the expression of these genes or a tendency to decrease in the treated cancer group leads to an increase in cancer invasion or metastasis formation.²³ However, interestingly, the analysis obtained from TCGA data sets (UALCAN-Gepia2-Oncodb, etc.) shows that low expression of the APC2 gene has a better survival rate. This contradiction needs to be elaborated in detail.

In our prominent genes, there was a tendency for EIF4E expression to decrease with treatment. EIF4E has a vital role in the translation mechanism. A crucial part of the eIF4F trimeric translation initiation complex, eIF4E binds to the 5' cap of eukaryotic mRNAs to control translation.²⁴ The increasing rate of EIF4E expression was found in many cancer studies. One of these studies was performed by²⁵ and shows that elevated eIF4E levels in CRC patients have a significant probability of liver metastasis, and eIF4E knockdown prevented CRC cell metastasis by controlling the production of MMP-2, MMP-9, VEGF, and cyclin D1.

In another study was demonstrated that the malignant phenotype of ovarian cancer is largely dependent on the activation of the eIF4E gene, and abnormalities in eIF4E expression are linked to ovarian cancer cell proliferation, migration, invasion, and chemosensitivity to cisplatin.²⁶ All studies show that downregulation of EIF4E may change the cancer progression.

Among the genes, bone morphogenetic proteins (BMP4), constituting a distinct subset of extracellular multifunctional signaling cytokines, they were first identified as osteogenic factors. They belong to the superfamily of transforming growth factor- β (TGF- β).²⁷ Due to their roles in tumor formation and spread, in addition to embryonic and postnatal development, the identification of BMPs has garnered a lot of attention.²⁸ Studies indicate that BMPs play a role in both tumor progression and suppression.²⁹ Although there are some contradictions, especially in colorectal cancer, studies have shown that BMP signaling inhibitors such as BMP type I receptor inhibitor (LDN-193189) induce growth inhibition³⁰ and apoptosis in cancer cells by decreasing highly expressed BMP4s. Moreover, the administration of this inhibitor to mice also had positive effects on decreasing tumor formation and inducing apoptosis.³¹ In our study, BMP4 tended to show a lower expression upon activation of the treatment. This suggests that BMP4 has a positive effect, especially on the apoptotic process.

The Wnt signaling pathway is mediated by a crucial transcription factor called lymphoid enhancer-binding factor 1 (LEF1). LEF1 is a regulator frequently increased in malignancies, such as colonic adenocarcinoma, and strongly linked to tumor aggressiveness. Using shRNA, LEF1 expression was suppressed in a study utilizing caco2 cells. It has been discovered that down-regulation of LEF1 inhibits microstructures linked to motility and malignancy, such as the polymerization of Lamin B1, β -tubulin, and F-actin in caco2 cells. The expression of genes associated

with the epithelial/endothelial-mesenchymal transition (EMT) was decreased by LEF1 inhibition. Additionally, it was reported to induce apoptosis.³² In vitro knockdown studies in HCT116 cells showed that LEF1 inhibits the proliferation of cancer cells by suppressing the therapeutic efficacy of β -sitosterol.³³ Our results show that LEF1 gene expression tended to decrease expression after treatment activation. Inhibition of LEF1 by this treatment method suggests that it activates apoptotic pathways and also blocks the blocks cell proliferation.

LDL receptor-related protein two is one of the genes that has gained attention since therapy began (LRP2/megalin). The multiliganded endocytic receptor LRP2 is expressed of many tissues, but it is most abundant in absorptive epithelial tissues like the kidney. Although low expression of LRP2 in some cancer types indicates poor survival,³⁴ with a very low chance of relapse following surgery, a study found that stage II CC cases with significant methylation in LRP2 had different clinical and biological impacts. This gene was shown to be specifically implicated in mechanisms linked to dendritic cell function and B cell immunity, as well as unique characteristics associated with mTORC1 and DNA repair signaling.³⁵ In our study, a tendency for LRP2 expression to decrease with treatment activation was also found. In addition, survival analysis showed that lower LRP2 expression was associated with better survival in colon cancer.

This study showed that ZnPc is greatly promising in clinical of cancer (especially human colorectal adenocarcinoma).

5. Conclusion

These comprehensive findings contribute significantly to our understanding of the nuanced interplay between ZnPc and a 660 nm laser, particularly within the context of HT-29 cells. The research sheds light on the intricate dynamics of energy absorption and subsequent biological responses, emphasizing the potential applications and implications of this light-matter interaction in cellular studies and photodynamic therapy.

Acknowledgment

We thank Kamil Çınar for his valuable contribution in developing the laser system for this research.

Conflict of Interest Statement

The authors have no conflicts of interest to declare.

Ethical Approval

This article does not contain any studies with human or animal subjects.

Funding

This research received no specific grant from funding agencies in the public, commercial, or not-for-profit sectors.

Availability of Data and Materials

Data is available on request from the authors.

6. References

- R.L. Siegel, K.D. Miller, A. Jemal, *CA. Cancer J. Clin.* **2019**, *69*, 7–34. DOI:10.3322/caac.21551
- M. O. Palumbo, P. Kavan, W. H. Miller, L. Panasci Jr., S. Assouline, N. Johnson, V. Cohen, F. Patenaude, M. Pollak, R.T. Jagoe, G. Batist, *Front. Pharmacol.* **2013**, *4*, 57. DOI:10.3389/fphar.2013.00057
- S. Sarkar, N. Cohen, P. Sabhachandani, T. Konry, *Lab. Chip.* **2015**, *15*(23), 4441–50. DOI:10.1039/C5LC00923E
- L. H. Nguyen, A. Goel, D. C. Chung, *Gastroenterology* **2020**, *158*(2), 291–302. DOI:10.1053/j.gastro.2019.08.059
- L. Niu, W. Yang, L. Duan, X. Wang, Y. Li, C. Xu, C. Liu, Y. Zhang, W. Zhou, J. Liu, Q. Zhao, L. Hong, D. Fan, *Mol. Ther. Nucleic Acids* **2020**, *23*, 42–54. DOI:10.1016/j.omtn.2020.10.030
- T. Matsuda, K. Yamashita, H. Hasegawa, T. Oshikiri, M. Hoso-no, N. Higashino, M. Yamamoto, Y. Matsuda, S. Kanaji, T. Nakamura, S. Suzuki, Y. Sumi, Y. Kakeji, *Ann. Gastroenterol. Surg.* **2018**, *2*(2), 129–136. DOI:10.1002/ags3.12061
- K. Van Der Jeught, H.C. Xu, Y. J. Li, X. Bin Lu, G. Ji, Drug resistance and newtherapies in colorectal cancer, *World J. Gastroenterol.* **2018**, *24*(34), 3834–3848. DOI:10.3748/wjg.v24.i34.3834
- A. Kawczyk-Krupka, A.M. Bugaj, W. Latos, K. Zaremba, K. Wawrzyniec, M. Kucharzewski, A. Sieroń, *Photodiagnosis Photodyn. Ther.* **2016**, *13*, 158–174. DOI:10.1016/j.pdpdt.2015.07.175
- A. F. Dos Santos, D. R. Q. De Almeida, L. F. Terra, M. S. Baptista, L. Labriola, *CA. Cancer J. Clin.* **2011**, *61*(4), 250–81. DOI:10.3322/caac.20114
- C.A. Robertson, D. H. Evans, H. Abrahamse, *J. Photochem. Photobiol. B.* **2009**, *96*(1), 1–8. DOI:10.1016/j.jphotobiol.2009.04.001
- A. Oniszczyk, K. Wojtunik-Kulesza, T. Oniszczyk, K. Kasprzak, *Biomed. Pharmacother.* **2016**, *83*, 912–929. DOI:10.1016/j.biopha.2016.07.058
- R. Baskaran, J. Lee, S. Yang, *Biomater. Res.* **2018**, *22*, 25. DOI:10.1186/s40824-018-0140-z
- N. Q. Khai and T. K. Vu, *Anticancer Agents Med. Chem.* **2024**, *24*(1), 18–29. DOI:10.2174/0118715206272112231102063919
- A. Gok, O. E. Baturhan, U. Salan U, A. R. Özkaya, M. Bulut, *Dyes and Pigments* **2016**, *133*, 311–323. DOI:10.1016/j.dyepig.2016.06.002
- H. Abrahamse, N. N. Houreld, *Int. J. Mol. Sci.* **2019**, *20*(13),

3254. DOI:10.3390/ijms20133254
16. A. G. Yurttas, A. M. Sevim, K. Çınar, G. Y. Atmaca, A. Erdoğan, A. Gül, *Dyes Pigment*. **2022**, *198*, 110012. DOI:10.1016/j.dyepig.2021.110012
17. S. Ozelcik, A. G. Yurttas, M. U. Kahveci, A. M. Sevim, A. Gul, *J. Mol. Struct.* **2023**, *1271*, 134019. DOI:10.1016/j.molstruc.2022.134019
18. P. Mega Tiber, S. Kocyyigit Sevin, O. Kilinc, O. Orun, *Gene* **2019**, *692*, 217–222. DOI:10.1016/j.gene.2019.01.015
19. A. G. Yurttas, Z. Okat, T. Elgun, K.U. Cifci, A. M. Sevim, A. Gul, *Photodiagnosis Photodyn. Ther.* **2023**, *42*, 103346. DOI:10.1016/j.pdpdt.2023.103346
20. T. Kirkegaard and M. Jaattela, *Biochim. Biophys. Acta*, **2009**, *1793(4)*, 746–54. DOI:10.1016/j.bbamcr.2008.09.008
21. A. Abedi, F. Tafvizi, P. Jafari and N. Akbari, *Sci Rep.* **2024**, *14(1)*, 3100. DOI:10.1038/s41598-024-53773-y
22. V. Jamier, W. Marut, S. Valente, C. Chereau, S. Chouzenoux, C. Nicco, H. Lemarechal, B. Weill, G. Kirsch, C. Jacob, F. Batteux, *Anticancer Agents Med. Chem.* **2014**, *14(7)*, 963–74. DOI:10.2174/1871520613666131224124445
23. Y. Sun, H. Tian, X. Xu and L. Wang, *Bioengineered* **2020**, *11(1)*, 1027–1033. DOI:10.1080/21655979.2020.1820823
24. M. L. Truitt, C. S. Conn, Z. Shi, X. Pang, T. Tokuyasu, A. M. Coady, Y. Seo, M. Barna and D. Ruggero, *Cell* **2015**, *162(1)*, 59–71. DOI:10.1016/j.cell.2015.05.049
25. T. Xu, Y. Zong, L. Peng, S. Kong, M. Zhou, J. Zou, J. Liu, R. Miao, X. Sun and L. Li, *Onco. Targets Ther.* **2016**, *9*, 815–22. DOI:10.2147/OTT.S98330
26. J. Wan, F. Shi, Z. Xu and M. Zhao, *Int. J. Oncol.* **2015**, *47(6)*, 2217–25. DOI:10.3892/ijo.2015.3201
27. X. Guo and X. F. Wang, *Cell Res.* **2009**, *19(1)*, 71–88. DOI:10.1038/cr.2008.302
28. J. C. Hardwick, L. L. Kodach, G. J. Offerhaus and G. R. van den Brink, *Nat. Rev. Cancer* **2008**, *8(10)*, 806–12. DOI:10.1038/nrc2467
29. S. Ehata, Y. Yokoyama, K. Takahashi and K. Miyazono, *Pathol. Int.* **2013**, *63(6)*, 287–96. DOI:10.1111/pin.12067
30. S. Nunomura, H. Ota, T. Irisawa, K. Endo and Y. Morita, *Appl. Phys. Express* **2023**, *16*, 061004. DOI:10.35848/1882-0786/acdc82
31. Y. Yokoyama, T. Watanabe, Y. Tamura, Y. Hashizume, K. Miyazono, S. Ehata, *Cancer Res.* **2017**, *77(15)*, 4026–4038. DOI:10.1158/0008-5472.CAN-17-0112
32. L. Xiao, C. Zhang, X. Li, C. Jia, L. Chen, Y. Yuan, Q. Gao, Z. Lu, Y. Feng, R. Zhao, X. Zhao, S. Cheng, Z. Shu, J. Xu, W. Duan, G. Nie, Y. Hou, *Int. J. Mol. Sci.* **2021**, *22(19)*, 10870. DOI:10.3390/ijms221910870
33. S. Gu, F. Liu, X. Xie, M. Ding, Z. Wang, X. Xing, T. Xiao, X. Sun, *Cell. Signal.* **2023**, *104*, 110585. DOI:10.1016/j.cellsig.2022.110585
34. M. Q. Rasmussen, G. Tindbæk, M. M. Nielsen, C. Merrild, T. Steiniche, J. S. Pedersen, S. K. Moestrup, S. E. Degn, M. Madsen, *Cancers (Basel)* **2023**, *15(6)*, 1830. DOI:10.3390/cancers15061830
35. B. Tournier, R. Aucagne, C. Truntzer, C. Fournier, F. Ghiringhelli, C. Chapusot, L. Martin, A. M. Bouvier, S. Manfredi, V. Jooste V, M. B. Callanan, C. Lepage, *Cancers* **2023**, *15(1)*, 158. DOI:10.3390/cancers15010158

Povzetek

Fotodinamična terapija (FDT) je način zdravljenja raka. Singletni kisik nastane kot posledica fotokemične reakcije med svetlobo, fotosenzibilizatorjem in molekularnim kisikom, ki uničuje celice. Pri raku debelega črevesa, za katerim na svetu boleha 1,23 milijona ljudi, je pogosto potrebna operacija, vendar je stopnja ponovitve bolezni in metastaz zelo visoka. FDT zato predstavlja alternativno pri zdravljenju raka debelega črevesa. V tej študiji so bili za oceno viabilnosti celic uporabljeni testi MTT, fotosenzibilizator cink(II) ftalocianin (ZnPc) pa je bil uporabljen na celični liniji adenokarcinoma debelega črevesa (HT-29) z namenom razjasnitve poti razvoja raka s pretočno citometrijo in q-PCR. Rezultati so pokazali, da je FDT z ZnPc znatno zmanjšala viabilnost celic HT-29 in povzročila apoptozo 53 % celic. Glede na rezultate q-PCR so bile vrednosti CT desetih od tridesetih genov signifikantne, zato je bila ovrednotena njihova povezava z rakom.



Except when otherwise noted, articles in this journal are published under the terms and conditions of the Creative Commons Attribution 4.0 International License

AUTHOR INDEX

Acta Chimica Slovenica
Year 2024, Vol. 71 No. 1–4

AbdElrahman Mohamed.....	421	Cheng Liu	685
Abdulghafar Banaz Arshad	398	Chetehouna Imane	492
Abdullah Salah	409	Chouana Toufik	186
Ahmadi Peni	619	Chumakov Yurii	609
Ahmed Faseehuddin	161	Ciber Luka	312
Aksöz Begüm Evranos	558	Cordes David B.	110
Akyuz Mehmet	566	Covaci Eniko	500
Alabidi Hawraa Mahdi	179	Čelić Andjelka S.....	256
Alispahić Amra.....	305	Dabhi Ravi A.....	334
Alwan Aseel.....	409	Dai Sheng-Ping.....	380
Amara- Rekkab Afaf	91	Dambagi Lawali Yabo	566
Angyus Bogdan Simion	500	Das Mouli	482
Apostolova Desislava	541	Das Tanisha	482
Arbi Ucu Yanu	619	Dascalu Izabella	197
Arsić Nebojša	170	Dash Rasmita	482
Arzhamova Ekaterina.....	528	Dedić Alema.....	305
Asiye Gok Yurttas	696	Deljanin Ilić Marina.....	170
Aslan Ali	566	Devetak Iztok	84
Aydogdu Seyda	437	Dey Biplab Kumar	161
Bah Yetiny Atuh.....	353	Dhaduk Milan P.....	334
Bardarov Ivo.....	541	Didi Mohamed Amine.....	91
Bari Sanjaykumar	66	Dimitrova Saravanska Antoaneta.....	519
Bayu Asep	619	Djaković Sekulić Tatjana	226
Bekić Sofija S.	256	Dobromirova Radkowska Ivelina.....	519
Belkhalifa Hakim	186	Dogan-Topal Burcu.....	558
Bhanwase Anil	26	Dong Xian	471
Bhatt Bhupesh S.....	334	Dong Xue.....	295
Bhatt Vaibhav D.....	334	Duran Gizem Nur	215
Biswas Ranu	421	Dutta Gouranga.....	421
Blazhev Gavazov Kiril.....	519	Dzoyem Jean Paul.....	353
Borisov Delchev Vassil.....	519	Džudžević-Čančar Huriya.....	305
Bouhadda Youcef.....	186	Egzar Hanaa Kadtem	179
Bouzidi Nebia.....	186	Enache Mirela	197
Brodnik Helena.....	312	Ercelen Sebnem	9
Bulkurcuoğlu Bünyamin	9	Erdogmus Ali	437
Burcin Erkal Cam.....	696	Ermanoğlu Mizgin	9
Cakir Ahmet	566	Evgeny Goreschnik	603
Chang-Wang Pan.....	685	Ezzat Mohammed.....	319
Chen Hai-Ying.....	236	Fajarwati Annisa Elcentia.....	619
Chen Liuxiu.....	236	Fan Ying-Cui.....	295
Chen Wen-Tong	380	Farhan Ali Mahdi	179
Chen Wu.....	236	Fatimah Nurul.....	619
Chen Yin-Bing	135		
Chen Zhuo.....	471		

Fei Hai-Yang.....	20	Li Wei.....	580, 587
Ferk Savec Vesna.....	143, 451	Liang Longchao.....	471
Findik Serap.....	123	Liu Cheng.....	380
Frentiu Tiberiu.....	500	Liu Chi.....	236
Gamal Mohammed.....	421	Liu Hao-Dong.....	380
Garbuz Olga.....	609	Liu Jiacheng.....	236
Genorio Bostjan.....	541	Liu Jiaxue.....	587
Göktaş Füsün.....	215	Liu Qiao-Ru.....	39
Graur Ianina.....	609	Liu Shu-Juan.....	135
Graur Vasilii.....	609	Liu Ya.....	288
Grošelj Uroš.....	312	Long-Hua Zeng.....	685
Gulea Aurelian.....	609	Lu Rundong.....	236
Guo Jin.....	595	Lu Zhi-Tao.....	595
Habibullah Sk.....	482	Luo Fangwen.....	471
Hadi Tri Aryono.....	619	Ma Jian-Ping.....	295
Han Yong-Jun.....	39	Majeed Atheer.....	409
Hao Yu-Mei.....	304	Mali Audumbar.....	26
Hao-Dong Liu.....	685	Mallick Subrata.....	482
Hardhiyuna Mutia.....	619	Mandal Suman.....	110
Hatipoglu Arzu.....	437	Marčetić Zoran.....	170
He Dan.....	509	Martins Pedro Farinazzo Bergamo Dias.....	541
He Xin.....	135	Masamba Wellington.....	500
He Zi-Jian.....	595	Massoumi Bakhshali.....	47
Heath Ester.....	56	Mathew Maris Minna.....	541
Henni Abdellah.....	186	Mazhukina Olga.....	528
Hermawa Adam.....	619	Melike Kefeli.....	696
Hočevár Jan.....	56	Mkounga Pierre.....	353
Hrast Špela.....	143	Moghadam Razieh Shekari.....	363
Isleroglu Hilal.....	204	Mosiur Rahaman Sk.....	421
İyidogan Ayşegül.....	566	Moussa Ines Ben.....	492
Jamaal Maryam.....	319	Msiedeen Ashraf Al.....	244
Ji Rui-Ying.....	509	Mulai Tsungom.....	99
Jia Qi-Ke.....	509	Murniasih Tutik.....	619
Kadri Meriem.....	186	Nandi Souvik.....	482
Kamil Cinar.....	696	Nangare Sopan.....	66
Karalı Nilgün.....	215	Narayan Sahoo Rudra.....	482
Keshtiban Marzieh Mahmoodi.....	47	Ndefonganga Jérôme Ndefo.....	353
Khan Zamir.....	66	Nikoo Abbas.....	47
Kharmawphlang Wanshanlang.....	99	Ningsih Febby Nurdiya.....	619
Kılıç Ömer.....	9	Nkengfack Augustin Ephrem.....	353
Klenina Olena.....	264	Nosan Miha.....	541
Kostadinova Toncheva Galya.....	519	Oancea Petruta.....	197
Kovač Kralj Anita.....	388	Obuseng Veronica.....	500
Kumar John Elisa.....	99	Öksüz Mustafa.....	9
Kutlu Oznur Dulger.....	437	Olgun Gamze Nur.....	204
Laib Ibtissam.....	492	Olha Panteleieva.....	603
Lazić Anita.....	226	Orel Mojca.....	451
Lei Jinkai.....	236	Özbil Mehmet.....	215
Lei Yan.....	288	Padariya Aelvish.....	334
Lenarčič Brigita.....	256	Pan Chang-Wang.....	380
		Panigrahy Shibashis.....	482
		Patel Mohan N.....	334

Patil Ashwini	66	Taskin Duygu	9
Patil Pravin Onkar	66	Taskin Turgut	9
Pattnaik Satyanarayan	161	Tian Xujiao	471
Pavšič Miha	256	Tlili Mohammed Laid	492
Peklaj Cirila	451	Toader Ana Maria	197
Petković Dejan	170	Tot Kristina	226
Petri Edward T.	256	Trifonova Stojnova Kirila	519
Plavša Jovana J.	256	Tsamo Armelle Tontsa	353
Požgan Franc	312	Tsapkov Victor	609
Putra Masteria Yunovilsa	619	Tsemeugne Joseph	353
Putri Dyaningtyas Dewi Pamungkas ...	619	Tsopmene Ulrich Joel	353
Qi Chen-Yu,	295	Tugba Elgun	696
Qi Fei-Yu	135	Vassileva Divarova Vidka	519
Qin Jie	295	Veselinovic Aleksandar	170
Qiu Ting-Qun	595	Vidmar Janja	56
Qiu Xiao-Yang	135	Wang Jing	20
Rassa Mehdi	1	Wang Meng	295
Rayaman Erkan	9	Wang Rong	509
Ribič Luka	84	Wang Ya-Pin	509
Rosyidah A'liyatur	619	Wei Wanlin	580
Saadi Nawzat S.	398	Wen-Tong Chen	685
Safavi-Mirmahaleh Seyede Khadije	1	Wu Chen	135
Saha Nitis Chandra	110	Wu Jiang Ning	363
Şahi Talip	9	Wu Yu-Hui	580
Sahoo Mihir Kumar	99	Xiao Xiuchan	288
Salem Mohamed M.	421	Xie Ya-Ping	295
Salem-Bekhit Mounir M.	421	Xie Zheng-Ping	595
Salemi Khadidja	492	Xi-Yu Shao	685
Samiey Babak	363	Xu Meng-Yuan	135
Sathe Bhushankumar	66	Xu Yu-Yue	380
Savaliya Nirbhay K.	334	Xue Ling-Wei	39
Senna Bame Sanah	500	Yan Shao-Peng	509
Setiawan Andi	619	Yang Feng	295
Shao Xi-Yu	380	Yang Meng	20
Sheng-Ping Dai	685	Yang Qiwen	288
Shoeili Zeinab Moradi	1	Yasin Suhad A.	398
Simonović Dejan	170	Yasin Suhad	409
Slapničar Miha	84	Yegorova Alevtina	528
Slawin Alexandra M.Z.	110	Yeole Pratik	66
Sokolović Dušan	170	Yi Xiu-Guang	595
Song Zi-Jie	295	Yilmaz Beyza Nur	9
Sopbué Emmanuel Fondjo	353	You Zhonglu	580, 587
Soylu-Eter Özge	215	Yuan Jun-Ru	295
Stojanović Milovan	170	Yu-Yue Xu	685
Stojanović Sanja	170	Zhang Cheng-Cai	20
Sugumaran Abimanyu	421	Zhang Shi-Yu	587
Sun Chang-Chun	304	Zhang Wei-Guang	462
Sun Juan	20	Zhang Yong-Han	295
Svete Jurij	312	Zhou Min	20
Swain Kalpana	161	Zhou Yang	20, 509
Swain Rakesh	482	Zhu Zhi-Yu	509
Špánik Ivan	305		
Štefan Bogdan	312		

DRUŠTVENE VESTI IN DRUGE AKTIVNOSTI SOCIETY NEWS, ANNOUNCEMENTS, ACTIVITIES

Vsebina

Podelili smo nagrade in priznanja Slovenskega kemijskega društva	S95
Koledar važnejših znanstvenih srečanj s področja kemije in kemijske tehnologije	S97
Navodila za avtorje	S98

Contents

Slovenian Chemical Society awards and prizes	S95
Scientific meetings – Chemistry and chemical engineering.....	S97
Instructions for authors	S98

Podelili smo nagrade in priznanja Slovenskega kemijskega društva

Slovensko kemijsko društvo z veseljem in ponosom sporoča, da je letos prvič podelilo stanovske nagrade in priznanja, s katerimi želimo nagraditi izjemne dosežke kemikov na različnih področjih znanstvenega, pedagoškega in gospodarskega dela. Te nagrade predstavljajo priznanje za prispevek posameznikov in skupin k napredku kemije v Sloveniji ter spodbudo za nadaljnji razvoj stroke.

Podelitev je potekala v sredo, 18.9.2024, v Portorožu v okviru konference Slovenski kemijski dnevi 2024, ki je letos obeležila 30 let. Konference se vsako leto udeleži okrog 300 udeležencev iz Slovenije in tujine, letos smo zabeležili goste iz 12 držav.

Na slovesnosti smo podelili štiri prestižne nagrade:

- **Nagrado za mlade kemike in kemijske inženirje na znanstvenem in pedagoškem področju** je prejel **dr. Matej Huš** za svoje izjemno delo na področju raziskav ter za pomemben prispevek k razvoju kemijske izobrazbe mladih.
- **Nagrado za mlade kemike in kemijske inženirje na gospodarskem področju** je prejel **dr. Martin Ocepek**, ki se je izkazal z inovativnostjo in naprednim delom v kemijski industriji.

*Dr. Matej Huš
prejemnik Nagrade za mlade kemike
in kemijske inženirje na znanstvenem
in pedagoškem področju*



*Dr. Martin Ocepek
prejemnik Nagrade za mlade kemike
in kemijske inženirje na gospodarskem področju*





Raziskovalna skupina iz Leka – prejemniki Nagrade za vrhunski dosežek na gospodarskem področju

- Nagrado za vrhunski dosežek na gospodarskem področju je prejela skupina iz Leka – dr. Rok Grahek, dr. Miha Drev, dr. Borut Zupančič, Matej Ošljaj, Andrej Bastarda, dr. Andrej Kocijan in dr. Zdenko Časar, ki je s svojim delom *Določitev mehanizma razkroja N-nitrozo-hidroklortiazida* pomembno prispevala k razvoju in uvedbi inovacij, ki imajo velik pomen tako za gospodarstvo kot za družbo nasploh.
- Nagrado za življenjsko delo na gospodarskem področju je prejel dr. Silvo Zupančič za svoj dolgoletni prispevek k razvoju kemijske industrije v Sloveniji ter za svojo vlogo mentorja in voditelja v tej pomembni panogi.



Dr. Silvo Zupančič – prejemnik Nagrade za življenjsko delo na gospodarskem področju

Ob tej priložnosti je predsednik Slovenskega kemijskega društva, dr. Peter Venturini, izjavil: »Slovensko kemijsko društvo je z uvedbo teh nagrad prepoznalo pomen odličnosti v kemijski stroki na vseh ravneh delovanja, od izobraževanja in raziskav do industrije. Ponosni smo na vse nagrajence, ki s svojim delom in predanostjo postavljajo visok standard in predstavljajo vzor mlajšim generacijam. Verjamem, da bodo te nagrade še naprej spodbujale inovativnost in napredek v naši družbi.«

»Ključna vodila skozi raziskovalno delo so ciljna usmerjenost, iskanje ustrezne poti do cilja ter vrednote kot so znanje, vztrajnost, zaupanje vase in v svoje sodelavce. S temi vodili lahko dosežemo preboje, ki prispevajo k napredku na področju kemije oziroma znanosti.« je svojo pot do uspeha opisal dr. Silvo Zupančič.

Dr. Matej Huš pa je dodal: »Zahvaljujem se za nagrado in dodajam, da so vsi dosežki tudi zasluga sodelavcev in okolja na inštitutu, ki me podpirajo pri mojem delu. Nagrado jemljem tudi kot zavezo, da v prihodnosti delam še bolje.«

»V Leku smo veseli, da je Slovensko kemijsko društvo s stanovskimi nagradami, ki so letos prvič podeljene, prepoznalo odličnost in prebojnost raziskovalnega dela Lekovih raziskovalcev, ki so s svojimi delom omogočili dostopnost zdravil za zdravljenje povišanega krvnega tlaka bolnikom po svetu,« je poudaril Matjaž Tršek, direktor Razvojnega centra Slovenija v Leku.

Dr. Martin Ocepek pa pravi: »Nagrada SKD za mlade kemike in kemijske inženirje iz gospodarstva mi pomeni priznanje dosedanjemu inoviranju in motivacijo po nadaljnjem ustvarjanju dodane vrednosti s pomočjo kemije.«

Zahvaljujemo se pokroviteljem stanovskih nagrad: Fakulteti za kemijo in kemijsko tehnologije Univerze v Ljubljani, Združenju kemijske industrije GZS in podjetjem Kansai Helios Slovenija, Labtim d.o.o. in Merck d.o.o.

Slovensko kemijsko društvo bo s podeljevanjem teh nagrad tudi v prihodnje prepoznavalo in nagrajevalo izjemne dosežke na področju kemije ter s tem krepilo pomen kemije v družbi in industriji.

KOLENDAR VAŽNEJŠIH ZNANSTVENIH SREČANJ S PODROČJA KEMIJE IN KEMIJSKE TEHNOLOGIJE

SCIENTIFIC MEETINGS – CHEMISTRY AND CHEMICAL ENGINEERING

2025

February 2025

- 2–7 EUROPEAN-WINTER SCHOOL ON PHYSICAL ORGANIC CHEMISTRY (E-WISPOC)
Bressanone, Italy
Information: <https://www.ewis poc.com/>
- 11 GWB2025
virtual
Information: <https://iupac.org/gwb/>
- 14–16 YOUNG CHEMISTS SUMMIT 2024 (YC SUMMIT 2024)
Salzburg, Austria
Information: <https://www.yc-summit.com/>

March 2025

- 10–13 ANAKON 2025
Leipzig, Germany
Information: https://veranstaltungen.gdch.de/microsite/index.cfm?l=11713&sp_id=2
- 17–19 CHEMIEDOZENTENTAGUNG 2025
Brunswick, Germany
Information: https://veranstaltungen.gdch.de/microsite/index.cfm?l=11723&sp_id=1

April 2025

- 1–4 FRONTIERS IN MEDICINAL CHEMISTRY
Erlangen-Nuremberg, Germany
Information: https://veranstaltungen.gdch.de/microsite/index.cfm?l=11738&sp_id=2&selMicrosite=126144
- 3–4 FLOW CHEMISTRY EUROPE
Málaga, Spain
Information: <https://flowchemistryeurope.com/>

Acta Chimica Slovenica

Author Guidelines

Submissions

Submission to ACSi is made with the implicit understanding that neither the manuscript nor the essence of its content has been published in whole or in part and that it is not being considered for publication elsewhere. All the listed authors should have agreed on the content and the corresponding (submitting) author is responsible for having ensured that this agreement has been reached. The acceptance of an article is based entirely on its scientific merit, as judged by peer review. There are no page charges for publishing articles in ACSi. The authors are asked to read the Author Guidelines carefully to gain an overview and assess if their manuscript is suitable for ACSi.

Additional information

- Citing spectral and analytical data
- Depositing X-ray data

Submission material

Typical submission consists of:

- full manuscript (PDF file, with title, authors, abstract, keywords, figures and tables embedded, and references)
- supplementary files
 - **Full manuscript** (original Word file)
 - **Statement of novelty** (Word file)
 - **List of suggested reviewers** (Word file)
 - **ZIP file containing graphics** (figures, illustrations, images, photographs)
 - **Graphical abstract** (single graphics file)
 - **Proposed cover picture** (optional, single graphics file)
 - **Appendices** (optional, Word files, graphics files)

Incomplete or not properly prepared submissions will be rejected.

Submission process

Before submission, authors should go through the checklist at the bottom of the page and prepare for submission.

Submission process consists of 5 steps.

Step 1: Starting the submission

- Choose one of the journal sections.
- Confirm all the requirements of the **checklist**.
- Additional plain text comments for the editor can be provided in the relevant text field.

Step 2: Upload submission

- Upload full manuscript in the form of a Word file (with title, authors, abstract, keywords, figures and tables embedded, and references).

Step 3: Enter metadata

- First name, last name, contact email and affiliation for all authors, in relevant order, must be provided. Corresponding author has to be selected. Full postal address and phone number of the corresponding author has to be provided.

- **Title and abstract** must be provided in plain text.
- Keywords must be provided (max. 6, separated by semicolons).
- Data about contributors and supporting agencies may be entered.
- **References** in plain text must be provided in the relevant text field.

Step 4: Upload supplementary files

- Original Word file (original of the PDF uploaded in the step 2)
- **List of suggested reviewers** with at least five reviewers with two recent references from the field of submitted manuscript must be uploaded as a Word file. At the same time, authors should declare (i) that they have no conflict of interest with suggested reviewers and (ii) that suggested reviewers are experts in the field of the submitted manuscript.
- All **graphics** have to be uploaded in a single ZIP file. Graphics should be named Figure 1.jpg, Figure 2.eps, etc.
- **Graphical abstract image** must be uploaded separately
- **Proposed cover picture** (optional) should be uploaded separately.
- Any additional **appendices** (optional) to the paper may be uploaded. Appendices may be published as a supplementary material to the paper, if accepted.
- For each uploaded file the author is asked for additional metadata which may be provided. Depending of the type of the file please provide the relevant title (Statement of novelty, List of suggested reviewers, Figures, Graphical abstract, Proposed cover picture, Appendix).

Step 5: Confirmation

- Final confirmation is required.

Article Types

Feature Articles are contributions that are written on Editor's invitation. They should be clear and concise summaries of the author's most recent work written with the broad scope of ACSi in mind. They are intended to be general overviews of the authors' subfield of research but should be written in a way that engages and informs scientists in other areas. They should contain the following (see also general guidelines for article structure below): (1) an introduction that acquaints readers with the authors' research field and outlines the important questions for which answers are being sought; (2) interesting, novel, and recent contributions of the author(s) to the field; and (3) a summary that presents possible future directions. Manuscripts should normally not exceed 40 pages of one column format (font size 12, 33 lines per page). Generally, experts who have made an important contribution to a specific field in recent years will be invited by the Editor to contribute a **Feature Article**. Individuals may, however, send a proposal (of no more than one page) for a **Feature Article** to the Editor-in-Chief for consideration.

Scientific articles should report significant and innovative achievements in chemistry and related sciences and should exhibit a high level of originality. They should have the following structure:

1. Title (max. 150 characters),
2. Authors and affiliations,
3. Abstract (max. 1000 characters),
4. Keywords (max. 6),
5. Introduction,
6. Experimental,
7. Results and Discussion,
8. Conclusions,
9. Acknowledgements,
10. References.

The sections should be arranged in the sequence generally accepted for publications in the respective fields and should be successively numbered.

Short communications generally follow the same order of sections as Scientific articles, but should be short (max. 2500 words) and report a significant aspect of research work meriting separate publication. Editors may decide that a Scientific paper is categorized as a Short Communication if its length is short.

Technical articles report applications of an already described innovation. Typically, technical articles are not based on new experiments.

Preparation of Submissions

Text of the submitted articles must be prepared with Microsoft Word. Normal style set to single column, 1.5 line spacing, and 12 pt Times New Roman font is recommended. Line numbering (continuous, for the whole document) must be enabled to simplify the reviewing process. For any other format, please consult the editor. Articles should be written in English. Correct spelling and grammar are the sole responsibility of the author(s). Papers should be written in a concise and succinct manner. The authors shall respect the ISO 80000 standard [1], and IUPAC Green Book [2] rules on the names and symbols of quantities and units. The Système International d'Unités (SI) must be used for all dimensional quantities.

Graphics (figures, graphs, illustrations, digital images, photographs) should be inserted in the text where appropriate. The captions should be self-explanatory. Lettering should be readable (suggested 8 point Arial font) with equal size in all figures. Use common programs such as MS Excel or similar to prepare figures (graphs) and ChemDraw to prepare structures in their final size. Width of graphs in the manuscript should be 8 cm. Only in special cases (in case of numerous data, visibility issues) graphs can be 17 cm wide. All graphs in the manuscript should be inserted in relevant places and **aligned left**. The same graphs should be provided separately as images of appropriate resolution (see below) and submitted together in a ZIP file (Graphics ZIP). Please do not submit figures as a Word file. In **graphs**, only the graph area determined by both axes should be in the frame, while a frame around the whole graph should be omitted. The graph area should be white. The legend should be inside the graph area. The style of all graphs should be the same. **Figures and illustrations** should be of sufficient quality for the printed version, i.e. 300 dpi minimum. **Digital images and photographs** should be of high quality (minimum

250 dpi resolution). On submission, figures should be of good enough resolution to be assessed by the referees, ideally as JPEGs. High-resolution figures (in JPEG, TIFF, or EPS format) might be required if the paper is accepted for publication.

Tables should be prepared in the Word file of the paper as usual Word tables. The captions should appear above the table and should be self-explanatory.

References should be numbered and ordered sequentially as they appear in the text, likewise methods, tables, figure captions. When cited in the text, reference numbers should be superscripted, following punctuation marks. It is the sole responsibility of authors to cite articles that have been submitted to a journal or were in print at the time of submission to ACSi. Formatting of references to published work should follow the journal style; please also consult a recent issue:

1. J. W. Smith, A. G. White, *Acta Chim. Slov.* **2008**, *55*, 1055–1059.
2. M. F. Kemmere, T. F. Keurentjes, in: S. P. Nunes, K. V. Peinemann (Ed.): *Membrane Technology in the Chemical Industry*, Wiley-VCH, Weinheim, Germany, **2008**, pp. 229–255.
3. J. Levec, Arrangement and process for oxidizing an aqueous medium, US Patent Number 5,928,521, date of patent July 27, **1999**.
4. L. A. Bursill, J. M. Thomas, in: R. Sersale, C. Collola, R. Aiello (Eds.), *Recent Progress Report and Discussions: 5th International Zeolite Conference*, Naples, Italy, 1980, Gianini, Naples, **1981**, pp. 25–30.
5. J. Szegezdi, F. Csizmadia, Prediction of dissociation constant using microconstants, http://www.chemaxon.com/conf/Prediction_of_dissociation_constant_using_microconstants.pdf, (assessed: March 31, 2008)

Titles of journals should be abbreviated according to Chemical Abstracts Service Source Index (CASSI).

Special Notes

- Complete characterization, **including crystal structure**, should be given when the synthesis of new compounds in crystal form is reported.
- Numerical **data should be reported with the number of significant digits corresponding to the magnitude** of experimental uncertainty.
- **The SI system of units and IUPAC recommendations** for nomenclature, symbols and abbreviations should be followed closely. Additionally, the authors should follow the general guidelines when citing spectral and analytical data, and depositing crystallographic data.
- **Characters** should be correctly represented throughout the manuscript: for example, 1 (one) and l (ell), 0 (zero) and O (oh), x (ex), D7 (times sign), B0 (degree sign). Use Symbol font for all Greek letters and mathematical symbols.
- The rules and recommendations of the **IUBMB** and the **International Union of Pure and Applied Chemistry (IUPAC)** should be used for abbreviation of chemical names, nomenclature of chemical compounds, enzyme nomenclature, isotopic compounds, optically active isomers, and spectroscopic data.
- **A conflict of interest** occurs when an individual (author, reviewer, editor) or its organization is in-

volved in multiple interests, one of which could possibly corrupt the motivation for an act in the other. Financial relationships are the most easily identifiable conflicts of interest, while conflicts can occur also as personal relationships, academic competition, etc. **The Editors** will make effort to ensure that conflicts of interest will not compromise the evaluation process; potential editors and reviewers will be asked to exempt themselves from review process when such conflict of interest exists. When the manuscript is submitted for publication, **the authors** are expected to disclose any relationships that might pose potential conflict of interest with respect to results reported in that manuscript. In the Acknowledgement section the source of funding support should be mentioned. The statement of disclosure must be provided as Comments to Editor during the submission process.

- **Published statement of Informed Consent.** Research described in papers submitted to ACSi must adhere to the principles of the Declaration of Helsinki (<http://www.wma.net/e/policy/b3.htm>). These studies must be approved by an appropriate institutional review board or committee, and informed consent must be obtained from subjects. The Methods section of the paper must include: 1) a statement of protocol approval from an institutional review board or committee and 2), a statement that informed consent was obtained from the human subjects or their representatives.
- **Published Statement of Human and Animal Rights.** When reporting experiments on human subjects, authors should indicate whether the procedures followed were in accordance with the ethical standards of the responsible committee on human experimentation (institutional and national) and with the Helsinki Declaration of 1975, as revised in 2008. If doubt exists whether the research was conducted in accordance with the Helsinki Declaration, the authors must explain the rationale for their approach and demonstrate that the institutional review body explicitly approved the doubtful aspects of the study. When reporting experiments on animals, authors should indicate whether the institutional and national guide for the care and use of laboratory animals was followed.
- To avoid conflict of interest between authors and referees we expect that not more than one referee is from the same country as the corresponding author(s), however, not from the same institution.
- Contributions authored by **Slovenian scientists** are evaluated by non-Slovenian referees.
- Papers describing **microwave-assisted reactions** performed in domestic microwave ovens are not considered for publication in *Acta Chimica Slovenica*.
- *Manuscripts that are **not prepared and submitted** in accord with the instructions for authors are not considered for publication.*

Appendices

Authors are encouraged to make use of supporting information for publication, which is supplementary material (appendices) that is submitted at the same time as the manuscript. It is made available on the Journal's

web site and is linked to the article in the Journal's Web edition. The use of supporting information is particularly appropriate for presenting additional graphs, spectra, tables and discussion and is more likely to be of interest to specialists than to general readers. When preparing supporting information, authors should keep in mind that the supporting information files will not be edited by the editorial staff. In addition, the files should be not too large (upper limit 10 MB) and should be provided in common widely known file formats to be accessible to readers without difficulty. All files of supplementary materials are loaded separately during the submission process as supplementary files.

Proposed Cover Picture and Graphical Abstract Image

Graphical content: an ideally full-colour illustration of resolution 300 dpi from the manuscript must be proposed with the submission. Graphical abstract pictures are printed in size 6.5 x 4 cm (hence minimal resolution of 770 x 470 pixels). Cover picture is printed in size 11 x 9.5 cm (hence minimal resolution of 1300 x 1130 pixels)

Authors are encouraged to submit illustrations as candidates for the journal Cover Picture*. The illustration must be related to the subject matter of the paper. Usually both proposed cover picture and graphical abstract are the same, but authors may provide different pictures as well.

* The authors will be asked to contribute to the costs of the cover picture production.

Statement of novelty

Statement of novelty is provided in a Word file and submitted as a supplementary file in step 4 of submission process. Authors should in no more than 100 words emphasize the scientific novelty of the presented research. Do not repeat for this purpose the content of your abstract.

List of suggested reviewers

List of suggested reviewers is a Word file submitted as a supplementary file in step 4 of submission process. Authors should propose the names, full affiliation (department, institution, city and country) and e-mail addresses of five potential referees. Field of expertise and at least two references relevant to the scientific field of the submitted manuscript must be provided for each of the suggested reviewers. The referees should be knowledgeable about the subject but have no close connection with any of the authors. In addition, referees should be from institutions other than (and countries other than) those of any of the authors. Authors declare no conflict of interest with suggested reviewers. Authors declare that suggested reviewers are experts in the field of submitted manuscript.

How to Submit

Users registered in the role of author can start submission by choosing USER HOME link on the top of the page, then choosing the role of the Author and follow the relevant link for starting the submission process.

Prior to submission we strongly recommend that you familiarize yourself with the ACSi style by browsing the journal, particularly if you have not submitted to the ACSi before or recently.

Correspondence

All correspondence with the ACSi editor regarding the paper goes through this web site and emails. Emails are sent and recorded in the web site database. In the correspondence with the editorial office please provide ID number of your manuscript. All emails you receive from the system contain relevant links. **Please do not answer the emails directly but use the embedded links in the emails for carrying out relevant actions.** Alternatively, you can carry out all the actions and correspondence through the online system by logging in and selecting relevant options.

Proofs

Proofs will be dispatched via e-mail and corrections should be returned to the editor by e-mail as quickly as possible, normally within 48 hours of receipt. Typing errors should be corrected; other changes of contents will be treated as new submissions.

Submission Preparation Checklist

As part of the submission process, authors are required to check off their submission's compliance with all of the following items, and submissions may be returned to authors that do not adhere to these guidelines.

1. The submission has not been previously published, nor is it under consideration for publication in any other journal (or an explanation has been provided in Comments to the Editor).
2. All the listed authors have agreed on the content and the corresponding (submitting) author is responsible for having ensured that this agreement has been reached.
3. The submission files are in the correct format: manuscript is created in MS Word but will be **submitted in PDF** (for reviewers) as well as in original MS Word format (as a supplementary file for technical editing); diagrams and graphs are created in Excel and saved in one of the file formats: TIFF, EPS or JPG; illustrations are also saved in one of these formats. The preferred position of graphic files in a document is to embed them close to the place where they are mentioned in the text (See **Author guidelines** for details).
4. The manuscript has been examined for spelling and grammar (spell checked).
5. The **title** (maximum 150 characters) briefly explains the contents of the manuscript.
6. Full names (first and last) of all authors together with the affiliation address are provided. Name of author(s) denoted as the corresponding author(s), together with their e-mail address, full postal address and telephone/fax numbers are given.
7. The **abstract** states the objective and conclusions of the research concisely in no more than 150 words.
8. Keywords (minimum three, maximum six) are provided.
9. **Statement of novelty** (maximum 100 words) clearly explaining new findings reported in the manuscript should be prepared as a separate Word file.
10. The text adheres to the stylistic and bibliographic requirements outlined in the **Author guidelines**.
11. Text in normal style is set to single column, 1.5 line spacing, and 12 pt. Times New Roman font is

recommended. All tables, figures and illustrations have appropriate captions and are placed within the text at the appropriate points.

12. Mathematical and chemical equations are provided in separate lines and numbered (Arabic numbers) consecutively in parenthesis at the end of the line. All equation numbers are (if necessary) appropriately included in the text. Corresponding numbers are checked.
13. Tables, Figures, illustrations, are prepared in correct format and resolution (see **Author guidelines**).
14. The lettering used in the figures and graphs do not vary greatly in size. The recommended lettering size is 8 point Arial.
15. Separate files for each figure and illustration are prepared. The names (numbers) of the separate files are the same as they appear in the text. All the figure files are packed for uploading in a single ZIP file.
16. Authors have read **special notes** and have accordingly prepared their manuscript (if necessary).
17. References in the text and in the References are correctly cited. (see **Author guidelines**). All references mentioned in the Reference list are cited in the text, and vice versa.
18. Permission has been obtained for use of copyrighted material from other sources (including the Web).
19. The names, full affiliation (department, institution, city and country), e-mail addresses and references of five potential referees from institutions other than (and countries other than) those of any of the authors are prepared in the word file. At least two relevant references (important recent papers with high impact factor, head positions of departments, labs, research groups, etc.) for each suggested reviewer must be provided. Authors declare no conflict of interest with suggested reviewers. Authors declare that suggested reviewers are experts in the field of submitted manuscript.
20. Full-colour illustration or graph from the manuscript is proposed for graphical abstract.
21. **Appendices** (if appropriate) as supplementary material are prepared and will be submitted at the same time as the manuscript.

Privacy Statement

The names and email addresses entered in this journal site will be used exclusively for the stated purposes of this journal and will not be made available for any other purpose or to any other party.

ISSN: 1580-3155

Koristni naslovi

Slovensko kemijsko društvo
Slovenian Chemical Society



Slovensko kemijsko društvo

www.chem-soc.si

e-mail: chem.soc@ki.si



Wessex Institute of Technology

www.wessex.ac.uk



SETAC

www.setac.org



European Water Association

<http://www.ewa-online.eu/>



European Science Foundation

www.esf.org



European Federation of Chemical Engineering

<https://efce.info/>



I U P A C

INTERNATIONAL UNION OF
PURE AND APPLIED CHEMISTRY

International Union of Pure and Applied Chemistry

<https://iupac.org/>

Novice evropske zveze kemijskih društev EuChemS najdete na:

 **EuChemS**
European Chemical Society

Brussels News Updates

<http://www.euchems.eu/newsletters/>



DONAU LAB Ljubljana
Member of LPPgroup



SEPIATEC SFC Supercritical Fluid Chromatography

The green standard for
fast compound isolation

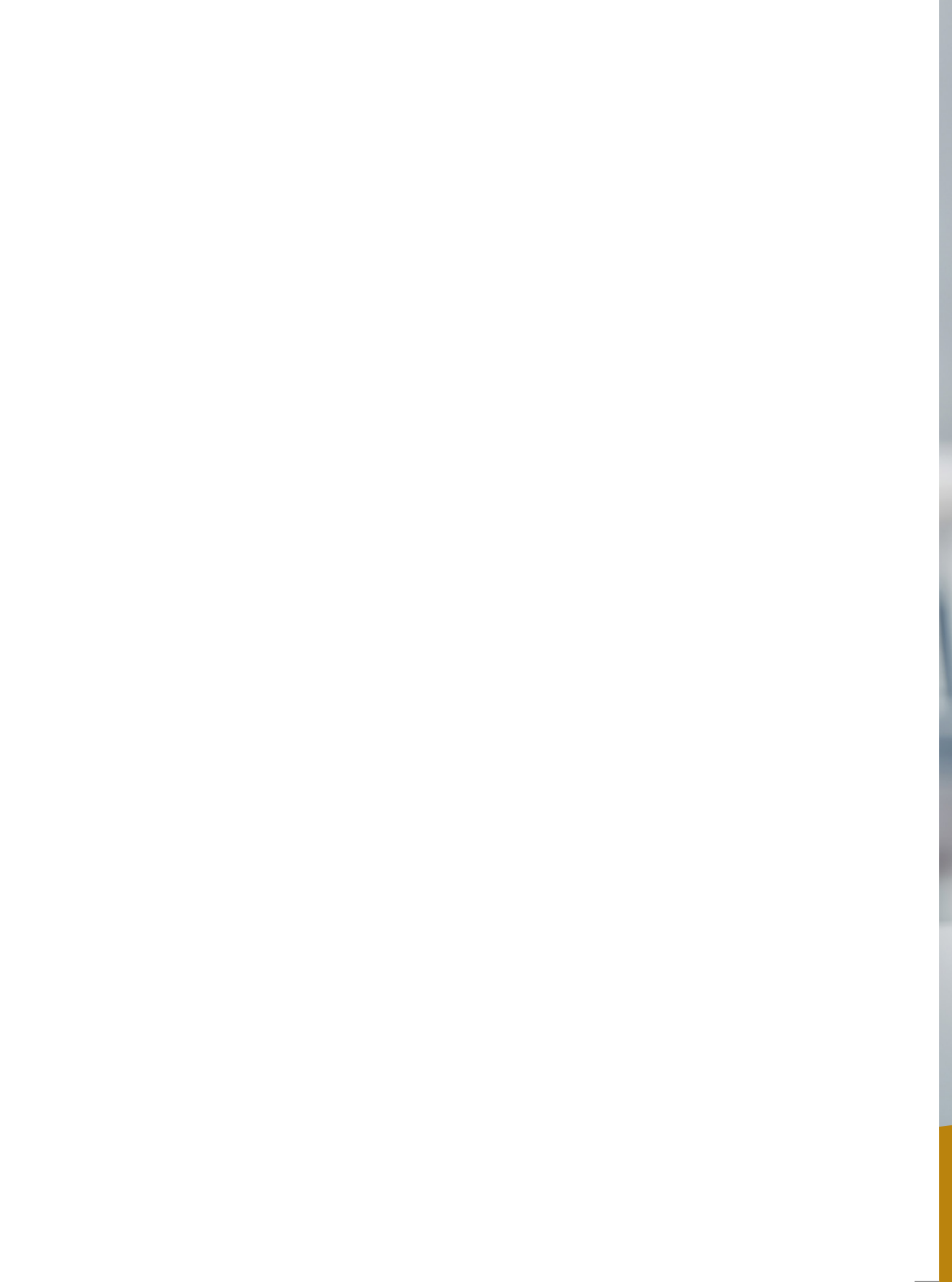


Donau Lab d.o.o., Ljubljana
Tbilisijjska 85
SI-1000 Ljubljana
www.donaulab.si
office-si@donaulab.com



*May health accompany you in the new year,
may courage lead you, and may understanding unite you.*

Happy 2025!



THE SECRET INSIDE **EXCELLENT PRODUCTS**

**Helios Resins and
Atcoat – specialists for
reliable coating and
composite solutions.**



www.atcoat.com
www.resinshelios.com

 **HELIOS RESINS** |  **ATCOAT**



NATIONAL INSTITUTE OF CHEMISTRY

Hajdrihova 19,
1000 Ljubljana
Slovenia
www.ki.si



research
EXCELENCE



Basic and applied research in materials, life sciences, biotechnology, chemical engineering, structural and theoretical chemistry, analytical chemistry and environmental protection.

In line with EU research and innovation priorities: nanotechnology, genomics and biotechnology for health, sustainable development, climate change, energy efficiency and food quality and safety.

We expand knowledge and technology transfer to domestic and foreign chemical, automotive and nanobiotechnology industries.

We are aware of the power of youth, so we transfer our knowledge to younger generations and offer many opportunities for cooperation.



contact: mladi@ki.si

ActaChimicaSlovenica

ActaChimicaSlovenica

An in-depth review of flash graphene, an innovative carbon nanomaterial synthesized by flash joule heating, focuses on recent electrocatalysis breakthroughs. The review explores the critical role of flash graphene in advancing renewable energy technologies and promoting sustainable electrocatalysis. For more details see p. 541.



Year 2024, Vol. 71, No. 4

